CRANFIELD UNIVERSITY

Paul J Bradley

Fundamental Study into the Governing Conditions of Rotor Thermal Bows in Hydrodynamic Bearings

School of Engineering

PhD Thesis
Academic Year :2011 - 2012

Supervisor : Professor David Mba
March 2012

Fundamental Study into the Governing Conditions of Rotor Thermal Bows in Hydrodynamic Bearings

School of Engineering

Paul J Bradley

CRANFIELD UNIVERSITY

6th March 2012

Declaration

The work contained in this thesis has not been submitted elsewhere for any other degree or qualification, and unless otherwise referenced it is the authors own work.

Abstract

This thesis presents an experimental investigation into the conditions generated within a high speed bearing system where thermally generated shaft bows can arise from differential journal heating, and under certain condtions this effect has been observed to result in unstable shaft vibration - the 'Morton Effect'. This thesis documents the development of a simplified analytical procedure for evaluating the thermal activity within an orbiting journal when running in hydrodynamic bearings. The aim of this work was to generate controlled experimental data regarding journal differential heating effects to support the understanding and development of appropriate modelling and predictive techniques.

A high speed rotor test rig, running in 50mm diameter bearings of fixed and variable geometry configuration, was used to obtain directly measured temperature distributions within the rotor when running under varying speed and unbalance response conditions.

Two separate rotor designs were used. The first is designed as a rigid rotor where no structurally influenced rotor dynamic phenomena are present within the running ranges. The second is a flexible rotor designed to operate in a super critical condition where conditions are replicated to provide a rotor that is sensitive to the variables required for thermal bow development and the rotordyanmic conditions promotional of associated instabilities. Existing theoretical models, in combination with operationally observed characteristics, were used to develop a design predicted to become unstable within the test running range.

Journal temperature measurements were obtained for rigid and flexible rotors over a range of speed conditions in intentionally introduced mechanical unbalance conditions. Journal temperature differentials were obtained with a clear correlation between journal orbit size and journal temperature differential. The flexible rotor was operated for prolonged periods of time in the predicted unstable region but instability was never initiated for any test condition. Peak journal temperature differentials were measured as 1.7 ^{o}C.

A new analytical model for the bearing oil film and journal thermal developments is presented which has reasonable correlation to other published literature.

Dedication

For Dad

Acknowledgements

I am most grateful to my supervisor, Professor David Mba for all his advice and support over the duration of the work. I am most thankful for the commitment he has shown to helping me reach the point of completion of the work, as without his help the project would never have been accomplished.

I am profoundly grateful to the large number of people who have helped throughout the duration of the work, right through from the test rig manufacture to the writing up of the thesis. Whilst the list is too long to mention everybody I would like to specifically thank the following for their extra special help and support. Bob Orgy, Nick Glover and Scott Morgan for all their help and advice with the test rig setup and instrumentation. Lee Partel, Carmine Pette and Martin Powers for their advice and assistance in fabricating various stands, brackets and widgets for the test rig at short notice. Particular thanks go to Colin Sims and Gordon Sims for their dedication in helping me on the manufacture on many of the test rig components, without their help the testing would not have been possible. I am also grateful to David Wilson for taking time out of his weekends and evenings to open up the factory, come rain or shine, to allow me to run the test equipment.

I would also like to thank the Whitworth Awards society for their support, both financially and as a society. Without the funding from the Whitworth Awards panel then the test rig construction would not have been possible.

I am extremely grateful to Allen Gears for providing the test facilities and data acquisition equipment to allow the test rig to be operated over the duration of the research. My utmost appreciation also goes to Professor Keogh for all of his input, support and advice on the theretical modelling.

Finally I would like to thank those people who without I could not have completed this research. Thanks go to all my friends for all their support and understanding over the last few years. In particular I would like to thank Alan Williams and Mark Saunders for giving up their time to help proof the thesis and analytical work. To my family, I am eternally grateful for all their patience and unfaltering faith in me, and in particular to my loving wife and new born daughter without whose support I could not have seen the project through.

Contents

List of Figures

List of Tables

Nomenclature

Chapter 3 – Section 3.3	
B_X, B_Y	Coefficients relating rotor bend to vibration amplitudes
c	Bearing radial clearance
c_B, c_L, c_J	Bearing, lubricant, journal material specific heat capacities
d	Fractional film width
D	Bearing diameter
G	Gain parameter for bend development
gmn, h_{mn}	Journal bearing thermal coefficients
h	Dimensional film thickness
h_B, h_J	Bearing, journal heat transfer coefficients
H	Dimensionless film thickness, h/c
I	Journal section second moment of area
k_B, k_L, k_J	Bearing, lubricant, journal material thermal conductivities
K_T	Rotor stiffness parameter
l_b, l_D	Rotor length parameters
L, L_J	Bearing, journal section lengths
m_b, m_d	Rotor mass parameters
N_B, N_J	Dimensionless bearing, journal heat transfer coefficients, Rh_B/k_B, Rh_J/k_J
p	Lubricant dimensional pressure
P	Lubricant dimensionless pressure, $p(c/R)^2/6$
Pe	Peclet number,
r	Dimensionless radial coordinate
r_o	Dimensionless outer bearing radius, R_o/R
R	Inner bearing radius
R_o	Outer bearing radius
t	Time
T	Dimensionless temperature
T_o, T_1, T_2	Dimensionless zero orbit and orbit perturbed lubricant temperatures
T_B, T_J, T_L	Dimensionless axially averaged bearing, journal, lubricant temperatures
T_A, T_S	Dimensionless ambient, lubricant supply temperatures
u, v, w	Flow velocity components
U, V, W	Dimensionless flow velocity components
W_b	Bearing steady load
z_{Xb}, z_{Yb}	Complex vibration amplitudes at bearing location
α	Journal material thermal expansion coefficient
β	Circumferential angular coordinate referred to fixed axes
β_c	Circumferential cavitation angular coordinate
γ	Orbit orientation parameter
γ_B, γ_J	Dimensionless parameters, $k_B\, c/k_L R$, $k_J c/k_L R$
Δ	Lubricant inlet temperature parameter
$\in_o$	Zero orbit eccentricity ratio

$\in_1, \in_2$	Backward, forward whirl circular orbit dimensionless radii
$\in_L$	Bearing parameter, $(L/D)^2$
η	Dimensionless cross-film coordinate, y/cH with $0<y<h$
θ	Circumferential coordinate referred to journal rotating axes,
Θ	Dimensional temperature
Θ_f	Reference temperature
κ_B, κ_J	Bearing, journal diffusivities
μ	Average lubricant viscosity
ξ	Dimensionless axial coordinate, $2z/L$
ξ_J	Journal section dimensionless axial length, L_J/L
ρ	Radial coordinate
ρ_B, ρ_L, ρ_J	Bearing, lubricant, journal material densities
τ	Dimensionless time
ϕ_0	Zero orbit attitude angle
ψ_x, ψ_y	Rotor bend angles referred to rotating axes
$\psi_C, \psi_{Ci}, \psi_{Ct}$	Complex rotor bend angles

Chapter 3 – Section 3.4	
A_x, A_y	Amplitude parameters for elliptic orbit
c_l	Lubricant specific heat capacity
C_b	radial bearing clearance
C_p	radial pad clearance
e	eccentricity
E	Young's Modulus
E_b	Rate of energy transfer to bearing
E_j	Rate of energy transfer to journal
E_{lub}	Rate of energy storage in lubricant
E_{visc}	Rate of visc. energy dissipation
f_p	Fractional angular position of pad pivot
h	Film thickness
H	Heat transfer coefficient
I	Area moment of inertia
L	Bearing length
L_d	Disk overhang length
m	Preload factor
m_d	Mass of overhung disk
N_{pads}	Number of pads
O_b	Bearing center
O_j	Journal center
O_p	Pad center of curvature
P	Hydrodynamic pressure within the bearing
P_o	Lubricant supply pressure
R_b	Bearing radius

R_j	Journal radius
R_p	Inner radius of curvature of pad
Re	Reynolds' number
Re_c	Critical Reynolds' number (Re > Rec => turbulent)
t_p	Pad thickness
T	Journal circumferential temperature
T_0	Lubricant supply temperature
T_{amb}	Ambient temperature
u_j	Surface velocity of journal
U	Resultant unbalance
U_m	Mechanical unbalance
U_t	Thermal unbalance
U_{thr}	Threshold unbalance
W	Rotor weight
W_b	Bearing load
x, y, z	Local coordinate system with origin on journal surface
X, Y, Z	Fixe coordinate system with origin at bearing center
y_d	Thermal deflection of disk
z	Axial dimension
β	Thermoviscosity coefficient
δ	Pad tilt angle
Δ_p	Angular dimension of pad
ε	Eccentricity ratio
θ	Circumferential angle
θ_c	Angle for line-of-centers
θ_j	Angle to journal center
θ_p	Pivot angle for pad
μ	Lubricant viscosity
μ_0	Lubricant supply viscosity
ζ	Angle used in PJB film thickness expression
ρ_l	Lubricant density
τ	Lubricant shear stress
φ	Angle between thermal and mechanical unbalances
φ_x, φ_y	Phase parameters for elliptical orbit
ψ_b	Thermal bend angle
ξ	Attitude angle
ω	Angular journal speed

Chapter 5	
C_A, C_B, C_C	Steinhart-Hart thermistor sensor constants
C_d	Diametral clearance
C_r	Radial clearance
p_R	Bearing pad pre-load
R_i	Fixed resistor resistance

R_{therm}	Thermistor sensor resistance
T	Temperature
V_G	Voltage across gauge
V_S	Supply voltage

Chapter 6	
χ_r	Bearing pad offset
ϕ_m	Bearing pad cant angle

Chapter 7	
A_o, A_m, A_g	Vibration amplitudes for glitch, measured and glitch extracted
k	Harmonic order
N	Number of data points
t	Time
t_K	Non harmonic residual of shaft journal temperature measurement
t_n	Temperature measurement of nth sensor
T_k	Measured journal 1st harmonic temperature amplitude
x_p, y_p	X and Y probe gap measurement
ϕ_{Tk}	Measured journal1st harmonic temperature phase angle
ϕ_o, ϕ_m, ϕ_g	Vibration phase angles for glitch, measured and glitch extracted
ω	Shaft rotation speed

Chapter 8	
$a_{1,2}$	Circular whirl orbit radii (1= forward, 2=backward)
c	Specific heat capacity
c_L	Specific heat capacity lubricant
c_r	Radial clearance
e	Journal eccentricity
e'	Journal effective dynamic eccentricity
$\dot{E}$	Energy transport
f_L	Oil film convective flow fraction
F_E	Bearing power loss coefficient
h	Oil film thickness / heat transfer coefficient
H	Non dimensional oil film thickness
I_h	Fractional film coefficient

Nomenclature

k	Thermal conductivity
k_L	Lubricant thermal conductivity
L_{inlet}	Oil inlet grove length
L_b	Length of bearing
p_{inlet}	Pressure at oil feed groove
$\dot{q}$	Heat flux
$\dot{q}_j$	Heat flux from lubricant to journal
$\dot{Q}$	Heat flow rate
Q_v, Q_p, Q_r	Lubricant flow rates, velocity, pressure, recirculation
r	Radial point
R_s	Journal radii
R_b	Bearing radii
T_m	Finite difference node temperature
T_∞	
T_L	Lubricant temperature
$T_{o1,2}$	Bearing pad lubricant inlet temperature
U	Journal velocity
α	Thermal diffusivity
β	angle from oil inlet to maximum film thickness
ε	Journal eccentricity ratio
ε'	Journal effective dynamic eccentricity ratio
ϕ	Angle around bearing
$\phi_{\Delta T}$	Journal 1st harmonic temperature differential phase angle
γ'	Angle between rotation vector and minimum film thickness
μ	Lubricant viscosity
θ	Angle around journal
θ'	Attitude angle of effective eccentricity
ρ	Density
$\sigma_{1,2}$	Non dimensional orbit radii (1= forward, 2=backward)
τ	Lubricant shear stress
ΔT	Journal 1st harmonic temperature differential

Chapter 1

Introduction

1. Introduction

Rotating machinery has been used as a means of providing labour saving devices to man for many hundreds of years. It is however in the last century, following the industrial revolution, that the most significant developments in rotating machinery have taken place and with it the development of their science.

The development of the theory behind the dynamics of rotating machines has been driven forward by the ever increasing power demands required for the various types of rotating machinery, such as steam turbines, gas turbines, electrical generators, pumps and compressors to name but a few. The requirement for modern machinery to be capable of delivering, absorbing and transmitting multi megawatt powers has driven the operating speeds of the rotors to higher and higher levels to enable practical designs to be realised. With these high operating speeds come a number of design challenges in that the physical limitations of the rotor materials restrict the diameters of the machine because of centrifugal loading and rotors need to become longer and consequently more flexible. This results in many of today's pieces of turbo-machinery operating above their first, second and sometimes third natural frequencies, defining the need for accurate and reliable methods for predicting the characteristics, response and stability of such super critical machines.

It is common in these rotating machines to experience vibration related problems, the causes of which can be diverse in nature. The most common cause of vibration in rotating machinery is synchronous to the rotor shaft speed and is most often due to the mechanical unbalance of the rotor. Well performed multi-plane balancing of the rotors helps to produce machines that run smoothly across their entire running range. However this process can be complex due to the number of influencing parameters (such as hydrodynamic and aerodynamic features etc) present within most rotating machinery and their variable nature during operation, specifically machines where the rotor is required to operate at super critical speeds. Even with these tools to control the vibration response of the rotors, other aspects and features of a rotor-

bearing system can result in unforeseen dynamic excitation and response yielding ‘vibration’ related problems.

At a top level vibration can be categorised into two types - those that are stable in nature and those that are unstable. Stable vibrations, although possibly high in magnitude, will remain at a constant level while operating in a steady state condition. Unstable vibrations however, while running at certain speeds, will increase in magnitude with time whilst operating at constant rotational speed. These unstable vibrations by their very nature have the potential to be most damaging and ultimately destructive, often preventing machines from achieving their required operating speeds and powers. Additionally the time dependant nature of these types of stability issues make them more complex to model, identify and predict at the design stage, presenting themselves as a significant problem to the rotordynamic engineer.

A significant amount of effort has been directed toward research and theory development into the prediction of rotating machinery performance over the last 100 or so years. Aside from the founding pioneers, such as Jeffcott [25] and Reynolds [26] the most significant developments have taken place in the last 30-40 years following the need for a large number of large high speed turbo-generators, super critical compressors and the introduction of the power gas turbine engine in the late 1960’s and early 1970’s.

In the majority of cases, high speed large industrial machines operate on fluid film bearings due to their relative insensitivity to high operating speeds and loads on large diameter shafts whilst providing non-finite life operating principles. As a result, a significant proportion of the work associated with rotating machinery has been directed toward the development and understanding of hydrodynamic bearing theory and measurement.

A fluid film bearing uses a liquid media (normally oil) to provide a hydrodynamic pressure field between a rotating shaft and stationary bearing resulting in a non contacting support for the shaft and its loads. Two principal types of hydrodynamic bearing are used in rotating machinery - journal bearings and thrust bearings. Journal bearings are used to support the radial loads of a shaft, and thrust bearings are required to accommodate any axial loads or location requirements of the rotating member. The bearing which is focused on within this work is the journal bearing and its interactions with the rotor and its’ dynamics. The journal bearing in its simplest form consists of a cylindrical rotating shaft and a stationary bearing shell of a slightly larger

diameter. The clearance between the two components results in a converging-diverging geometry which, when filled with the lubricant, generates the necessary hydrodynamic pressures required to support the shaft and produces, whilst it does so, a series of relatively complex dynamic conditions between the oil film and rotor.

The analytical, computational and diagnostic techniques involved with rotating machinery analysis have developed significantly in the last 80 years with the most significant theoretical advances being made in the 1970's and 1980's with respect to both bearing and rotordynamic performance evaluation, such as the work of Lund [27,28] etc. The exponential increase in computational power available to implement some of the earlier developed analytical methods now allows for large numerical representations of complex rotor systems to be characterised in relatively short computation times of a few minutes, as opposed to several hours or even days that 1980's technology allowed. This, coupled with the more advanced sensor technology and diagnostic tools such as the dynamic FFT analyser and digital data recorders, allows for the highly dynamic conditions present within high speed rotating machinery to become better understood and more advanced evaluation techniques developed.

The specific topic of this research is unstable synchronous vibration which is thermal in nature. The vibration has been observed on large and medium sized high speed rotating machines [11], resulting in the need for significant modifications to overcome the problem. Measurements taken during acceptance testing of one of the machines has shown that at constant speed, the vibration magnitude increases with a corresponding change in shaft vibration phase angle. Subsequent inspections have ruled out the possibility of a seal rub being the cause of the vibration.

The phenomenon described, often referred to as the 'Morton Effect' [13] after the author of a paper describing such a vibration, is attributed to the variation of viscous oil shear occurring within a hydrodynamic journal bearing oil film due to synchronous orbit of the shaft rotor. The change in viscous shear in the oil film gives rise to thermal fluctuation, which results in the formation of a temperature differential across the rotor journal. A static bow in the rotor forms as a function of the differential shaft temperature, causing an increase in the unbalance of the shaft and hence orbit magnitude. The increase in journal orbit widens the temperature differential, increasing the unbalance, hence

providing a positive feedback loop where, under certain conditions, unstable spiral vibrations occur.

It is the intention of this research to perform a series of experimental tests to provide actual data for a rotor specifically engineered to be susceptible to experiencing the synchronous thermal Instability due to differential bearing journal heating. The aim is to quantify the impact and influence characteristics and various operating parameters and practical features.

The principal focus of the research is to design, produce and operate a rotor test rig suitable for the investigative research into high speed rotor performance with respect to bearing journal thermal differential heating, more specifically the association spiral vibration instabilities. The test rig should be suitably instrumented to enable quantification of the governing physical properties which are understood to influence hydrodynamic bearing thermally induced rotor instability. A more detailed breakdown of the specific objectives is provided in the following list:

1. Provide a thorough review of the published literature in the relevant subject areas linked to synchronous thermal rotor bows, thermal instabilities and spiral vibrations.

2. Perform a detailed analytical review of the relevant theories, analytical procedures and modelling techniques, benchmarking analysis techniques where appropriate.

3. Using well documented practical reference cases perform a detailed review of the rotor-bearing systems design by means of rotordynamic and appropriate thermal modelling techniques. This will enable the common characteristics to be assessed, in rotors where bearing induced thermal rotor bows and unstable vibrations have been observed, giving a qualitative, and where possible, quantitative account of the apparent governing terms. Summarising this information to establish qualitative observations as to a rotor's sensitivity to thermal rotor bow and thermal instability, and use of it to assist in the experimental rotor design.

4. Specify, analyse and design an appropriate test rig for the evaluation of journal bearing induced thermal rotor bow, with the ability to capture both comprehensive dynamic response and vibration modes, but more

significantly obtain live shaft journal temperature measurement. Use available data from known thermally sensitive or thermally unstable rotating machines to develop appropriate design guidance and evaluation procedures.

5. Build and commission a test rig with appropriate physical characterisation and measurement validation procedures.

6. Carry out an extensive programme of experimental testing to characterise rotor journal temperature differential measurement for a range of operating parameters and configurations, such as; lubrication conditions, operating speeds, rotor geometry, bearing type, introduced mechanical unbalance.

7. Obtain experimental test data for a rotor operating under conditions identified as being sensitive to journal bearing induced thermal rotor bow, and capture rotor performance data across areas of high rotor bow sensitivity and possible thermal instability.

8. Audit existing analytical procedures against generated test data and suitable practical case studies. Introducing qualitative, and where practical quantitative, evaluation techniques. Also, where beneficial, applying or adapting appropriate existing analytical procedures.

9. Provide state of the art evaluation of journal bearing induced synchronous thermal rotor bow and instability phenomenon in rotating machines, covering design considerations and detailing appropriate evaluation techniques with guidance as to application, applicability and limitation.

Chapter 2

Literature Review

2. Literature Review

2.1 Rotor Rubs (Newkirk Effect)

In 1925, in an article from the magazine of the association of German engineers, Dr D. Thoma [29] described a vibration problem for a four journal bearing, single thrust bearing vertical rotor of a water-wheel generator that had an operating speed of 600 rpm. The unit experienced a high vibration problem which developed within a few minutes, occurring after the machine had been operating satisfactorily for a prolonged period. The machine was shut down and restarted. Once again after months of satisfactory operation the vibration was experienced resulting in the machine being shut down. Observations showed that immediately after the shut down a bow was present in one end of the shaft which disappeared over the next few minutes. It had been observed during operation that the bearing at this location had been running warmer than the others. Dr. Thoma documented that the vibration was due to a point on the bearing journal being heated along one element which resulted in a thermal bow, which in turn caused the journal to move closer still to the bearing, resulting in more heat and shaft bow, and so on. The net result of this was an unstable vibration of the rotor.

Where Dr. Thoma [29] had experienced and documented this type of vibration phenomena, giving some physical description, it was Burt Newkirk [1] who went some way further to understanding the problem of unstable vibrations in rotors due to thermal bowing of a rotor. Newkirk [1] published an article titled 'Shaft Rubbing' in 1926 giving a qualitative analysis of a thermally-induced phenomena that would describe Dr. Thoma's [29] observations. It was supported by a series of experimental observations.

Newkirk [1] described how a rotor operating below its critical speed can have a 'heavy spot' (residual unbalance) which causes this point in the shaft to distort and move radially outward. If this point then comes into contact with a stationary component causing a rub, heat is generated. This heat results in the material around the 'heavy spot' expanding and thus causes the rotor to

bow out about this location. The rotor proceeds to dig in harder at the rub location generating more heat, which causes the feedback cycle described above to take place.

Newkirk [1] then went on to state that rotors operating above their critical speed are not subject to this cycle and resulting instability. In rotors that operate above their critical speed, the ‘heavy spot’ is no longer located on the outside of the rotor, but the inner. Any heating of the shaft due to a rub will cause the rotor to bow in a direction which moves the ‘heavy spot’ inward and toward the shaft centre line. This reduction in unbalance means that there is no positive feedback aspect to the rub and thermal bow as the shaft moves inward, away and clear of rub producing stable operation of the machine. However, shafts which are in perfect balance or rub at a point due to a raised section of geometry of the shaft, are an exception to the above. For rotors where the rub occurs at raised points along the shaft, although the heavy spot may not be at the same location, the light rubbing will bow the shaft about this location and very soon becomes the heavy spot and starts to respond as previously described.

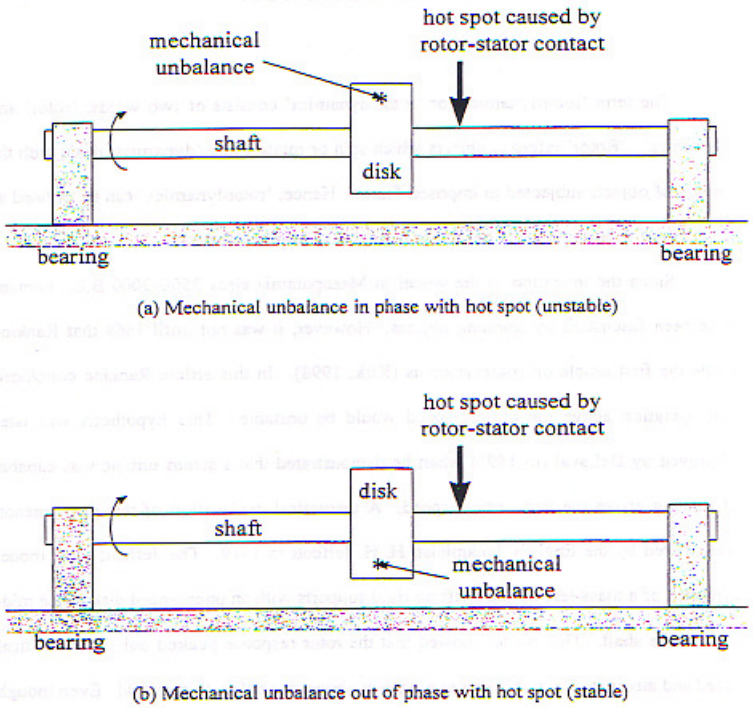

Figure 1 Diagram of Newkirk Effect Above and Below 1st Critical Speed [19]

Newkirk [1] performed a number of experiments in conjunction with Mr. H.D. Taylor [22] at the General Electric Company. The first were performed with a

carefully balanced rotor to which an out of balance of known mass and location was introduced. The rotor was run at various speeds and with a slight rub added onto the shaft surface. For the rotor operating below its first critical speed, the vibration increased rapidly until severe rubbing occurred with high levels of vibration. Whereas when the operating speed was above the critical of the rotor and light rubbing was applied, vibration did not increase and rubbing did not build up with the rotor eventually clearing itself completely from the rub.

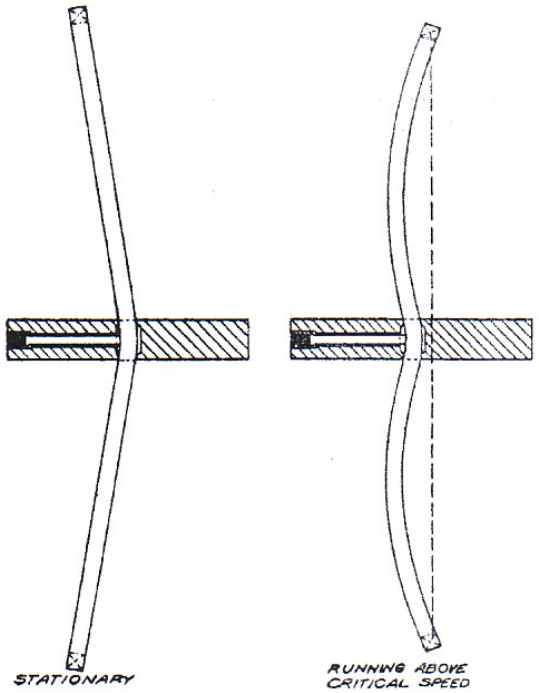

Figure 2 Diagrammatic Representation of the Backward Bending of Shaft Running Above Critical Speed [1]

Marking blue that had been put onto the shafts before the tests showed that the rubbing had occurred at the location of the out-of-balance below the critical speed and on the opposite side to the unbalance when above the critical speed.

A second type of test was performed by introducing a bow into the rotor shaft by means of elastically deflecting the shaft in the static state. The mechanical out of balance was now produced by the mechanical bow in the shaft. The rotor was run above and below its critical speed. It was again observed that below its critical, the out of balance (and thus bow) were outward facing and above the critical inward facing. Although no rubbing tests were performed,

this confirmed that the same phenomena would occur in rotors where an initial bow causes the mechanical unbalance.

2.2 Spiral Vibrations

In 1939 Kroon and Williams [2] later went on to give a more qualitative analysis of what was now known as the Newkirk Effect.

They describe a mathematical model in which a rotor experiences a steady increase in vibration amplitude with a continuous change in phase angle relative to time. A method was proposed that allowed the identification for the cause of 'unstable' increases in synchronous vibrations with time. Kroon and Williams [2] indicated how the problem could be categorised into a change of system state or a change in the unbalance of the rotor. A change in system state is where either or both of the stiffness and damping characteristics are changing with time. This is identified by the modification in resonant characteristics displayed, particularly when running close to a resonate region. In general this sort of change in amplitude in one direction would have little effect in the orthogonal direction, resulting in small changes in phase angle, if any.

However, where there is a change in unbalance due to a distortion etc. then the shift in phase angle is essentially unlimited. Such a change in balance results from an alteration in shaft distortion due to a thermal effect caused by such things as rubs, i.e. the Newkirk effect. These vibrations, when plotted in a polar form, have the appearance as shown in Figure 3 and hence go to explain the title of 'Spiral Vibrations' for such phenomenon. The large changes in phase and steady increase in amplitude show consistent geometrical relations for vibrations in opposite directions which is consistent with a change in unbalance. The time taken for the large changes in phase (several times 360^{o}) were observed by Kroon and Williams [2] as being as short as 16 minutes to as long as 5 hours. These points support the model of a thermally distorting rotor giving rise to a continually changing magnitude and vector of unbalance.

The mathematical model produced by Kroon and Williams [2] explains how for a shaft with an out of balance force (due to a static shaft eccentricity vector 'x') has a dynamic unbalance vector 'y' with a lag of ϕ, see figure 4a. If rubbing occurs then the contact will be initially made at the point of vector 'y'. This rub will cause asymmetric heating to be generated in the rotor, causing a bow in

the direction of vector 'y'. The increase in bow causes an additional unbalance vector Δx which when combined with the original static vector x' gives rise to a new instantaneous unbalance vector x_1' and hence dynamic unbalance vector y_1. This results in a corresponding increase in phase angle, see Figure 4 (b). With the magnitude of rotor displacement increased, contact now occurs with greater force and at a position further round the shaft circumference, causing the cycle described above to repeat giving rise to an unstable vibration.

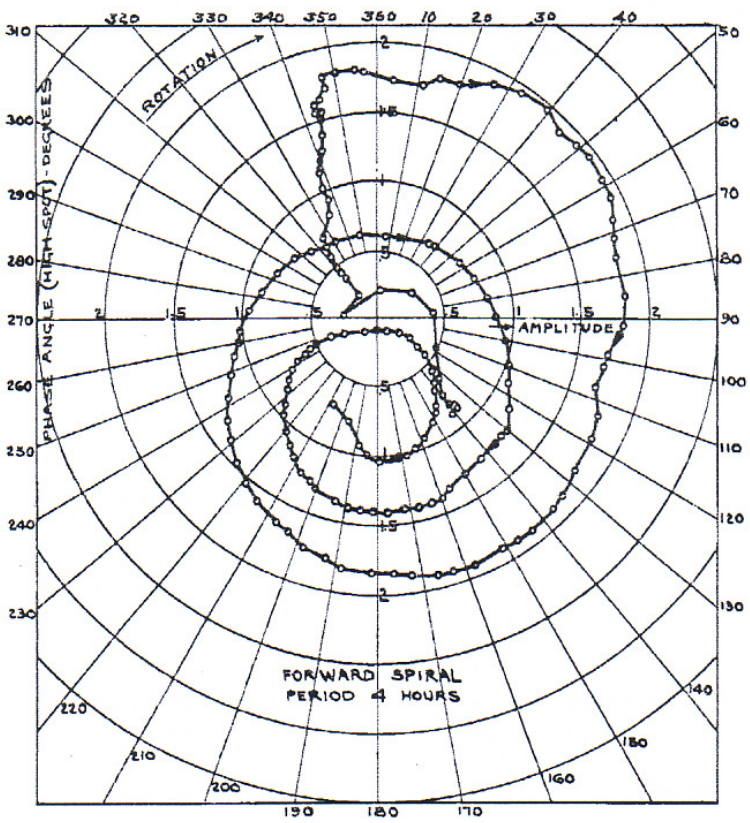

Figure 3 Vibration for a Rotor Displaying the Newkirk Effect [2]

Kroon and Williams [2] performed a number of simple tests on specifically simplified rotors where the distortions resulting from heating a fixed spot were measured. A quantitative assessment was produced using dimensional analysis where it was found that the rotor could be accurately modelled using two equations for the heating and cooling curves. See Figure 5.

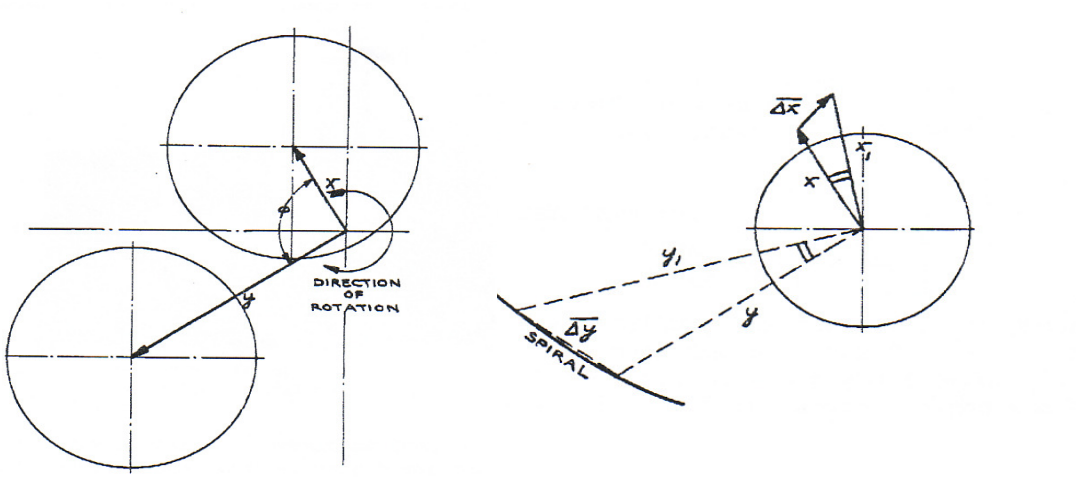

Figure 4 (a) Relationship Between Static and Dynamic Bow (b) Development of Spiral [2]

A fully analytical model was developed for the case of an infinitely long thin walled cylinder subjected to local heating. Solutions were provided for heat distribution and resulting deflection. The analysis was based upon some significant assumptions in the definitions of the applied boundary conditions.

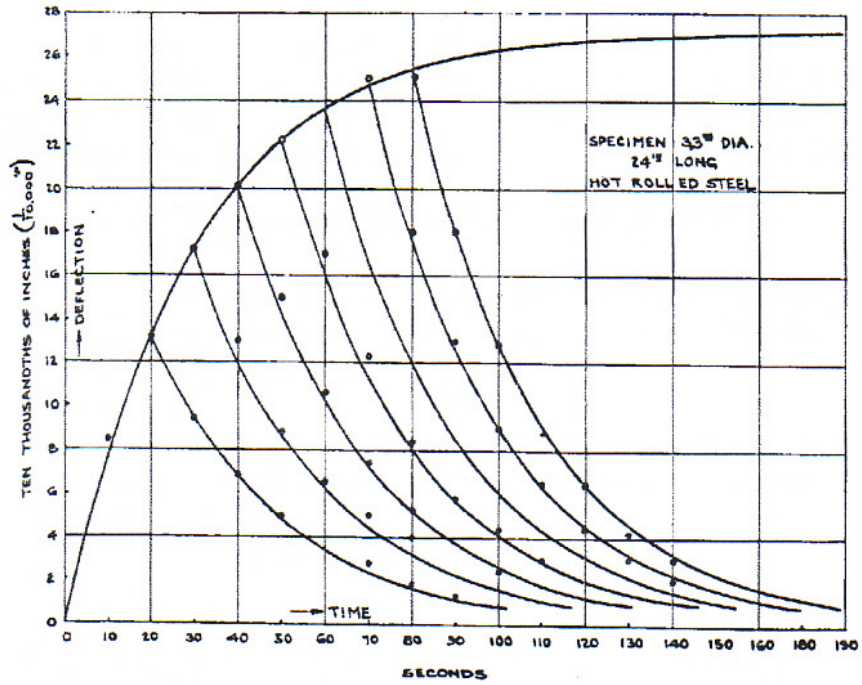

Figure 5 Typical Experimental Results Obtained by Kroon and Williams [2]. Solid Lines are True Exponential Curves, Datapoints were Obtained by Test [2]

The work does not provide an accurate or exact method of solution but offers a method of diagnosis as to the potential cause of a particular vibration problem by means of the measured 'spiral vibrations'.

A full quantitative analysis of the thermal state in a rubbing rotor was not tackled until 1973 by Dimarogonas [3,4]. A full analytical solution was developed for a rotor in which the static bow due to an arbitrary heat input could be determined as a function of a source bow and heat function [5]. The dynamic response of the system was used to calculate the corresponding dynamic bow. Dimarogonas [3,4] found that the heat generation and heat function resulting from the dynamic bow could be determined as well as stability / response of the rotor with respect to time. The rotor system was modelled using two non-linear differential equations solved by the Runge-Kutta method, using a digital computer program to calculate the system response with respect to time.

The analysis established three separate modes associated with the Newkirk effect which describe the stability of the system. These modes are spiralling, oscillating and constant modes. Spiralling is an unstable mode, constant is a stable mode and oscillating is a transitional state between the former two. A number of experimental results compared well with the solutions for the spiralling, constant and osolating modes. No analytical solution was available for the oscillating mode [5].

The fundamental conclusions from the work are that the main factor determining the mode in which the system will respond is the phase angle between the static and corresponding dynamic bow. It also shows that the mode is indirectly affected by the critical speed of the rotor, but is not the principle influencing feature [5].

2.3 Rotor Differential Heating

A quantitative analysis of the Newkirk [1] effect was performed by Kellenberger [6] with respect to Turbogenerator seal rings causing rotor differential heating around the circumference. Unlike Dimarogonas [4] a number of simplifying assumptions are made and more significantly the system equations remain linear. The analysis is dominated by two parameters '*p*' and '*q*' expressing the power entering and being removed from the rotor respectively. The stability of the system can be shown to be governed by the ratio of *p/q*, where above some threshold, unstable increasing spiral vibrations will exist. Stability is defined as the point at which the amplitude and phase, when plotted in polar form, produce a circle.

The qualitative analysis compared well with published results - even with the inclusion of the simplifying elements used in calculation. Spirals were identified as normally opposing the rotation direction of shaft but could be reversed if sufficiently high damping or inertia is present within the seal ring (stator).

Kellenberger [6] concludes that the time taken to complete one 360^{o} phase shift is governed by the power entering the rotor only. Also the shaft critical speed is not a significant factor in the production of spiral vibrations produced in this manner. This is an important point as this is in some contradiction to the rubbing mechanism identified and quantified by Newkirk [1]. The location of the running frequency with respect to the critical speeds and shaft mode shapes can determine the stabilising or destabilising effects under such conditions.

To the author's knowledge, the first published identification for the problem of differential heating of the journal due to synchronous vibrations within the bearing was made by Ericsson [7]. The work was an entirely analytical study which observed the temperature distribution within a bearing pad (more specifically a tilting pad bearing) due to synchronous vibrations. The work was split into two specific aspects, the 'static' solution and the 'perturbation' solution (vibrating).

A series of idealising and simplifying assumptions are made which allow the static and perturbation equations for pressure, temperature and viscosity to be uncoupled. A number of numerical solution procedures are provided for in the

solution of the equations for static and perturbation hydrodynamic conditions within the oil film by means of direct integration, difference methods and finite element method.

The effect of the variable parameters were investigated in non dimensional form along with some numerical examples based on specific assumptions related to bearing vibration magnitude, vibration orbit and pad oil inlet temperature. The solutions are considered to be adiabatic and provide no account for heat transfer into either of the bearing pad or journal.

The analysis provides a method of solution (by means of application of numerical methods using a digital computer) for establishing the temperature variation around an infinitely long journal bearing (specifically tilting pad) surface and within the oil film due to a harmonically varying film thickness. However, the calculations rely heavily upon a series of assumptions - specifically oil pad inlet temperatures, oil film viscosity and oil conductivity. It shows that assumptions regarding the oil, (particularly viscosity and fluid conductivity) and frequency of vibration have significant effects on the temperature distribution around the slider surface. Ericsson's [7] analysis method does not numerically or specifically address the heat transfer between the fluid and rotor, rotor bow nor any feedback resulting from changes in dynamic operating conditions due to harmonic vibration amplitude.

The potential for hydrodynamic bearings to produce a thermal differential heating of the rotor was again recognised by Schmied [8] who also identified slip rings as a potential source for spiral vibrations. Schmied [8] developed a method for the solution of spiral vibrations using finite elements. The model uses the linear relationship between thermal and mechanical effects and solution procedure presented by Kellenberger [6] for seal rings. Although recognising the importance of bearing hydrodynamics in the subject area the analysis procedure is approximate and does not address the thermodynamic and heat transfer effects present in initiating spiral vibrations. Also the operating parameters of the bearing are not specifically incorporated, in that orbits are assumed circular and of a known radius.

Schmied's [8] model provides a generic solution procedure using finite elements for multi bearing and slip ring machines. The work of Kellenberger [6] is extended slightly in that an attempt is made to equate the proportionality factors p, p^* and q (identified by Kellenberger) as opposed to estimation from

real machine data. However, the results are approximate and practically indicative in application.

2.4 Morton Effect

It was Keogh and Morton [9] who produced the first fully qualitative and quantitative analysis of a spiral vibrations in a rotor system due to thermal effects within a hydrodynamic journal bearing. It is due to the work conducted by Keogh et al [9,10] that from that point onward spiral vibration problems associated with rotor bearings are referred to as the 'Morton Effect'.

The initial published work of Keogh et al [9,10] provides an analytical assessment of the thermohydrodynamic process that occurs within a plain journal bearing due to synchronous perpetrations in the oil film with respect to time. Morton [9] gives reference to some industrial applications where spiral vibrations have been observed where the cause was found not to be attributed to rubs or seal rings, notably in machines with overhung sections.

It is an important feature that the analysis looks at the bearing solution thermodynamically, as all previous analyses had not provided a thorough account for the thermal conditions within the bearing. The qualitative analysis of the 'Morton Effect' for a rotor running in hydrodynamically lubricated bearings, shows that it will undergo a synchronous orbit due to unbalance. This orbit will cause one specific circumferential section of the shaft to experience slightly smaller clearances at the position of the minimum film thickness than the section of shaft 180 degrees opposed. Generally, smaller film thickness are associated with higher rates of viscous shear stresses, thus a difference in film operating temperature will occur at shaft rotation frequency. The result of this is to generates a 'hot spot' on the shaft journal approximately at the position of the minimum film thickness resulting in a temperature differential across the shaft and producing a thermal bow. This mechanism will then, under certain conditions, continue to follow the process of feedback already described.

A time dependant analysis is provided, calculating the thermal bend by coupling the heat transfer effects with the rotor dynamic calculations. The analysis developed by Dimarogonas [3] is used to determine the rotor bend associated specifically with the thermal influences. By converting the thermal bend response into the frequency domain, a positive feedback loop is used to

assess the system stability by means of Nyquist plots and Eigenvalues with respect to shaft speed.

A simple model of a single bearing overhung shaft section was used as an example model. The solution of this predicted a speed range of instability which gave Eigenvalue results producing a system gain where G>1.

The analysis showed that temperature differences of 4^{o}-10^{o} C can develop under certain synchronous vibration orbits. Agreement was made with Kellenberger's [6] observations that unstable vibrations result in a 'spiral' progressing in the direction of rotation, whereas stabilising vibrations rotate in the opposite direction.

Analysis also showed that conditions for stability are speed dependent and are usually in the vicinity of a critical speed due to the level of dynamic magnification of rotor unbalance response. A significant feature identified is that the position of maximum shaft heating is not coincident with the position of minimum film, but with a significant lag due to convective heat transfer within the lubricant film. A lag of approximately 50-55 degrees was calculated in the numerical example performed by Keogh et al [9].

A practical example of the Morton effect was investigated by de Jongh and Morton [11] when a synchronous instability, caused problems during API (American Petroleum Institute) testing of a centrifugal compressor on the manufacturers test bed. The compressor rotor, having a mass of 450 kg, was mounted on two tilting pad hydrodynamic journal bearings. It was found on test that the rotor could not achieve the full running speed of 11,947 rpm due to high synchronous vibrations although the closest critical was at 14,500 rpm. It was observed that at a speed below approximately 9000 rpm vibrations were stable, but as speed was increased in incremental steps neither the vibration magnitude nor phase stabilised. At 11,400 rpm the vibrations began to grow rapidly and the run was reduced back down to 10,000 rpm. However the vibrations did not decrease immediately - after a short dwell the vibrations returned to about normal, see Figure 6. From this it was deduced that the problem was thermal in nature and the diagnosis of the Newkirk effect was identified and attributed to a seal rub.

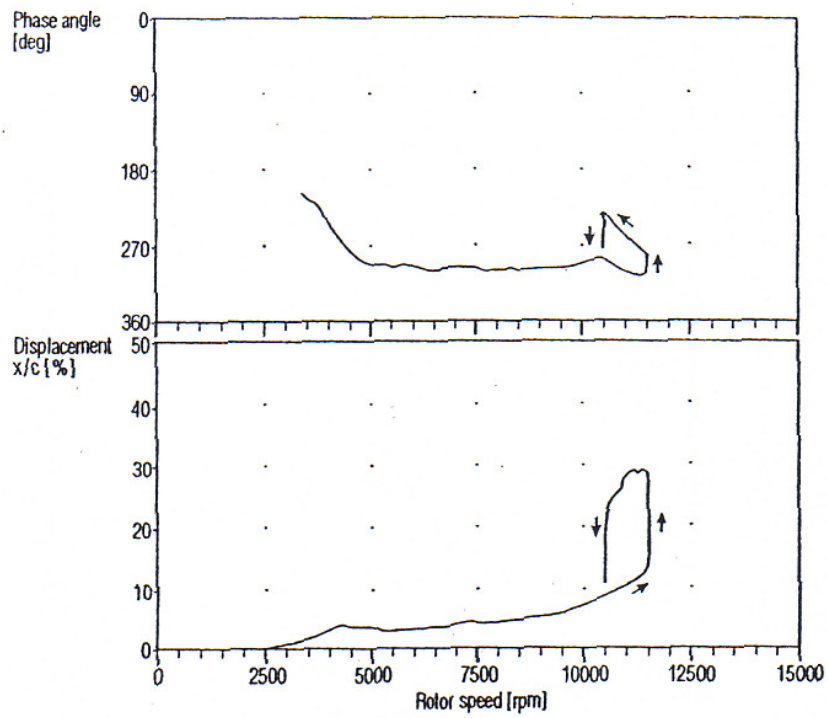

Figure 6 Fundamental Component (1x) of Relative Shaft Vibration [11]

As a result the test was repeated with the labyrinth seals removed, however the vibration problems again demonstrated the same pattern, ruling out the Newkirk Effect. To enable the compressor to get through test, the overhung mass of the rotor was reduced by use of alternative materials. The resolution of the problem, although not fully understood, pointed towards the Morton effect being the prime cause.

To enable a fuller understanding of the problem, a test rotor was constructed having effectively identical dynamic characteristics as the actual compressor rotor. After some prior testing, small Resistance Temperature Detectors (RTD's) were located within the rotor bearing journal. Four sensors were used to allow the full temperature profile to be obtained based on the assumption of harmonic distribution. Glue and slight interference fits were used to ensure good thermal contact and the electrical signals were passed through a slipringless transmitter to the stationary measuring equipment. Temperature in the bearing pads was also monitored as well as the shaft displacement at various positions along its length. All were referenced to a once per revolution pulse marker.

Results from the test rig showed that at speeds above 10,500 rpm, significant temperature differentials across the journal developed - from 3^{o} C and upward. It should be noted at this point that the magnitude at which the

temperature differential will become significant with relation to rotor stability is very closely linked to the rotor and bearing geometry. For a rotor which has a high thermal bow gain, temperature differentials as low as 1^{o}C could be sufficient to trigger unstable vibration growth.

As the rotor speed was increased spiral vibrations occurred, in the same direction as shaft rotation, with large unstable amplitudes occurring at approximately 11,500 rpm. At constant speed it was observed that the vibration levels were increasing at approximately 15% of the bearing clearance per minute which coincided with continually increasing differential journal temperatures. Further testing showed that the location of the onset of instability could be moved by around 900 rpm by quite small changes in overhung mass, demonstrating the sensitivity of the problem to overhung rotors.

Further examples of the Morton effect were encountered by Falkner, Strong and Kirk [12,13] during testing of an overhung turbocharger rotor. After some initial problems with loose fitting rotors, another problem was experienced further up the speed range. The problem demonstrated the characteristics of the Morton effect and was identified as such. Although phase measurements were not made, the time dependent vibration amplitude increases and vibration hysterisis loops pointed toward the phenomenon. In this case the problem was overcome by modifications to the bearing, producing an increase in operating eccentricity ratio and resulting in a less centered orbit which allowed increased cooling of the shaft 'hot spot'.

De Jongh and van der Hoeven [14] describe another example of the Morton effect in which a compressor experienced unacceptable levels of synchronous vibrations during operation, after successfully completing a full API shop test. After some examination and further testing, the seal rub was eliminated and the Morton effect identified as the cause in one of the machine bearings. Due to machine specific constraints, modification of the bearing was not possible and an alternative method of overcoming the problem was required. A heat barrier sleeve was incorporated to introduce a discontinuity in the heat transfer in the shaft journal, see Figure 7. The result of this was to reduce the amount of temperature variation around the journal and hence the rotor thermal bend. Additional testing confirmed the success of the modification and stable operation of the machine was experienced in the field.

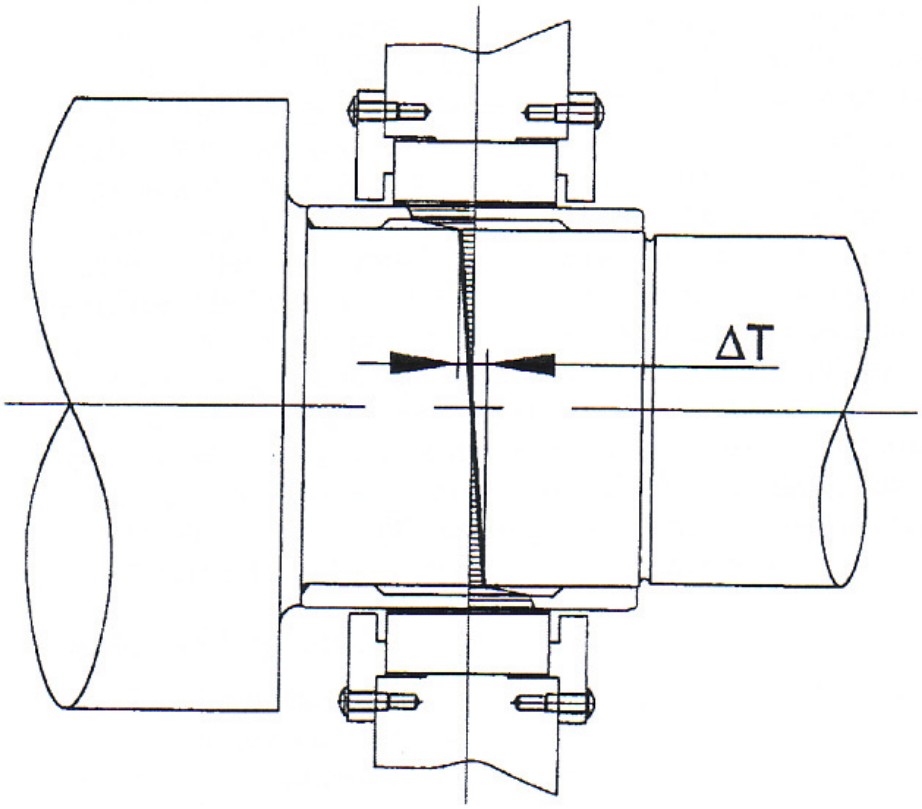

Figure 7 Typical Temperature Distribution with Heat Barrier Sleeve [14]

More recently some further analytical research has been conducted associated with the Morton effect. Larson [15,16] extends the thermal modelling of Keogh and Morton [9,10] by the inclusion of tilting pad bearings whilst making some simplifications in the solution procedure. Tucker and Keogh [17] and Gomiciaga and Keogh [18] have employed CFD techniques to analytically determine the temperature distribution around and across a rotating bearing journal with a perturbating orbit. Dynamic cavitation effects are determined (rather than initially estimated) in an attempt to obtain more accurate temperature differentials. The results of the analysis demonstrate that the journal does not behave in a isothermal fashion and can have significant static temperature differentials across the rotating shaft journal.

Possibly the most extensive amount of research conducted into the Morton effect since Keogh and Morton [9,10] has been presented by Balbahadur [19] and Balbahadur and Kirk [20,21,23,24]. Balbahadur [19,20,24] developed a simplified model in which a steady state analysis is performed with the objective of determining the onset of the Morton effect. The analysis is based on determining an unbalance threshold force which is a function of the total rotor mass. Account is taken for both plain and tilting pad journal bearings and a suite of software was developed to perform the analysis determining a

stability speed threshold. The criteria used to establish the thermal unbalance force thereshold is to take the product of a constant factor and the rotor total mass.

Balbahadur and Kirk [21,23] use a number of published examples of the Morton instability [11,13,14] as case studies for comparison with the results of the technique developed, to identify the onset of instability based on an unbalance force threshold. The results give reasonable agreement between the experimental and theoretical model. Balbahadur and Kirk [19,20] identify the significance of the orbit centre position and orbit magnitude on the onset of Morton instabilities. The analysis indicates that rotors operating with small eccentricity ratios and large circular orbits are more susceptible to Morton instabilities than those of large operating eccentricities. Some discrepancy is apparent as to the factor used to determine the unbalance force threshold. In Kirk and Balbahadur [24] a factor of 35% or rotor weight is reported to provide good correlation of a instability speed threshold whereas in later work [19,20,21,23] this factor is reduced to 15%. The precise causes for this change is not apparent in the available literature, however it is the author's assumption that when a wider field of case studies was evaluated [19] then a better aggregate correlation was observed with a factor of 15%, which is consistent with the results presented in [19].

Balbahadur [19] performed some preliminary experimental testing of a rotor intended to demonstrate the Morton effect, the results of this testing however did not culminate in the presence of the Morton effect. The experimental rig monitored shaft vibration; however it did not have the ability to measure rotor journal temperatures. Little meaningful data was obtained from the rig as a result of other unresolved dynamic issues within the test rotor system.

The analysis presented by Balbahadur [19] does not provide a full account for all of the variables involved in the Morton effect, but does provide a tool which appears to serve as a useful guide on the susceptibility of a rotor to instability. It is also a useful simplified analytical method to model the impact of the bearing operating characteristics, such as shaft orbit, on the stability of a rotor.

Kirk and Guo [30] go onto present some minor developments of Balbahadur's [19] work, but principally the same analytical and computational process is applied. The only significant apparent analytical modification to the procedure is the method by which the considered journal hot and cold spot locations are

determined. Balbahadur [19] defined the journal hot and cold spots by static geometrical means where the hot spot is defined as the point which is closest to the bearing sleeve at a time constant t=0, identified by Kirk et al [30] as method #1. Kirk et al [30] propose two further approaches that can be considered to define these locations. The same static geometrical approach is applied but now the hot spot can also be defined as either the closest point to the bearing sleeve at time constant t=tm, method #2 or the hot spot is defined as the point at which the journal is found to have the maximum temperature found in one orbit cycle, method #3. Kirk et al [30] do not provide an account as to which method provides a more accurate representation of the physical situation but later go on to conclude that, based on the two case studies presented, it is recommended that method #2 be applied for both plain and tilting pad bearing approaches. This is substantiated by the principle that method #2 produced better correlation to the case studies considered for tiling pads and the plain bearing solution is relatively insensitive to the method based on the analytical procedure being employed.

Kirk et al [30] conclude that, in addition to the key influencing criteria identified by Balbahadur [19] on sensitivity to thermal instability (low bearing eccentricity and circular obits), the relative phase angle between the initial mechanical unbalance and the thermal unbalance is also of significant importance. This intuitive statement relates to the fact that at large phase angles, (around 180 degrees) the thermal and mechanical unbalances would combine to result in a lower effective mechanical unbalance condition, favouring stability. As part of the tilting pad case study Kirk et al [30] investigate the effects of bearing clearance and pre-load on the sensitivity and location of thermally induced instability. It is stated that the increasing of bearing clearance has the greatest effect on improving instability risk, while changes in pad pre-load seem to have no serious effect on the thermal instability when considered within the same clearance range. The small impact made by the changes in pre-load were stated to provide some improvements to instability for a relative decrease in pad pre-load, however these impacts were relatively limited.

A further case study was published by Marscher and Illis [31,65] where the unexplained cyclic vibration of an integrally geared compressor supported in tilting pad bearings, was attributed to a form of the Morton effect. Following installation of an improved oil cooling system the compressor, which had been in service for some years, began to experience high vibration which cycled over approximately a six minute period. The vibration at both support bearings was seen to increase from ~18 microns pk-pk to 31 microns pk-pk over a

specific period in time during which any change in vibration amplitude was accompanied by an associated phase change. The phase change during cycling equated to approximately $+60^{o}$ for both support bearings. The problem was confirmed to not be associated with any critical speeds of the rotor, the fundamental of which was 195 Hz and the rotor operating speed was 255 Hz. It was also observed that the thermal cycling was in some way coupled between each end of the shaft, with the two bearing vibration amplitudes maintaining different phase angles which reduced and increased with time.

The Newkirk effect was ruled out by the authors as it was concluded that if a rotor-stator/seal rub was the principle cause the rub would 'burn' itself out and clear over a given period of time. A significant element which pointed toward a thermal influence in the rotor system was the fact that the cyclic increase in vibration was initially triggered when the oil inlet temperature was dropped below a specific threshold temperature, which was found to be ~52 degrees C. Further reductions in inlet temperature below this level only served to further increase the magnitude of the high vibration cycles. Whilst not fitting the traditional model of the Morton effect amplitude-phase relationship, several of the conditions within this reference do indicate some characteristics symptomatic of the Morton effect. In particular the potential for interaction between opposing bearings raises some further complex coupled thermal-rotordynamic aspects not yet discussed within the literature.

Schmied et al [32] present another example of a physical machine experiencing a synchronous vibration problem. The machine was a double overhung turbo-expander for the cryogenic industry running in 5-pad tilting pad bearings operating at a top end running speed of ~18000 rpm. The problem clearly demonstrated the forward spiral vibration characteristics associated with a thermal instability at both support bearings and it is stated by Schmied et al [32] that all other possibilities were eliminated and a journal bearing hot spot condition was considered the principle cause. The rotor was a short stiff rotor and as such was running in a sub critical condition. A number of practical changes were attempted on the test bench such as changing oil inlet conditions and bearing clearance - all of which introduced minor changes but did not overcome the problem. A form of hot spot analysis was performed based on the thermal stability sensitivity procedure presented by Schmied [32] and incorporated the hot spot model of Kellenburger [6]. The procedure uses a coupled rotordynamic matrix solution similar to that given by Keogh et al [10] where the thermal conditions are based on [8]. The stability assessment procedure compares the added heat (heat generated within the

oil film) to the eliminated heat (heat lost to the rotor/bearing structure) and is expressed as $\frac{p.\Omega}{q}$ where p = the proportionality factor for added heat, q = proportionality factor for eliminated heat, and Ω = shaft speed. The application of the method used is independent of bearing geometry and therefore it is stated by Schmied et al [32] that this simplifying assumption will affect the accuracy of the heat input terms. As such, to determine sensitivity, only 50% of the calculated values are used in the analysis. The result of the hot spot evaluation predicted that the rotor would be sensitive to thermal instability therefore some proposed changes were evaluated in an attempt to determine their impact. The physical changes that were implemented to the rotor, which resulted in an acceptable dynamic performance on the test bench, was to increase the diameter of the centre section of the rotor and to reduce the support bearing width. The effect of which increases the stiffness of the shaft in the overhung deflection mode and the reduction in bearing width reduces the thermal bend sensitivity, due to a reduced level of proportional thermal strain in the rotor. In addition to the geometrical changes the lubricant viscosity was also reduced from ISO VG46 to VG 32 to reduce the amount of heat being generated due to oil film shearing.

Schmied et al [32] also states that spiral vibration problems have been experienced on highly load bearings with highly elliptical orbits. This is in some contradiction to the proposal by Balbahadur [19] who comments that centred shafts with circular orbits are most sensitive. Schmied et al [32] however, does not include any evidence or references of such examples.

In 2008 Frits de Jongh [33] published a technical paper in which a collective summary of the published work and field examples linked to the Morton effect is presented. de Jongh [33] details the principle areas of activity that have been undertaken with regard to the phenomenon giving examples of practical cases where the Morton Effect has been attributed to rotating machinery vibration problems. The details of the work are consistent with the references already outlined earlier in this chapter. However, de Jongh [33] also gives commentary on some as yet unpublished work based on internal works conducted by Morton conducted at GEC in the UK. De Jongh [33] states that Morton performed tests on a large low speed test rig where circumferential temperature measurements were taken by means of 12 thermocouples placed on the rotating shaft journal. The test rig uses a bearing diameter of approximately 28 inches with an operating speed of 1800 rpm. No specific

details are provided of the detailed bearing geometry, operating clearances or lubricant type/viscosity.

It was found during the tests, that significant temperature differentials were observed even for relatively small shaft orbits ("only a few % of bearing radial clearance" [34]). It was also stated that a near linear relationship between shaft orbit size and journal temperature differential was observed. This is also consistent with the work presented by Larson [15,16] detailed earlier in this chapter, where a linear response between journal differential heating and vibration amount is stated. However, it should be noted at this point that no detail is provided as to the size of the vibration orbits as a percentage of radial clearance over which a near linear response with temperature differential was observed. Also no comment is made as the temperature distribution profile around the shaft journal circumference, i.e. harmonic and non harmonic components.

De Jongh [33] groups the various examples of rotating machinery vibration issues that have been reported as a result of the Morton effect. De Jongh [33] identifies that in all of the cases presented they share some common characteristics, in that they are all supported by plain hydrodynamic bearings and to a greater or lesser degree have relatively large overhung moments. De Jongh [33] makes a useful summarisation that whilst all the rotors have some common elements and features, the actual rotors do have different types of configuration and a breakdown of these is presented in Table 1. (It should be noted that de Jongh's [33] table is no longer current due to the addition of two further case studies published since this work).

	Rotor Configuration	Case Studies
1	 Single Overhung Wheel	Berot, et al., (1999); Kocur, et al., (2000); de Jongh, et al., (1998); Kirk, et al., (2003)
2	 Double Overhung Wheels	Faulkner, et al., (1997b), Schmied, et al., (2008)
3	 1 Overhung Coupling	Kocur, et al., (2000)
4	 2 Overhung Couplings (drive-through)	de Jongh, et al., (1994)
5	 Integrally Geared, 1 Overhung Wheel	Carrick, (1999)
6	 Integrally Geared, 2 Overhung Wheels	Marscher, et. al., (2004)

Table 1 Breakdown of Various Rotor Types Identified as Experiencing the Morton Effect [33]

de Jongh [33] provides details the approach taken by de Jongh and Van derhooven [14] to establish the sensitivity of a rotor set to synchronous thermal instability due to shaft bending, was introduced as standard to the rotordynamic assessment of a rotor assembly. De Jongh [33] states that the procedure consisted of determining the rotor mechanical unbalance for unit thermal bending at the bearing location. From this condition, the rotor response at the bearing locations is determined. Using some empirical data, the non uniform temperature distribution is estimated based on the operating conditions under evaluation. The estimated temperature differential is then used to determine the resulting shaft thermal bend. The modulus of the complex thermal bend angle is determined as a ratio of the unit input and output complex bend angle and it is this ratio which is used as a criterion for stability.

De Jongh [33] notes some possible practical corrective actions for machines that are considered to be subject to the Morton Effect instability.

- Limit the design speed
- Reduce overhung moments
- Change bearing clearances
- Reduce bearing length
- Change bearing type or geometry
- Heat barrier sleeve
- Increase specific bearing loading and eccentricity
- Change shaft material
- Change lubrication oil viscosity
- Increase inlet oil flow

It is also noted that the Morton effect not only applies to new machinery but can also be experienced on established machinery in the field, such as compressors, where it is common to upgrade certain components to obtain increased performance or capacity, as observed by Faulkerner et al [13].

Childs and Saha [35] present an iterative algorithm for the synchronous response analysis for analysing the Morton effect. The procedure is dependent on a suitable thermal model being applied to solve for the journal thermal conditions and thermal sensitivity to shaft orbit size. Childs et al [35] state that a procedure similar to that presented by Keogh et al [9] is required

to obtain the necessary journal temperature differentials and phase angles, such that these can be applied to the rotordynamic model. The procedure uses the results of a complex thermal analysis to calculate the shaft temperature differentials and thermal phase angle for 5 orbit radii conditions for a given bearing operating condition. These results are then interpolated between data points when applied to the rotordyanmic model. The algorithm in principle then involves performing an iterative procedure of rotor response (the initial condition of response is determined for the shaft mechanical unbalance). From this, the resulting degenerated forward and backward whirl amplitudes are extracted. Applying these amplitudes to the thermal analysis results, appropriate forward and backward whirl journal temperature differentials and phase angles can be interpolated as appropriate. Childs et al [35] then determine a resultant maximum journal temperature differential and phase angle by:

$$\Delta T_1 = \sqrt{\Delta T_f^2 + \Delta T_b^2 + 2.\Delta T_f.\Delta T_b.\cos\left(2.\beta^* + \varphi_{Tf} + \varphi_{Tb}\right)} \qquad \text{Eq. 2.4.1}$$

$$\varphi_T = \tan^{-1}\left(\frac{\Delta T_f.\sin\left(\beta^* + \varphi_{Tf}\right) - \Delta T_b.\sin\left(\beta^* + \varphi_{Tb}\right)}{\Delta T_f.\cos\left(\beta^* + \varphi_{Tf}\right) - \Delta T_b.\cos\left(\beta^* + \varphi_{Tb}\right)}\right) \qquad \text{Eq. 2.4.2}$$

Where $\Delta T_f, \varphi_{Tf}, \Delta T_b, \varphi_{Tb}$ are the temperature differential and phase for forward and backward whirl respectively, computed from the complex bearing energy model. β^* is the shaft bend angle present from the previous iteration calculation.

The resulting shaft bend angle is then calculated from Dimoragonas [8] and importantly, this is used to determine the moments at the bearing location which are then directly applied to the rotordynamic model to generate the excitation (as opposed to other methods which determine an equivalent mechanical unbalance force due to the eccentric overhung mass).

The unbalance components are combined and a new thermal unbalance solution is performed, this procedure is repeated until a converged solution for the shaft orbit is obtained. The gain factor following each iteration is stated by Childs et al [35] as:

$$G_{aT} = \frac{F_i + B_i}{F_{i-1} + B_{i-1}} \qquad \text{Eq. 2.4.3}$$

Where F_i and B_i are the forward and backward whirl amplitudes respectively.

Childs et al [35] state that the analysis is heavily dependent on the availability of appropriate data from a bearing thermal model of some sort (which provides both temperature and phase data for complex shaft orbits). To date the only models available - Keogh et al [9] or CFD (Computational Fluid Dynamics) solutions - are prohibitively complex and computationally/time intensive for practical application. Childs et al [35] also state that if a computational method is employed, where data is interpolated between a set of given conditions from the bearing thermal analysis, then it is possible to encounter a numerically unstable condition if too few orbit data points are available for interpolation, resulting in an oscillating result which tends to diverge.

Most recently Murphy and Lorenz [36,37] have published several works addressing rotor thermal hot spot development and corresponding spiral instabilities. Murphy et al [37] present an industrial case study where a variable speed electrical machine was found to exhibit unstable time dependant shaft vibrations when running at its maximum design speed of 4175 rpm for prolonged periods (~2 hours). The rotor was supported in partial arc plain bearings and was designed to run through several critical speeds, the fourth of which was predicted to be at a frequency close to running speed, with a calculated frequency of 4000 cpm. The natural mode at this speed was associated with high vibration activity exhibited by the overhung sections of the rotor, although no specific qualification of predicted stability/damping for this mode was quoted in the literature. Although, it is noted by Murphy et al that this mode is sensitive to unbalance at the overhung shaft section.

The unstable vibration was observed to occur whilst running at operating speeds over 4000 rpm for some 100+ minutes before excessive exponential growth was encountered. A significant aspect was the time history characteristic of vibration which showed symptoms of a harmonic function with an exponential growth curve, suggesting an oscillatory nature, before instability becomes onset (see Figure 8). An interesting feature of this case study is that several units of identical design were produced with each machine displaying slightly different characteristics with respect to any Morton effect instability. Murphy et al [37] state that of four machines produced, one machine showed no clear signs of instability during shop testing, another showed an oscillating mode but no instability and another machine showed very rapid unstable growth. Murphy et al [37] identify that from the test data

presented, it is clear that the time taken for an instability to show itself, or be present, are very sensitive to the physics involved in the Morton effect phenomenon; such as variations of bearing clearance, bearing alignment ambient temperature, machine operating temperature, lubricant properties, overhung mass, support stiffness, etc.

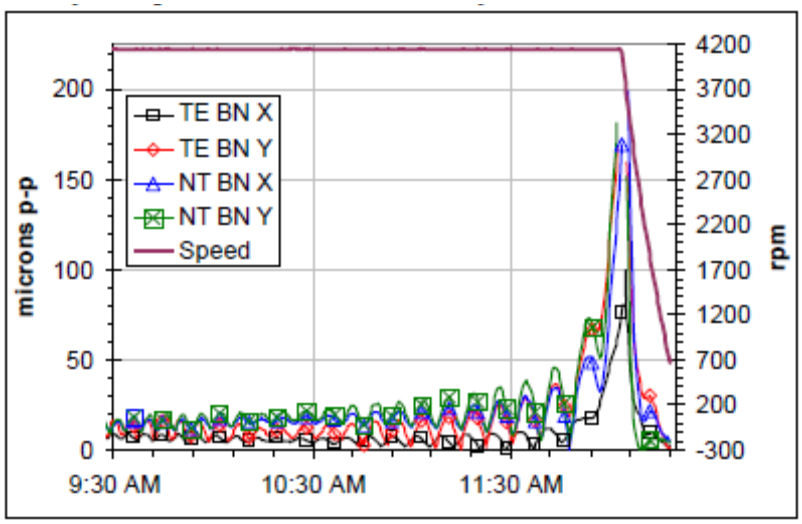

Figure 8 4150 RPM Constant Speed Factory Test Proximity Probe 1x Vibration Amplitude vs Time [37]

For the each of the tests performed over the four different machines Murphy et al [37] present the relative growth factors and time constants experienced for the vibration oscillations and divergent cases. Murphy et al [37] document shaft vibration growth rates ranging from 7 %/min to 177 %/min. Differences of up to 160 %/min were published for the same machine between different runs.

It was observed by Murphy et al [37] that, for the machines that showed the least resistance to experiencing the Morton effect, synchronous response of the machine when first reaching running speed was lower than that of the other machines. It is postulated by Murphy et al [37] that this effect of lower synchronous response close to the Morton instability threshold could be indicative of a less stable configuration. The qualification for this was that the thermal bow condition could result in a lower state of mechanical unbalance prior to the instability threshold being reached or instability taking hold.

The spiral vibration problem in the machine described above was stated as being overcome by the introduction of an alternative bearing design. The original partial arc bearing arrangement was replaced with a 4-lobe plain bearing configuration. The introduction of this bearing design was seen to

eliminate the presence of the Morton effect instability. The proposed justification by Murphy et al [37] for the 4-lobe bearing eliminating the Morton effect, was given to be the increased cooling effect introduce by the 4-lobe bearing.

Murphy et al [37] outline a procedure to evaluate the sensitivity of a rotor thermal instability on the Morton effect. The procedure was applied to assist in evaluating the case study presented in [37]. It outlines how the application of a number of sensitivity terms can be combined to establish how sensitive a system is to instability. The sensitivity terms relate to shaft temperature differential as a function of vibration magnitude, thermal bend unbalance sensitivity as a function of thermal differential and other more typical rotor dynamic elements. The product of these terms yields a first order differential equation where the solution results in a single complex eigenvalue s. Stability of the system is defined by Murphy et al [37] as any result where the real component of the eigenvalue is < 1. Murphy et al [37] identify 3 possible modes of stability: (1) $\mathrm{Re}\,s$ < 1 stable-converging spiral vibration (2) $\mathrm{Re}\,s$ = 1 stability threshold-oscillating but not divergent (3) $\mathrm{Re}\,s$ > 1 unstable-divergent spiral vibration. These modes of stability reflect those identified by Dimigronas [5] when associated with rotor rubs.

A significant area highlighted by Murphy et al [36,37] is that the requirement for an accurate thermal model of the bearing is critical for accurate predictions of rotor stability to be achieved. The principle suggested by Murphy [36] to establish the temperature distribution around the journal uses similar principles as that applied by Balbahadur [19] with the exception that a full circumferential temperature distribution is extracted for each orbit location instead of just the hot and cold spot locations. It is noted by Murphy et al [36] that accurate definition of the temperature differential is difficult to achieve and whilst the complex procedure employed by Keogh et al [9,10] provides the necessary data, it is not practical to implement these complex procedures at an industrial level. In particular Muphy et al [36] indicates that the phase angle, which cannot be calculated with the presented approach, of the hot spot around the journal is of critical importance when defining the sensitivity of a system's stability performance. No approach or solution for solving the journal thermal problem is proposed or presented within the literature. Any account for the phase angles involved is included by means of introduction of assumed phase lags based on some associated data or intuitive estimates; although Murphy et al [36] does state that there is the need for experimental

verification and/or data of the thermal temperature differential and phase angles.

Lorenz [38] presents a study in which a propriety CFD modelling package is used to attempt to model the thermal conditions associated within the bearing oil film, shaft journal and bearing housing. The principle objective of the work was to be able to determine the necessary thermal data points required for implementation in any thermal stability rotordynamic analysis such as that of Childs et al [35] and Murphy et al [36]. The research investigates some practical aspects of the CFD modelling techniques used to represent the fluid-film bearing model such as mesh density, boundary conditions and solution methods. A periodic iterative approach is adopted over a full transient solution technique in an attempt to overcome the associated physical and computational difficulties that would be involved in the latter.

The conclusion of the work of Lorenz [38] was that it was possible to establish appreciable temperature differentials across the shaft journal, however the magnitude did not agree with that of other referenced literature such as [9,11]. The magnitudes predicted by Lorenz [38] were systematically higher than those of Keogh et al [9]. Although Lorenz [38] states the results did compare well to that presented by Dowson [39].

Another key element within the research was the determination of the phase angle of the hot spot on the journal. The work of Lorenz [38] showed not to be in agreement with that of Keogh et al [9]. For a circular forward whirl orbit, the phase angle was predicted to lag the minimum film thickness point by ~60^{o}, whereas the results of Lorenz [38] showed that the phase led by approximately 42^{o} degrees. In addition to the numerical results, it is of notable observation that for the single point solution cases undertaken in the research, the solution times required are expensive both computationally and in time. Typical solution times for a single orbit converged solution were given by Lorenz [38] as 16 hours with significant further time and effort required to extract the solved results and post process.

2.5 Hydrodynamic Bearing Theory

When considering the influences taking place in rotors exhibiting thermal instability due to shaft bow, an appropriate appreciation of the hydrodynamic effects and analytical modeling techniques involved is necessary. It is not the intention to cover in detail here the very numerous sources of material covering this subject matter, however, the principle aspects relating hydrodynamic theory are described in the landmark paper by Reynolds [26]. Here the governing equations relating the hydrodynamic principles in fluid bearings are described and presented. From this founding work many hundreds of other significant works are available addressing the many important hydrodynamic features and effects present in rotating machinery and in particular plain bearings. Significant contributions in recent times have been the works of Sommerfeld [40], Ovkirk [41], Lund [27,28], Garner [42] and Cameron [43] to name but a few who have all contributed significantly to the development of hydrodynamic theory relating to journal bearings for rotating machinery. The references covered here, whilst far from exhaustive, provide sufficient account to cover the generalised hydrodynamic conditions which are of interest within the scope of this research.

Chapter 3

Analytical Review of Bearing Journal Differential Heating

3. Analytical Review of Bearing Journal Differential Heating

3.1 Introduction

This chapter presents the analytical methods applied in the evaluation of bearing journal differential heating and more specifically, the assessment of thermally induced rotor bend stability evaluation by several published methods. Two specific methods evaluated in detail are: (1) those presented by Keogh and Morton et al. in their papers on 'Journal bearing differential heating evaluation with influence on rotor dynamic behaviour' and 'The dynamic nature of rotor thermal bending due to unsteady lubricant shearing within a bearing' [9,10], (2) that presented by Balbahadur and Kirk in several papers [20,21,23,24] and in more detail in the thesis 'A thermoelastichydrodynamic model of the Morton effect operating in overhung rotors supported by plain or tilting pad bearings' [19]. In recent times several other works have been presented on this topic as outlined in the previous section, however these are effectively subtle variations on the principles summarised in this chapter with the founding work of Keogh et al and Balbahadur et al being the most comprehensive works available today in the published domain.

Much of the founding analytical procedures involved the thermal bend analysis procedures relate to well published quantitative techniques for the assessment of hydrodynamic bearings and lateral rotordynamic behaviour/response. As such only a brief analytical summary is provided here for the above two methods by way of an introduction to the thermal bend stability theory developed in each case.

3.2 Hydrodynamic Lubrication in Bearings

3.2.1 Brief Overview of Hydrodynamic Lubrication

Lubrication in some form or another is a fundamental principle in the working of all machines where relative motion is present between the moving parts. Without the presence of lubrication the losses and forces introduced would result in the workings of all machines, be they rotating or linear, to become impractical.

The mechanism of lubrication is the principle where two surfaces that have some form of relative movement are separated by a film of material which can be sheared in some way without causing unacceptable levels of damage or wear to the associated working surfaces. Principally four generic regimes of lubrication can be considered and, dependant on the functional requirements of a given mechanism, the type of lubrication experienced can consist of one or several of the conditions given below across its operating range.

Four principle lubrication regimes :

1. **Full or Hydrodynamic Lubrication**: two surfaces are completely separated by a fluid film with applied loads supported by the lubricating media.
2. **Elastohydrodynamic Lubrication**: two surfaces are separated by a very thin fluid film operating under high pressures where significant interaction with the elastic deformations of the sliding surfaces exist.
3. **Mixed Lubrication**: two surfaces are partly separated by a film and partly in contact (usually by asperities in the sliding surfaces surface roughness)
4. **Boundary Lubrication**: two surfaces mostly are in contact where a fluid or gas lubricant may be present but the lubricating properties are the result of the physical interaction between the two sliding surfaces.

For the purposes of this work, the principles and theories associated with full hydrodynamic lubrication are those which are relevant to the application of plain bearings for high speed rotating machinery. It is the interaction between these lubricating principles and the rotordynamic characteristics of a rotor that interact to produce the thermal instability of interest.

The advantageous principles of hydrodynamic lubrication have been employed for over two centuries. Hydrodynamic lubrication was given

scientific context in the mid 1800's where several works presented qualitative accounts of the principles of pressure generation in fluid films of two sliding bodies. However, it was not until the work of Reynolds [26] in 1886 that a detailed analytical analysis was presented showing how a converging wedge shaped film was required to generate a pressure profile in the lubricating fluid capable of supporting load. It is this keystone paper that has provided the foundation on which all subsequent hydrodynamic analysis principles have been based.

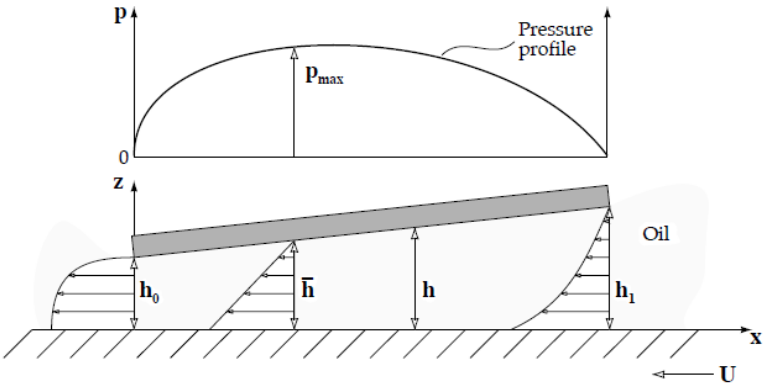

Figure 9 Principle of Hydrodynamic Lubrication Between Two Inclined Surfaces – figure taken from [44]

3.2.2 Equations Governing Hydrodynamic Lubrication in Journal Bearings

The work conducted by Reynolds [26] provided a mathematical description of the hydrodynamic pressure profile that is generated between two converging surfaces of differential sliding speeds separated by a fluid. The pressure in the lubricant film is generated by the action of the viscous fluid being stationary at the boundaries of the two working surfaces and, due to the relative velocities, the lubricant is dragged into the converging gap. Working on a principle of virtual incompressibility of the lubricant, a pressure field is generated which is capable of supporting a load nominally normal to the direction of sliding. Reynolds derived a differential equation which related the influences of lubricant viscosity, sliding velocity and pressure, which was based upon a given geometric description of the gap between the two working surfaces.

The partial differential equation presented by Reynolds in three dimensions is:

$$\frac{\partial}{\partial x}\left(\frac{h^3}{\eta}.\frac{\partial p}{\partial x}\right)+\frac{\partial}{\partial z}\left(\frac{h^3}{\eta}.\frac{\partial p}{\partial z}\right)=6\left(\frac{\partial}{\partial x}(U_1+U_2)h+\frac{\partial}{\partial z}(W_1+W_2)h+2\frac{\partial h}{\partial t}\right) \quad \text{(Eq 3.2.1)}$$

The Reynolds partial differential equation in its full three dimensional form is generally too complex to solve practically. To overcome this degree of complexity several methods have been developed to simplify it to a form which can more readily be solved.

$$\frac{\partial}{\partial x}\left(\frac{h^3}{\eta}.\frac{\partial p}{\partial x}\right)+\frac{\partial}{\partial z}\left(\frac{h^3}{\eta}.\frac{\partial p}{\partial z}\right)=6\left(\frac{\partial h}{\partial x}U+2\frac{\partial h}{\partial t}\right) \quad \text{(Eq. 3.2.2)}$$

Equation 3.2.2 shows the Reynolds equation with several of these simplifications applied to equation 3.2.1, such as the recognition that generally no relative sliding occurs in the axial direction and the velocity is constant throughout the film, i.e $\frac{\partial}{\partial x}(Uh)\equiv U\frac{\partial h}{\partial x}$. A further simplification can be made for bearings running at steady conditions without perturbation of the oil film where the squeeze film pressure term can be equated to zero $\frac{\partial h}{\partial t}=0$ and yields the Reynolds equation as typically written:

$$\frac{\partial}{\partial x}\left(\frac{h^3}{\eta}.\frac{\partial p}{\partial x}\right)+\frac{\partial}{\partial z}\left(\frac{h^3}{\eta}.\frac{\partial p}{\partial z}\right)=6U.\frac{\partial h}{\partial x} \quad \text{(Eq. 3.2.3)}$$

3.2.3 Solution of the Reynolds Equations for Journal Bearings

As the Reynolds second order partial differential equation cannot be solved directly, it is necessary to implement further assumption and simplification to enable discrete analytical solutions to be obtained. The two principle simplifications applied to journal bearings are typically known as the Infinitely Long Bearing and the Infinitely Short Bearing. The Infinitely Long Bearing theory was introduced by Sommerfeld [40] whereby the bearing length is assumed infinite and hence the pressure variation in the axial direction is zero. This allows the term $\frac{\partial p}{\partial z}$ to be set to zero which results in the Reynolds equation being reduced to one dimension as given by equation 3.2.4. The application of this approach means that it can only be considered as representative of the centre portion of the bearing.

$$\frac{\partial}{\partial x}\left(\frac{h^3}{\eta}.\frac{\partial p}{\partial x}\right)=6U.\frac{\partial h}{\partial x} \quad \text{(Eq. 3.2.4)}$$

Infinitely Short Bearing theory conversely considers the bearing to be of infinitely short length. It was presented by Ocvirk [41] and results in a pressure profile where the gradient in the *z* direction is much greater than that in the x direction. This enables the first term from equation 3.2.3 to be considered as zero, $\frac{\partial}{\partial x}\left(\frac{h^3}{\eta}.\frac{\partial p}{\partial x}\right)=0$, and results in Ocvirk's Reynolds equation :

$$\frac{\partial}{\partial z}\left(\frac{h^3}{\eta}.\frac{\partial p}{\partial z}\right)=6U.\frac{\partial h}{\partial x} \quad \text{(Eq. 3.2.5)}$$

Ocvirk's equation provides a method to solve the differential equation by practical means for relatively simple film thickness relationships and, as it retains two dimensions, generally results in a more accurate result than the Infinitely Long Bearing approach for length to diameter ratios between 0.3 and 1. For this reason it is more widely used for the solution of practical plain journal bearings which most commonly have L/D ratios of ≤ 1.

Where more accurate results are being sought, or with more complex film thickness relationships such as journal misalignment or use of variable geometry pads, a form of numerical solution needs to be applied. These techniques employ the same fundamental principles and arrangements of the Reynolds equation but reach solutions of the Reynolds equations by means of approximations. This yields results within predefined or acceptable tolerance ranges. Many numerical techniques are available for the solution of such mathematical problems with the likes of finite element and finite difference techniques providing common means of obtaining a solution to equation 3.2.3 (2D Reynolds equation).

The solution of the Reynolds equation is of significant importance to the topic of synchronous thermal instabilities as it provides the basis around which the shaft journal quasi-static and dynamic bearing positions within the bearing are determined. From this, the corresponding pressure profiles and film thickness shear rates can be established by some relationship which in turn provides a means for extraction of journal temperature variations to be established. The

basic principles of the above Reynolds theory is in some form applied to both of the analytical procedures reviewed here as presented firstly by Keogh and Morton [9] and then Balbahadur [19]. Details of which are outlined in the remained of this chapter.

3.3 Keogh et al [9] Procedure

Keogh and Morton presented several works [9,10] which evaluate the principles associated with the differential heating of a bearing journal when running in hydrodynamically lubricated bearings. A summarised review of the work is contained in the literature review in chapter 2, and a detailed overview of the analytical procedures is now covered in the following sub section. Of the works reviewed, the work given in reference [9] is covered in detail here, which addresses the models used to describe both the thermal conditions at the bearing-oil-journal interfaces and the coupling interaction with the rotordyanmic behaviour and response due to the induced thermal bend. The work reviewed in [10] goes to build on the work given in [9] to introduce a time dependant control logic which establishes a measure of system stability and the associated time constants involved in the thermal oil film developments and stability development. The review focus is placed on the theory surrounding the actual modelling of the thermal bend development and sensitivity, without account for the analytical procedure.

The principle approach of the method presented by Keogh et al [9] is to tackle the problem by means of development of a full thermohydrodynamic model of the oil film, bearing and shaft journal. The interrelations within the bearing are evaluated for the thermal and spatial conditions present, with a plain bearing handling the dynamic and steady conductive heat flux terms between the lubricant and physical elements. The technique seeks to provide a holistic approach to coupling the complex energy, hydrodynamic, thermal and structural aspects of the dynamic thermal bow problem.

The principle of this section is to present and discuss the governing equations derived and presented by Keogh and Morton [9]. Where possible the derivation and expression developments are followed through in this text, however in some areas the analytical developments and resulting expressions are presented without proof. This is a reflection of the complex nature of the analytical procedure and the intention of this paper is provide a sufficient account of the methodology and expressions used to model the dynamic

thermal conditions, only to enable suitable observations and comparisons made to the scope of work embodied with the author's research.

The analytical account of the work of Keogh et al [9] is presented by addressing the following aspects of the analytical model in turn. Keogh et al [9] breaks the problem down as per the list below to develop the necessary expressions and boundary conditions required to solve and couple the various dynamic and steady state conditions of interest.

- Lubricant flow terms
- Lubricant energy terms
- Lubricant film thickness
- Lubricant temperature and temperature perturbations
- Bearing and journal conduction
- Lubricant temperature development
- Prediction of rotor bend
- Thermal bend influence on rotordynamics

3.3.1 Lubricant Flow Terms

First, the hydrodynamic formulations and lubricant flow terms are expressed for the thermohydrodynamic oil film model. Keogh et al [9] presents the general Reynolds equation as given previously in equation 3.2.2, in non dimensional form (equation 3.3.1). This non dimensional equation is then reduced by means of applying Ovkirk's equation for short bearing theory but now following through the non dimensional approach, equation 3.3.2.

$$\frac{\partial}{\partial\beta}\left(H^3\frac{\partial P}{\partial\beta}\right)+\frac{1}{\in_L}.\frac{\partial}{\partial\xi}\left(H^3\frac{\partial P}{\partial\xi}\right)=\frac{\partial H}{\partial\beta}+2.\frac{\partial H}{\partial\tau} \quad \text{Eq. 3.3.1}$$

$$P=\frac{1}{2.H^3}.\left(\frac{\partial H}{\partial\beta}+2.\frac{\partial H}{\partial\tau}\right).\left(\xi^2-1\right).\in_L \quad \text{Eq. 3.3.2}$$

The common assumptions for the short bearing theory are applied here in that only positive pressure (P >= 0) can exist, negatively calculated pressure are taken as 0.

The accompanying non dimensional velocity components for the full film region can be expressed for the three principle directions as given in equation 3.3.3.

$$U = \eta \quad \text{(Eq. 3.3.3-a)}$$

$$V = \left(\frac{c}{R}\right).\left(\eta^2 + \eta^2.(1-\eta).\frac{\partial H}{\partial \beta} + \left(3.\eta^2 - 2.\eta^3\right).\frac{\partial H}{\partial \tau}\right) \quad \text{(Eq. 3.3.3 -b)}$$

$$W = -\frac{3.\eta.(1-\eta)}{H}.\left(\frac{\partial H}{\partial \beta} + 2.\frac{\partial H}{\partial \tau}\right).\xi.\sqrt{\epsilon_L} \quad \text{(Eq. 3.3.3-c)}$$

Flow continuity considerations need to be accounted for due the divergent section of the oil film beyond the minimum film thickness point. Beyond this location the oil film enters a cavitatived state where the oil breaks into a number of streamers [45]. It is considered by Keogh et al [9] that the velocity terms described in equation 3.3.3 are maintained but are now local to the various oil streamers in the divergent section with reference to any axial ordinate terms.

3.3.2 Lubricant Energy Terms

Whilst, to the author's knowledge, no commonly adopted form of the non dimensional energy equation for journal bearings is commonly applied, Keogh et al [9] presents a non dimensional form of the energy balance relationship by applying the full dimensional energy equation as given in equation 3.3.4 and introducing the non dimensional flow terms of equation 3.3.3 to result in the dimensionless energy equation for short bearings given in equation 3.3.5.

$$\rho_L.c_L.\left(u.\frac{\partial \Theta}{\partial x} + v.\frac{\partial \Theta}{\partial y} + w.\frac{\partial \Theta}{\partial z} + \frac{\partial \Theta}{\partial t}\right) = k_L.\left(\frac{\partial^2 \Theta}{\partial x^2} + \frac{\partial^2 \Theta}{\partial y^2} + \frac{\partial^2 \Theta}{\partial z^2}\right) + \Phi \quad \text{(Eq. 3.3.4)}$$

$$\eta.\frac{\partial T}{\partial \beta} + \frac{\eta.(1-\eta)}{H}.\left(\eta.\frac{\partial H}{\partial \beta} + (2.\eta - 1).\frac{\partial H}{\partial \tau}\right).\frac{\partial T}{\partial \eta}..... \\ -\frac{3.\eta.(1-\eta)}{H}.\left(\frac{\partial H}{\partial \beta} + 2.\frac{\partial H}{\partial \tau}\right).\xi.\frac{\partial T}{\partial \xi} + \frac{\partial T}{\partial \tau} = \frac{1}{P_e.H^2}\frac{\partial^2 T}{\partial \eta^2} + \frac{1}{H^2} \quad \text{(Eq. 3.3.5)}$$

Where P_e is the Peclet number $P_e = \frac{\rho_L.c_L.\Omega.c^2}{k_L}$ which is a non dimensional term which links the rate of lubricant advectation with the diffusion flow rate. Θ_f is a specific reference temperature which is defined by Keogh et al [9] as $\Theta = \frac{\mu.\Omega.}{\rho_L.c_L}.\left(\frac{R}{c}\right)^2$ which is then used to non dimensionalise the temperature terms by $T = \frac{\Theta}{\Theta_f}$. The presented equation 3.3.5 does not provide terms of axial and circumferential conduction within the lubricant and the heat source term $\frac{1}{H^2}$ is independent of axial coordinate. A further reduction of equation 3.3.5 is achieved by introducing an axially averaged temperature across the wetted bearing width where $T_L = \int_0^1 T.d\xi = T$, removing the axial dependant terms $\frac{\partial T}{\partial \xi}$ giving equation 3.3.6.

$$\frac{\partial^2 T_L}{\partial \eta^2} - \frac{P_e.\eta.(1-\eta)}{2}.\left(\eta.\frac{\partial H}{\partial \beta} + (2.\eta - 1).\frac{\partial H}{\partial \tau}\right).\frac{\partial T_L}{\partial \eta} - P_e.\eta.H^2.\frac{\partial T_L}{\partial \beta} - P_e.H^2.\frac{\partial T_L}{\partial \tau} = -P_e$$

(Eq. 3.3.6)

To account for continuity of heat flux at the boundaries between the fluid film and the bearing/journal, use of an axial fractional film function is introduced $d(\beta,\tau)$ to account for the cavative areas around the bearing circumference. This allows consistency to be maintained for the axially averaged temperature and heat flux in the bearing and journal surfaces.

The boundary conditions on the lubricant for the bearing and journal interfaces are now written as :

$$T_L(0,\beta,\tau) = T_B(1,\beta,\tau) \qquad \frac{\partial T_L}{\partial \eta}(0,\beta,\tau) = -\gamma_B.\frac{H(\beta,\tau)}{d(\beta,\tau)}.\frac{\partial T_B}{\partial r}(1,\beta,\tau) \quad \text{(Eq. 3.3.7)}$$

$$T_L(0,\beta,\tau) = T_B(1,\beta,\tau) \qquad \frac{\partial T_L}{\partial \eta}(1,\beta,\tau) = -\gamma_J.\frac{H(\beta,\tau)}{d(\beta,\tau)}.\frac{\partial T_J}{\partial r}(1,\theta,\tau) \quad \text{(Eq. 3.3.8)}$$

Where r is non dimensionalised bearing ordinate, $r = \frac{\rho}{R}$, and θ is a circumferential coordinate but now referred to a fixed axis on the rotating shaft journal.

3.3.3 Lubricant Film Thickness

The definition of the lubricant film thickness function is expressed in non dimensional form in equation 3.3.8. The film thickness function *H* consists of both the steady film thickness H_o as defined by the steady eccentricity ratio $\in_o$, and the film thickness perturbations resulting from the shaft elliptical orbit. The elliptical orbit is represented by decomposed circular forward and backward whirl orbit components. It is possible to analytically represent an elliptical orbit with two cylindrical orbits of opposing rotation. This method of representation is described in a little more detail later in chapter 8.

$$H = H_o + \in_1 .H_1 + \in_2 .H_2 \quad \text{(Eq. 3.3.9)}$$

where the non-dimensional form for $h(\beta)$ is given by $H_o(\beta) = 1 + \in_o .\cos(\beta)$ for the plain cylindrical bearing under consideration and the film thickness components due forward and backward whirl are given by:

$$H_1(\beta,\tau) = \sin(\beta + \tau + \phi_o - \gamma) \qquad H_2(\beta,\tau) = \sin(\beta - \tau + \phi_o - \gamma) \quad \text{(Eq. 3.3.10)}$$

3.3.4 Lubricant Temperature Oscillations

Keogh et al [9] considers the perturbation terms $\in_1, \in_2$ as small parameters and linearises the energy balance relationships which then lead to the temperature perturbed relationships as expressed in equation 3.3.11.

$$\begin{aligned} T_L &= T_o + \in_1 .T_1 + \in_2 .T_2 \\ T_B &= T_{Bo} + \in_1 .T_{B1} + \in_2 .T_{B2} \\ T_J &= T_{Jo} + \in_1 .T_{J1} + \in_2 .T_{J2} \end{aligned} \quad \text{(Eq. 3.3.11)}$$

The energy equations for the zero and perturbed orbits are now written :

Zero orbit energy equation :

$$\frac{\partial^2 T_o}{\partial \eta^2} - \frac{P_e.\eta^2(1-\eta)}{2}.\frac{\partial H_o}{\partial \beta}.\frac{\partial T_o}{\partial \eta} - P_e.\eta.H_o^2.\frac{\partial T_o}{\partial \beta} - P_e.H_o^2\frac{\partial T_o}{\partial \tau} = -P_e \quad \text{(Eq. 3.3.12)}$$

Perturbed orbit energy equation :

$$\frac{\partial^2 T_j}{\partial \eta^2} - P_e.\eta^2.(1-\eta).\frac{\partial H_o}{\partial \beta}.\frac{\partial T_o}{\partial \eta} - P_e.\eta.H_o^2\frac{\partial T_j}{\partial \beta} - P_e.H_o^2\frac{\partial T_j}{\partial \tau} = ...$$

$$P_e.\eta.(1-\eta).\left(\eta.\frac{\partial}{\partial \beta}\left(H_o H_j\right) + (2.\eta - 1).\frac{\partial}{\partial \tau}\left(H_o H_j\right)\right).\frac{\partial T_o}{\partial \eta} + 2.P_e.\eta.H_o.H_j\frac{\partial T_o}{\partial \beta} + 2.P_e.H_o.H_j.\frac{\partial T_o}{\partial \tau}$$

(Eq. 3.3.13)

The following equation can be established to involve the oil film thickness *H* :

$$\frac{H(\beta,\tau)}{d(\beta,\tau)} = A_o(\beta) + \in_1 .A_1(\beta,\tau) + \in_2 .A_2(\beta,\tau) \quad \text{Eq. 3.3.14}$$

Where:

$$A_o(\beta) = \begin{cases} H_0(\beta) & 0 \le \beta \le \pi \\ \dfrac{H_o(\beta)}{H_o(\pi)} & \pi \le \beta \le 2.\pi \end{cases}$$

$$A_j(\beta,\tau) = \begin{cases} 0 & 0 \le \beta \le \pi \\ \dfrac{H_j(\beta,\tau).H_o(\pi) - H_o(\beta).H_j(\pi,\tau)}{H_o(\pi)^2} & \pi \le \beta \le 2.\pi \end{cases}$$

Therefore the boundary conditions can now be expressed for the zero orbit and the perturbed orbit by equations 3.3.15 and 3.3.16. The formulation of the boundary conditions require an understanding of the thermal conditions in the bearing and journal, and the orbit perturbed temperatures are functions of the zero orbit temperature.

Zero orbit boundary conditions:

$$T_o(0,\beta,\tau) = T_{Bo}(1,\beta,\tau) \qquad \frac{\partial T_o}{\partial \eta}(0,\beta,\tau) = -\gamma_B . A_o(\beta) . \frac{\partial T_{Bo}}{\partial r}(1,\beta,\tau)$$

$$T_o(1,\beta,\tau) = T_{Jo}(1,\theta,\tau) \qquad \frac{\partial T_o}{\partial \eta}(1,\beta,\tau) = -\gamma_J . A_o(\beta) . \frac{\partial T_{Jo}}{\partial r}(1,\theta,\tau)$$

(Eq. 3.3.15)

Perturbed orbit boundary conditions:

$$\left.\begin{aligned} & T_j(0,\beta,\tau) = T_{Bj}(1,\beta,\tau) \\ & \frac{\partial T_j}{\partial \eta}(0,\beta,\tau) + \gamma_B . A_o(\beta) . \frac{\partial T_{Bj}}{\partial r}(1,\beta,\tau) = -\gamma_B . A_j(\beta,\tau) . \frac{\partial T_{Bo}}{\partial r}(1,\beta,\tau) \\ & T_j(1,\beta,\tau) = T_{Jj}(1,\theta,\tau) \\ & \frac{\partial T_j}{\partial \eta}(1,\beta,\tau) + \gamma_J . A_o(\beta) . \frac{\partial T_{Jj}}{\partial r}(1,\theta,\tau) = -\gamma_J . A_j(\beta,\tau) . \frac{\partial T_{Jo}}{\partial r}(1,\theta,\tau) \end{aligned}\right\} \quad \text{(Eq. 3.3.16)}$$

3.3.5 Bearing and Journal Conduction

As the model presented by Keogh et al [9] provides a full thermodynamic account of the oil film bearing and journal interactions, the relationships governing this interaction are developed and presented. The equations, coefficients and boundary conditions developed by Keogh et al [9] for the conduction terms are presented here without proof in equations 3.3.17 and 3.3.18.

It is shown by Keogh et al [9] that the periodic heat inputs via the lubricant film for the axially averaged bearing and journal and journal temperatures at the lubricant interface can be expressed in the following non dimensional form:

$$T_B(1,\beta,\tau) = T_A + \sum_{-\infty}^{\infty}\sum_{-\infty}^{\infty} \frac{q_{mn}}{h_{mn}} . e^{i(n\beta + m\tau)}$$

(Eq. 3.3.17)

$$\frac{\partial T_B}{\partial r}(1,\beta,\tau) = \sum_{-\infty}^{\infty}\sum_{-\infty}^{\infty} q_{mn}.e^{i(n\beta+m\tau)}$$

$$T_J(1,\theta,\tau) = T_A + \sum_{-\infty}^{\infty}\sum_{-\infty}^{\infty} \frac{p_{mn}}{g_{mn}}.e^{i(n\theta+m\tau)}$$

(Eq. 3.3.18)

$$\frac{T_J}{\partial r}(1,\theta,\tau) = T_A + \sum_{-\infty}^{\infty}\sum_{-\infty}^{\infty} p_{mn}.e^{i(n\theta+m\tau)}$$

The terms p_{mn} and g_{mn} are thermal coefficients of the axially averaged temperatures and heat fluxes which relate the time and special Fourier components at the lubricant interfaces for the journal and bearing. Keogh et al [9] states that for typical material, geometric and operating parameters, the time harmonic coefficients have significantly higher magnitudes than those of the stationary coefficients (where *m*=0). These coefficients are used to implement the boundary conditions on the lubricant at the shaft journal and bearing interfaces. The appropriate form for the feature of interest, the shaft journal temperature is given by equation 3.3.19. As the elements which dictate the steady rotor bend are primarily of interest and it is stated by Keogh that it is shown that the thermal shaft bend is governed by the magnitude of the thermal coefficient g_{mn} where m=0 and n=-1.

$$T_J(1,\theta,\tau) = T_A + \sum_{-\infty}^{\infty}\sum_{-\infty}^{\infty} \frac{p_{mn}}{g_{mn}}.e^{i(n\theta+(m-n)\tau)}$$

(Eq. 3.3.19)

$$\frac{T_J}{\partial r}(1,\theta,\tau) = \sum_{-\infty}^{\infty}\sum_{-\infty}^{\infty} p_{mn}.e^{i(n\beta+(m-n)\tau)}$$

Details of the methods used to determine and solve for p_{mn} and g_{mn} are given in appendix B of reference [9].

3.3.6 Lubricant Temperature Development

The next step is to consider expressions for the development of the lubricant around the bearing in both space and time. The expressions below are for steady state conditions of orbit whirl where the temperatures are seen to oscillate in time periodically with the shaft rotation, and where transient effects are ignored. From the assumptions and evaluations previously taken, it can

be considered that the zero orbit temperatures are steady and the orbit temperatures vary steadily with time, consisting of fundamental harmonic components only. The following expressions are used to describe the temperature conditions for the zero and perturbed orbit components :

$$T_o(\eta,\beta,\tau) = T_A + S_o(\eta,\beta) \quad \text{(Eq. 3.3.20)}$$

$$T_j(\eta,\beta,\tau) = S_j(\eta,\beta).e^{i\tau} + \overline{S_j(\eta,\beta).e^{-i\tau}} \quad \text{(Eq. 3.3.21)}$$

Equation 3.3.20 requires term *So* to be determined. Due to the discontinuity in temperature distribution at the oil inlet, a Fourier series in isolation cannot be applied to obtain a solution and some account for the 'step' change that takes place at the inlet is required. The discontinuity at the inlet is as a result of the re-circulating oil within the bearing being refilled with fresh supply oil to maintain the continuity of flow around the bearing. Keogh et al [9] presents a form of expression where for a bearing with a single inlet, the discontinuity can be described by means of two terms V_o and U_o. The orbit temperature is then written :

$$S_o(\eta,\beta) = U_o(\eta).\beta + \frac{V_o(\eta).\beta^2}{2} + \sum_{-\infty}^{\infty} W_{ok}(\eta).e^{ik\beta} \quad \text{(Eq. 3.3.22)}$$

As the oil film is being considered in two dimensions some knowledge of the form of the discontinuity across the oil film is required, which will be governed by the mixing conditions around the oil inlet. Due to the complexity of this problem Keogh et al [9] defines expressions for the approximation of V_o and U_o by developing and applying the following conditions and relationships :

$$S_o = s_o = 0 \qquad \text{at } \beta = 0$$

$$\frac{\partial S_o}{\partial \beta} = 2.\pi.V_o = 0$$

$$\frac{\partial^2 S_o}{\partial \eta^2} = \ddot{s}_o$$

$$s_o(\eta=0) = s_o(\eta=1) = 0 \qquad V_o(\eta=0) = V_o(\eta=1) = 0$$

Keogh et al [9] proposes the approximation given by equation 3.3.23 to allow a solution for the temperature due to the unknown mixing conditions present at the inlet.

$$\ddot{s}_o(\eta) = \Delta.\eta^2.(1-\eta) \quad \text{(Eq. 3.3.23)}$$

Where V_o and s_o would now be given:

$$V_o(\eta) = \frac{\Delta.\eta.(1-\eta)}{2.\pi.P_e.H_o(0)^2} \quad \text{(Eq. 3.3.24)}$$

$$s_o(\eta) = \Delta.\eta.\left(-\frac{1}{30}+\frac{\eta^3}{12}-\frac{\eta^4}{20}\right) \quad \text{(Eq. 3.3.25)}$$

The parameter Δ defines the magnitude of the temperature change at the inlet due to the mixing of the 'hot' re-circulating oil and 'cool' supply oil. To do this a mean cross film temperature is used where the inlet step change is given by :

$$[T_M]_{\beta=0} = 2.\int_0^1 \eta.s_o(\eta).d\eta = -\frac{99}{11340}.\Delta \quad \text{(Eq. 3.3.26)}$$

This value of Δ can by adjusted until the desired pad inlet conditions are obtained.

Keogh et al [9] applies a refill law at the inlet, where it is assumed the supply oil is sufficient to replenish the oil flow lost around the bearing, giving equation 3.3.27 which calculates the temperature of the pad oil inlet temperature.

$$T_S = \frac{1}{1-\left(\frac{H_o(\pi)}{H_o(2.\pi)}\right)}.[T_M]_{\beta=0} + T_M(2.\pi) \quad \text{(Eq. 3.3.27)}$$

With the procedure and expressions defined for determining the steady orbit lubricant pad inlet temperature and inlet discontinuity conditions, attention can now be given the development of the expressions used to solve for the infinite Fourier series terms $W_{0,k}$. For the steady zero orbit the application of equation

3.3.22 to the energy equations for the zero orbit conditions given in equations 3.3.12 and 3.3.15 , without proof, is given by Keogh et al [9] as the ordinary differential equation having the form :

$$\ddot{W}_{0,n} + P_e.\sum_{-\infty}^{\infty}\left(b_{n,-k}.\ddot{W}_{0,k} - ik.\eta.c_{n,-k}.W_{0,k}\right) = r_n \quad \text{(Eq. 3.3.28)}$$

Where the boundary conditions for the lubricant-bearing interface $(\eta = 0)$ is defined as :

$$\dot{W}_{0,n} + \gamma_B.\sum_{-\infty}^{\infty} a_{n,-k}.h_{0,k}.W_{0,k} = \begin{cases} -\pi.\left(\frac{2}{3}.\pi.\dot{V}_o + \dot{U}_o\right), n = 0 \\ -\frac{\dot{V}_o}{n^2} + \frac{\pi.\dot{V}_o + \dot{U}_o}{i.n}, n \neq 0 \end{cases} \quad \text{(Eq. 3.3.29)}$$

And at the lubricant-journal interface $(\eta = 1)$ is defined as :

$$\dot{W}_{0,n} + \gamma_J.\sum_{-\infty}^{\infty} a_{n,-k}.g_{k,k}.W_{0,k} = \begin{cases} -\pi.\left(\frac{2}{3}.\pi.\dot{V}_o + \dot{U}_o\right), n = 0 \\ -\frac{\dot{V}_o}{n^2} + \frac{\pi.\dot{V}_o + \dot{U}_o}{i.n}, n \neq 0 \end{cases} \quad \text{(Eq. 3.3.30)}$$

For the non zero orbit temperature solutions the same principle can be applied the orbit perturbed conditions. In this case however the solution is considered purely periodic with no discontinuity at the inlet location. As such the expression can be developed to consider only the fundamental harmonic components only. Therefore the non zero orbit temperature can be expressed by the following equation :

$$S_j(\eta, \beta) = \sum_{-\infty}^{\infty} W_{j,k}(\eta).e^{i.k.\beta} \quad \text{(Eq. 3.3.31)}$$

And similarly to the zero obit condition the ordinary differential equation to be solved for the perturbed condition is given, again without proof, by Keogh et al [9] as :

$$\ddot{W}_{j,n} + P_e.\sum_{-\infty}^{\infty}\left(b_{n,-k}.\dot{W}_{j,k} - ik.\eta.c_{n,-k}.W_{j,k} - ic_{n,-k}.W_{j,k}\right) = r_{j,n} \quad \text{(Eq. 3.3.32)}$$

With the applied boundary conditions at the lubricant interfaces of :

At the lubricant-bearing interface $(\eta = 0)$:

$$\dot{W}_{j,n} + \gamma_B.\sum_{-\infty}^{\infty} a_{n,-k}.h_{1,k}.W_{j,k} = s_{j,n}, \eta = 0 \quad \text{(Eq. 3.3.33)}$$

At the lubricant-journal interface $(\eta = 1)$:

$$\dot{W}_{j,n} + \gamma_J.\sum_{-\infty}^{\infty} a_{n,-k}.g_{1+k,k}.W_{j,k} = t_{j,n}, \eta = 1 \quad \text{(Eq. 3.3.34)}$$

Expressions for the coefficients $s_{j,n}$ and $t_{j,n}$ are presented in appendix A of [9]. Where they are expressed in terms of the steady state zero orbit condition. The infinite system of resulting differential equations describing the lubricant film temperatures is solved by truncation of the infinite series using Chebyshev collocation techniques [46]. The zero orbit condition is first solved which then allows the orbit perturbed solutions to be determined, with the procedures for both the zero and perturbed orbit solutions following the same procedure. It is stated by Keogh et al [9] that the infinite series were typically truncated to 10 harmonics.

3.3.7 Prediction of Rotor Bend

The shaft bend can be expressed in terms of bend angles in the referenced transverse axis of the journal, ψ_x, ψ_y as shown in Figure 10. The methods presented by Dimogronas [3] for the description of shaft bend due to thermal influences, is applied for the analysis of the shaft bend. Applying this analysis process, the shaft bend angle is expressed in complex form by:

$$\psi_C = \psi_x + i\psi_y = \frac{2.\alpha}{I}.e^{i\left(\phi_o + \frac{\pi}{2}\right)}.\int_0^R \int_0^{2.\pi} \int_0^{\frac{L_J}{2}} \Theta.\rho^2.e^{i\theta}.dz.d\theta.d\rho \quad \text{(Eq. 3.3.35)}$$

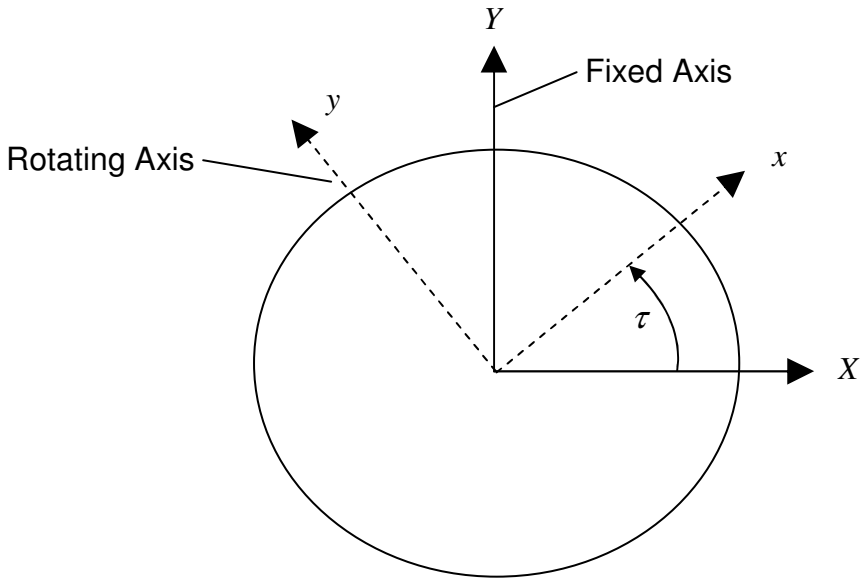

Figure 10 Axis About which Rotor Bend Angles are Defined

It can be concluded that the complex bend angle can take the form of equation 3.3.35. As the procedure involves the integration of the temperature distribution across the entire journal cross section (assuming an axially averaged temperature distribution), it can be seen that the only steady bend conditions in the rotor are produced as a result of the fundamental perturbed orbit harmonic. Other higher order harmonics will only result in small osolations during the shaft rotation, due principally to the thermal inertia of the shaft when running at operating conditions and speeds typical for such machines. Therefore as the synchronous rotor dynamic response is governed only by the steady rotor bend, it can be written that the bend angle can be expressed by equation 3.3.37.

$$\psi_C = \psi_{C0} + \in_1 .\psi_{C1} + \in_2 .\psi_{C2} \quad \text{(Eq. 3.3.36)}$$

$$\psi_C = \in_1 .\psi_{C1,0} + \in_2 .\psi_{C2,0} + \text{ small oscillating terms} \quad \text{(Eq. 3.3.37)}$$

Where $$\psi_{Cj,0} = iP_{0,-1}.W_{j,-1}(1).e^{i\phi_o} \quad \text{(Eq. 3.3.38)}$$

3.3.8 Bend Influence on Rotor Dynamic Systems

To now handle the dynamic response of the shaft, the bend angle ψ_C needs to be translated into dynamic rotor displacement characteristics capable of being modelled using typical rotordynamic evaluation techniques. Initially the bend angle must be described and is given by Keogh et al [9] as :

$$\psi_C = B_X . z_{Xb} + B_Y . z_{Yb} \quad \text{(Eq. 3.3.39)}$$

Where, when expressed in terms of radial clearance, the dimensionless terms B_X and B_Y are calculated in terms of the non zero orbit conditions by :

$$B_X = \frac{\psi_{C1,0} + \psi_{C2,0}}{2}$$

$$B_Y = \frac{i\left(\psi_{C1,0} + \psi_{C2,0}\right)}{2} \quad \text{(Eq. 3.3.40)}$$

The degenerated bend angle ψ_C needs now to be incorporated in the equations of motion governing the rotordynamic system. To do this, using typical solution methods, the system degree of freedom matrix χ needs to embody not only the generalised deflections in the two principle axis but also the components resulting from the bend angle χ_B, where the total system degree of freedom matrix is given by :

$$\chi_T = \chi + \chi_B \quad \text{(Eq. 3.3.41)}$$

Where if the influence of any external forces are ignored, the equation of motion for a rotordynamic system can now be expressed by :

$$M_R . \ddot{\chi}_T + \left(C_b + \Omega . I_R\right) . \dot{\chi}_T + \left(K_R + K_b\right) . \chi_T = K_R . \chi_B \quad \text{(Eq. 3.3.42)}$$

Where M_R, I_R and K_R are the rotor mass, gyroscopic and stiffness matrices respectively. The bearing performance characteristics are included into the equation of motion by the C_b and K_b matrices which define the bearing stiffness and damping oil film coefficients.

Keogh et al [9] partitions the degree of freedom vector into the X and Y fixed coordinate directions where the bend angle is then expressed as :

$$\chi_B = \mathrm{Re}\left(c.\psi_{Ci}.U_B.e^{i\Omega.t}\right) \quad \text{(E1. 3.3.43)}$$

Where U_B is of the form :

$$U_B = \begin{bmatrix} U \\ -iU \end{bmatrix}$$

The complex synchronous response Z is then solved by means of the steady state particular solution of the equation of motion (3.3.42) which satisfies equation 3.3.44, D is given by equation 3.3.45 and describes the constant elements of the equation of motion:

$$\chi_T = \mathrm{Re}\left(c.Z.e^{i\Omega.t}\right) \quad \text{(Eq. 3.3.44)}$$

$$D.Z = \psi_{Ci}.K_R.U_B \quad \text{(Eq. 3.3.45)}$$

$$D = -\Omega^2.M_R + i\Omega.\left(C_b + \Omega.I_R\right) + K_R + K_b \quad \text{(Eq. 3.3.46)}$$

Once the system of linear equations has been solved for the steady state synchronous response the complex bend angles can be extracted at the bearing location and the resulting thermal bend as a result of the system response determined using equation 3.3.46 to obtain z_{Xb} and z_{Yb}.

In order to identify some means of qualification of the system sensitivity to thermal rotor bending, Keogh et al [9] presents a procedure whereby the resulting thermal bend is determined for an initial static shaft bend and the gain of the bend development can be expressed by equation 3.3.48.

$$\psi_{Ct} = B_X.z_{Xb} + B_Y.z_{Yb} \quad \text{(Eq. 3.3.47)}$$

$$G = \frac{\psi_{Ct}}{\psi_{Ci}} \quad \text{(Eq. 3.3.48)}$$

Keogh et al [9] clarifies that the analysis gives no indication of time dependant development of the thermal bend due to the steady state assumption for the thermal conditions within the lubricant for both zero and perturbed forms. However, it is stated by Keogh et al [9] that where thermal bend development is considered significantly slower than the dynamic response, $\mathrm{Im}G > 0$ then rotor vibration will spiral with the direction of rotation and when $\mathrm{Im}G < 0$ the it will spiral in an opposing direction. With regards to commentary as to a systems stability Keogh et al [9] summarises that if follows that if $\mathrm{Im}G = 0$ then $\mathrm{Re}G > 1$ would result in unstable development of the thermal bend for synchronous orbit excitations.

3.4 Balbahadur [19] Procedure

A method of analysis is presented by the work of Balbahadur [19] where a simplified analytical evaluation is presented. Here a thermal bend development and stability assessment criteria is developed. The procedure is principally concerned with developing a technique in which the film thickness equation is established for both plain and tilting pad journal bearings, where an energy equation is then used to establish a temperature condition at specific locations in the bearing. Finally this is used to establish a thermally developed bend which is compared to a defined stability threshold. The analytical procedures applied and presented by Balbahadur [19] are reworked here with the associated derivations where relevant.

3.4.1 Relationships for film thickness

To enable the Reynolds conditions and subsequent thermal conditions within the bearing to be evaluated, two sets of equations are presented to describe the oil film thickness around the bearing. The two conditions described by Balbahadur [19] were for the simple plain cylindrical bearing and the central pivot tilting pad bearing.

Plain Bearing

The oil film thickness function derived by Balbahadur [19] is consistent with that presented in most literature for a plain cylindrical bearing with no misalignment present and is stated (without proof) by equation 3.4.1.

$$h = C_r(1+\varepsilon.\cos\beta) \quad \text{(Eq. 3.4.1)}$$

Figure 11 shows the geometric relationships for film thickness in a plain cylindrical bearing.

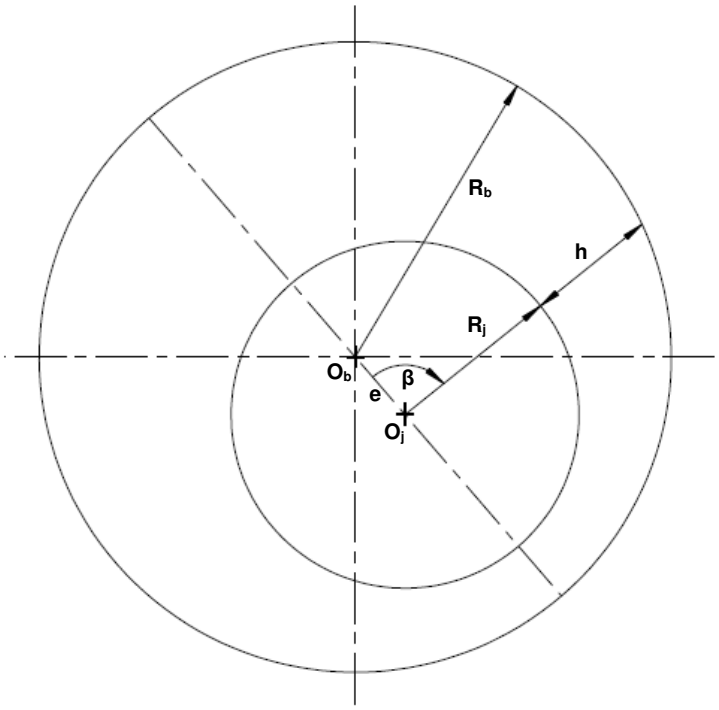

Figure 11 Plain Cylindrical Bearing Film Thickness Function

Where $\varepsilon = \frac{e}{C_r}$

Tilting Pad Bearing

The analytical description of the oil film function for the titling pad bearing requires a slightly more complex derivation and a specifically derived film function is presented in [19]. Figure 12 shows a schematic diagram of the geometry relations present in a tilting pad bearing. The figure shows a bearing with 5 pads but bearings with any practical number of pads can be employed.

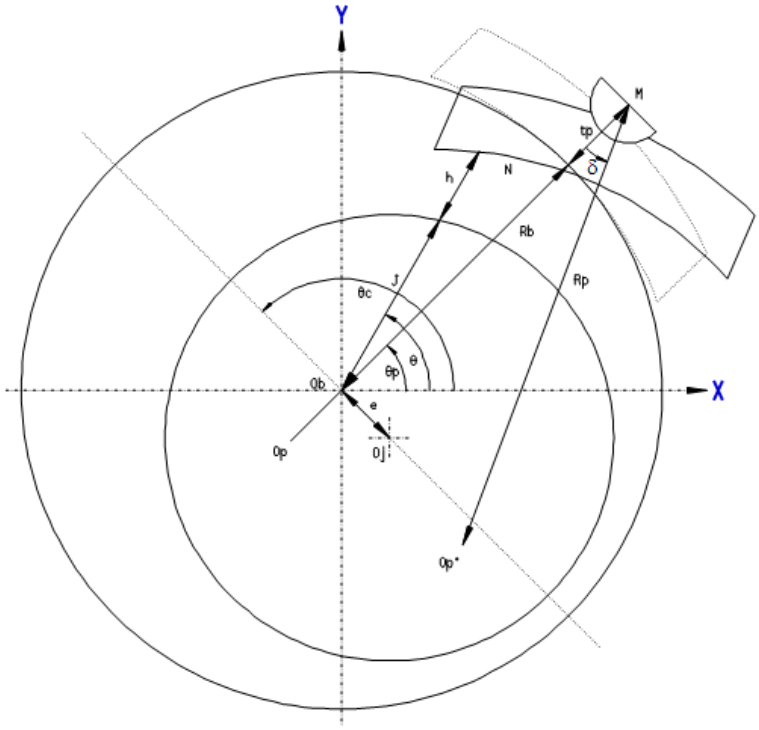

Figure 12 Tilting Pad Bearing Geometric Relationships

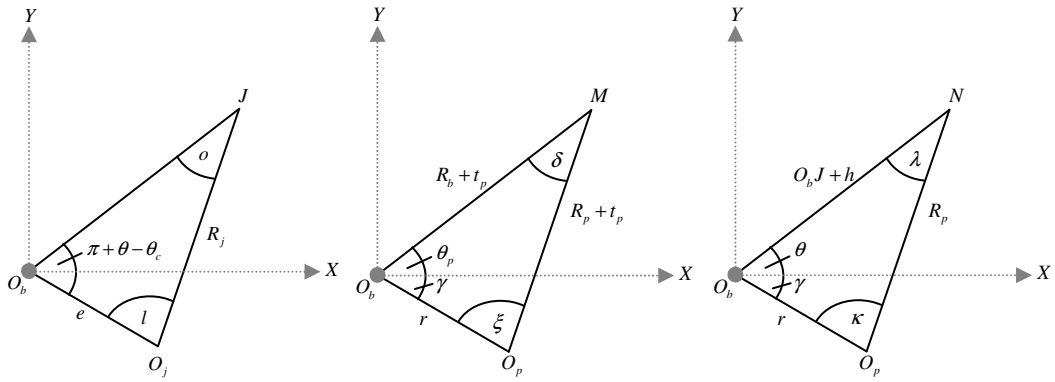

(a) (b) (c)

Geometric relationships from Figure 12

From Figure 12 it is possible to determine :

$$\frac{R_j}{\sin\left[\pi-\theta_c+\theta\right]}=\frac{e}{\sin(o)}=\frac{O_bJ}{\sin(\iota)} \quad \text{(Eq. 3.4.2)}$$

Solving this equation for o, ι and O_bJ gives :

$$o = \sin^{-1}\left[\frac{e.\sin(\pi - \theta_c + \theta}{R_j}\right] \quad \text{(Eq. 3.4.3)}$$

$$\iota = \pi - \left[\pi - \theta_c + \theta + o\right] = \theta_c - \theta - \sin^{-1}\left[\frac{e.\sin\left(\pi - \theta_c + \theta\right)}{R_j}\right] \quad \text{(Eq. 3.4.4)}$$

$$O_bJ = \frac{R_j.\sin(\iota)}{\sin(\pi - \theta_c + \theta)} \quad \text{(Eq. 3.4.5)}$$

Substituting equation 3.4.4 in to 3.4.5:

$$O_bJ = \frac{R_j}{\sin(\pi - \theta_c + \theta)}.\sin\left[\pi - \theta_c + \theta - \sin^{-1}\left[\frac{e.\sin\left(\pi - \theta_c + \theta\right)}{R_j}\right]\right] \quad \text{(Eq. 3.4.6)}$$

As the amount of eccentricity can be considered to be small relative to the bearing journal radius for practical bearings it follows that the $\sin^{-1}$ term will approximate to be equal to is argument.

$$\sin^{-1}\left[\frac{e.\sin\left(\pi - \theta_c + \theta\right)}{R_j}\right] \approx \left[\frac{e.\sin\left(\pi - \theta_c + \theta\right)}{R_j}\right]$$

Hence

$$O_bJ = \frac{R_j}{\sin(\pi - \theta_c + \theta)}.\sin\left[\pi - \theta_c + \theta - \left[\frac{e.\sin\left(\pi - \theta_c + \theta\right)}{R_j}\right]\right] \quad \text{(Eq. 3.4.7)}$$

Applying trigonomic identities and expanding gives :

$$O_bJ = \frac{R_j}{\sin(\pi - \theta_c + \theta)}.\left[\begin{array}{l}\sin\left(\pi - \theta_c + \theta\right).\cos\left[\frac{e.\sin\left(\pi - \theta_c + \theta\right)}{R_j}\right] - \ldots\ldots \\ \ldots\ldots\cos\left(\pi - \theta_c + \theta\right).\sin\left[\frac{e.\sin\left(\pi - \theta_c + \theta\right)}{R_j}\right]\end{array}\right] \quad \text{(Eq. 3.4.8)}$$

By the application of small angle approximation for cos and sin terms, the significant analytical simplification results for equation 3.4.8 gives :

$$O_bJ = R_j - e.\cos(\pi - \theta_c + \theta) \quad \text{(Eq. 3.4.9)}$$

Now applying the sine rule to Figure 11 it can be shown that :

$$r = \sqrt{(R_p + t_p)^2 + (R_b + t_p)^2 - 2.(R_p + t_p).(R_p + t_p).\cos(\delta)} \quad \text{(Eq. 3.4.10)}$$

From Figure 11the following relationship can also be established:

$$\frac{R_p}{\sin(\theta + \gamma)} = \frac{r}{\sin(\lambda)} = \frac{O_bN}{\sin(\kappa)} \quad \text{(Eq. 3.4.11)}$$

Solving for λ:

$$\lambda = \sin^{-1}\left[\frac{r.\sin(\theta + \gamma)}{R_p}\right] \quad \text{(Eq. 3.4.12)}$$

For practical bearings the ratio of *r* to R_p will be much less than 1 which allows equation 3.4.12 to be simplified to :

$$\lambda \approx \left[\frac{r.\sin(\theta + \gamma)}{R_p}\right] \quad \text{(Eq. 3.4. 13)}$$

Equation 3.4.11 is then further rearranged and with the application trigonomic identities yields:

$$O_bN = \frac{R_p}{\sin(\theta + \gamma)}.\left[\sin(\theta + \gamma).\cos\left(\frac{r.\sin(\theta + \gamma)}{R_p}\right) + \cos(\theta + \gamma).\sin\left(\frac{r.\sin(\theta + \gamma)}{R_p}\right)\right]$$

(Eq. 3.4.14)

Again significant simplification is achieved by applying the principle of r<<Rp, and small angle assumptions resulting in:

$$O_bN = R_p \_ r.\cos(\theta + \gamma) \quad \text{(Eq. 3.4.15)}$$

Taking the following relationships from Figure 11

$$\gamma = \pi - \theta_p - \delta - \xi \quad \text{(Eq. 3.4.16)}$$

$$r.\sin(\xi) = (R_b + t_p).\sin(\delta) \quad \text{(Eq. 3.4.17)}$$

Substituting equation 3.4.16 into into equation 3.4.15 yields:

$$O_bN = R_p - r.\cos(\delta + \xi).\cos(\theta - \theta_p) - r.\sin(\delta + \xi).\sin(\theta - \theta_p) \quad \text{(Eq. 3.4.18)}$$

It is then shown that :

$$r.\cos(\xi) = \sqrt{r.(1 - \sin^2(\xi))} = \sqrt{r^2 - (R_b + t_p)^2.\sin^2(\delta)} \quad \text{(Eq. 3.4.19)}$$

Substituting for r into equation 3.4.19 gives :

$$r.\cos(\xi) = (R_p + t_p) - (R_b + t_p).\cos(\delta) \quad \text{(Eq. 3.4.20)}$$

From equations 3.4.17 and 3.4.20 and applying trig identities :

$$r.\cos(\delta + \xi) = r.\cos(\delta).\sin(\xi) = (R_p + t_p).\cos(\delta) - (R_b + t_p) \quad \text{(Eq. 3.4.21)}$$

$$r.\sin(\delta + \xi) = r.\sin(\delta).\cos(\xi) + r.\cos(\delta).\sin(\xi) = (R_p + t_p).\sin(\delta) \quad \text{(Eq. 3.4.22)}$$

A simplification is again presented where δ (pad angle) is considered to be very small and as such small angles would yield the following reduced equation :

$$r.\cos(\delta + \xi) = R_p - R_b \quad \text{(Eq. 3.4.23)}$$

and

$$r.\sin(\delta + \xi) = \delta.(R_p + t_p) \quad \text{(Eq. 3.4.24)}$$

Substituting equations 3.4.23 and 3.4.24 into equation 3.4.18 :

$$O_bN = R_p - (R_p - R_b).\cos(\theta - \theta_p) - \delta.(R_p + t_p).\sin(\theta - \theta_p) \quad \text{(Eq. 3.4.25)}$$

Using Figure 12 it can be seen that film thickness, h, can be expressed as:

$$h = O_b N - O_b J \quad \text{(Eq. 3.4.26)}$$

The full film thickness function is now assembled by substituting for equations 3.4.9 and 3.4.25:

$$h = \left(R_p - R_j\right) + e.\cos\left(\theta_c - \theta\right) - \left(R_p - R_b\right).\cos\left(\theta - \theta_p\right) - \delta.\left(R_p + t_p\right).\sin\left(\theta - \theta_p\right)$$

(Eq. 3.4.27)

This gives the fluid film function for tilting pad journal bearings as derived by Balbahadur [19].

A comparison is presented with another published film function algorithm for tilting pads bearings. The comparison is presented in Figure 13 is for the method presented by Balbahadur [19] and that of San Andres [47].

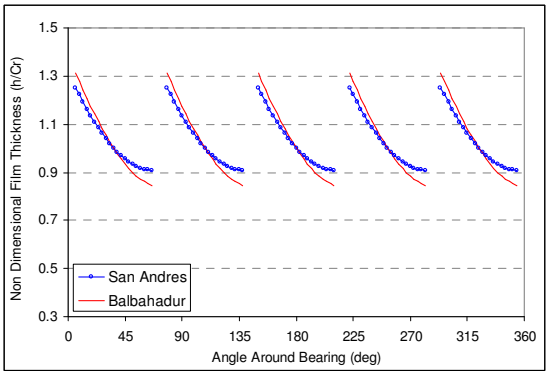

$\delta = 0.05, t = 9, \varepsilon = 0$

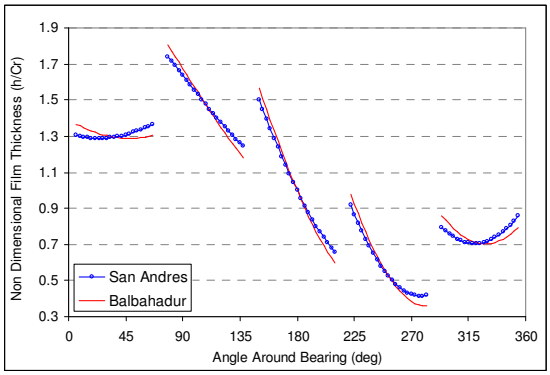

$\delta = 0.05, t = 9, \varepsilon = 0.5$

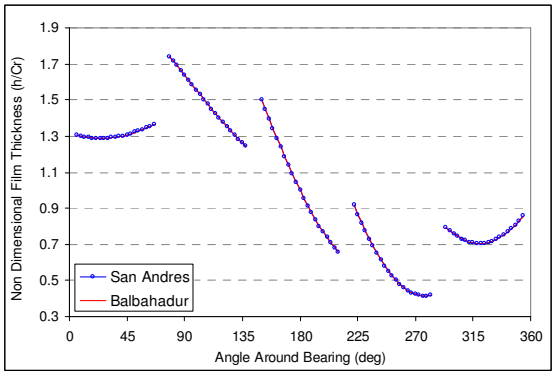

$\delta = 0.05, t = 0, \varepsilon = 0.5$

Figure 13 Tilting Pad Bearing Film Thickness Function Comparison 5 Pad, R_j=25 mm, C_d=0.125 mm, Pre-load=0.375, Load angle = 90°

As can be seen from Figure 13 the method derived here as presented by Balbahadur [19] generally compares well with that of San Andres [47] and other published data, although some discrepancies are apparent at the pad leading and trailing edges under certain conditions. Balbahadur [19] generally results in thinner oil films at the trailing edges of the pad. As can be seen from the Figure 13, the principle difference between the two methods is the influence of the account for the pad thickness. When the pad thickness is neglected the two methods produce the same result.

3.4.2 Journal Position and Perturbation (Solution of Reynolds equation)

To establish the static position of the bearing journal and dynamic translations of the shaft journal it is necessary to solve the Reynolds equation and determine the dynamic stiffness and damping bearing characteristics.

3.4.2.1 Plain Bearings

The solution of the Reynolds equation (Eq. 3.2.4), whilst subject to some transposition, is as presented by Cameron [43] for a plain cylindrical bearing. It is used to determine the steady state eccentricity ratio and attitude angle for a given journal load. Detailed derivations are not included as this is presented in detail by Cameron [43] and is the solution of the Reynolds equation applying short bearing theory and Ocvick and DuBois [41] boundary theory applying the half Somerfeld conditions. As such, no specific details of the derivation are presented here.

$$\frac{W_b.C_b^2}{\mu.\omega.R_j.L^3} = \sqrt{\frac{\pi^2.\varepsilon_0^2}{16.\left(1-\varepsilon_0^2\right)^3} + \frac{\varepsilon_0^4}{\left(1-\varepsilon_0^2\right)^4}} \quad \text{(Eq. 3.4.28)}$$

and for attitude angle :

$$\tan\left(\psi_{a0}\right) = \frac{\pi.\sqrt{1-\varepsilon_0^2}}{4.\varepsilon_0} \quad \text{(Eq. 3.4.29)}$$

To solve equation 3.4.29 for a specific load, it is necessary to know the viscosity conditions around the bearing which is a function of the oil film thickness and hence eccentricity ratio. This interdependency presents a

problem in the solution. The approach applied by Balbahadur [19] is that of an effective viscosity which now allows equation 3.4.28 to be solved for ε_o. Balabahadur [19] uses a curve fitted 8th order polynomial describing the right hand side (RHS) of equation 3.4.28 which is used to determine ε_o as a function of the left hand side (LHS) of equation 3.4.28. The polynomial solution presented by Balbahadur [19] can be found in appendix A of [19], although it should be noted that ε_o can be solved by using standard iterative techniques also.

The synchronous perturbation of the shaft journal is described as an elliptical orbit around the steady state journal centre O_j. Figure 14 shows the geometrical relationships of the elliptical orbit experienced by the synchronously orbiting journal. The locus of any point P on the journal surface is mathematically described by equation 3.4.30. The elliptical orbit geometric descriptions presented in Figure 14 can be linked to the geometric relationships used in the oil film thickness equations by equation 3.4.31.

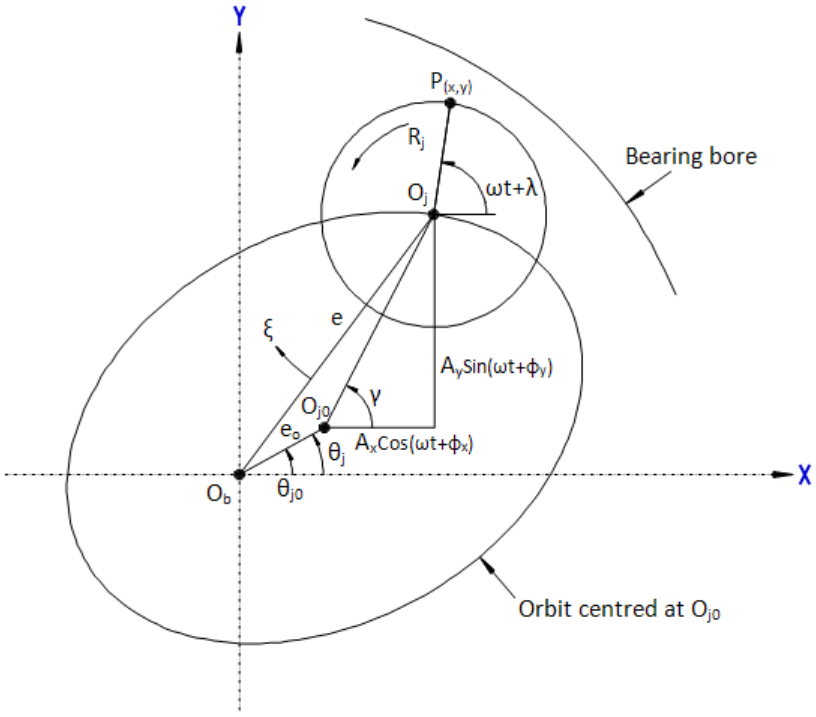

Figure 14 Geometric Relationships of Elliptical Synchronous Orbit

$$x = e_0.\cos\left(\theta_{j0}\right) + A_x.\cos\left(\omega.t + \phi_x\right) + R_j.\cos\left(\omega.t + \lambda\right) \quad \text{(Eq. 3.4.30 – a)}$$

$$y = e_0.\sin\left(\theta_{j0}\right) + A_y.\sin\left(\omega.t + \phi_y\right) + R_j.\sin\left(\omega.t + \lambda\right) \quad \text{(Eq. 3.4.30 – b)}$$

$$\xi = \pi - \left(\omega.t + \lambda - \theta_j\right) \quad \text{(Eq. 3.4.31)}$$

Where

$$\theta_j = \tan^{-1}\left[\frac{e_0.\sin\left(\theta_{j0}\right) + A_y.\sin\left(\omega.t + \phi_y\right)}{e_0.\cos\left(\theta_{j0}\right) + A_x.\cos\left(\omega.t + \phi_x\right)}\right] \quad \text{(Eq. 3.4.32)}$$

and $$\theta_{j0} = \frac{3.\pi}{2} + \psi_{a0} \quad \text{(Eq. 3.4.33)}$$

The hot spot on the shaft due to oil film shearing temperatures is defined by Balbahadur [19] as the point on the journal surface which is closest to the bearing surface at time (t)=0. Which when applied to Figure 14 yields the following at t=0:

$$\gamma = \gamma_0 = \tan^{-1}\left(\frac{A_y.\sin\left(\phi_y\right)}{A_x.\cos\left(\phi_x\right)}\right) = \lambda \quad \text{(Eq. 3.4.34)}$$

Where the assumption is that $\gamma = \omega.t + \lambda$ which results in the points O_{j0}, O_j and point P aligning on a common straight line.

Taking the definition for γ_0 and applying this to equations 3.4.30 (a) and (b) allows the hot and cold spots to be defined for any point on the elliptical orbit locus, i.e. $t > 0$.

$$x_H = e_0.\cos\left(\theta_{j0}\right) + A_x.\cos\left(\omega.t + \phi_x\right) + R_j.\cos\left(\omega.t + \gamma_0\right)$$

$$y_H = e_0.\sin\left(\theta_{j0}\right) + A_y.\sin\left(\omega.t + \phi_y\right) + R_j.\sin\left(\omega.t + \gamma_0\right) \quad \text{(Eq. 3.4.35)}$$

$$x_C = e_0.\cos\left(\theta_{j0}\right) + A_x.\cos\left(\omega.t + \phi_x\right) + R_j.\cos\left(\omega.t + \gamma_0 + \pi\right)$$

$$y_C = e_0.\sin\left(\theta_{j0}\right) + A_y.\sin\left(\omega.t + \phi_y\right) + R_j.\sin\left(\omega.t + \gamma_0 + \pi\right) \quad \text{(Eq. 3.4.36)}$$

In the polar coordinate system of reference the following results :

$$\xi_H = \pi - \left(\omega.t + \gamma_0 - \theta_j\right) \quad \text{(Eq. 3.4.37)}$$

$$\xi_C = \theta_j - \omega.t - \gamma_0 \quad \text{(Eq. 3.4.38)}$$

For the solution of the perturbation equations it is a pre-requisite that the amplitude and phase terms in the X and Y axis $\left(A_X, A_Y, \phi_X, \phi_Y\right)$ are known. Balbahadur [19] extracts these parameters by means of a rotordynamic software package which solves the rotor system under consideration for a forced response condition by means of the Transfer Matrix method - although any suitable rotordyanmic analysis software or procedure can be used to establish this information.
The stiffness and damping coefficients associated with the bearing are determined by the procedures presented by Vance [48]. The coefficients for stiffness K_{xx}, K_{xy}, K_{yx}, K_{yy} and damping C_{xx}, C_{xy}, C_{yx}, C_{yy} are then computed for the specific operating condition and used by the computer programme solving for the mechanical unbalance response characteristics. Details of the analytical procedures used to determine the stiffness and damping characteristics of plain journal bearings are presented in several literature sources and as such details of the derivations are not presented here.

3.4.2.2 Tilting Pad

To solve the more geometrically complex tilting pad bearing accounting for the introduced angular degrees of freedom, a numerical procedure is necessary to determine a solution. In the work presented by Balbahadur [19] a finite element method (FEM) is applied to establish the journal static equilibrium position within the bearing. As with the plain bearing, a method of solution of the Reynolds equation is required to determine the pressure distribution, and based on the calculated pad pressure distribution, the resulting forces and moment must be resolved to establish a point of equilibrium for each pad and collectively between all pads.

Balbahadur's [19] finite element formulation for the pressure distribution calculations is based around the solution of the reduced Reynolds equation for two dimensional flow and uses the equation 3.2.3 as presented earlier in this chapter.

A brief overview of the analytical model is presented here, however specific details of the finite element formulations and matrices assemblies is not repeated here as it does not directly related to the topic of this paper.

Balbahadur [19] solves the Reynolds equation problem by means of a discreatised domain of the pad surface as shown in Figure 15. The FEM modelling techniques applied incorporate the use of 'h' type linear quadrilateral elements where mesh refinement was used to obtain acceptable levels of convergence for the pad pressure distributions.

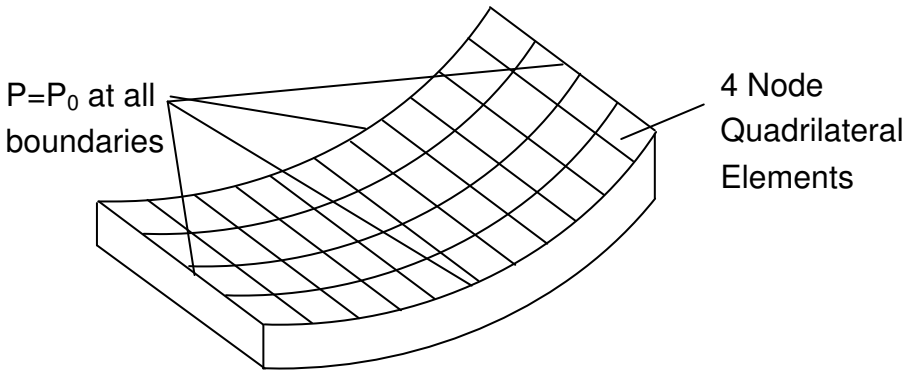

Figure 15 Discreatised FEM mesh of a single tilting pad

After some work the finite element formulation of the Reynolds approximation is given as:

$$\sum_{j=1}^{NPE} KE_{i,j}.P_j = FE_i \quad \text{(Eq. 3.4.39)}$$

Where $KE_{i,j}$ is the element stiffness matrix and $FE_{i,j}$ is the vector of the element loads and these are given by :

$$KE_{i,j} = \iint_{element} \frac{h^3}{\mu}.\left[\frac{\partial \phi_i}{\partial x}.\frac{\partial \phi_j}{\partial x} + \frac{\partial \phi_i}{\partial z}.\frac{\partial \phi_j}{\partial z}\right].dA \quad \text{(Eq. 3.4.40)}$$

$$FE_i = -\iint_{element} \phi_i.\left[6.u_j.\frac{\partial h}{\partial x}\right].dA \quad \text{(Eq. 3.4.41)}$$

Using equation 3.4.39 the associated global stiffness and force matrices are assembled using linear basis functions and their associated derivatives. The boundary conditions are then applied to the global matrices and the system of equations solved for the nodal pressure values. Balbahadur [19] details a

computer based programme to conducted the procedure of building and solving the associated finite element formulations which are included in appendix B of ref [19]. The boundary conditions applied to the pad by Balbahadur [19] are that the pressure P, at the four boundaries of the pad under evaluation, are set equal to the lubricant supply pressure P_0.

The converged equilibrium solution is obtained by determining the moment on each pad based on the approximated pad pressure distributions, and for equilibrium to be present, the pad moment must be equal to zero. The resulting forces on the journal are also evaluated. By movement of the shaft it is possible to establish the forces in the X and Y directions, the resultant of which has to balance the radial load applied to the bearing W_b. The balanced solution is achieved for a given set of operating parameters by varying the individual pad angles δ and the journal eccentricity e_o. An iterative technique based on Newton-Raphson is employed to solve the finite element formulations to a specified level of force convergence between the *X, Y* loads on the bearing journal and the applied radial load.

The method for defining the synchronous shaft orbit uses the same method as that adopted for the plain bearing problem (I.e. the response is calculated by a third party rotordynamic package for a given set of bearing film stiffness and damping coefficients and rotor unbalance condition). Balbahadur determines the stiffness and damping coefficient by means of the same finite element formulation but now also introducing the time dependant term $\frac{\partial h}{\partial t}$ in to the Reynolds equation. The bearing pad tilt angle velocity is considered to be $\frac{\partial \delta}{\partial t} = 0$. The stiffness and damping terms are then used to solve the rotordyanmic response shaft orbits across the desired speed range for synchronous unbalance.

3.4.3 Energy Equations and Journal Temperature

A key feature of the thermal instability model is to establish the temperature distribution around the circumference of the shaft journal. To enable a quantities assessment to be undertaken the development and application of some form of energy relationship is required which considers both the oil film and journal as a minimum.

A simple energy model is presented by Balbahadur [19] which considers the energy flow in a plain journal bearing which consists of a control box encompassing the oil film and a section of the bearing and journal surfaces. The model assumes steady state conditions within the control box, no axial heat flow and significantly that the net journal temperature is obtained by averaging the distribution determined for each dynamic location within the orbit.

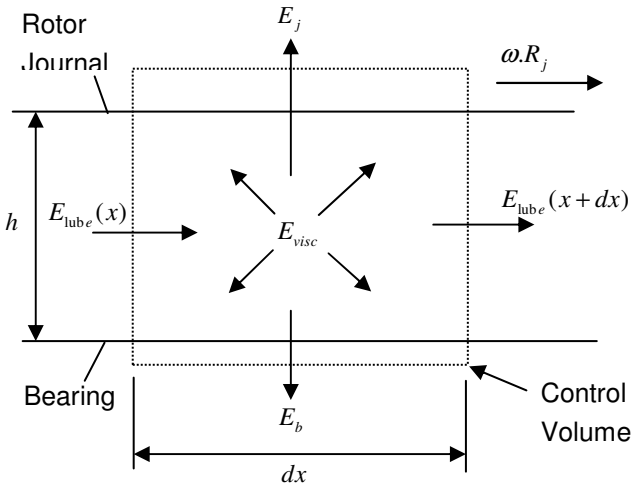

Fig 15b Simple Energy Model Presented by Balbahadur [19]

To maintain the conservation of energy and hold true to the steady state assumption, the following energy equation is presented, where the energy accumulation rate is zero.

$$\dot{E}_{visc} = \left(\dot{E}_{\mathrm{lub}(x+dx)} - \dot{E}_{\mathrm{lub}(x)} + \dot{E}_j + \dot{E}_b \right) \quad \text{(Eq. 3.4.41)}$$

Of the energy generated due to the viscose shear stress in an element (dx,dz) of the oil film for a specific point around the bearing, the energy lost to the journal and bearing is written by Balbahadur [19] as :

$$\dot{E}_j + \dot{E}_b = f.H.dx.dz.\left(T - T_{amb}\right) + \left(1 - f\right).H.dx.dz.\left(T - T_{amb}\right) \quad \text{(Eq. 3.4.42)}$$

Where H is the heat transfer coefficient for the bearing and journal between the lubricant oil film, f is a fraction which defines the proportion of energy that is transferred to the journal with the remainder being dispersed into the bearing shell, housing and surroundings.

Applying substitutions into equation 3.4.41 and introducing appropriate terms to describe the heat source in the oil film, the energy present within the oil flowing into and out of the element *dx* gives equation 3.4.43 as presented by Balbahadur [19]:

$$\omega.R_j.\tau = \rho_1.h.\frac{\omega.R_j.c_1}{2}.\frac{dT}{dx} + H.\left(T - T_{amb}\right) \quad \text{(Eq. 3.4.43)}$$

A key assumption to note at this point is that the total energy loss equates to $H.dx.dz.\left(T - T_{amb}\right)$ where T_{amb} = mean ambient journal temperature = mean ambient bearing housing temperature.

Applying a linear shear stress profile simplification, expressing *dx* in a polar domain and simplifying results in the following governing differential equation as presented by Balbahadur [19] :

$$\frac{d\,\overset{\square}{T}}{d\xi} + \frac{2.H}{\rho_1.c_1.\omega.h}.\overset{\square}{T} - \frac{2.\mu.\omega.R_j^2}{\rho_1.c_1.h^2} = 0 \quad \text{(Eq. 3.4.44)}$$

Where $\overset{\square}{T} = \left(T - T_{amb}\right)$ and is the temperature rise of the lubricant above ambient.

To enable the differential equation 3.4.44 to be solved, it is necessary to have some prior knowledge of the operating viscosity around the bearing. Balbahadur [19] selects to apply an ISO viscous model where an effective viscosity approach is applied. The effective viscosity is established by setting the bearing eccentricity to 0, setting $h = c_r$ and calculating the temperature rise over 180 degrees of the bearing for an oil inlet temperature and viscosity equal to the lubricant supply conditions. Using this temperature rise an effective viscosity μ_0 is calculated using Reynolds viscosity equation [43]. The application of the effective viscosity allows for equation 3.4.44 to be solved numerically for circumferential temperature distribution. The method of solution of the differential equation used by Balbahadur [19] was to apply a proprietary ordinary differential equation solver within the Matlab [49] software programming system.

Tilting Pad Bearings

The energy equation used for the temperature distribution in the tilting pad bearings uses the same fundamental expressions as defined above for the plain bearing problem, using equation 3.4.41. However due to the more complex film function descriptions, it is stated by Balbahadur [19] that a numerical solution method is required to solve the energy equation. Balbahadur employs a finite difference (FD) technique to solve the differential equation across a 1D discreatised grid, using Euler's method, and presents the FD solution to the energy equation as:

$$T_{i+1} = \left[1 - \Delta_\theta . \left(\frac{2.H}{\rho_1 . c_1 . \omega . h}\right)_i\right] . T_i + \Delta_\theta . \left(\frac{2.H.T_{amb}}{\rho_1 . c_1 . \omega . h} + \frac{2.\mu . \omega . R_j^2}{\rho_1 . c_1 . h^2}\right)_i \quad \text{(Eq. 3.4.45)}$$

To provide the required lubricant inlet temperature conditions Balbahadur [19] assumes a relationship between the lubricant supply temperature, average temperature rise (estimated) and ratio of oil film thickness for the pad under consideration. This relationship is defined as :

$$T_{in} = T_0 + \frac{h_{\min}}{h_{in}} . \Delta T_{mean} \quad \text{(Eq. 3.4.46)}$$

Where ΔT_{mean} = estimated average temperature rise

The purpose of the above equation is to provide some account for the principle that higher entry film thickness to a pad will result in lower pad inlet temperatures.

Different to the plain bearing, a specific relationship is used to determine the heat transfer coefficient H (into the bearing and journal) in equation 3.4.45 for the bearing based on work presented by Ettels [50] for the convective energy loss in variable geometry bearing pads, which is given by Ettels [50] as :

$$H = 25.5 . u_j^{0.7} . \mu_0^{-0.2} . \left(R_j . \Delta_p\right)^{-0.4} \quad \text{(Eq. 3.4.47)}$$

Where $R_j . \Delta_p$ = pad angular length

The effects of lubricant mixing, different heat transfer effects (journal to bearing) and the convective heat transfer in the bearing pockets were neglected and not considered in the analysis.

For both the plain and tilting pad bearing the temperature differential ΔT across the shaft journal is obtained by straight forward averaging of the temperature at point P for a number of positions around the shaft orbit. In the example case provided by Balbahadur [19], ten or more positions around the orbit for each condition are typically employed.

3.4.4 Thermal Unbalance and Stability Evaluation

With a model applied to determine the temperature conditions present within the bearing, it is now necessary to develop a relationship to this temperature distribution and the thermally induced synchronous forcing function and corresponding stability measure.

Balbahadur [19] uses a simple relationship equating a quasi-static bending moment to the shaft due to a linear transverse thermal strain. This strain is the then used to determine the bend angle of the shaft line at the non drive side of the bearing sleeve. The resulting angle is then used to calculate an eccentricity at the free end of the overhung shaft and the corresponding unbalance force is determined from the eccentricity, lumped overhung mass and operating shaft speed.

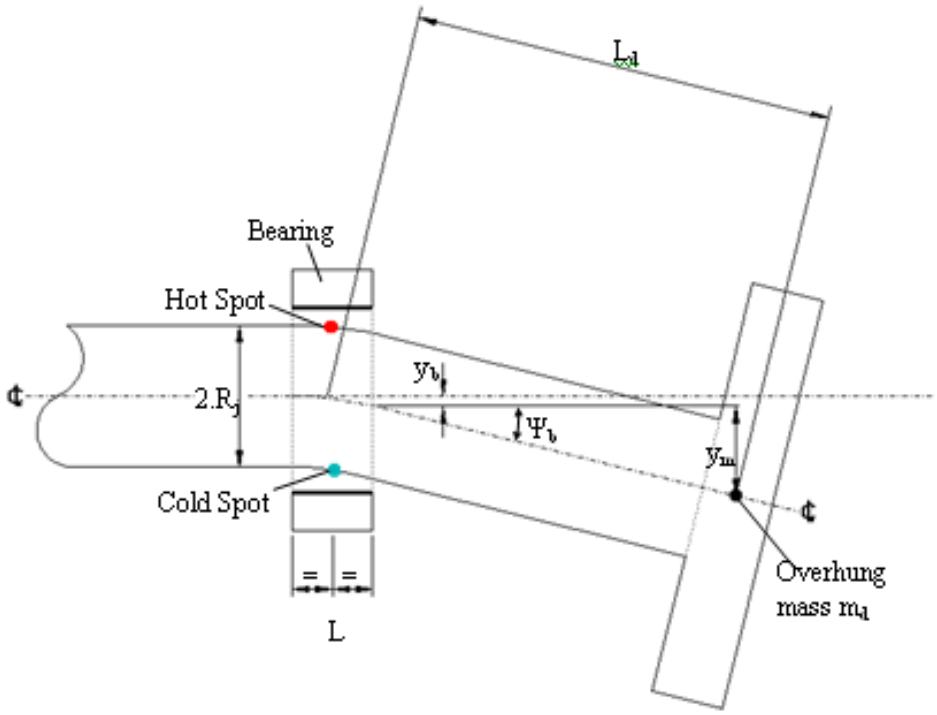

Figure 16 Rotor Thermal Bend Model

The following relationships are established to determine the unbalance force due to the overhung mass and thermal shaft bend:

Using Figure 16 the bending moment in the shaft can simply be described by:

$$M = E.I.\frac{d\psi}{dz} \quad \text{(Eq. 3.4.48)}$$

Where the stress is

$$\sigma_{\max} = \frac{R_j.M}{I} = E.\alpha.\Delta T \quad \text{(Eq. 3.4.49)}$$

and Balbahadur [19] introduces a relationship between the thermal expansion and ΔT, where ΔT is as defined in the previous energy equation solutions. ΔT is assumed to be constant across the bearing width.

Substituting the above yields:

$$\frac{d\psi}{dz} = \frac{\alpha.\Delta T}{R_j} \quad \text{(Eq. 3.4.50)}$$

Where integration with respect to *dz* and applying boundary conditions 0 and L gives :

$$\psi_b = \frac{\alpha.\Delta T.L}{R_j} \quad \text{(Eq. 3.4.51)}$$

Noting that $\psi = \frac{dy}{dz}$ and further integrating with respect to *dz* yields the centre line deflection at L as :

$$y_d = \frac{\alpha.\Delta T.L^2}{2.R_j} \quad \text{(Eq. 3.4.52)}$$

Where $y_d = y_b + y_m$

Applying the assumption of small angles :

$$y_d \approx \left(L_d - L/2\right).\psi_b \quad \text{(Eq. 3.4.53)}$$

Combining equations 2.34 and 2.35 :

$$y_d = \frac{\alpha.\Delta T.L.L_d}{R_j} \quad \text{(Eq. 3.4.54)}$$

With thermal unbalance being defined as :

$$U_t = m_d.y_d \quad \text{(Eq. 3.4.55)}$$

With a relationship for determining the magnitude of thermally induced unbalance presented, it is necessary to define a means of establishing some form of stability criterion.

The method presented by Balbahadur [19] vectorially combines the forces resulting from the thermally induced bend with the residual mechanical unbalance loads to produce a net unbalance force. These loads are combined applying the relative angular phase conditions of the hot spot and the residual mechanical unbalance. This can be analytically described as:

$$U = \sqrt{U_t^2 + U_m^2 - 2.U_t.U_m.\cos\left(\omega.t - \theta_{CH}\right)} \quad \text{(Eq. 3.4.56)}$$

The method by which Balbahadur [19] assesses the stability of the bearing rotor system is to define a constant threshold unbalance force which is then compared to the calculated resultant unbalance force for a given speed and response condition. If the thermal unbalance force is greater than the specified threshold the rotor is considered to be thermally unstable.

$$U_{thr} = \frac{f_{thr}.W}{\omega^2} \quad \text{(Eq. 3.4.57)}$$

Where f is a factor relating to a fraction of the rotor weight.

The value proposed by Balbahadur [19] to define the point at which instability would occur is when the value of $f_{thr} = 0.15$, i.e. 15% of the rotor weight. This level is suggested by Balbahadur [19] based on that it provides reasonable correlation with the case studies presented in Keogh and Morton [10], Faulkernker et al [12, 13] and de Jongh et al [11] rotor models within [19]. The

procedure applied to determine stability is to graphically plot U and U_{thr} for a specified speed range. Where the plots intersect, the instability threshold point is determined.

Chapter 4

Benchmark Examples

4. Benchmark Examples

4.1 Introduction

To enable a suitable test rig design to be produced it is necessary to obtain a suitable understanding of the coupled rotordynamic and hydrodynamic conditions present in rotors that have been observed to be susceptible to the Morton effect. Whilst little data is available for machines known to have experienced the phenomenon several pieces of published work are available which have be reported to have been subject to synchronous instabilities matching the characteristics of the Morton effect, see [11,13,14,31,32,37]. As it is well known that the rotordynamic conditions of the bearing system play such a significant part in the sensitivity of a rotor to thermally induced type instabilities, it has been the approach in this research that each of the cases is evaluated in detail rotordynamically to provide a summarised account of the specific conditions and performance conditions under which thermal instabilities are observed to be prevalent. The deliverable from this element of work is to provide a qualitative assessment and if possible identify some quantitative parameters that can be used, to guide as to whether a systems qualities make it susceptible to bearing induced thermal instability. These assessments are then taken to provide the principles on which the design rational for the experimental test rig can be based.

Detailed rotordynamic analysis is performed as part of this research for some selected published examples and the results and analysis of this work are presented here.

4.2 Benchmark example cases

The cases selected to provide the benchmark studies were obtained from the published literature and a single unpublished example. In total three rotor bearing systems were evaluated, each with subtly different operating and

physical parameters, but in all cases it was concluded that the instabilities observed were due to bearing thermally induced rotor bends.

The three cases taken that were studied:

1. deJong and Morton Rotor [11]
2. Faulkner, Strong and Kirk [12,13]
3. High Speed Overhung Compressor (HSOC)

Case studies 1 and 2 are covered in some detail in chapter 2 whereas case study 3 is an industrial example provided by a large OEM in support of this research. Case study 1 is considered the most informative benchmark case due to the greater amount of machine operation data being available, and also the inclusion of some temperature measurements. Cases 2 and 3 were industrial machines that were seen to observe instability characteristics consistent with the Morton effect, where only limited measurements were taken before practical in service solutions were implemented. The information available in all three cases is sufficient to enable definition of rotordynamic models to be created with the requirement for application of some relatively limited assumptions. The most significant area of assumption is around the specific detail of some of the bearing profiles and clearances; however the effects of small variations to these bearing properties can be tested and was performed in the cases shown here.

In each of these cases some basic rotordynamic data is provided in the published literature, however, to enable a suitable level of detail to be evaluated for this research it was considered necessary to conduct a separate rotordynamic analysis of each of the rotor-bearing systems during the research. The method of rotordynamic evaluation was conducted using a number of different systems during the initial research and design phases. Early work was carried out using a custom developed code using MatLab [49] applying a relatively simple transfer matrix modelling technique, however, whilst suitable initial characterisation of the rotordynamic performance was obtained, a more detailed and flexible rotordynamic approach was required. The final rotordyanmic analysis work was conducted using a proprietary package called Xlrotor [51] provided by RMA Inc, and all rotordynamic results presented within the thesis have been evaluated using this software package. Xlrotor [51] is a comprehensive rotordynamic evaluation suite which allows all necessary analytical procedures to be conducted, such as damped

eigenvalue extraction, rotor mode shapes, unbalance response and the use of unsymmetrical bearing stiffness-damping matrices.

All of the rotordynamic analysis and results data presented in this chapter hereafter has been performed, processed, assessed and presented as part of this research.

4.2.1 Rotordynamic principles applied in XLRotor [51]

Xlrotor [51] is a rotordynamic software package produced by Rotating Machinery Analysis, Inc (RMA) of the USA. The programme is a set of tools that are embeded within a proprietary spreadsheet environment, it allows the undamped and damped natural frequencies of rotor bearing systems to be computed. The software capability covers many rotordynamic procedures, not only lateral but also torsional and branched rotordynamic systems.

The features used for the work presented in this thesis are related to the lateral rotordynamic analysis features only. More specifically the undamaped natural frequency, damped eigenvalue, unbalance response and rotor deflected shapes analysis procedures have been employed.

The rotor dynamic model is based on a lumped mass model where the rotor is split into a number of elements or sections. Each section is represented by an elastic beam section where the beam mass for that section is split proportionally between each end of the beam element. The beam formulation used in the software is the Euler beam analytical model, where for longer beam sections (with L/D ratios > ~0.6) a correction factor is required to account for the additional moment inertia that results from the lumped mass distributions. Additional mass and/or inertias can be applied at each station by explicitly specifying the magnitudes required at a given station or location.

Bearings or supports are introduced as linear stiffness and damping components at a given station in the rotor model. As many support locations as desired can be introduced into the rotordynamic model. The mathematical model allows for unsymmetrical stiffness matrices and uses 8 specified oil film linearised stiffness and damping coefficients, i.e. both the direct and cross coupled coefficients K_{xx}, K_{xy}, K_{yx}, K_{yy} and C_{xx}, C_{xy}, C_{yx}, C_{yy}.. The bearing data is specified for a number of speed conditions and the stiffness and damping data is curve fitted across the required speed range and then calculated for each speed step in the solution process.

The principal theory governing the solutions of the dynamic models are by application of the governing equations of motion. Where the free-free damped natural frequency of a rotor-bearing system is governed by equation 4.2.1, and the unbalance response of the rotor system is similarly determined by application of the non trivial solution of the forced response relationship presented in equation 4.2.2.

Principal Equations of Motion

$$m.\frac{d^2u}{dt^2} + c.\frac{du}{dt} + k.u = 0 \quad \text{Eq. 4.2.1}$$

Forced harmonic excitation

$$m.\frac{d^2u}{dt^2} + c.\frac{du}{dt} + k.u = f.\cos(\omega.t) \quad \text{Eq. 4.2.2}$$

when applied to a discrete rotor system and expressed in matrix form is written :

$$M.\ddot{U} + (D+G).\dot{U} + K.U = F(\omega,t) \quad \text{Eq. 4.2.3}$$

where

m = mass	M = mass matrix
c = damping	C = damping matrix
k = stiffness	G=gyroscopic force matrix
u = displacement	K = stiffness matrix
ω = angular velocity	U = displacement vector
f = excitation force	F = time dependant force vector

The stiffness K and damping C matrices are unsymmetrical due to the cross coupling effects introduced by the journal bearing oil film interactions.

The numerical solution method used to solve for the eigen analysis and response analysis can be of the transfer matrix or FEM method. The transfer matrix method provides a quick and efficient solution but is restricted to non branched systems. The FEM method allows for the solution of branched systems but requires longer solution times. As the analysis required within the work presented in this thesis was limited to a single shaft line, then the Transfer Matrix solution was used exclusively for all of the rotordynamic work presented. The transfer matrix technique consists of considering the rotor as a

series of mass/inertia stations and beam/stiffness elements. Each station and element is represented by a pair of stiffness and mass matrices describing the analytical relationships for the principle degrees of freedom. The product of these matrices is then used to form the system matrix which can be solved iteratively for the associated eigenvalues of the system, where the iteration variable is rotational velocity ω. Any specific model will have as many eigen values as there are numbers of stations in the system. The associated eigen vector for a given eigenvalue allows for the rotor mode shapes to be expressed for any speed condition.

4.2.2 Case Study 1 – deJong and Morton [11]

In the work presented by de Jongh and Morton [11] two rotors are referenced which display the spiralling instability phenomenon associated with the Morton effect (see Figure 18). The second rotor is a slightly smaller rotordynamically scaled version of the first and it is this second rotor that is modelled because a more compressive set of data is available for its operation and measurement. A more detailed account of this example is given in the review of literature in chapter 2 and [11].

The data for the rotor was taken from that presented in de Jongh et al [11].

It was observed by de Jongh and Morton [11] that the rotor was very sensitive to unbalance in the overhung section of the rotor and, as part of the production testing, several overhung masses were evaluated. During the running of the rotor the vibration and phase data were recorded and plotted relative to time. It was observed that at a specific running speed of 11000 rpm the shaft vibration became unstable and steadily rose whilst at steady state speed and inlet temperature. This characteristic showed a hysteresis effect during the run up and run down phases. Here the rotordynamic conditions present during the running range observed are modelled. The following model looks at the original rotor overhung mass and also the impact of the reduced shaft end mass.

Figure 19 shows the discretised rotordynamic model used for the analysis of the rotor-bearing model. As the test compressor used in the work of de Jongh et al [11] consisted of a number of shrunk on discs, account was taken for these in the model by considering the additional stiffening effect of these components and the slight damping properties that such fits offer in flexible

rotors of this type. By means of comparison evaluation of the undmaped critical speeds is made with those presented by de Jongh et al [11], Figure 17. The results of this analysis are presented in Figure 20 by means of a critical speed map.

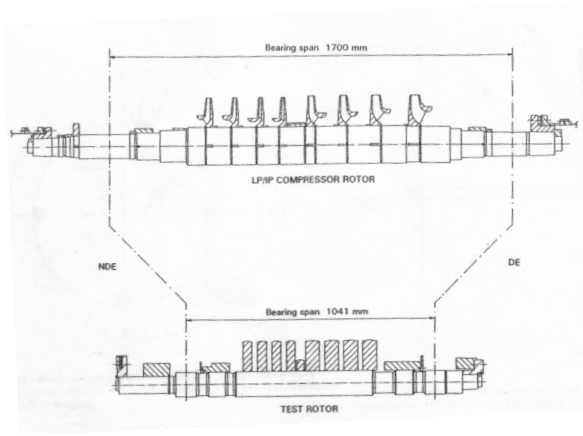

Figure 18 de Jongh and Morton [11] Compressor Rotors

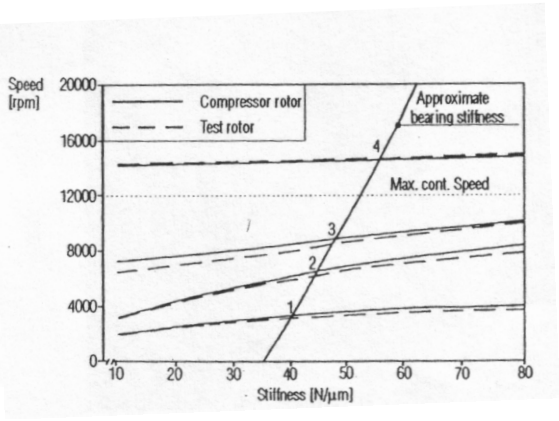

Figure 17 Undamped Critical Speed Map for Test Compressor Rotor

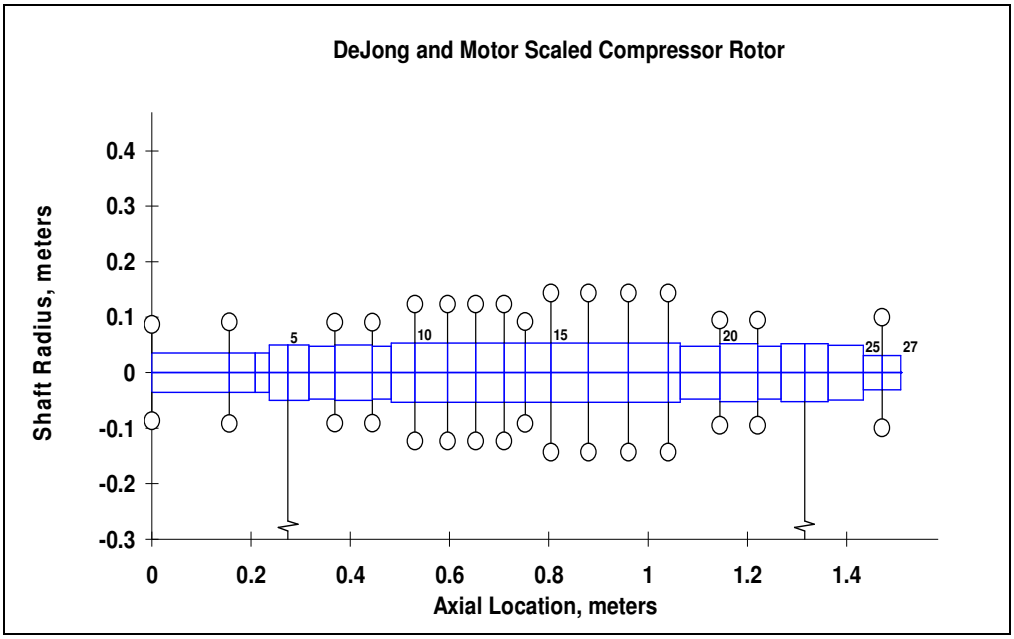

Figure 19 Rotordynamic Model of de Jongh et al [11] Rotor

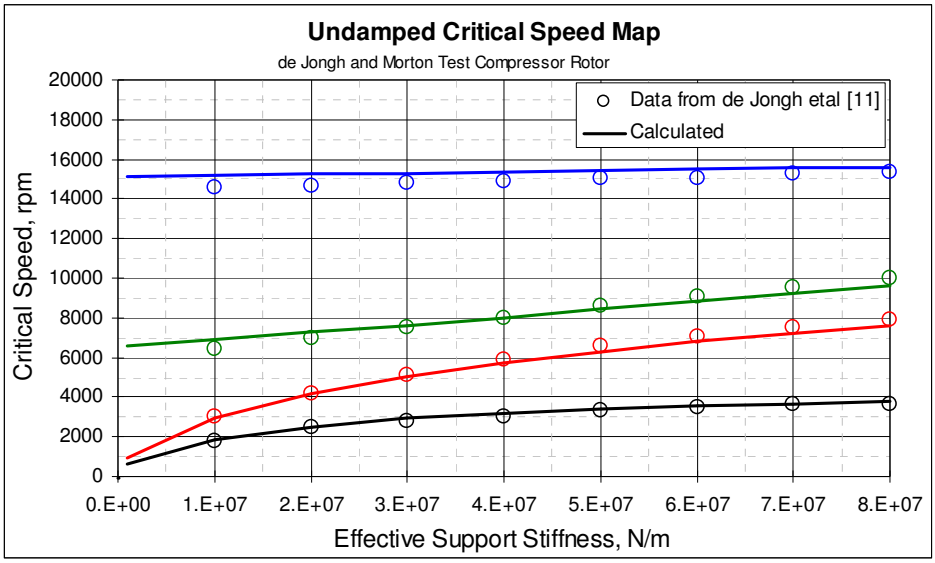

Figure 20 Calculated Critical Speed Map of de Jongh et al [11] Rotor Including Comparative Data Presented within the Literature

To compare the rotordynamic model used here to that presented in the paper by de Jongh et al [11] a response analysis was performed using the support stiffness data provided by de Jongh et al [11]. This was based on the stiffness and damping conditions in the 'XX' and 'YY' planes being identical with no cross coupling terms. Figure 21 to Figure 23 show the bearing stiffness and rotordynamic response predictions of de Jongh et al [11] and that of the model used within this thesis. No bearing damping data was provided in the paper and values appropriate for this size and type of bearing were calculated and used in the model. Performed in this research, the response model and analysis was conducted with a 100 g.mm unbalance mass located at the non drive end (NDE) flange of the rotor with a 0^{o} phase lag, with the response evaluated at the NDE bearing centre location.

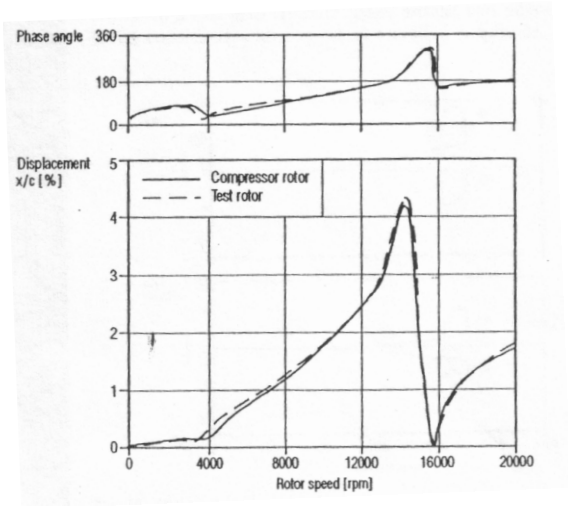

Figure 21 Unbalance response prediction presented by de Jongh et al [11]

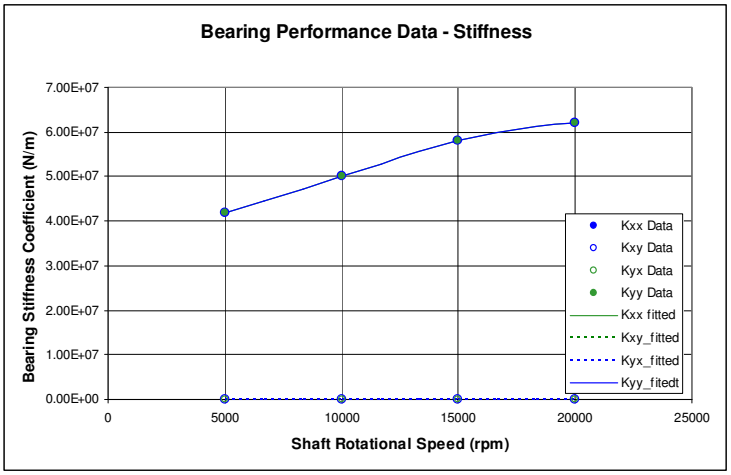

Figure 22 Bearing stiffness data used in rotordynamic model of de Jongh et al [11] rotor

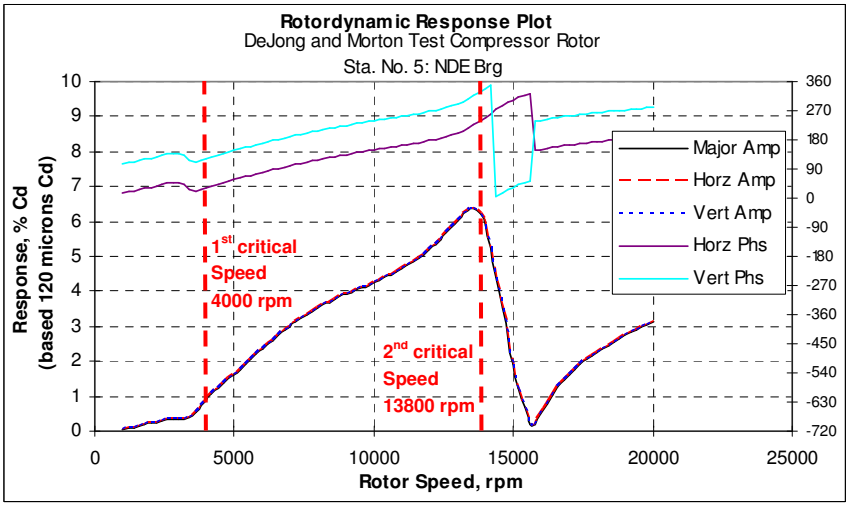

Figure 23 Calculated Unbalance Response of de Jongh et al [11] Rotor - using approximate stiffness coefficients from [11]

From Figure 21 and Figure 23 the results of the initial analysis can be seen to correlate well with those presented by de Jongh et al [11] for the undamped critical speed map and simple response evaluation, Figure 20 and Figure 23 respectively (where $\%C_d$ is pk-pk vibration as a % of bearing diametral clearance). The critical speed map frequencies tie up well across the running speed range with relation to support stiffness, with the 4th vibration mode presenting the biggest difference with this being approximately 200-300 rpm higher than that predicted by de Jongh et al [11]. This could in some part be attributed to the slight differences in mass distribution and account for additional stiffness presented by the shrunk on discs. However for a model of this type, the level of correlation is suitable for the purposes of this characterisation.

The simple response analysis (Figure 23) also correlates well that presented in the published work (Figure 21). The location of the natural modes and general characteristic of the response are well positioned with relation to the model results presented by de Jongh et al [11]. The model presented by de Jongh et al [11] gives a slightly more pronounced 'ramp' toward the second bending mode but this aspect would be influenced by the level of damping used in the support bearings for the analysis. For this there will be some difference between the two models. A significant feature for the subject of interest is the phase relationship, and it can be seen that this also correlates well with the conditions around both the first and second critical speeds showing the same characteristics and closely matched magnitudes.

In summary, the initial evaluation shows that sufficient correlation exists in this model for it to be applied for the more detailed characterisation required.

To allow the full rotordynamic characterisation of the test compressor shaft rotordynamic performance, the actual dynamic bearing oil film stiffness and damping coefficients need to be predicted. The bearing performance was evaluated across a range covering the operating range (0-12500 rpm) of interest. The bearing conditions were solved for 5 operating speeds within the running range and then curve fitted using a 3rd order polynomial to provide speed dependant stiffness and damping data for use in the rotordynamic model. Table 2 gives a summary of the calculated bearing conditions, and Table 3 and Figure 24 provide the bearing oil film characteristics calculated.

Basic Bearing Geometry and Performance Data				
Bearing diameter (mm)	100			
Bearing pad length (mm)	50			
Number of pads	5			
Load direction	Load on pad (LOP)			
Angle of Pad (degrees)	60 degrees			
Diametral clearance (microns)	120			
Specific load (kPa)	450			
Pivot type	Centre pivot			
Shaft speed (rpm)	5000	10000	15000	20000
Eccentricity ratio	0.2055	0.1323	0.0856	0.0550
Minimum film thickness (microns)	35	37	36	34

Table 2 Calculated support bearing basic performance data

Speed	Kxx	Kxy	Kyx	Kyy	Cxx	Cxy	Cyx	Cyy
rpm	N/m	N/m	N/m	N/m	N.s/m	N.s/m	N.s/m	N.s/m
5000	208617	192	257	238498	219011	0	0	235090
10000	338786	-86	-196	356838	169415	0	0	174363
15000	526039	-104	-241	537587	159286	0	0	161067
20000	813713	-89	-264	821619	160538	0	0	161212

Table 3 Calculated support bearing oil film stiffness and damping coefficients

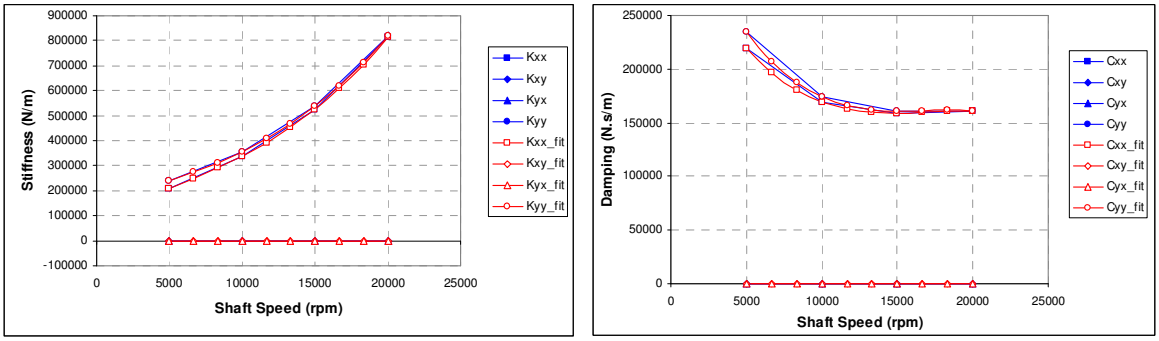

Figure 24 Curve fitting of calculated support bearing stiffness and damping coefficients

Hydrodynamic bearing solutions for the tilting pad bearings were performed using a custom code 'Vickers – JPU Tilting Pad Journal Bearing Performance Program' V3.21' [52]. The program is able to evaluate either fully flooded or direct fed lubricated bearings with central or offset pivots. Performance data for oil film thickness, shaft eccentricity ratio, operating temperatures and stiffness and damping characteristics is calculated within the code. The pad minimum film thickness typically occurs at the point of the trailing edge of the pads, where the film thickness is a function of both the shaft eccentricity and pad tilt angle.

The rotordynamic model was then solved to extract the eignvalues for the rotor with relation to operating speed and the Campbell chart in Figure 25 shows the locations of the predicted natural frequencies. From Figure 25 it can be seen that the predicted locations for the first and second critical speeds are at ~4400 rpm and ~12300 rpm respectively. The associated calculated logarithmic decrements for the first and second critical speeds are 0.673 and 0.227 respectively. The bearing performance data used for the analysis presented here was based on the lower bearing diametral clearance of 120 microns.

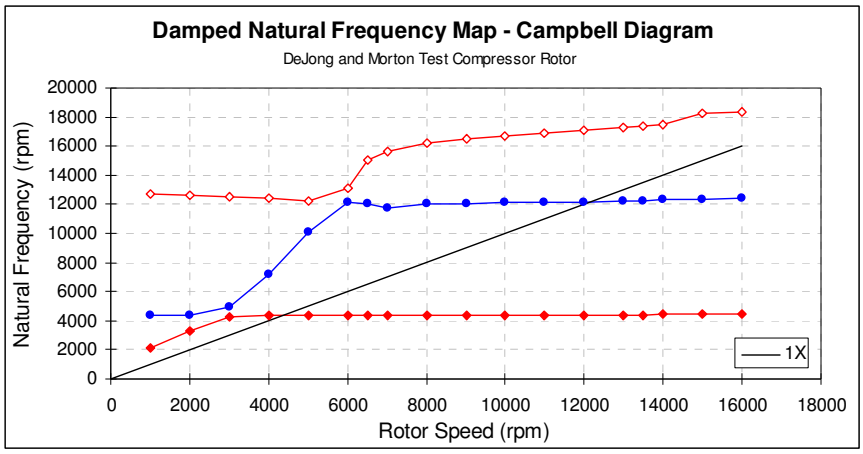

Figure 25 Calculated forward whirl damped natural frequencies for de Jongh et al [11] rotor

In order to gain a good understanding and characterisation of the rotrodynamic conditions within the rotor the modes shapes, response at the non drive end bearing and operating deflection shapes were extracted. Figure 26 to Figure 32 show the calculated mode shapes and responses. The response analysis was performed using a mechanical unbalance force vector of 100 g.mm at a 0 degrees phase angle positioned at the NDE overhung rotor flange. During the rotor analysis an investigation was performed as to the sensitivity of the rotor to unbalance elsewhere on the shaft. It was observed that the response at the NDE bearing was relatively insensitive to imbalance elsewhere in the centre of the rotor. The effect of this can be seen in Figure 35 where an imbalance load was applied at the rotor bearing mid-span (equal to 50% of the API [53] limit) and the response evaluated. The imbalance mass was rotated into several phase positions to determine not only the sensitivity to imbalance magnitude elsewhere on the rotor, but also to the relative phase. The above activity cannot fully establish how the rotor will respond to the distribution of balance elsewhere on the rotor due to the near infinite number of combinations possible. It does however show that the overhung section characteristics do not appear to be particularly sensitive to these effects, allowing the characteristics analysed to be considered as relatively general characteristics for the rotor.

As is the case for any practical machines, a certain level of residual unbalance would also reside elsewhere in the rotor. To provide for this a representation was included for unbalance on the rotor between the bearing span. The phase of this unbalance was opposed to that of the overhang unbalance by 180 degrees. The magnitude of this unbalance was 50 g.mm which is based on

25% of the calculated API [53] limit for compressor rotors of this size and operating speed.

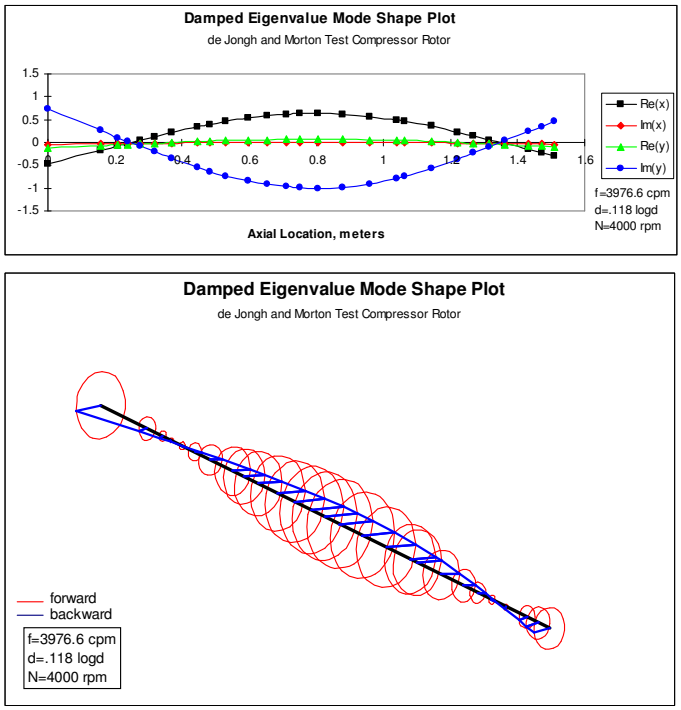

Figure 26 Calculated damped mode shape for first critical speed for de Jongh et al [11] rotor

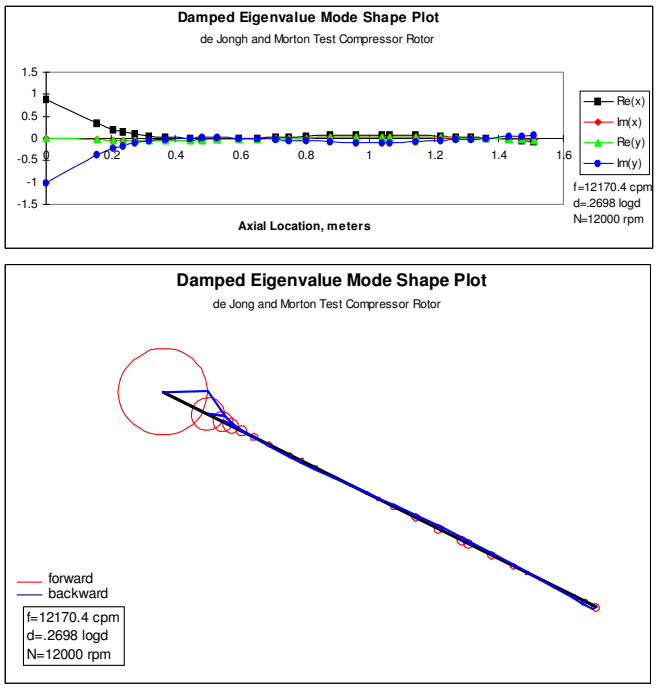

Figure 27 Calculated damped mode shape for second critical speed for de Jongh et al [11] rotor

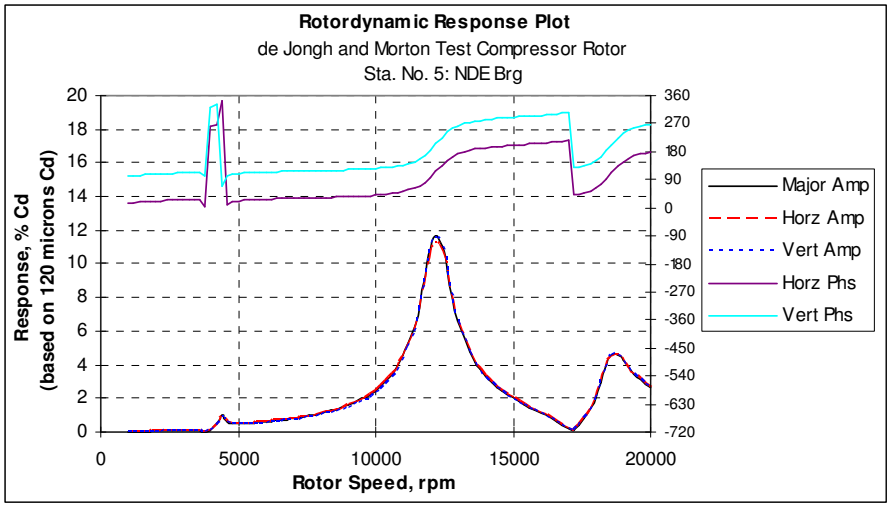

Figure 28 Calculated unbalance response for the de Jongh et al [11] rotor with 100 g.mm unbalance at the NDE overhung mass

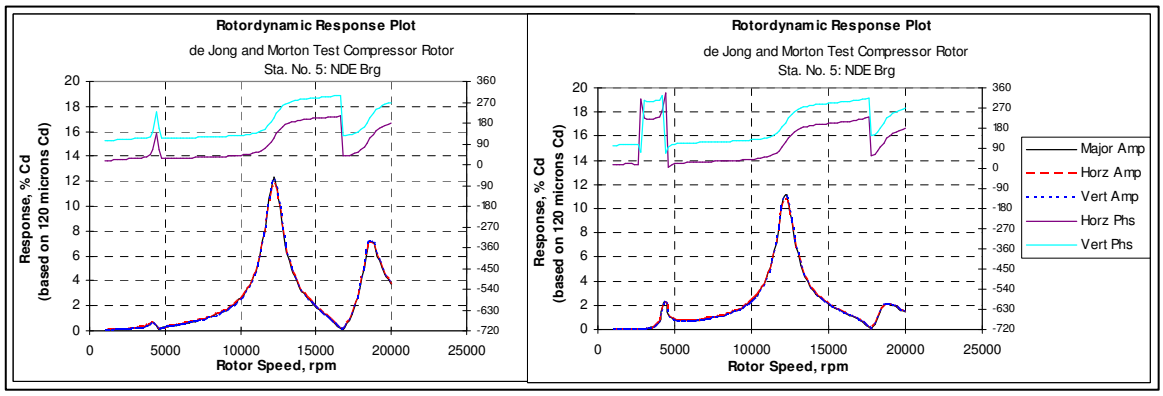

(a) (b)

Figure 29 Calculated unbalance response for the de Jongh et al [11] rotor with 100 g.mm unbalance at the NDE overhung mass and 100 g.mm at the bearing mid-span at (a) 0o phase lag and (b) 180o phase lag

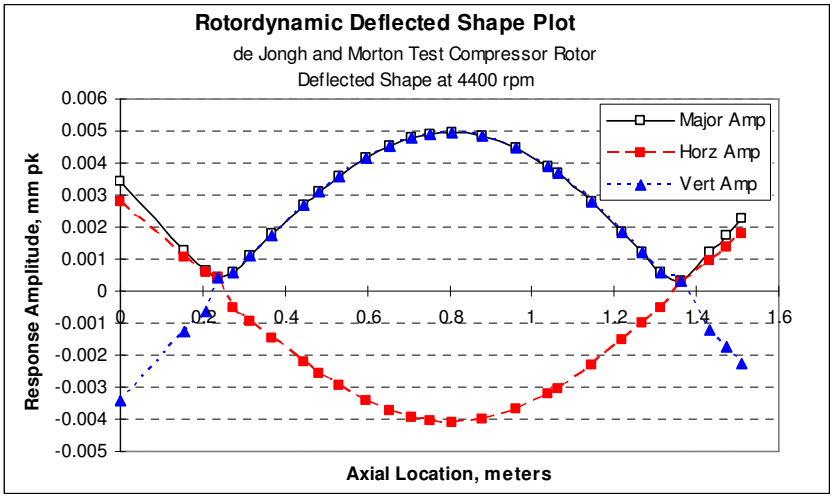

Figure 30 Calculated rotor deflection shape of de Jongh et al [11] rotor at location of 1st critical speed

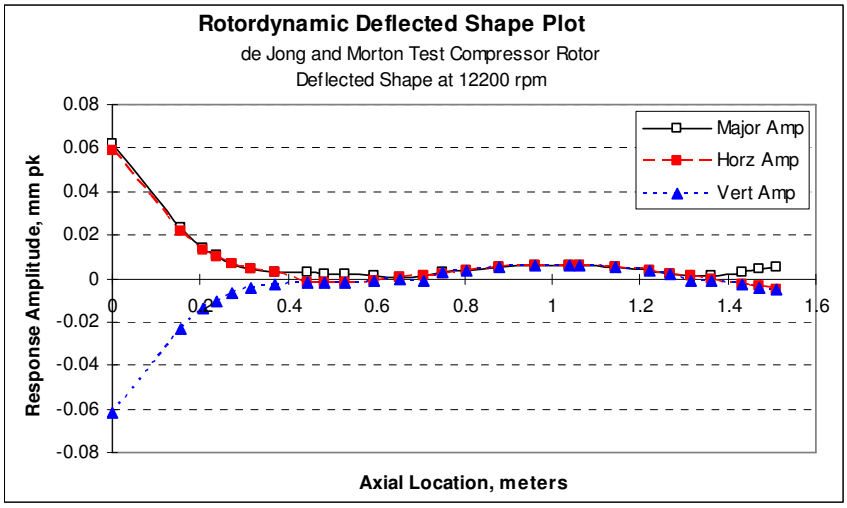

Figure 31 Calculated rotor deflection shape of de Jongh et al [11] rotor at location of 2nd critical speed of 12200 rpm

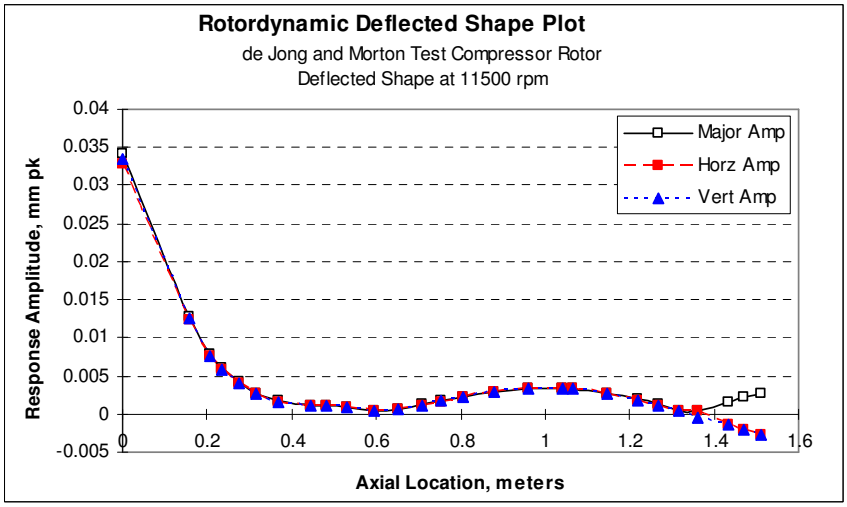

Figure 32 Calculated rotor deflection shape of de Jongh et al [11] rotor at observed thermal stability threshold speed of 11500 rpm

As a further check to the correlation of model predictions of the actual rotor performance when under test, the response of the rotor due to unbalance located at the rotor centre and overhung mass were performed. These results can then be directly compared for characteristics with the physical measurements presented by de Jongh et al [11].

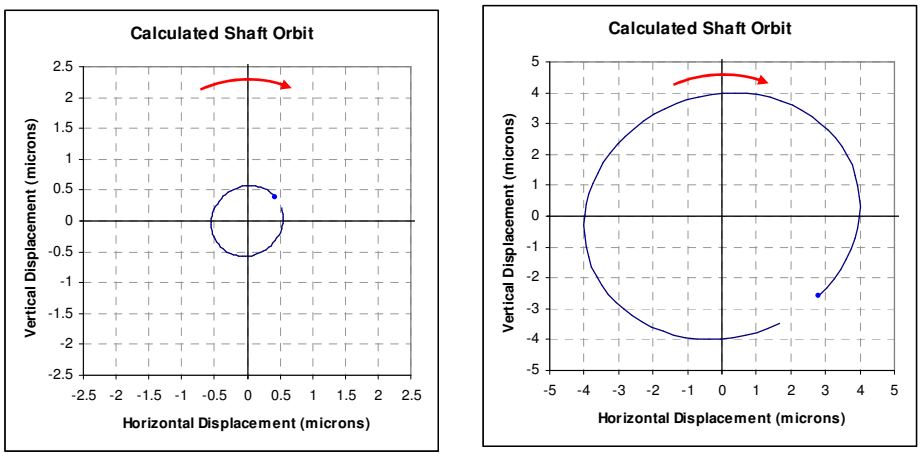

(a) (b)

Figure 33 Predicted shaft whirl orbits at NDE bearing of de Jongh et al [11] rotor at (a) 4500 rpm – location of 1st critical and (b) 11500 rpm – thermal instability threshold speed

The specific magnitudes cannot be readily compared due the particular amounts of introduced unbalance not being available via the literature [11], but as the authors analysis is based on a linear response model, the characteristics can be taken as representative for any scalable unbalance condition where the relative proportions or phase of unbalance are nominally maintained and linear bearing response characteristics remain valid. This can be a significant assumption where larger vibration amplitudes are present.

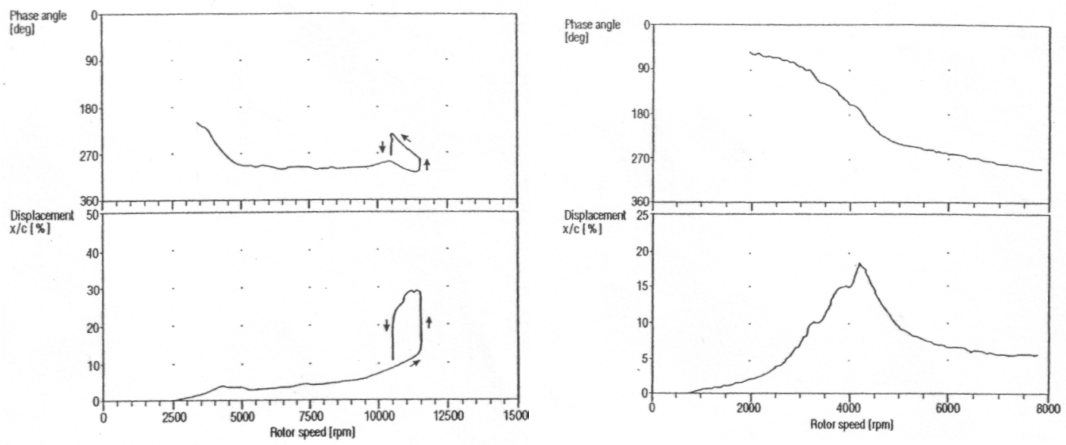

Figure 34 Measured 1X response data for test compressor rotor with introduced centre unbalance presented by de Jongh et al [11] – figure taken from [11]

An additional test was performed by de Jongh et al [11] where an imbalance load was introduced into the centre of the test compressor rotor. The vibration

response of which are given in Figure 34. The purpose of the evaluation was to observe if any significant temperature differential or instability was observed. It was observed [11] that an appreciable temperature differential could be identified when crossing the critical speed but the rotor remained stable at all times.

To capture this condition in the rotordynamic work performed by the author, a case which reflects this was evaluated. The results of this can be seen in Figure 35. It was identified that to obtain the level of response observed in [11] that a significant unbalance load was required (many times that of the API [53] limit). It is the opinion of the author that this would be to ensure a sufficient level of vibration takes place at the NDE bearing this close to a nodal point for the 1st critical mode to generate conditions where a measurable temperature difference would be generated. This principle is also supported by the fact the rotor was only run up to approximately 60% of full speed as the vibration levels beyond this would be unacceptable as a result of the much higher imbalance loads.

Comparing the results given in Figure 35 to those presented by de Jongh et al [11] in Figure 34 shows good correlation of the critical speed and the general response characteristic is maintained. One notable observation however, is that the quality factor Q, see Blake [67], between the two responses is much lower on that of the calculated data. The appearance of the response in Figure 35 would suggest that more damping is present with the actual test rotor than is being predicted in the author's rotordynamic model. Possible sources for this discrepancy are small variations on the bearing performance, but a more probable source would be the additional damping introduced by the rotor structure itself and that of the contribution of the main bearing support housings for which damping is not considered within the mathematical model.

The work conducted on the de Jongh and Morton [11] rotor has shown that the rotordynamic models appear to satisfactorily predict the rotordynamic conditions observed within the super critical rotors, with the fundamental rotordynamic characteristics comparing well with the presented data. Further in-depth analysis of the model then allows for the more detailed understanding of the rotor conditions during running and instability phases to support in the design of the test rotor for the research of this thesis.

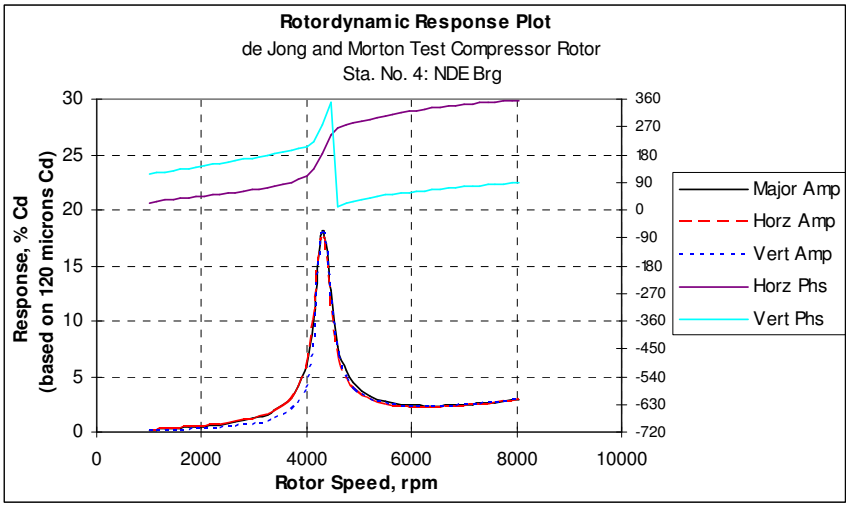

Figure 35 Calculated unbalance response of de Jongh et al [11] rotor where centre only imbalance introduced

The same modelling principles are now applied by the author to the two further case studies to extract the same rotordynamic characteristic information.

4.2.3 Case Study 2 – Faulkner, Strong and Kirk [12,13]

The rotor used in this case study is based on several papers presented by Faulkner, Kirk and Strong [12,13]. Here a high speed overhung turbocharger was seen to display unstable operating vibrations when running at constant speed. Following an initial design modification due to a loose impellor rotor when at speed, increasing vibrations were observed with time at constant speed with an associated continually shifting phase. The machine was observed to show signs of instability when a running speed of 9800 rpm was reached. Some operational vibration measurements were taken and on exhausting other root causes thermal synchronous instability 'Morton Effect' was attributed. The machine was fitted with modified bearings of the pocket type which provided increased eccentricity in the bearing and resulted in the machine no longer demonstrating the phenomenon. This enabled full operating speed to be achieved indefinitely. The following analysis looks at the rotor and bearing conditions prior to the introduction of the pocket bearing assemblies.

An undamped critical speed map has been produced and this used as a measure of the rotor response in line with the data presented for turbocharger [12,13]. The analysis shows that three critical speeds are present below

40,000 rpm as is presented in Figure 37, with the associated rotordynamic model compiled for the analysis shown in Figure 38. The undamped critical speed map determined by Faulkner et al [12,13] is shown in Figure 36.

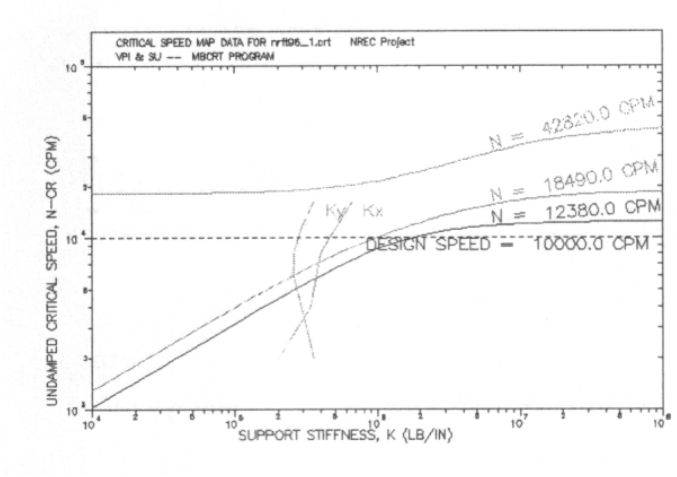

Figure 36 Undamped critical speed map for Turbocharger rotor presented by Faulkner, Strong and Kirk [12,13] – figure taken from [12,13]

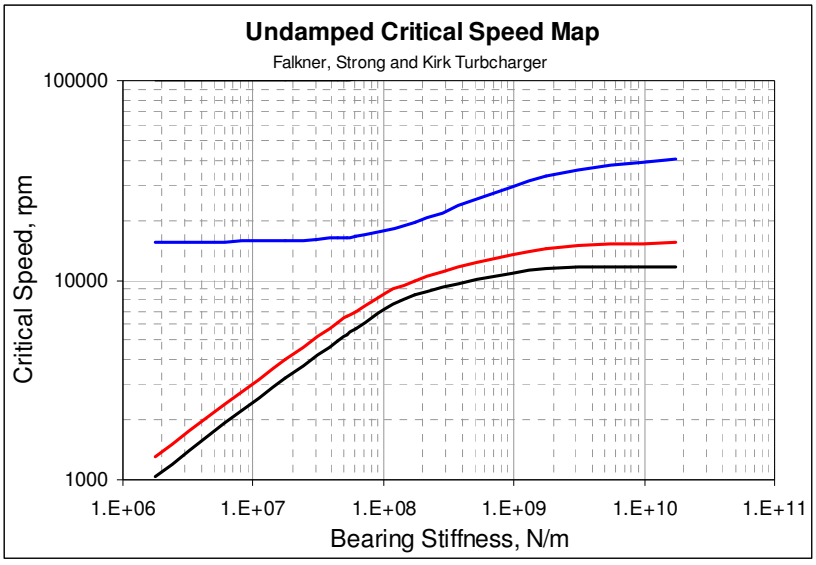

Figure 37 Calculated undamped critical speed map of Faulkner et al [12,13] rotor

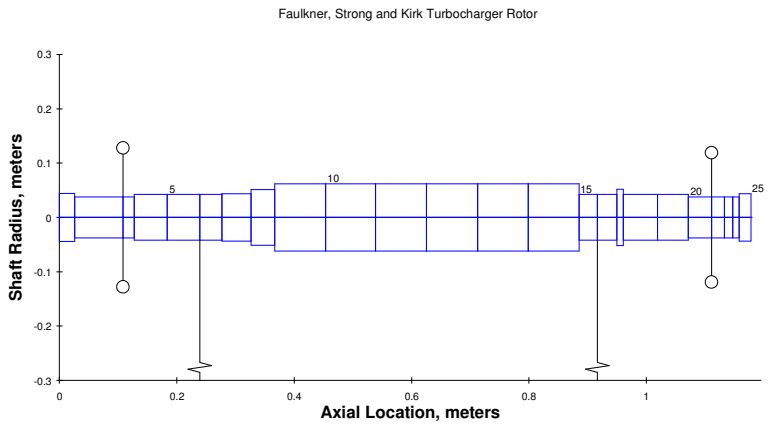

Figure 38 Rotordynamic model of Faulkner et al [12,13] rotor

The bearing types used for the analysis are the 3 lobe type which is consistent with those present within the machine prior to the bearing modifications conducted at the turbine bearing end [12]. The bearing performance data was calculated across the running speed range and the stiffness and damping data used for the damped eigenvalue extraction and response analysis.

The mode shapes at the rotor bearing assembly critical speeds were extracted for a running speed up to 16000 rpm. The first two modes are strongly linked to the bearing stiffness characteristics and can be characterised as the rocking and bounce modes respectively. The second 'bounce' mode does however include some component of rotor shaft bending associated with the overhung masses of the rotor, and this point has some significance with relation to the process of shaft thermal bend development. The third mode is principally a 1^{st} shaft flexural bending mode and sits approximately 4000 rpm above the max running speed of the rotor. Figure 39 a, b and c show the rotor mode shapes for the first, second and third damped natural frequencies respectively.

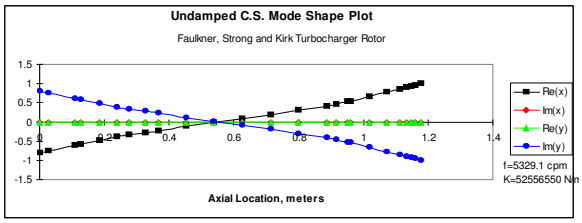

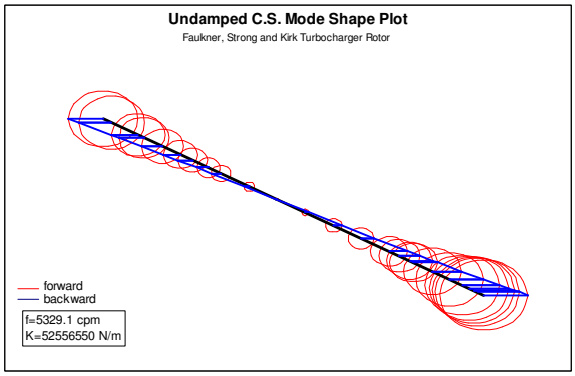

(a) Bearing associated 'rocking' mode

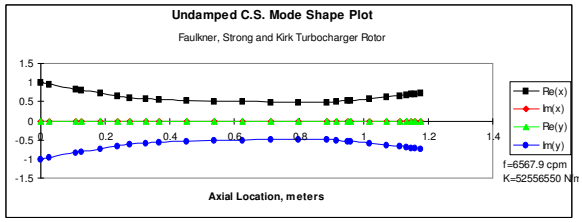

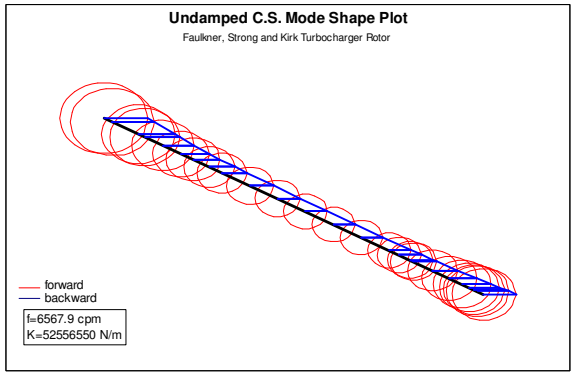

(b) Bearing and shaft associated 'bounce' mode

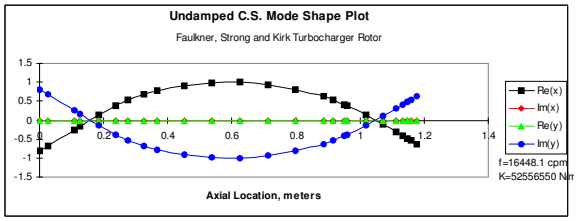

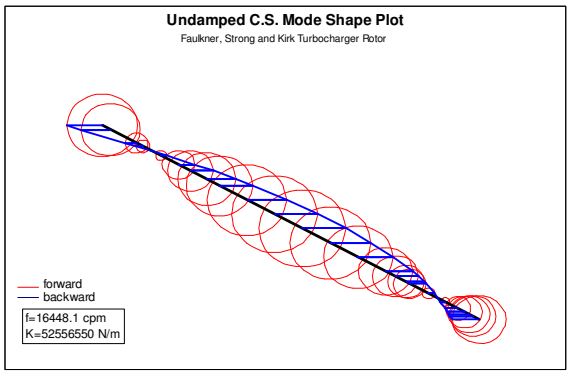

(c) Shaft 1st flexural bending mode

Figure 39 Calculated damped modes shapes for Faulkner et al [12,13] Turbocharger rotor

The rotor response analysis was performed by the author through introducing an unbalance level of 350 g.mm at the turbine rotor shaft end. The magnitude of unbalance is based on 0.5 oz.in as presented by Faulkner et al [12,13]. The response data is presented in Figure 40, Figure 41 and Figure 42 for the compressor bearing, turbine bearing and turbine disc locations respectively. The deflected rotor shapes have been extracted for the locations of the

second critical speed and the instability running speed of ~10000 rpm. These calculated operating deflection shapes are provided in Figure 44 and Figure 45.

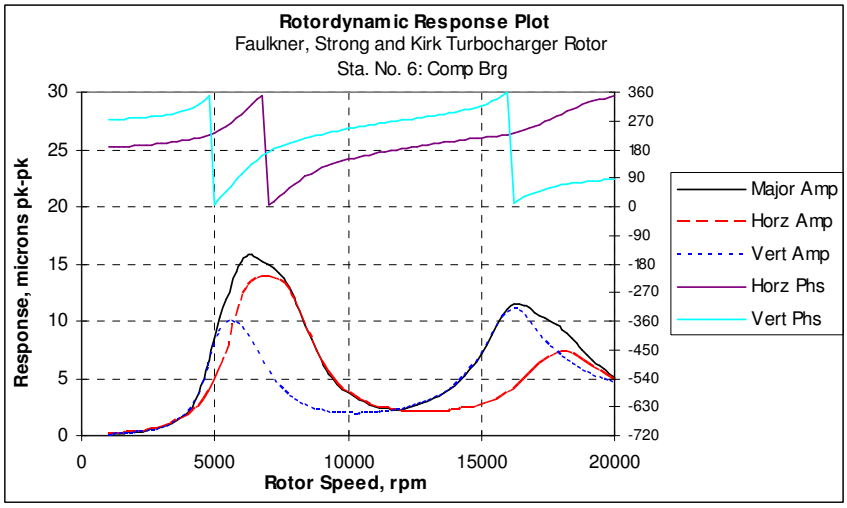

Figure 40 Calculated unbalance response for Faulkner et al [12,13] rotor compressor bearing

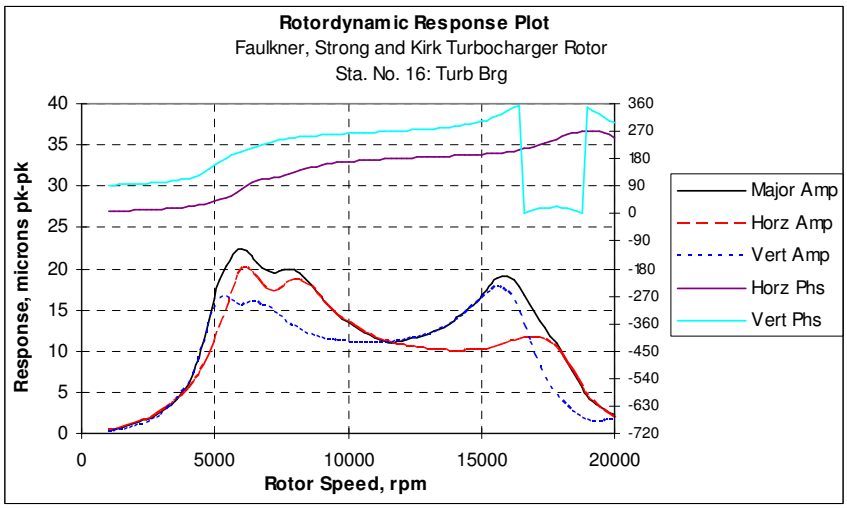

Figure 41 Calculated unbalance response for Faulkner et al [12,13] rotor turbine bearing

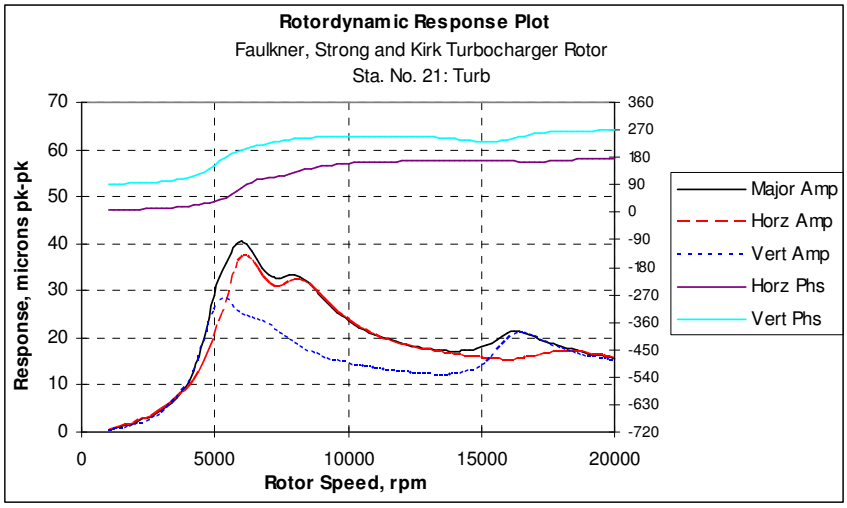

Figure 42 Calculated unbalance response for Faulkner et al [12,13] rotor turbine disc

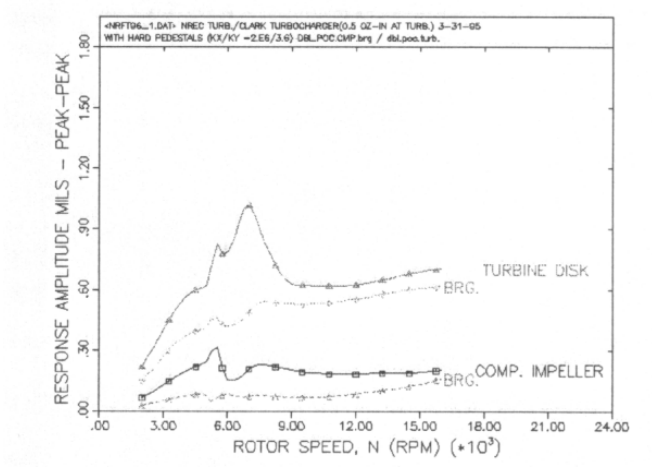

Figure 43 Predicted rotor response for turbocharger rotor presented by Faulkner, Strong and Kirk [12,13]

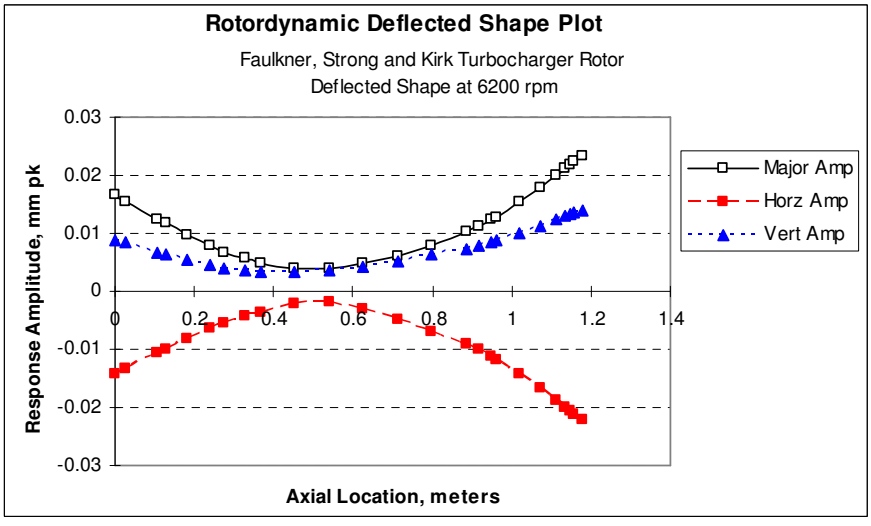

Figure 44 Calculated operating rotor response for Faulkner et al [12,13] rotor

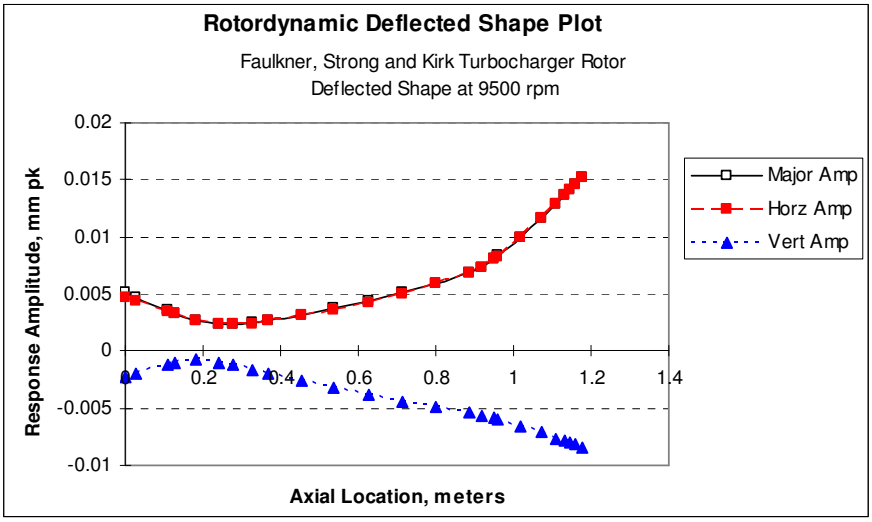

Figure 45 Calculated operating rotor response for Faulkner et al [12,13] rotor

The predicted shaft obits at the machine running speed of 9500 rpm are shown in Figure 46 (a) and (b) for the compressor and turbine end bearing respectively.

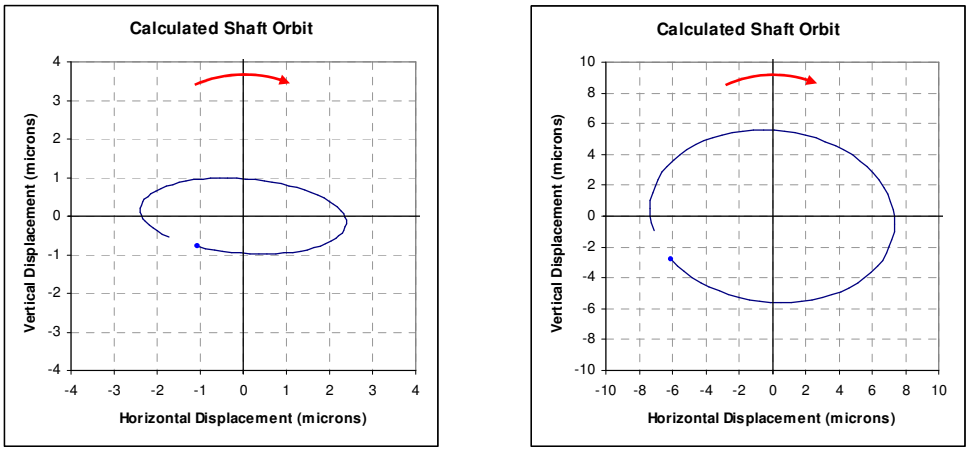

(a) Compressor bearing (b) Turbine bearing

Figure 46 Predicted bearing whirl orbits for Faulkner et al [12,13] rotor

4.2.4 Case Study 3 – High Speed Overhung Compressor (HSOC)

The final case study is based on an unpublished example where a high speed single impellor compressor rotor was seen to experience high and short term unstable vibrations whilst undergoing performance evaluation on the test bed. The rotor was designed and manufactured by a large multinational Original

Equipment Manufacturer (OEM) with extensive experience in the design, manufacture and operation of high speed rotating machinery. The rotor design is a radial flow CF high speed compressor driven by a gas turbine for use in the Oil and Gas industry. The bearing assembly used to support the rotor was by means of two 5 pad tilting pad journal bearings. The bearings at the Drive End (DE) and Non-Drive End (NDE) are of different diameters and length, with the larger diameter, longer bearing being present at the non drive compressor rotor end.

Whilst undergoing testing the machine was seen to operate with typical vibration response characteristics within normal levels when running at normal operating temperatures. However, when the machine underwent a cold start up, a condition of high vibration was experienced when run up to full speed (~14250 rpm). The vibration level was seen to increase slowly with time and when the unit was slowed back down to its steady running speed (11695 rpm), the vibration was seen to remain at a high level and then slowly reduced back to its 'normal' levels. Associated with the changing vibration was the characteristic change in phase observed when a thermal stability event is taking place. The phase shift in this case was not particularly significant compared to other examples, but is clearly present. The lower phase shift could be related to the shorter time constants involved when running at the maximum speed before slowing back down to the steady running speed. The characteristic hysteresis effect can be seen in the Bode plot shown in Figure 48.

The high vibration levels were observed in only one of the two support bearings. The high vibrations were seen at the DE bearing with levels at the NDE being significantly lower and not displaying the same steady increase with vibration and only very small movement in phase taking place. A significant observation of this particular case is that the unstable vibration is observed at the bearing location opposite to the end where the large shaft overhung section is positioned, i.e. the DE bearing (Figure 47). This significance is that in previous examples, the unstable vibration characteristic has been principally associated with the bearing located at the same end as the overhung section or, in the case of overhung rotors both bearings see increased vibration.

Following some initial investigative work by the OEM the possibility of thermal instability was considered and a basic evaluation of the rotor sensitivity to this issue was investigated by Dr G Kirk of Virginia Tech University, USA. Based

on this work it was concluded that the most probable cause was due to differential rotor heating. Also the conditions under which the vibration was observed was as a result of the higher viscous shearing effects seen when operating with the bearing pad lower temperature inlet oil at higher viscosity, this is present when the machine is starting up before full thermal soak has occurred in the rotor and housings.

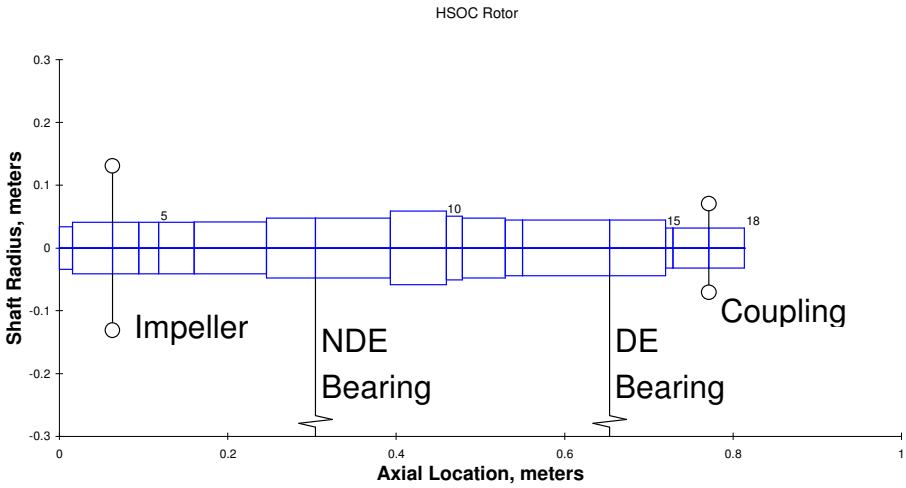

Figure 47 Rotor dynamic model of HSOC compressor rotor

The solution to the presence of the problem was a modification to the bearing by the introduction of increased bearing clearance which resulted in a slight increase in oil film thickness and reduction in circumferential viscous shear rate. The qualitative assumption of this is to result in a lower temperature differential being generated at the bearing journal location and reducing the thermal bend feedback into the unbalance cycle.

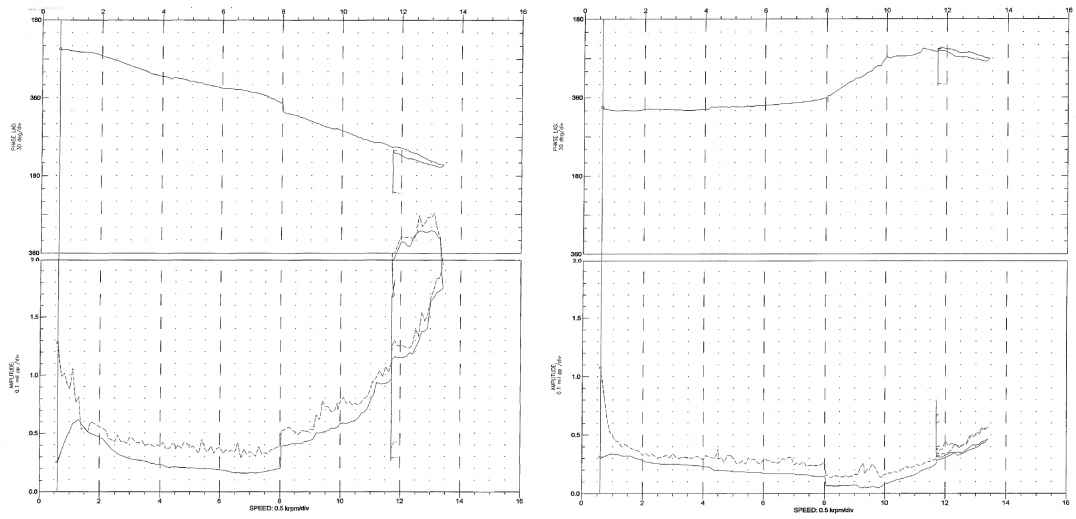

Figure 48 Measured shaft vibration for (a) DE bearing location and (b) NDE bearing location of HSOC compressor rotor

As with the previous two case studies, the author has evaluated the rotor to obtain an understanding of the rotordynamic and hydrodynamic characteristics present across the running range. In addition to the principle rotordynamic evaluation a brief evaluation of the effect of the bearing characteristics on the rotordynamic performance has been included so as to understand the difference in conditions when running at lower bearing pad lubricant inlet viscosities and how this could influence the conditions at the rotor with respect to thermal bend stability sensitivity.

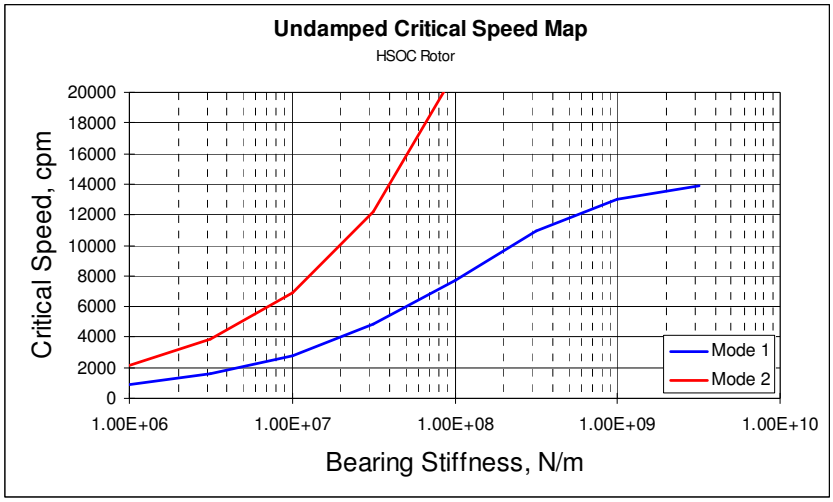

Figure 49 Calculated undmaped critical speed map for HSOC compressor rotor

The undamped critical speed map was calculated as is shown in Figure 49. Within the speed range of interest, two natural modes were identified and both these showed significant sensitivity to support stiffness with reference to the mode frequency location. There would also be a notable change in associated mode shape within the support stiffness range considered.

To allow the full rotordynamic characterisation of the HSOC compressor shaft, the dynamic bearing oil film stiffness and damping coefficients were calculated. The bearing performance was evaluated across the operating range of interest and split into 4 operating speed sets. As described previously the data was curve fitted to yield speed dependant stiffness and damping data for use in the rotordynamic model. Table 4 and Table 5 summarise the bearing oil film characteristics calculated. It was found when calculating the critical speeds of the rotor, that to match the observed dynamic response it was necessary to use a DE support bearing with lower support stiffness. This was incorporated by using a bearing clearance which would be at the top clearance for a bearing of this size.

Speed	Kxx	Kxy	Kyx	Kyy	Cxx	Cxy	Cyx	Cyy
rpm	N/m	N/m	N/m	N/m	N.s/m	N.s/m	N.s/m	N.s/m
5000	366720000	123972	-328728	371823000	154557	63403	-63662	156486
10000	597312000	-19671	-51126	600675000	120520	47555	-47590	121190
15000	885927000	-52809	-83859	888141000	112390	42136	-42145	112699
20000	1272729000	-58026	-86625	1274235000	111145	38768	-38767	111311

Table 4 Bearing oil film coefficients across speed range for NDE bearing

Speed	Kxx	Kxy	Kyx	Kyy	Cxx	Cxy	Cyx	Cyy
rpm	N/m	N/m	N/m	N/m	N.s/m	N.s/m	N.s/m	N.s/m
5000	6204400	919.3	-3945.4	6233500	77415	33578	-33627	77946
10000	10005700	1675.2	-4028.3	10014500	60789	25555	-25568	60945
15000	13477200	-472.8	-344	13492200	52527	21347	-21345	52634
20000	18363000	-748	-555	18373400	51232	19889	-19887	51297

Table 5 Bearing oil film coefficients across speed range for DE bearing

Resolving the model with the calculated bearing support stiffness and damping characteristics the damped natural frequencies shown in Figure 50 were obtained. The Campbell diagram shown in Figure 50 suggests that two critical speeds will be experienced within the running range. However in practice the lower red curve in Figure 50 is associated with a reverse precession whirl mode and under typical operating conditions this would not be excited by simple unbalance response. The results predict that the rotor will experience a critical speed at 14000 rpm. The mode shape associated with this point is given in Figure 51. It can be seen that the mode is a combination of bearing and shaft governed elements, with significant rotor deflection taking place in the area of the NDE overhung section with relatively low bearing activity. At the DE the displacement at the bearing is comparatively high but there is little rotor deflection taking place at this point of the shaft.

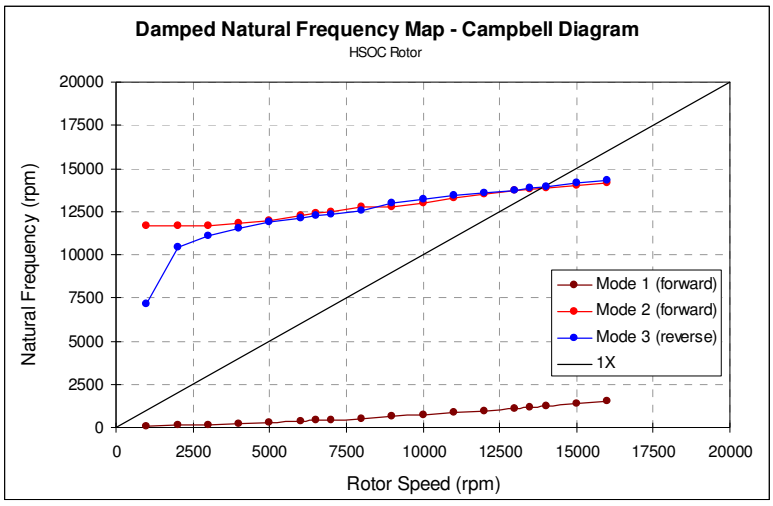

Figure 50 Calculated damped natural frequency map for HSOC compressor rotor

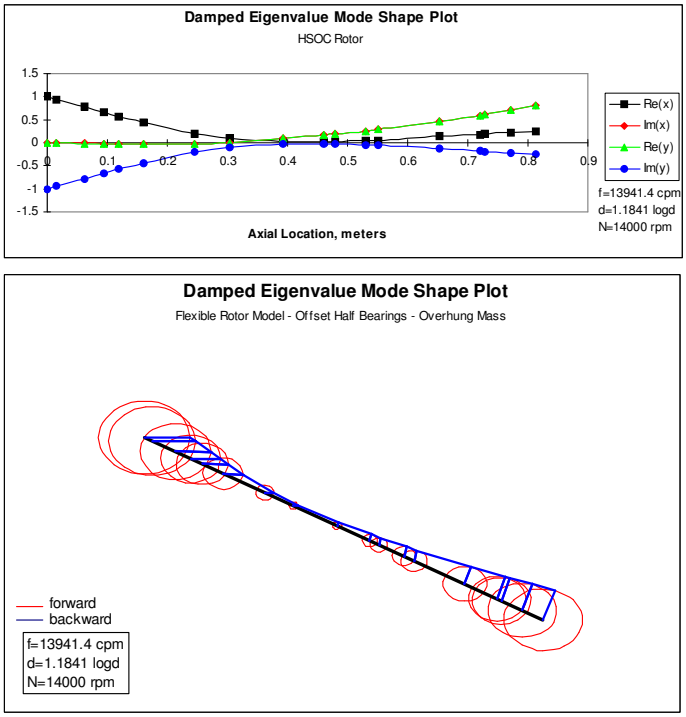

Figure 51 Calculated damped mode shape for natural frequency at 13941 cpm

The response of the rotor was evaluated by introducing an imbalance force equating to 150 g.mm (0^o phase) located at the impeller rotor location. Figure 52 and Figure 53 show the response of the rotor at the NDE and DE bearing locations respectively. It can be seen that the general characteristics of the response between ~5000 rpm and the full speed ~1400 rpm compare well to the measured data shown in Figure 48. The response in the lower frequency range however does not agree quite so well. It is unclear as to the cause of the relatively high vibration observed in the lower frequency range as it does not show any common traits with typical rotor dynamic issues, here the level of vibration is highest at very low speeds where dynamic balance forces are at their lowest. Also it can be seen that there is also a significant amount of non synchronous vibration activity in this area which can be seen from the dashed line in Figure 48. It is not uncommon to observe these types of characteristics in rotating machines where other external effects can give rise to observed moderate vibration levels at lower running speeds where, in this case, aerodynamic effects, coupling loads or even shaft measurement glitch can influence the actual or perceived vibration levels. For the purposes of this evaluation little focus is placed on this apparent discrepancy between the predictive tool and observed vibration as it is not considered that these aspects are significant to the thermal problem in the rotor, due to the lower levels of heat generation in the bearings at these speeds.

The NDE bearing shows significantly lower response than the DE bearing by a factor of ~7 which is consistent the observed measurements, these show an ~5 times increase at the DE bearing relative to the NDE. The impact on rotordynamic performance of a higher lubricant viscosity in the bearings is also considered in an attempt to understand if the thermally induced effect is driven by the rotordynamic as well as the increased oil shear heat flux when running with higher oil viscosity. The impact of the higher viscosity rotordynamically is to result in nominally higher stiffness and damping values, which in this case is a factor of some 50% when at ~12000 rpm. Figure 54 and Figure 55 present the response results for the higher viscosity condition. It can be observed that predicted impact of the higher viscosity on the rotordynamic performance conditions is limited. A very slight reduction in amplitude is seen at the NDE bearing and there is a shift to bring the peak critical speed down closer to running speed. Conversely the amplitude at the DE bearing reduces by a slightly higher amount by ~25% even though the critical speed has been pulled down closer to the running speed.

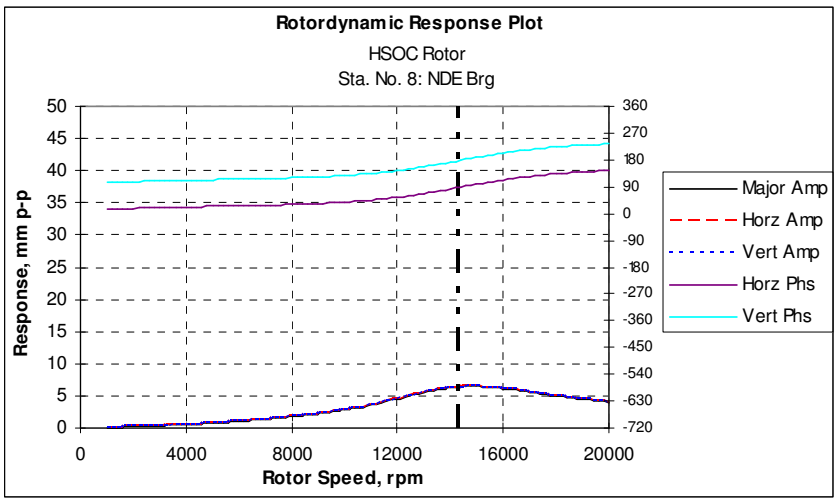

Figure 52 Calculated response for NDE bearing location of HSOC compressor rotor (normal viscosity)

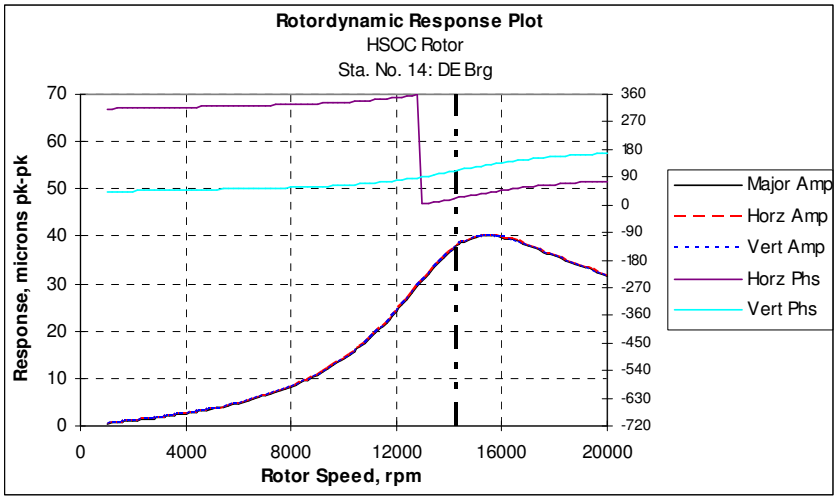

Figure 53 Calculated response for DE bearing location of HSOC compressor rotor (normal viscosity)

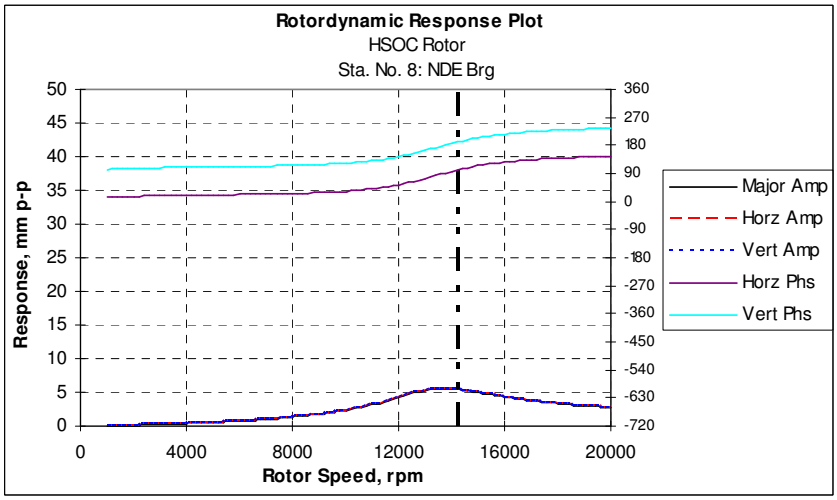

Figure 54 Calculated response for NDE bearing location of HSOC compressor rotor (higher viscosity)

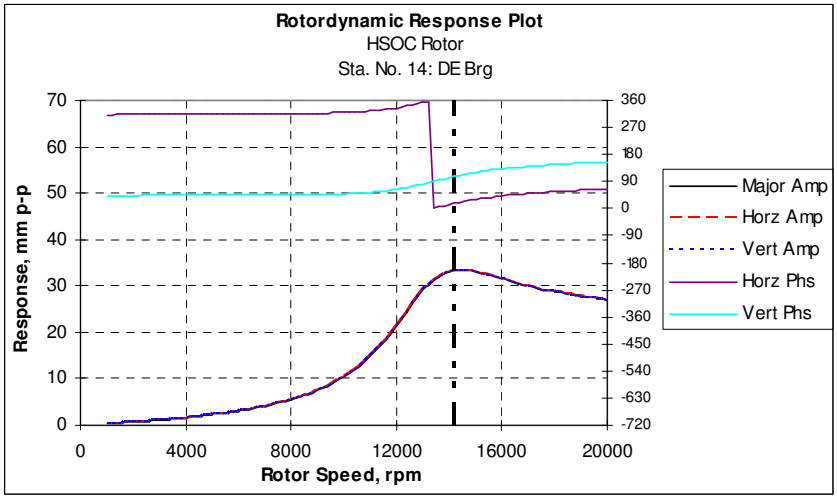

Figure 55 Calculated response for DE bearing location of HSOC compressor rotor (higher viscosity)

The associated rotor deflection shapes at the steady running speed of 11695 rpm and the maximum running speed of 13400 rpm are given in Figure 56 and Figure 57. The deflected rotor shape is also provided for the high inlet viscosity condition when running at 11695 rpm in Figure 58. Predicted shaft whirl orbits are shown in Figure 59 and Figure 60 for the NDE and DE bearings. The observed shaft whirl orbits from the measured HSOC compressor rotor are shown in Figure 61. These have been re-synthesised from the synchronous amplitude and phase data presented in the HSOC test data. A notable difference in the calculated vs measured shaft orbits is the highly circular form of the predicted orbits, whereas the DE bearing for the measured data displays a significant ellipse.

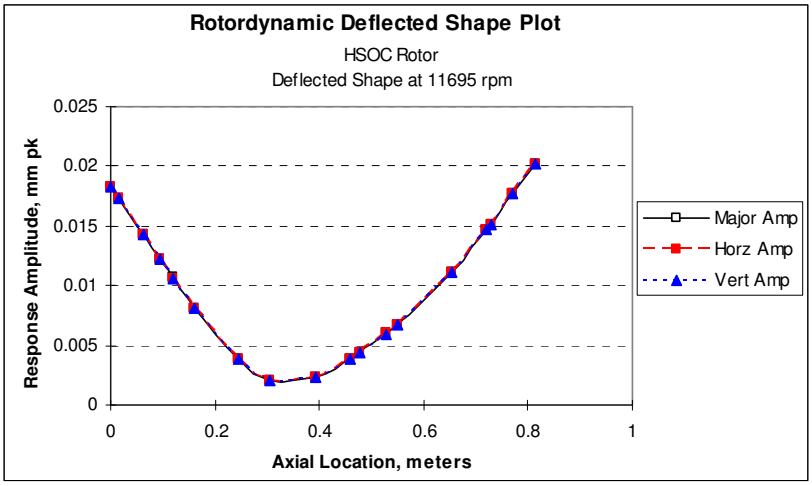

Figure 56 Calculated operating deflection shape for HSOC compressor rotor at endurance running speed of 11695 rpm

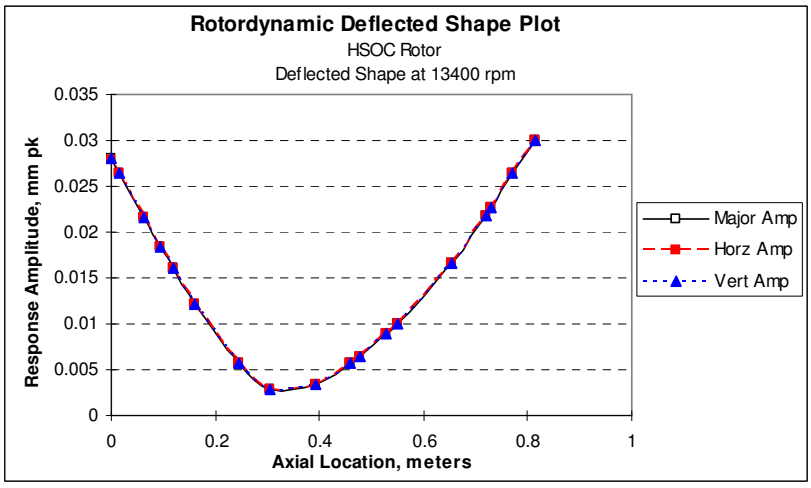

Figure 57 Calculated operating deflection shape for HSOC compressor rotor at maximum running speed of 13400 rpm

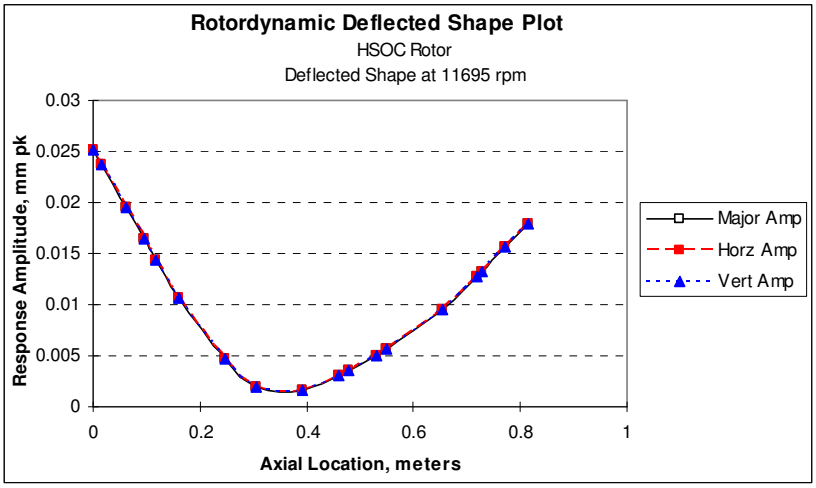

Figure 58 Calculated operating deflection shape for HSOC compressor rotor at endurance running speed with low bearing pad inlet viscosity

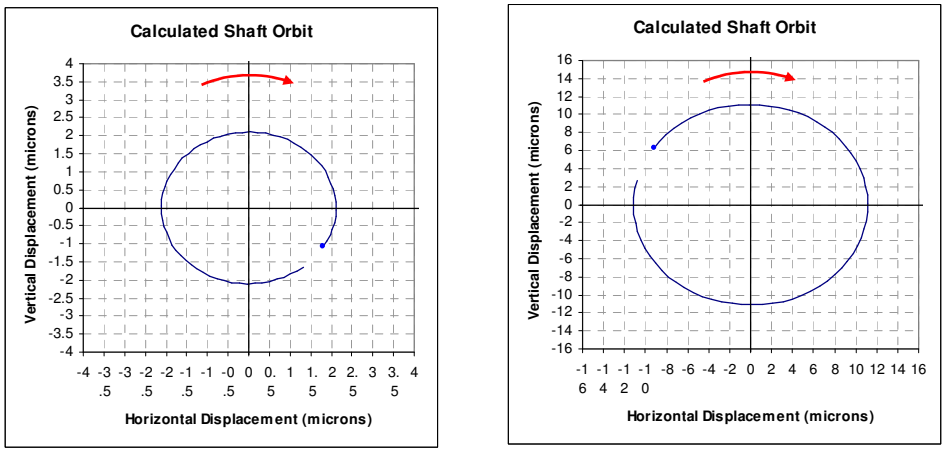

Figure 59 Predicted whirl orbits for HSOC compressor rotor for NDE and DE end bearings rotating at endurance running speed 11695 rpm

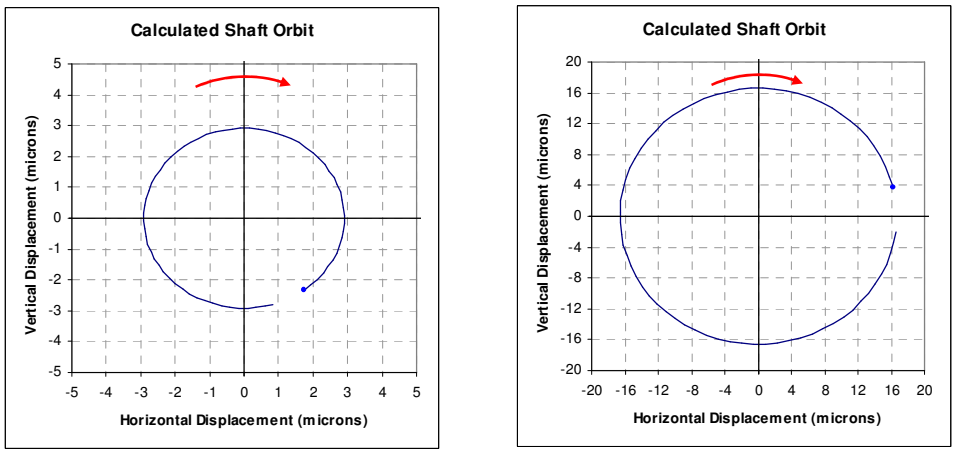

Figure 60 Predicted whirl orbits for HSOC compressor rotor for NDE and DE end bearings rotating at maximum running speed 13400 rpm

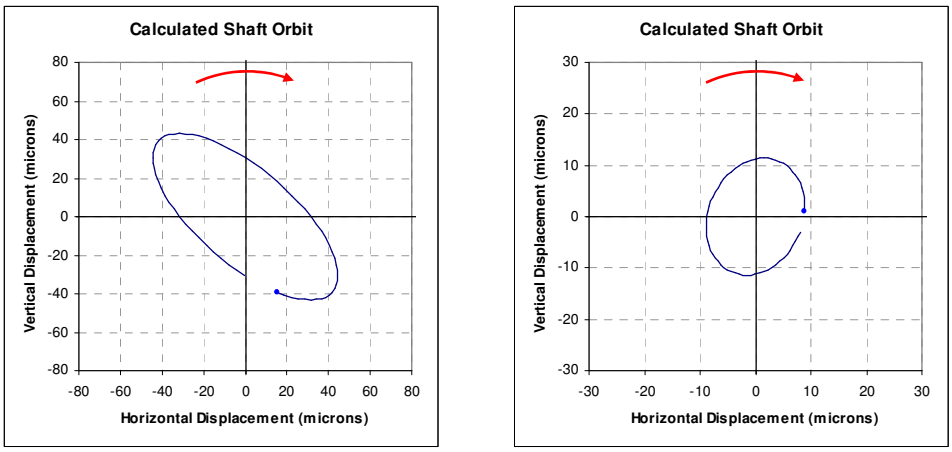

Figure 61 Generated shaft whirl orbits from measured HSOC compressor rotor test data for NDE and DE bearing locations running at 13400 rpm

4.3 Discussion

Taking the author's rotordynamic work presented here in combination with physical data presented in the literature, the principle observations, conditions and relationships are now briefly discussed. The author concludes with a short summary of the principal rotordynamic and bearing performance characteristics that can be associated with the Morton effect instability for use in predictive sensitivity assessments and moreover the design of the experimental test rig.

Of the cases considered in this chapter all machines showed the time dependant hysteresis effect (as shown in Figure 34 and Figure 48) on shaft vibration whereby, once the machine had reached a point of instability and was slowed, the vibration level did not immediately reduced to its initial level but remained higher during the run down, it only approached its original run-up levels after a period of time. This effect was accompanied in all cases by some shift in phase angle, where this was observed to be 70-80^{o}, 160-180^{o} and 130-150^{o}, for the de Jongh et al [11], Faulkner et al [12,13] and HSOC rotors respectively. Of the cases evaluated, the time constant involved for the unstable nature of the vibration to take hold was between 1 and 5 minutes. With the de Jongh et al [11] rotor increasing from 15%C_d microns to 30%C_d microns in 60 seconds, Faulkner et al [12,13] rotor stability cyclic period taking ~90 seconds and steadily increasing in amplitude over a loner time base of

15-20 minutes. Finally the HSOC rotor increasing from ~21%C_d to ~33%C_d in ~400 seconds.

Bearing loadings for all bearings were relatively low, with specific loadings always below 0.3 MPa. This was accompanied by lower levels of eccentricity ratio within the bearing (ranging from 0.1-0.3) which is directly associated with the low specific loadings. Both fixed geometry and variable geometry bearings have been seen to initiate thermal instability conditions. It is also observed that the shaft whirl orbit shapes in the region of instability are very circular, although the re-synthesised orbits generated from the measured data of the HSOC rotor show higher elliptical components than the predictions.

In the cases examined not all rotors were operating at, or necessarily close to, a region of a predicted rotordynamic critical. The de Jongh et al [11] and HSOC rotors were both operating close to critical speeds. However, in the case of the Faulkner et al [12,13] rotor, it was operating in a super critical region but away from the next shaft bending mode by a suitable separation margin > 30%. In all cases the shaft critical modes are associated with some shaft rotor bending. In the case of the de Jongh et al [11] rotor the first simple support bending mode is traversed and the rotor is operating closely to the second shaft bending mode, whereas in the Faulkner et al [12,13] and HSOC rotor the modes are coupled shaft overhung-bearing modes. In all the cases examined the calculated rotor operating deflection shape at the unstable operating speed is associated with a rotor bend point at the bearing location where the shaft overhang is present. From these observations it is possible to state that the operating vibration mode shape will tend to be sympathetic to a rotor bow of an overhung section, it does not necessarily need to be associated with a region of amplified dynamic response by operation close to or at a critical speed, which is in slight contradiction to that presented by de Jongh et al [11].

From the rotordynamic work presented here and the information presented in the literature, it is clear that one of the most significant aspects in the thermal stability of the rotors is the phase conditions present at the overhung rotor bearing section. The deflected rotor response shapes are consistent with a ‘typical’ shaft bend mode being present at the overhung section of the rotor. However the calculated mode shapes for the rotor critical speeds give rise to conditions where the journal surface on the inside of the bow is closest to the bearing surface (i.e. minimum film thickness and hence heat flux). Therefore from a qualitative perspective, this condition would tend to generate a thermal

differential such that the thermal bow, as a result a predominately forward whirl orbital, would result in a stabilising effect with respect to the mechanical unbalance. However the speeds at which instability have been observed to initiate are where the calculated phase lag begins to shift to a point of ~between 80 and 150 degrees or greater. This condition would then result in a vectorial contribution which will begin to compliment or add to the level of mechanical unbalance as a result of any thermal bow. The observation that the phase difference is less than 90 degrees would require that a further lag between the minimum film thickness and the thermal bend formation be present to provide a condition where a positive feedback loop is created to result in a system gain >1. This condition of phase lag between the shaft hot spot and rotor peak response was identified by Keogh et al [9] in the plain bearing THD model for a simple shaft model and also by deJongh et al [11]. The rotordynamic work presented here indicates that a significant thermal phase lag would be needed in addition to the presence of rotordynamic phase lag to be present to provide a suitably strong positive gain via the shaft thermal bow. This would provide the necessary threshold point to initiate instability. Typically the phase lag would need to be somewhere in the region of 15+ degrees in the fully unstable cases and between 0 and 40 degrees for the marginal cases based on the calculated rotordynamic cases considered here.

The unbalance response characteristics of the rotors considered is predicted to be quite different in each case. The de Jongh et al [11] rotor was found to be very sensitive to unbalance (which correlates with the predicted low level of log decrement seen for the rotor second critical speed) at the overhung mass with a vibration to unbalance ratio of 0.025 $\%C_d$/g.mm at 10000 rpm with this increasing to 0.052 $\%C_d$/g.mm at the instability speed of 11500 rpm. The Faulkner et al [12,13] and HSOC rotor were found to have lower sensitivities at 0.028 $\%C_d$/g.mm at 10000 rpm for Faulkner et al [12,13] and 0.03 $\%C_d$/g.mm for the HSOC rotor. The unbalance sensitivity conditions correlate with the more aggressive thermal instability response observed on the de Jongh et al [11] rotor when compared to the less aggressive conditions seen on the Faulkner et al [12,13] and HSOC cases. It should be noted however, that the unbalance distribution in the rotor elsewhere was seen to significantly modify the response characteristics at the bearings and also the operating deflection shape. This could therefore modify the response sensitivity and phase conditions at the overhung mass bearing in terms of altering the rotor's response to thermal instability and the location of the stability speed threshold.

A closer inspection of the results for the HSOC rotor would suggest that the change in rotordynamic conditions, due to an increased inlet viscosity, were associated with the cooler start up conditions, is very slight. The more influential aspect that drives the instability threshold is the increased viscous shearing in the oil and corresponding heat generation.

In the Faulkner et al [12,13] rotor, whilst the unstable threshold speed is not apparently closely associated with a critical speed, it does run in fairly responsive rotor-bearing mode in the high speed range. During this, significant and progressive phase change is predicted in the analysis. This phase change (if linked with an additional thermal phase shift), when coupled to the predicted shaft rotor deflection shape, would provide a positive gain to the magnitude of rotor unbalance response at the turbine shaft end.

An interesting feature of note from both the Faulkner et al [12,13] and HSOC rotor is the interaction between the DE and NDE bearings where significant influence is seen between the two locations. From which it is apparent that this interaction is significant in driving the instability. This coupled relationship is one that would require additional consideration when linking any rotordynamic and thermal instabilities, where existing attempts at thermal bowing analysis have generally been limited to sub-modelling a particular section of the dynamic system focused around the bearing and overhung shaft sections.

It is clear from the conditions outlined above, that the combination of various operating parameters and the methods in which they react make the precise analysis of the thermal stability condition a very complex one. It should also be noted that, whilst rotordynamic and hydrodynamic analyses have developed to a level of accuracy once thought impossible, there remain a number idealisations and assumptions in the analytical and numerical procedures which result in a residual level of error in the performance predictions. As such it can be understood how the precise evaluation of thermal instabilities is a very difficult one where no prior knowledge of the thermal or rotordynamic conditions of the machine are available.

The principle observations and conditions concluded from the examined cases are:

- Regions of thermally induced instability are associated with areas of rotordynamic shaft bending at or around the bearing location.
- Fundamental modes of the vibration result in high spots being on the inner bend point therefore suitable phase lag is required to generate a positive feedback condition. I.e. any instability will occur at some point below or above a natural frequency where the level of separation is heavily governed by the system damping.
- The combined rotordynamic and phase conditions are key to the conditions promotional for unstable conditions within a system.
- Orbit shape is typically circular and centred in the bearing (low eccentricity ratios)
- All shafts are running above or in close proximity to a critical speed.
- Both fixed and variable geometries have shown the phenomenon.
- All rotors have significant overhung sections on the rotor.
- Sensitivities to overhung section imbalance range from 0.025 to 0.052 $\%C_d$/g.mm. Rotors with higher sensitivities show more aggressive instability conditions.
- All published cases have been seen to occur on relatively high speed machines operating between 9000 rpm and 14000 rpm.

Chapter 5

Design of Experiment - Experimental Test Rig

5. Design of Experiment - Experimental Test Rig

5.1 Introduction

This chapter describes the methods and process used to specify, analyse and latterly design the experimental apparatus used to obtain the empirical data presented within this thesis. Whilst some prior studies had been undertaken into this topic area within the Cranfield rotating machinery department no suitable test rigs were in existence at the outset of the research, hence the necessity for the complete design and construction of suitable test equipment to be undertaken.

The principle need for the creation of the test equipment was driven firstly by the requirement to generate some controlled experimental data for a high speed rotor specifically engineered to be prone to the Morton effect. The generation of this data is needed due to a lack of quality data being available in the field. In particular the need for coupled rotordynamic measurement and rotor journal temperature is an area, that to the author's knowledge, no dedicated empirical data has been published to date with the exception of the one industrial example presented de Jongh et al [11]. A secondary function of the rotor test rig was to provide a means of practically benchmarking the current analytical procedures presented in published work to provide practicable means of assessing the susceptibility of high speed rotors to bearing initiated synchronous thermal instability, such as that presented by Balbahadur [19].

5.2 Experimental Rig Design Requirements

At the outset it is critical to ensure that the requirement of the test equipment are well defined and achievable. The principle for the objective of the testing work been generally outlined earlier in this thesis but a more prescriptive set of requirements is outlined in the following points.

The experimental test apparatus should be specified and designed with capability to address the following functional criteria:

- Rotor-bearing system rotordynamic design to be sympathetic to the conditions considered to be promotional of the Morton effect as defined in chapter 4 of this thesis.
- Rotor is to operate above the first shaft bending critical speed and within an appropriate proximity of second bending critical.
- Operating speed is to be representative of appropriate industrial machines where thermal instability has been observed. A minimum peak operating speed of 10000 rpm should be applied.
- Dynamic shaft journal temperature measurement of the bearing journal at the non-drive overhung mass section of the rotor is required. Sensors are to be suitable to capture a fundamental harmonic temperature distribution at an accuracy level of +/- 0.15 degrees of peak absolute operating temperature. The selected measurement solution must not significantly impact on rotordynamics or thermal distribution of the rotor.
- A clean, constant and controlled lubrication oil supply system is required, allowing for the adjustment of supply pressures and temperatures to be made. Oil inlet temperatures should be representative of appropriate industrial machines, i.e. 40 ^{o}C.
- Rotor speed should be able to operate at any speed between 0 rpm and full speed (i.e. variable speed operation) by means of an independent drive system.
- Test rotor journal bearing temperature shall be measurable to enable suitable operating temperature profiles to be obtained from the test bearing and for safety purposes on non test bearing locations.
- Dynamic shaft vibration measurements are required, capable of capturing both phase and amplitude of vibration.

- Steady state shaft position measurement of test bearing is required.
- Vibration measurements along the rotor length to enable basic operating mode shapes to be interpreted.
- Data acquisition equipment must be suitable of capturing dynamic data at a sampling rate which allows for accurate frequency analysis and high speed shaft spatial movements to be adequately expressed. All low frequency thermal data must be capable of being captured and logged at a sampling frequency of no less than 10 samples per minute.
- Rotor must be capable of being operated in a safe and controllable manner for extended periods of time by a single operator.

5.3 Measurement, Instrumentation and Control

As part of the experimental activity, a key element of the work is to obtain suitable measurements of sufficient accuracy to fully characterise and observe the principal features of interest relating to the thermal instability.

The rotordynamic aspects are clearly a fundamental feature that requires close monitoring and measurement. To physically observe this sufficient instrumentation is needed to qualify the dynamic response of the rotor at key points along the rotor's length. This should be achieved by means of dynamic displacement measurements at the bearing locations and at several significant points on the rotor to enable the operating deflection shape of the shaft to be measured. Suitable means of phase referencing is needed to enable a full planar spatial description at each location and correlation between various points on the rotor.

Thermal measurement is again a fundamental parameter of interest and this is both in the bearings, shaft journal and lubrication oil. The thermal conditions in and around the bearing need to be measured sufficiently to obtain either a suitable means of benchmarking theoretical predications or an as measured map of the temperature conditions within and around the bearing. The accuracy of instruments used should be such that the resolution and absolute measurement obtained is several orders less than the expected temperature variations around the bearing shell. Whilst the temperature conditions at both bearings is of interest, a fuller understanding at the test bearing is necessary as it is the circumferential thermal distribution in the bearing which dictates the resulting temperature distribution within the shaft journal.

Of all the parameters involved in system instability, the temperature distribution around the shaft journal provides the most significant condition required to drive the time based response of the system and interaction with the rotor geometric conditions. This parameter, whilst very significant, is the one feature which is least analytically described and also to date very little practical measurement has been reported or published. As part of this research, direct measurement of the shaft journal will be needed to provide a direct observation of the thermal conditions present within the shaft rotor and how they develop across the dynamic operating range of the rotor. The measurement of this area of the machine is more challenging due to the nature of the rotating high speed shaft combined with the relatively high resolution of temperature measurement needed to sufficiently describe the temperature conditions for the expected temperature differentials around shaft. Based on the case studies presented and the work discussed by Keogh et al [9] then temperature variations across the shaft journal could range from ~2 to 10 degrees at the point of instability. This requires that, to ensure suitable measurement under stable conditions is obtained, absolute measurement accuracies should in the range of +/- 0.15 ^{o}C or better.

Several other parameters associated with the lubrication supply to the bearings requires monitoring and control. The two principle parameters being the supply viscosity, which can be monitored and controlled by means of inlet temperature, and also the supply pressure to the bearing which will influence the rate of bearing flow and hence cooling conditions. These parameters need to be carefully controlled and monitored so as to ensure a good level of repeatability in the running conditions at the bearings for the range of test conditions evaluated. The potential sensitivity of the thermal conditions within the bearing and shaft due to the oil inlet viscosity are inferred in the example case study 3 summarised in chapter 4 where the instability was only incurred when operating at lower oil inlet conditions.

All instrument outputs need to be suitably logged and acquired to enable the necessary post processing activities. For dynamic signals such as the shaft vibration and any seismic measurement, this should be carried out at a suitable frequency to enable both harmonic analysis and real time description of the shaft movements when considered with relation the rotor running speed (i.e. sufficient points are acquired per shaft rotation to geometrically describe the shaft's position and loci). Temperature measurements for the purposes of this study can be considered as quasi-static due to the steady state or slowly moving nature of the thermal differentials and thermal inertias involved. The

changes of temperature with time have been observed to be slow with relation to shaft rotation frequencies in the work presented by Keogh et al [10]. As such the sampling frequency for the temperature measurements can be as low as 0.25 Hz without influencing the quality of measurement.

5.4 Experimental Test Rotor and Bearing Design

5.4.1 Bearing Design and Selection

Two types of bearing have been initially identified for use within the rig. The selection consists of one fixed geometry bearing and one variable geometry bearing. The design and selection procedure for each of the bearings is described in the following sub sections.

5.4.1.1 Fixed Geometry Bearing

A fixed geometry bearing is, as the name suggests, one in which the profile of the bearing bore that is produced by its manufacturing process to the required design specifications and remains consistent during operation. A number of established fixed geometry bearings are available, each providing slightly different operating characteristics. The basic necessity for different bearing types being required is to ensure that, within the operating speed ranges shaft stability can be maintained and the occurrence of a potentially aggressive vibration termed as 'Half Speed Whirl' or 'Shaft Whirl' be avoided. Whilst the specific limiting ranges (such as speed or load) for bearing type is dependent on the actual rotor-bearing arrangement, Table 6 provides a brief summary of the general performance measures for different fixed geometry bearing types.

For the experimental test rig two types of fixed geometry bearing were considered, the taper dam and the offset half. Each of these bearings offers some resistance to whirl by introducing pre-load into the oil film using a form of geometrically forced converging oil film. The taper dam is a simpler bearing to manufacture and as such less costly, so this would have been the preferred option if a workable solution could be identified. However due to the shaft speeds and static shaft loads involved it was felt unlikely that this type of geometry would provide a suitably stable design. It was evaluated for completeness.

The fundamental design constraint with reference to the bearings was the amount of available drive power as dictated by the test drive motor and inverter. As such it was necessary to ensure that the motor/inverter torque speed characteristic was matched to the bearing speed power loss characteristics. At full speed the max motor output shaft power was limited to 4.5 kW. After calculating and evaluating some approximate bearing power losses for a range of bearing journal sizes and comparing these against the available motor torque, a nominal bearing journal diameter of 50mm with a length to diameter ratio of 0.7 was selected as the limiting constraint. With the nominal bearing size determined, a number of bearing designs were analysed and the various relevant operating parameters extracted for comparison. Table 7 presents the data for the taper dam and offset half bearing designs for a range of assembled bearing diametral clearances. Stiffness and damping values are not included in the table due to the quantity of data generated but a measure of stability is included by means of the critical mass and whirl frequency. It should be noted that the stability requirement is based on a critical mass being more than half the shaft mass, i.e. approx. 15 kg, and to provide a sufficient margin for calculation error, a value of +25% was applied to his half mass criteria. The bearing performance calculations were performed using the Franklin Institute HYBJRN AGSL custom Fortran routine [54].

From the data in Table 8 it can be seen that the taper dam bearing variants do not provide a stable bearing at all running speeds and also bearing temperatures can be seen to exceed 100 deg C. For satisfactory operation and to ensure no unwanted dynamic or functional performance complications are present which could cloud any evaluations relating to the presence of the 'Morton Effect' the bearings must operate in a fully stable range with respect to bearing whirl and operate within peak metal temperatures of 95 degrees C.

Bearing Type	Load Capacity	Resistance to Whirl	Stiffness & Damping	Comments
Cylindrical Bore 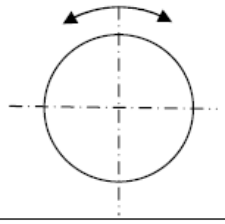	1 = Poor 10 = Excellent			
	8	2	4	Reversible and easy to manufacture.
Taper Dam Groove 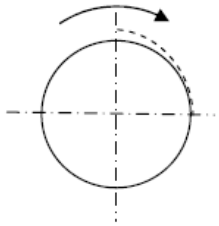	8	3	4	Uni-Directional and more complex manufacture.
Lemon Bore/Elliptical 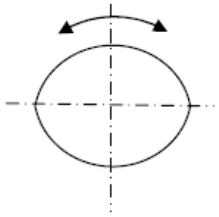	7	4	5	Reversible easy to manufacture. Horizontal stiffness weak.
3 Lobe 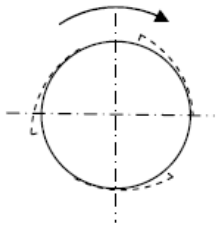	5	6	7	Uni-Directional and difficult to make. Can suffer with wear during start up with static loads > 0.4 MPa.
Offset Half 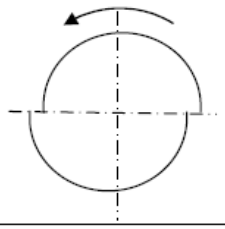	6	8	8	Uni-Directional. Provides good damping.

Table 6 Fixed Geometry Bearing Types

It has been suggested, in several of the published works relating to Morton Effect instabilities, that hydrodynamic bearing conditions where the rotor is sensitive to instability [10,19,23], the quasi-static shaft running position remains relatively central with respect to the bearing centre, having eccentricity ratios ε_o generally operating at < 0.3. Additional to this is the requirement that a reasonably circular orbit with moderate amplitude is

attained. For this to occur the bearing must not have too higher values for stiffness and damping or this could produce an over stable system with low response to synchronous unbalance. It is the balance between having a stable system but also a responsive system that requires careful and considered selection of the bearing arrangement and geometries.

Bearing Design	Bearing Type	Diametral Clearance C_d (mm)		Bearing Pre-load p_R	
		minimum	maximum	maximum	Minimum
2	Offset Half	0.102	0.143	0.5	0.3
3	Offset Half	0.127	0.168	0.5	0.3
4	Offset Half	0.153	0.193	0.5	0.3
5	Offset Half	0.102	0.143	0.3	0.3
6	Offset Half	0.127	0.168	0.3	0.3
7	Offset Half	0.153	0.193	0.3	0.3
8	Taper Dam	0.127	0.168	0.1	0.16
9	Taper Dam	0.153	0.193	0.1	0.16
10	Taper Dam	0.178	0.219	0.1	0.16
11	Taper Dam	0.203	0.244	0.1	0.16
12	Plain Cyln	0.102	0.143	0.1	0.16

Table 7 Fixed Geometry Bearing Designs

Using the evaluations outlined above the fixed geometry bearing type selected was an offset half type. Considering the specific operating parameters of oil film thickness, stability, operating temperature, stiffness and damping the following designs 2, 3, 4 and 5 provide acceptable functional solutions, see Table 8. For the final selection of the bearing geometry and clearances the rotordynamics and bearing dynamics need to be considered in combination. This aspect is covered in the following sections rotordynamic analysis.

Bearing Design	Shaft Speed (rpm)	Eccentricity Ratio		Minimum Film Thickness (mm)		Maximum Bearing Temperature (deg C)		Stability. Critical Mass (kg) (> 15)	
		min c_d	Max c_d	min c_d	max c_d	min c_d	max c_d	min c_d	max c_d
2	5000	0.017	0.043	0.025	0.046	68	63	296	3483
	10000	0.01	0.023	0.025	0.046	84	75	119	1390
	15000	0.007	0.016	0.025	0.043	94	84	66	729
	20000	0.006	0.013	0.025	0.043	102	92	43	459
3	5000	0.026	0.06	0.030	0.056	62	57	188	1927
	10000	0.014	0.032	0.030	0.056	74	70	64	821
	15000	0.01	0.022	0.030	0.053	83	76	34	479
	20000	0.008	0.018	0.030	0.053	90	82	32	308
4	5000	0.037	0.078	0.036	0.064	59	56	133	1149
	10000	0.019	0.042	0.038	0.064	68	66	48	513
	15000	0.013	0.029	0.038	0.064	75	71	27	313
	20000	0.011	0.022	0.038	0.061	81	76	17	214
5	5000	0.023	0.044	0.033	0.046	72	63	295	683
	10000	0.013	0.023	0.030	0.046	91	75	118	236
	15000	0.01	0.017	0.030	0.043	103	84	66	126
	20000	0.008	0.013	0.036	0.043	113	92	43	80
6	5000	0.036	0.06	0.041	0.056	67	57	188	389
	10000	0.019	0.032	0.041	0.056	80	70	64	150
	15000	0.014	0.022	0.038	0.053	90	76	34	83
	20000	0.011	0.018	0.038	0.053	98	82	32	53
7	5000	0.049	0.078	0.051	0.064	62	56	133	247
	10000	0.026	0.042	0.048	0.064	72	66	48	102
	15000	0.019	0.029	0.048	0.064	81	71	27	57
	20000	0.015	0.022	0.046	0.061	88	76	17	37
8	5000	0.201	0.154	0.051	0.071	91	76	40	86
	10000	0.192	0.166	0.051	0.071	118	101	5	24
	15000	0.187	0.157	0.051	0.071	136	117	4	15
	20000	0.183	0.153	0.051	0.071	151	130	3	9
9	5000	0.168	0.171	0.061	0.081	81	71	33	66
	10000	0.199	0.173	0.061	0.079	104	91	7	17
	15000	0.192	0.163	0.061	0.081	120	106	3	9
	20000	0.188	0.157	0.061	0.081	133	117	2	7
10	5000	0.159	0.19	0.076	0.089	73	67	27	37
	10000	0.169	0.128	0.074	0.097	97	84	5	8
	15000	0.16	0.169	0.074	0.091	112	97	3	4
	20000	0.154	0.162	0.076	0.091	124	107	1	2
11	5000	0.18	0.21	0.084	0.097	70	63	23	31
	10000	0.119	0.143	0.084	0.104	88	78	2	6
	15000	0.166	0.116	0.084	0.102	102	89	2	2
	20000	0.159	0.167	0.086	0.102	113	99	1	2
12	5000	0.075	0.106	0.046	0.064	99	77	17	5
	10000	0.119	0.15	0.089	0.104	78	70	5	6
	15000	0.099	0.117	0.091	0.107	92	79	2	3
	20000	0.086	0.102	0.091	0.109	102	88	1	2

Table 8 Summary of Fixed Geometry Bearing Calculations

5.4.1.2 Variable Geometry Bearing

A variable geometry bearing is a partial arc design configuration of a plain bearing. The configuration is made of multiple individual bearing pads which are allowed to pivot or tilt to conform with the dynamic loads from the lubricant and shaft, generate a converging oil film wedge capable of supporting radial loads. The principle benefit of tilting pads bearings is that they are capable of operating at high speeds under light load conditions whilst maintaining a high degree of stability and resistance to whirl. A tilting pad bearing however generally has a lower load carrying capacity than a plain bearing and also, due to its increased complexity, carries a higher cost.

The pads are produced with a greater radii of curvature than the radii at which they are mounted relative to the bearing centre. This condition introduces the pre-load effect which helps to generate the oil film wedge and as such directly influences the bearing load carrying capacity and specifically the dynamic properties of the bearing. The bearing can be configured with a varying number of pads, typically 4 or 5, which are either configured with a central pivot or an offset pivot which allows bi-directional and uni-directional operation respectively. Figure 62 shows a schematic of a typical tilting pad bearing configuration.

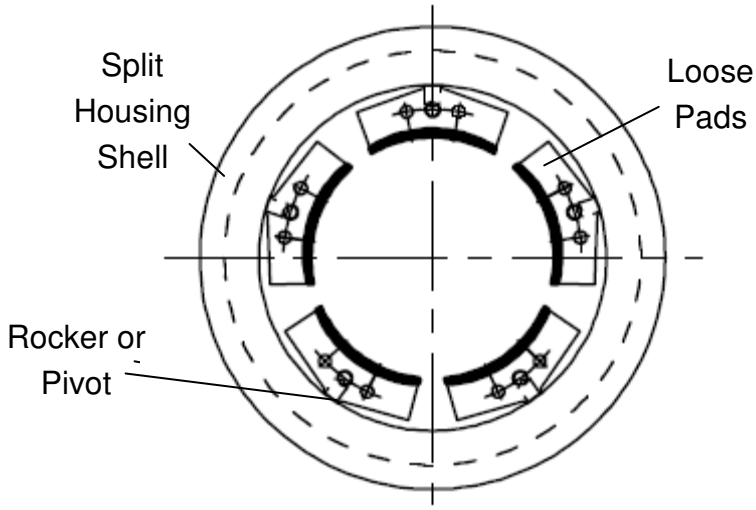

Figure 62 Tilting pad bearing schematic.

The design of the tilting pad bearing for the experimental rig was based around a 5 pad central pivot configuration. The bearing diameter was pre-determined at 50mm by the previous work conducted on the fixed geometry bearing selection. It was originally intended that an existing bearing design would be procured from an established bearing manufacturer. However, due

to the cost constraints of the project and the high cost of the bearings, it was decided that the bearings would be specifically designed and manufactured.

The detailed parameters of the bearing design were determined such that the fixed geometry bearing and tilting pad bearing would be fully interchangeable. Clearance and pre-load ranges for the bearing were selected to be consistent with the internal geometry used in industrial variable geometry bearings when running under light loads. Table 9 gives a summary of the tilting pad bearing specifications.

Bearing Design Ref	Diametral Clearance C_d (microns)	Shaft Speed (rpm)	Eccentricity Ratio	Minimum Film Thickness (mm)	Maximum Bearing Temperature (deg C)
13	70	5000	0.099	0.025	64.0
		10000	0.063	0.025	77.0
		15000	0.050	0.025	87.0
		20000	0.041	0.024	95.2
14	90	5000	0.157	0.032	60.9
		10000	0.105	0.033	71.6
		15000	0.082	0.033	79.5
		20000	0.068	0.033	86.4
15	100	5000	0.190	0.035	59.9
		10000	0.127	0.036	69.7
		15000	0.098	0.037	76.9
		20000	0.084	0.037	83.6
16	125	5000	0.270	0.041	57.6
		10000	0.186	0.044	66.5
		15000	0.146	0.045	72.9
		20000	0.123	0.046	78.7
17	140	5000	0.312	0.044	56.5
		10000	0.221	0.048	64.9
		15000	0.176	0.05	71.4
		20000	0.150	0.051	76.9
18	160	5000	0.365	0.047	55.4
		10000	0.261	0.053	62.8
		15000	0.214	0.055	69.2
		20000	0.186	0.057	75.1

Table 9 Summary of Variable Geometry Bearing Parameters Evaluated

Bearing performance predictions were calculated for range of operating speed conditions and clearances. The limiting bearing operational constraints were consistent with those defined for the fixed geometry bearing design. Table 9 provides a summary of the bearing performance data for the running speeds evaluated. The fixed geometry bearing calculations were performed using a custom code referenced as HYDJRN [54], which is custom code developed by Allen Gears in conjunction with the Franklin Institute hydrodynamic bearing codes. The computational procedure uses a 2D finite difference grid to solve the Reynolds equations and flow conditions within the bearing oil film. Bearing performance criteria for lubricant temperatures, pressures, film thickness and stiffness and damping data are produced by the analysis.

5.4.2 Rotor Dynamic Analysis

From the observations made in chapter 4 and from comments presented by both Keogh et al [10] and Balbahadur et al [19], it is suggested that a significant element in creating conditions promotional for thermal instability to occur is the presence of a critical speed within, or of close proximity to, shaft running speeds. From the work conducted in chapter 4 this has not been the situation in all industrial cases, however a 'lively' rotor is required. As such it was defined that that the experimental rotor should be designed to operate above or close to a suitable natural frequency. However care must be taken to ensure that the high vibrations experienced at and around critical speeds are within acceptable and controllable levels. This to some extent can be managed through the stiffness and damping properties in the bearings.

To aid in producing a rotor design that would be susceptible to displaying the Morton Effect, an approach was taken whereby the experimental test rotor bearing system would be designed so as to produce similar dynamic characteristics as defined in chapter 4 section 4.3. The rotor dynamic characteristics were intended to follow those observed in the de Jongh et al [11] rotor, where the rotor was seen to be very sensitive to the thermal instability experienced. This methodology dictates that the rotor is capable of running supercritical, i.e. the rotor runs above its first shaft bending natural frequency.

The specification for the rotor was targeted to have a running range above the first bending natural frequency and up to or very close to that of a second shaft bending mode of the rotor with the maximum rotation speed limited to 10000 rpm. This criterion presents two beneficial features. Firstly, the impact of the first bending natural frequency as well as the second can now be investigated, and secondly, conditions similar to those presented for the compressor rotor produced by de Jongh et al [11], which was shown to display the 'Morton Effect' thermal instability, will be introduced.

A speed limitation of 15000 rpm was established to ensure that some margin remained for the total power consumption of the test rig, which would be limited by the drive motor and frequency inverter capacity (~4.5 kW). Also at speeds beyond 15000 rpm it becomes very problematic and costly to provide methods of extracting the shaft temperature sensor signals from the rotor. The method selected for the extraction of the temperature sensor signals was by means of electrical slip ring. To operate at speeds much above 15000 rpm

without significant signal distortion or excessive wear would require very specialist instrumentation and slip ring technology which would beyond the budget constraints of this research.

5.4.2.1 Preliminary Lateral Rotordynamics

With the basic experimental design criteria established, as a starting position to determine preliminary shaft rotor dimensions, some basic rotor critical speeds were calculated. The shaft diameter was kept fixed nominally at 50mm in line with the bearing dimensions and the bearing span altered to produce a range of shaft natural frequencies. As the shaft overhang has been identified as a key feature in the thermal instability process a nominal shaft overhang length of 200mm was kept constant for all bearing spans. The bearing support stiffnesses were varied across a range to provide indication of the impact of the support effects on the natural frequencies and mode shapes.

The location the natural frequencies is not the only element that needs to be considered at this stage. The associated mode shapes are of great significance especially where they have been attributed to being one of the necessary driving elements observed to provide conditions susceptible to the manifestation of when thermal instabilities can occur [10,11]. As such nominal support stiffnesses were taken from the bearing calculations that had already been performed, and this used to develop a series of un-damped critical speed maps. As the stiffness and damping effects in the bearing are complex and consist of not only directional stiffnesses but also cross-coupling effects, only the Kxx and Kyy stiffness data was considered for simplicity at this point.

The undamped critical speed map was evaluated for the support stiffness range of 1e+5 to 1e+10 N/m. See Table 10. The associated critical speeds for the rotor configurations were established for bearing oil film stiffness range Kxx and Kyy. The resulting natural frequencies that were calculated were assessed and the mode shape categorised in line with the modes shapes as shown in Figure 63. It is important the mode shapes for the natural frequencies encountered within the test rig speed range are suitably described and that they satisfy the previously established criterion with relation to shaft bending modes etc. The mode shapes shown in Figure 63 provide very distinct and separate deflected vibration modes, however in reality the interaction of bearing and rotor stiffness increases the complexity of the modes and in some cases combine to give more complex deflected

shapes. Where this occurs the assigned mode shapes in Table 10 are classified by the combination of the two most relevant mode shapes.

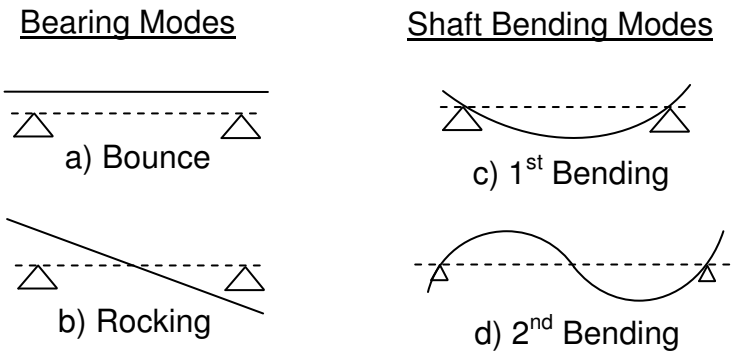

Figure 63 Rotor Mode Shapes Supported in Two Hydrodynamic Mode Shapes

Table 10 shows each of the calculated natural frequencies for the bearing spans considered and assigns the associated mode shapes for each frequency. It can be seen from the data that some of the natural frequencies, although within the speed range, are not specifically shaft bending modes but essentially bearing dominated modes. As such these are not the dynamic conditions that have been defined as those desired for creating conditions sensitive to the Morton Effect as has been specified for the experimental test rotor design. Also damping levels for these bearing modes are invariably high due to being governed by the oil film specifically. For this reason the rotors of 625mm and 500mm bearing span were disregarded as the associated shaft stiffnesses were too high to introduce the desired mode shapes.

Other more practical considerations in the rotor design were aspects such as physical size, manufacture capability and ability to balance etc. Due to these points the preference was to have as short a bearing span rotor as possible whilst providing the desired rotordynamic conditions. This approach identified the 750mm bearing span as being the most preferred arrangement. However, the natural frequency locations for neither the nominal support stiffness or the rigid supports fulfilled the specification for operating speed range. In an attempt to modify the location of the natural frequencies without radically altering the mode shapes, a larger diameter section of 150mm was added to the centre of the shaft for a length of 100mm. The objective of introducing this feature was to add some significant mass to the rotor centre without increasing the shaft stiffness by a similar order of magnitude and pushing natural frequencies up. For comparative purposes all of the rotor bearing

spans were again assessed with the change in rotor geometry. Figure 64 presents the results for the 750mm bearing span in an un-damped critical speed map with approximated nominal support stiffness Kxx and Kyy.

Rotor Bearing Span (mm)	Support Stiffness (N/m)	Natural Frequency (cpm)	Mode Shape
1000	3.2E+07	5695	C
1000	3.2E+07	14684	D
1000	1.00E+07	5793	C
1000	1.00E+07	17584	D
875	3.2E+07	7222	C
875	3.2E+07	14907	D
875	1.00E+07	7381	c
875	1.00E+07	19013	d
750	3.2E+07	9342	c
750	3.2E+07	15169	a/d
750	1.00E+07	9595	c
750	1.00E+07	20401	d
625	3.2E+07	12077	c
625	3.2E+07	15855	a
625	1.00E+07	12544	c
625	1.00E+07	22448	a/d
500.0	3.2E+07	13931.0	c
500.0	3.2E+07	19029.0	a
500.0	1.0E+07	15665.0	c
500.0	1.0E+07	26997.0	a

Table 10 Natural Frequency of Plain Rotors of Varying Bearing Span

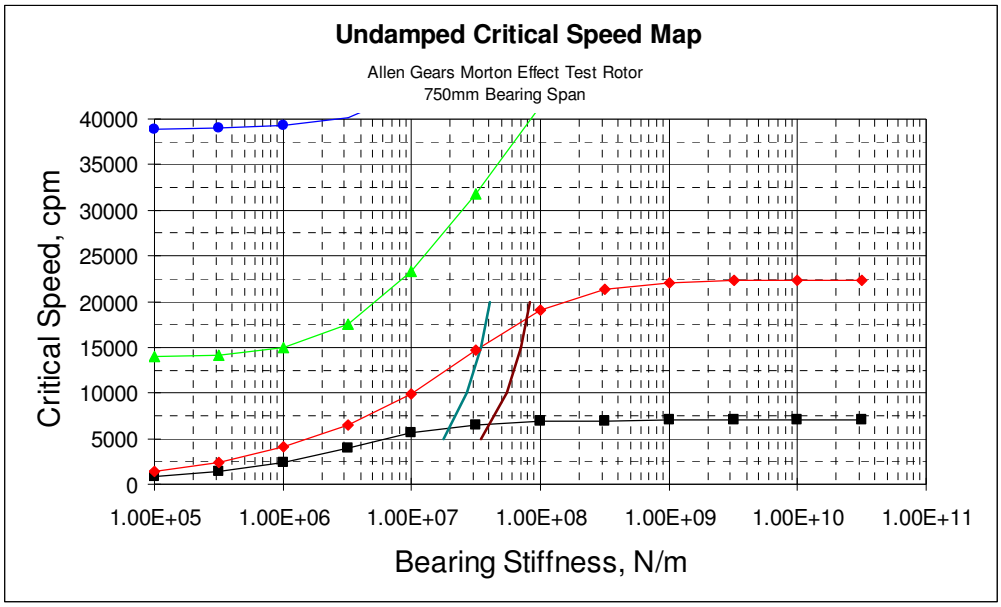

Figure 64 Un-damped Critical Speed Map for 750mm Bearing Span With Added Mass at Shaft Centre

The resulting natural frequency ranges of 6565-6876 and 14649-19087 cpm for the first and second natural frequencies respectively are now close enough to the specified running range that, as part of the detailed rotor design and analysis with specific bearing coefficient data, the desired rotordynamic properties can be obtained. Specifically the introduction of the oil film damping effects onto the rotor will cause a reduction in the natural frequency locations to take place, bringing down the second bending mode closer to the proposed running range capability of the experimental apparatus.

5.4.2.2 Detailed Lateral Rotordynamics

With the nominal rotor dimensions determined, the detailed rotordynamics were performed. In this stage of the design an increased number of operating parameters were considered, such as rotor stability, response, orbit size and phase, unbalance location and fundamentally the damped natural (eigen) frequencies of the system.

In the process of analysing the rotor, a number of bearing designs as established in section 5.4.1 were considered (based upon fixed and variable geometry). For each design the maximum and minimum clearance conditions were considered in combination with different oil inlet conditions. The number of various rotor-bearing combinations generated significant amounts of data and only a summary of those results is presented here. However, it can be said that the controlling feature in the design evaluation and selection of the rotor-bearing arrangement was the system rotordynamic stability.

For the majority of bearing designs considered (essentially clearance and pre-load changes), the natural frequency locations were acceptable through the implementation of some minor geometry changes. It was found that for many of the system combinations the logarithmic decrement (log dec), which is a measure of the system stability (see chapter 4), was low at the location of the first shaft bending natural frequency. It is normal for a system to be considered stable by means of analysis when the log dec value is 0.2-0.3 or greater. Many of the designs produced negative values which is a strong indication that system would become fully unstable and therefore practically inoperable.

There are two principle reasons for the instability. One is that due to excessive clearance and insufficient preload in the fixed geometry bearing

'Half Speed' or 'Shaft' whirl was present. The second was that it appeared that if the bearings were too stiff there was little movement at the bearing supports and hence little damping contribution from the hydrodynamic bearings. As it is also important to have a bearing design where a moderate orbit due to mechanical unbalance is present, then a compromise was struck between the amount of clearance in the bearing, the rotor system stability and the bearing performance.

The calculated natural frequencies and associated mode shapes were extracted for each combination of bearing clearance and oil inlet temperature. The specific natural frequencies were established by means of a Campbell diagram for each case the results of which is presented in Table 11. A Campbell diagram for the nominal bearing clearances is provided in Figure 67 with the associated mode shapes for the 1st and 2nd critical speed presented in Figure 68. The data and associated hydrodynamic and rotordynamic models are based on final dimensions produced following the detail design of the experimental test rotor and components such as couplings etc. An overview of the detailed design is provided later in this chapter. It should be noted at this point that the initial design specification was engineered around the use of fixed geometry bearings as the use of variable geometry bearings was only introduced later in the research programme.

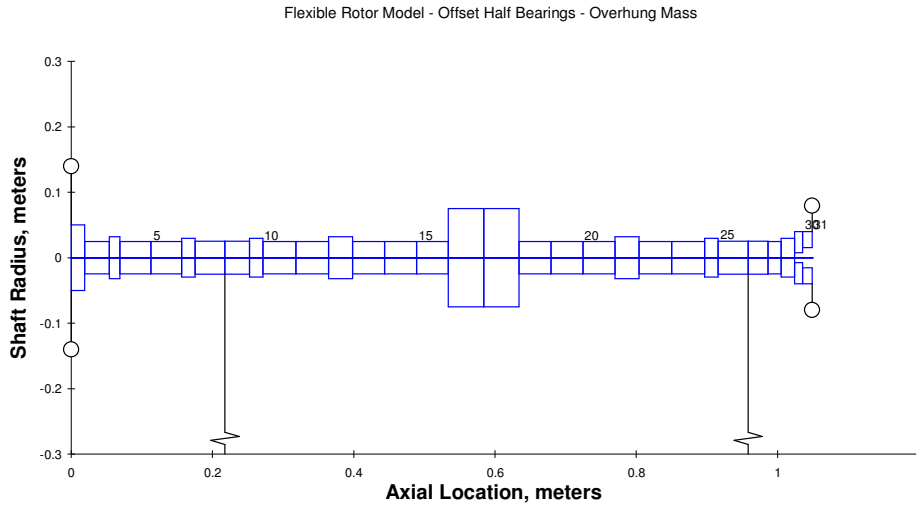

Figure 65 Rotordynamic Model of Flexible Rotor – with Added Mass

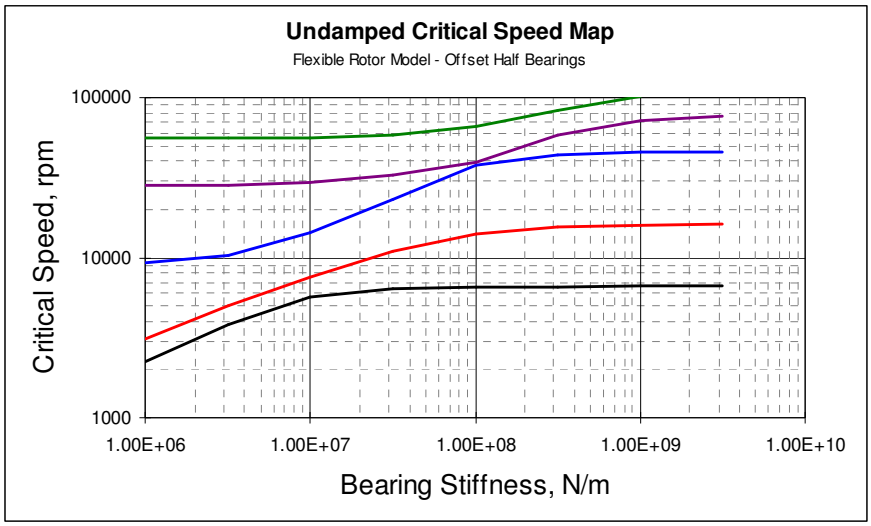

Figure 66 Undamped critical speed map for flexible rotor without added mass

In addition to the model for the plain rotor a number of further calculations were performed where an added mass was included on the overhung section of the rotor. This additional mass allows for modification of the rotordynamic characteristics and also provides a mechanical gain function to the conditions influencing the mechanism of the Morton Effect.

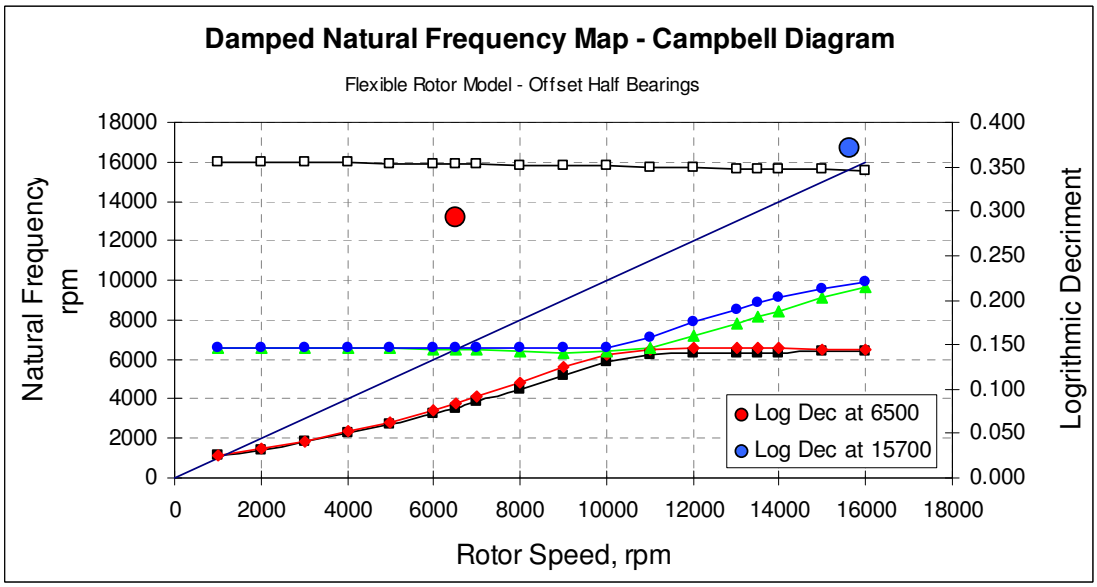

Figure 67 Damped natural frequency map for rotor in fixed geometry bearings, mean clearance, normal inlet temperature with no added mass

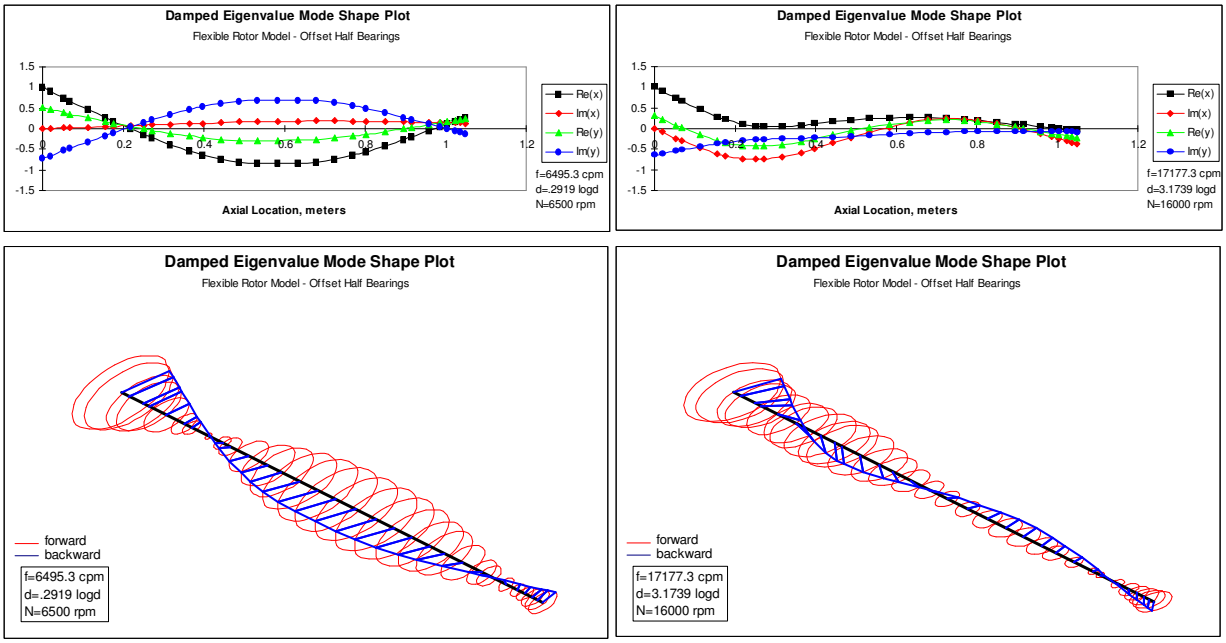

(a) (b)

Figure 68 Mode shapes for rotor in fixed geometry bearings, mean clearance, normal inlet temperature with no added mass (a) is first critical at 6500 rpm and (b) is second critical at 15750 rpm

The effect of the overhung mass is to provide a rotordynamic gain function whereby any thermal differential generated at the NDE rotor journal results in the corresponding bow. This bow then in effect generates further unbalance excitation due to the effectively eccentric mass of the overhung section of shaft and results in a corresponding movement on the journal due to the increased unbalance forces. This is a basic feedback loop mechanism and if the overhung mass amount is increased this results in a greater amplification for any unit thermal bend at the bearing journal.

			Critical Speed 1			Critical Speed 2			Critical Speed 3		
Bearing Type	Clearance range	OHM	Frequency (cps)	Log dec	Mode Type	Frequency (cps)	Log dec	Mode Type	Frequency (cps)	Log dec	Mode Type
Fixed Geometry	minimum	1.3	836	3.994	a/b	6793	0.361	c	20253	1.544	d
	mean	1.3	1105	3.754	a/b	6464	0.302	c	17177	3.174	d
	maximum	1.3	1743	3.644	a/b	6682	0.59	c	24108	1.811	d
Fixed Geometry	minimum	5.0	839	3.969	a/b	6128	0.173	c	12486	3.168	d
	mean	5.0	1120	3.647	a/b	6111	0.214	c	13971	3.647	d
	maximum	5.0	1447	3.673	a/b	6088	0.282	c	18253	3.743	d
Variable Geometry	minimum	5.0	6060	0.0861	c	10339	0.7866	d	-	-	-
	mean	5.0	5972	0.1391	c	8940	1.0447	d	-	-	-
	maximum	5.0	5951	0.1517	c	8557	1.0819	d	-	-	-

Table 11 Summary of Test Rotor Critical Speeds and Mode Shapes

The results of this work are also summarised in Table 11, with some of the critical speed maps and modes included in Figure 69 through to Figure 73. It should be noted however that the introduction of a larger mass at the shaft overhang does not necessarily always result in a higher gain function for the

thermal instability due to the complex relationship between rotor shaft deflection, shaft phase and unbalance response. Conditions can occur where increased mass results in a higher gain which tends to a stabilising thermal condition as opposed to an instability. In some conditions the increase in mass modifies the rotor response characteristics sufficiently that the net effect is to provide a more thermally stable rotor with regards to the Morton effect. This is considered more commonly to be due to reduced response at the bearing as opposed to any phase changes but this is not exclusively the case and is specifically dependant on the rotor geometry and bearing performance characteristics.

Fixed Geometry 'Offset Half' Bearing Design Specification		
Bearing Diameter	50	mm
Bearing Length	35	mm
Minimum Diametral Clearance	0.142	mm
Minimum Diametral Clearance	0.168	mm
Maximum Pre-load	0.3	
Minimum Pre-load	0.3	
Bearing Radial Load	135	N
Bearing Specific Pressure	0.075	MPa
Oil Inlet Temperature	40	^{o}C
Oil Type (Grade)	ISO VG 46	

Table 12 Fixed geometry bearing basic design specification

	Stiffness Oil Film Coeficients (N/m)				**Damping Oil Film Coefficients (N.s/m)**			
Rotational Speed	**Kxx**	**Kxy**	**Kyx**	**Kyy**	**Cxx**	**Cxy**	**Cyx**	**Cyy**
5000	29693312	13350590	-48663248	15089423	90485	-57024	-56849	145932
10000	45732257	21006240	-73393558	22610441	70426	-47126	-43972	114486
15000	59531680	27282193	-95433935	29193587	60966	-42308	-38016	99157
20000	70499356	32270247	-112950771	34425066	54133	-34600	-33636	88032

Table 13 Fixed geometry bearing oil film stiffness and damping coefficients for mean clearance and normal oil inlet temperature

Variable Geometry Tilting Pad Bearing Design Specification		
Bearing Diameter	50	mm
Bearing Pad Length	20	mm
Minimum Diametral Clearance	0.100	mm
Minimum Diametral Clearance	0.125	mm
Maximum Pad Pre-load	0.6	
Minimum Pad Pre-load	0.4	
Number of Pads	5	
Length of Pad	60	°C
Pivot Location	Centre	
Radial Load Direction Load on pad (LOP) Load between pad (LBP)	LBP	
Bearing Radial Load	135	N
Bearing Specific Pressure	0.135	MPa
Oil Inlet Temperature	40	°C
Oil Type (Grade)	ISO VG 46	

Table 14 Variable geometry bearing basic design specification

	Stiffness Oil Film Coeficients (N/m)				Damping Oil Film Coefficients (N.s/m)			
Rotational Speed	Kxx	Kxy	Kyx	Kyy	Cxx	Cxy	Cyx	Cyy
5000	15771000	5254	-3894	17930000	19516	9644	-10184	21399
10000	23397000	20060	12480	24922500	14684	7204	-7366	15346
15000	29565500	7134	-11882	30788000	12352	6008	-6092	12694
20000	34900000	-10647	-24629	35944500	10815	5189	-5254	11031

Table 15 Variable geometry bearing oil film stiffness and damping coefficients for mean clearance and normal oil inlet temperature

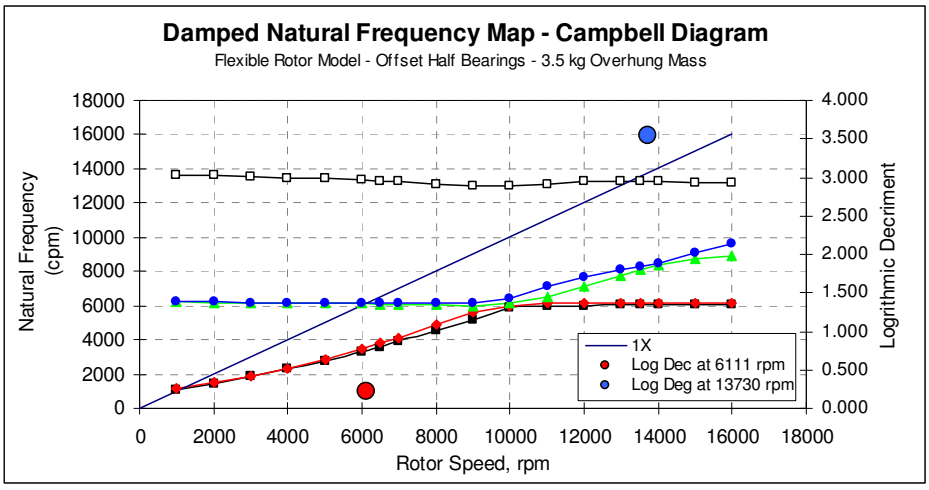

Figure 69 Damped natural frequency map for final rotor design with fixed geometry bearings, mean clearance and 3.5 kg added overhung mass

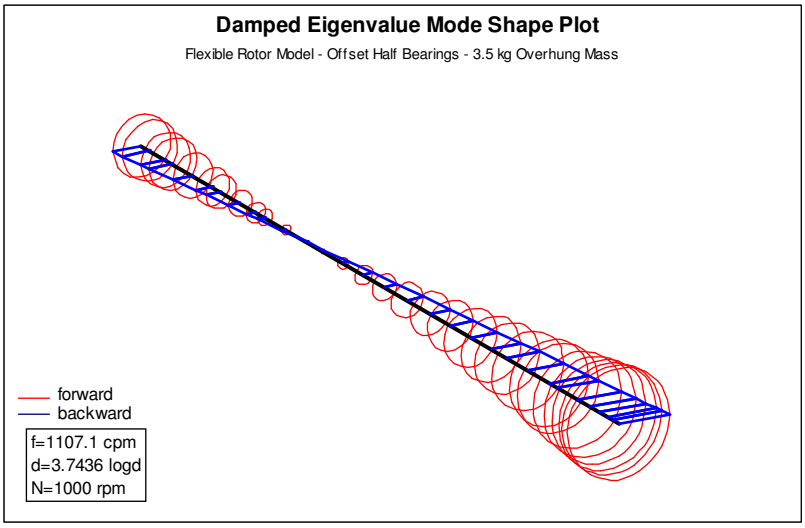

Figure 70 Damped mode shape for final rotor design with fixed geometry bearings, mean clearance and 3.5 kg added overhung mass at 1107 rpm critical (bearing rock mode) with log decrement of 3.743

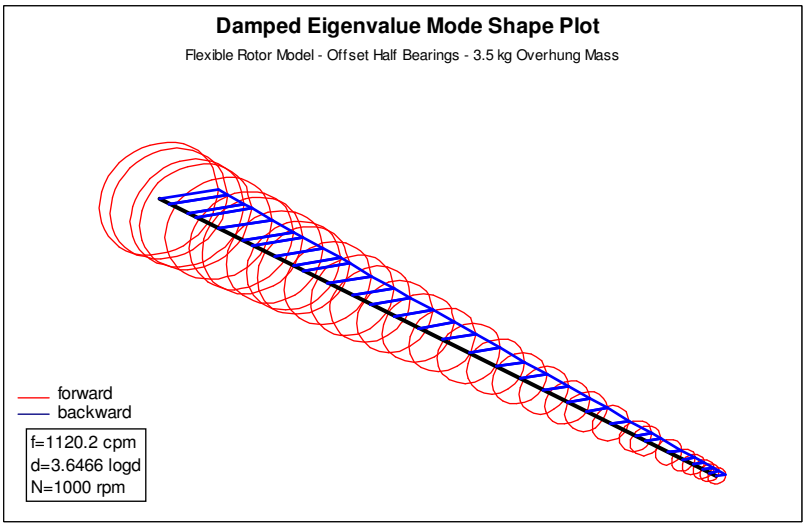

Figure 71 Damped mode shape for final rotor design with fixed geometry bearings, mean clearance and 3.5 kg added overhung mass at 1120 rpm critical (bearing rock mode) with log decrement of 3.646

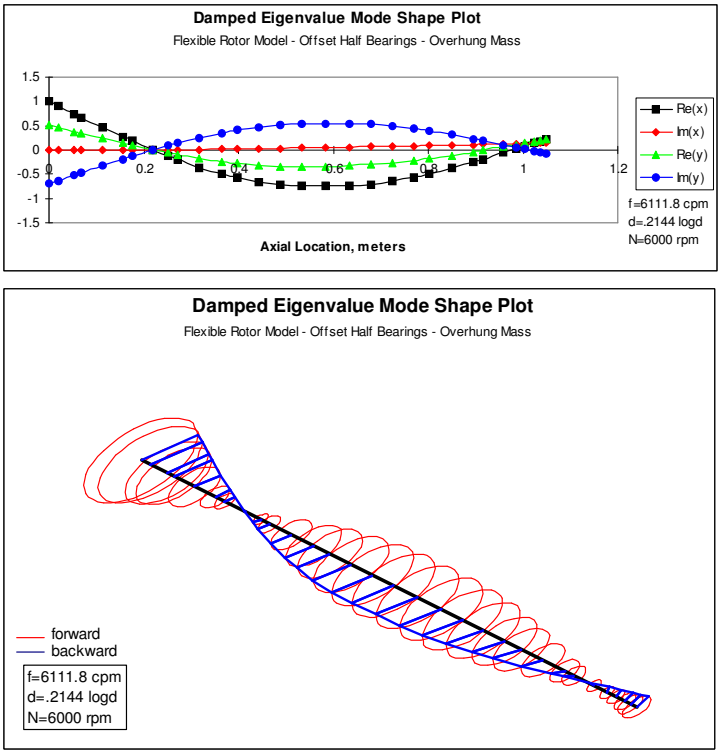

Figure 72 Damped mode shape for final rotor design with fixed geometry bearings, mean clearance and 3.5 kg added overhung mass at 6111 rpm critical with log decrement of 0.214

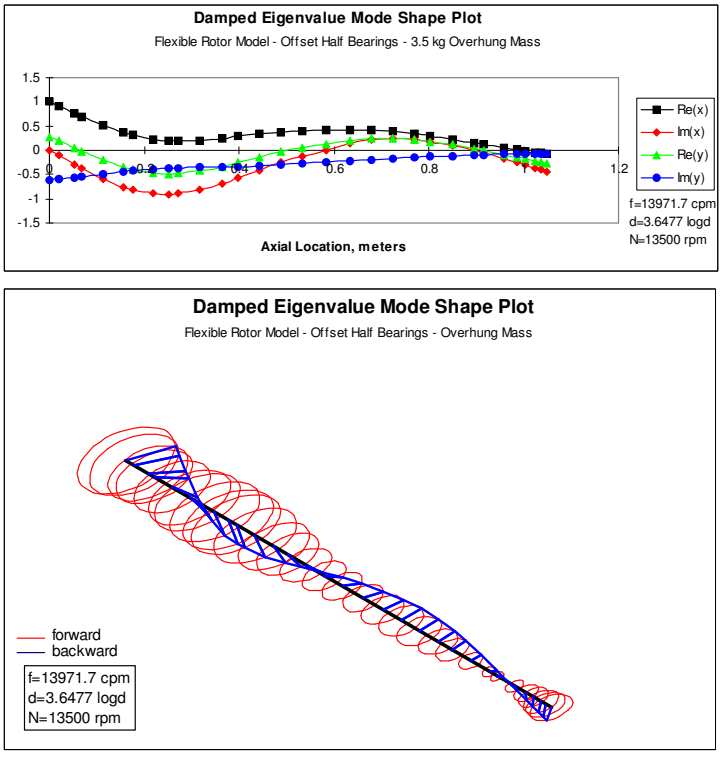

Figure 73 Damped mode shape for final rotor design with fixed geometry bearings, mean clearance and 3.5 kg added overhung mass at 13971 rpm critical (bearing rock mode) with log decrement of 3.647

To establish predictions for the rotors response across the operating speed range, several response analyses were performed for the various combinations of bearing, lubrication and overhung mass. The results of this analysis were used to understand the anticipated conditions of displacement that would be expected across the rotor length. The level of unbalance used to evaluate the rotor response was consistent with an unbalance mass of 750 mg at a radii of 50mm at station 1 (the overhung non drive end flange) of the model. This level of imbalance is in accordance with ISO 1940 [55] grade G2.5 for a rotor of this weight. (ISO 1940 is a balancing standard which is used to determine permissible levels of residual unbalance in rotating machinery and grade G2.5 is typical for machines such as industrial compressors of gas turbines).

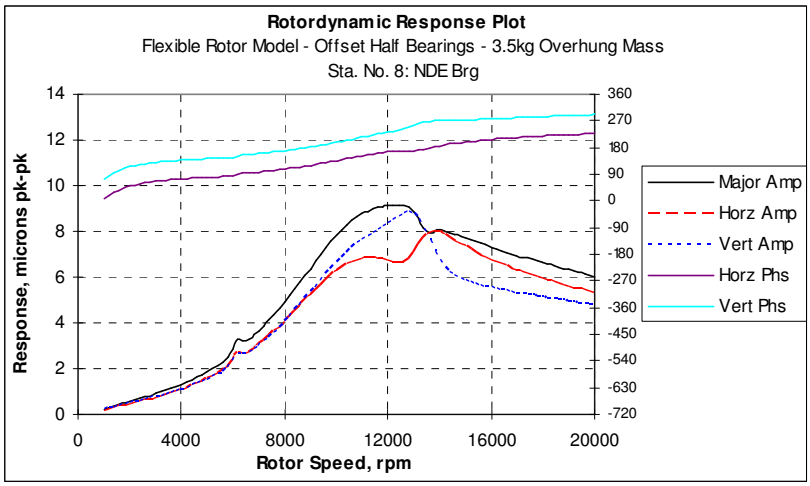

Figure 74 Damped response plot for final rotor design with fixed geometry bearings, mean clearance and 3.5 kg added overhung mass at NDE bearing

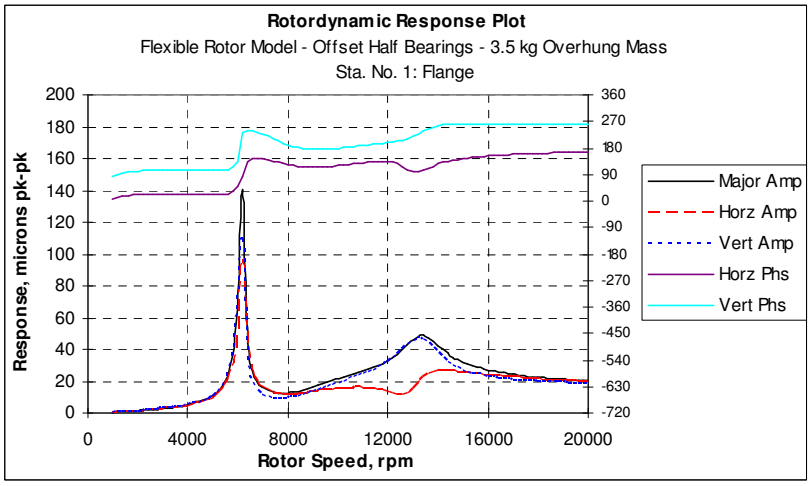

Figure 75 Damped response plot for final rotor design with fixed geometry bearings, mean clearance and 3.5 kg added overhung mass at NDE flange

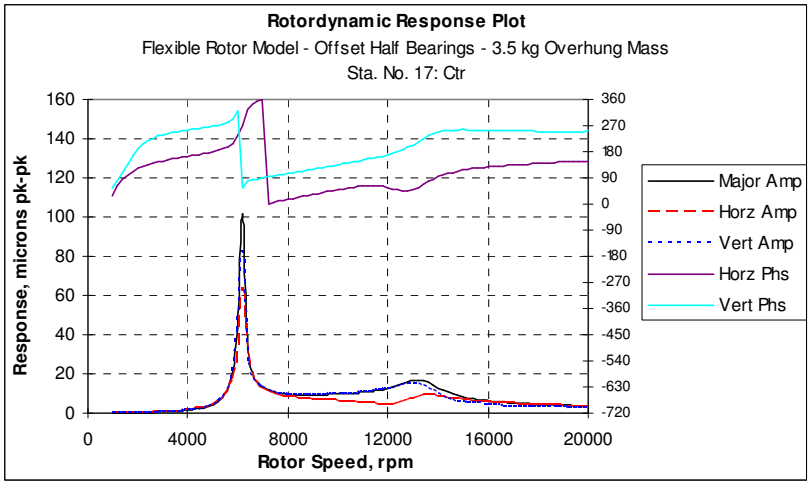

Figure 76 Damped response plot for final rotor design with fixed geometry bearings, mean clearance and 3.5 kg added overhung mass at centre mass

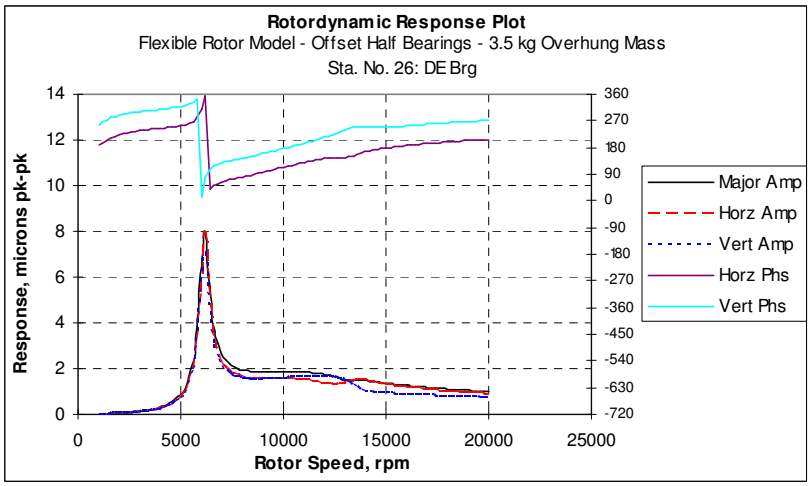

Figure 77 Damped response plot for final rotor design with fixed geometry bearings, mean clearance and 3.5 kg added overhung mass at DE bearing

In addition to evaluating the impact of imbalance at the overhung flange of the rotor, imbalance was also included at the shaft centre. Combinations of imbalance at both locations simultaneously were also assessed, considering both in and out phase conditions. Figure 74 to Figure 77 present the unbalance response for the rotor at the stations 1, 8, 17 and 26 which correspond to the NDE flange, NDE end bearing, rotor centre and DE bearing respectively. The response data presented in Figure 78 to Figure 80 is with a 3.5 kg added overhung mass and a residual unbalance values of 37.5 g.mm and 12.5 g.mm applied to the NDE flange and shaft centre mass respectively, 0 degrees phase lag was applied between the unbalance vectors located at the NDE flange and rotor centre. The 12.5 g.mm applied to the rotor centre is to account for a proportion of the unbalance mass to be distributed at this

location as would be in place in a practical component (i.e. no matter how well balanced, practically a proportion of the unbalance mass will be located at the shaft centre due to its high proportion of weight of the total shaft). It should be noted that only synchronous excitation was applied as is consistent with imbalance forces in rotating machinery. No account for higher order excitations were considered in the rotor response analysis.

For each of the response conditions the deflected rotor shapes was extracted. These deflected rotor shapes provide an understanding of the conditions that will be experienced at the bearings when considered in combination with phase. With a means of quantifying the conditions at the bearings across the running speed range it is possible to qualitatively determine that the conditions are consistent with the criteria defined as promotional to the initiation of thermal instability, as per chapter 4. Orbit shapes were also extracted at the NDE bearing location at or around the rotor critical speeds. Figure 78 to Figure 80 present the deflected shapes for the rotor with and without the overhung mass for the critical speed locations.

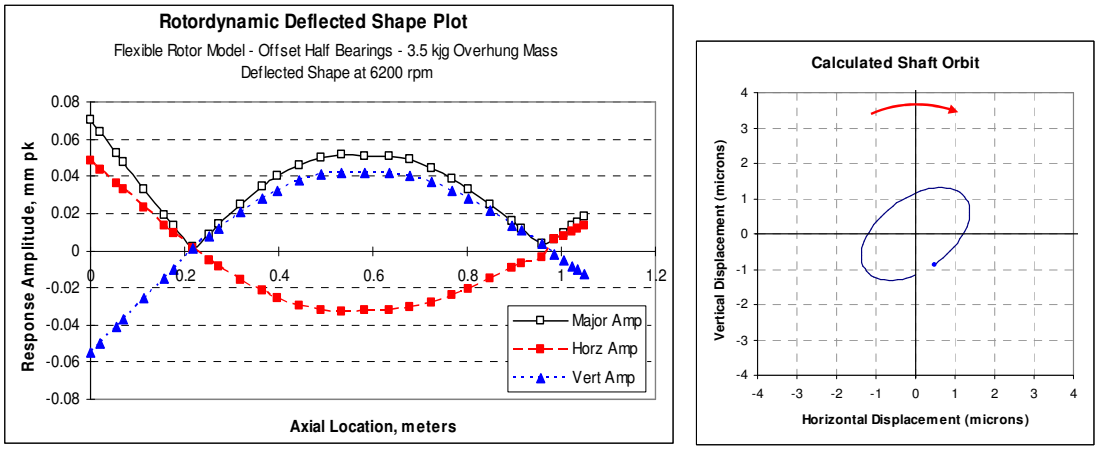

Figure 78 Damped response operating deflection shape and NDE bearing whirl orbit for final rotor design with fixed geometry bearings, mean clearance and 3.5 kg added overhung mass at DE bearing at 6200 rpm.

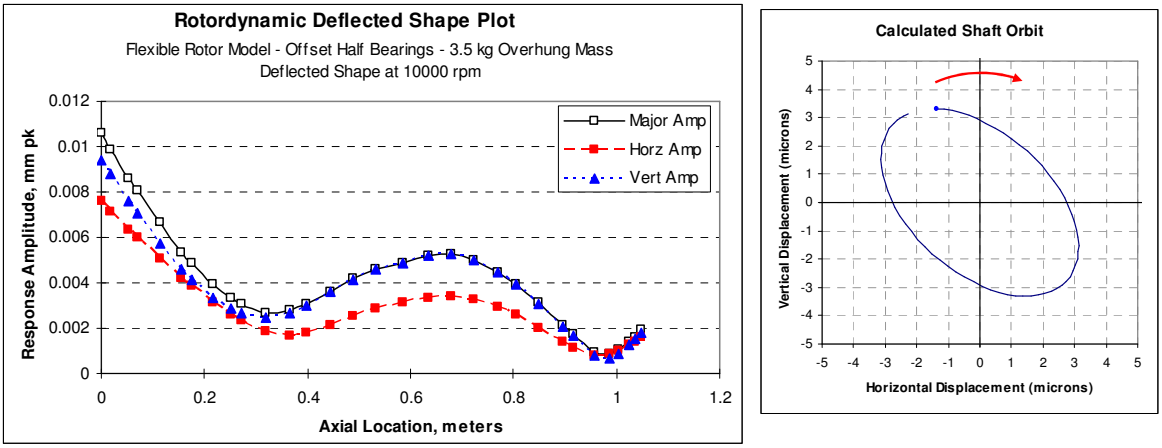

Figure 79 Damped response operating deflection shape and NDE bearing whirl orbit for final rotor design with fixed geometry bearings, mean clearance and 3.5 kg added overhung mass at DE bearing at 10000 rpm.

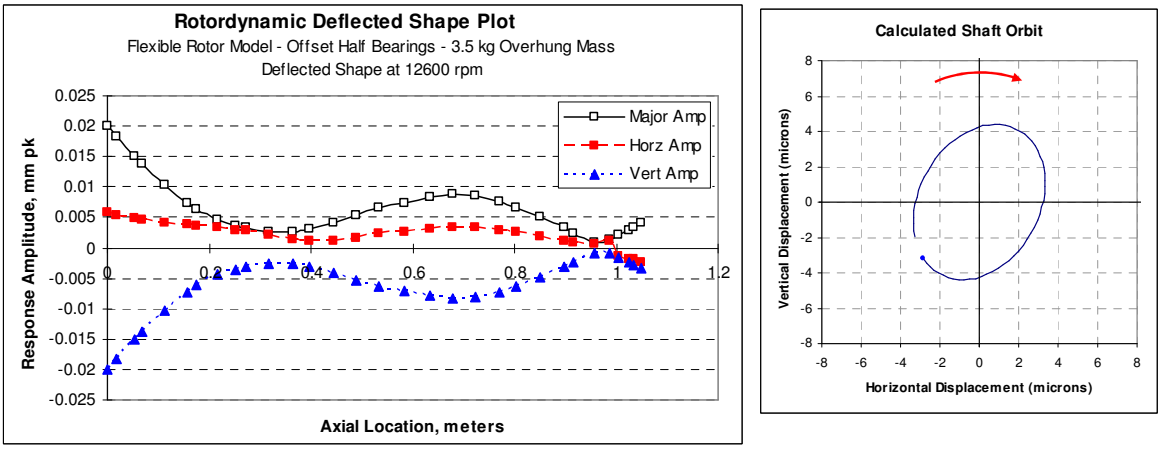

Figure 80 Damped response operating deflection shape and NDE bearing whirl orbit for final rotor design with fixed geometry bearings, mean clearance and 3.5 kg added overhung mass at DE bearing at 12600 rpm.

The rotordynamic data presented in the preceding figures relates to the fixed geometry offset half type bearing configuration. The same procedure was applied for the evaluation of the flexible rotor for the tilting pad (TP) bearings. Figure 81 to Figure 83 present the damped critical speed map (Campbell diagram), rotor damped mode shapes, rotor response at the NDE bearing and the rotor deflected shape at 10000 rpm for the nominal TP bearing clearance condition with normal oil inlet temperature.

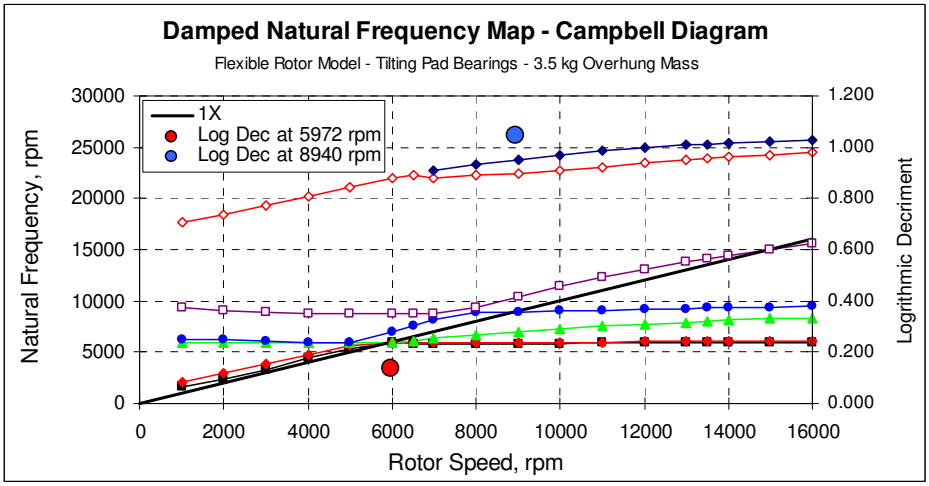

Figure 81 Damped natural frequency map for final rotor design with variable geometry bearings, mean clearance and 3.5 kg added overhung mass

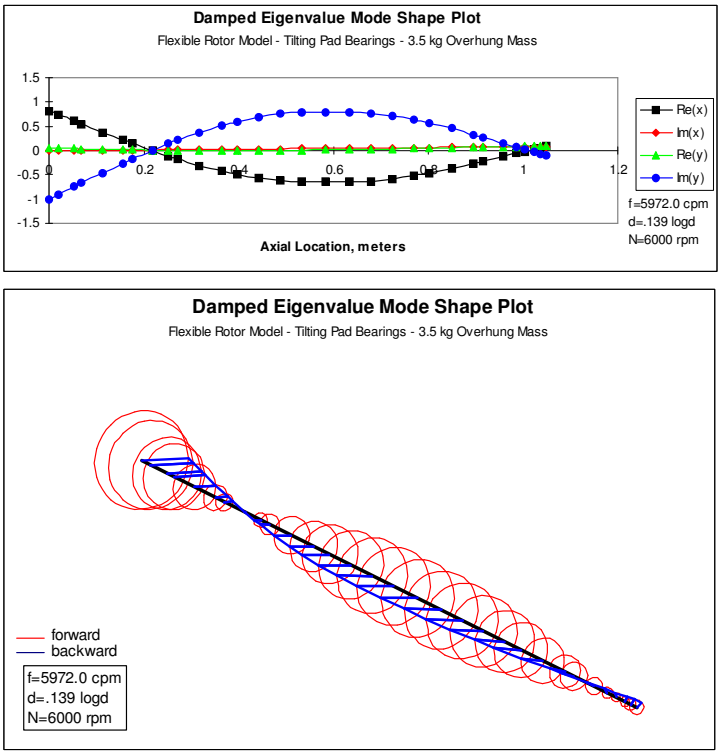

Figure 82 Damped mode shape for final rotor design with variable geometry bearings, mean clearance and 3.5 kg added overhung mass at 5972 rpm critical with log dec of 0.139

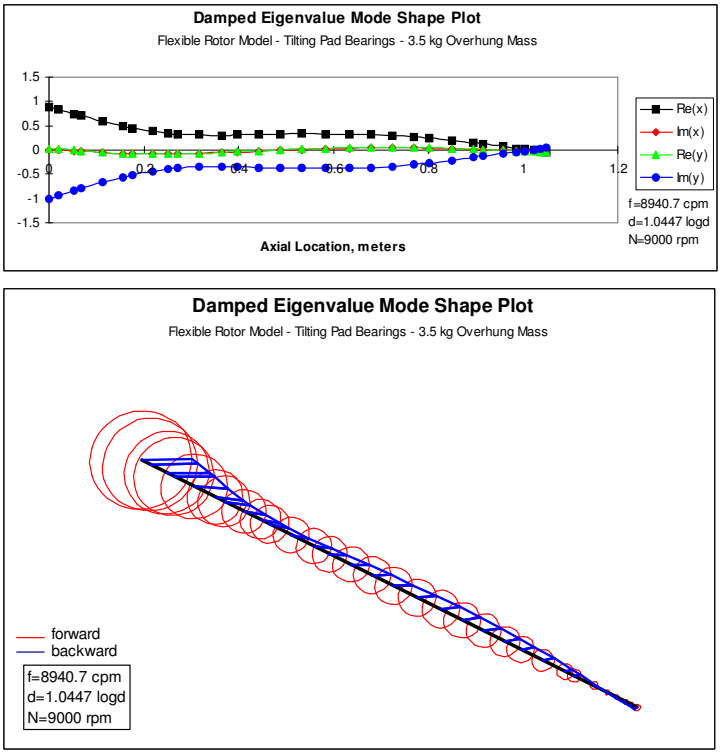

Figure 83 Damped mode shape for final rotor design with variable geometry bearings, mean clearance and 3.5 kg added overhung mass at 8940 rpm critical with log dec of 1.044

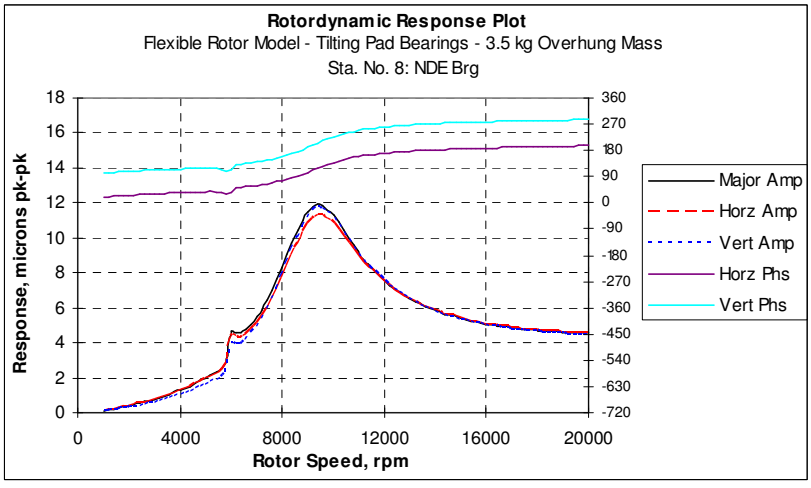

Figure 84 Damped response plot for final rotor design with variable geometry bearings, mean clearance and 3.5 kg added overhung mass at NDE bearing

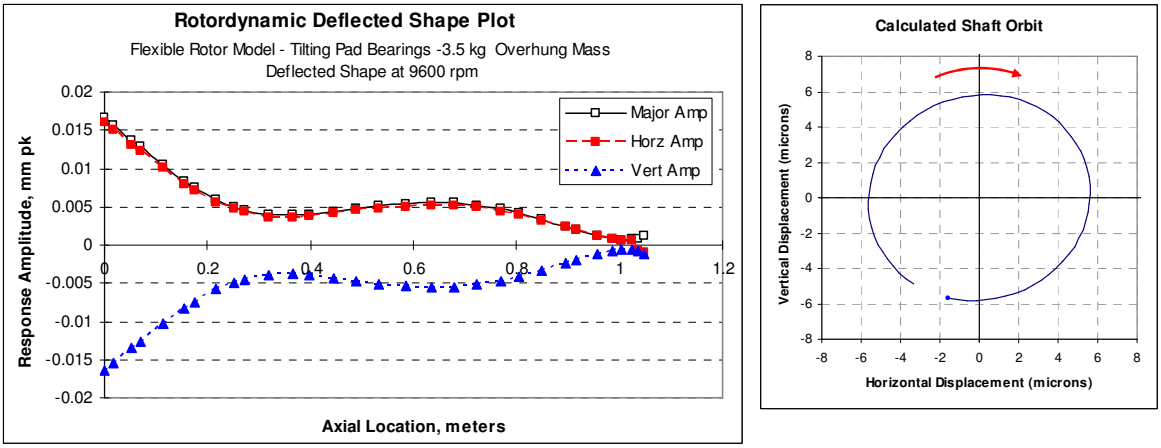

Figure 85 Damped response operating deflection shape and NDE bearing whirl orbit for final rotor design with variable geometry bearings, mean clearance and 3.5 kg added overhung mass at NDE bearing at 9600 rpm.

Considering the results of the rotordynamic design and analysis of the test rig, rotor and bearing configuration with respect to the observations taken from the literature and those highlighted in chapter 4, the following comments can be made.

The test rotor design encounters several areas of significant unbalance response within the running range which are coupled with rotor bending modes. The rotor is capable of operating above the first critical bending mode under all bearing and rotor configurations, and runs close to, at or above a second shaft bending mode. The second shaft bending mode is largely associated with the overhung section and NDE bearing. The response at the NDE bearing remains active across the entire range, showing a similar characteristic to the displayed in the de Jongh et al [11] rotor. This similarity in characteristics to the de Jongh et al [11] rotor is also apparent in the predicted mode shapes.

Also in line with observations made from case studies in chapter 4, the operating deflection shape is associated with a rotordynamic bend at the NDE bearing location when approaching the second bending mode, where the inner bend surface is closest to bearing wall when a zero degree phase lag exists. Therefore the requirement for phase change is present as was observed in the case study rotors. The rotordynamic predictions of the test rotor are such that a significant phase change takes place in the high speed region (~8-12 krpm) which, when coupled with a thermal lag of 20-0 degrees would give a phase range of over 90 degrees. This should provide a

speed/phase band suitable to traverse a condition where the thermal and mechanical unbalance components would combine (although this condition alone does not guarantee instability as suitable conditions for the rate of thermal differential heating and coupled unbalance response are also required, See Figure 84 and Figure 85.

The bearing operating eccentricity ratios are predicted to run at low levels of typically <0.15 for speeds above ~3000 rpm, with the NDE shaft obits in the regions of high response or critical speed locations having significant circular form. Also the NDE bearing response is shown to be sensitive to unbalance located at both the shaft centre, and more significantly, the overhung NDE flange.

In summary, it has been possible to rotordynamically design a test rotor-bearing system which is predicted to display the principle governing characteristics and conditions, as established in chapter 4, that can be typically associated with machines having been reported as suffering journal differential heating instability. Both the fixed and variable geometry bearings show the characteristics sympathetic to being sensitive to the instability. One feature where some difference between the case study rotors and that of test rotor exists is in that the surface journal velocities of the test rotor are somewhat lower than those cases considered in chapter 4. The test rotor peak journal velocity is ~35 m/s and the case study bearing velocities being 40 to 66 m/s. This effect however is somewhat countered by the fact that lower clearances employed in the bearings result in similar operating temperatures within the oil films and also the lower stiffness and damping properties of the system make it comparative in sensitivity to unbalance than the larger rotors in the case studies.

5.4.2.3 Rigid Rotor

In addition to the main experimental test rotor, which has been specified as a flexible rotor in that it runs in a super critical condition, a smaller rigid rotor was also designed. The concept behind the creation of a shorter rigid rotor was to allow for operation of the experimental rig using the main test bearings without any significant influence or feedback mechanism from the rotordynamic conditions within the rotor shaft. The use of a rigid rotor, which does not introduce any significant rotordynamic complexities, provides a means for characterising the thermal journal conditions within the bearing and any associated relationships with unbalance and shaft journal displacements.

The absence of any significant phase changes also helps to provide conditions which provide more stable operating conditions on which to found a baseline. The application of this type of rotor also allows for the journal temperature measurement instrumentation to be tested and verified.

The rigid rotor is designed such that the rotor journal static load on each bearing is very close to that of the main test rotor, replicating the basic conditions within the bearings as for the flexible rotor. The rigid rotor geometry has been defined such that the rotor does not encounter, with suitable separation, any shaft bending natural modes within the experimental rig operating speed range. This is principally achieved by means of reducing the rotor bearing span, increasing shaft diameter in the centre of the rotor and reducing the overhung section of the NDE for the rotor. Figure 86 shows the rotordynamic model of the rigid rotor configuration. It can be seen in Figure 86 that the rotor bearing span has been reduced from 750mm to 430mm.

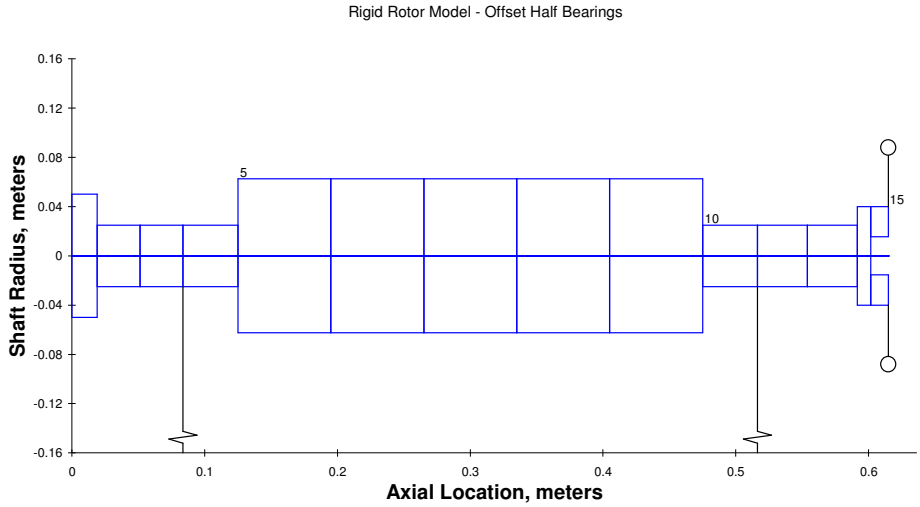

Figure 86 Rigid rotor dynamic model

Rotordynamic analysis of the rigid rotor was again performed in line with the procedures as outlined for the flexible rotor. Full details of this analysis are not presented here but the general rotor response characteristics are summarised in Figure 87 to Figure 91 providing the undamped critical speed map, Campbell diagram and rotor response to unbalance.

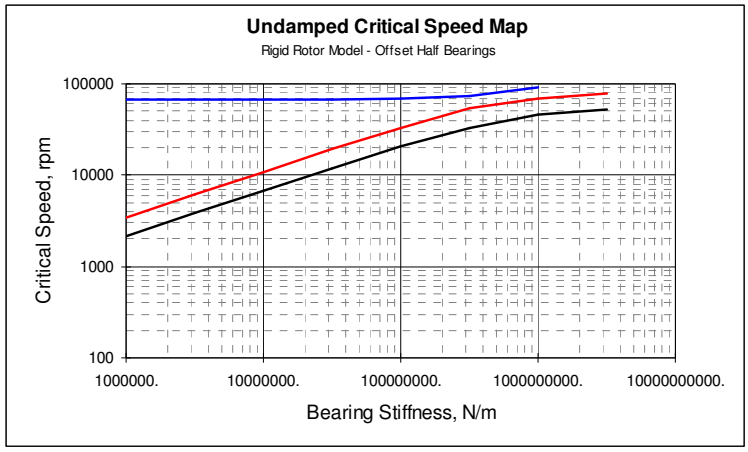

Figure 87 Rigid rotor undamped critical speed map

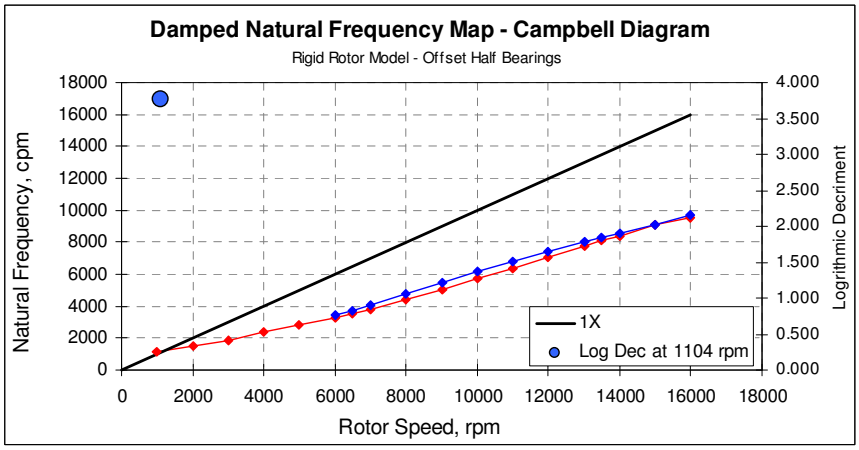

Figure 88 Damped natural frequency map for rigid rotor design with fixed geometry bearings, mean clearance

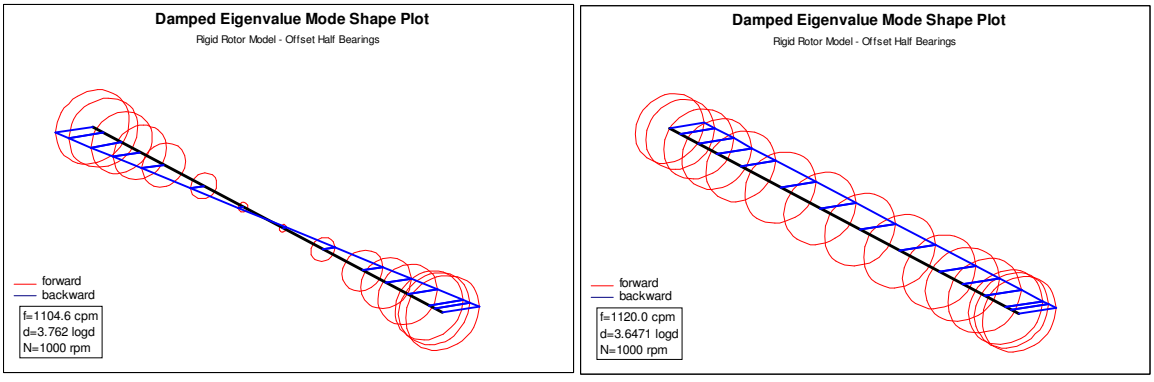

Figure 89 Damped mode shapes for rigid rotor design with fixed geometry bearings and mean clearance (a) 'rocking' mode at 1104 rpm with log dec of 3.762 (b) 'bounce' mode at 1120 rpm with log dec of 3.647

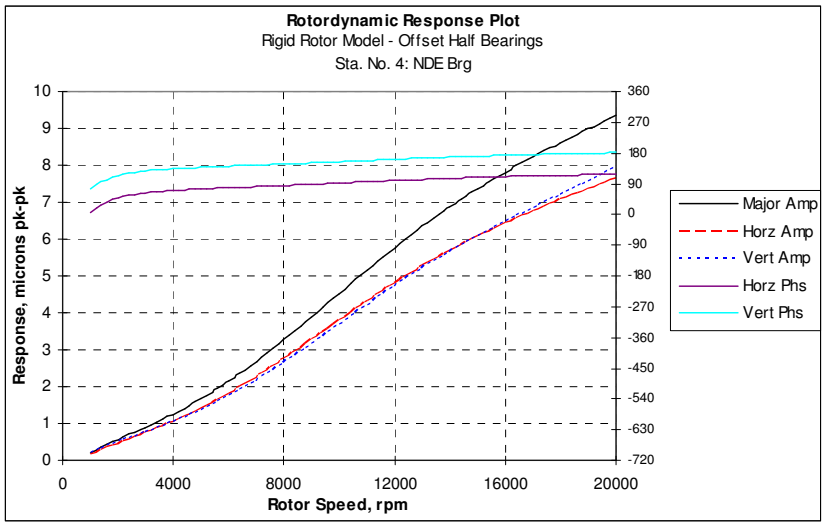

Figure 90 Damped response plot for rigid rotor design with fixed geometry bearings and mean clearance 12.7 g.mm at NDE flange

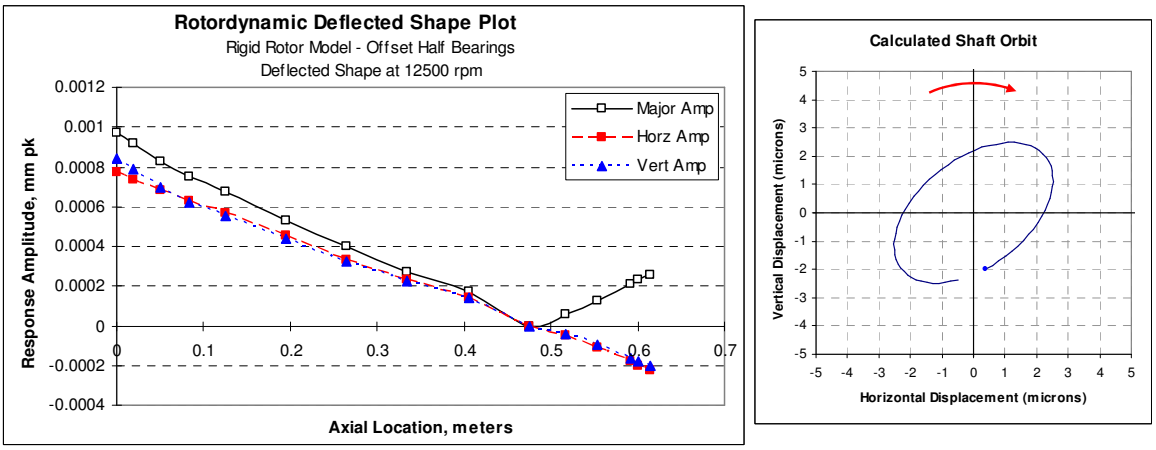

Figure 91 Damped response operating deflection shape and NDE bearing whirl orbit for rigid rotor design with fixed geometry bearings and mean clearance at 12500 rpm.

5.4.3 Synchronous Thermal Instability (Morton Effect) Analysis

Having evaluated the rotordynamics with respect to thermal sensitivity of the rotor, some consideration is given to the thermal evaluation of the rotor. This consideration is addressed using two approaches. The first was to evaluate the rotor design in line with the physical, rotordynamic and hydrodynamic observations taken from the case studies presented in chapter 4. The second was to apply the appropriate analytical techniques presented in the published literature. This element of the design evaluation is an important one, in that not only is it being used as a tool on which consider the design criteria with regard to the promotion of instability, but it will also provide a benchmark as to the capability of the existing analytical methods to predict the thermal and stability response of a real rotor with respect to journal differential heating.

The analytical procedure applied is that as presented by Balbahdur [19] in his PhD thesis as opposed to the analytical CFD approach applied by Keogh et al [9]. The principle reason behind this is that the Keogh et al [9] method is a highly analytically intense process which, without significant mathematical and computational development, cannot be readily applied to non cylindrical bearings such as those considered in this work. Also, as a practical rotordynamic tool it would prove too computationally and time intensive. Conversely the method presented by Balbadur [19], whilst having some significant idealisations and assumptions, is more readily applicable. It also allows for an experimental validation of the presented theory in [19] to be made both from a dynamic response and journal thermal response consideration.

Whilst the Balabadur [19] analytical procedure was used as a tool to assess the detail design of the rotor to thermal instability, the principle design considerations were based on producing physical conditions in the rotor operational performance which is consistent or representative with the observations identified in section 4, which resulted in the rotordynamic design criteria for the shaft as detailed in section 5.4.2.2.

The definitive criteria in the Balabahadur [19] thermal stability modelling method for calculating the points of instability, is the resultant level of unbalance generated by the rotor due to the thermal bow about the bearing journal. This is represented as a fraction of the rotor mass. Fifteen percent was the level used by Balbahadur [19] in his research which was based upon running a number of practical examples through the analysis procedure. For

the purposes of consistency (and in the absence of any other credible data with which to determine a suitable thermal unbalance threshold level by the application of this technique) the same 15% threshold was applied but in combination with a band pass type approach where an upper threshold criteria of 30% was also applied. This allowed for some indication of how sensitive to the calculated and input data the predicted stability of the rotor would be.

5.4.3.1 Fixed Geometry Bearings

System information from the analysis according the Balbahadur [19] method for the amplitude and phase data for the non-drive end bearing journal was extracted from the rotordynamic analysis performed in section 5.4.2.2. The phase data was manipulated to be in a form that could be used in the Morton Effect stability analysis and other system information such as bearing dimensions etc included. The analysis was performed using a number of unbalance values for all of the rotor system configurations, e.g. bearing clearances added mass etc.

The results of the analysis showed that for the bearing and test rotor design used, dependant on the level of initial residual unbalanced, all of the rotor bearing configurations were predicted to go unstable at some point within the operating speed range. As would be expected, the point at which the analysis suggested the rotor would go unstable was directly related to areas of high response. When the unbalance condition is linked to the rotor centre location, the point of instability can be seen to associate with the first critical speed at around 6000 rpm. If the unbalance level is significantly reduced, or more notably moved to the overhung flange, the analysis shows that instability is reached at some point between the first and second natural frequencies. The movement in the instability location is not only due to the change in unbalance location but also the change in rotordynamic conditions used as inputs for the analysis, i.e. amplitude and phase responses at the NDE bearing location.

The results of some of the analysis predictions are shown in Figure 92 through to Figure 95. Figure 93 and Figure 94 show the stability predictions for the rotor in fixed geometry bearings (mean clearance) with 20 g.mm and 50 g.mm unbalance respectively located at the NDE flange, with 3.5 kg of added overhung mass. The rotor unbalance curve is derived from the calculated thermal bend unbalance for any given speed condition and the unbalance threshold curve is based on a specified % of the total rotor mass.

Instability is defined as occurring where the rotor unbalance and threshold curves intersect. It can be seen that instability is predicted between 11000 and 12635 rpm for the 20 g.mm case and 8862 and 10820 rpm for the 50 g.mm case.

The predicted journal temperature differential with respect to speed can be seen in Figure 95.

Similar results are shown for the variable geometry conditions in Figure 96 to Figure 99. Figure 97 shows the stability prediction for the tilting pad bearings running with maximum clearance and a 20 g.mm unbalance force. The stability range was calculated as 8148 to 8940 rpm. With the Figure 98 showing the same unbalance condition but now for mean clearance conditions, with instability predicted between 8292 and 9288 rpm. Predicted journal temperature differentials are given in Figure 96 and Figure 97 for the maximum and mean clearance conditions respectively.

It should be noted here that for reasons explained in literature review in chapter 2 this analysis is not exhaustive and remains essentially unproven with some areas having some significant simplifications and assumptions. As such the analysis has been used only as an indicative guide in the specific design of the test rig rotor and bearings, with the actual design criteria also being strongly based on more practical and operational requirements such as rotor mode shapes, response phase, shaft orbit geometry and bearing characteristics as identified by de Jongh and Morton [11].

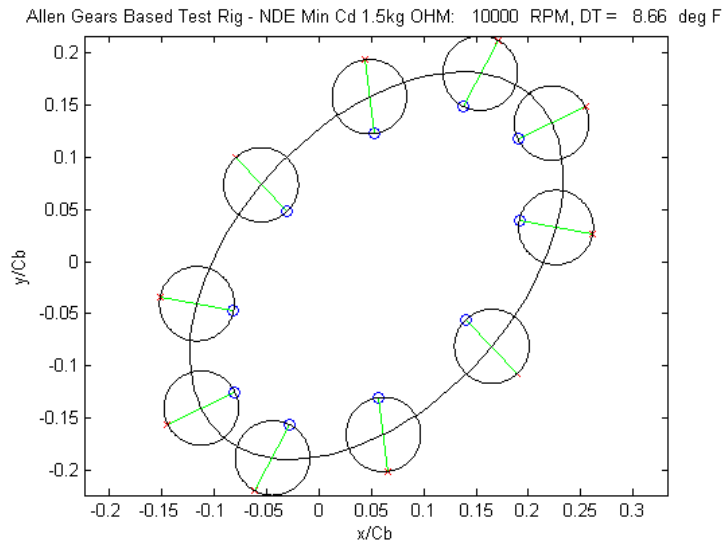

Figure 92 Shaft orbit showing hot and cold spots on rotor journal for flexible rotor in fixed geometry bearings

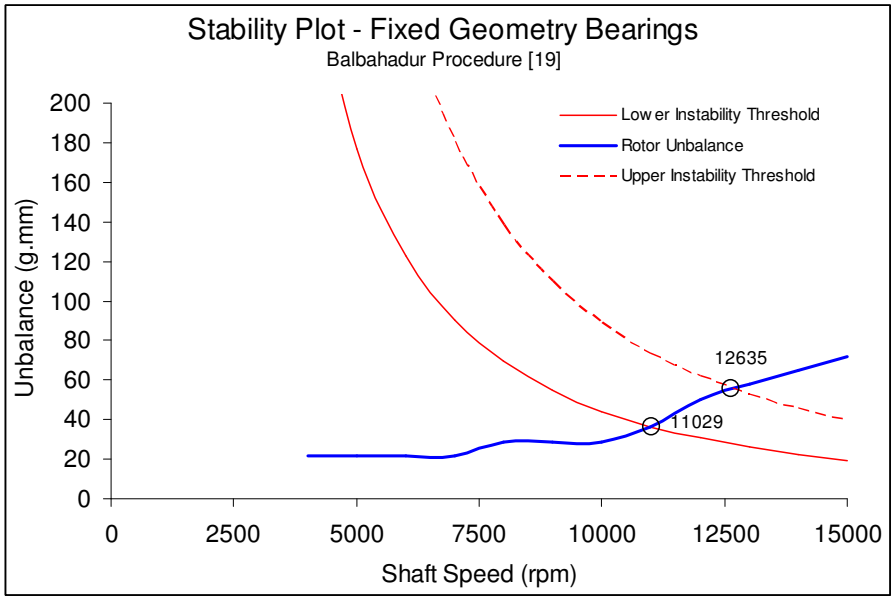

Figure 93 Morton stability analysis of fixed geometry bearings with 20 g.mm unbalance at overhung flange, 3.5 kg added mass and mean bearing clearance

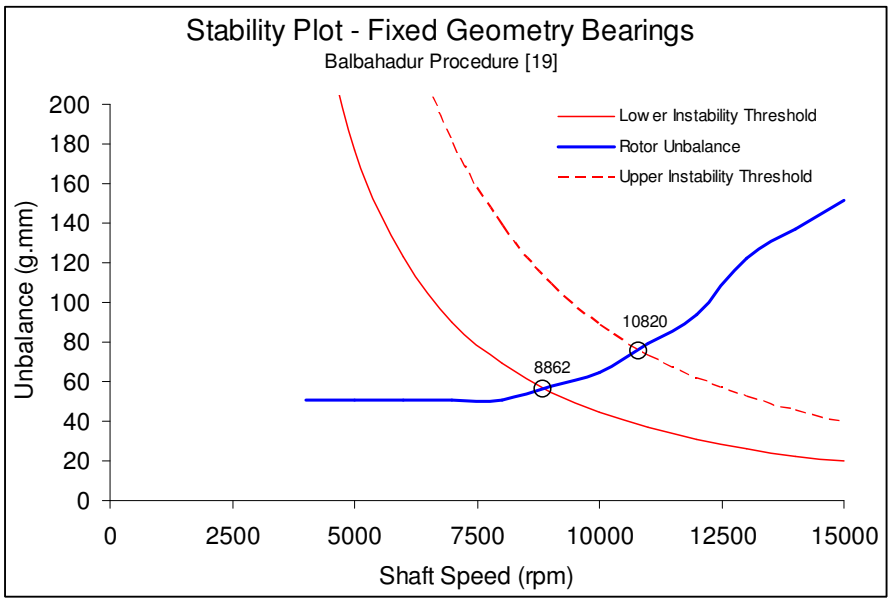

Figure 94 Morton stability analysis of fixed geometry bearings with 50 g.mm unbalance at overhung flange, 3.5 kg added mass and mean bearing clearance

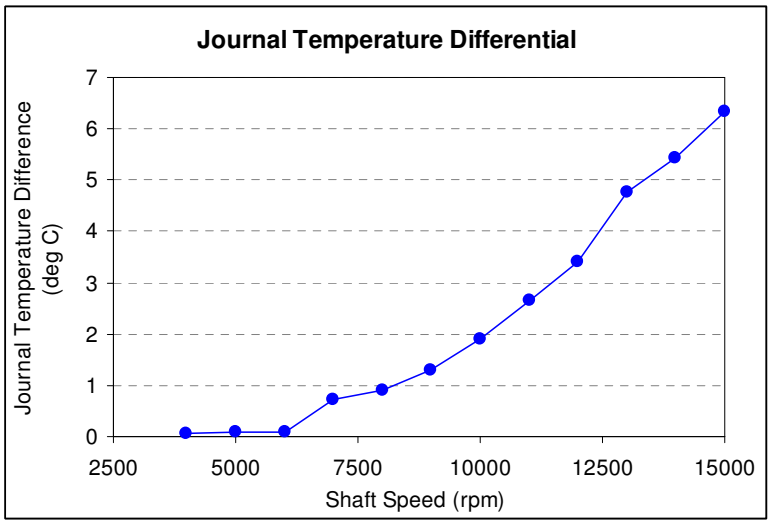

Figure 95 Journal temperature differential fixed geometry bearing at NDE journal with 50 g.mm unbalance, 3.5 kg added mass and mean bearing clearance

5.4.3.2 Variable Geometry Tilting Pad Bearings

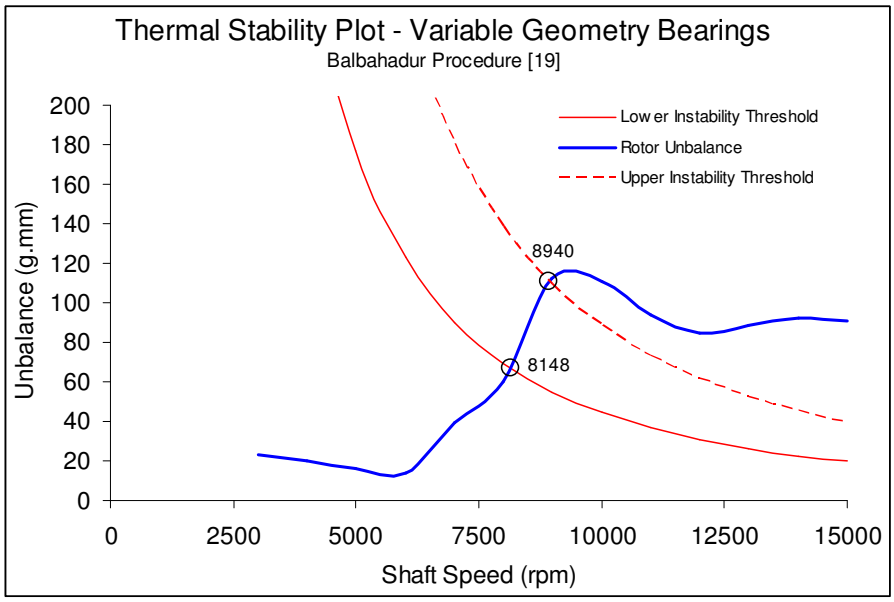

Figure 96 Morton stability analysis of variable geometry bearings with 20 g.mm unbalance at overhung flange, 3.5 kg added mass and maximum bearing clearance

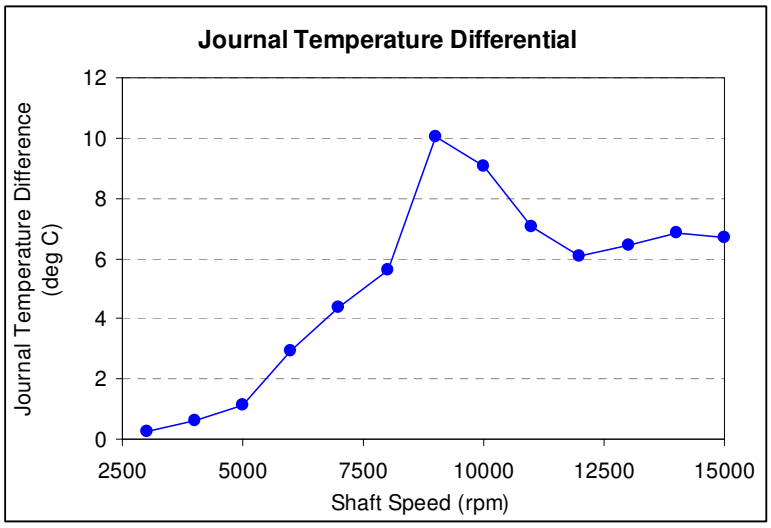

Figure 97 Journal temperature differential variable geometry bearing at NDE journal with 20 g.mm unbalance, 3.5 kg added mass and maximum bearing clearance

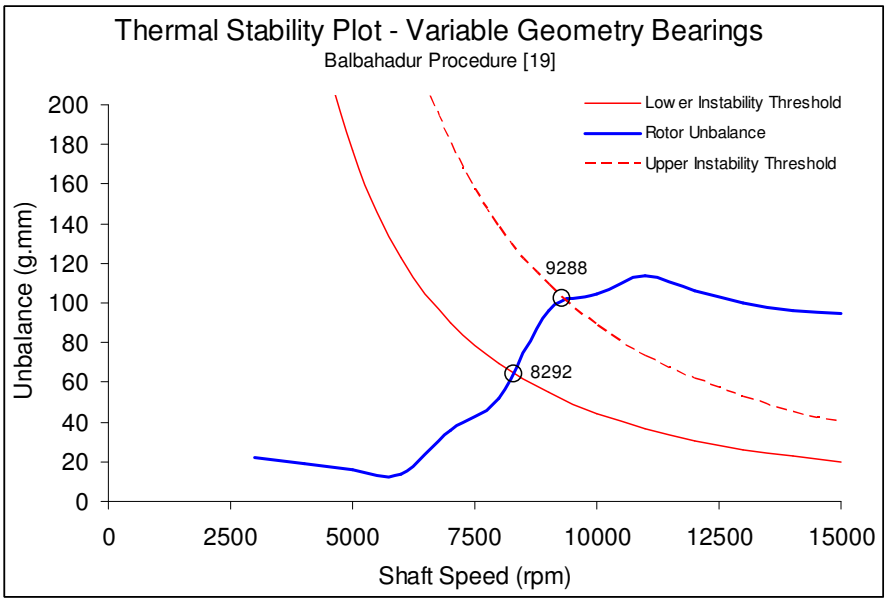

Figure 98 Morton stability analysis of variable geometry bearings with 20 g.mm unbalance at overhung flange, 3.5 kg added mass and mean bearing clearance

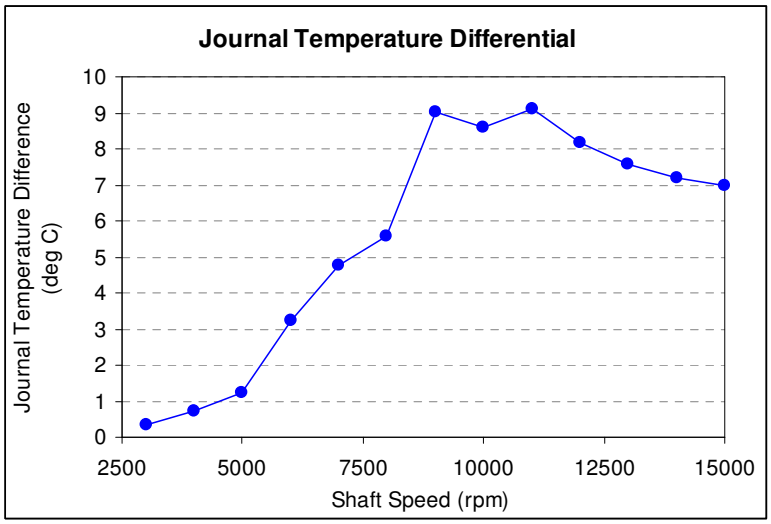

Figure 99 Journal temperature differential variable geometry bearing at NDE journal with 20 g.mm unbalance, 3.5 kg added mass and mean bearing clearance

From the results of the thermal instability analysis, in accordance with [19], it was observed that the rotor would be considered as sensitive to instability and expected to go unstable within the running range for a moderate level of mechanical unbalance. The fixed geometry bearing was predicted as having a higher instability threshold with notably lower journal temperature differentials being predicted than for the tilting pad. The tilting pad configuration showed a journal temperature differential prediction of up to 10 deg C. The predicted temperature differentials for the tilting pad, in the opinion of the author, would seem somewhat high for the conditions under analysis, however even if overestimated, the procedure would predict a rotor that is sensitive to the Morton effect instability.

An interesting point of note is that the rotor without the added mass is shown to have a lower stability threshold than that with the larger overhung mass. Whilst this might immediately seem counter intuitive as the mechanical gain has been increased by the increased overhung mass, the implication is that the rotordynamic conditions at the NDE bearing are notably different for the two cases. It is these complex rotordynamic relationships which could result in the introduction of the overhung mass actually pushing up the threshold speed by means of altering the mode shape, frequency and response at the bearing of interest.

It should also be noted that the polynomial expression for steady shaft eccentricity ratio as a function of applied load was found to be sensitive to

load magnitude. In particular at low loads of specific bearing pressures some cases would not resolve due to the low journal bearing specific pressures in the test rotor. In these cases this was overcome by artificially increasing the load by ~50% (still only a small load). The effect of this is not highly significant on the steady bearing conditions for higher speeds, although it does result in a slightly higher journal eccentricity ratio. In the case of running speed at 8000 rpm, this increased the eccentricity ratio from ~0.25 to ~0.3 (max clearance condition) which will have some impact on the bearing temperature calculations.

5.5 Detail Design

Following the analytical assessment and key design criteria definition the practical and detail design aspects of the test rig have to be considered. The complete test rig configuration has been broken down into the following six sections:

1. Main Test Rotor and Bearings
2. Drive System
3. Transmission
4. Lubrication System
5. Instrumentation
6. Monitoring, Data Logging and Data Management

5.5.1 Main Test Rotor and Bearings

The principle design features and criteria for the test rotor and bearings have been covered in the preceding sections in this chapter. However, a number of design features worthy of mention and are summarised here.

In the design of the rotor, care was taken to ensure that the manufacturing specifications were consistent with maintaining a good state of balance across the running range and provide good quality surfaces from which to measure shaft movements. To provide these conditions the shaft was precision ground on all diameters to provide both good dimensional control and runout errors. The shaft was also thermally stress relived at several stages throughout the manufacturing cycle to provide good shaft stability to residual stress distortions during finishing machining and also whilst in service.

The location points for the shaft temperature measurements were achieved by means of providing small axial holes drilled just below the shaft surface into the centre of the shaft journal. The holes were 4.75 mm diameter and positioned such that a wall thickness of 2.0 mm was produced from the journal surface.

The number of sensors to include under the journal surface was an area of investigation during the early stages of the research. Several publications [11] indicate that only 4 measurement points are required as the expected journal temperature distribution would be harmonic as a result of the synchronous unbalance and associated oil film thickness function. It is only the first harmonic component that will cause the shaft to develop a steady state thermal bow. Other higher order harmonic distributions would serve to produce polar equilibrium stresses which do not result in a geometric displacement of the shaft overhang mass. Whilst these assumptions hold true for the analytical problem described, it is quite possible that when using more complex bearing geometries combined with complex vibration orbits temperature distributions other than harmonic are quite plausible. To fully understand the generation of the thermal state in the bearing and rotor journal a greater number of measurement points could offer increased understanding of this feature. A downside of considering the inclusion of more than 4 sensors on the shaft diameter is that an increase in sensors results in a distortion of the thermal mass/inertia of the rotor journal and also the stiffness of the shaft. Also, whilst with 4 sensors only the first harmonic amplitude can be reliability attained, it will be possible to observe the level of non fundamental temperature distribution around the shaft.

Based on the potential practical issues that would be introduced with high sensor numbers due to the risk to the measurement and modelling accuracy, also that the necessary fundamental harmonic thermal distribution is the principle area of interest, the number of sensors included in the shaft journal was specified as 4.

Detailed manufacturing specifications for the main test rotor and rigid shaft rotor were designed and produced applying the same philosophy and processes. Full manufacturing specifications for the test rotors and key test rig components are provided in appendix B.

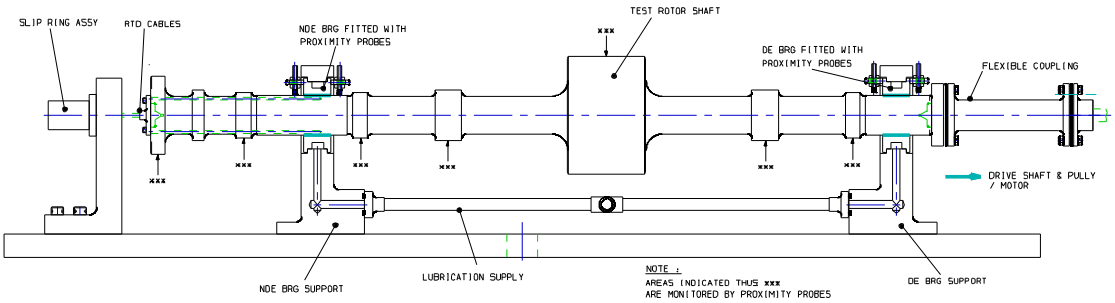

Figure 100 Main test (flexible) rotor assembly schematic

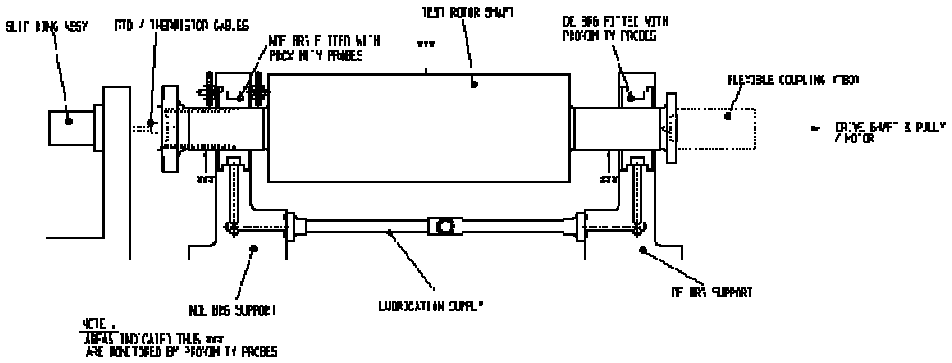

Figure 101 Rigid test rotor assembly schematic

5.5.2 Drive System

As the rotor is required to run at a range of speeds some sort of variable speed drive is required. The drive is to be supplied by electric motor and the variable speed aspect can be achieved by one of two means. One is by using a DC motor and thyristor type control, the other is to use an AC induction type motor and a frequency inverter. The preferable method was to use an AC induction motor and frequency inverter drive due to the low cost and ready availability of AC induction motors. However, frequency inverters can be quite costly for powers of around 7.5 kW. However, due to a fortunate circumstance, a Jaguar CDII750 7.5 kW frequency inverter became available and was donated to the project and a 5.75 kW ABB M2AA 112 M4 Aluminium body electric motor was selected for the prime mover. With the correctly designed transmission this provided a more than sufficient power supply to the test rig, covering the required operating speed range.

5.5.3 Transmission

In order to obtain the required maximum rotor running speed of 15000 rpm, a means of step up transmission was required to increase the motor output

speed from 2160 rpm. Two options were considered to achieve this, one being the use of a set up gearbox and the other use of a belt drive arrangement. For reasons of reduced cost, complexity and lead time a belt drive system was selected. The operating speed and powers are somewhat outside the normal operating bounds for most belt drives. As such designing and sourcing suitable components presented some problems.

One supplier of high performance belts (Conti-Tech) was, after some discussion, able to offer a solution with a pulley wheel ratio of 9:1, achieved in one stage. The running conditions of the belts was outside normal operating limits but for the purposes of research purposes the predicted belt life of the belts was sufficient to meet the estimated testing requirements.

The belt arrangement selected was a multi ribbed V belt ContiTech 1143/540 J12. The arrangement consists of two drive wheels one of 30mm diameter and another of 270mm diameter. The smaller wheel had to be specially designed due the high speeds, high ratio and bearing arrangement required which was performed by the author and manufactured by Allen Gears.

The drive transmission is coupled to the main rotor via a flexible element coupling. The coupling is a multi-disc pack type with one set of flexible elements at each end, capable of accommodating both offset and axial misalignment errors up to 2.5 and 1.0 mm respectively. For practical reasons the coupling size had to be 80mm diameter and as such was capable transmitting much higher torques than required.

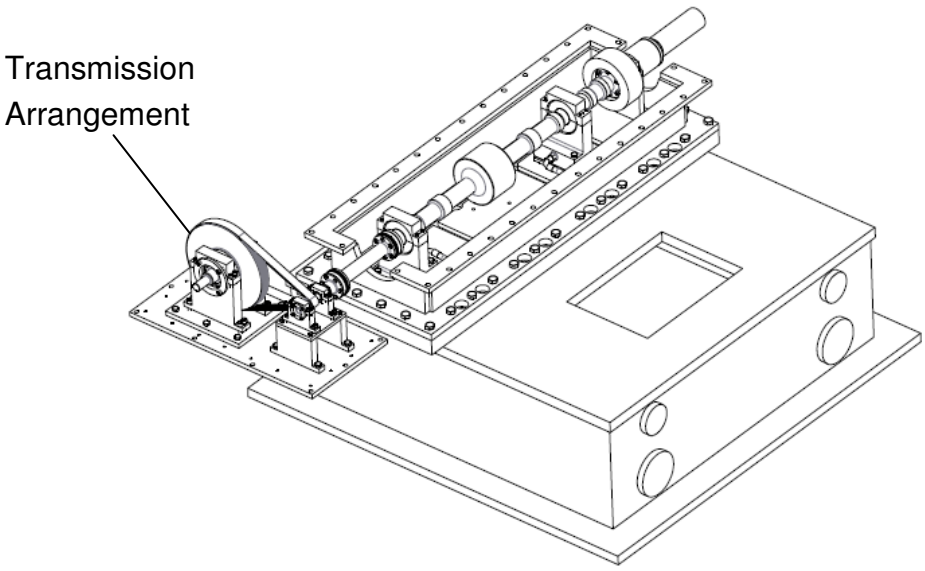

Figure 102 Test rotor and transmission assembly

5.5.4 Lubrication System

The lubrication system consists of a relatively straight forward arrangement. It comprises of an electric motor driven pump, filter, oil heater, cooling system and pressure control valve. The supply pump was an existing piece of equipment available through Allen Gears with a pumping flow capacity of 70 l/min with a peak discharge pressure of 6.0 bar.

The filter is a 10µm PAL cylinder cartage filter with a 150 l/min flow capacity and is again an existing piece of equipment available at Allen Gears.

The oil heater is a Chromaloy low power 4.0 kW immersion heater with a variable thermostat, and is located in the base of the lubricating oil test stand sump.

Oil cooling capability is provided by means of a Boman 1425-2 shell-tube cooler with a 8 kW(max) heat rejection capacity, which uses pressure fed fresh water cooling media. It was specifically selected and procured specifically for use with the experimental test apparatus.

The oil tank forms part of the main test stand base and has a maximum oil capacity of 70 litres. The oil type used for all of the commissioning and experimental activity was an ISO VG46 viscosity mineral oil with properties as given in Table 16. This particular viscosity grade of oil was selected as it is a commonly used oil type in the types of high speed turbo machinery observed to be sensitive to the Morton Effect, such as compressors, steam turbines, turbochargers gearboxes etc.

Manufacturer : Castrol
Brand : Hyspin AWS 46 – Hydraulic Mineral Oil

Kinematic Viscosity at 40 Deg C	46.0	Cst
Dynamic Viscosity at 40 Deg C	3.96E-2	$N.s/m^2$
Relative Density at 40 Deg C	0.857	
Specific Heat Capacity at 40 Deg C	1.947	kJ/kg Deg C
Kinematic Viscosity at 100 Deg C	6.94	Cst
Dynamic Viscosity at 100 Deg C	5.683E-3	$N.s/m^2$
Relative Density at 100 Deg C	0.819	
Specific Heat Capacity at 100 Deg C	2.165	kJ/kg Deg C

Table 16 Lubrication Oil Summary

5.5.5 Instrumentation

5.5.5.1 Shaft Vibration

The method of shaft vibration and displacement measurement was achieved by means of non contacting eddy current proximity probes. The specific probe types selected were 5.0mm tip diameter SKF M65 probes and extension leads used in conjunction with SKF osolator demodulator proximiter probe drivers. The output of the proximity probes is a voltage signature which consists of an 'AC' component (the shaft vibration) and a DC component (shaft position or gap) which can be directly input to the DAQ equipment. A total of ten proximity probes were specified to measure four different positions along the test rotor length ; DE bearing, shaft centre, NDE bearing and NDE flange (Figure 103).

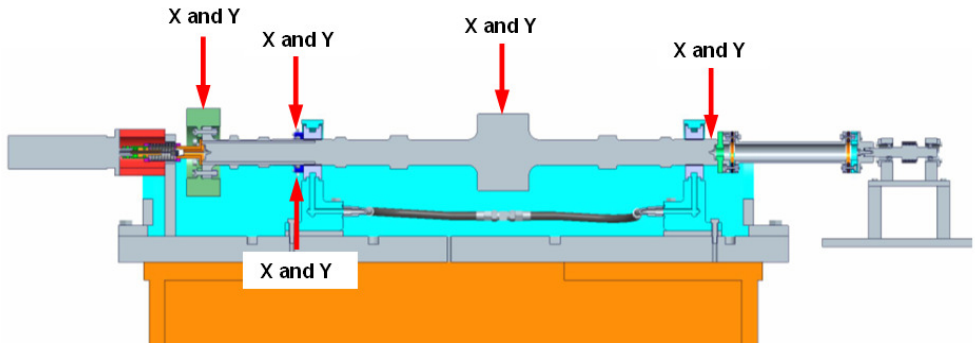

Figure 103 Test rotor shaft proximity probe locations

The bearing journal probes were mounted directly to the bearing shells to minimise the effects of relative thermal growth. At the NDE test bearing, four probes were configured in a 'push – pull' arrangement to minimise the errors in shaft position measurement introduced by relative thermal growth of the shaft and bearing/housing. The application of the push pull arrangement allows for direct measurement of the relative change in bearing operating clearance and provides an approximate measurement of the operating oil film thickness. The probes were mounted as close as practical to the bore of the bearing to reduce the effects of thermal dimensional changes on the gap measurement due to bearing shell temperature. Figure 104 shows a schematic of the probe arrangement on the test bearing.

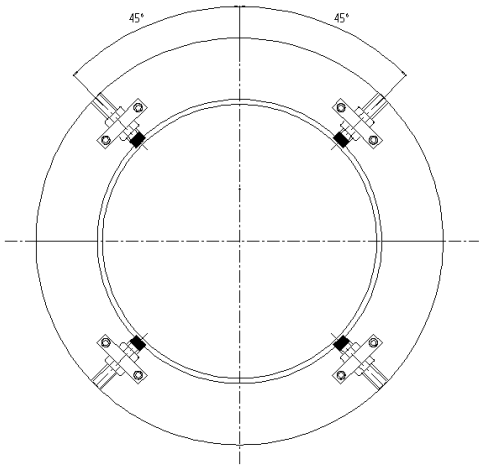

Figure 104 Push-Pull Test Bearing Proximity Probe Arrangement

(Note: the diagram shows the fixed geometry bearing but same principle applied on tilting pad bearings)

5.5.5.2 Bearing Temperature Measurement

Bearing temperature measurement was made by using simplex PT100 Resistance Temperature Detectors (RTD's), 3 wire type. These sensors are located axially in centre of the bearing at a radial position of 2mm below the surface of the babbitt. The location holes for the RTD canisters are produced to provide a tight fit on the diameter of the sensors to aid heat transfer in combination with a heat transfer compound during installation. Both the test bearing and the drive end bearing have provision for 10 sensors position circumferentially around the bearing. The NDE test bearing was fitted with RTD sensors at all 10 locations and the DE bearing being fitted with only four, see Figure 105.

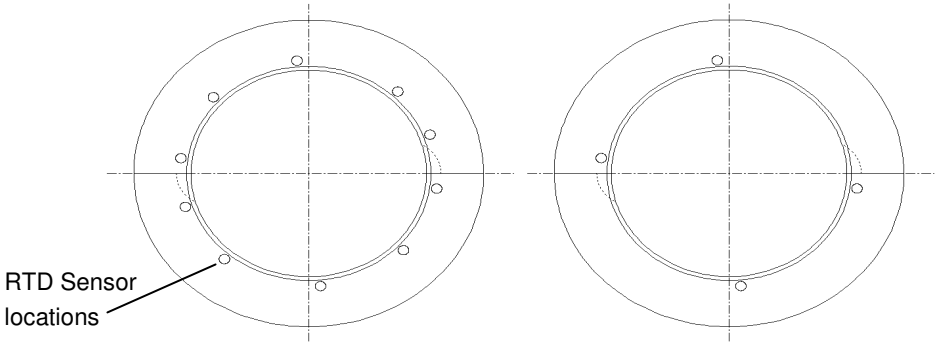

NDE Test Bearing DE Bearing

Figure 105 Bearing Temperature RTD Sensor Locations

The RTD sensors fitted to the tilting pad bearing were again axially located at 2mm below the babbitt surface at the leading and trailing edges of the pad, with 10 (2/pad) sensors again fitted to the test bearing and four in the DE bearing. Sensors were located at the leading and trailing edges of each pad.

5.5.5.3 Shaft Temperature Measurement

The most challenging measurement to be made was that of the shaft journal temperature distribution due to the requirement to provide power to and receive a signal from some kind of temperature measurement sensor in the high speed rotating shaft. A number of options were explored to achieve this objective. The initial choice would have been to use the PT100 RTD sensors as used in the bearing, as these have a good inherent absolute accuracy and an adequate operational temperature range. However the use of these sensors requires a low noise, low resistance method of electrical coupling to the sensor due to the very low inherent resistance levels and sensitivity of measurement to resistance change. To practically achieve this for the accuracy levels required, it would necessitate the use of a wireless option due to the concern that surrounded the use of an electrical slip ring with RTD's (i.e. slip ring noise and resistance). The possibility of such a telemetric option was explored with several specialist instrumentation providers, the conclusion of which was that due to the high operating speed requirements, whilst achievable, the associated equipment and signal conditioning costs would be high and beyond the restrictive budget of this work.

Alternative options as to how to achieve the required measurements without compromising on the required measurement accuracy capability were continued, with focus being around a solution which allowed the use of a high speed low noise electrical slip ring. The conclusion of the work was that the use of high quality ceramic thermistors could provide a suitable solution to conduct the required journal measurements. The selection of thermistors was made due to the high resistance and low sensitivity to signal noise characteristics. This allowed the concerns relating to the electrical slip ring to be negated, with typical slip/ thermistor ring resistance ratio of approximately $1.35x10^{-4}$ without any requirement for significant on rotor signal conditioning.

A principal disadvantage of selecting thermistors is that a suitable usable sensor construction is not readily available on the market. As such the design and construction of the sensors had to be carried out specifically for the project.

The sensor construction used miniature high quality 100kΩ @ 20°C NTC(Negative Temperature Coefficient - reducing resistance with temperature) thermistors with minimum absolute accuracy levels of +/-0.2°C, and sensor repeatability within <0.01°C within a temperature range of 20°C to 100°C. Small brass canisters were manufactured to house the sensors with the sensor 'potted' in the canister with a high integrity epoxy resin. Special attention was applied during the 'potting' process to ensure no air pockets were present in the epoxy so as not to effect the heat transfer within the sensor. PTFE high temperature oil resistant signal sheathing was used to insulate the signal wires and then sealed in high temperature oil resistant heat shrink sleeve. Figure 106 shows the basic thermistor sensor construction.

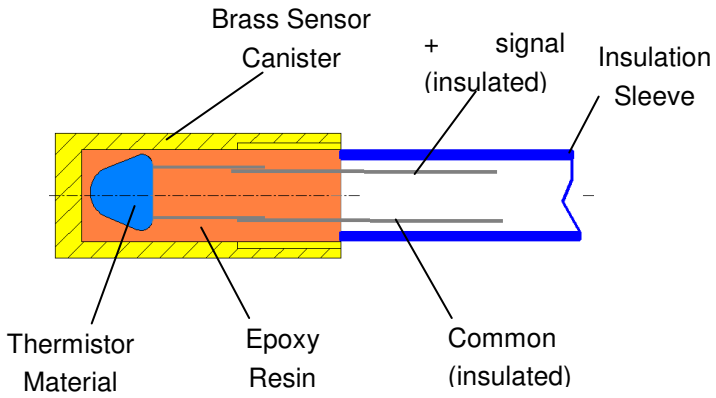

Figure 106 Thermistor sensor basic construction

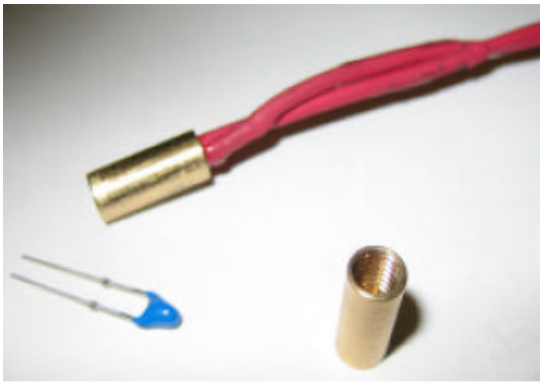

Figure 107 Thermistor sensor assembly

Several problems are presented with the use of thermistors as the method of temperature measurement. The principle difficulties are the non-linear relationship with temperature and the second is how to obtain a suitable output voltage or current than can be recorded.

To enable a suitable output signal relating to the thermistor resistance value to be obtained, a simple signal conditioning circuit was designed and

constructed. The circuit was based on a traditional Wheatstone bridge circuit consisting of 3 fixed high accuracy resistors. The bridge was configured such that the thermistor acted as a variable resistor in the forth leg of the circuit, see Figure 108. Each thermistor had a dedicated bridge circuit with a common power supply rail. The signal conditioning board was configured such that removal links allowed for direct measurement of the fixed resistors to enable accurate quantification of the resistance of each leg of the bridge, minimising the residual errors measured for the thermistor resistance. The bridge circuit shown in Figure 109 was used for each thermistor, and the measured resistance of the thermistor for any given temperature condition was establish by the application of the relationship in equation 5.5.1.

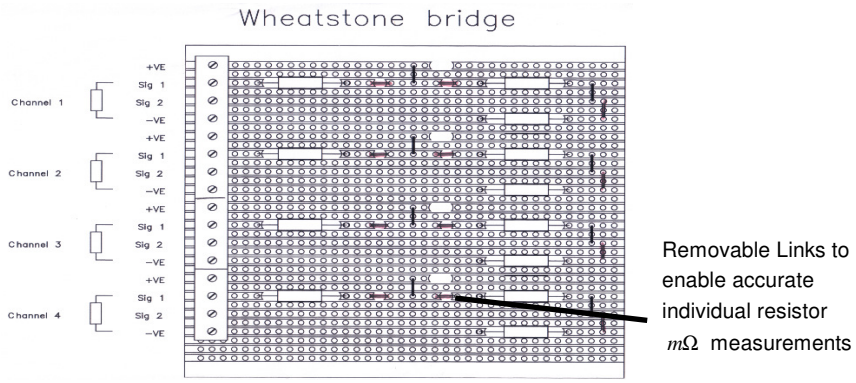

Figure 108 Thermistor Wheatstone bridge signal circuit (signal conditioning unit not shown)

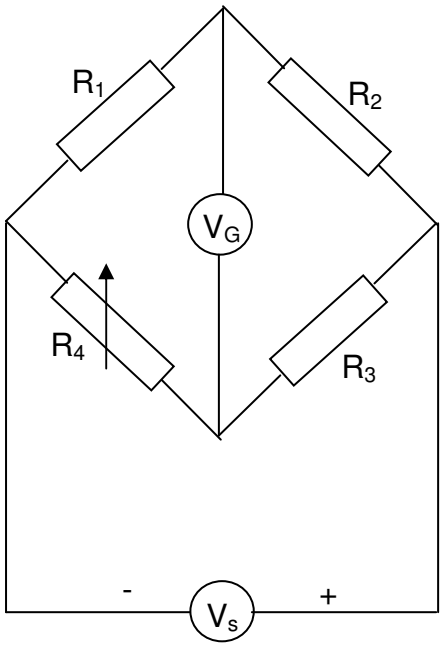

Figure 109 Thermistor Wheatstone bridge configuration

$$R_{therm} = \frac{\left(\frac{V_G}{V_S}\right).R_3 + \left(\frac{R_2.R_3}{R_1+R_2}\right)}{1-\left(\frac{R_2}{R_1+R_2}\right)-\left(\frac{V_G}{V_S}\right)} \quad \text{(Eq. 5.5.1)}$$

where R_{therm} = unknown thermistor sensor

R_1, R_2, R_3 = Fixed resistors

The gauge voltage from Figure 109 was taken as the input signal to the data acquisition as a measure of the thermistor resistance.

The second problem presented by the application of thermistors is in two parts. The highly nonlinear response of the sensors resistance change to temperature presents difficulties in practically interpreting the corresponding bridge voltages to a temperature accurately without the need for cumbersome or inaccurate discreatised data tables (Figure 110). Additionally the absolute accuracy of the sensor across the temperature range of interest can result in accuracies of +/- 0.2 degrees. This level of variability is outside the required measurement accuracy as outlined earlier in this chapter.

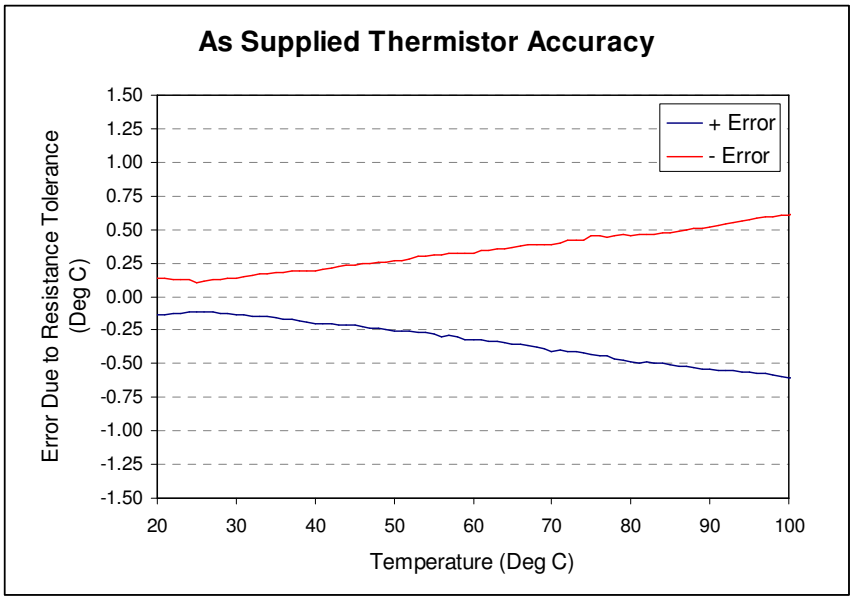

Figure 110 As supplied thermistor accuracy due to resistance variance

By using the inherent high degree of repeatability of the thermistor sensors, a technique was used to analytically characterise the resistance-temperature

relationship which allowed for the direct determination of temperature for a given measurement of resistance or equivalent voltage. The method applied can also result in the ability to significantly increase the absolute accuracy of the sensor by obtaining an accurate analytical description of the resistance curve for each sensor. The technique used was that as presented by Steinhart et al [56] and is commonly known as the Steinhart-Hart equations. It states that the application of this relationship can increase the absolute accuracy of any given thermistior to +/-0.01°C or better over a 200°C temperature range. The principle equation presented by Steinhart et al is derived from empirical curve fitting of the resistance-temperature characteristic of thermistor devices and described using the natural log of resistance relative to the inverse of temperature, where (1/T) is expressed in terms of a polynomial expression as :

$$\frac{1}{T} = A_0 + A_1\left(\ln\left(R\right)\right) + ... + A_N\left(\ln\left(R\right)\right)^N \qquad \text{(Eq. 5.5.2)}$$

where T = temperature in degrees Kelvin
A_0 to A_N are polynomial coefficients

It is presented in the accepted literature [57] that a 3rd order polynomial is able to accurately describe the nonlinear response for any specific thermistor and equation 5.5.2 can be reduced to equation 5.5.3 and is known as the Steinhart-Hart equation.

$$\frac{1}{T_i} = C_A + C_B.\left(\ln\left(R_i\right)\right) + C_C.\left(\ln\left(R_i\right)\right)^3 \qquad \text{(Eq. 5.5.3)}$$

The coefficients C_A, C_B and C_C are the Steinhart-Hart constants for the specific thermistor which requires analytical modelling. The coefficients for each specific thermistor need to be established and this can be achieved by accurate determination or specification of the resistance of the thermistor within the desired temperature measurement range. For example, for a given temperature resistance curve such as that in Figure 111, the resistance for three specific temperature conditions can be taken. With this data it is possible to solve for the three unknown coefficients by constructing 3 sets of linear simultaneous equations. To provide an efficient and direct solution, expressions for the coefficients were developed within the thesis and following

some work the following equations 5.5.4, 5.5.5 and 5.5.6 are presented to express each of the coefficients for a given thermistor sensor.

$$C_C = \frac{\left(\frac{1}{T_2}-\frac{1}{T_1}\right).\left(\ln(R_3)-\ln(R_2)\right)-\left(\frac{1}{T_3}-\frac{1}{T_2}\right).\left(\ln(R_2)-\ln(R_1)\right)}{\left(\ln(R_3)-\ln(R_2)\right).\left(\ln(R_2)^3-\ln(R_1)^3\right)-\left(\ln(R_3)^3-\ln(R_2)^3\right).\left(\ln(R_2)-\ln(R_1)\right)}$$

(Eq. 5.5.4)

$$C_B = \frac{\left(\frac{1}{T_2}-\frac{1}{T_1}\right)-C_C.\left(\ln(R_2)^3-\ln(R_1)^3\right)}{\left(\ln(R_2)-\ln(R_1)\right)} \quad \text{(Eq. 5.5.5)}$$

$$C_A = \frac{1}{T_1}-C_B.\ln(R_1)-C_C.\ln(R_1)^3 \quad \text{(Eq. 5.5.6)}$$

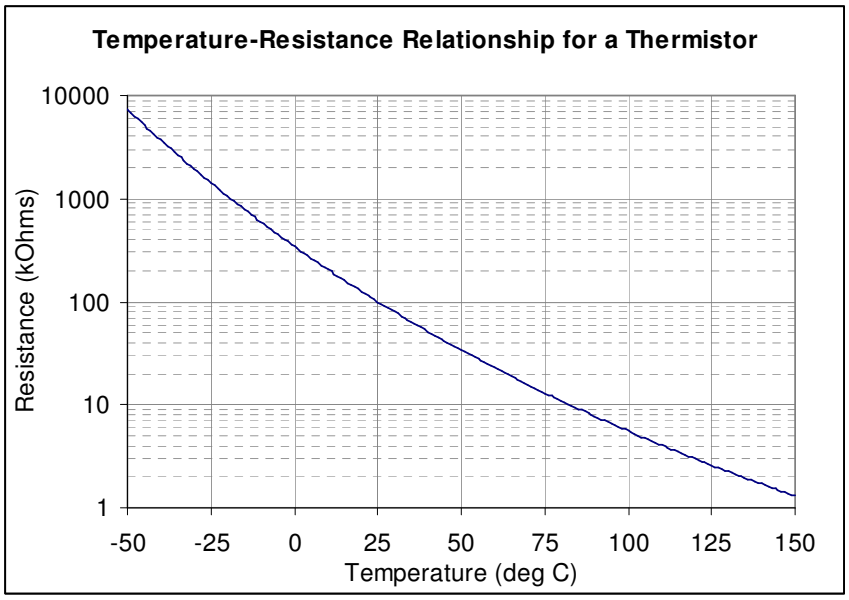

Figure 111 Typical thermistor temperature-resistance curve

With the three Steinhart-Hart coefficients it is possible to determine the temperature for each thermistor accurately based on the measured resistance.

Applying and solving the Steinhart-Hart equation for each thermistor allows the associated coefficients to be determined. To be able to solve the equations, the resistance of each sensor at three temperatures needs to be accurately known. The method used to determine this data was to measure the resistance response of each thermistor against the temperature measurement of a 'master' sensor. The sensor used to provide the master measurement for the purposes of calibration was a specially calibrated PT100 RTD which had been previously calibrated to an accuracy measurement of +/- 0.01 ^{o}C.

Calibration

A calibration block was constructed into which the four themistor sensors were mounted along with the master RTD and two further PT100 RTD's Figure 122. The calibration block was a steel disc which was introduced to provide a degree of thermal inertia to the measurement point. This was to reduce any effects caused by air movement and forced convection within the heating medium that could be experienced if the sensors were exposed directly to the heating atmosphere. All four shaft sensors were calibrated together in the same runs to enable a high degree of relative accuracy in that any absolute errors in the master RTD were principally negated by the fact that all thermistor sensors and the RTD were at the same temperature reading, irrespective of the small absolute error in the master PT100.

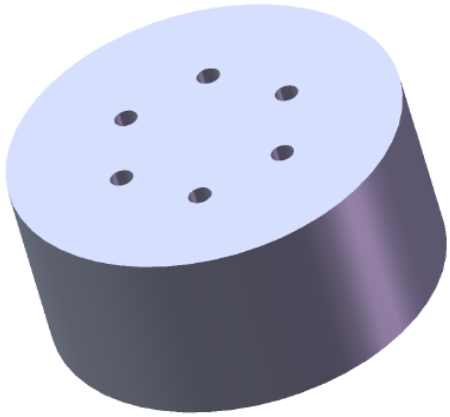

Figure 112 Heat sink block used for thermistor sensor calibration

The calibration block was placed into an accurately controlled heat treatment furnace. All sensors were monitored and recorded during a heating cycle in which the furnace temperature was steadily raised to 100^{o}C or just over. Once at temperature the furnace was switched off and all forced circulation

disengaged. The furnace temperature allowed to cool slowly down to ambient. The typical time required to heat the furnace and allowing to cool to ~25°C took around 22 hours. Figure 113 shows a typical calibration cycle for the thermistors, the temperature shown is that of the master sensor.

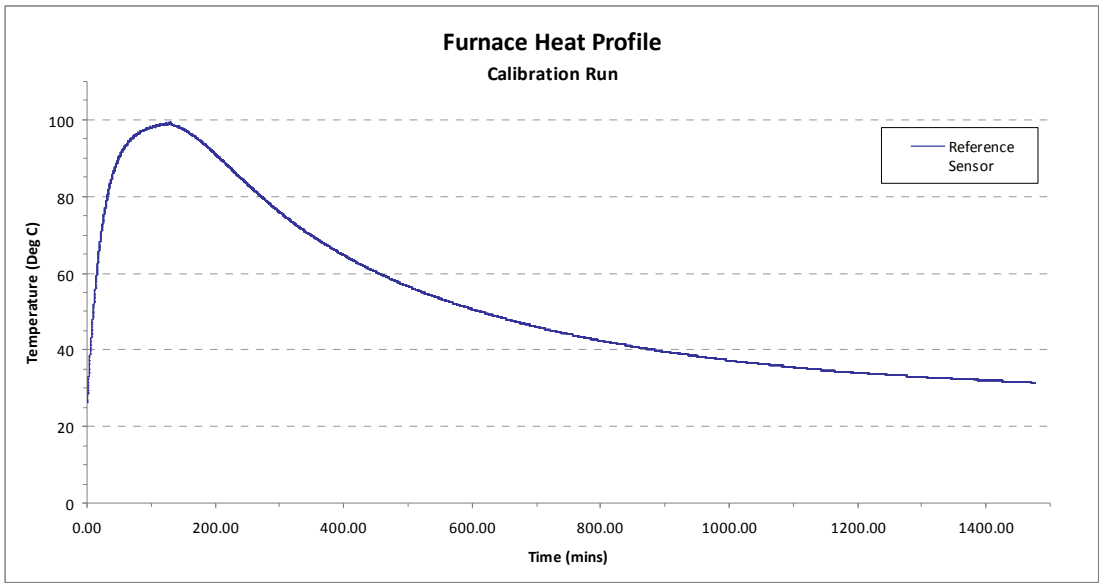

Figure 113 Time-temperature curve for thermistor calibration

From the measured calibration data the three thermistor resistances were obtained and the Steinhart-Hart constants established for each sensor. The constants were taken to give an operating temperature range of the sensor of 25°C to 100°C. Table 17 gives the three temperature constants obtained for both sets of thermistor sensors for the rigid and flexible rotors.

	Steinhart-Hart Constants		
Sensor	**C_A**	**C_B**	**C_C**
G(1)	0.007744	-0.00444	4.3643E-07
B(1)	0.007635	-0.00043	4.0807E-07
R(1)	0.007739	-0.00044	4.3356E-07
W(1)	0.007691	-0.00043	4.2176E-07
G(2)	0.000884	0.00020	7.3626E-08
B(2)	0.000818	0.00021	4.6681E-08
R(2)	0.000901	0.00020	7.9879E-08
W(2)	0.000843	0.00021	5.9158E-08

Table 17 Thermistor sensors Steinhart-Hart constants

To establish the functional accuracy and repeatability of the thermistor sensors when applying the Steinhart-Hart coefficient from Table 17, several repeat heat cycles were carried out in the furnace and the measured thermistor temperature computed with the previously determined Steinhart-Hart coefficients. The computed thermistor temperatures were compared with

the master sensor (RTD PT100) temperature. Also the relative temperatures of each of the thermistors sensors were compared to each other. The most relevant measure of accuracy for the measurement of interest is the relative accuracy of the thermistors sensors. A plot of the temperature measurement error for each of the thermistors against the master sensor is presented in Figure 114 to Figure 117. It can be seen that for the temperature range between 30°C and 75°C, all sensors are within +/- 0.025°C whereas at the higher temperatures the accuracy levels reduce slightly up 100 °C. The data shown in Figure 114 to Figure 117 is for the sensors used in the flexible rotor. However similar characteristics were obtained for the sensors used in the rigid rotor and the accuracy ranges defined were consistent with those presented in Table 18 between the temperatures of 25 and 80 °C. The temperature measurement error is defined as T_{error} is defined as:

$$T_{error} = T_{sensor} - T_{master}$$

where T_{sensor} = the as measured temperature from the thermistor

T_{master} = the temperature as measured with the master sensor

Table 18 summarises the derived sensor accuracies when considered across several temperature ranges. Each of the four different thermistor sensors is identified by the colours green, blue, red and white.

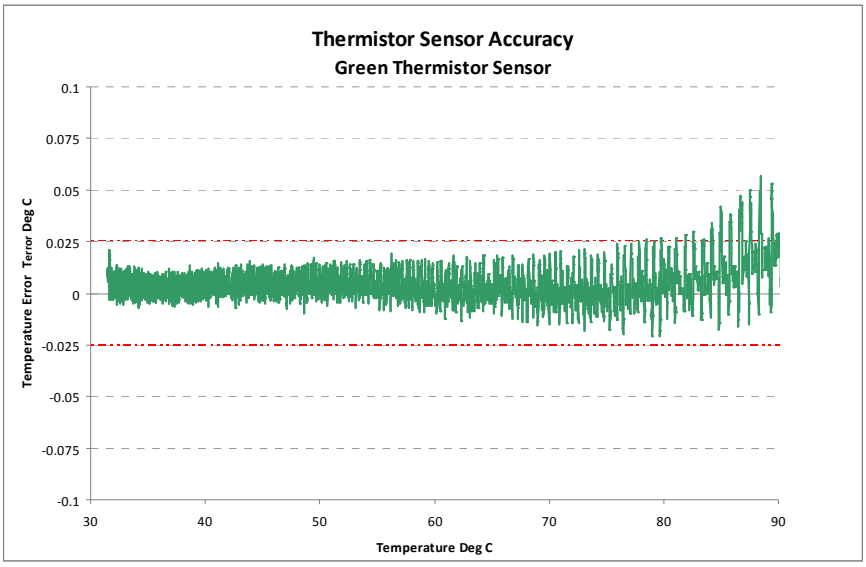

Figure 114 Thermistor sensor error measurement (Green sensor)

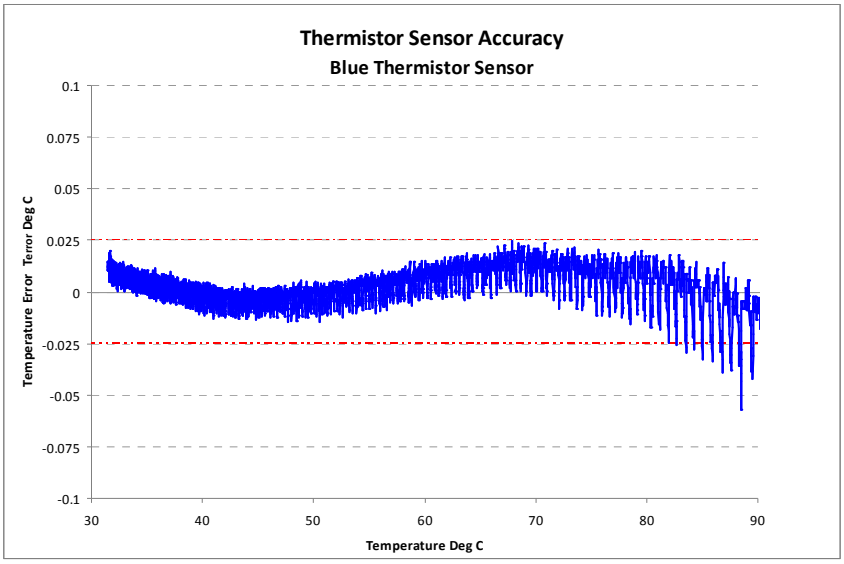

Figure 115 Thermistor sensor error measurement (Blue sensor)

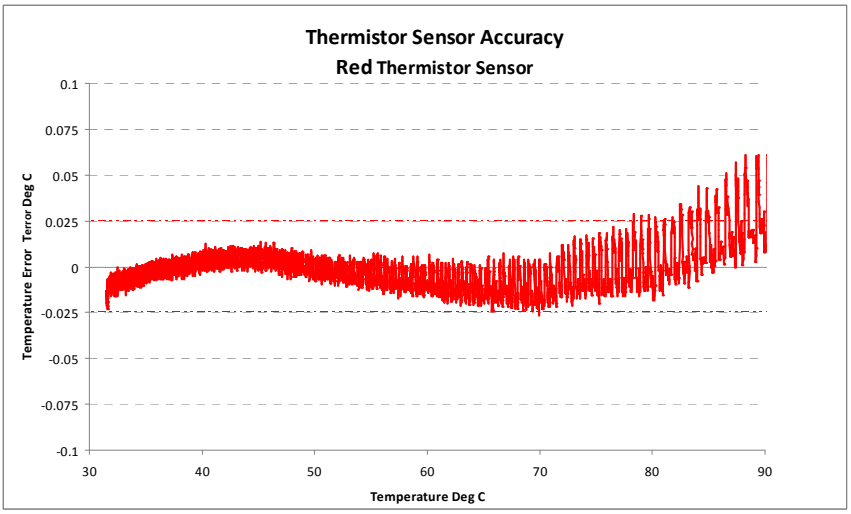

Figure 116 Thermistor sensor error measurement (Red sensor)

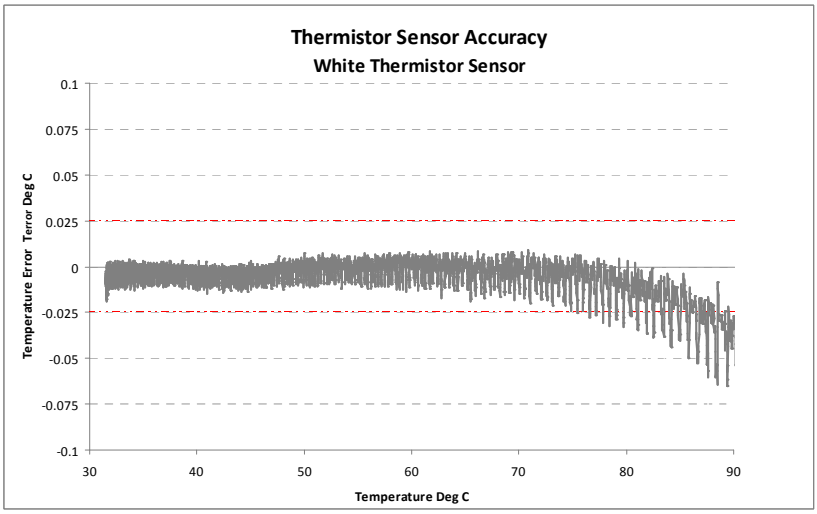

Figure 117 Thermistor sensor error measurement (White sensor)

The repeatability of the sensor accuracies was also verified by repeating the furnace heating cycle two further times. In each of the following cases the temperatures were maintained within the accuracy ranges identified in Table 18.

	Temperature Range / Measurement Accuracy and Repeatability					
	30-75 °C		75-85 °C		85-95 °C	
Thermistor	+ °C	- °C	+ °C	- °C	+ °C	- °C
Green(1)	0.025	0.025	0.050	0.025	0.075	0.025
Blue (1)	0.025	0.025	0.025	0.050	0.025	0.075
Red (1)	0.025	0.025	0.050	0.025	0.075	0.025
White (1)	0.025	0.025	0.025	0.050	0.025	0.075

Table 18 Individual sensor calibrations/accuracy for flexible and rigid rotor

The thermistor signals were fed to the rotor via a 12 channel (24 way) high speed IML-Moog slip ring. The arrangement in which the signal wires were coupled between the slip ring and rotor underwent a number of design iterations. Two key elements were, firstly the means by which the slip ring and rotor were coupled and the second was the means of making the connections between the signal wires to the slip ring. As it was a requirement to be able to remove the rotor from the rig several times a relatively quick and reliable way of joining the signal wires was important.

The coupling was achieved by a custom designed and manufactured coupling which is based on a coil spring with coupling ferrules on each end. This allowed for the necessary drive to be obtained, whilst accommodating any static of dynamic misalignment between the two components. The means of connecting the signal wires was more challenging with several problems incurred during the commissioning and testing phases. Early designs were based around the signals being made by means of soldering joints in the rig. However, following a number of failures, it was concluded that a more robust and quick release method of coupling the sensors was needed. The use of a pin type connection was finally selected with a specialist connector and aluminium housing assembly produced. The rotor side housing was made as a split aluminium housing to both provide ease of access to the signal cables during initial fitting and the use of aluminium limited the impact of the mass of the instrumentation assembly. Figure 118 shows the failure of the initial soldered arrangement and Figure 120 is the final design arrangement used throughout the testing phase.

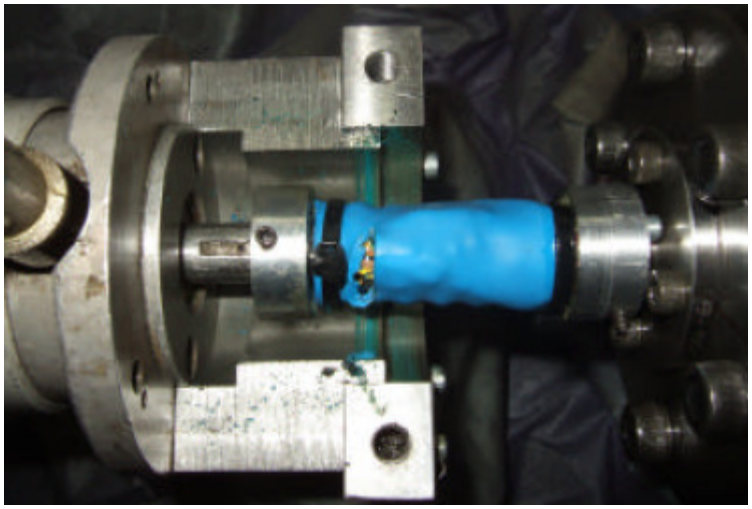

Figure 118 Original slip ring coupling signal wire failure

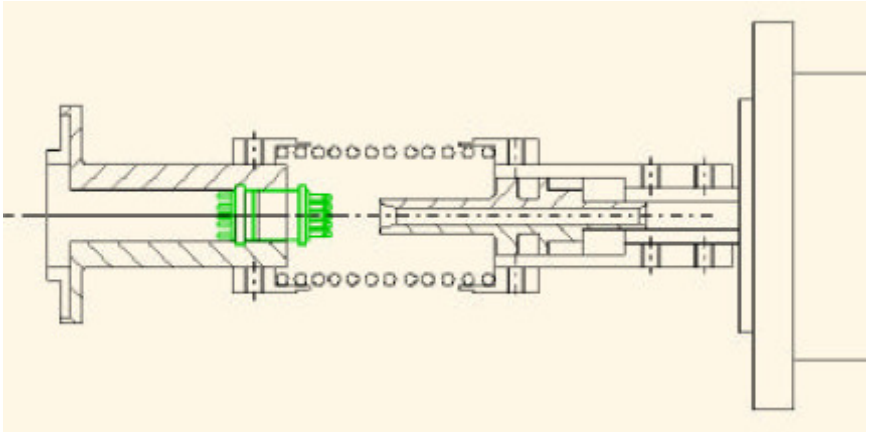

Figure 119 Schematic of final slip ring instrumentation design

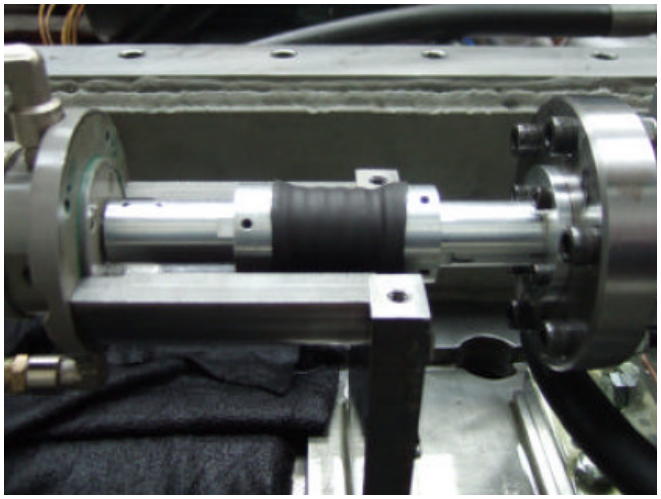

Figure 120 Final slip ring instrumentation design

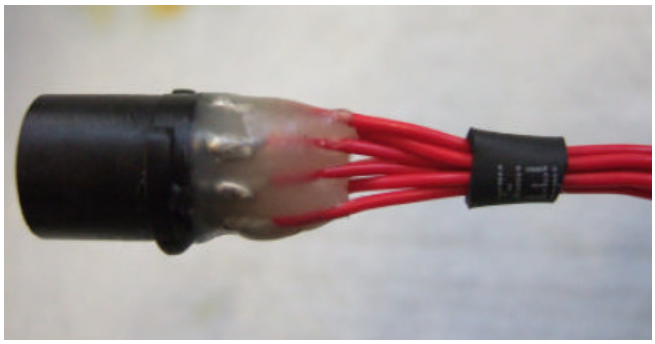

Figure 121 'Potting' of signal wire soldered joints to prevent fatigue failures

5.5.5.4 General Measurements

A number of other sensors were also used across the rig predominantly associated with the lubrication oil supply. Table 19 summarise the instrumentation and sensors used across the test apparatus. The sensors locations can be seen in Figure 122.

Sensor Type	Qty	Sig Type	Measurement	Units	Instrument
Eddy Current Proximity Probe	10	V	Vibration	microns	Sony & NOIS & OROS
Eddy Current Proximity Probe	4	V	Gap	microns	Sony
Accelerometer	2	mV	Vibration	m/s^2	Sony
Resistance Temperature Detector RTD	14	mV	Temperature	Deg C	Anvil & NOIS
Key Phasor	1	V	Pulse	V	Sony & OROS
Shaft Thermistor Sensors	4	V	Temperature	mV	Anvil
Thermistor Bridge Voltage Supply	1	V	Voltage	V	Anvil
Shaft Speed Tachometer	1	V	Speed	rpm	Anvil & NOIS
Pressure Transducer	1	mA	Pressure	psi	NOIS
Thermocouples	4	mA	Temperature	Deg C	Anvil & NOIS

Table 19 Test rig sensor summary

5.5.6 Monitoring, Data Logging and Data Management

To enable the desired number of channels and sensor types to be monitored, a number of different systems were used to perform the data logging and monitoring. The most desirable situation would be to use a common data logger to perform all the recordings of signals, however this would require some 42 channels covering 8 sensor and signal types which was neither available to the researcher or affordable within the research project. By using multiple systems care had to be taken as a number of problems had to be

overcome to eliminate issues with interference and incompatibility between different equipment. In total four different logging systems were employed. These systems covered both low frequency logging and high frequency vibration data.

The four systems used were :

- Newlyme Special Purpose DAQ System (NL)
- Anvil Instruments General Purpose DAQ System (AV)
- Sony EX Dynamic Signal Recorder (SX)
- OROS Dynamic Signal Analyser (OROS)

The Newlyme (NL) system is an existing data logging system at Allen Gears. The system has a specific number of dedicated channels with built in signal conditioning for certain sensor types. The system is used to provide the active monitoring system by which the test rig is controlled and monitored. All measured parameters (with the exception of the shaft temperature sensors) are displayed on the system and a basic digital log is generated. Using the NL system, peak-peak shaft vibration readings are acquired. No frequency data is processed within NL.

The digital recordings of all the temperature sensors (including shaft journal sensors) are fed into the Anvil instruments DAQ module. This is an existing piece of equipment at Allen Gears. The system records all of the RTD and Thermocouple readings digitally to the computer hard disk at a sampling frequency of 1s/s. Signal conditioning for the RTD's and Thermocouples is managed within the instrument itself, making calibration a more straightforward procedure. The shaft temperature measurements are supplied as DC voltages to the instrument via the signal conditioning circuit outlined in the previous section.

The high frequency data was acquired using the Sony Ex (SX) which is a 16 channel dynamic digital data recorder and analyser. This unit is used to give basic frequency information whilst acquiring data and has limited amount of analysis capability. The data recorded is later post processed using Matlab to provide frequency spectra, shaft orbits and phase relationships etc. The dynamic signals for the proximity probes, accelerometers and key phasor are recorded with the SX.

DAQ System	Channel Ref	Sensor/Reading Type	Sampling Rate (Hz)	
Sony (SX)	chan 1 - 10	Proximity Probe - vibration	10k	
	chan 11 - 14	Proximity Probe - DC gap	2k	
	chan 15	Accelerometer	25.6k	
	chan 16	Key phasor	10k	
Oros (OROS)	Chan 1 - 10	Proximity Probe - vibration	5.12k	*
	chan 11	Key phasor	5.12k	
Newlyme (NL)	chan 20 - 30	Proximity Probe - vibration	1	**
	chan 1-4	Thermocouples - Lube sys	1	
	chan 32	Speed tachometer	1	***
	chan 60	Pressure - Lube sys	1	
	chan 70 - 84	RTD - Bearing temperature	1	
Anvil (AV)	chan 1 - 12	RTD - Bearing temperature	2	
	chan 13 - 16	Thermistors - Shaft temperature	2	
	chan 17 - 20	Thermocouples - Lube sys	2	
	chan 21	Pressure - Lube sys	2	
	chan 22	Speed tachometer	2	

* Time domain filtered 1X is logged every 1s
** Signal is pre-conditioned at a sample rate of 5k Hz to determine pk-pk
** Tachometer unit acquires at higher rate to provide output DC voltage proportional to speed

Table 20 Data acquisition rates for all mesasurement equipment and channels

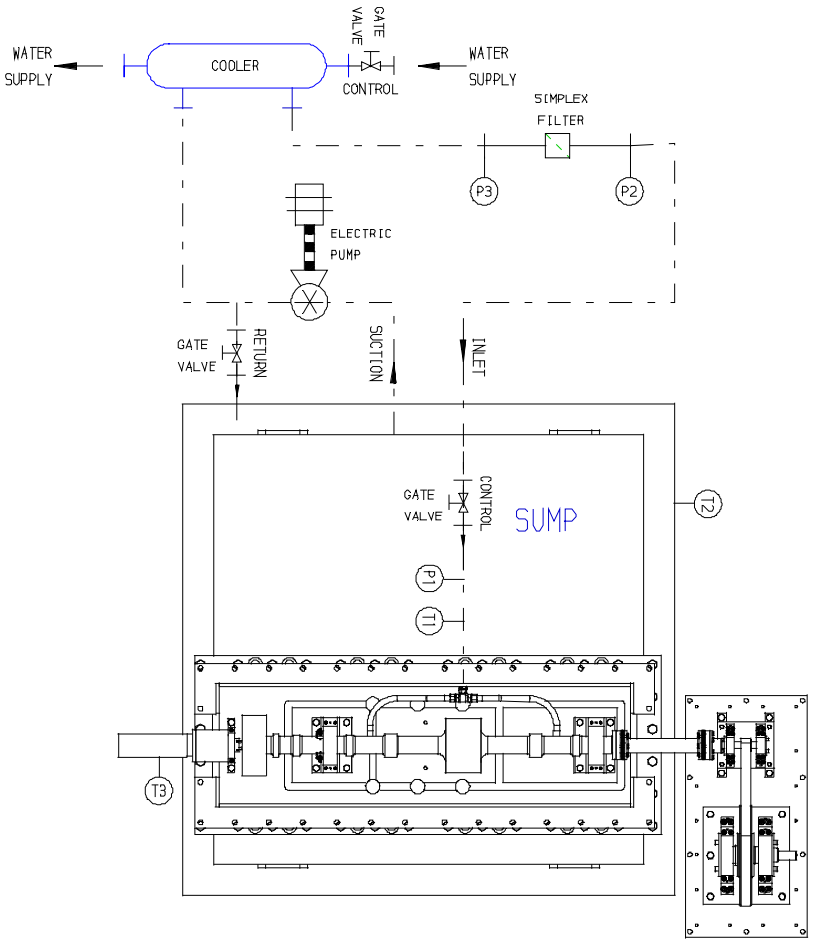

Figure 122 Pipework and instumentation layout for test rig

An OROS dynamic signal analyser was used to track and record the filtered synchronous order of the shaft vibration. The shaft vibration 1st order was filtered and tracked with the processed information presented both visually live to the monitor screen and recorded digitally to disk. Post processing of this data was later performed using Matlab and Microsoft Excel.

The high volume of data acquired during the testing was stored and referenced within a structured file naming system and entered into an access database for ease of future referencing.

Chapter 6

Experimental Rig Commissioning and Test Procedure

6. Experimental Rig Commissioning and Test Procedure

6.1 Introduction

This chapter describes the physical test apparatus used for the experimental testing, and details the commissioning and system calibration verification procedures applied. The test rig arrangement is consistent with the design specifications presented in chapter 5. An overview of the testing programme is also provided in this section which specifies the various test conditions and variable parameters that were defined at the outset of the experimental programme. Whilst testing was underway results were reviewed and the test programme was modified. This is reflected in the information provided here.

The process of commissioning is defined as the activities of test rig installation, instrumentation verification, measurement and sensor calibration and finally principle characterisation of the operational equipment. Characterisation is principally associated with demonstrating that the test equipment performs as expected for fundamental operating parameters when compared to the design assumptions and predictions.

6.2 Test Rig Preparation and Assembly

The experimental test arrangement consists principally of the main test rotor support stool assembly, the transmission drive motor assembly, drive control panel and data acquisition equipment. Figure 123 shows a general arrangement of the test equipment key components. The fully assembled test rig is shown in Figure 124 to Figure 127.

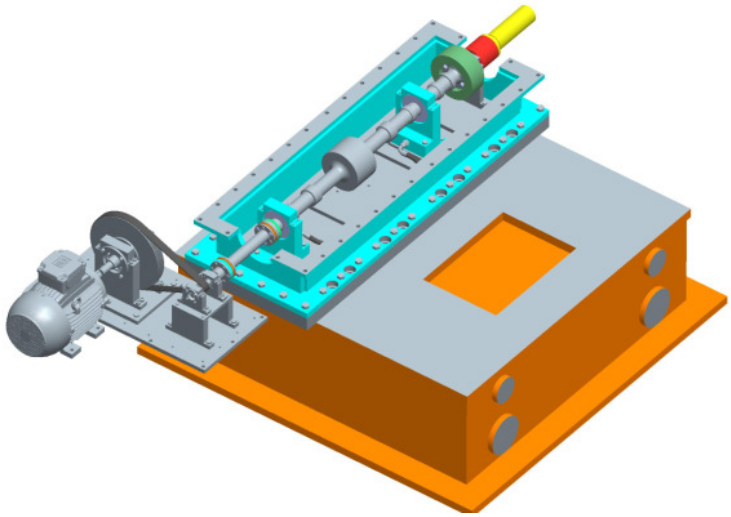

Figure 123 Test Rig General Arrangement

During the initial commissioning of the test apparatus the rigid rotor was used to verify the functionality of the instrumentation, drive system and lubrication system. This was then directly followed by the rigid rotor test programme. The flexible rotor commissioning took place later in the experimental work once the rigid rotor-fixed geometry bearing work had been completed. Figure 124 to Figure 127 show the test rig assembly with both the rigid and flexible rotor assemblies.

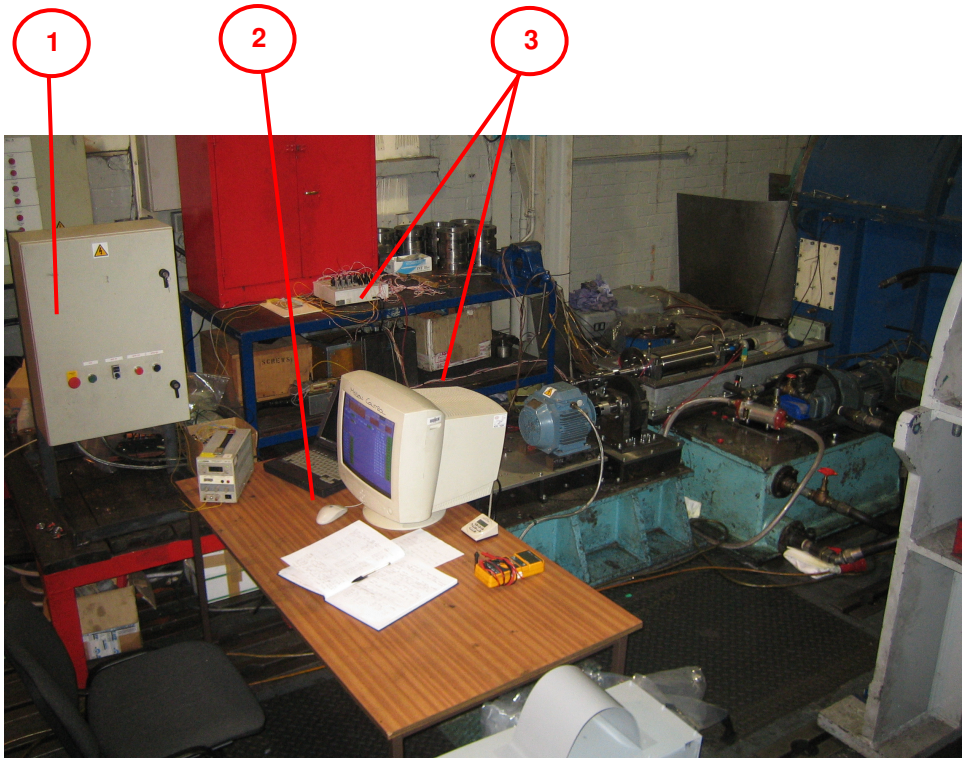

Figure 124 Test Rig Basic Equipment (1)

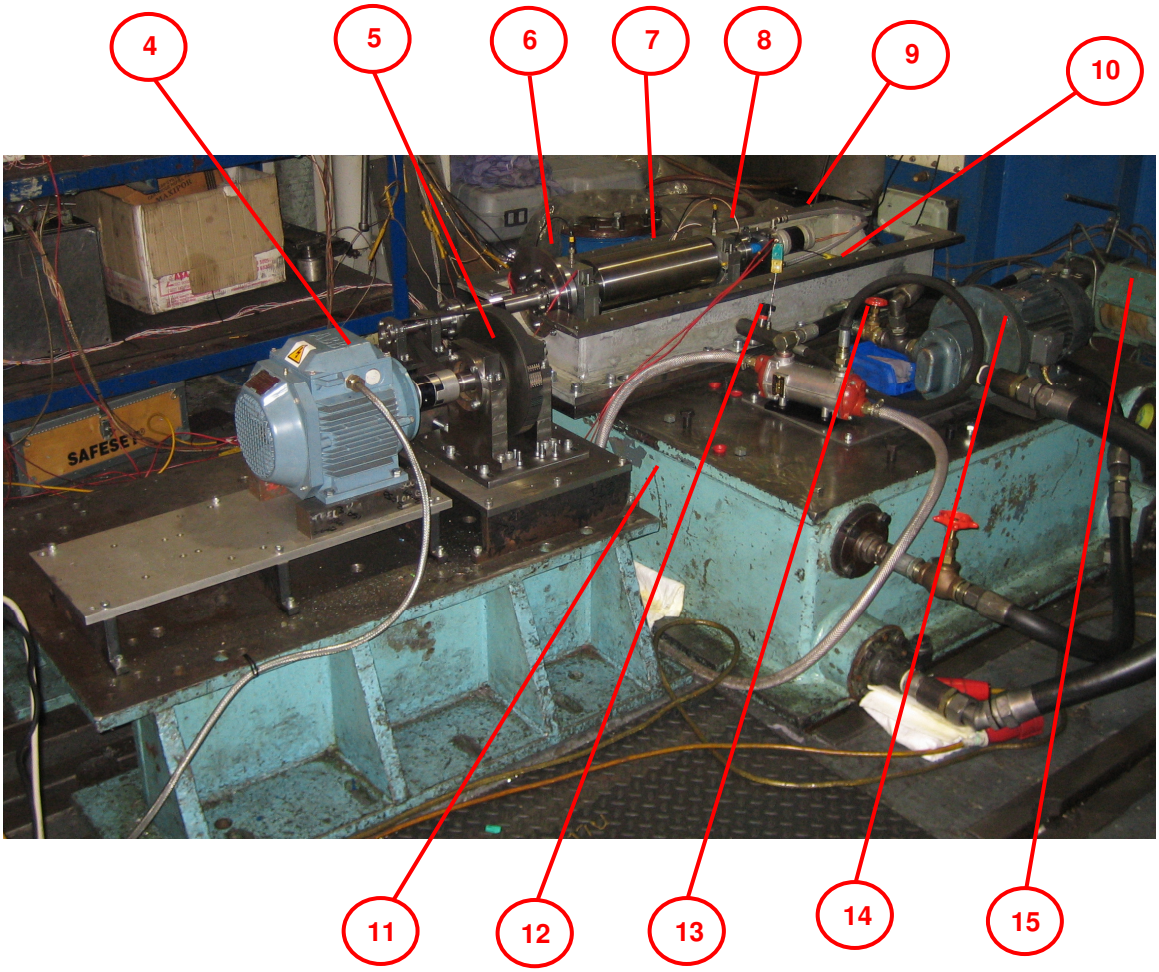

Figure 125 Test Rig Basic Equipment (2)

1. Test Rotor Control Panel
2. Monitoring Stations
3. Data Acquisition and Instrumentation Equipment
4. Electric Drive Motor
5. Pulley Transmission
6. Test Rotor Labyrinth Seal
7. Test Rotor (Dummy)
8. Test Rotor Bearings and Pedestals
9. Slip Ring Assembly
10. Test Rotor Housing and Base Plate
11. Test Rotor Support Stool and Lube Oil Sump
12. Lube Oil Inlet and Pressure and Thermocouple Sensors
13. Lube Oil Inlet Pressure Control Valve
14. Electric Motor Pump Set
15. Lube Oil Element Filter

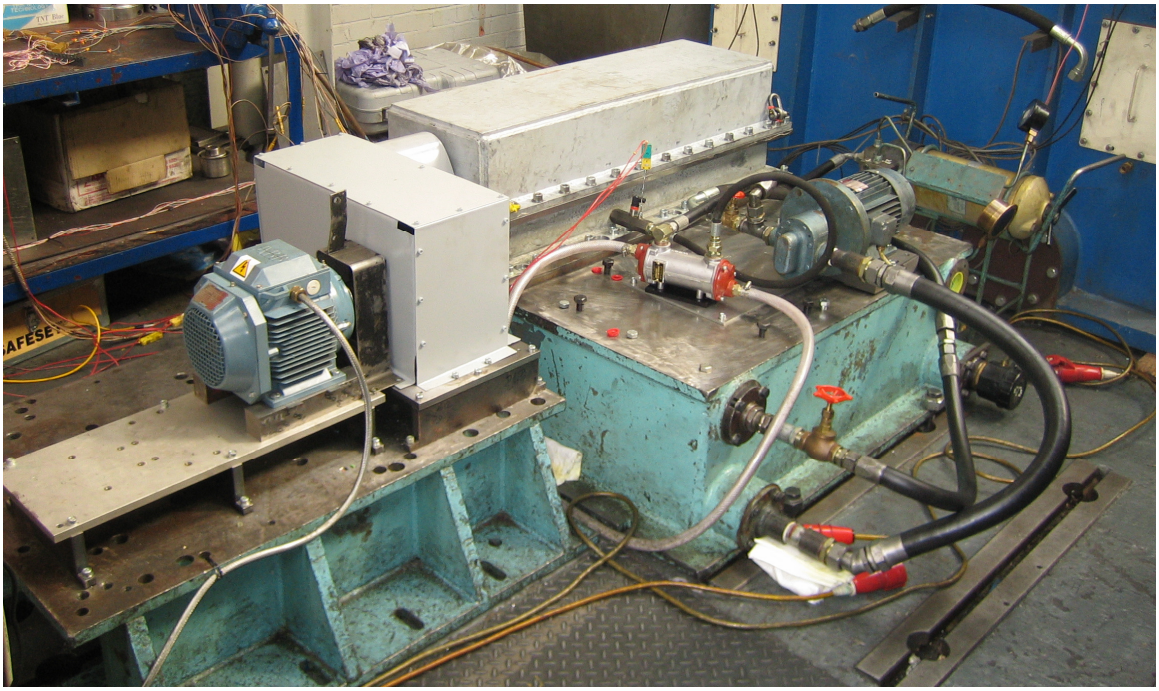

Figure 126 Test rig with main rotor housing and guards fitted

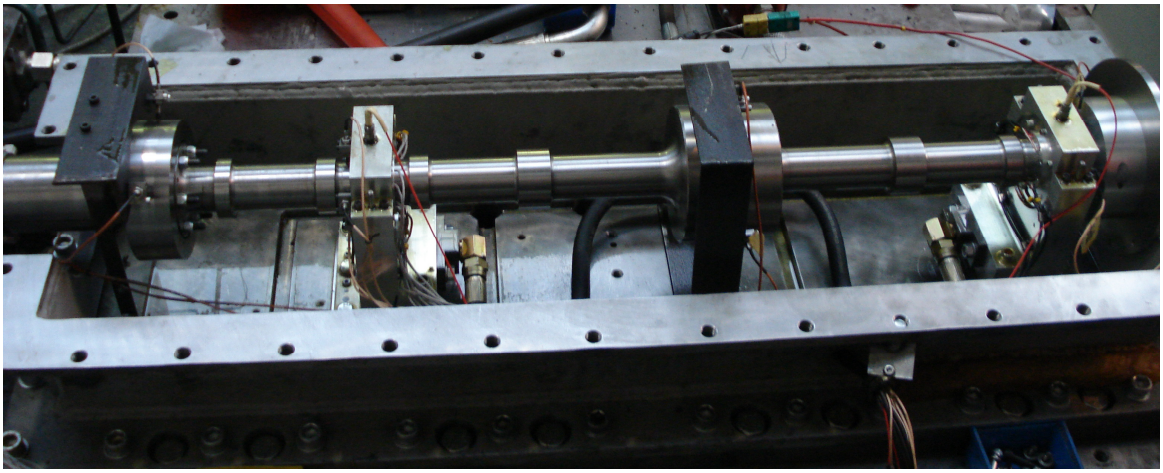

Figure 127 Test rig with main flexible rotor

As part of the commissioning process, several notable activities were performed prior to the final assembly or operation of the rig that could have a significant influence on the rotor performance. A brief detail of how these aspects were considered and controlled is covered in the next few sections.

To ensure that no significant parasitic and/or undesirable rotordynamic features were introduced to the test rotors or rig, it was imperative that the alignment and unbalance states were defined, controlled and understood.

6.2.1 Rotor Balancing

To provide the best possible initial dynamic conditions for both test rotors they were dynamically balanced as discrete components using an independent Shenk multi plane dynamic balancing machine to achieve the lowest practical levels of residual mechanical unbalance. The rigid test rotor was twin plane balanced with corrections made by removing material by grinding small chamfers on the corners of the large outside diameters at two correction planes. The rotor was balanced at a speed of 3000 rpm with the final residual unbalance values of 0.97 g.mm and 2.1 g.mm at the two planes.

The main flexible rotor was initially single plane balanced to get the rotor to such a state where the residual unbalance level permitted higher speed balancing to be performed. The initial single plane balancing was focused on the large diameter at the shaft centre where the largest level of unbalance would be expected. The large centre diameter is also the point at which the rotor is most sensitive to the 1^{st} bending natural mode. By single plane balancing at this location it became practical to run the rotor up the necessary balancing speeds for complete balancing of the rotor.

Once the initial balancing was completed, the rotor was twin plane balanced with corrections made in three planes in total. As the rotor was running above its first natural bending mode it was necessary to balance at multiple locations and this was achieved be means of an iterative balancing procedure. Again balance corrections were made by means of material removal with chamfers ground on the corners of the various shaft diameters. The final mechanical residual unbalance levels at the bearing locations was 0.039 g.mm and 0.028 g.mm for the DE and NDE journal respectively and 0.033 g.mm when run at a balance speed of 2500 rpm (below first bending critical).

Balancing of the flexible test rotor was repeated with the two overhang weights fitted to shaft. For these cases, balancing was performed below the predicted rotor critical speeds with correction material removed only for the overhung mass discs by means of axially drilled holes.

6.2.2 Test Rig Alignment

As with the rotor unbalance the alignment of the test rotor to the drive transmission is a critical feature that influences the rotor response and excitation. To minimize any dynamic forces generated from the flexible element coupling between the rotor and pulley pinion, alignment was tightly maintained during the set up process. To further minimise the magnitude of the dynamic forces presented to the test rotor, the number flexible element blades used in the coupling was reduced. The flexible element membrane blades were reduced to the practical minimum for the level of torque being transmitted which gives a lower angular stiffness and hence lower parasitic force transmission where operating misaligned. Care was taken when selecting the final number of blades so as not to introduce any dynamic issues relating to the axial vibration mode of the coupling.

The alignment procedure was performed with the test rotor as the fixed component and the transmission and motor aligned to it. The alignment of the transmission to the rotor was positioned to give both correct vertical, horizontal and face alignments. The height adjustment was achieved by grinding the transmission support feet to the desired dimensions. Allowance was made for the rise in the bearing when operating and thermal growth of the support pedestal due to the rotor operating temperature. The final alignment figures were as shown in Figure 128.

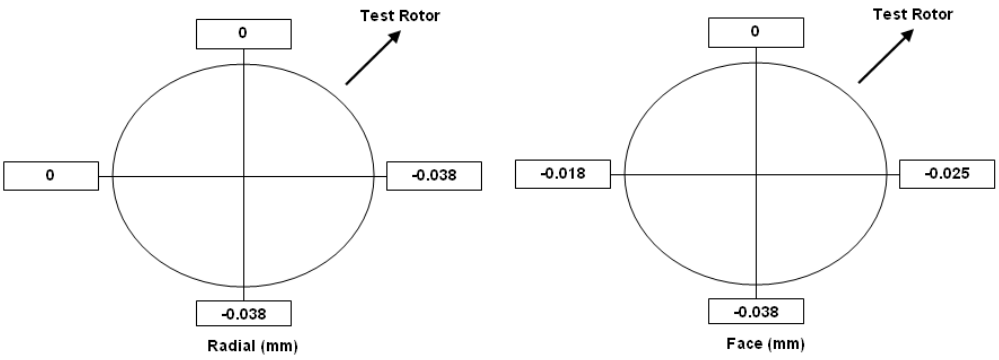

Figure 128 Test rig transmission to test rotor alignment readings

A similar alignment procedure was repeated for the low speed pulley to motor coupling; however it is noted that the alignment at this interface would have a far less significant effect on the test rotor dynamic performance.

6.2.3 Mechanical – Electrical Runout Measurement

In the areas where shaft proximity probes observe the running surfaces of the shaft a pre-assembly check was performed to measure the level of residual mechanical and electrical runout or 'glitch' on the rotors (shaft 'Glitch' is discussed in more detail in chapter 7). The rotors were mounted in a vee block assembly and the level of mechanical runout was measured with a traditional dial test indicator (finger type). Finally the combined electrical-mechanical runout was measured using a master proximity probe, with the results recorded on a paper trace as the shaft was slowly rotated. The initial results showed that the residual electrical runout was over 8 microns, to improve this, the observed surfaces were burnished in a grinding machine using a diamond burnishing tool to a surface finish of ~0.4µm. The process of burnishing improves the homogeneity of the magnetic signature from the shaft surface and results in lower electrically measured variations by the proximity probe.

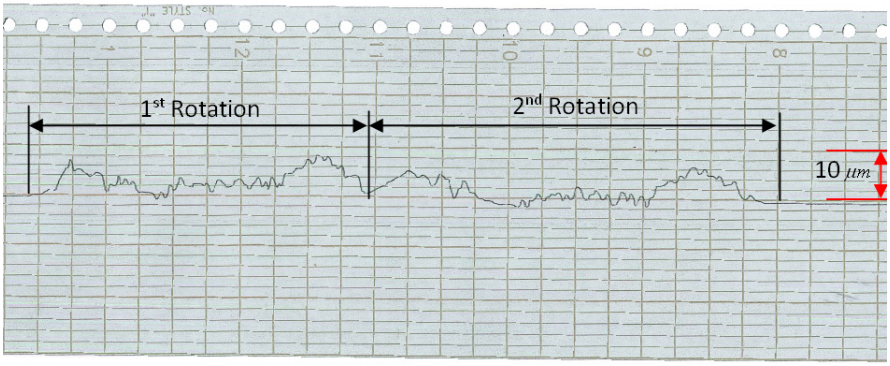

Figure 129 Electrical Mechanical Runout for Rigid Rotor
NDE Observed Surface

The burnishing process was able to reduce the electrical-mechanical runout in all cases but some magnitudes (although low by typical industrial standards) remained higher than desired. To avoid any further machining operations it was decided these residual errors would be compensated for when in the test rig. Detail of the principle and procedure to accomplish this is provided later in this and the following chapter.

6.2.4 Bearing Geometry Measurement

An important feature to verify was the as manufactured sizes and geometry of the bearings. With both the fixed geometry offset half and tilting pad bearings, the topology of the bearing geometry is of critical importantance with respect

to both the running responses of the rotor and the thermal conditions within the bearing. It has been observed from the published literature and the case studies presented in chapter 4 that the operational clearance of the bearing can have a significant influence on the sensitivity to the thermal instability.

The fixed geometry bearings were measured by using a specific process to ascertain the level of pre-load offset and actual joint and crown clearances within the bearing. The procedure was based around obtaining a number of clock readings around both the bore and outside diameter of the bearing and using this data to curve-fit the results to obtain the cylindrical pad geometry with relation to the bearing datums.

The as manufactured geometry of the bearing was obtained by means of clocking the bearing on a rotary table and measuring the deviations of the clock with respect to the datum of the bearing assembly. Analytically these readings were then curve fitted using a least squares fit procedure to determine the effective diameter of each pad, its magnitude of offset and rotational error relative to the datum halving joint of the bearing. Figure 130 provides a schematic of the principal applied. The set of equations in matrix form given in equation 6.2.1 are shown to express the least squares fit for the top and bottom pads of the bearing. Details of the derivations are given in appendix A.

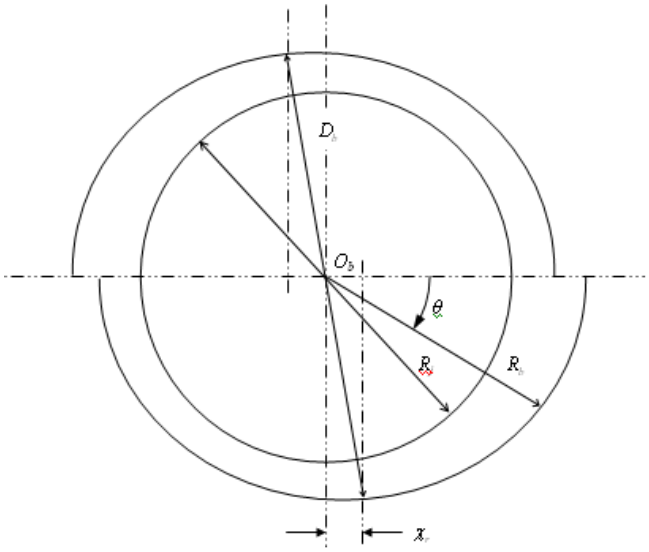

Figure 130 Offset Half bearing geometric measurement relationships

$$\begin{bmatrix} n & \sum\cos(\theta) & \sum\sin(\theta) \\ \sum\cos(\theta) & \sum\cos^2(\theta) & \sum\sin(\theta).\cos(\theta) \\ \sum\sin(\theta) & \sum\sin(\theta)\cos(\theta) & \sum\sin^2(\theta) \end{bmatrix}.\begin{bmatrix} C_r \\ \chi_r.\cos(\theta) \\ \chi_r.\sin(\theta) \end{bmatrix} = \begin{bmatrix} \sum C_H \\ \sum C_H.\cos(\theta) \\ \sum C_H.\sin(\theta) \end{bmatrix}$$

(Eq. 6.2.1)

where n = number of data points

From equation 6.2.1 the equations can now be solved for $C_r, \chi_r.\cos(\phi_m), \chi_r.\sin(\phi_m)$ and $\chi_r.\sin(\phi_m)$ from which χ_r and ϕ_m can be given by 6.6.2 and 6.2.3.

$$\chi_r = \left(\left(\chi_r.\cos(\phi_m)\right)^2 + \left(\chi_r.\sin(\phi_m)\right)^2\right)^{\frac{1}{2}} \quad \text{(Eq. 6.2.2)}$$

$$\phi_m = \tan^{-1}\left(\frac{\chi_r.\sin(\phi_m)}{\chi_r.\cos(\phi_m)}\right) \quad \text{Eq. 6.2.3)}$$

Where pad pre-load = $m = \frac{\chi_r}{C_r}$

The results of the bearing measurements for the offset half bearings are presented in Table 21 for both the DE and NDE bearing.

	Pre-Load		Cant Angle		
Bearing Ref	Top Half	Bottom Half	Top Half (degrees)	Bottom Half (degrees)	Diametral Clearence (microns)
A	0.388	0.304	-37.4	-16.3	139
B	0.44	0.319	-32.1	2.1	152

Table 21 Fixed Geometry Offset Half Bearing Manufactured Measurements

A similar procedure was applied for the measurement of the tilting pad bearing assembly. In this case, due to the variable geometry arrangement, the bearings are not measured as an assembled unit as this cannot practically and reliably be achieved. Instead each of the components is measured individually. The main bearing housing was measured using a micro vertex instrument which provided a typical dimensional measurement but to a high degree of accuracy (0.001 mm). The reading was taken at several points around the bore of the bearing to ensure both the size of the bore was consistent and that the form (i.e. roundness) of the feature was acceptable.

The pads were measured in two ways. The first was to establish the pad thickness which ultimately will determine the operational bearing clearance (when combined with the housing bore measurement). Each pad was measured using the micro vertex with a spherical ruby tip. The second measurement was to establish the curvature of the bearing pad which would control the level of pre-load present within the pad. This measurement was achieved by using a CMM to acquire special co-ordinates across the pads length. These co-ordinates were then curve fitted to extract the effective radius of the pad by the same analytical procedure describe above. The final assembled diametrial clearances for the variable geometry tilting pads were 111 and 128 microns.

Using the as measured bearing data, all bearings were recalculated for their operational performance predictions and used in the rotordynamic evaluations to obtain data for the as manufactured conditions.

As a final practical check, in the case of both the offset halve and tilting pad bearings, shaft lift checks were also performed in the fully assembled test rig. This process involves taking a reading of the shaft position with it sat in the bottom of the bearings and then a second reading with the shaft raised into the top halve of the bearings. The results of which were consistent with the as measured clearances for the bearings.

6.2.5 Lubrication System

The lubrication system was flushed without any of the test rotor bearing or pedestals fitted for a period of 12 hours at 50 degrees C. The test rotor pedestals were then fitted and the process repeated. Finally a third flush was performed with the entire rig assembled without the test rotor fitted. This process was performed to ensure that all remaining contamination and debris had been flushed through the filter before running the rotor in its bearings. This provided an oil quality and cleanliness that would not have any significant impact on the integrity of performance of the test apparatus.

A number of other checks were conducted relating to alignments, lubrications system, balancing and transmission components etc, most of which were conducted on the test rig assembly. Whilst these features are necessary for satisfactory performance of the test arrangement they do not directly affect the

test rotor and are not of specific interest to the presented topic. As such they are not covered in detail here.

6.3 Instrumentation Calibration and Validation

6.3.1 Proximity Probes

The sensors used to measure the shaft vibration and position were eddy current type proximity probes. The specific sensors used were SKF 6mm tip 8 mV/µm in conjunction with SKF osolator demodulator (ODM) probe drivers which were separately housed in an instrumentation cabinet to minimise background interference.

Each of the proximity probe sensors used on the test equipment was first calibrated as individual sensors to a master ODD driver to obtain the displacement voltage characterise for that specific sensor. This was performed to ensure that each sensor was within acceptable full scale errors before building up into the system. Similar checks were performed for each of the ODM by using a master proximity probe sensor. The method of calibration was to use a special micrometer stand Figure 131 which is used to accurately record the voltage reading for a known set of gaps. The probes were calibrated across a range of 0 to 2280 microns. The power supply was provided by means of a calibrated and condtioned DC power supply system at 24v DC.

With all the sensors and ODM driver checked, the instruments were built up into the test and data acquisition system. With a complete system in place it was now necessary to perform the final calibration of the probes. This was carried out in the complete DAQ system to minimise the errors in data readings which result from the cumulative effect of multiple sensors, instruments and cables on the overall system calibration. The calibration procedure was performed using the same equipment and procedure as outlined above. The ODM drivers were supplied by means of a steady 24v DC power supply provided through the data logging equipment.

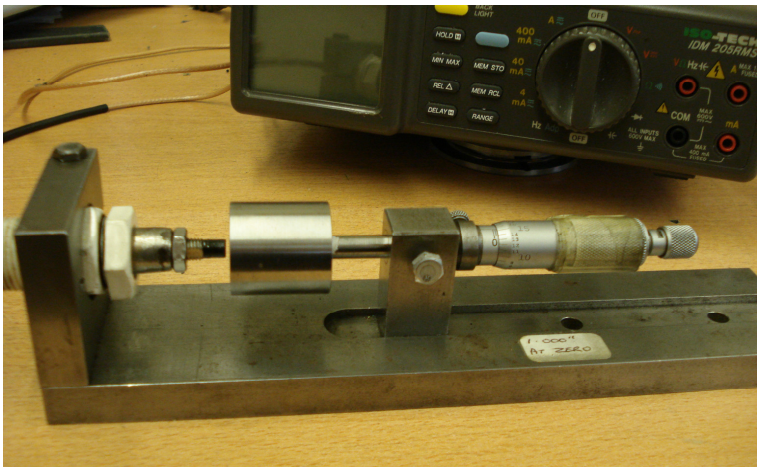

Figure 131 Shaft proximity probe calibration

The specific calibrations for each probe location were then set in the data acquisition equipment for each respective channel.

When the proximity probes were installed into the test rig it was necessary to set the gap between the probe and measured surface to a dimension within the useable probe range. For the sensors used, the distance at which the best linear response is achieved was 10 volts which equates to a gap of ~1250 microns. Each of the sensors used was fitted to this nominal gap setting.

6.3.2 Shaft Temperature Sensors

A detailed description of the shaft sensor design, construction and calibration methodology was presented in chapter 5. The sensor calibrations performed were as discrete sensors using a common bridge circuit. Applying the same approach as that taken for the proximity probes, an additional calibration verification was undertaken of the shaft thermistors as a complete acquisition system.

The purpose of the verification was to gain a measurement of the thermisor accuracy when coupled through the entire DAQ system and, more significantly, the slip ring assembly. An accurate means of verifying the measurement accuracy of the thermistors is difficult to achieve in the dynamic system, principally due to the fact that a rotating system is required. More significantly, a means of establishing a well distributed, stable and defined temperature on the rotor is required.

The dynamic calibration accuracy measurement was performed with the rotor fully assembled in the test stand and connected to the ANVIL DAQ via the slip ring assembly. The method for introducing a controlled temperature was to run the rotor at low speed (~60 rpm) with the oil being circulated with inlet conditions presented at air ambient temperatures. The oil sump heater was then switched on and the oil inlet temperature allowed to rise steadily over a period of time. As the rotor rotation was so slow the temperature generated at the oil film due to shear was considered to be negligible. The very low levels of shaft vibration would mean any temperature perturbation in the oil film would also be very small. With negligible heating from the oil film the dominate temperature source to the shaft and bearing was by means of conduction from the lubricating oil supply. The bulk temperature measurements of the shaft were then compared to provide an in situ measurement of shaft temperature sensor relative accuracy.

The time taken for the shaft to increase from ~25 ^{o}C to ~75 ^{o}C was nominally 12 hours. As with the individual sensor calibrations, the process was repeated two further times. The results from these checks gave an absolute sensor to sensor variation error for the thermistors of 0.06^{o}C. Repeatability was shown to be consistent with a variation of 0.06^{o}C being the largest absolute error within the 3 runs.

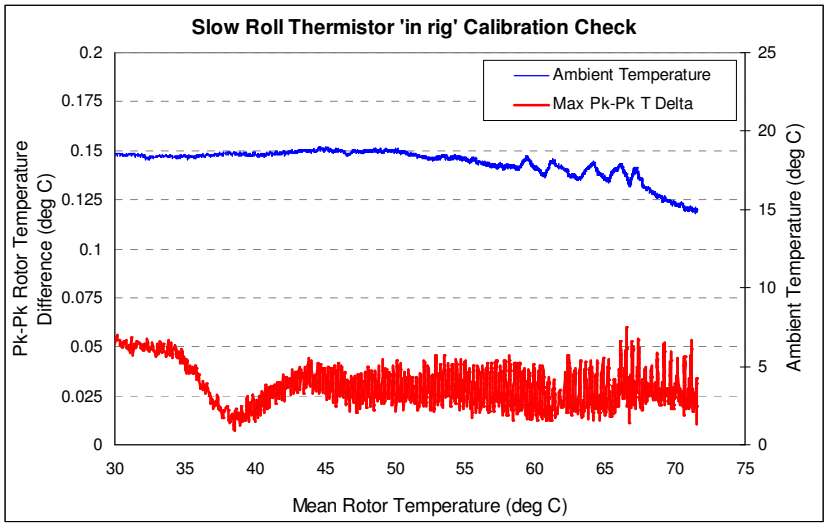

Figure 132 Measured variation in temperature measurement from shaft thermistors during slow roll gradual oil temperature increase

The results of the slow roll calibration verification gave results that were in line with those seen for the individual sensor calibration accuracies when the additional contribution of slip ring noise and DAQ thermal instrument wander

(note changes in ambient temperature across test) are considered. The measured error level of 0.06^{o}C is considered to be acceptable for the journal shaft temperature measurement requirements of the experimental work.

6.3.3 General Sensor Calibration

All other sensors used were calibrated within normal operating accuracies by means of standardised calibration procedures. The calibration accuracies for each of the sensor types is in line with specifications as defined in chapter 5.

6.4 Running Commissioning

Before undertaking the full testing program, several running commissioning tests were performed. This activity involved running the test rig with primarily the rigid test rotor to establish the integrity and performance of the test apparatus, instrumentation, bearings and drive system.

Several test runs were carried out where the rotor was run up in incremental speed steps to a maximum speed of 14000 rpm. Further run up and run down tests were performed to characterise the rotordynamic behaviour of the rotors. During the final commissioning runs, the rotor was run up in speed steps of 1000 rpm and the speed maintained until thermal stability in the bearings and shaft had been reached. This processes tended to take approximately 10 minutes between each speed increment, dependant on operating speed. During the commissioning runs the rotors were operated both with and without intentional mechanical unbalance weights introduced. The introduction of the unbalance mass was applied to establish that safe operating conditions were achieved when running in a forced excitation condition.

Throughout the test runs all of the temperature and shaft vibration parameters were recorded and monitored to ensure that the readings were being received correctly and to ensure that the bearing temperatures were satisfactory and generally in line with expectations. The shaft vibration peak-peak levels were monitored to ensure that the dynamic performance was stable and within acceptable operating levels.

6.4.1 Bearings

6.4.1.1 Fixed Geometry Bearings

The first commissioning runs were carried out with the rigid rotor in fixed geometry offset half bearings. The bearing temperatures at both the drive and non drive end bearings were recorded and monitored across the running range of the rig. The maximum temperatures were measured to be well within acceptable operating limits across the entire speed range of the rotor. The maximum temperature measured in the DE and NDE bearings was measured to be 70 and 67 ^{o}C respectively which occurred when running at 12500 rpm. Comparing the predicted and measured peak temperatures shows a good correlation across the entire speed range, with temperatures differences of ~6 ^{o}C when running at 12500 rpm with the measured temperatures being the lower.

The lower temperatures measured on the actual bearing would be expected due to the fact the temperature measurement is taken a some point below the surface, and the magnitude of the difference is acceptable within the boundaries of the analytical prediction techniques available.

6.4.1.2 Tilting Pad Bearings

In the latter part of the test programme tilting pad bearings were fitted onto the main test rotor. The rotor used for operating in these bearings was limited to the flexible rotor only. As for the fixed geometry bearing arrangement a commissioning procedure was undertaken to validate the functionality of the new features introduced to the test set up which was principally limited to the bearings themselves and the RTD sensors fitted to the bearing. The bearing temperatures were again monitored across the running range of the rotor up to a speed of 12500 rpm (a lower maximum speed was limited during commissioning due to precautionary measures due to previous damage to shaft temperature instrumentation). Bearing pad temperatures of 58 ^{o}C at 10000 rpm were observed. This compares to a calculated peak pad temperature of 69 ^{o}C resulting in a –11 ^{o}C difference. This level of discrepancy is slightly higher than expected but could be as a result of the level of oil flow presented to the bearing pads via the radial oil spray orifices. Unfortunately the actual flow into the bearings could not be determined on the rig due to a manufacturing defect resulting in some oil leakage within the

bearing pedestal preventing an accurate reading being obtained. The temperature difference, however, between the leading and trailing edge of the bearing is consistent with that analytically predicted.

6.4.2 Shaft Journal Temperature Sensors

Commissioning checks on the thermistor sensors in the shaft journal were conducted prior to the running tests. As the temperature measurements are a fundamental feature for the experimental work, significant efforts were focused on the verification and validation of the shaft temperature measurements.

As the sensor supply voltage from the bridge circuits were provided by means of a brush type slip ring, continuity checks were performed to verify the electrical resistance to earth and indications of any cross interference between channels. Each slip ring way was checked for resistance to earth with all channels demonstrating resistances greater than 16MΩ and no voltage leaks identified across ways for any of the slip ring channels. The maximum resistance measured across any of thermistor channels when short circuited was 74mΩ compared to a minimum thermistor resistance within the expected operating range of 7.697kΩ at 90 ^{o}C. This equates to a nominal error of +0.0003 ^{o}C at 90 ^{o}C .

Some problems were experienced with earth leakage of thermistor signals within the slip ring later in the testing. This was found to be due to build up of carbon deposits creating a short circuit path. The issue was resolved by stripping and cleaning of the slip ring. For all future tests it was routine to clean the slip ring inner housing following each test run.

Once the continuity checks and measurements had been made the thermistor signals were recorded during the commissioning running tests and the signals assessed for general quality and stability. The rotor was run up in speed increments of 1000 rpm and held at a constant speed for a period of time. During each dwell period the shaft temperatures were allowed to stabilise before accelerating up to the next speed increment, to a maximum speed of 12500 rpm. The absolute temperature levels showed reasonable stability within a short duration (<10s), with absolute temperature measurements fluctuating by no more than 0.05^{o}C pk-pk at 12500 rpm constant running conditions. This suggests some level of electrical and slip ring noise but at a

manageable level. Typical durations to reach stable shaft temperatures were between 5 and 15 minutes dependant on the running speed, with the response of the sensors showing high sensitivity to change in operating conditions with little sign of hysteresis with relation to shaft speed increases and decreases.

To provide increased accuracy of the shaft temperature readings, the input voltage to the bridge circuit from the DC power supply was also logged with the DAQ system. The DC supply system was set to a nominal supply voltage of 10 VDC but, due to instrument stability and ambient temperature variation, the supply voltage could vary by ~80 mV. By recording the output from the power supply this could then be used in the bridge resistance calculations at each discreet data point and any associated error resulting from deviation from the 10 VDC negated.

Repeatability checks were performed and the results showed that the stability and consistency of results was maintained for each test run. A specific measure cannot be meaningfully applied between each test run due to the sensitivity of the shaft temperatures to supply lubricant temperature and specific operating speeds.

6.4.3 Rotor Vibration Response

The rotordynamic response was evaluated by means of a steady run up test and free rundown. The results were verified with the nominal predicted natural frequency and response data generated at the test rotor design stage. For both the rigid and flexible rotor, acceptable vibration responses were obtained across the entire running range of 0 – 14000 rpm with pk-pk vibration maximum of 5 microns and 8 microns for the rigid and flexible rotors respectively. No imbalance loads were introduced onto the shafts for this test verification.

To measure the level of ‘in rig’ electrical mechanical runout ‘glitch’ at each of the observed surfaces, a slow roll check was performed at ~80 rpm (so as limit any effects of dynamic movements within the bearing) during which the ‘phantom’ vibration signature was recorded. Figure 133 shows an example of the shaft ‘glitch’ reading for the rigid rotor NDE bearing observed band. This data was used during the vibration analysis by subtracting it from the operational vibration data. The method used to establish and remove the shaft glitch from the vibration signature is described in more detail in chapter 7.

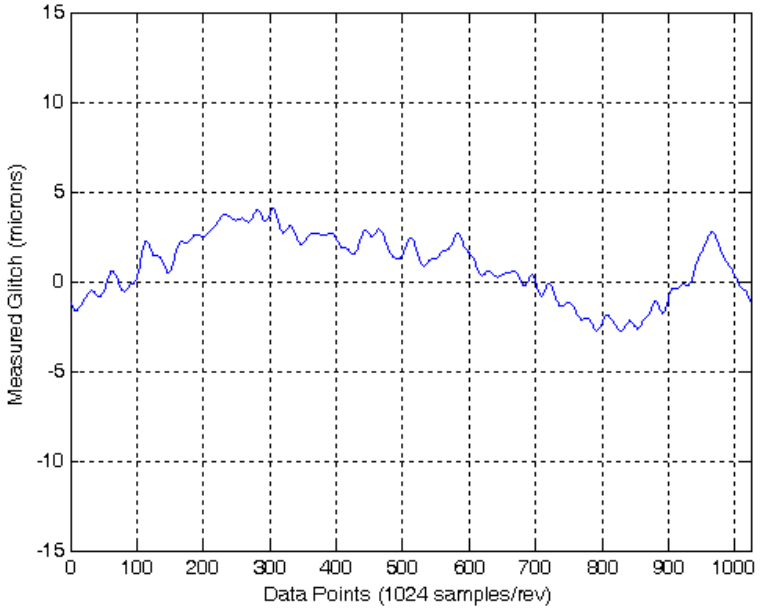

Figure 133 Slow roll glitch for rigid rotor NDE

Figure 134 shows the measured response data for the NDE bearing of the flexible rotor in fixed geometry bearings with no unbalance introduced to the shaft.

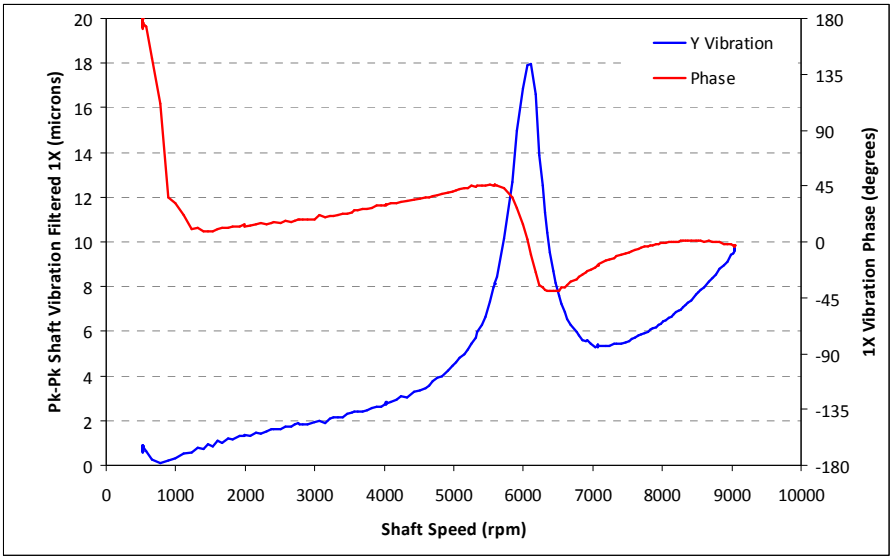

Figure 134 Synchronous (1X) vibration amplitude and phase response (Bode Plot) of rigid rotor in fixed geometry bearings

6.5 Rotor Commissioning Summary

The commissioning activities outlined above provided satisfactory and safe operating conditions across the intended operating range. Some changes in the instrumentation configurations and equipment was required to obtain reliable and acceptable data but the final result of the systems was to give data that satisfied the design specification brief.

Measured performance conditions such as thermal and vibration measurements were in line with those expected from theoretical predictions. The largest discrepancy was observed in the tilting pad bearing temperatures, but a significant element of this could be attributed to the offset introduced by the location of the RTD's in the pads being several mm below the babbit surface and in an area of greater cooling.

In conclusion, the rig was deemed suitable to undertake the experimental programme.

6.6 Test Procedure

A specific series of test programmes was compiled to cover the experimental testing. The test programmes were added to and adapted as the work progressed and as results became available. However the basic programmes remained largely unchanged across the testing duration. The original programme of work was focused around four testing work packages, DR01, DR02, DR03 and DR04. These test programmes were focused around commissioning and testing both the rigid and flexible rotors in fixed geometry offset half bearings. A second batch of work was defined in principle to look at a similar test programme for the rotors running in tilting pad bearings. It was not originally envisaged that the tilting pad bearing work would make up part of this research, but it was decided to include the work to provide a wider range of data within the test programme. The additional test programme was introduced for the running of the flexible rotor in tilting pad bearings and is identified as DR06 work package. As such the number of tests and testing time was increased significantly. Table 22 summarises each work package conducted within the testing programme.

The following tables provide details of the test programmes for DR03, DR04 and DR06.

Testing streams
DR01 Rigid Rotor Commissioning with Fixed Geometry Bearings
DR02 Flexible Rotor Commissioning with Fixed Geometry Bearings
DR03 Rigid Rotor with Fixed Geometry Bearings Test Programme
DR04 Flexible Rotor with Fixed Geometry Bearings Test Programme
DR05 Flexible Rotor Commissioning with Tilting Pad Bearings
DR06 Flexible Rotor with Tilting Pad Bearings Test Programme

Table 22 Specific test activity streams

For each testing programme, a number of specific tests and test conditions were defined. For each test the basic test parameters and speed ranges were specified.

Two separate speed ranges were defined for the test programme as high speed and low speed tests. This was carried out due to the problems experienced with the shaft temperature measurement instrumentation when running at high speed. To reduce the risk of damaging the instrumentation at high speed and prevent significant delay to the testing, the low speed tests were generally performed at the begining of each specific phase, and the high speed tests were performed at the end. A number of tests were added into the programme and several conditions repeated a number of times to validate repeatability of readings.

Table 23 to Table 25 provide a detailed breakdown of the tests conducted under each test phase.

Test No.	Test Description	Inlet Temp	Speed Range	Added Unbalance Amount (g)	Unbalance Angular Location
T3.1	No unbal 40 deg C Inlet (0-8000)	40	Low	0	-
T3.2	No unbal 30 deg C Inlet (0-8000)	30	Low	0	-
T3.3	-0.1g unbal 40 deg C Inlet (0-8000)	40	Low	-0.1	180
T3.6	-1.00g unbal 40 deg C Inlet (0-8000)	40	Low	-1	180
T3.7	-2.50g unbal 40 deg C Inlet (0-8000)	40	Low	-2.5	180
T3.8	-5.00g unbal 40 deg C Inlet (0-8000)	40	Low	-5	180
T3.11	No unbal 40 Deg C Inlet (8000-12500)	40	High	0	-
T3.21	-7.5g unbal 40 deg C Inlet (0-8000)	40	Low	-7.5	180
T3.22	25.5g unbal (no bolt fitted) 40 deg C Inlet (0-4500)	40	Low	-25.5	180
T3.24	-7.5 unbal 40 deg C Inlet (0-8000)	40	Low	-7.5	0

Table 23 Rigid rotor test programme DR03 – fixed geometry bearings

Test No.	Test Description	Inlet Temp	Speed Range	Dummy Weight Fitted	Added Unbalance Amount (g) (Unbalance angle)
T4.1	No unbal 40 deg C Inlet (0-10000)	40	Medium	No	0
T4.6	-1.00g unbal 40 deg C Inlet (0-11000)	40	Medium	No	-1 (180)
T4.7	-2.50g unbal 40 deg C Inlet (0-10000)	40	Medium	No	-2.5 (180)
T4.27	No unbal 40 deg C Inlet Dummy Weight (0-10000)	40	Medium	Yes	0
T4.28	-1.025g unbal @ flg 0g @ ctr 40 deg C Inlet Dummy Weight (0-10000)	40	Medium	Yes	-1.025 (180)
T4.29	-2.021g unbal @ flg 0g @ ctr 40 deg C Inlet Dummy Weight (0-10000)	40	Medium	Yes	-2.021 (180)
T4.51	-1.1g ubal @ ctr 0g unbal @ flg 50 deg C Inlet (0-10000)	40	Medium	No	-1.1 (C0)
T4.53	-2.5g ubal @ ctr 0g unbal @ flg 50 deg C Inlet (0-10000)	40	Medium	No	-2.5 (C0)

Table 24 Flexible rotor test programme DR04 – fixed geometry bearings

Test No.	Test Description	Inlet Temp	Speed Range	Dummy Weight Fitted	Added Unbalance Amount (g) (Unbalance angle)
T6.1	No unbal 40 deg C Inlet (0-10000)	40	Medium	No	0
T6.6	-1.00g unbal 40 deg C Inlet (0-11000)	40	Medium	No	-1.0 (180)
T6.7	-2.50g unbal 40 deg C Inlet (0-11000)	40	Medium	No	-2.5 (180)
T6.51	No unbal 40 deg C Inlet Dummy Weight (0-12500)	40	High	Yes	0
T6.66	-1.1g ubal @ ctr 0g unbal @ flg 50 deg C Inlet (0-11000)	40	Medium	No	-1.1 (C0)
T6.67	-2.5g ubal @ ctr 0g unbal @ flg 50 deg C Inlet (0-11000)	40	Medium	No	-2.5 (C0)
T6.73	-1.025g unbal @ flg 0g @ ctr 40 deg C Inlet Dummy Weight (0-11000)	40	Medium	Yes	-1.025 (180)
T6.74	-1.025g unbal @ flg 0g @ ctr 40 deg C Inlet Dummy Weight (0-11000)	40	Medium	Yes	-1.01 (270)
T6.75	-1.025g unbal @ flg 0g @ ctr 40 deg C Inlet Dummy Weight (0-11000)	40	Medium	Yes	-1.025 (0)
T6.76	-1.025g unbal @ flg 0g @ ctr 40 deg C Inlet Dummy Weight (0-11000)	40	Medium	Yes	-1.01 (90)

Table 25 Flexible rotor test programme DR06 – variable geometry bearings

Chapter 7

Experimental Results

7. Experimental Results

7.1 Introduction

This chapter presents the experimental results obtained and the methods used to extract and post processes the measurements and data captured throughout the experimental testing of the rotor bearing rig. The results data captured can be divided into three principle categories, these being mainly associated to the various types of measurements taken during the testing as outlined in the previous chapters. The test data result groups are (1) shaft vibration and position, (2) journal bearing temperatures and (3) shaft journal temperatures. A more detailed breakdown of the test data for each group is provided in the following sections.

To enable meaningful interpretation of the measured data, an extensive amount of post processing was required for the various data measurements and a detailed overview of the procedures developed and applied is presented within this chapter.

7.2 Data Conditioning and Post Processing

This subsection provides details of the techniques and procedures used to extract results data from the raw data captured during the practical experimental testing. Much of the data captured is in a raw format and it is important that appropriate methods are used to condition the signals into meaningful quantities without introducing significant errors and unwanted numerical filtering.

7.2.1 Shaft Vibration and Position

The data for both the shaft vibration and position was captured by means of the non contacting proximity probes as described in chapters 5 and 6. The sensors were placed at various locations along the shaft length enabling the

dynamic response of the rotor to be captured across the range of operating conditions.
The data from the proximity probes was captured in the three ways using the three different acquisition instruments. The DAQ instruments used captured both low frequency sampling and high frequency acquisition data. Three of the data capture instruments were used to obtain shaft vibration related data and for convenience will be referred to as following for the remainder of this chapter.

System I = Low frequency data logger (Newlyme - NY)
System II = High frequency digital data recorder (Sony - SO)
System III = High frequency signal analyzer (Oros - OROS)

A detailed description of the equipment used and the respective configurations is provided in the preceding chapter 6.

Data captured by system I for the proximity probes was used to provide a peak to peak total vibration level for each sensor position. The data was used as a real time monitor throughout the testing with a data log reading being captured once every 60 seconds. (Real time updates to the digital display were once every second). The data captured with this system was predominantly used for control and monitoring during the test operation. As such the data is not processed further or presented here as the dynamic recorded data is captured by system I and II.

System II was used to capture the raw data from each of the proximity probes at various points throughout the testing sequence. The data captured by this method is for the purpose of post processing following the test itself and has been used to determine high resolution shaft vibration trends, direct measurement of unfiltered shaft orbits and direct measurement of shaft position. The data was captured at ‘high’ frequency to enable a suitable frequency range to be evaluated and sufficient resolution of shaft orbits and vibrations to be achieved. The sampling rates of the channels ranged from 2048 samples/s to 16384 samples/s. Due to the resulting size of the digital files, data was captured for short bursts throughout the testing of the rotor. Approximately ten second bursts were acquired at each running speed condition. Where run-ups/run downs or conditions of transient activity were being assessed then data was captured for the entire duration of the event.

System III was used specifically to captured the filtered once per revolution (1X) shaft vibration amplitude and associated phase. The rate at which the data was sampled was again considered high at 4092 samples/s (19.6 s/rotation a 12500 rpm) to ensure good quality data capture. However the output data was recorded as a simple synchronous filtered total vibration component with the associated phase angle and was logged at 1 sample per second. This information was then later post processed and presented to give the rotor unbalance response characteristics and synthesized once per rev filtered shaft orbits.

7.2.1.1 Shaft Glitch

In rotating machinery diagnostics and measurement, the term ‘shaft Glitch’ or combined electrical mechanical run out is often used to describe the effects of inherent residual errors presented in measurement of shaft vibration by means of non contacting probes and in particular those of the eddy current operating principle (as presented in chapter 6). The term shaft Glitch was widely introduced by proximity probe manufacturer Bentley Nevada and has been given good account in a number of publications, one of which was presented by Biggs [58]. The feature gives specific account for the resulting measurement error introduced on a rotating shaft due to the mechanical effect of relative run out and inconsistent magnetic response around the proximity probe observed surface.

When producing a shaft with eddy current observed surfaces special precautions are made in the preparation of the monitored shaft diameters as outlined in section 5.5. Careful manufacture of the shaft journals and observed diameters is required in combination with a low level demagnetization and burnishing of the on the observed diameter surface. This typically enables combined residual mechanical-electrical run out errors to be limited to ~8 microns. However where accurate measurements are required, such as those within this research, further account has to be taken of these residual errors.

To provide account for the residual error present within the shaft proximity probe measurements a ‘slow roll’ compensation technique was applied. This consisted of running the shaft in its bearings at as slower speed (~30 rpm) as practical and recording the resulting proximity probe data for every location. This data was captured simultaneously with a shaft once per rev key phasor to provide visibility of the relative phase of the captured data to a point on the

test rotor. Once captured and processed this data can be used to subtract from the running vibration data to 'filter' out the unwanted phantom vibration components. Figure 135 gives a simple example of how the principle of the slow roll glitch extraction technique was implemented and later applied.

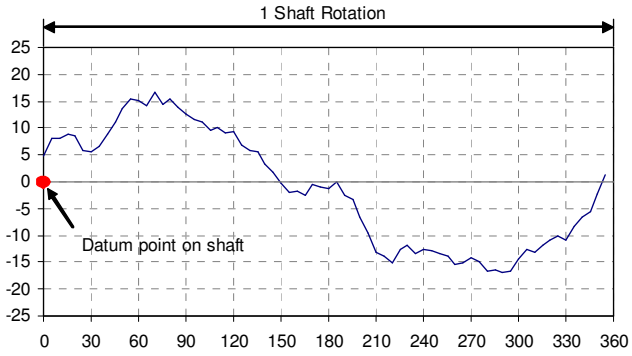

Measured vibration signal of running shaft shaft

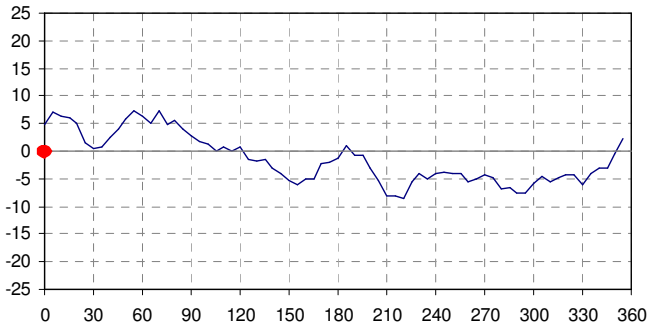

Measured slow roll signal from (Glitch)

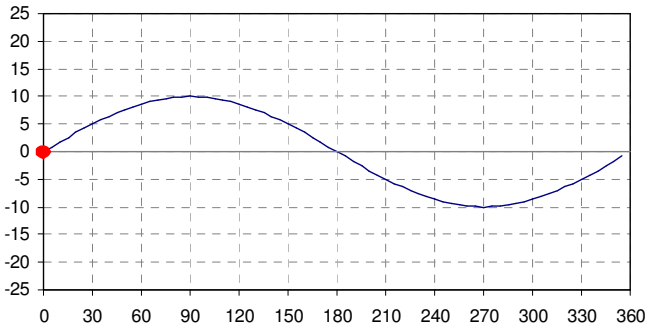

Measured signal subtracting shaft glitch

Figure 135 Shaft 'glitch' extraction principle using slow roll measurement

The slow roll data captured was taken at the beginning and end of every test. This was carried out because, whilst the mechanical component of the shaft glitch remains, constant the magnetic response component (due to the eddy current field interacting with the observed surface microstructure etc.) can vary as a result of proximity probe gap or precise axial position. As most of the proximity probes had to be reset following each test due to disruption to the bearings or unbalance weights, account for this potential source of variation/error had to be accommodated.

Slow roll data was captured and compensated for in two ways. The first method was based around extracting the first order components from the captured data and applying this to the running data in the frequency domain. The second more involved procedure was based around using the captured raw signal data and conditioning this with the running data in the time domain.

The two separate methods were applied to the data captured by System III and System II respectively.

Glitch Data Extraction for system III

The vibration data is processed by the Oros software to extract the 1st order synchronous vibration amplitude and phase lag angle. These 1st order components are obtained for the slow roll 'glitch' $\left(A_g, \phi_g\right)$ and measured vibration $\left(A_m, \phi_m\right)$. Where, using these components, the time domain vibration response can be described by :

$$\begin{aligned} x_m &= A_m.\cos\left(\omega.t + \phi_m\right) \\ x_g &= A_g.\cos\left(\omega.t + \phi_g\right) \end{aligned} \quad \text{Eq 7.2.1}$$

Considering x_m and x_g in complex form :

$$\begin{aligned} x_m &= a_m.\cos\left(\omega.t\right) + b_m.\sin\left(\omega.t\right) \\ x_g &= a_g.\cos\left(\omega.t\right) + b_g.\sin\left(\omega.t\right) \end{aligned} \quad \text{Eq 7.2.2}$$

Following some work it can be shown that :

$$\begin{aligned} a_m &= A_m.\cos\left(\phi_m\right), a_g = A_g.\cos\left(\phi_g\right) \\ b_m &= A_m.\sin\left(\phi_m\right), b_g = A_g.\sin\left(\phi_g\right) \end{aligned} \quad \text{Eq 7.2.3}$$

Having obtained the complex factors for the measured and glitch data the necessary relationships to extract the actual vibration are developed. Again, following some work, the amplitude and phase lag angle of the 'true' or glitch filtered measurement of the shaft vibration can be shown to be given by:

$$A_o = \sqrt{\left(a_m - a_g\right)^2 + \left(b_m - b_g\right)^2} \quad \text{Eq. 7.2.4}$$

$$\phi_o = \tan^{-1}\left(\frac{b_m - b_g}{a_m - a_g}\right) \quad \text{Eq. 7.2.5}$$

Where A_o and ϕ_o are the amplitude and phase lag angle of the conditioned shaft vibration. From these constants the synchronous response data can be determined for the rotor with the 'glitch' effects removed.

Glitch Data Extraction for system II

- Import raw signal data into Matlab as a matrix
- Attribute associated variables
- Identify trigger point (0 deg phase location)
- Write data point increments into trigger matrix
- Modify number of points in real-time to match sample rate of trigger blocks
- Extract blocks for each trigger increment
- Modify number of points in block to a standard number of samples(i.e. 1024)
- Write vector to vibration matrix
- Average vibration matrix over sample length to give single glitch vector

It should be noted that of the two methods described above, the latter is the more informative as this gives a direct representation of the physical measurements around the shaft observed surface and can be used as a true time domain measurement.

The first method provides a quick and direct method extracting 1X shaft vibration and orbit shape around which the current thermal instability theory is principally developed, whereas the second procedure allows for more detailed evaluation of actual shaft orbits to be evaluated and its effects on effective film thickness etc around the bearing journal observed. The first method was applied more generally as this can be more readily applied to the results data in an effective way without requiring a significant amount of numerical processing, whilst still retaining the key dynamic information of the shaft synchronous vibration. Also, due to the analytical evaluation being conducted before the data is logged to disk, it means manageable data files can be obtained. This allows the records to be taken for the entire duration of the test as opposed to the high frequency data captured as in the second procedure which applies only of relatively short bursts as key points of the running. The time domain glitch extraction was only applied where the high frequency raw data was used for further analysis or investigation of the shaft orbits or vibration at specific test conditions.

To perform the numerical processing with the first method, the procedure was applied to the data by means of a spreadsheet type environment due to the relatively simple computational effort. The second time domain procedure was performed by application of a specific code developed in Matlab [49] by the author.

7.2.1.2 Shaft Vibration and Orbits

Shaft vibration data was captured through applying the same principles as outlined in section 7.2.1.1 for the slow roll 'glitch' extraction. Synchronous filtered shaft vibrations were captured using the system II acquisition system and raw time domain data was captured by system III.

The method for data processing was similar to that outlined in section 7.2.1.1 in that the captured data was structured in synchronous blocks which were then combined into a single matrix for each section of data. From each of these blocks the electrical mechanical residual run out error was then subtracted to leave only the contribution of the dynamic vibration to the as measured data. This data was then used to establish the following key parameters:

- Total Level Peak to Peak Shaft Vibration
- Time averaged synchronous vibration sample
- Harmonic content
- Direct unfiltered shaft orbits
- Shaft Running Position
- Filter 1X peak to peak shaft vibration and phase (Bode plots)
- Filtered 1X shaft orbits

Total Level Peak-Peak Vibration

Total level peak to peak vibration was extracted from the captured data by means of a short MatLab routine to interrogate the data and identify the peak-peak level identified form data block sizes of 0.1X filtered. The peak-peak result for each block was averaged on a rolling consecutive 8 block basis to give a stable measurement, removing any random elements in the acquired signal.

Time Averaging

Averaging is often used in the measurement and post processing of vibration data. The use of averaging produces statistically more reliable and repeatable data where significant variation from one data sample and the next is often observed. The most popular method for averaging is carried out in the frequency domain as is commonly applied in dynamic analysers where the Fast Fourier Transform (FFT) is used to extract the harmonic distribution of a given data sequence. The FFT for each data bock is then averaged in the frequency domain to provided more statistically reliable results.

Time averaging was used when running at a constant speed to provide a means of harmonic filtering to the data samples whilst retaining the actual time domain signal for further analysis and post processing. This method of averaging is useful as it retains all amplitude and phase data relating the synchronous only vibration components of the rotor. This avoids converting to the frequency domain which can often result is certain components of the data being truncated or lost such as phase.

The time averaging process was conducted within the MatLab [49] routines used to process the data samples.

It should be noted that handling data in the time domain can be computationally demanding and result in significant processing time. Careful thought is need as how to manipulate the data to make the process practical and efficient. It is especially a problem when using high sampling rates and running at relatively low speeds where synchronous block sizes can become very large resulting in unwieldy vectors and matrix sizes that require numerical truncation for further analysis. For this reason the time domain procedures have not been routinely used on all test result sets and are only applied where specific areas of interest are identified.

Harmonic Analysis

To provide a simple breakdown of the frequency components contained in the data samples, a harmonic analysis was performed on the conditioned blocks of synchronous data. The harmonic analysis was applied to the data blocks following the subtraction of the residual mechanical-electrical run out. Harmonic extraction was applied to 0.1X filtered data blocks. This was

conducted so that both sub-synchronous and super synchronous components were identified.

The harmonic components were extracted by application of a discrete Fourier analysis to the data block samples. Averaging was performed in the frequency domain to the block wise harmonic signatures. To show the level of variation seen across a given data set the amplitude of preceding harmonic components was tracked for the entire data sample. Suitable processing was used to give block sizes on 2^n that enable the Fast Fourier Transform (FFT) algorithm to be applied for ease of post processing on some data sets.

The aforementioned MatLab routine was developed to perform the computational procedure to apply the discrete Fourier transform to the data samples.

Unfiltered Shaft Orbits

The unfiltered shaft obits were extracted by taking 1X post processed data blocks of 1024 data points for a given test condition for a specific probe. 16 consecutive blocks were averaged to give a more statistically reliable result (effectively a short duration time average). The resulting single (time averaged) block for each probe the X and Y probe for a given location can then be plotted against each other in a Cartesian coordinate system to give the shaft orbit. As at each location the orientation of the probes was not the same, the coordinates then had to be rotated by the appropriate clocking angle to present them relative to a common datum. The coordinate translations were performed by application of a rotation matrix of the form :

$$\begin{bmatrix} \cos(\theta_p) & -\sin(\theta_p) \\ \sin(\theta_p) & \cos(\theta_p) \end{bmatrix} \cdot \begin{bmatrix} X \\ Y \end{bmatrix} = \begin{bmatrix} X_p \\ Y_p \end{bmatrix}$$

$$\begin{bmatrix} X_p \\ Y_p \end{bmatrix} = \begin{bmatrix} x_1 & x_2 & .... & x_{n-1} & x_n \\ y_1 & y_2 & .... & y_{n-1} & y_n \end{bmatrix}$$

Where $\begin{bmatrix} X \\ Y \end{bmatrix}$ is the cartesian coordinate orbit matrix were x_i and y_i are the specific coordinates of a given data point *i* for the X and Y probe respectively and θ_p is the clocking angle of rotation required for the specific pair of probes being considered.

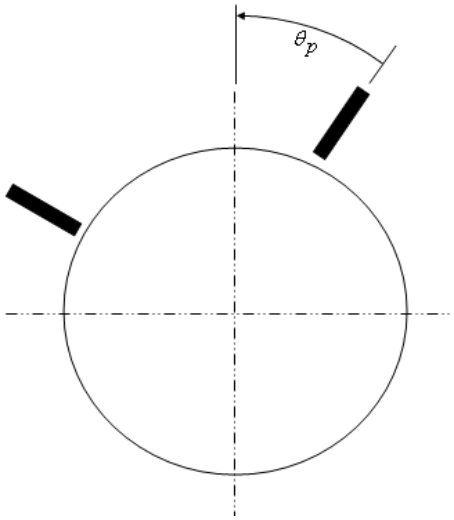

Figure 136 Coordinate system for clocking angle of radial proximity probes

Running Shaft Position

The process used to determine the shaft running position was to take the DC component of the proximity probe signals. The DC component is the mean value taken over a specified period of time (the length of time would be related to the shaft speed to ensure integrity of the reading is not removed by over or under averaging) of the vibrating signature from the proximity probe when the effect of the steady state gap is not removed prior to processing.

The acquired DC proximity probe data was block-wise averaged in the time domain in a similar manner to that carried out for the time averaged vibration data. The specific relationship to the shaft phase trigger is less critical here though as the dynamic vibration element of the signal is not of interest. For each mean block-wise value this was written to a new vector which can then be used as record of the steady state probe gap reading for a given operating point or condition.

To obtain the gap, the understanding of some of the physical bearing dimensions and the static starting position must be known. The bearing dimensional data was obtained earlier by means of component measurements and then also by a direct lift check measurement in the test rig. The static shaft position measurement is needed to know what the static DC gap readings are from the proximity probes observing the rotor. This data was obtained by means of taking a static shaft position reading at the start of every

test at ambient conditions prior to any oil being circulated around the rotor or bearings (i.e. rotor temperature would nominally be at ambient conditions). This static measurement can then be subtracted from the dynamic gap measurement to give the change in gap and hence shaft positional change relative to the bearing pedestal.

Another feature, which must also be considered as it can result in errors in measurement if overlooked, is the effect of relative thermal expansion between the observed surface and point of measuring instrument. In this case the rotor journal thermal growth relative to the thermal growth of the probe mounting point. This was addressed by means of the 'push-pull' probe arrangement as shown in figure 103 chapter 5. This arrangement allows for compensation to be taken for the reduction or increases of effective internal bearing clearance as the simple addition in readings of diametrically opposed probes. The residual of this summation should be 0 for no relative change due to thermal growth and any positive value corresponding to an effective reduction in bearing internal clearance and vice versa for a negative residual. The shaft running position relative to the bearing centre point, datum O, for a specific probe plane can then be obtained by :

$$X_{Pos}, Y_{Pos} = \frac{-C_d.\left(\Delta X_{Gap} + \Delta Y_{Gap}\right)}{4} + X_T, Y_T \quad \text{(Eq. 7.2.6)}$$

Where $X_T = X_{Dyn} - X_{Static}$, $Y_T = Y_{Dyn} - Y_{Static}$ and ΔX_{Gap}, ΔY_{Gap} are the residual of the push-pull probe measurements.

Once the X_{Pos}, Y_{Pos} vectors have been extracted for the required speed conditions then, as with the orbit special vectors, the data points were translated into the correct orientation by means of the rotation matrix.

Some care needs to be taken when no circular geometry profiles or variable geometry profiles are being used in the bearings. In the case of the fixed geometry bearings used here, no special consideration was required as, although modified geometry is present, the bearing is split horizontally in the pedestal. This means the diametrical clearance C_d used in equation 7.2.6 is the same as the measured crown clearance for the bearing. In the case of variable geometry bearings then a factor is applied which accounts for the effect of the increased drop of the shaft in the bearings due to the load between pad condition. This relationship for a five pad bearing is the total lift

value multiplied by $f_{lift} = 0.894$. Where when considered for the running position measurements the expected radial lift to the bearing centre would become $fr_{lift} = \frac{1}{2.f_{lift} - 1}$.

Filtered Shaft Vibration

Filtered shaft vibration was obtained using the analysis routines provided in the OROS frequency analyzer software. The procedure takes the high frequency data from the proximity probes and performs a FFT on this signal. Using a low number of frequency domain averages it extracts the amplitude and phase for the frequency that corresponds to the shaft order of interest. The shaft specific order is limited by the sampling frequency, number of spectral lines and shaft running speed range. For the analysis performed here the fundamental shaft order 1 was specified for extraction. The amplitude and phase values are then logged at a much slower sampling rate to give a typical Bode plot of peak vibration amplitude and phase with reference to either time or shaft speed.

Filtered Shaft Orbits

The filtered shaft orbits were produced by using the data obtained from for the filtered shaft vibration described above. From the amplitude and phase data for a pair of corresponding probes, it is possible to synthesize the orbit in Cartesian coordinates in the same manner as done for the unfiltered orbits, but in this case only the 1X orbit component is retained. The resulting orbit ellipse is rotated by the appropriate clocking angle by application of the following trigonomic relationship:

$$\begin{aligned} x_p(\omega.t) &= x(\omega.t).\cos(\theta_p) - y(\omega.t).\sin(\theta_p) \\ y_p(\omega.t) &= x(\omega.t).\sin(\theta_p) + y(\omega.t).\cos(\theta_p) \end{aligned} \quad \text{(Eq. 7.2.7)}$$

Where $x(\omega.t) = A_x.\cos(\omega.t + \phi_x)$ and $y(\omega.t) = A_y.\cos(\omega.t + \phi_y)$

7.2.2 Bearing Temperatures and Lube Oil/Air Temperatures

The bearing temperatures and lube oil/air temperatures were measured using PT100 RTD's and K type thermocouples respectively. In the case of both types of sensor the signal conditioning and calibration aspects were managed within the DAQ systems. The only requirement was to determine each specific sensor sensitively (established as outline in chapter 6) and provide this to the appropriate DAQ post processing software. The measured temperature is then provided directly in the logged data files from the respective instrument.

7.2.3 Shaft Temperatures

The shaft journal temperature measurements were acquired as voltages by the Anvil DAQ system and logged at a sample rate of 1 samples/s. These voltages were then translated into temperature measurements by application the Steinhart-Hart constants applying the methods presented in chapter 6 which are not repeated here. The non linear voltage responses acquired from the thermistors bridge circuits were processing into actual temperature values for further processing and diagnosis by means of spreadsheet program created in Excel. This program used the individual constants, calibration settings and associated data to determine the temperature readings with reference to speed and/or time.

Having now obtained temperature data for the journal for all four shaft sensors, it is necessary to further process these measurements to give a more meaningful account of the temperature conditions present within and around the rotor journal. The temperature measurements for each of these sensors is ordered to reflect the sequence as they appear around the rotor journal with respect to the shaft key phasor in the direction of rotation of the test. Further processing and interrogation is then performed to extract the temperature differential data relevant to the thermal bowing conditions and how they associate/correlate to the vibration data.

Whilst the peak-peak temperature differential is of interest, the principle features of interest for the journal temperatures are the form of the temperature distribution and more so the magnitude and location of the fundamental harmonic temperature distribution i.e. amplitude and phase of the 1^{st} harmonic temperature differential. Of additional interest is the bulk

operating temperature of the journal and also the level of non fundamental harmonic components in the thermal distribution.

To extract the fundamental harmonic component from the measured data points, a Discrete Fourier Transform (DFT) analysis was applied each data record. The temperature distribution can be expressed by the following Fourier description for a discreet set of data consisting of N data points. The greater the number of data points the higher the number of frequency orders that are incorporated. This gives a result which better matches the true result for the complete periodic data set. Equation 7.2.8 gives the temperature distribution $T(\theta)$ in terms of the Fourier coefficients and angle theta around the shaft journal.

$$T(\theta)_0^{2.\pi} = \frac{t_o}{2} + \sum_{k=1}^{N/2} a_k.\cos(k.\theta) + b_k.\sin(k.\theta) \quad \text{(Eq. 7.2.8)}$$

The Fourier coefficients for the order of interest can be determined by:

$$t_o = \frac{\sum_{n=1}^{N} t_n}{N} \quad \text{(Eq. 7.2.9)}$$

$$a_k = \frac{2}{N}.\sum_{n=1}^{N} t_n.\cos\left(\frac{k.2.\pi.(n-1)}{N}\right) \qquad b_k = \frac{2}{N}.\sum_{n=1}^{N} t_n.\sin\left(\frac{k.2.\pi.(n-1)}{N}\right)$$

The amplitude and phase data of the relevant order can now by determined as follows:

$$T_k = \sqrt{a_k^2 + b_k^2} \qquad \phi_{T_k} = \tan^{-1}\left(\frac{b_k}{a_k}\right) \quad \text{(Eq. 7.2.10)}$$

For the measured temperatures of the shaft journal, 4 sensors were used making N=4. The temperature distribution that will result in a thermal bend it is the first order content that is of interest where $k = 1$. This process allows for the peak to peak amplitude $(2.T_1)$ and phase angle (ϕ_{T1}) to be established from the measured temperatures. It should be noted that, whilst it is numerically valid to be able to extract the second order harmonic content of the temperature distribution (i.e. the limit N/2, where N=4), there are only 2 points to describe a single cycle of the second order content significant amplitude and phase errors. For orders higher than the fundamental, a

number of data points must equate to ≥ 2.56 per cycle to be statistically valid for amplitude data (as is stated by Shannon and Nyquist [59]). In the case of the data obtained here the signature content that is non harmonic can be presented by taking the 1st harmonic component for a given angular location from the measured value at this point. The residual of this measurement t_K can be considered as the non fundamental harmonic content and is presented in the results data.

$$t_{K(n)}(\theta) = t_n - T_1.\cos(\theta + \phi_{T1}) \quad \text{(Eq. 7.2.11)}$$

The processing of the data in accordance with the method outlined above was conducted within the spreadsheet program mentioned earlier. The above procedure can be applied to the entire data captured during the testing providing a thermal Bode plot with reference to time and/or shaft speed, which also includes some information of the non harmonic content.

7.3 Test Results

This section presents the results data acquired from the experimental testing of the three test programmes undertaken. Not all results are presented here due to the large volume of information, but a number of significant test conditions show the key aspects observed from the testing. This allows qualitative and quantitative analysis to be made from the conditions observed during running.

The results section is broken down into two principle sections of vibration related data and thermal data. The vibration data looks at the measured shaft dynamic and spatial features, whereas the thermal data is based around the temperature conditions in the bearings - more specifically the shaft journal.

General data logs were taken during every test which captures all conditions such as oil drain temperatures, oil supply temperatures, oil supply pressures, motor power and ambient temperature etc. These are not presented in detail here due to the repetitive nature and the data being of passive interest only. Some aspects of the general test data are used in the following chapter when analysing the results of interest with respect to the operating conditions.

7.3.1 Shaft Vibrations

This section presents the rotor shaft vibration and spatial test results for the test programmes DR03, DR04 and DR06.

A large amount of data was gather and processed for the shaft rotordynamics during the testing. Only a summary of the key features is presented here to enable the principle performance features to be understood. Results data for filtered and unfiltered shaft vibration, whirl orbits and running shaft position was evaluated for each of test conditions.

7.3.1.1 Rigid Rotor Test Programme DR03

This sub section covers some of the vibration results for the rigid rotor test DR03 programme running fixed geometry bearings. The two test conditions for which some vibration results are presented here are:

DR0301 No unbalance, oil inlet temp 40°C
DR0321 -7.5g (-300 g.mm) unbalance position 1, oil inlet temp 40°C

The filtered 1X vibration for the base line condition of test DR0301 for no unbalance at the NDE bearing is given in Figure 137.

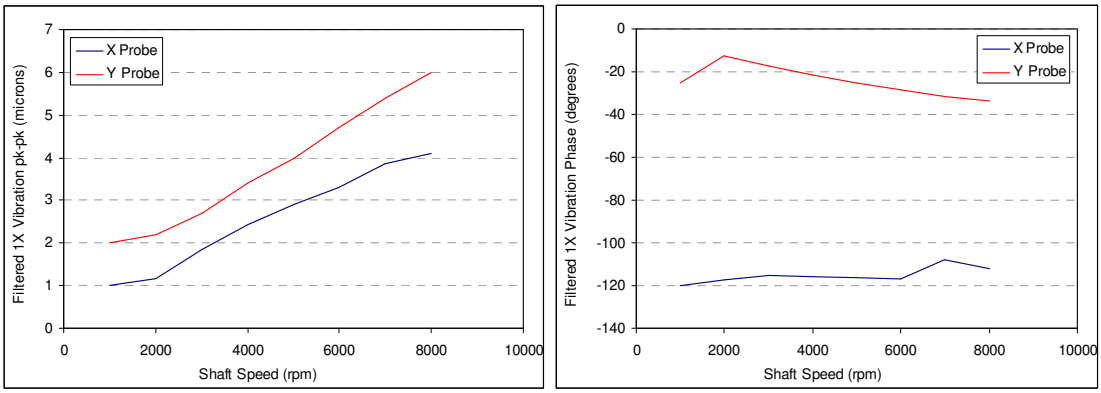

Figure 137 NDE Bearing filtered shaft vibration DR0301

The total level pk-pk vibration (glitch removed) and filtered 1X response results the NDE bearing for test DR0321 is presented in Figure 138.

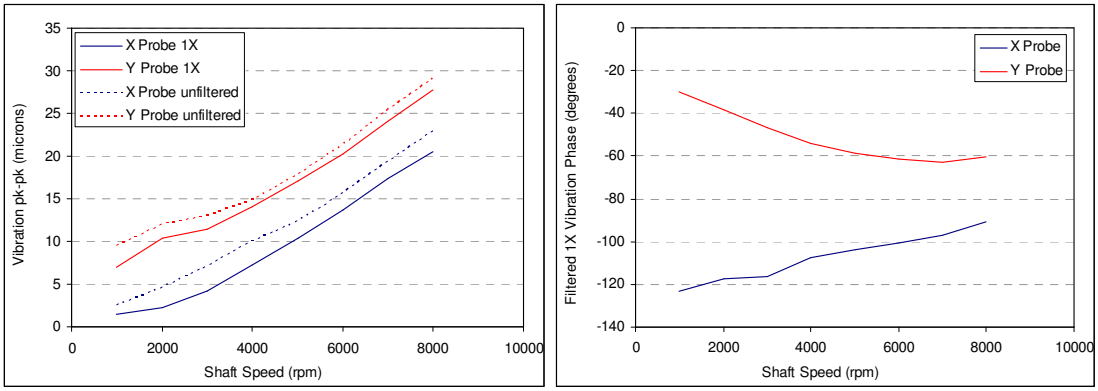

Figure 138 NDE Bearing filtered and unfiltered shaft vibration DR0321

The 1X filtered orbit at the NDE bearing is given in Figure 139 for the DR0321 test condition running at 8000 rpm.

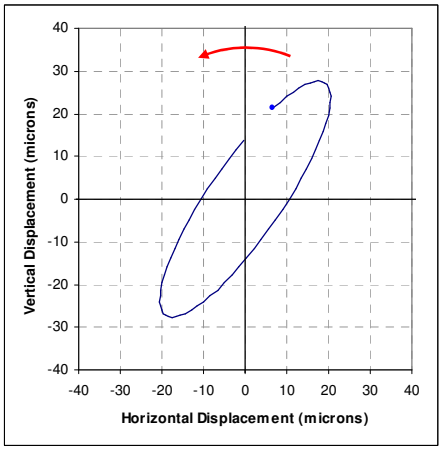

Figure 139 NDE 1X filtered orbit 8000 rpm DR0321

The shaft running positions were seen not to varying significantly between different test conditions performed within the conditions (principally the introduction of unbalance) covered within this work. It is noted that shaft position is clearly influenced by running speed, as would be expected.

A harmonic frequency analysis of the NDE bearing time domain signal is shown in Figure 140 for DR0301 and DR0321 respectively.

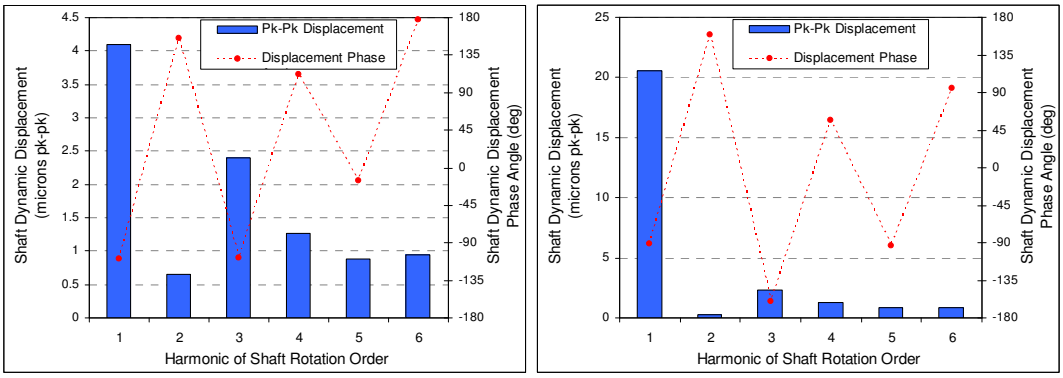

DR0301 DR0321

Figure 140 Harmonic Analysis of NDE Vibration for DR0301 and DR0321 at 8000 rpm

A summary of the key vibration characteristics for the rigid rotor is given in Table 26.

Test Ref	Added Unbalance Mass (g)	Shaft Speed (rpm)	X Probe 1X pk-pk (microns)	X Probe 1X Phase (degrees)	Y Probe 1X pk-pk (microns)	Y Probe 1X Phase (microns)	X Probe Raw pk-pk (microns)	Y Probe Raw pk-pk (microns)
DR0301	0	8000	4.1	-112.32	8.02	-18.82	7.12	10.48
DR0303	0.1	8000	3.1	-131.16	8.51	-14.95	7.02	11.07
DR0306	1	8000	4.57	-115.92	10.12	-42.25	7.47	12.21
DR0307	2.5	8000	8.32	-110.69	14.02	-53.7	10.29	15.3
DR0308	5	8000	14.62	-94.81	20.94	-59.9	16.91	22.19
DR0321	7.5	8000	20.52	-90.9	27.71	-60.42	22.91	29.08

Table 26 Results summary of vibration data for DR03 test programme

7.3.1.2 Flexible Rotor Test Programme DR04

This sub section covers some of the vibration results for the flexible rotor test programme running in fixed geometry bearing, DR04. Four test conditions for which vibration results are presented here are :

DR0401 No added unbalance mass, oil inlet temp 40°C

DR0407 -2.5g (-100 g.mm) added unbalance position x, no added mass oil inlet temp 40°C

DR0428 -1.02g (-41 g.mm) added unbalance position x, 3.5kg added mass, oil inlet temp 40°C

DR0353 -2.5g (-150 g.mm) added unbalance position x shaft centre, oil inlet temp 40°C

Figure 141 to Figure 144 give results data for the flexible rotor without any added overhung mass applied at the NDE flange.

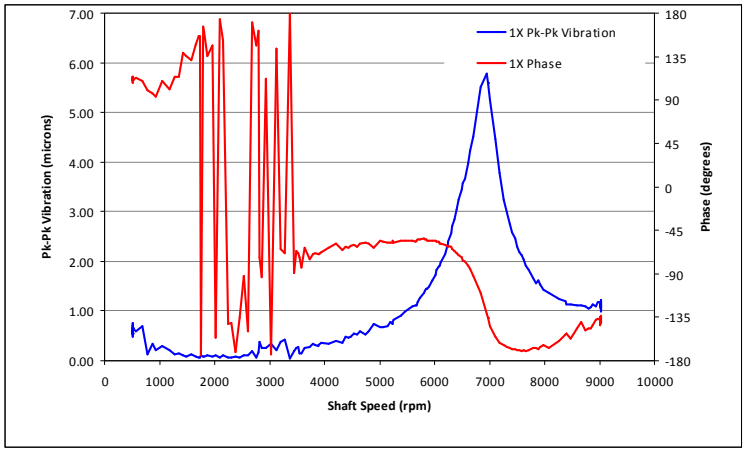

X Probe

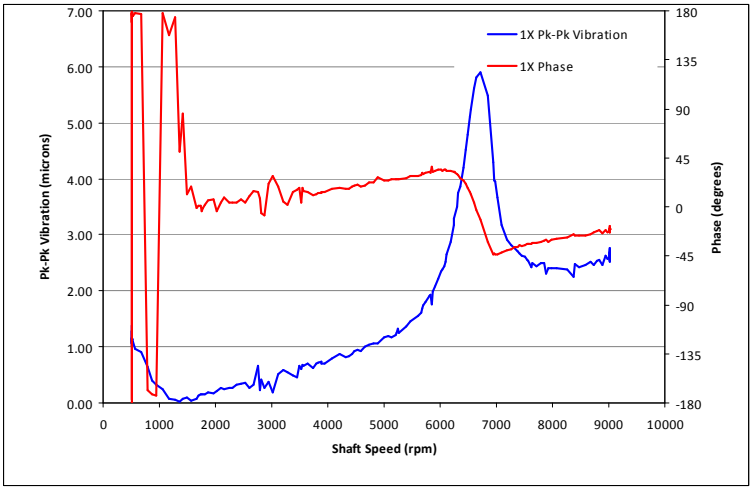

Y Probe

Figure 141 NDE Bearing filtered shaft vibration DR0401 – Run-up Test

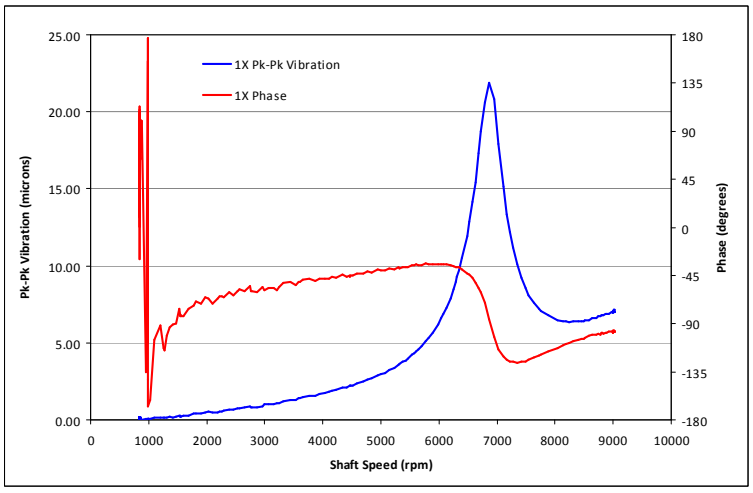

X Probe

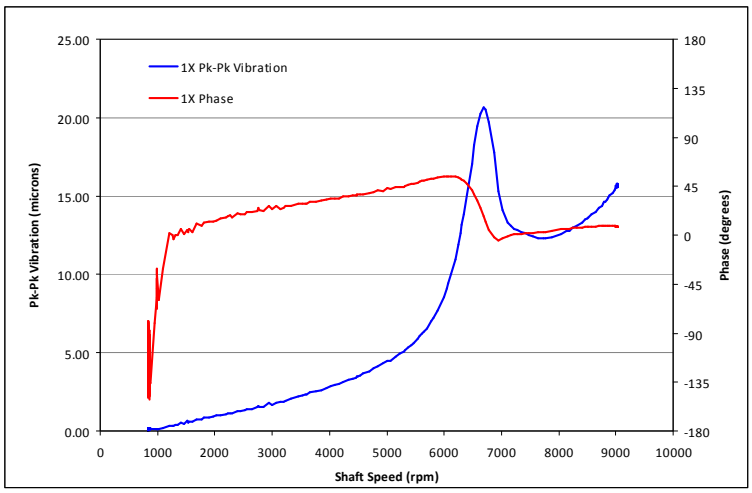

Y Probe

Figure 142 NDE Bearing Filtered Vibration DR0407 – Run-up Test

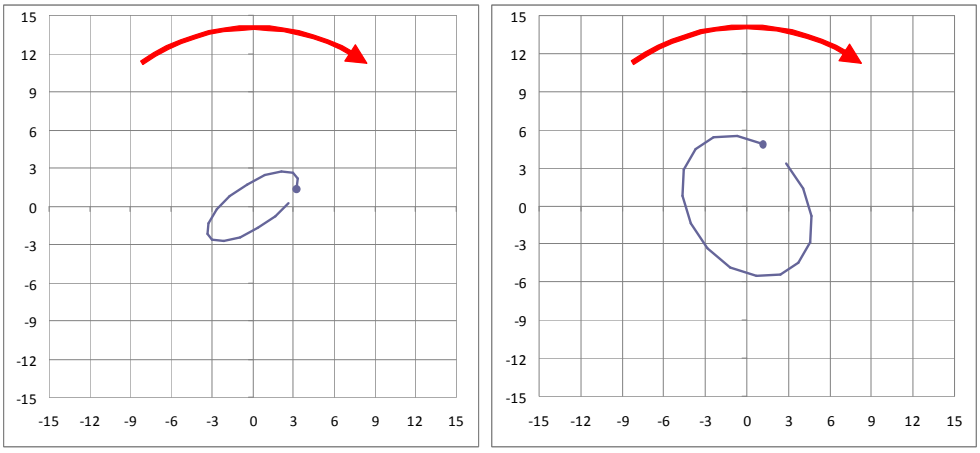

DE Bearing NDE Bearing

Figure 143 Synchronous (1X) flexible rotor shaft orbits at 6250 rpm - DR0407

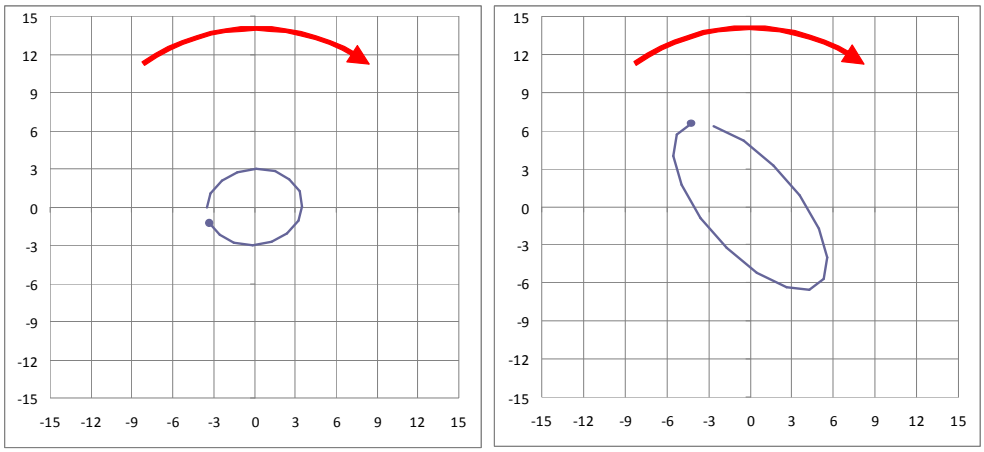

Figure 144 Synchronous (1X) flexible rotor shaft orbits at 9000 rpm - DR0407

The following Figure 145 and Figure 146 are the same vibration characteristics but now for the rotor with the 3.5 kg added mass applied to the NDE flange end for test condition DR0428.

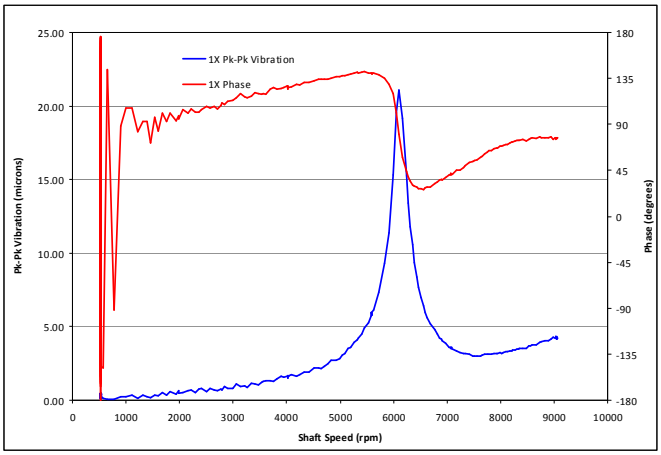

X Probe

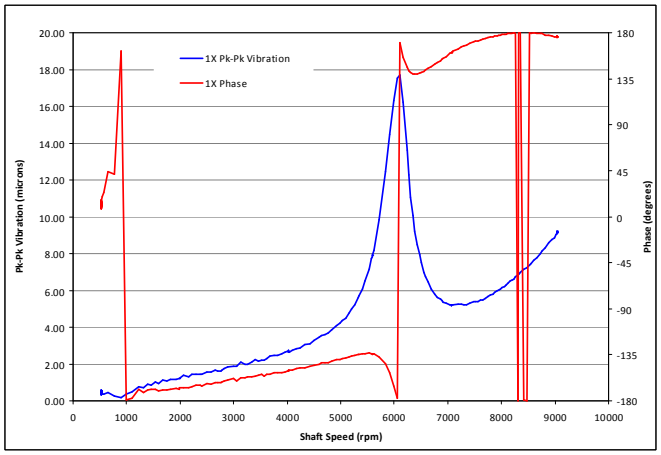

Y Probe

Figure 145 NDE Bearing Filtered Vibration DR0428 – Run-up Test

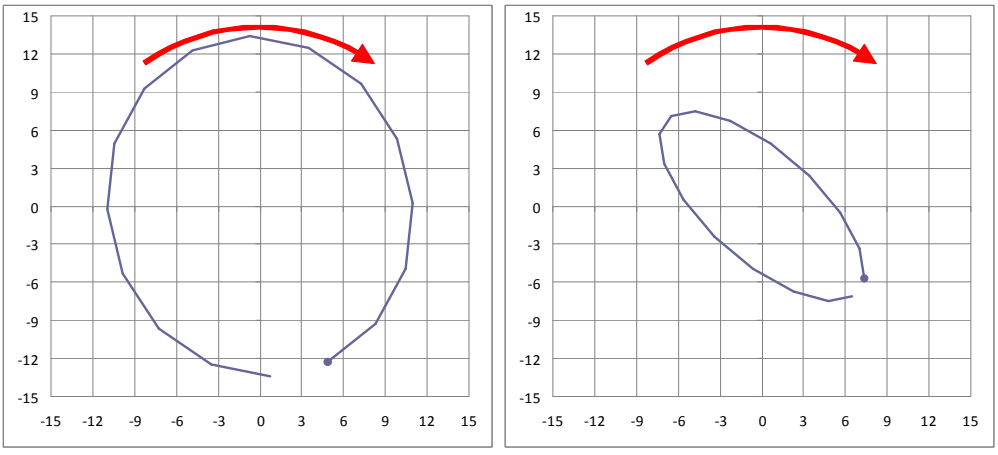

6250 rpm 9000 rpm

Figure 146 NDE Synchronous (1X) flexible rotor shaft orbits - DR0428

The final set of figures for the DR04 test programme vibration results are for the test condition DR0453 where no unbalance is introduced at the NDE flange but 150 g.mm is applied to the shaft rotor centre. Figure 147 and Figure 148 give the filtered shaft vibration response at the NDE bearing and shaft orbits respectively.

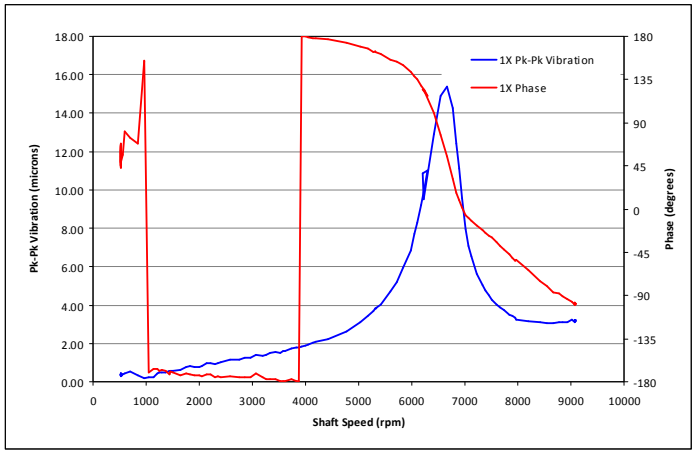

X Probe

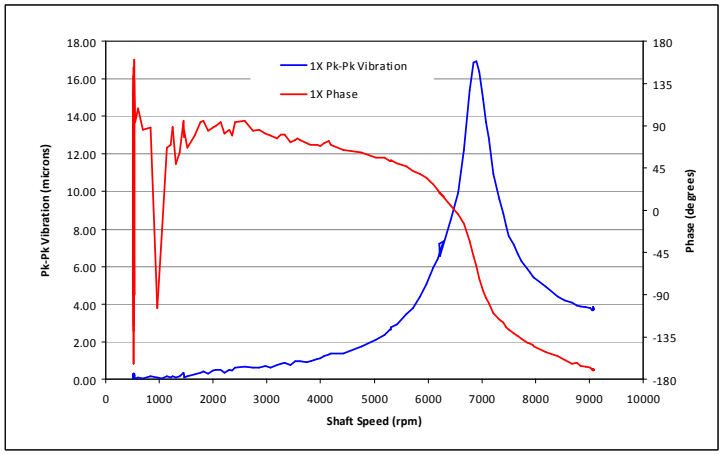

Y Probe

Figure 147 NDE Bearing Filtered Vibration DR0453 – Run-up Test

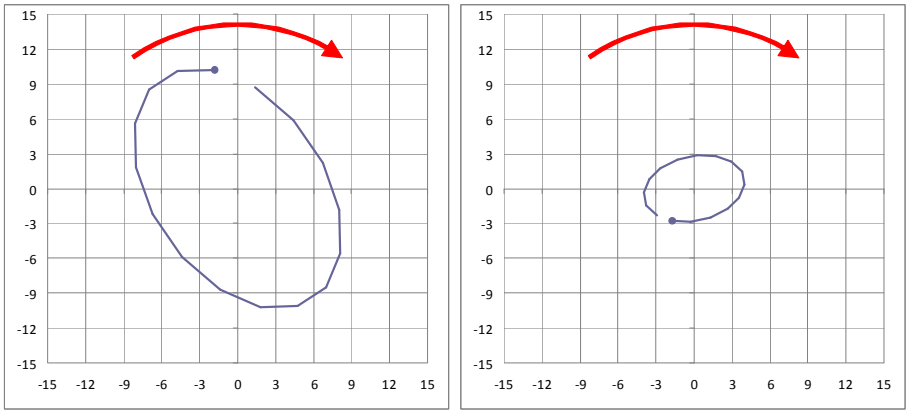

6250 rpm 9000 rpm

Figure 148 NDE Synchronous (1X) flexible rotor shaft orbits - DR0453

7.3.1.3 Flexible Rotor Test Programme DR06

This sub section covers some of the vibration results for the flexible rotor test programme running in variable geometry bearings, DR06. Two test conditions for which vibration results are presented here are :

DR0651 -No added unbalance, no added mass, oil inlet temp 40°C

DR0473 -1.02 (-41 g.mm) unbalance position x, 3.5kg added mass, oil inlet temp 40°C

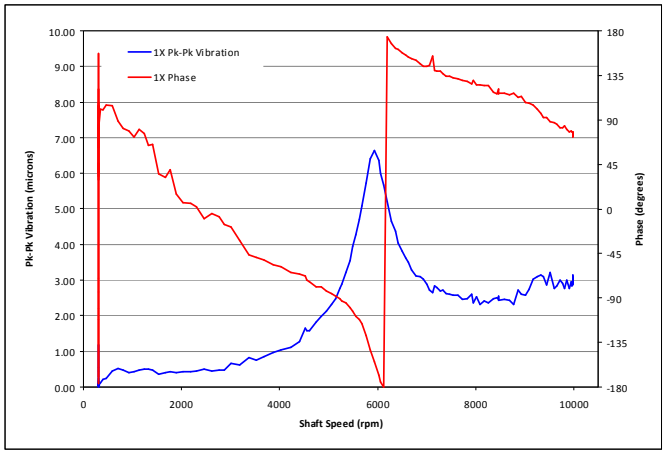

X Probe

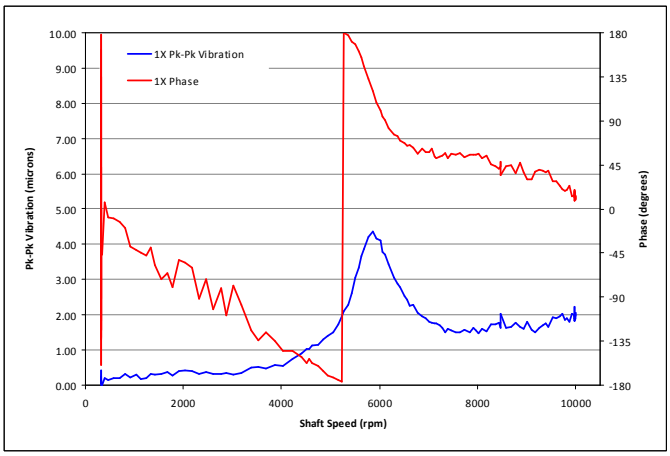

Y Probe

Figure 149 NDE Bearing Filtered Vibration DR0651 – Run-up Test

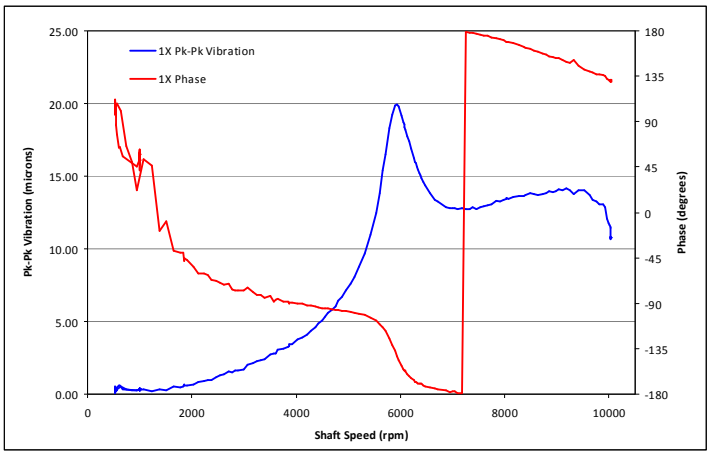

X Probe

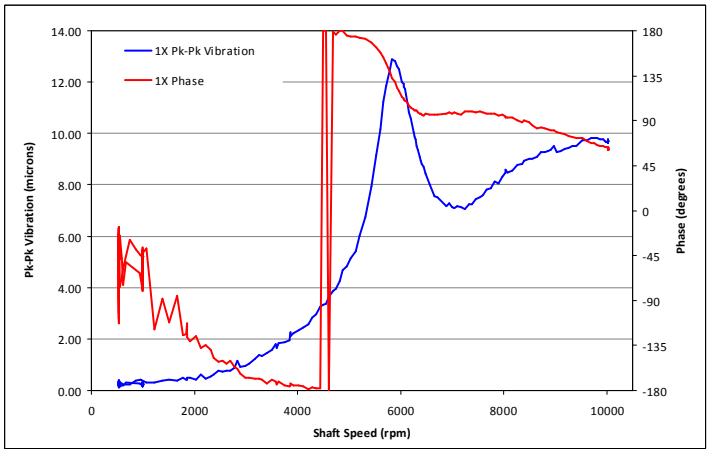

Y Probe

Figure 150 NDE Bearing Filtered Vibration DR0673 – Run-up Test

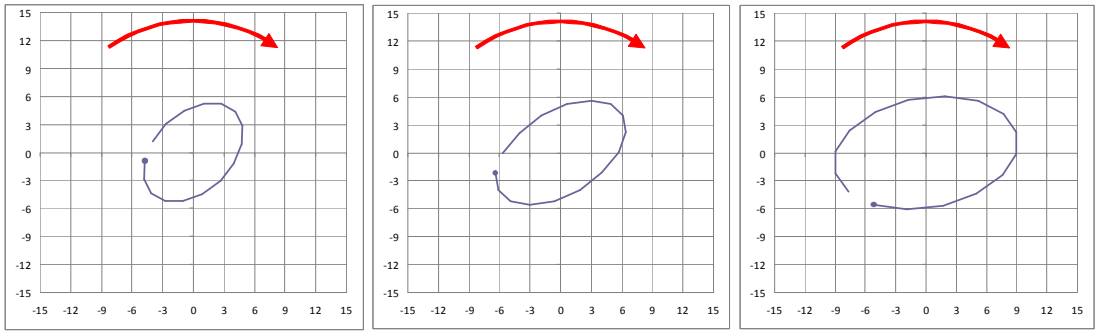

6000 rpm 9500 rpm 10000 rpm

Figure 151 NDE Synchronous (1X) flexible rotor shaft orbits - DR0673

7.3.2 Shaft Temperatures

This section presents temperature data for the test bearing and shaft journal for a number of the test conditions covered by programmes DR03, DR04 and DR06.

Results data for the test bearing temperatures is presented for all the NDE measurement locations and referred to test time and operating speed. Also, for several locations, the circumferential temperature distribution is presented.

Shaft journal temperature differential temperature is presented over the test duration providing 1st harmonic pk-pk temperature differential and associated phase. On the same presentation the as-measured pk-pk temperature differential is also shown. For each steady running condition the journal circumferential temperature distribution is displayed giving the as measured, 1st harmonic and non harmonic residual. Error bars are included on the as measured data points to provide an indication of the expected accuracy range of the sensor based on the individual sensor calibrations.

The results information presented in this section is a summarised selection of the test data for ease of presentation.

7.3.2.1 Rigid Rotor Fixed Geometry Bearings (DR03 Tests)

DR0301 – No added unbalance 0-12500 rpm

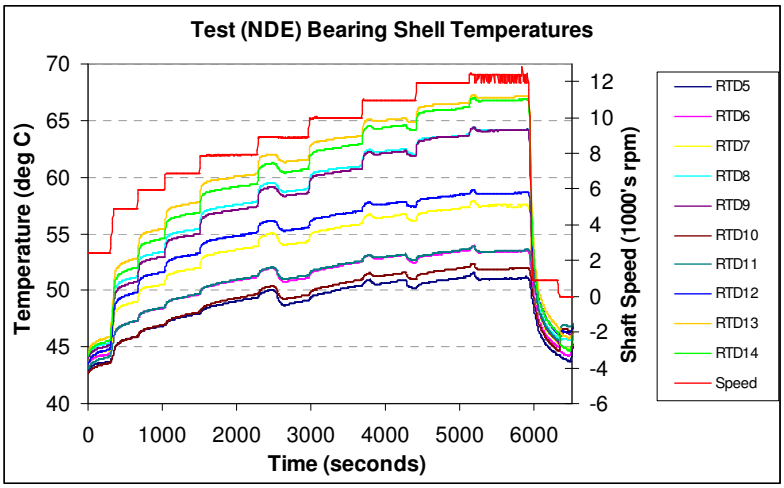

Figure 152 NDE Test Bearing Temperature Measurements Throughout Test DR0301

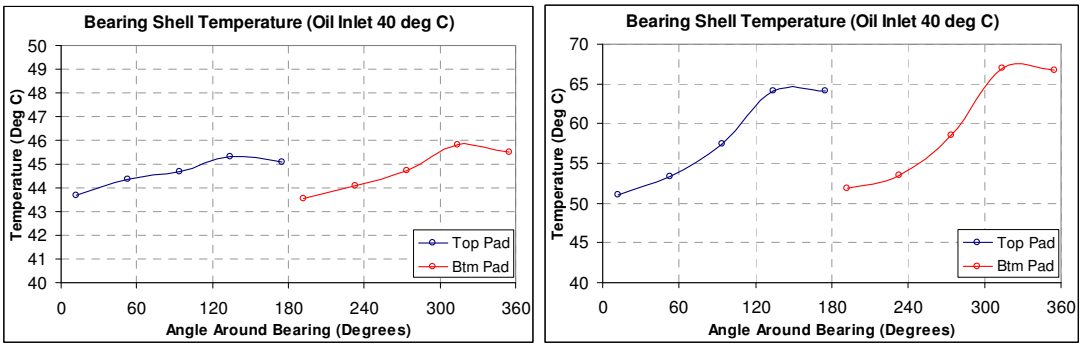

(a) 2500 rpm (b) 12500 rpm

Figure 153 NDE circumferential bearing shell temperature measurements DR0301

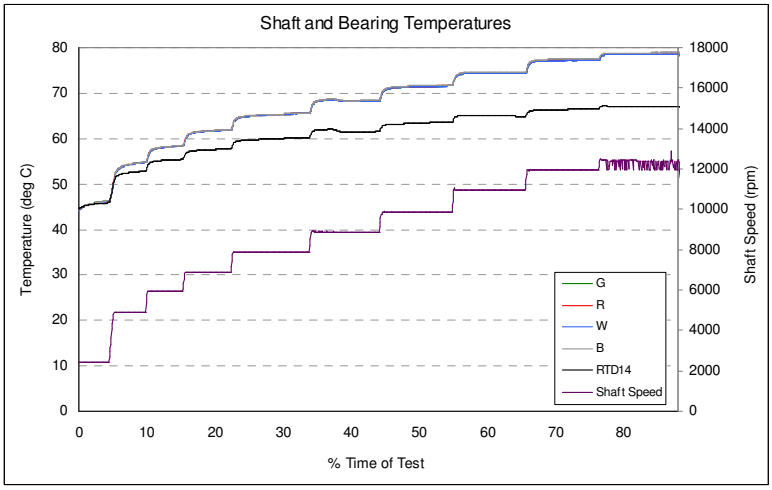

Figure 154 Shaft Journal and NDE Bearing (RDT14) Temperatures for DR0301

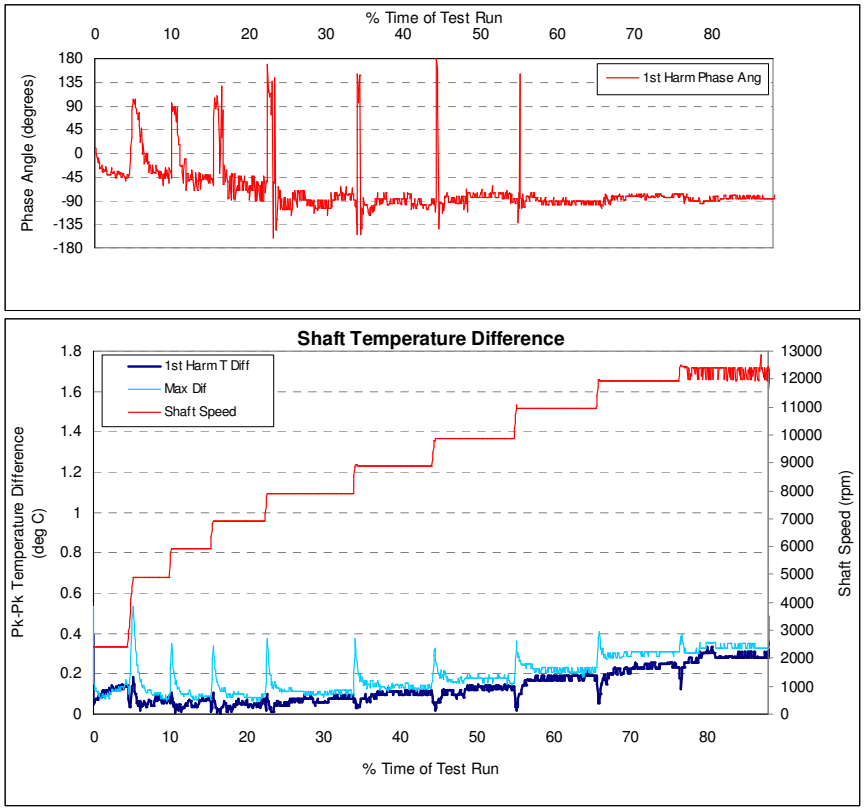

Figure 155 Shaft journal temperature differential measurements for DR0301

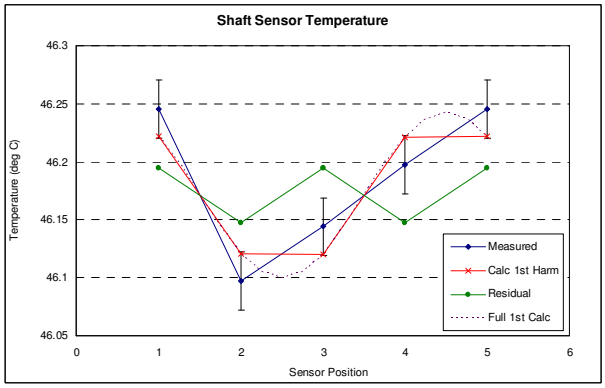

2500 rpm

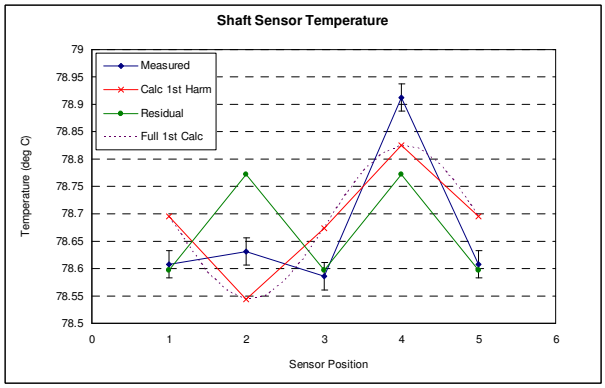

12500 rpm

Figure 156 Journal Circumferential Temperatures for DR0301

DR0321 – 7.5 g unbalance 0-8000 rpm (position 4)

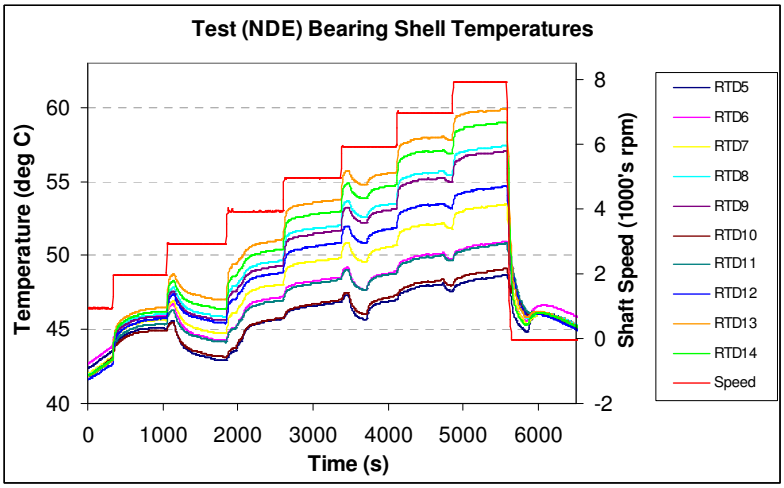

Figure 157 NDE Test Bearing Temperature Measurements Throughout Test DR0321

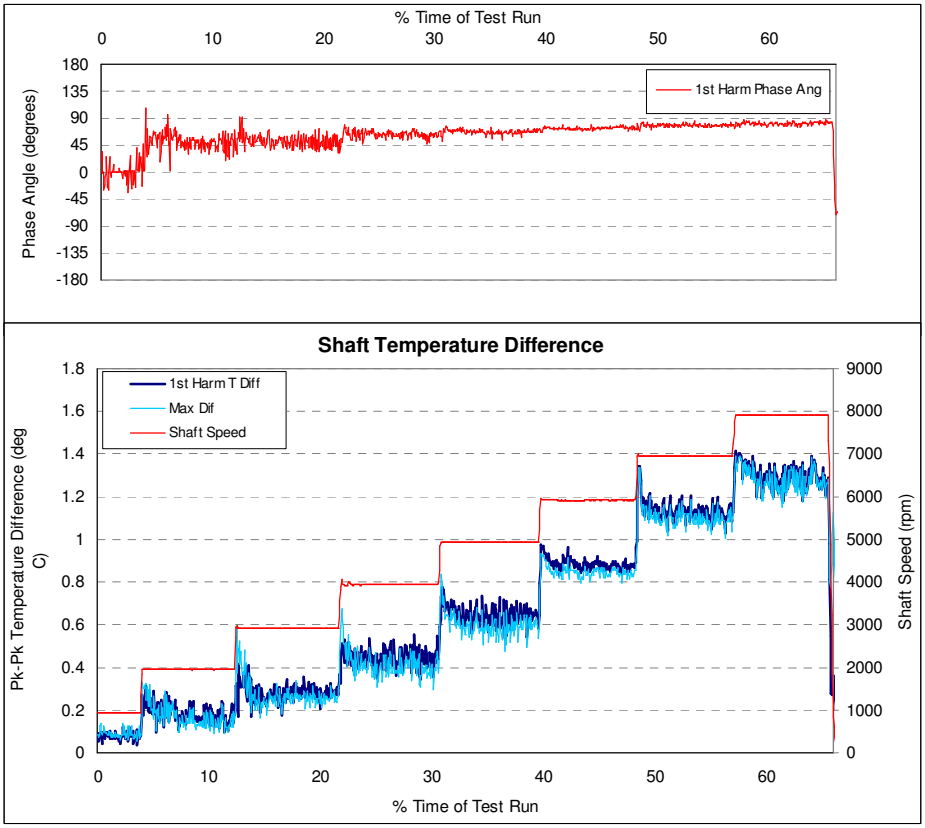

Figure 158 Shaft journal temperature differential measurements for DR0321

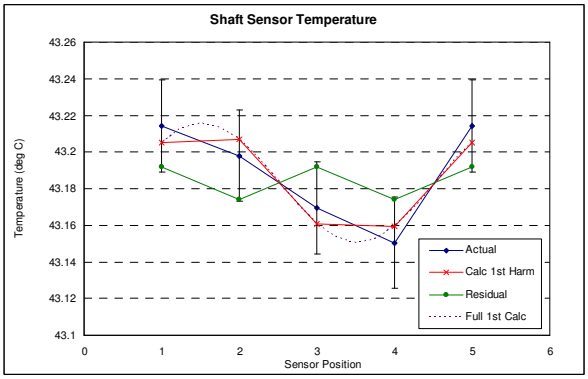

1000 rpm

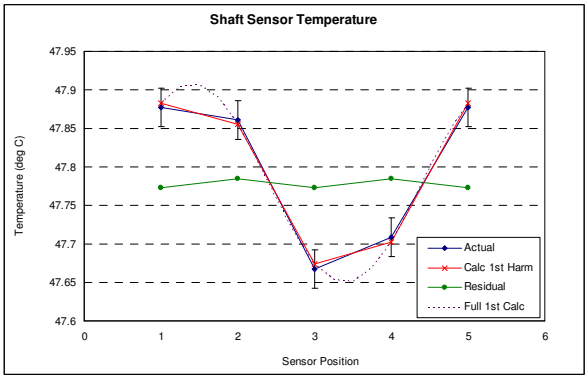

3000 rpm

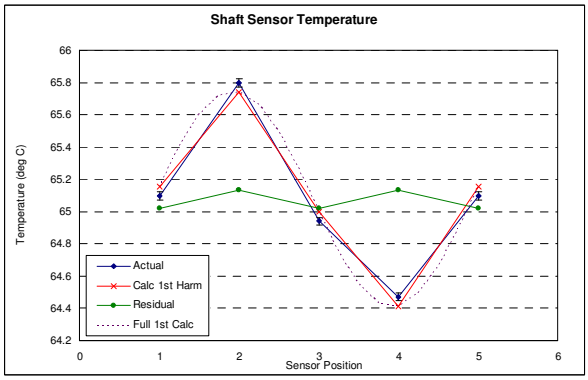

8000 rpm

Figure 159 Journal Circumferential Temperatures for DR0321

DR0399 - 7.5 g unbalance 0-8000 rpm (position 1)

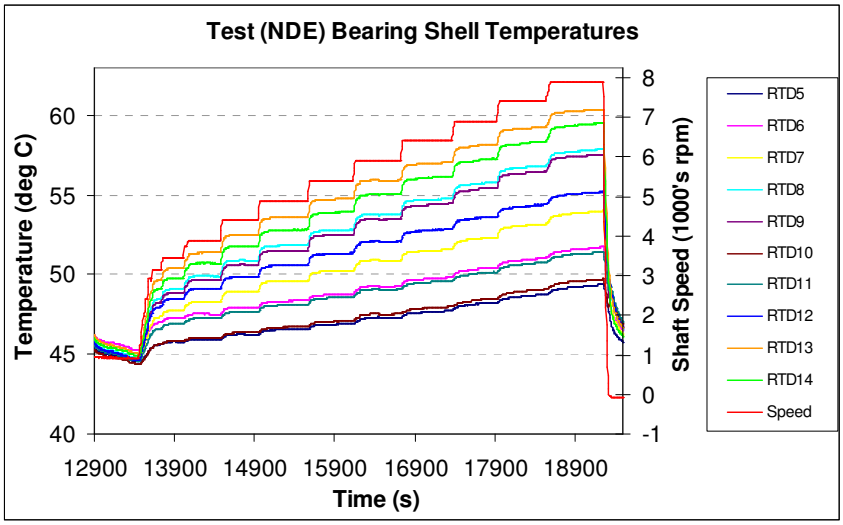

Figure 160 NDE Test Bearing Temperature Measurements Throughout Test DR0321

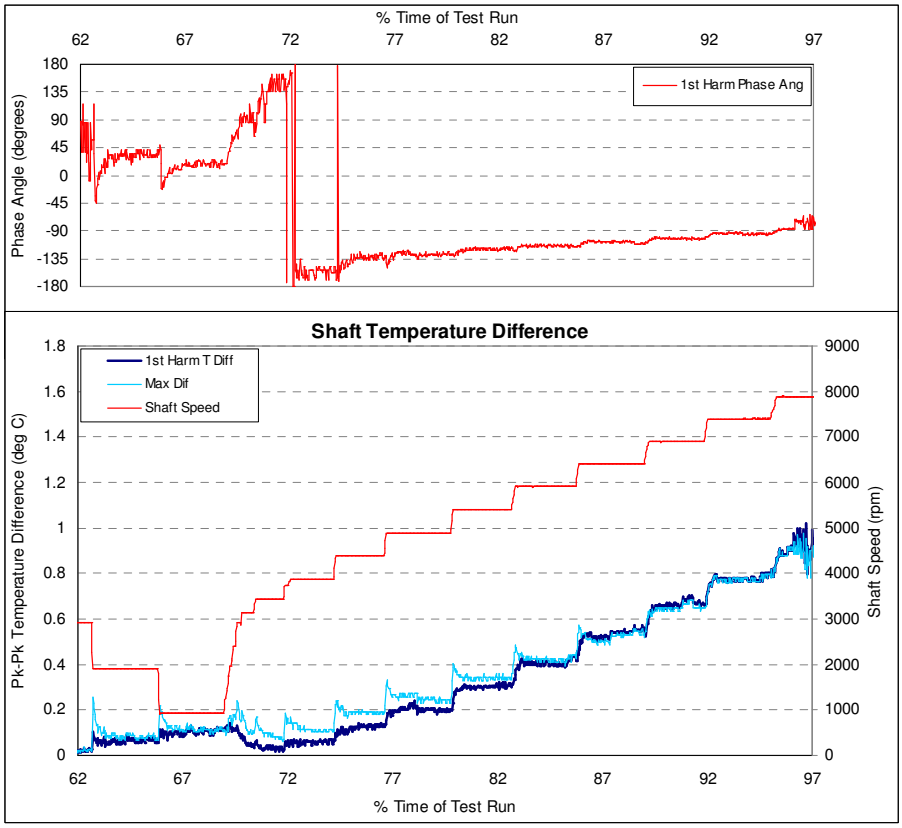

Figure 161 Shaft journal temperature differential measurements for DR0399

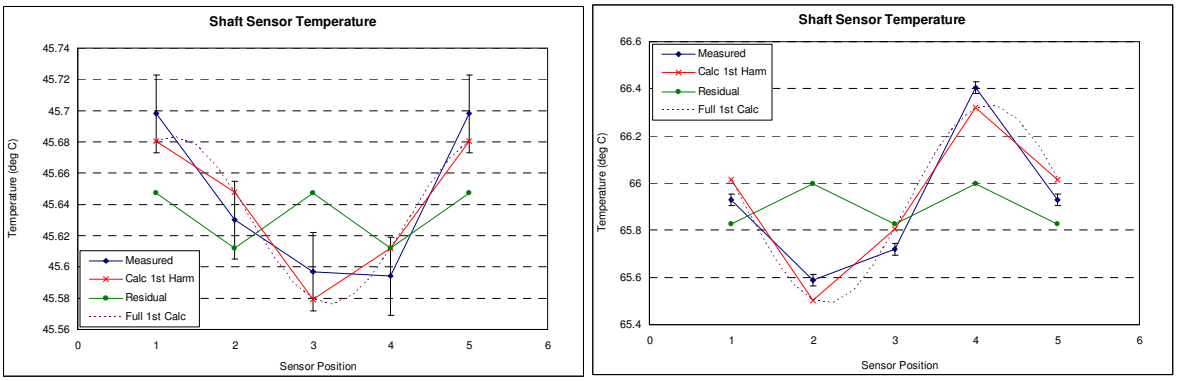

1000 rpm 8000 rpm

Figure 162 Journal Circumferential Temperatures for DR0399

7.3.2.1 Flexible Rotor Fixed Geometry Bearings (DR04 Tests)

DR0401 – 0 g unbalance 0-9000 rpm 1.5 kg OHM

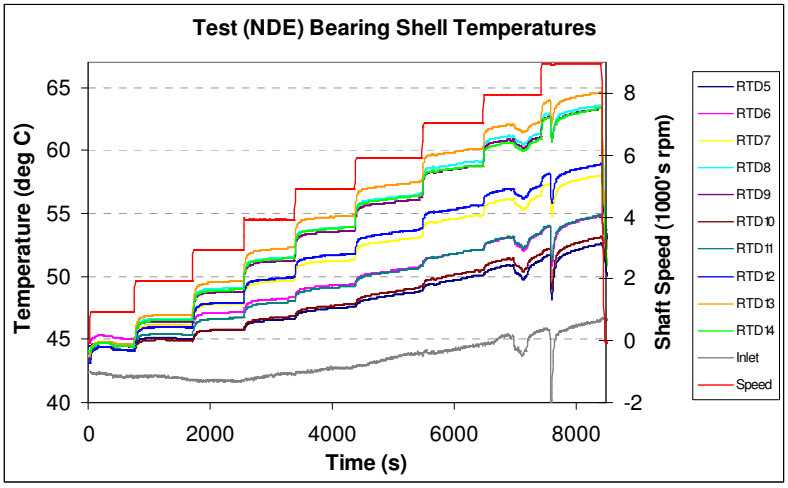

Figure 163 NDE Test Bearing Temperature Measurements Throughout Test DR0321

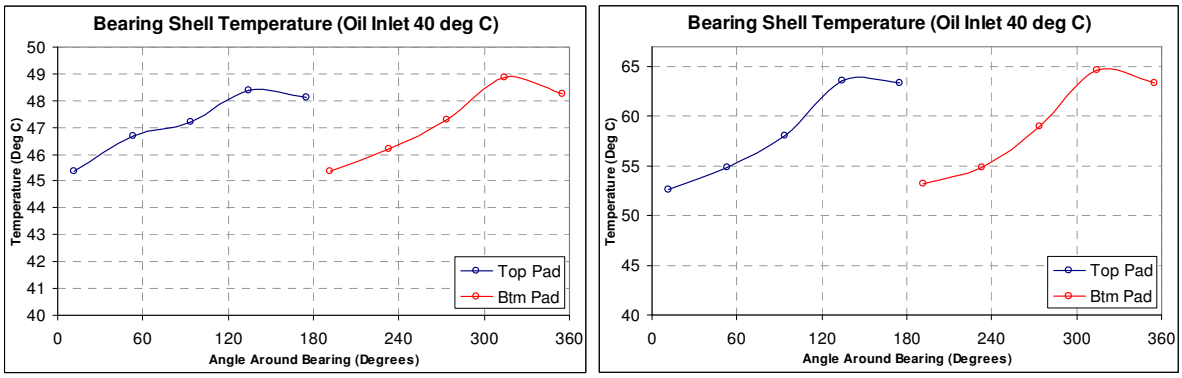

(a) 3000 rpm (b) 9000 rpm

Figure 164 NDE circumferential bearing shell temperature measurements DR0401

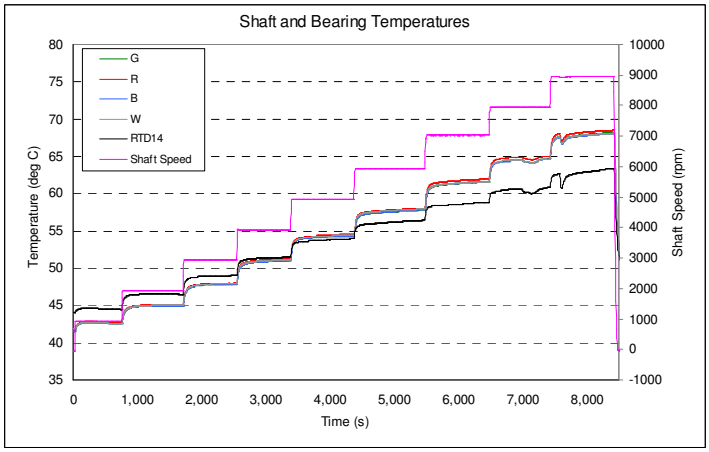

Figure 165 Shaft Journal and NDE Bearing (RDT14) Temperatures for DR0401

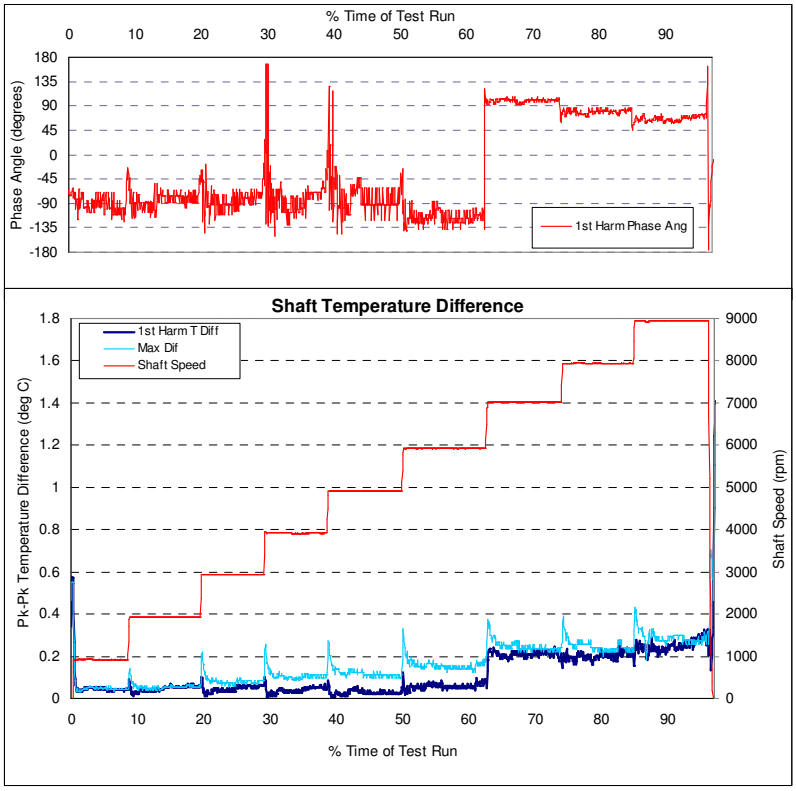

Figure 166 Shaft journal temperature differential measurements for DR0401

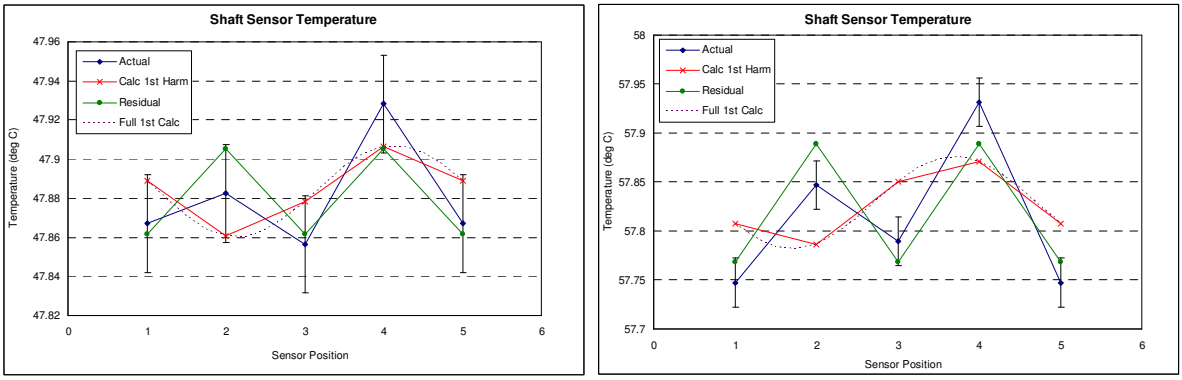

3000 rpm 6000 rpm

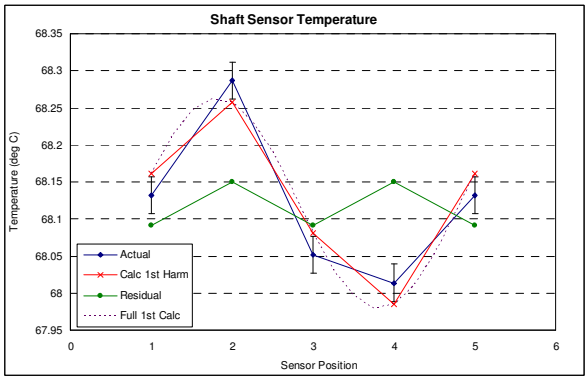

9000 rpm

Figure 167 Journal Circumferential Temperatures for DR0401

DR0407 - 2.5 g unbalance 0-9000 rpm (postion 4) 1.5 kg OHM

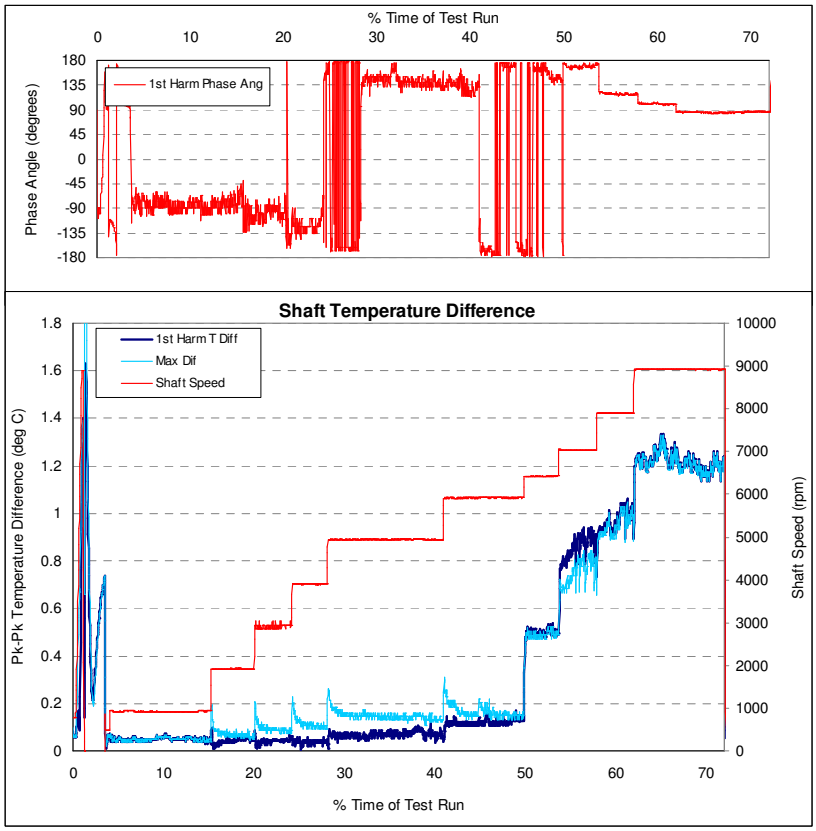

Figure 168 Shaft journal temperature differential measurements for DR0407

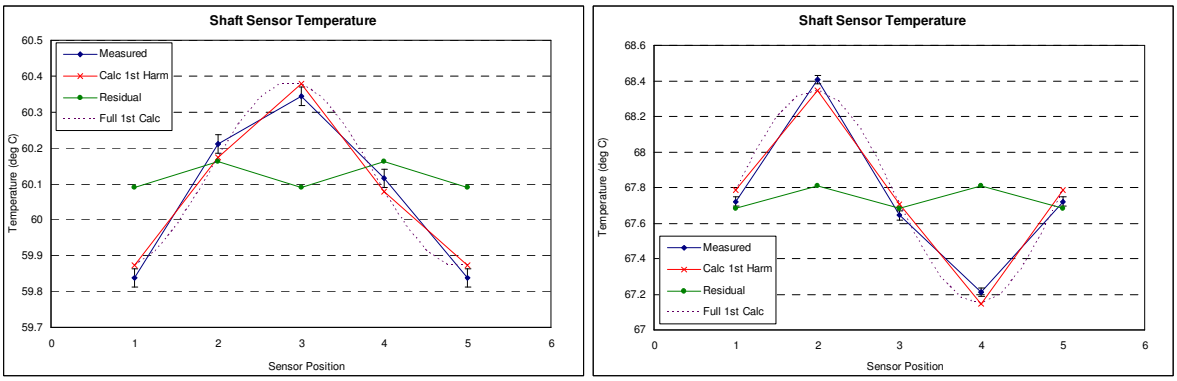

6500 rpm 9000 rpm

Figure 169 Journal Circumferential Temperatures for DR0401

DR0427 – 0 g unbalance 0-900 rpm @ flange 5 kg OHM

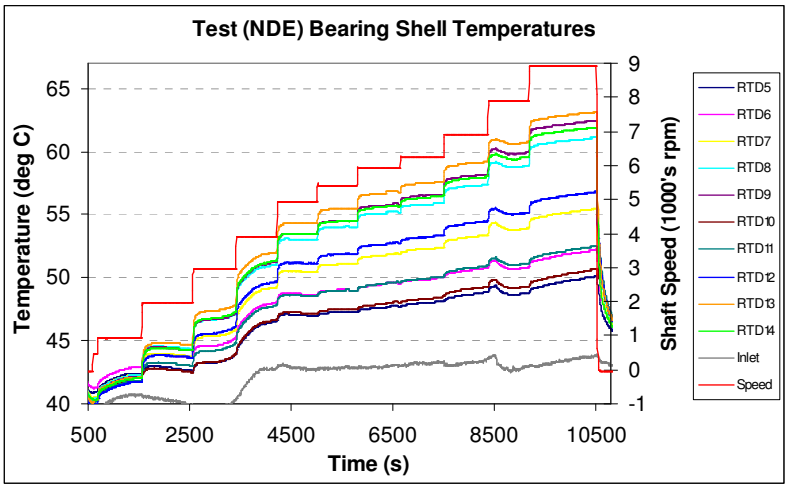

Figure 170 NDE Test Bearing Temperature Measurements Throughout Test DR0427

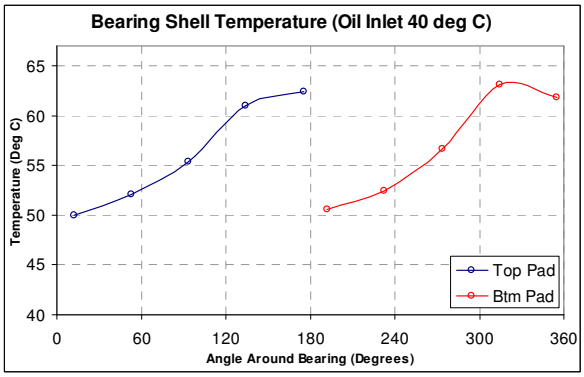

9000

Figure 171 NDE circumferential bearing shell temperature measurements DR0427

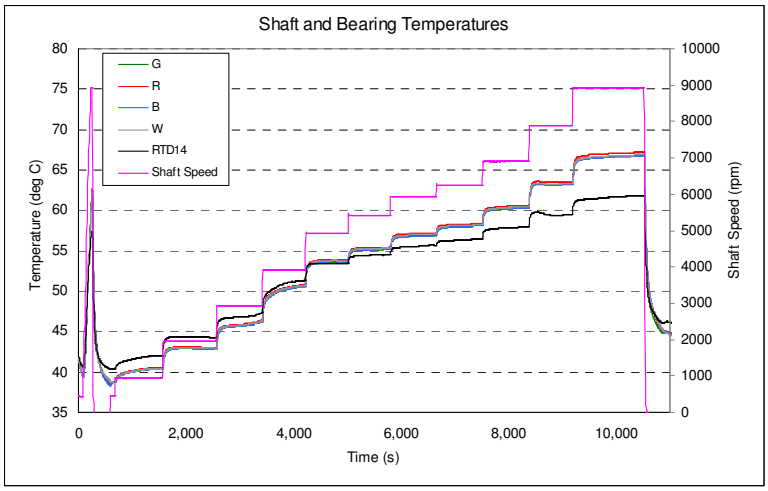

Figure 172 Shaft Journal and NDE Bearing (RDT14) Temperatures for DR0427

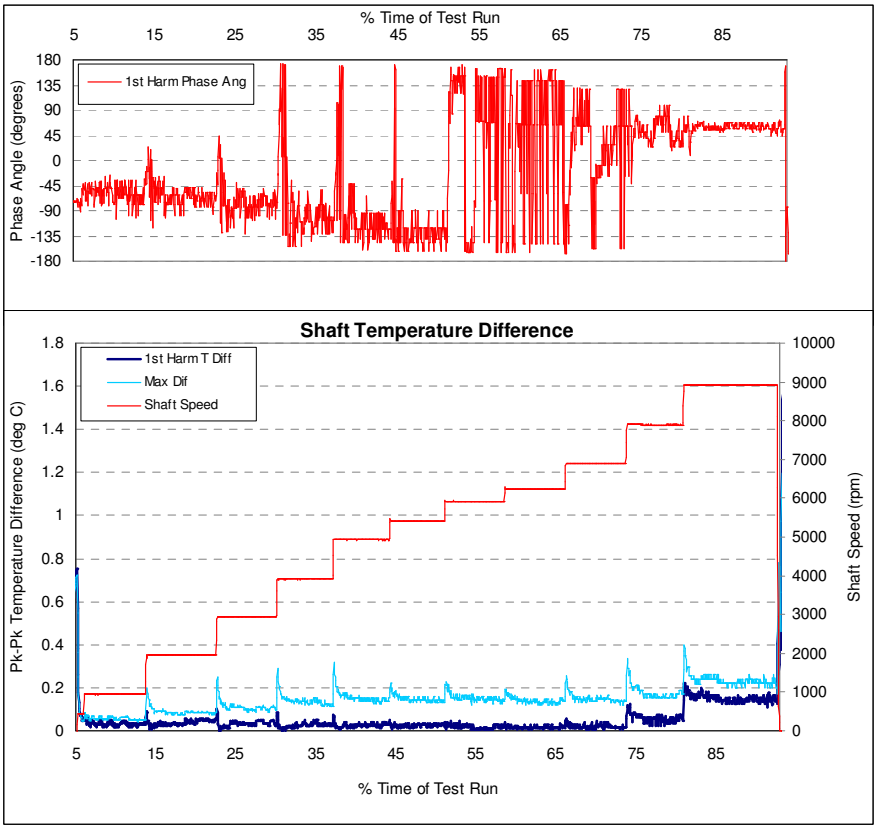

Figure 173 Shaft journal temperature differential measurements for DR0427

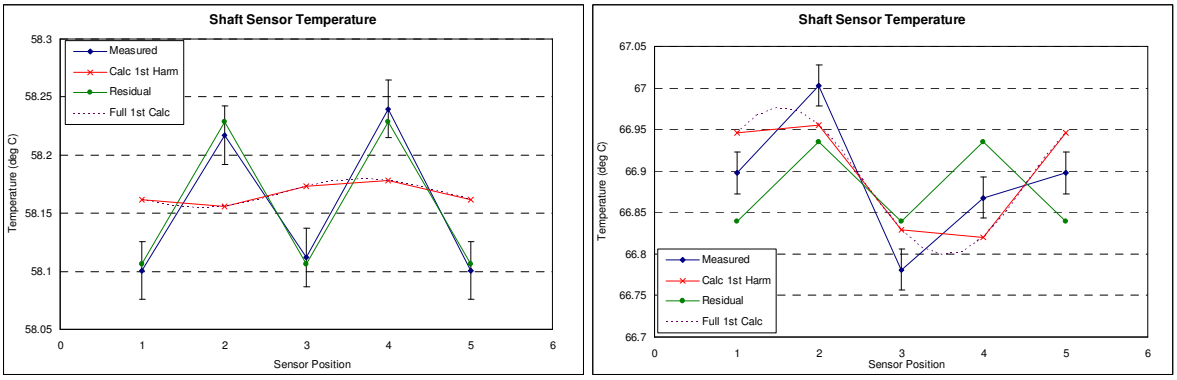

6250 rpm 9000 rpm

Figure 174 Journal Circumferential Temperatures for DR0427

DR0428 – 1g unbalance @ flange 0-9000 rpm (position 4) 5 kg OHM

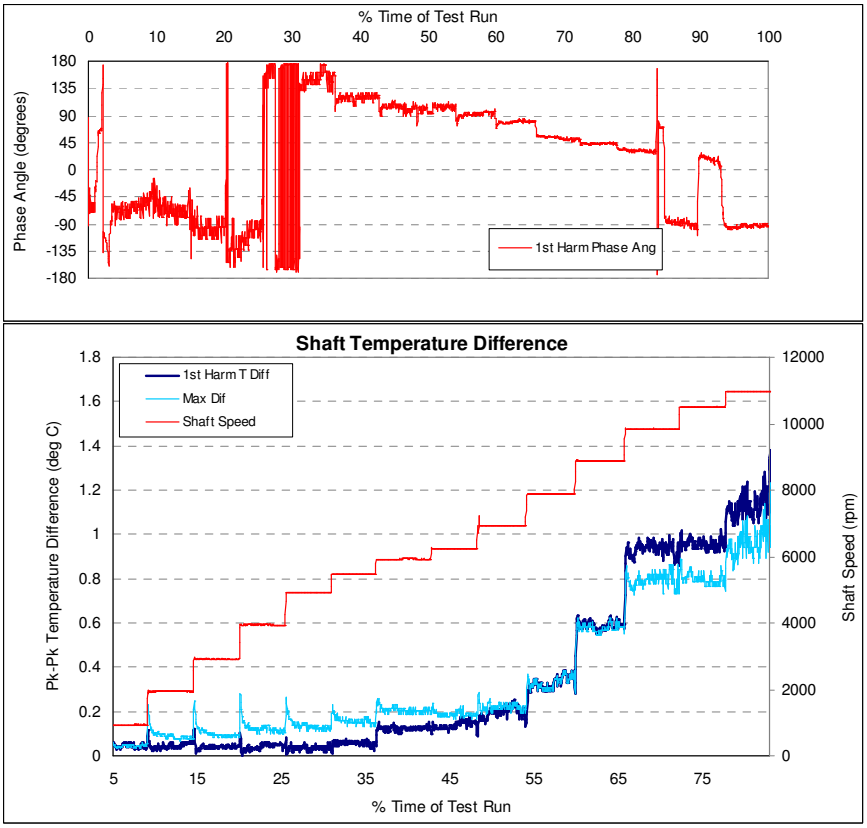

Figure 175 Shaft journal temperature differential measurements for DR0428

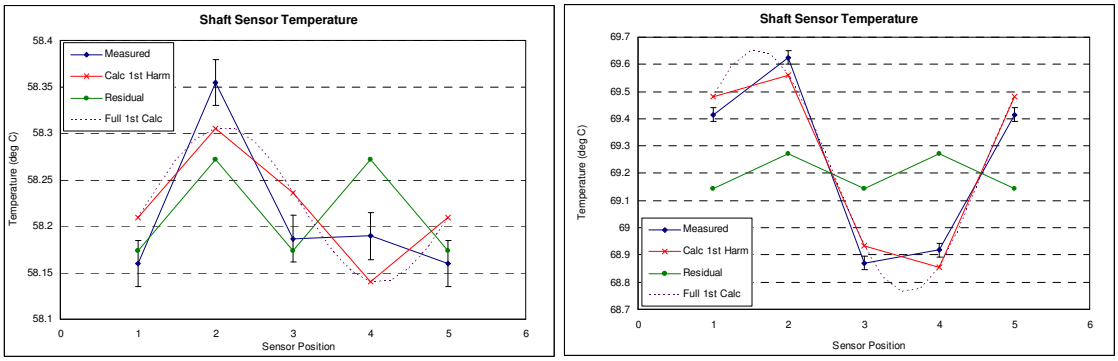

6250 rpm 10000 rpm

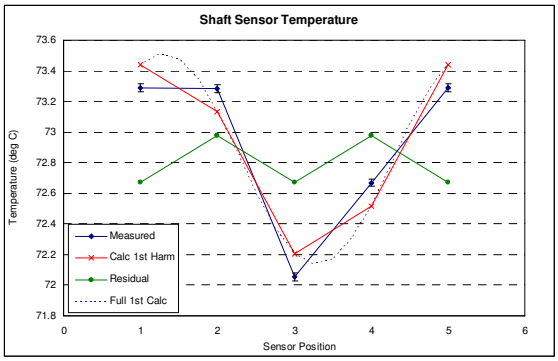

11000 rpm

Figure 176 Journal Circumferential Temperatures for DR0428

DR0453 – 2.5 g @ centre unbalance 0-9000 rpm (positon 1) 1.5 kg OHM

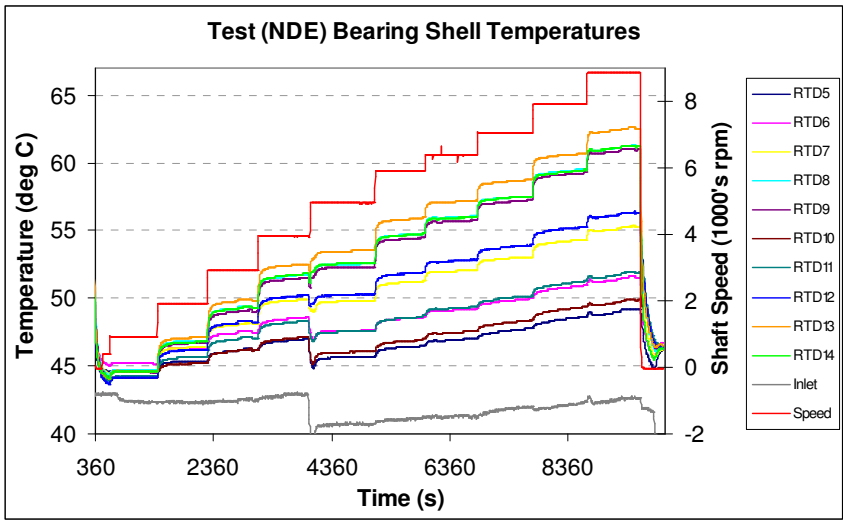

Figure 177 NDE Test Bearing Temperature Measurements Throughout Test DR0453

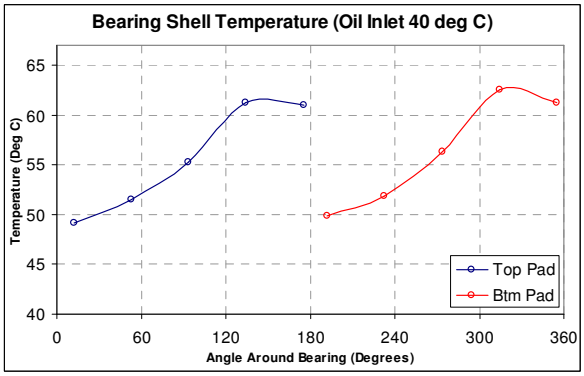

9000

Figure 178 NDE circumferential bearing shell temperature measurements DR0453

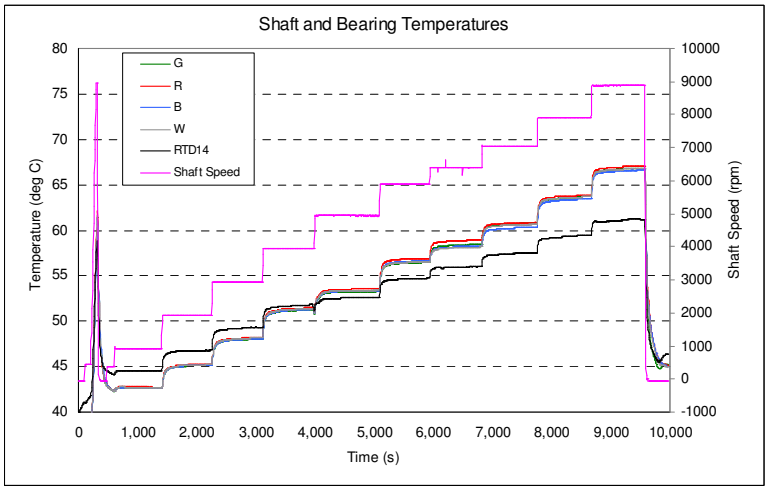

Figure 179 Shaft Journal and NDE Bearing (RDT14) Temperatures for DR0453

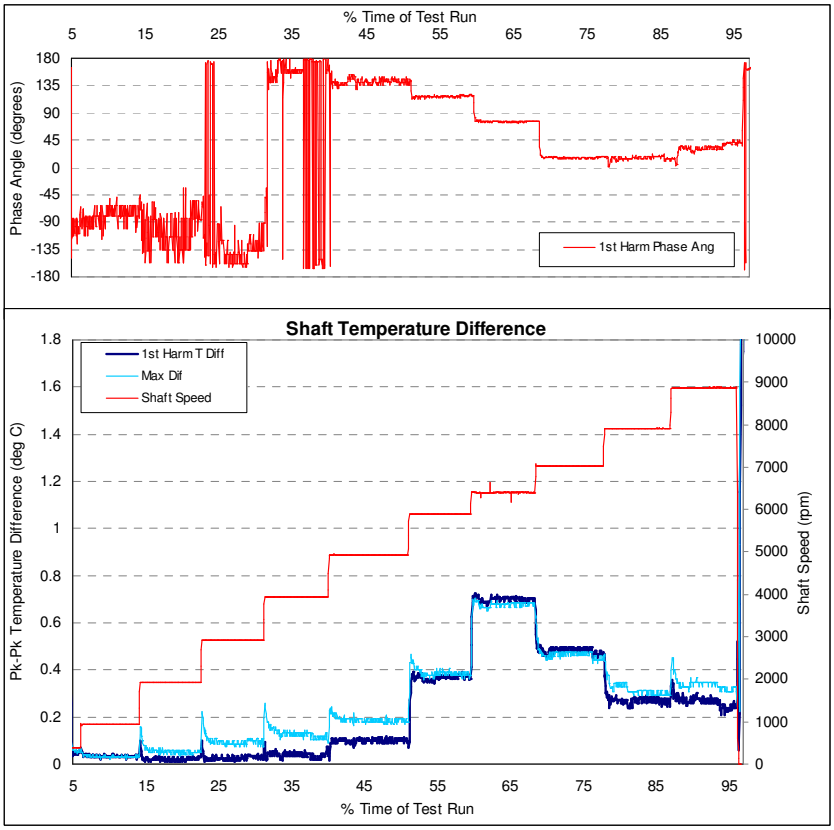

Figure 180 Shaft journal temperature differential measurements for DR0453

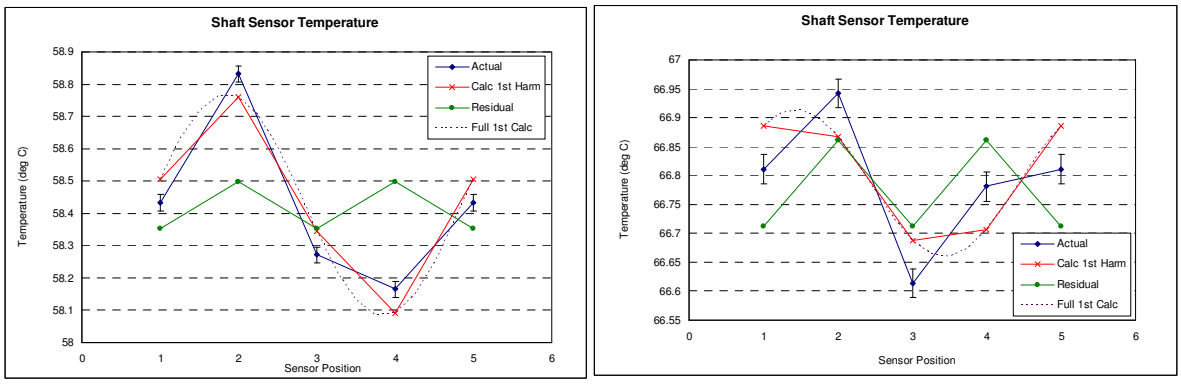

6450 rpm 9000 rpm

Figure 181 Journal Circumferential Temperatures for DR0453

7.3.2.1 Flexible Rotor Variable Geometry Bearings (DR06 Tests)

DR0651 – 0 g unbalance @ flange 0-9000 rpm 5 kg OHM

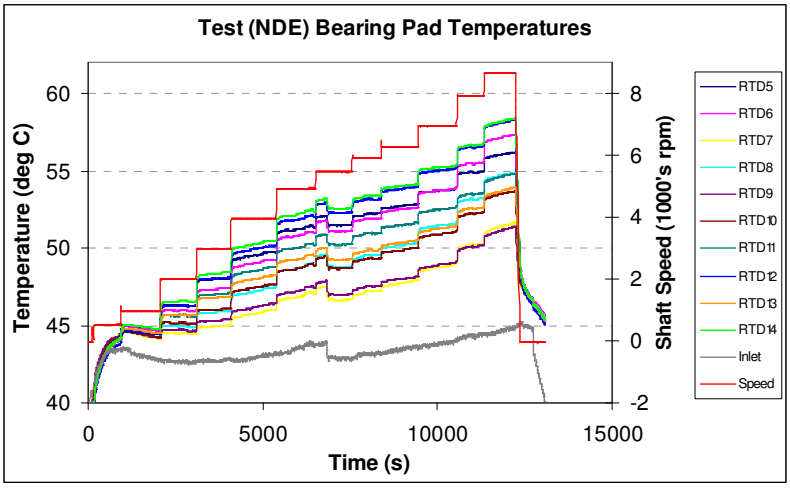

Figure 182 NDE Test Bearing Temperature Measurements Throughout Test DR0651

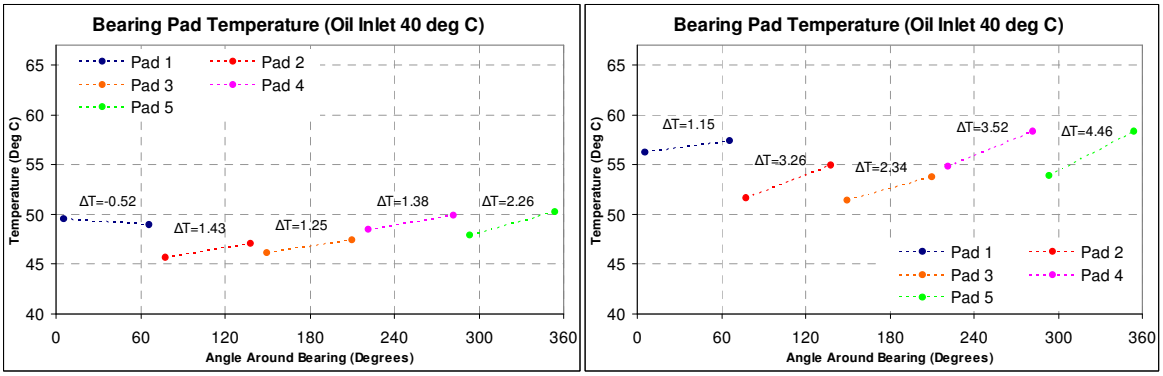

4000 rpm 9000 rpm

Figure 183 NDE bearing pad temperature measurements DR0651

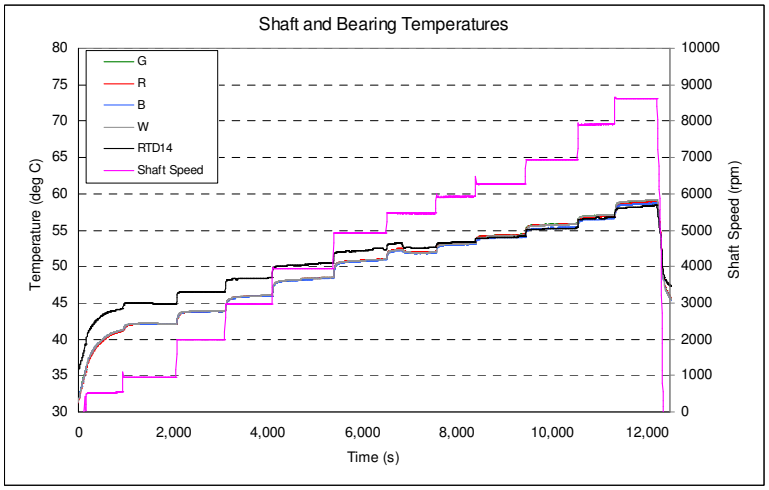

Figure 184 Shaft Journal and NDE Bearing Temperatures for DR0651

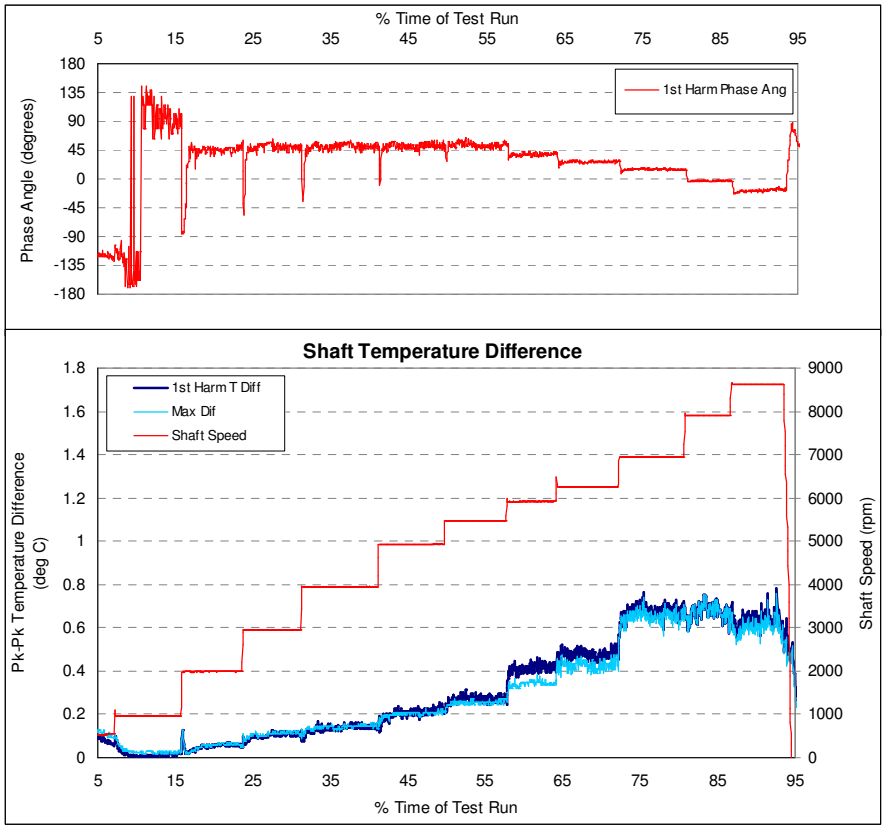

Figure 185 Shaft journal temperature differential measurements for DR0651

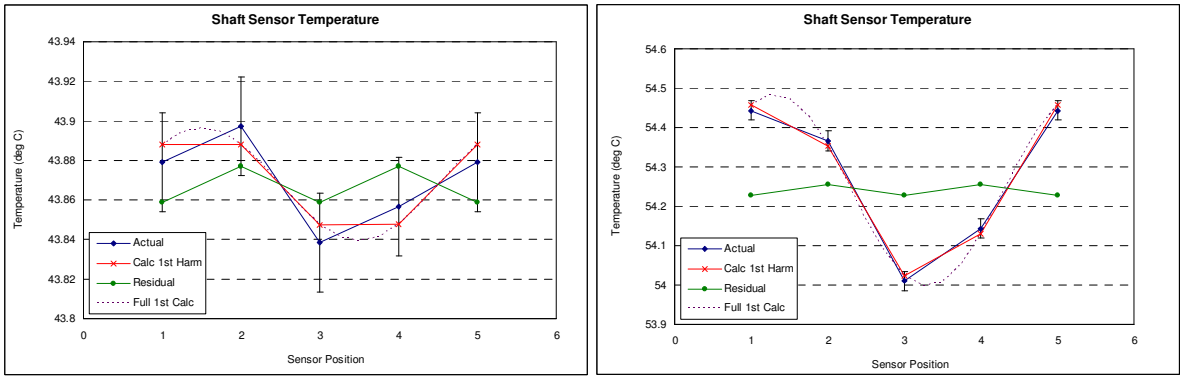

1000 rpm 6250 rpm

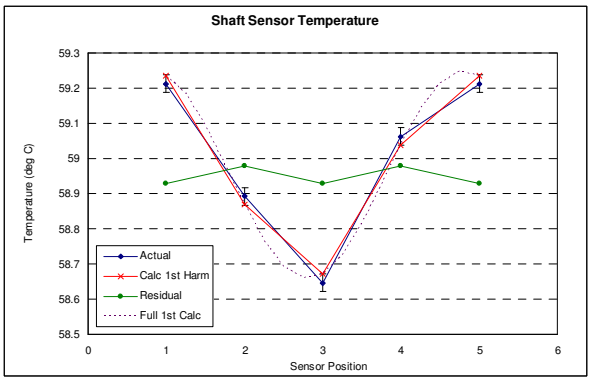

9000 rpm

Figure 186 Journal Circumferential Temperatures for DR0651

DR0673 - 1 g unbalance @ flange 0-9000 rpm (position 4) 5 kg OHM

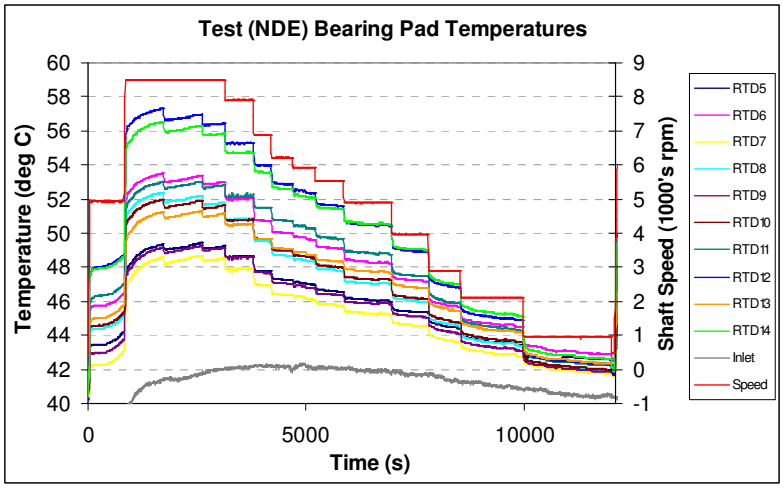

Figure 187 NDE Test Bearing Temperature Measurements Throughout Test DR0673

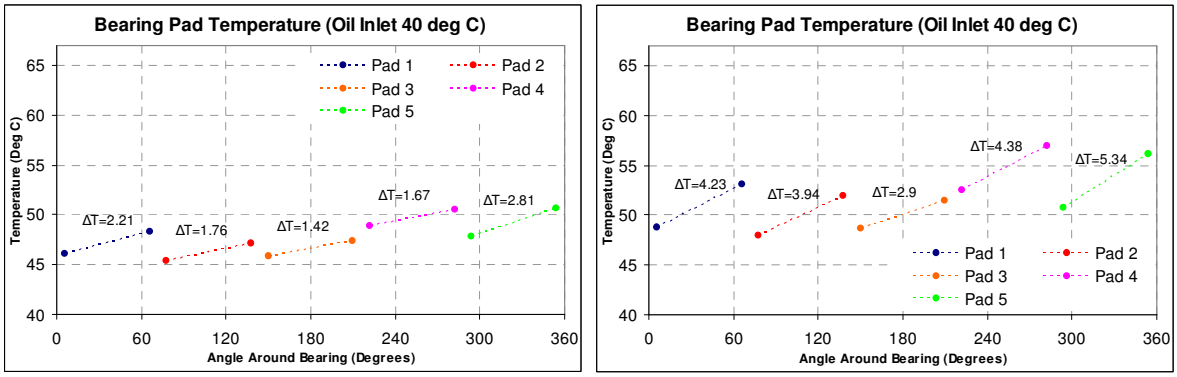

5000 rpm 10000 rpm

Figure 188 NDE bearing pad temperature measurements DR0673

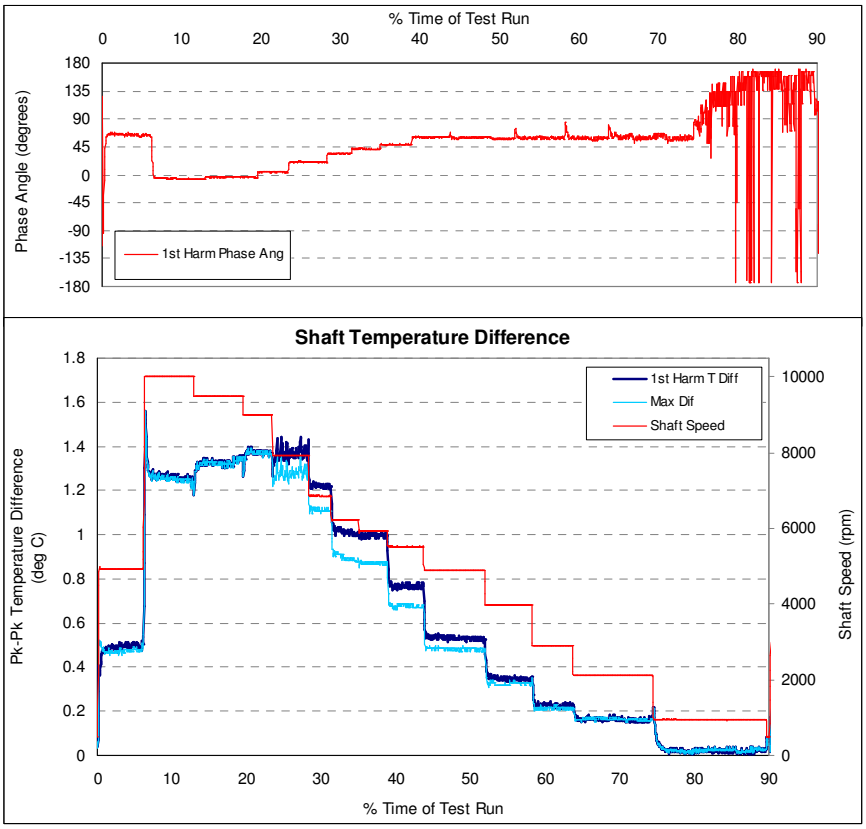

Figure 189 Shaft journal temperature differential measurements for DR0673

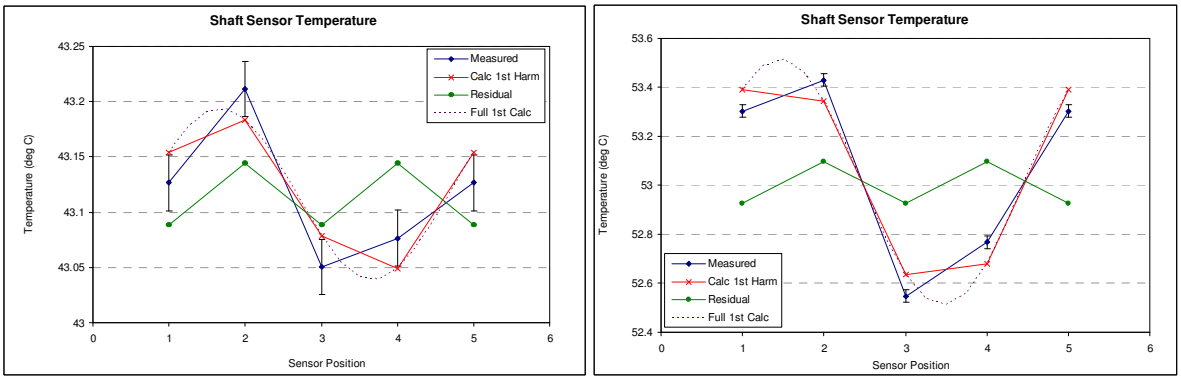

2200 rpm 6250 rpm

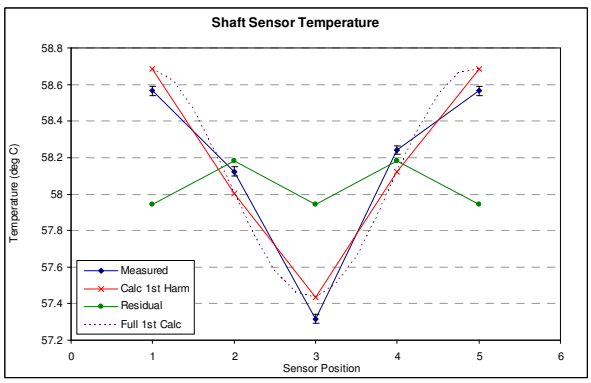

10000 rpm

Figure 190 Journal Circumferential Temperatures for DR0673

Chapter 8

Analytical Evaluation and Development of Journal Temperature Distribution

---

8. Analytical Evaluation and Development of Journal Temperature Distribution

8.1 Introduction

This chapter presents some methods developed for the qualitative and quantitative description of bearing journal temperature distribution. The principal focus of the work presented here is to attempt to provide a means of suitable approximation for the expected temperature distribution around the circumference of an whirling journal without the requirement for complex CFD type analysis. The intention is to present a method which can be developed for use in conjunction with typical rotordynamic packages for the coupled evaluation of the rotor response and differential journal heating stability. The work presented here provides only an initial presentation of some new methods for the modelling of the journal thermal conditions and further development and development is intended to provide models suitable for integration into existing rotordynamic procedures.

Two distinct aspects of evaluation are tackled. The first is associated with introducing an approach that allows for the effects of more complex bearing geometries to be evaluated for a specific vibration condition. Here the temperature distribution can be described with suitable resolution for the entire journal circumference. The intent here is not to develop complex thermohydrodynamic analysis models, but to apply the fundamental principles of the energy and temperature relationships within a hydrodynamic bearing and develop expressions and/or numerical procedures to allow for the application to journal temperature differential heating. The principle objective of this modelling work is to develop a suitable means of establishing the thermal boundary conditions that can be applied to a suitable model of the bearing journal. In particular, specific focus will be placed on the development

of the 1st harmonic temperature differential and arguably more significantly its phase relative to the point of minimum film thickness.

The second area of analytical assessment addresses the transfer of heat energy into the journal from the oil film. The analysis procedure is based around the development of a model of the shaft bearing journal where a pre-described thermal boundary condition is applied to the shaft circumference. The applied boundary condition is dynamic and is related to the associated operating speed of the shaft. This allows for a description of the shaft thermal distribution in the time domain to be developed. The method used to approach this problem was by the application of the Finite Difference Method. The results from the shaft temperature distribution are then used in a closed form algorithm to determine the associated shaft thermal bend angle and resulting shaft unbalance vector. A more detailed description of the analytical methods considered and the technique used are provided later in this chapter.

8.2 Finite Difference Heat Transfer Model

To enable a measure of the time dependant nature of the thermal bow development and corresponding dynamic interaction, a means of understanding the temperature development within the shaft is needed. As has been outlined in the literature, several methods for carrying out this type of analysis have been presented. In all cases reviewed thus far the techniques that have been employed are highly analytically intensive and either computationally intensive such as the CFD approaches or analytically complex to the point where practical implementation of real dynamic systems becomes impractical.

The intention of the modelling work presented here is to provide a computational technique which allows a practical compromise between the computational complexity and the notably simplified time independent methods as presented in the literature. When considering the problem the various techniques that can be applied were considered with respect to the level of analytical complexity and the probable computation requirements needed to provide solutions of acceptable accuracy. Following some initial evaluation, it was considered that a form of numerical solution was more preferable to that of a detailed analytical description. The reason was to maintain flexibility to enable application to real dynamic systems and features. In addition, the application of an analytical approach would require significant

assumption with relation to the real features or bearing geometries present within practical rotor systems, some of which would require some form of numerical solution in any case due to complex features or interactions being present. The implication of discontinuity features in analytical systems can introduce significant complexity whilst still requiring significant assumptions about those discontinuity features such as bearing oil inlets or the complex boundary conditions created by the oil film temperature and energy states. Whilst the accuracy or certainty around these features when incorporated into a numerical analysis offer little if any gain over that of the analytical methods the implication and control of such areas is much more readily implemented and more importantly adjusted.

A number of numerical techniques are available for the solution of such problems but it is the finite difference modelling technique which is adopted here. The use of finite elements or finite volume techniques were considered however, for the solution of the temperature distribution in the shaft journal, the finite difference technique allows for the most effective and least complex model to be developed. The use of the finite volume technique (in place of the differencing technique) was considered as this would allow for the thermohydrodynmic modelling of the oil film to be coupled with the shaft journal. However an approach was taken to attempt to separate the solution for the boundary conditions from the conduction heat transfer analysis of the shaft. The benefit is maintaining a practically applicable and quick (less computationally intensive) solution. It is important that if a practical approach can be implemented, the results are generated with quick, efficient computational procedures.

8.2.1 The Heat Transfer Model

The principle of the temperature distribution within the shaft journal is governed by the transient heat flux at the journal surface and the flow of heat within the shaft section. The one dimensional flow of heat within a body is given by Fourier's differential equation of heat conduction:

$$\frac{d^2T}{dx^2} + \frac{\rho.c}{k} = 0 \quad \text{eq. 8.2.1}$$

The above differential equation (eq 8.2.1) provides a description of the steady state heat transfer in a body. For the time dependent problem of the shaft journal it is therefore necessary to introduce a time dependant relationship with the rate of heat conduction known as the diffusion term. By introducing a time dependant temperature term into equation 8.1 $\partial T / \partial t$ the one dimensional equation for heat diffusivity can be written :

$$\frac{\partial^2 T}{\partial x^2} + \frac{\rho.c}{k}.\frac{\partial T}{\partial t} = 0 \quad \text{eq. 8.2.2}$$

where

$$\frac{\rho.c}{k}.\frac{\partial T}{\partial t} = \frac{1}{\alpha}.\frac{\partial T}{\partial t}$$

$\alpha = \frac{k}{\rho.c}$ is the thermal diffusivity of the body which is a measure of how quickly a material can transfer heat from a higher energy location to a lower one.

Whilst it is possible to derive analytical solutions to the heat diffusion differential equation for specific bodies, the assumptions and simplifications required, significantly limit the return on analytical effort when handling the difficult boundary conditions presented by the whirling shaft in the hydrodynamic bearing. The application of the finite difference technique allows for closely approximated solutions to the heat transfer problem and the definition of complex dynamic boundary conditions and discontinuity features within the bearing.

8.2.2 The finite Difference Technique

As with all the numerical the solution techniques, the governing equations are solved by means of representing the differential terms using an algebraic relationship. The finite difference method uses this approach by substitution the derivative terms with difference terms.

The principle of the finite difference method is based on approximating the derivative equation with a linear interpolation between successive points. If we

take Figure 191 to represent a second order derivative (as presented in the heat equations) then by dividing the X axis into a number of sections, it is possible to establish an approximation of the first derivative by taking the difference between the adjacent points along the curve. As the heat equation is a second order derivative, the first order derivative in finite difference terms must first be established.

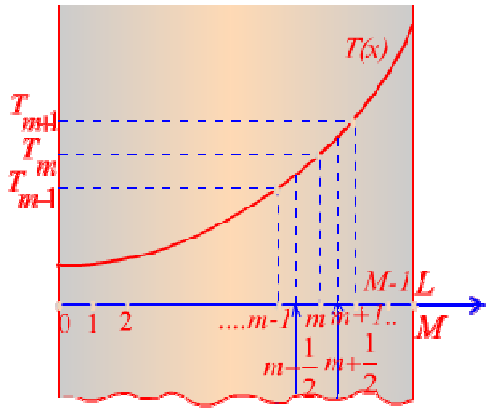

Figure 191 Discretisation of the analytical derivative solution [60]

To solve the second order partial derivatives presented in equation 8.2.2 the first and second order derivatives need to expressed in finite difference formulation.

The 1st order approximation with central differencing is given by :

$$\left.\frac{dT}{dx}\right|_{m-\frac{1}{2}} \cong \frac{T_m - T_{m-1}}{\Delta x}$$

And Eq. 8..2.3

$$\left.\frac{dT}{dx}\right|_{m+\frac{1}{2}} \cong \frac{T_{m+1} - T_m}{\Delta x}$$

And from this the formulation for the second order derivative can be determined:

$$\left.\frac{d^2T}{dx^2}\right|_{m-\frac{1}{2}} \cong \frac{\left.\frac{dT}{dx}\right|_{m+\frac{1}{2}} - \left.\frac{dT}{dx}\right|_{m-\frac{1}{2}}}{\Delta x} = \frac{\frac{T_{m+1} - T_m}{\Delta x} - \frac{T_m - T_{m-1}}{\Delta x}}{\Delta x} \quad \text{Eq. 8.2.4}$$

Therefore

$$\left.\frac{d^2T}{dx^2}\right|_{m-\frac{1}{2}}^{m+\frac{1}{2}} \cong \frac{T_{m+1} - 2.T_m + T_{m-1}}{\Delta x^2} \quad \text{Eq 8.2.5}$$

Where Δx represents the dimensional grid spacing in the dimension of heat transfer. Applying the above approximation for the second derivative to the heat equation 8.2.2, gives the finite difference equation for heat transfer :

$$\frac{d^2T}{dx^2} + \frac{\rho.c}{k} \cong \frac{T_{m+1} - 2.T_m + T_{m-1}}{\Delta x^2} + \frac{\rho.c}{k} = 0 \quad \text{Eq. 8.2.6}$$

The application of the finite difference method requires the medium under consideration to be discretised by a series of control volumes with an interior node to which the heat fluxes are subjected. The discretisation of a domain must typically be of uniform distribution across the generated grid to ensure continuity across the differencing (although there are techniques that can be applied to overcome this restriction such as Sundqvist et al [66]). A typical one dimensional gird is shown in Figure 192 where it can be seen at the boundary nodes consideration must be given to the control volume now being ½ of the discretisation increment.

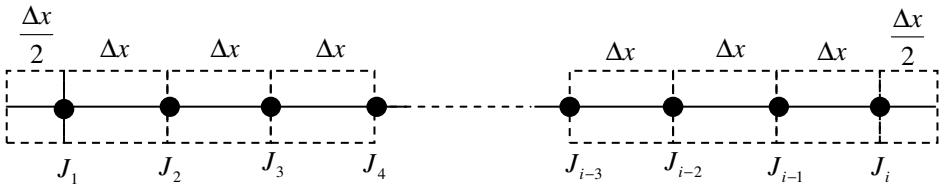

Figure 192 1 dimensional finite difference discreatisation grid with equal spacing

8.2.2.1 Boundary Conditions

Where external nodes exist, care must be taken as the finite difference formulation needs to be considered differently at the these locations. Typically external nodes are typically located at the boundary conditions. As such the descriptions of the conditions are based on the specific type of boundary condition being applied. The main principle behind the conditions required at external nodes is that formulations are written such that they observe the energy balance:

$$\sum_{m+1,m-1,n+,n-1} \dot{Q} + \dot{Q}_{m,n} = 0$$

The specific formulation of the conditions for external nodes is specific to the type of boundary condition applied. For the purposes of the analysis of the shaft journal, the boundary conditions considered are that of an insulated boundary, a convective boundary(heat flux and temperature specified boundary constraint. The specific temperature boundary condition is the simplest of the boundary conditions as the formulation is based on temperature values being defined or assigned specifically to an external node. Where :

$$T_n = T_\infty \quad \text{Eq. 8.2.7}$$

The formulation of the convection and heat flux boundary conditions can be constructed as follows for a 1 dimensional case :

$$0 = h.A.(T_\infty - T_o) + k.A\frac{(T_1 - T_o)}{\Delta x} + q_o.A.\left(\frac{\Delta x}{2}\right) \quad \text{Eq. 8.2.8a}$$

$$0 = q_o.A + k.A\frac{(T_1 - T_o)}{\Delta x} + q_o.A.\left(\frac{\Delta x}{2}\right) \quad \text{Eq. 8.2.8b}$$

Where the associated differential equation is given by :

$$0 = k.\frac{\partial T}{\partial x} + h.T - h.T_\infty \quad \text{Eq 8.2.9}$$

8.2.2.2 Discretisation Accuracy

Equations 8.2.5 and 8.2.6 are of the 1st order approximation and with this there is an associated error in its approximation. It is possible to increase the accuracy of the approximations of the finite difference equations by the application of higher order formulations. A brief study of the relative accuracies and computational requirements involved was made to establish which formulation would provide the most suitable when applied to the

differencing model of the rotor. Second and third order formulations for the first and second derivatives were also explored.

The results from the finite differencing analysis evaluation were assessed and the relative accuracies compared for the three formulations of both 1st and 2nd order derivatives, observation is made as to the level of increased complexity and computational effort incurred with each solution. The level of increased computational effort required for the higher order equations is significant as when a finite difference grid is constructed, the calculations will be performed many thousands of times which can have a profound effect on the associated solution times even on a modern computer.

From the evaluation it was considered that sufficient accuracy can be obtained with the application of the 1st order approximations when used with a sufficiently refined grid. The use of the lower order approximation means that the CPU intensity is kept to a minimum to speed up solution times with acceptable impact on solution accuracy.

8.2.2.3 Two Dimensional Grid Formulation

The above equations have been presented for a 1 dimensional representation. The analysis of the bearing journal requires that a two dimensional grid be developed. The application of the above formulations can be readily applied to a 2 dimensional grid construction. For a 2D grid with equal spacing the 1st order formulation for a given node will be :

$$\frac{T_{m+1,n} - 2.T_{m,n} + T_{m-1,n}}{\Delta x^2} + \frac{T_{m,n+1} - 2.T_{m,n} + T_{m,n-1}}{\Delta y^2} + \frac{\dot{q}_{m,n}}{k} = 0 \quad \text{Eq. 8.2.10}$$

Writing equation 8.2.10 for $dT_{m,n}$ and introducing the implicit transient solution using α gives :

$$dT = \alpha.dt.\frac{T_{m+1,n} - 2.T_{m,n} + T_{m-1,n}}{\Delta x^2} + \alpha.dt.\frac{T_{m,n+1} - 2.T_{m,n} + T_{m,n-1}}{\Delta y^2} \quad \text{Eq. 8.2.11}$$

Polar Coordinates

To suitably represent the 2 dimensional section or the shaft journal it is necessary to develop the above finite difference equations in the polar coordinate system. The control volume grid construction and coordinate system as presented in Figure 193 is used.

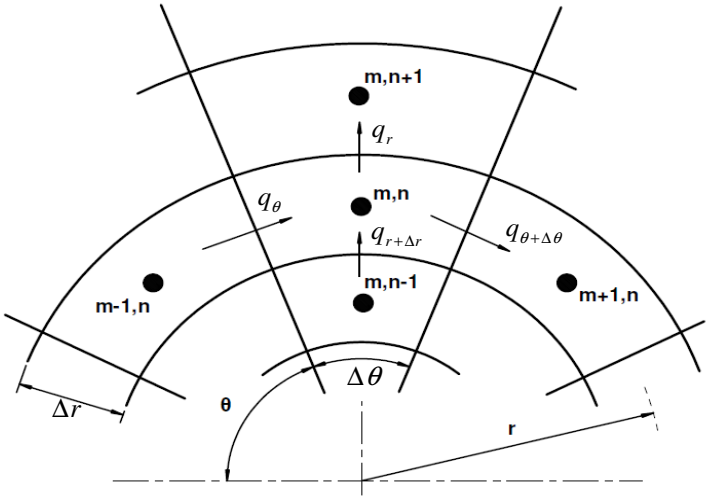

Figure 193 Finite difference control volume and node construction in polar coordinates

Applying the same formulation principles as for the Cartesian equations the energy balance for an internal node m can be developed as :

$$q_r.(r-0.5.\Delta r).\Delta\theta - q_{r+\Delta r}.(r+0.5.\Delta r).\Delta\theta + q_\theta.\Delta r - q_{\theta+\Delta\theta}.\Delta r..... \\ +q_g.r.\Delta\theta.\Delta r = 0 \qquad \text{Eq. 8.2.12}$$

Where r, θ, Δr and $\Delta\theta$ are the polar terms used for describing the control volume.

Where the heat fluxes can be expressed by:

$$\left.\begin{aligned}
\dot{q}_r &= k_{m,n-\frac{1}{2}}.\frac{T_{m,n-1}-T_{m,n}}{\Delta r} \quad \text{(a)}\\
\dot{q}_{r+\Delta r} &= k_{m,n+\frac{1}{2}}.\frac{T_{m,n}-T_{m,n+1}}{\Delta r} \quad \text{(b)}\\
\dot{q}_{\theta} &= k_{m-\frac{1}{2},n}.\frac{T_{m-1,n}-T_{m,n}}{r.\Delta\theta} \quad \text{(c)}\\
\dot{q}_{\theta+\Delta\theta} &= k_{m,n+\frac{1}{2}}.\frac{T_{m,n}-T_{m,n+1}}{r.\Delta\theta} \quad \text{(d)}
\end{aligned}\right\} \text{Eq . 8.2.13}$$

Combining equations 8.2.13 and substituting into 8.2.12 yields the finite difference formulation for a 2D internal node in polar coordinates, also substituting steady state heat transfer constant k for transient heat diffusion α gives :

$$dT = \frac{\alpha.dt}{r^2}.\left[T_{m+1,n}-2.T_{m,n}+T_{m-1,n}\right]+\alpha.dt.\left[T_{m,n+1}-2.T_{m,n}+T_{m,n-1}\right]+.... \quad \text{Eq. 8.2.14}$$
$$\frac{\alpha.dt}{2.r}.\left[T_{m,n+1}-T_{m,n-1}\right]$$

The central node

A feature presented in the polar coordinate system not experienced in the cartesian grid construction is the node at the centre of a solid shaft or disc. The central node is a singularity and as such cannot be treated with the previously presented equations for other internal nodes. The formulation of the conditions for the central node derived here are consistent with those presented by Muneer et al [61].

Considering the control volume of $\frac{\Delta r}{2}$ as shown in Figure 193 the energy balance equation can be expressed as

$$0 = -(\dot{q}_{r1,2} + \dot{q}_{r1,2} + \dot{q}_{r1,2} + ... + \dot{q}_{r1,2}).\frac{\Delta r.\Delta\theta}{2} + \dot{q}_g .\pi.\left(\frac{\Delta r}{2}\right)^2 \quad \text{Eq. 8.2.15}$$

Were *i* is the number of segments connected to the central node within the central control volume boundary $q_{i,j}$ and is the radial heat flux between the corresponding control volume boundary from nodes *i* and *j*. Where q_{ij} can be expressed as

$$\dot{q}_{r.m,2} = k\frac{T_{1,1} - T_{m,2}}{\Delta r} \quad \text{Eq. 8.2.16}$$

Substituting into equation 8.2.14, introducing transient conditions and simplifying yields the finite difference formulation for the central node with respect to time :

$$dT \cong \frac{4.\alpha}{i.\Delta r^2}.(T_{1,2} + T_{2,2} + T_{3,2} + ... + T_{i,2}) - T_{1,1} \quad \text{Eq. 8.2.17}$$

It is also necessary to express the boundary conditions in the polar coordinate system. For the convective boundary condition the finite difference equation for transient heat transfer as :

$$dT = \frac{\alpha.dt}{\left(r - \frac{\Delta r}{4}\right).r.\Delta\theta^2}.\left[T_{m+1,n} - 2.T_{m,n} + T_{m-1,n}\right] + \frac{\alpha.2.(r - 0.5.\Delta r).dt}{\left(r - \frac{\Delta r}{4}\right)\Delta r}.\left[T_{m,n-1} - T_{m,n}\right] + ...$$
$$.....\frac{2.h.r.dt}{\rho.c_s.\Delta r.\left(r - \frac{\Delta r}{4}\right)}.\left[T_\infty - T_{m,n}\right]$$

Eq. 8.2.18

Where T_∞ is the temperature of the fluid at the boundary with the solid surface.

8.2.2.4 Numerical Stability

When undertaking transient finite difference analysis using an implicit method, it is possible to result in unstable numerical isolations. In this case the time

steps involved between each iteration can become too large and result in and oscillating divergent and unstable nodal calculations.

The conditions under which unstable characteristics are observed is when the time step increment in relation to the grid spacing results in errors that are either increasing in size or at a rate greater than the rate of convergence. The errors are generally in the form of truncation or discretisation errors where the error is a direct result of the error in the difference approximation, and round-off errors where the numerical precision in the calculations is insufficient and the effect accumulates with each increment or time step. The latter of the two error sources is not typically a problem with modern high bit computers but the grid discretisation is influential and is managed by means of reducing grid size relative to time step Δt. It is possible to determine a minimum time step/mesh size to ensure stability is maintained across the difference mesh, and is given by Li [62] for the heat equations as in equation 8.2.19 , where the minimum time step required for a given Δx is :

$$dt \leq \frac{\Delta \overset{\vee}{x}^2}{2.\alpha} \quad \text{Eq. 8.2.19}$$

The problem with this time step stability requirement is that in transient analysis it can result in much higher computational effort to evaluate a given time period. The issue is that as the mesh density to improve accuracy is increased a reduction in the time step is necessary, resulting in more solutions per time step and increased number of time steps. This compounding effect significantly increases the processing times required to solve the models. A notable additional effect in the polar system is that, as the radii approaches the centre, the arc length of the circumferential control volumes become very small. This is not a problem typically encountered in Cartesian grids due to the grid spacing typically being evenly spaced across the entire model.

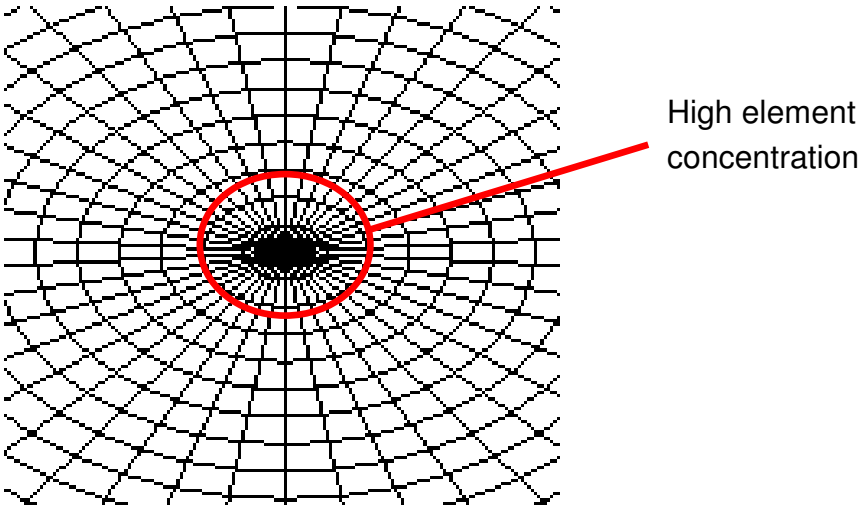

Figure 194 Small grid discreatisation effect around centre node in polar coordinates

With the above conditions in mind, the finite difference model grid resolution should be kept to as course grid as possible (within acceptable accuracy limits) to provide the most effective model solution durations.

The application the finite difference relationships developed above now provide a means by which a two dimensional representation of the shaft journal section at the bearing location can be modelled in the time domain. The remaining key element required to solve the thermal conditions is the suitable description of the dynamic journal boundary conditions defined and expressed at the grid boundaries (shaft outer surface).

8.3 Bearing Oil Film Temperature Distribution Model

To successfully create a model that in some way represents the dynamic thermal conditions present with the bearing rotor system a suitably detailed description of the steady state and transient thermal conditions present with the bearing oil film are necessary. The work presented here has been developed as part of the research to provide a calculation method and procedure which predicts the thermal conditions present within the lubricant oil film at the journal bearing boundaries. The equations and relationships have been developed to attempt to reduce the highly involved computational requirements typically needed for detailed modelling of the oil film energy relationships present within the oil film. The intention is not to provide an alternative procedure to give a complete description of the thermal and

dynamic properties present within the three oil film dimensions, but to present appropriate energy and temperature conditions for application to shaft journal heat transports from the lubricant oil film. In particular focus on representation and modelling of non circular bearing geometries is presented as this is an area which to date has not received any popular attention within the subject area. At an industrial level this limits the applicability of the existing procedures when attempts are made to apply procedures to practical high speed machines.

8.3.1 The Oil Film Function

To gain a suitable understanding of the thermal conditions within the lubricant film it is necessary to characterise the oil film thickness function around the bearing for any given point in space and/or time, and from this characterisation develop a means of understanding the heat generation development around the bearing-journal surfaces.

8.3.1.1 Geometric Relationships

The first step in defining the oil film function $h_{(\theta)}$ is to develop a series of equations and relationships that can be used to fully describe the oil film spatial conditions between the bearing and journal surfaces. This geometrical relationship is commonly referred to as the oil film function. This a geometrically related function which is principally dependant on the bearing surface topology and the operating position of the rotating shaft or journal (when perfectly round bearing journal are assumed and local thermal influences on the surface of the bearing are assumed negligible).

Many authors have derived and presented algorithms for the determination of the oil film thickness for journal bearings. The mostly commonly encountered is that of plain cylindrical bearing. It is the plain cylindrical bearing which will be considered first here. The following derivations are based on the most widely adopted analytical description which is compressively covered by Cameron [43]. The development of these oil film functions will then be adapted to describe the oil film functions for the non circular fixed and variable bearing geometries used in the experimental research of this project.

Figure 195 shows the coordinate system adopted for the following equations and derivations.

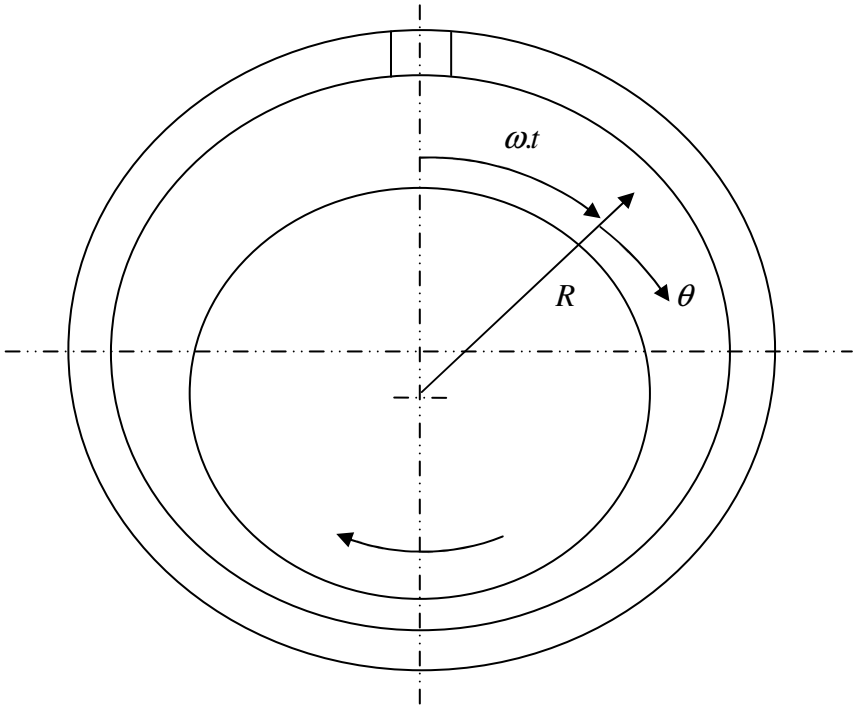

Figure 195 Basic coordinate system used in the bearing geometry and energy formulations

Plain Cylindrical Bearing

Under steady state conditions the normal section of the shaft and bearing presented in Figure 196 is assumed. The geometrical conditions are dictated by the level of eccentricity (e) present between the centre of bearing Ob and the centre axis of the rotating shaft journal Os, i.e. e=Ob.Os. It is typical to non dimensionalise this offset with reference to the bearing radial clearance Cr to yield the factor known as the eccentricity ratio ε, (where 0 is gives a fully centred shaft journal relative the bearing and eccentricity ratio of 1 is where the shaft journal comes into contact with the bearing surface).

$$\varepsilon = \frac{e}{C_r} \qquad \textit{where } C_r \textit{ = radial clearance}$$

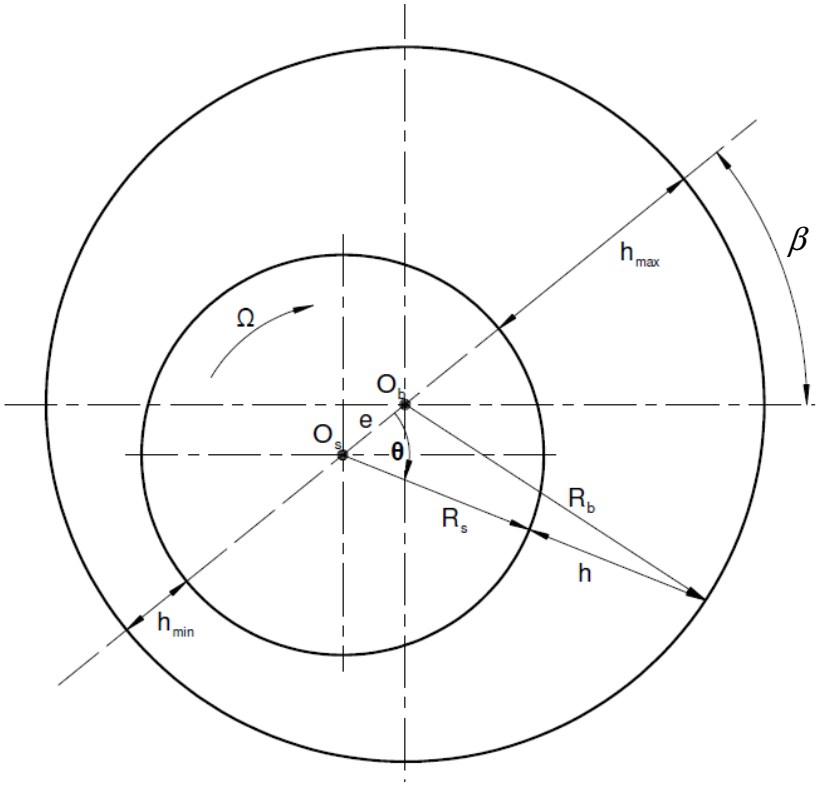

Figure 196 Plain bearing geometric relationships

Examining the trigonomic arrangement from Figure 197 in more detail, the following description in terms of triangles can be established.

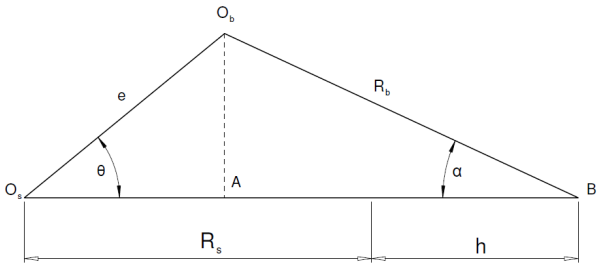

Figure 197 Triangles from Figure 196

.

Using Figure 197:

$$O_sB = O_sA + AB = R_s + h \quad \text{Eq. 8.3.1}$$

This in trigonometric terms is given by:

$$O_sB = e.\cos(\theta) + R_b.\cos(\alpha) \quad \text{Eq. 8.3.2}$$

Therefore

$$h = e.\cos(\theta) + R_b.\cos(\alpha) - R_s \quad \text{Eq. 8.3.3}$$

Applying the sine rule and writing for α by:

$$\frac{e}{\sin(\alpha)} = \frac{R_b}{\sin(\theta)} \quad \text{Eq. 8.3.4}$$

where

$$\sin(\alpha) = \frac{e.\sin(\theta)}{R_b} \quad \text{Eq. 8.3.5}$$

and applying the trigonomic identity $\cos^2(\alpha) + \sin^2(\alpha) = 1$ yields:

$$\cos(\alpha) = \sqrt{1 - \sin^2(\alpha)} \quad \text{Eq. 8.3.6}$$

substituting for $\sin(\alpha)$

$$\cos(\alpha) = \sqrt{1 - \left(\frac{e}{R_b}\right)^2.\sin^2(\theta)} \quad \text{Eq. 8.3.7}$$

At this point it should be noted that for practical bearings the ratio of the radial clearance is generally of the order of 0.1-0.2% of R_b. This results in the angle α being a very small value. Also $\left(\frac{e}{R_b}\right)^2$ will be of the order $1 - 2\times10^{-6}$ % of R_b resulting in $\cos(\alpha) \approx 1$. Substituting this into equation 8.3.3 yields :

$$h = e.\cos(\theta) + R_b - R_s = e.\cos(\theta) + C_r \quad \text{Eq. 8.3.8}$$

Re-writing with ε for eccentricity ratio gives :

$$h = C_r(1+\varepsilon.\cos(\theta)) \quad \text{Eq. 8.3.9}$$

Where equation 8.28 is the oil film function for plain cylindrical bearings and for bearings with clearance ratios of <~0.5% yiels results with errors within 0.1% for h.

In real bearing applications the steady state eccentricity ratio and the angle at which it acts relative to a datum need to established for any given load vector and operating speed. These two features are calculated by means of solving the Reynolds equation for a steady state operation. The principal derivations and application of hydrodynamic lubrication and the Reynolds equation to cylindrical bearings is summarised in chapter 3 and will not be re-addressed here.

The solution of the Reynolds equation for various bearing types is extensively covered in the available literature applying a wide range of solution techniques. As the principal aspects of the work undertaken here are derived from the geometric and operating conditions in the bearing, it is not necessary to solve the pressure distribution within the bearing to derive the desired relationships required to define the required thermal boundary conditions. The information needed from the solution of the hydrodynamic problem is the eccentricity ratio ε and attitude angle φ for a given operating condition. As such it is not the intention of this work to address specifically the solution of the Reynolds equation for a given bearing configuration, as the application of one of the many existing techniques provides a satisfactory and effective means of establish the necessary geometric data. For the purpose of the work detailed in this section, it is assumed that the steady sate conditions for the shaft journal position are known and used as an input to the analytical evaluation.

Currently equation 8.3.8 is expressed with referenced to the point of maximum film thickness where $\theta = 0$. In real bearing configurations the orientation of the bearing is typically such that a physical datum is used with which to reference the geometric and other performance data (see Figure 198). As such for a plain cylindrical bearing equation 8.3.9 can be re-written :

$$h = C_r(1 + \varepsilon.\cos(\theta - \beta)) \quad \text{Eq. 8.3.10}$$

where *h* can now be expressed with reference to any arbitrary point around the bearing.

The film function defined above is consistent with the form presented by many sources in the literature for the steady state condition in the bearing where the shaft rotation axis remains at point Os. Generally when evaluating bearing performance it is only the steady state condition which is of interest and dynamic perturbations are considered to have only a minor and/or transient effect on bearing oil film temperatures. However for the purposes of the subject matter of the research, these transient conditions of direct interest and importance with relation to the journal thermal conditions. For this reason it is necessary to develop here the geometric conditions present during the dynamic orbit with respect to time.

The shaft orbits can be functions of any order of shaft rotation and the resulting shaft movements will, in almost all cases, be a combination of multiple shaft orders. The most dominant and common order considered is that of the synchronous orbit, whereby the shaft movement is directly related to the shaft rotation frequency. During the synchronous orbit the shaft journal centre Os will traverse a circular or elliptical path about the steady eccentricity location Os.

To obtain the dynamic oil film function for any value of $\Omega.t$ it is necessary to consider the geometric time based conditions presented by the shaft synchronous orbit. Now consider the conditions shown if Figure 198 for a cylindrical orbit.

When considering the dynamic shaft orbit it is now necessary to determine the new relationships between the oil film thickness function and the dynamic position of the shaft. Due to the additional time dependant geometric component of the bearing–rotor the oil film function equation 8.3.10 cannot be defined with respect to only one variable θ. Now also it is a function of time t. The approach taken here is to determine an effective eccentricity ratio for any given point of the shaft rotation cycle, this is denoted as e' in Figure 198. This dynamic eccentricity can then be used in direct substitution of *e* in equation 8.3.8 to obtain the oil film thickness for any given point in time of the rotating shaft.

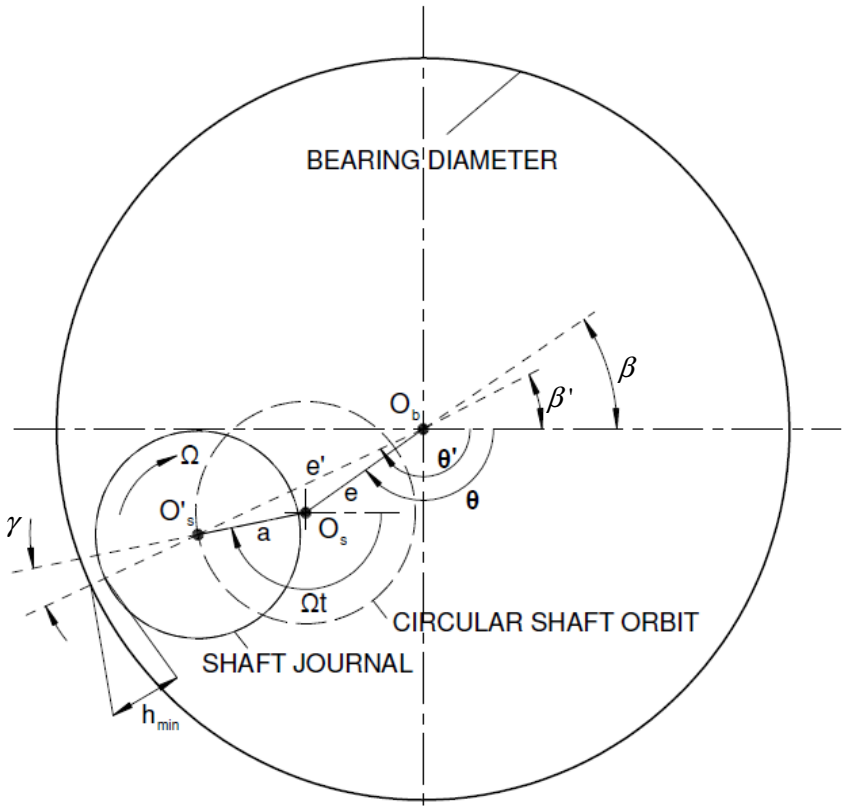

Figure 198 Cylindrical whirl orbit geometric conditions in a plain bearing

However it has to be recognised that associated with the magnitude of the new dynamic eccentricity there is an associated change in the instance at which the direction of eccentricity occurs with respect to the shaft rotation angle. Account must be taken of this angular variation γ when referencing it to the datum point or point of interest, see Figure 198.

The corresponding angle θ' is established to define the dynamic location of the minimum film thickness around the bearing with respect to the fixed coordinate system at the bearing centre and the rotating shaft journal centre.

The introduction of a synchronous shaft orbit means that a single location for the minimum film thickness with reference to the bearing shell is no longer true. Account of how this changes with relation to a single revolution needs to be considered when relating the film thickness to the rotating shaft journal. In a steady state assumption, the point of minimum film thickness at any point of rotation will follow the trajectory of the eccentricity ratio *e*. However with a shaft orbit introduced, the location of the minimum film thickness on the

bearing surface will oscillate around the bearing circumference as the shaft rotates and the orbit is traversed. As can be seen from Figure 198 for a circular orbit when the points O_b, O_s and O'_s are in line, (i.e. at $\Omega.t = \theta = \theta + \pi$), the relative angle that is generated between $O_bO'_s$ and the minimum film thickness for any point in the shaft rotation is denoted by γ. This angle is important as this point has an influence on where the cavatitive region in the bearing begins and how the thermal conditions generated in the oil film relate to the journal rotational datum's.

In the referenced literature [19,30] it has been taken that the point of minimum film thickness is the hot spot for the rotating journal and this point tracks around the shaft. The geometric relationships discussed above suggest that this assumption may not always be appropriate as, due to the shift in minimum film thickness location, other sections of the rotating journal may see lower aggregate film thickness than the point at which $\Omega.t = \theta$. Also any time dependant functions with regard to the heating of the lubricant or the heat transfer to the journal will result in the location of the shaft hot spot being moved to some other circumferential location on the journal, i.e. the time derivative effects seen in the model of Keogh et al [9].

The equations relating the dynamic geometric conditions for the plain bearing are now derived. From Figure 198 the dynamic effective eccentricity ratio can be expressed as :

$$e'^{\,2}_{(t)} = (e.\cos(\theta) + a.\cos(\Omega.t))^2 + (e.\sin(\theta) + a.\sin(\Omega.t))^2 \quad \text{Eq. 8.3.11}$$

Expanding out equation 8.3.11 yields

$$e'^{\,2}_{(t,\theta)} = e^2.\cos^2(\theta) + 2.a.\cos(\Omega.t).e\cos(\theta) + a^2.\cos^2(\Omega.t).....$$
$$e^2.\sin^2(\theta) + 2.a.\sin(\Omega.t).e\sin(\theta) + a^2.\sin^2(\Omega.t) \quad \text{Eq. 8.3.12}$$

Noting the trigonometric identify $\cos^2(\theta) + \sin^2(\theta) = 1$ then

$$e^2.\cos^2(\theta) + e^2.\sin^2(\theta) = e^2$$
$$a^2.\cos^2(\Omega.t) + a^2.\sin^2(\Omega.t) = a^2 \quad \text{Eq. 8.3.13}$$

Substituting into equation 8.3.2 with some work gives

$$e'_{(t)}{}^2 = e^2 + a^2 + 2.e.a.(\cos(\Omega.t).\cos(\theta) + \sin(\Omega.t).\sin(\theta)) \quad \text{Eq. 8.3.14}$$

Finally applying the trigonometric identity

$$\cos(a \pm b) = \cos(a).\cos(b) \mp \sin(a).\sin(b)$$

allows equation 8.3.3 to be reduced to

$$e'_{(t)} = \sqrt{e^2 + a^2 + 2.e.a.\cos(\theta - \Omega.t)} \quad \text{Eq. 8.3.15}$$

Where equation 8.3.15 is the expression for determining the effective eccentricity ratio for any point in a circular shaft orbit.

The angle of instance θ' of the dynamic eccentricity in the bearing is given by:

$$\theta'_{(t)} = \tan^{-1}\left(\frac{e.\cos(\theta) + a.\cos(\Omega.t)}{e.\sin(\theta) + a.\sin(\Omega.t)}\right) \quad \text{Eq. 8.3.16}$$

Equations 8.3.15 and 8.3.16 can be written in non dimensional from by introducing $C_{r,}$ where equation 8.3.17 and 8.3.18 are the non dimensional eccentricity ratio and angle of instance respectively for any point around the shaft orbit.

$$\varepsilon'_{(t)} = \sqrt{\varepsilon^2 + \sigma^2 + 2.\varepsilon.\sigma.\cos(\theta - \Omega.t)} \quad \text{Eq. 8.3.17}$$

$$\theta'_{(t)} = \tan^{-1}\left(\frac{\varepsilon.\cos(\theta) + \sigma.\cos(\Omega.t)}{\varepsilon.\sin(\theta) + \sigma.\sin(\Omega.t)}\right) \quad \text{Eq. 8.3.18}$$

where σ is non dimensional circular orbit radii $\frac{a}{c_r}$

From Figure 198 and the above equations it is now possible to describe the angle $\gamma'_{(t)}$ relating the minimum film thickness and the angle of rotation of the shaft $\Omega.t$.

Where $\theta_A = \theta - \theta'$, therefore

$$\gamma'_{(t)} = \Omega.t - \theta_A - \theta = \Omega.t - 2.\theta + \theta' \quad \text{Eq. 8.3.19}$$

Equation 8.3.17, 8.3.18 and 8.3.19 can now be introduced to equation 8.2.10 to give the film thickness as a function of time t for any angle $\Omega.t$ around the shaft orbit.

$$h_{(t,\theta)} = C_r(1 + \varepsilon'_{(t)}.\cos(\theta - \beta - \gamma'_{(t)})) \quad \text{Eq. 8.3.20}$$

The details necessary to establish the whirl orbit parameters need to be determine from either experimental results or by means of a rotordyanmic response analysis. The whirl orbit characteristics are heavily dependant on the stiffness and damping conditions within a bearing oil film and also the rotordynamic conditions in the rotor itself can also have a notable influence. For the purposed of the work presented here the orbit data is assumed to be a known set of data.

It should be noted at this point that in most bearings, a purely circular whirl orbit rarely occurs and that some form of ellipse generally results. The same principle of calculation can be applied to a shaft exhibiting an elliptical shaft orbit as defined in chapter 2 Figure 14. However for the purposes of the oil film perturbation analysis the orbit ellipse can be considered as separate forward and backward circular whirl orbits. The effective journal centre can then be determined for any point around the shaft whirl orbit at time *t*.

It was presented by Keogh et al [9] that it is possible to degenerate any elipse into forward and backward whirl orbit components. The forward and backward whirl components for a given elliptical shaft orbit can be established by :

$$\sigma_1 = \frac{a+b}{2} \ , \ \sigma_2 = \frac{a-b}{2}$$

where : a and b are the ellipse major and minor axis
σ_1 and σ_2 are forward and backward non dimensional whirl radii respectively
ψ is the ellipse rotation angle

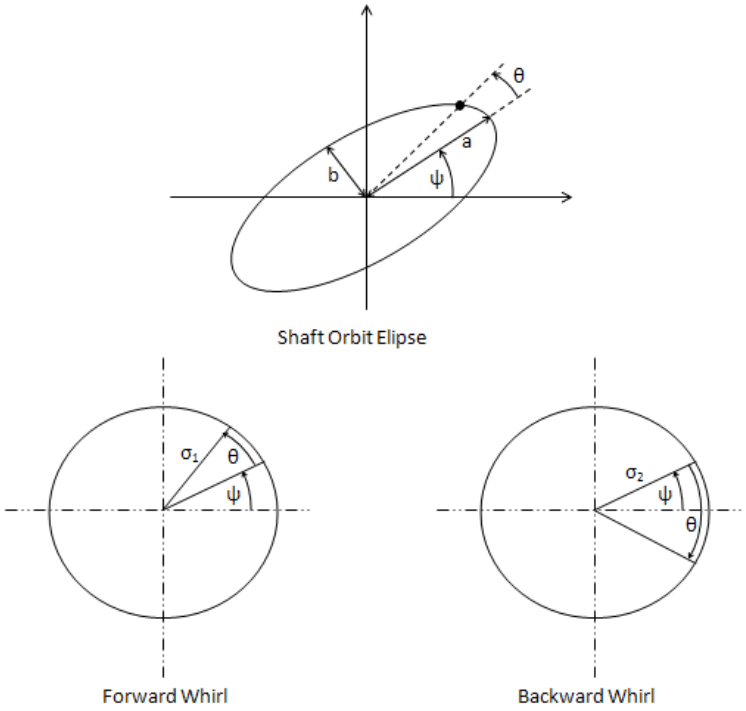

Figure 199 Forward and backward whirl orbits from vibration ellipse

Application to Non Cylindrical Offset Half Bearing

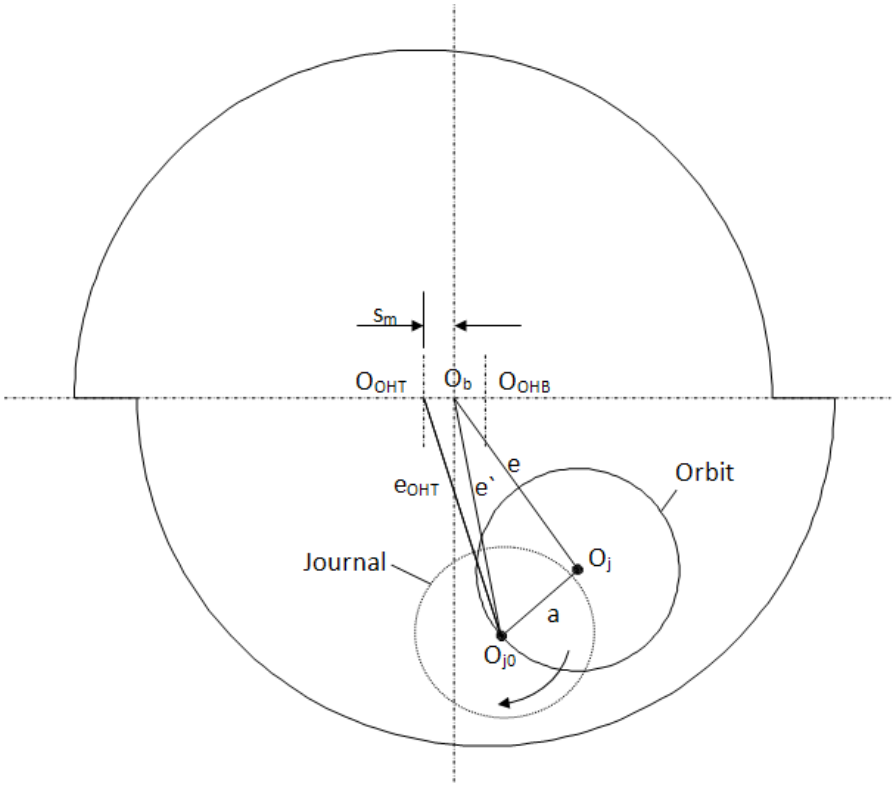

Figure 200 Fixed Geometry Offset Half Dynamic Orbit Relationships

In the same way the effective dynamic eccenticty *e`* for a time *t* was used for the plain cylindrical bearing we can now define an effective eccentricity with respect to either the top or pottom pads by introduing the pad offset s_m. The effective dynamic eccentricity for the top pad then becomes defined by $O_{OHT}O_{j0.}$ e_{OHT} can then be used to for the necesary dynamic orbit calculations as is outlined above. For the steaty running postion relative to each pad the effective steady state eccentricity is given by $O_{OHB}O_j$ and $O_{OHT}O_j$ for bottom and top pads respectivley.

The oil film and energy solutions are then applied to the top and bottom pad for the appropriate θ range. In that when θ is in the top half pad then e_{OHT} is used and when in the bottom range then e_{OHB} is applied. The conditions for the energy solution are the same as that used for the two oil inlet bearing case.

8.3.2. Bearing Temperature Distribution Model

To suitably represent the temperature conditions and distribution within the bearing, it is necessary to considerer the coupled conditions of the hydrodynamics and the thermodynamics. A number of models have been presented in the literature to this end but generally what they all share in common is that for a single load case the level of complexity associated with both analytical or numerically building and then solving the model is high. In all but a small few [9,10,17,18] the shaft journal is considered either isothermal or of uniform temperature during the analysis. The intent of the work covered here is to present a simplified model which can be applied and computed with relative ease when applied to a range of bearing geometries.

The approach developed here is based on the development of a model which considers the hydrodynamic conditions as interrelated but not analytically coupled. This is attempted by considering a pre-determined solution to the Reynolds equation to establish the geometric conditions governing the oil film geometric characteristics. These geometric conditions are then used to establish an energy development model which is used to calculate the temperature distribution within the bearing. The hydrodynamics and thermodynamics can be associated by an initial iterative routine which can be used to determine an acceptably converged condition for the bearing geometric running position. This is done by re-evaluating the Reynolds

equation for new ‘effective’ operating oil film temperatures. However, it must be pointed out here that the focus of information presented in this section is not associated with developing this process, it is principally intended as a method to enable the necessary temperature boundary conditions to be established for a dynamically vibrating shaft, based on initial steady state running conditions and response characteristics when the Reynolds solution problem has been converged.

To establish the desired temperature distribution within the bearing oil film a form of energy balance model has to be established. As the purpose of the work is to allow for a high number of calculations to be performed in a cumulative procedure within the time domain, it is necessary to develop a numerically effective analytical description of the temperature to provide the necessary boundary conditions. To this end a number of assumptions have to be introduced to allow acceptable solution simplifications, methods and computation times to be achieved whilst maintaining, what the author considers to be, an acceptable level of accuracy when modelling the thermally dynamic physical system.

Firstly consideration of the oil film in the bearing is required and the energy balance within the system. In practice we are dealing with a three dimensional system with energy flows in each of these planes. To reduce the complexity of the problem the model will be reduced to a two dimensional case. In this simplification it assumed that the lubricant film temperature and heat flux to the bearing shell and journal are constant in the z direction and are represented as axially averaged values/functions. Now considering the element dx shown in figure 201 and making the following principle assumptions:

1. Temperature is constant across oil film (i.e. averaged cross film temp)
2. Steady state conditions are assumed within the element and all convective heat transfer has reached steady conditions.
3. The temperatures at the bounding surfaces of the bearing shell and the journal are equal to the temperature of the oil film
4. Conduction terms within the oil film are not considered
5. ISO viscous conditions are assumed within the lubricant
6. Thermal effects are not considered to alter film function geometry
7. Bulk flow laminar conditions are assumed

It can be seen from the assumptions that (2) presents a slight contradiction as the assumption of steady state conditions is incompatible with the transient type analysis to be performed within the finite difference model. The problem that this presents is explored and discussed later with justifications as to how the assumption can be applied without significant impact of the accuracy of the boundary conditions within the model presented.

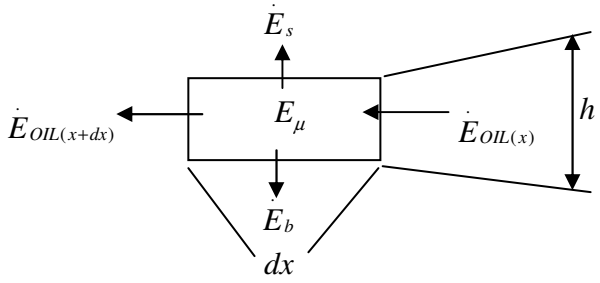

Figure 201 Energy balance in an element of lubricant *dx*

Applying an energy balance to the model described above it is possible to write that:

$$\dot{E}_{OIL(x+dx)} = \dot{E}_\mu + \dot{E}_{OIL(x)} - \dot{E}_b - \dot{E}_s \quad \text{Eq. 8.3.21}$$

The energy generated in the element dx is produced as a result of the viscous shear that takes place in the oil film between the bearing surface and the rotating journal. The velocity profile in the oil film will vary between a linear and parabolic type relationship due to Couette and Poiseuille flow terms. This type of profile results in variable shear stress across the oil film, making analytical description more difficult. To aid in simplification of the analytical description a Petroff type of assumption is applied whereby a linear velocity profile is assumed across the oil film, as has been commonly applied by several of the literature sources [19,43].

The assumption relating to the cross film linear oil film profile for shear stress and also for circumferential flow terms can be justified by the simplicity it introduces and by the small effects it has for moderately loaded bearings. For bearings where the eccentricity ratio and developed pressures are in the region of <0.8 ε then the velocity profile will follow very closely to the assumption. Only where high eccentricities and high pressure gradients are present does the flow profile have a very significant effect on the net shear forces.

The shear stress in the oil film is given by $\tau = \mu.\frac{du}{dy}$ where $\frac{du}{dy}$ is the gradient of the velocity profile across the oil film. Applying the linear velocity profile assumption this can now by written as :

$$\tau = \mu.\frac{U}{h} = \frac{\Omega.R_s}{h} \quad \text{Eq. 8.3.22}$$

Considering the element *dx* the energy in the element due to viscous shear is given by :

$$dE_\mu = U.\tau.du \quad \text{Eq. 8. 3.23}$$

Substituting for τ and noting that $du \approx R_s.d\phi$ into equation gives the following, where *h* is dependent on ϕ so it is possible to substitute *h* for the oil film function into equation 8.3.23 yielding :

$$dE_\mu = \frac{\Omega^2.R_s{}^3.\mu.L_b}{h_{(\phi)}}.d\phi = \frac{\Omega^2.R_s{}^3.\mu.L_b}{c_r.(1+\varepsilon.\cos(\phi))}.d\phi \quad \text{Eq. 8. 3.24}$$

From equation 8.3.24 it is possible to describe the energy accumulation around the bearing as the advection or circulating oil passes through the bearing oil film gap. Solution of the above equation can, with some work, be solved by direct integration with respect to ϕ. The $\frac{1}{(1+\varepsilon.\cos(\phi))}$ term presents some analytical challenge but applying the following integration procedure equation 8.3.30 results.

Separating out effective constants

$$E_\mu = \frac{\Omega^2.R_s{}^3.\mu.L_b}{c_r.}.\int \frac{d\phi}{(1+\cos(\phi))} \quad \text{Eq. 8. 3.25}$$

Using substitutes for $t = \tan\left(\frac{\phi}{2}\right)$ where

$$1+\varepsilon.\cos(\phi)=1+\varepsilon.\frac{(1-t^2)}{(1+t^2)} \quad \text{Eq. 8.3.26}$$

With some work gives

$$\int\frac{d\phi}{1+\cos(\phi)}=2.\int\frac{dt}{A_1-(1+\varepsilon).t^2} \quad \text{where} \quad A_1=1+\varepsilon \quad \text{Eq. 8.3.27}$$

Using the standard integrals $\int\frac{1}{1+x^2}.dx=\tan^{-1}(x)+C$

and $$\int\frac{1}{A+x^2}.dx=\frac{\sqrt{A}}{A}.\tan^{-1}\left(\frac{\sqrt{A}.x}{A}\right)+C \quad \text{Eq. 8. 3.28}$$

Equation 8.3.28 can be reduced to the following equation with subs for A_1

$$\int\frac{d\phi}{1+\cos(\phi)}=\frac{2}{1+\varepsilon}.\sqrt{\frac{1+\varepsilon}{1-\varepsilon}}.\tan^{-1}\left(\frac{1-\varepsilon}{1+\varepsilon}.\sqrt{\frac{1+\varepsilon}{1-\varepsilon}}.\tan\left(\frac{\phi}{2}\right)\right)+C \quad \text{Eq. 8. 3.29}$$

Substituting into equation 8.3.25 gives

$$E_\mu=\frac{2.\Omega^2.R_s^3.\mu.L}{c_r.(1+\varepsilon).\sqrt{\eta}}.\tan^{-1}.\left(\frac{\eta}{\sqrt{\eta}}.\tan\left(\frac{\phi}{2}\right)\right)+C \quad \text{Eq. 8. 3.30}$$

where $\eta=\frac{1-\varepsilon}{1+\varepsilon}$

Equation 8.3.30 allows direct calculation of the energy accumulation in the oil around the bearing. The final step is to solve for the constant of integration which is dependent on the oil inlet location relative to the minimum oil film thickness point. In all information presented to date, and that provided in the literature, the oil inlet is assumed to be 180 degrees around from the point of minimum film thickness. Using this assumption the boundary conditions become $E_\mu=0$ when $\phi=0$ and therefore $C=0$, resulting in equation 8.3.32 proving the complete solution. However in practical bearings this is rarely the case. Just as in situations where the type of bearing has 2 or more inlets or due to variation in the direction of applied loads the attitude angle changes. As

an example, in the bearings on the experimental test rig, the minimum oil film thickness point was ~120 degrees from the inlet. To cover these more probable conditions, the boundary conditions can be applied such that if we say $E_\mu = 0$ when $\phi = \pi - \theta$ (See Figure 198) then the constant of integration becomes:

$$C = -\frac{2.\Omega^2.R_s^3.\mu.L}{c_r.(1+\varepsilon).\sqrt{\eta}}.\tan^{-1}.\left(\frac{\eta}{\sqrt{\eta}}.\tan\left(\frac{\beta}{2}\right)\right) \quad \text{Eq. 8.3.31}$$

Substituting into equation 8.3.30 and simplifying gives

$$E_\mu = \frac{2.\Omega^2.R_s^3.\mu.L}{c_r.(1+\varepsilon).\sqrt{\eta}}.\left(\tan^{-1}\left(\frac{\eta}{\sqrt{\eta}}.\tan\left(\frac{\theta+\beta}{2}\right)\right)-\tan^{-1}\left(\frac{\eta}{\sqrt{\eta}}.\tan\left(\frac{\beta}{2}\right)\right)\right) \quad \text{Eq. 8. 3.32}$$

Equation 8.3.32 describes the rate of heat generation accumulated around the bearing and can be used to gain an understanding of the power loss and amount of energy being distributed around the bearing. It is used later in the finite difference model help establish the bearing inlet conditions. However, in order to obtain the required temperature conditions of the oil film, the continuity of flow conditions must be maintained whereby the volume of oil available in the oil gap is considered. The above equation 8.3.32 does not allow for continuity of flow around the bearing and as such film temperatures cannot be established from this equation.

As the oil gap converges the volume of oil is reducing with the surplus lubricant being expelled from the sides of the bearing, i.e. side leakage. This side leakage takes some of the accumulated energy out of the bearing and oil film, leaving only the remainder in the oil film to continue its route around the bearing circumference. Therefore the application of equation 8.3.32 would result in artificially high temperatures being progressively established around the bearing. To account for the effects of continuity of flow it is necessary to account for the cumulative rate of side leakage, as the lubricant moves around the bearing, into equation 8.3.32. To do this in energy terms alone, as above, becomes a more challenging with respect to the associated direct integration. Therefore the same energy balance principle is applied to the model only this time introducing temperature into the bounding equations. The energy balance model can now be considered as below:

$$\dot{E}_{\mu} = \dot{E}_{OIL(x+dx)} - \dot{E}_{OIL(x)} + \dot{E}_b + \dot{E}_s \quad \text{Eq. 8. 3.33}$$

where $\dot{E}_b$ and $\dot{E}_s$ are assumed to be 0.

The above base model construction is now similar to the one applied by Balbahadur [19] but in this case the journal and bearing interfaces are considered to be isothermal with respect to the oil film, and in effect the energy dissipated from the film into the journal and bearing have been neglected. This assumption significantly simplifies the resulting differential equation. However the impact of this assumption must be validated for the range of conditions that would be experienced in such bearings in application to ensure this does not significantly impact the temperature result of the oil film and journal.

Justification of Isothermal Assumption

Considering the viscous shear energy term and the energy loss term due to heat transfer into the journal to be given by :

$$E_{\mu} = \omega.R_j.\tau.dx.dz = \frac{\omega^2.R_j^2.\mu.dx.dz}{h} \qquad E_b = E_s = H.\left(T_{b,s} - T_{amb}\right).dx.dz \quad \text{Eq. 8.3.34}$$

The fraction of energy lost from the oil due to the viscous oil shear for a given element can be determined.

$$\frac{E_{b,s}}{E_{\mu}} = \frac{\omega^2.R_j^2.\mu}{h.H.\left(T_{b,s} - T_{amb}\right)} \quad \text{Eq. 8.3.35}$$

Using typical values for a bearing running under fairly moderate conditions where the journal velocity $V_j = \omega.R_j$, these can be considered to be V_j=15m/s, operating viscosity μ = 0.05 N.s.m^{-1}, film thickness h=75 μm, $\Delta T_{j\text{-}b}$=50°C. A heat transfer coefficient H=50 W/m^2 is applied between the lubricant and shaft/journal. This results in a fraction of heat lost from the film to the journal of ~1.5%. This demonstrates that the impact on the energy state in the oil film due to the heat loss to the journal can be neglected for typical operating conditions without significant impact on the calculated lubricant temperature. As the bearing speed increases, this error would also tend to reduce due to the higher rate of energy generation and reduced $\Delta T_{j\text{-}b}$ as the shaft temperature increases.

Removing the journal-bush energy transfer term from equation 8.3.33 results in the simplified equation :

$$0 = E_{\mu} - (E_{OIL(x+dx)} - E_{OIL(x)}) = E_{\mu} - E_{OIL(x+dx)} + E_{(x)} \quad \text{Eq. 8.3.36}$$

Substituting the relevant terms :

$$0 = \Omega.R_s.\tau.L.dx - \frac{\rho.h.\Omega.R_s.c_L.L_b}{2}.(T + dT) + \frac{\rho.h.\Omega.R_s.c_L.L_b}{2}.T \quad \text{Eq. 8. 3.37}$$

Where simplification gives:

$$0 = \Omega.R_s.\tau.L.dx - \frac{\rho.h.\Omega.R_s.c_L.L_b}{2}.dT \quad \text{Eq. 8. 3.38}$$

Re-writing and further simplifying the change in film temperature term *dT* can be expressed by

$$dT = \frac{2.\tau.L_b}{\rho.h.c_L}.dx \quad \text{Eq. 8. 3.39}$$

Substituting for τ , h and $dx = R.d\phi$

$$dT = \frac{2.\mu.R_s^2.\Omega.L_b}{\rho.c_L.c_r^2.(1+\varepsilon.\cos(\phi))^2}.d\phi \quad \text{Eq. 8. 3.40}$$

Integrating to obtain *T* as a function of ϕ

$$T = \frac{2.\mu.R_s^2.\Omega.L_b}{\rho.c_L.c_r^2}.\int \frac{d\phi}{(1+\varepsilon.\cos(\phi))^2} \quad \text{Eq. 8. 3.41}$$

Where it can be found that :

$$\int \frac{d\phi}{(1+\varepsilon.\cos(\phi))^2} = -\frac{2.\sqrt{\eta}}{(\varepsilon^2-1)}.\tan^{-1}\left(\frac{\tan\left(\frac{\phi}{2}\right)}{\sqrt{\eta}}\right).\left[\frac{\varepsilon}{1+\varepsilon}-1\right] + \frac{2.\varepsilon.\tan\left(\frac{\phi}{2}\right)}{(\varepsilon^2-1).(1+\varepsilon).\left(\frac{1}{\eta}.\tan^2\left(\frac{\phi}{2}\right)+1\right)} + C$$

Eq. 8.3.42

and $\eta = \dfrac{1+\varepsilon}{1-\varepsilon}$

Substituting equation 8.3.42 into equation 8.3.41

$$T_L = \frac{4.\mu.R_s^2.\Omega.L_b.\sqrt{\eta}}{\rho.c_L.c_r^2.(1-\varepsilon^2)}.\tan^{-1}\left(\frac{\tan\left(\frac{\phi}{2}\right)}{\sqrt{\eta}}\right).\left[\frac{\varepsilon}{1+\varepsilon}-1\right]+\frac{2.\varepsilon.\tan\left(\frac{\phi}{2}\right)}{(\varepsilon^2-1).(1+\varepsilon).\left(\frac{1}{\eta}.\tan^2\left(\frac{\phi}{2}\right)+1\right)}+C$$

Eq. 8.3.43

To obtain the constant of integration the boundary condition can be applied that $T_L = 0$ when $\phi = \pi - \theta$.

$$C = -\frac{4.\mu.R_s^2.\Omega.L_b.\sqrt{\eta}}{\rho.c_L.c_r^2.(1-\varepsilon^2)}.\tan^{-1}\left(\frac{\tan\left(\frac{\beta}{2}\right)}{\sqrt{\eta}}\right).\left[\frac{\varepsilon}{1+\varepsilon}-1\right]-\frac{2.\varepsilon.\tan\left(\frac{\beta}{2}\right)}{(\varepsilon^2-1).(1+\varepsilon).\left(\frac{1}{\eta}.\tan^2\left(\frac{\beta}{2}\right)+1\right)}$$

Eq. 8.3.44

Substituting into equation 8.3.43 gives the general solution for oil film lubricant temperature around the bearing.

$$T_L = T_{SUP} + \frac{4.\mu.R_s^2.\Omega.L_b.\sqrt{\eta}}{\rho.c_L.c_r^2.(1-\varepsilon^2)}.\left[\tan^{-1}\left(\frac{\tan\left(\frac{\theta+\beta}{2}\right)}{\sqrt{\eta}}\right)-\tan^{-1}\left(\frac{\tan\left(\frac{\beta}{2}\right)}{\sqrt{\eta}}\right)\right].\left[\frac{\varepsilon}{1+\varepsilon}-1\right]+.....$$

$$.....\frac{2.\varepsilon}{(\varepsilon^2-1).(1+\varepsilon)}.\left[\frac{\left(\tan\left(\frac{\theta+\beta}{2}\right)\right)}{\left(\frac{1}{\eta}.\tan^2\left(\frac{\theta+\beta}{2}\right)+1\right)}-\frac{\left(\tan\left(\frac{\beta}{2}\right)\right)}{\left(\frac{1}{\eta}.\tan^2\left(\frac{\beta}{2}\right)+1\right)}\right]$$

Eq. 8.3.45

Due to the fairly involved integration process full details are not provided here for the solution of $\int \frac{d\phi}{(1+\varepsilon.\cos(\phi))^2}$ but details can be found in appendix C.

The application of the equation 8.3.45 results in the following oil film temperature profile around the bearing for a single and dual oil inlet arrangement respectively. The characteristic of the oil film temperature profile

will change significantly as the angle between the oil inlet and the minimum film thickness is varied. This results in a more drastic increase temperature occurring as the distance between the inlet and minimum film point is decreased below $\theta < \pi$. Figure 202 shows the temperature profile for the same bearing geometry but now with two inlets and θ reduced from π to $\frac{\pi}{2}$.

It should be noted here that the temperatures are non dimensional as an arbitrary heating term has been used for convenience with an effective oil inlet temperature of 0 to each pad. The data is presented only for comparative purposes to demonstrate the temperature profiles generated by a particular bearing with the eccentricity ratio and attitude angles applied.

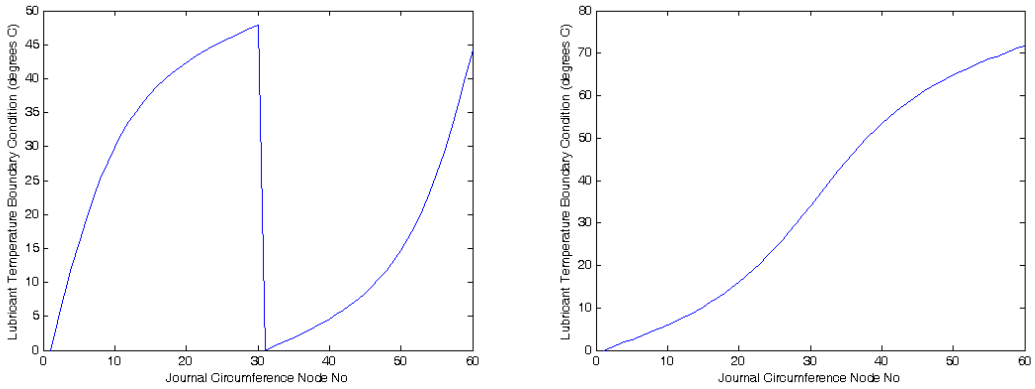

Figure 202 Calculated lubricant temperature distributions for a single and double inlet bearing

8.4 Cavatitive Region

As mentioned earlier in the section, once the oil film passes the minimum oil film point the circulating oil breaks down and forms a cavative region within the bearing due to continuity of flow. The oil in this region has been shown to form a number of streamers or fingers whereby the remaining space is filled by air drawn in through the sides of the bearing at atmospheric pressure (i.e. no hydrodynamic pressure/lift). In some previous works this area has been considered as an air oil mixture but it has been shown by testing using transparent bearings full oil films are maintained but across a reduced portion of the bearing width [45]. Figure 203 shows the generalised characteristics observed in the cavative region.

Generally the full film region of the bearing extends from the oil inlet to the point of minimum film thickness $h_{\min}$. Where several inlets are present within the bearing there will be several areas where both full film and cavatitive regions exist. In all of these cases, consideration must be paid to the effects on the temperatures in the oil film and shaft journal due to this partial film or cavatitive region. Additionally care must also be taken as it is possible, although uncommon in practical bearings, under certain circumstances that the cavitation region can be adjacent to an oil inlet. This condition is created due to the eccentricity condition, resulting in a diverging section in the direction of rotation at the location of an oil inlet.

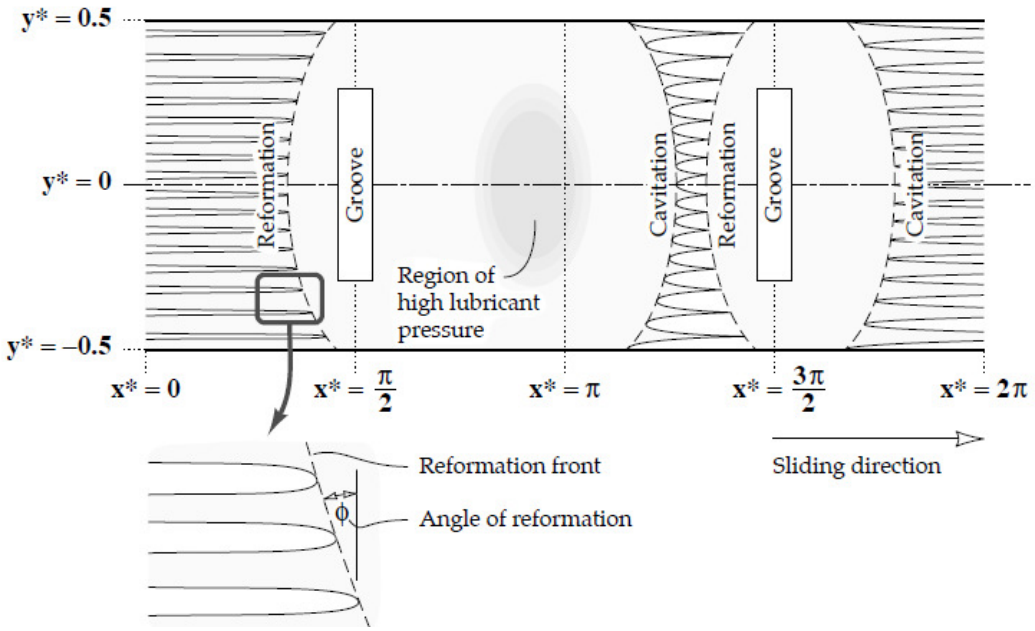

Figure 203 Cavitation region in plain bearing with oil streamers –figure taken from [44].

In practice the temperatures generated in the oil film will remain nominally the same for streams that follow round into the partial film area of the bearing as at a local level full films being maintained (although some heat cooling effects will take place between the streamers and the entrained air). However the amount of energy that is transmitted to the bearing in these locations will be reduced to the wetted area and account for this needs to be provided in the associated equations.

The method for introducing this effect here follows a similar approach as presented by Keogh et al [9] where a fractional film coefficient is used in the cavatitive region. The assumption within the oil film is that the temperatures

are axially averaged across the bearing width. The same principle can be applied to the heat flux in that the cavatitive region the oil film temperature is axially averaged by means of a fractional oil film coefficient. Therefore by modifying equation 8.3.45 to include the fractional film coefficient such that:

$$T_L = I_{h(\theta)}.T_L \quad \text{Eq. 8.4.1}$$

Where $I_{h(\Omega.t)}$ is the fractional film coefficient with boundary conditions:

$$I_{h(\Omega.t)} = 1 \qquad \text{for } 0 < \theta < \theta_{h_{\min}}$$

$$I_{h(\Omega.t)} = \frac{h_{\min(\Omega.t)}}{h_{(\Omega.t)}} \qquad \text{for } \theta > \theta_{h_{\min}}$$

The effect of this on the axially averaged oil film temperature can be seen for the single oil inlet example in figure Figure 204.

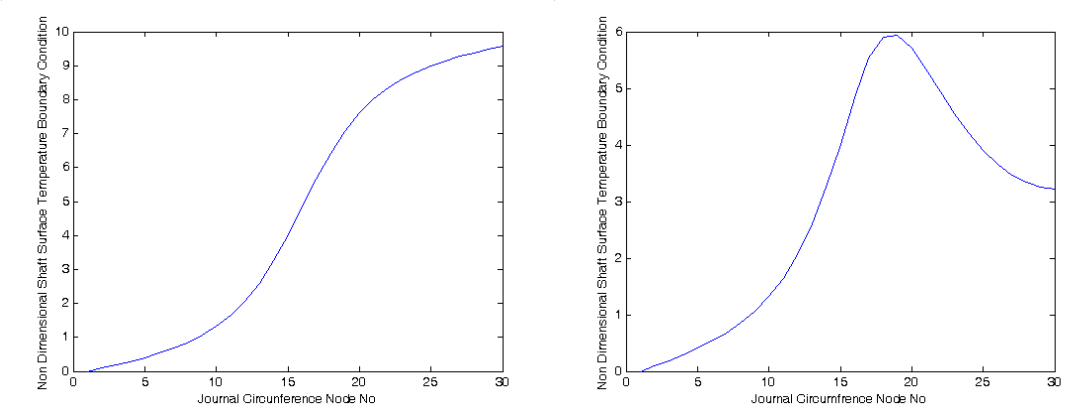

(a) No account for cavitation (b) with fractional film function

Figure 204 Axially averaged oil film temperature for a single oil inlet bearing

Care must be taken to define the converging and diverging sections of the bearing when considering the perturbed orbit solutions as, during the shaft orbit the location of minimum film thickness will oscillate about the peak minimum film thickness location. This is governed by γ as defined earlier in equation 8.3.19.

When considering tilting pad bearings there is no need for the fractional film coefficient as due to the variable geometry and preload within the bearing the pads always tend to result in a converging geometry and full oil film (subject to sufficient oil supply being provide at the pad inlet). However some

consideration is need of the cooling effect at the oil galleries between the operating pads.

The effect of the cavitation region is to lower the effective temperatures in the journal where the net heat flux from the oil film is reduced to the reduction in wetted area. This in turn has an effect on the magnitude of the temperature distribution around the journal.

8.5 Oil Inlet boundary conditions

The final aspect relating to the shaft oil film boundary conditions is to determine the oil inlet temperature to each of the pads. The lubricant supplied to the pad is a mixture of the recirculation flow within the bearing and fresh lubricant supplied via the oil inlets. The determination of the mixing of the oil at the inlet is not a straight forward one and it is not the intention to conduct a detailed evaluation here. However, an attempt is taken to derive an algorithm suitable to provide approximations as to provide sufficient for the bearing oil film model. Keogh et al [9] tackles the problem of the pad oil inlet temperature and the mixing effects that take place, however the methods presented are not applicable here due to the fact no cross film dimension is considered in the thermodynamics.

Considering the fixed geometry bearings, a means of establishing the level of mixing that takes place is required. In fixed geometry bearings the fresh oil supplied to the bearing is principally related to the volumetric difference created in the cavitation region due to the divergent section of the bearing. As the oil inlet is a discontinuity in the temperature distribution model, an algorithm that can determine the effective step temperature change is required.

The oil flow into and around a bearing consists of several mechanisms, which can be considered separately as components of velocity flow, pressure flow, side leakage and recirculation flow.

8.5.1 Side leakage

The side leakage has been highlighted previously in this section and is associated with the oil lost from the bearing during the divergent sections of the bearing due to a reduction in volume of oil film gap. Account for this oil

flow loss is managed within the fundamental film temperature equations presented earlier, Eq 8.3.45 and Eq. 8.4.1.

8.5.2 Re-circulation flow

The recirculation flow is the body of oil that remains following the end of the positive pressure curve in the direction of rotation just after the minimum film thickness point. The oil continues to flow around the bearing accumulating heat until it reaches an oil inlet were it mixes with the fresh supply oil or a further divergent section is encountered and further oil is lost by side leakage. The former of these two conditions is most common in fixed geometry bearings.

The volume flow rate of the re-circulating oil can be expressed by

$$Q_r = \frac{U.h_{(\theta)}.L_b}{2}.I_{h(\theta)} \quad \text{Eq. 8.5.1}$$

8.5.3 Velocity flow

This is the oil that is 'pumped' into the bearing at the oil inlet by means of the rotating shaft and oil velocity profile. The rate of flow is principally governed by the surface velocity of the shaft and the size of the oil inlet. The velocity flow forms the principle means of oil replenishment into the bearing. Taking the Reynolds equation component for circumferential direction flow as given by equation 8.5.2 and applying substitutions we get equation 8.5.3 for the velocity flow component. The velocity flow is calculated from the start of the pressure profile.

$$q_x = \frac{-h^3}{12.\mu}.\frac{\partial p}{\partial x} + (U_1 + U_2).\frac{h}{2} \quad \text{Eq. 8.5.2}$$

$$Q_v = \frac{\omega.R_j.h.L_{inlet}}{2}.\left[1 - \frac{h^2}{6.C_r^2}.\frac{\partial P}{\partial \theta}\right] \quad \text{Eq. 8.5.3}$$

Where L_{inlet} = oil inlet groove length

8.5.4 Pressure Flow

The pressure flow is the flow that is associated with the oil expelled through the sides of the bearing in the region of the oil inlet due to the oil supply pressure. This flow effectively mixes with the re-circulating and velocity flow at the inlet and contributes to the pad inlet temperature. It can have a significant effect on the supply temperature where bearings are operating with low eccentricity.

The amount of pressure flow can be estimated be equation 8.5.4 as presented by Martin [63,64] by :

$$Q_p = \frac{C_d^3 \cdot p_{inlet}}{8.\mu} \cdot \frac{1.25 - 0.25.L_{inlet}}{6.L_b.\left(\frac{L_b}{L_{inlet}} - 1\right)^{\frac{1}{3}}} \cdot \left(\frac{h_{\theta 1}^3 - h_{\theta 2}^3}{C_r^3}\right) + \frac{2.R_j}{6.L_b.\left(1 - \frac{L_b}{L_{inlet}}\right)} \cdot \frac{\theta_2 - \theta_1}{5} \cdot \sum_{\theta=\theta_1}^{\theta=\theta_2} \frac{h(\theta)^3}{C_r^3}$$

Eq 8.5.4

Where θ_1 and θ_2 are the angular extents of the oil inlet.

The above components of flow combine to provide the lubricating and cooling oil within the bearing. Figure 205 presents a single bearing pad and shows how the various components of oil enter and exit the bearing. For bearings with several oil inlets a similar arrangement can be considered for each pad.

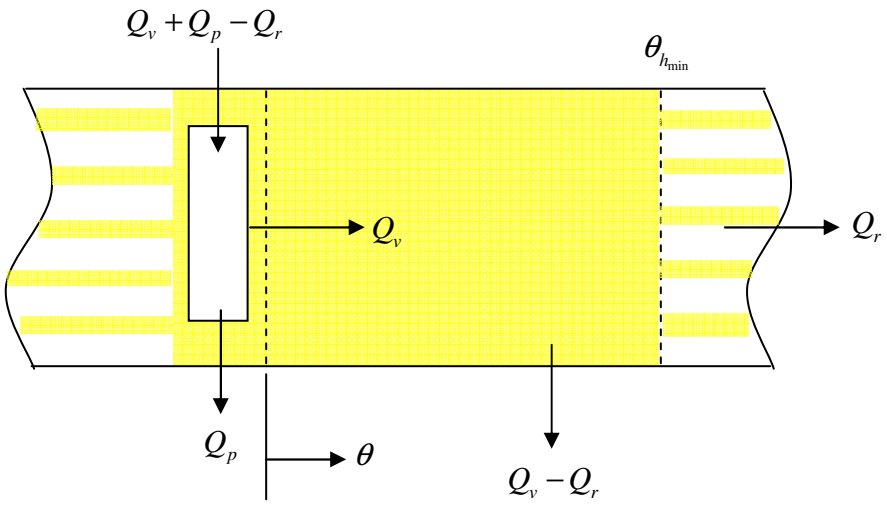

Figure 205 Oil flow schematic for a single inlet bearing

The components of flow can be considered to combine as stated in Figure 205 where the velocity and pressure flow 'top up' the gap left by the cavitation in the divergent section of the bearing.

The following expressions have been derived within this research to determine the oil inlet temperatures to each bearing pad. If perfect mixing is assumed at the oil inlet the pad inlet temperature can be described by equations 8.5.5 and 8.5.6 for a bearing with two oil inlets.

$$T_{o1} = \frac{Q_{r2}.T_{o2} + Q_{r2}.\Delta T_2 + Q_{v1}.T_{SUP} + Q_{p1}.T_{SUP}}{Q_{r2} + Q_{v1} + Q_{p1}} \quad \text{Eq. 8.5.5}$$

$$T_{o2} = \frac{Q_{r1}.T_{o1} + Q_{r1}.\Delta T_1 + Q_{v1}.T_{SUP} + Q_{p2}.T_{SUP}}{Q_{r1} + Q_{v2} + Q_{p2}} \quad \text{Eq. 8.5.6}$$

With some work, the above equations can be resolved to obtain T_{o1} in terms T_{o2} in equation 8.5.7 and hence solve for T_{o2}. Following which T_{o1} can be determined from equation 8.5.5.

$$T_{o2}.\left(1 - \frac{Q_{r1}.Q_{r2}}{(Q_{r2} + Q_{v1} + Q_{p1}).(Q_{r1} + Q_{v2} + Q_{p2})}\right) =$$

$$\frac{Q_{r1}.\Delta T_1 + T_{SUP}.(Q_{v2} + Q_{p2})}{(Q_{r1} + Q_{v2} + Q_{p2})} + \frac{Q_{r1}.(Q_{r2}.\Delta T_2 + Q_{v1}.T_{SUP} + Q_{p1}.T_{SUP})}{(Q_{r1} + Q_{v2} + Q_{p2}).(Q_{r2} + Q_{v1} + Q_{p1})} \quad \text{Eq. 8.5.7}$$

Care needs to be taken when running in bearings with two oil inlets, as dependant on the direction of eccentricity, it is possible for the oil to be supplied into a divergent section with respect to the direction of sliding. Therefore the oil supplied will be insufficient to fully replenish the oil film for a certain distance around the bearing until a convergent section with oil gap condtions matching the oil volume is again reached.

8.6 Lubricant Thermal Perturbations

Having established geometric and energy relationships for the bearing both for the zero orbit and dynamic orbit cases, consideration must now be given to the thermal developments resulting from the shaft synchronous orbit.

It would be a reasonable approach to use the expressions derived above to calculate the energy/temperature conditions around the circumference of the journal for a point around the dynamic whirl orbit and use these as the boundary conditions for the journal finite difference model. The process would then be repeated for a successive number of locations around the dynamic orbit with an appropriate increment of Δt until convergence is attained and the steady temperature differential can be extracted. It was this process that was initially developed and used to solve the journal time domain heating problem.

However this approach introduces several issues due to the physics of the problem. As the fundamental assumption in this approach is the application of steady state conditions for discrete dynamic positions around the whirl orbit, i.e. ‘quasi’ dynamic conditions, this introduces erroneous energy distributions within the oil film. Neglecting the time dependant function of the orbit perturbed temperatures results in a condition where the heat accumulation due to the advection of lubricant is over estimated, and more significantly, results in incorrect dynamic temperature distributions with higher temperatures being tended toward the outflow pad side.

The impact of this energy development discrepancy is a tendancy to over predict the temperature differential present within the shaft journal, which in the limited cases evaluated would appear to equate to approximately 30-40%. Also, and possibly more significantly, is the effect on the circumferential location of the hot spot of the temperature differential with respect to the point of minimum film thickness, in effect the ‘hot spot’ phase angle. The resulting

'hot spot' phase angle with reference to the point of minimum film thickness on the journal produced by the 'steady state' process described above, results in a phase lead when the journal is subjected to a forward circular orbit. This phase lead is in contradiction to the analytical predictions presented in [9] and [18] where phase lag angles between 35° and 55° for plain cylindrical bearings where predicted for the conditions assessed. Also the physical observations presented by de Jongh et al [11] quoted a measured phase lag angle of ~20° between the journal hot spot location and the point of minimum film thickness for the rotor journal, which was running in tilting pad bearings.

The temperature distribution in Figure 206 shows the results of an analysis performed following the above procedure for a bearing within eccentricity ratio of 0.65, running at 10000 rpm with a $0.1C_d$ whirl orbit diameter. The resulting converged ΔT and phase angle was 13.1°C and +61.8° respectively. The temperature distribution was seen to consist of predominantly the fundamental harmonic component, but some small non harmonic components are present, seeFigure 207.

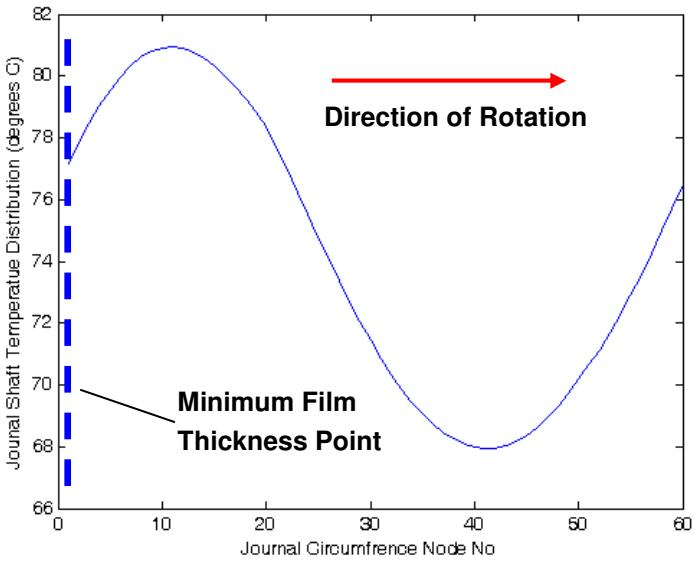

Figure 206 Journal Circumferential Temperature Distribution for 'Steady State' Assumption Boundary Conditions

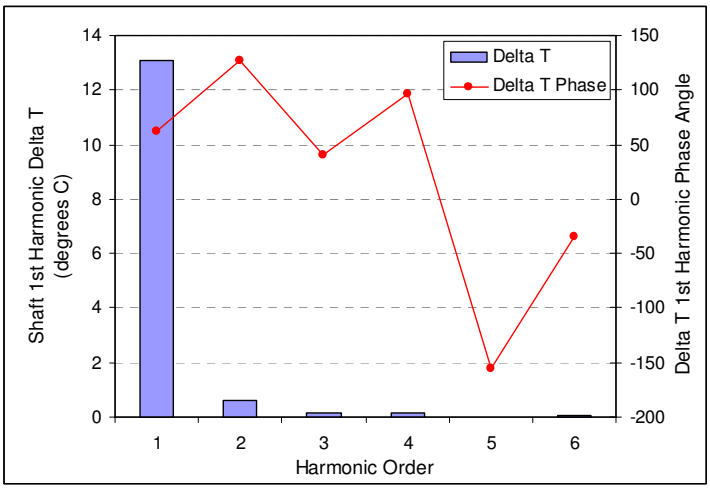

Figure 207Journal Circumferential Harmonic Temperature Distribution for 'Steady State' Assumption Boundary Conditions

As the phase angle is so influential for the rotordyanmic/thermal shaft bend development and in particular the stability of the rotor, it is necessary for any method of temperature differential prediction to introduce a means for establishing this phase angle, of which the 'hot spot' lag contributes a significant amount. The principle effect being overlooked with the procedure described above is the way in which the time dependant energy function (by which heat is generated in the lubricant film) is created and how the mass dependant heat transfer then develops around the bearing, i.e. convective heat transports. It is the convective heat transfer within the lubricant film which results in conditions whereby the greatest thermal source at the journal surface is found upstream of the direction of lubricant flow (i.e. opposite to the direction of shaft rotation) for a forward whirl orbit. This observation of the convective heat transfer being responsible for the hot spot phase lag was briefly quoted by Keogh et al [9] when summarising the analytical results presented in [9].

The evaluation of the transient thermal conditions and resulting convective heat transports presents two notable challenges with respect to its evaluation. Firstly, to model the convective heat transfer effects around the bearing an understanding of the flow conditions around the bearing, and across the film is generally required. It is this cross film aspect which presents the first challenge. The analysis procedure being discussed here has been reduced to a 1 dimensional heat flow problem within the oil film, i.e. no cross film ordinate exists. As previously discussed, significant computational efforts are

introduced when looking in detail at the mass and heat flows within the oil film itself which detracts from the purpose of this modified analysis procedure.

The second significant challenge is that direct simulation of the thermal developments within an orbiting bearing introduces the need for long time constants to allow for a converged 'steady state' periodic dynamic condition to be reached. The solution of such a condition requires many rotations of the shaft and as such many journal orbits which, dependant on the time step, can result in a significant number of calculations. Therefore the use of more complex modelling methods of the oil film become prohibitive and any method developed here is required to result in short to moderate solution times.

The approach presented here to simulate the orbit perturbed oil film temperatures is based around developing a method to provide account for the convective heat transport whilst retaining the 1 dimensional thermal oil film model (i.e. cross film averaged temperature conditions). The associated heat fluxes between the lubricant film and shaft journal are then determined in the time domain from the 1 dimensional film temperature distribution by application of the 2 dimensional oil film/journal spatial conditions. This approach allows for a less complex numerical and computational solution for any given operating condition.

Convective Model

Solution of the time dependant lubrication film temperature due to the orbiting shaft is approximated by considering the oil film to consist of two boundary layers. One of the layers is associated with the static bearing shell and the other is coupled to the rotating shaft surface. The mean cross film temperature at any point in time is the volumetrically averaged temperature of the two layers for any specific location around the bearing.

If an element as per Figure 208 with a specific velocity profile of the oil film is considered then the proportion of lubricant mass affecting to the adjacent element (in direction of sliding) will be a factor *f* of the element volume *dx.h*. Where *f* relates to the proportion of mass flow transporting from one element to another in the direction of sliding. The two bodies of lubricant are now considered to mix together along with any additional heat variation introduced to the element to develop a new bulk temperature for the element *dx*. As the

shaft rotates by the next time step Δt the process repeats to develop a modified temperature condition for *dx*. Hence the film can be considered to consist of 'static' and dynamic lubricant elements both of which vary in temperature over time as the shaft rotates and the orbit processes. The process embodies/provides account of the spatial time derivative element of the energy equation $\frac{\partial T}{\partial t}$ with respect to a fixed location around the bearing.

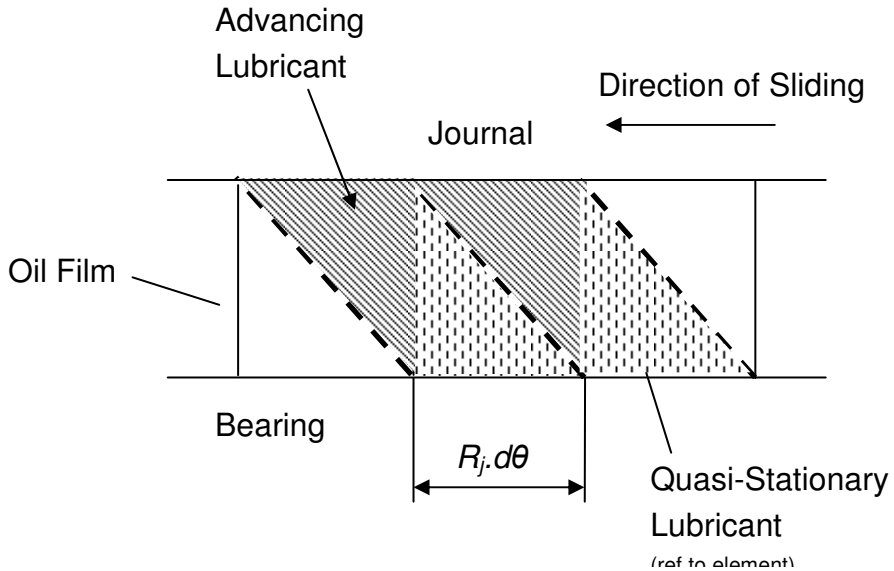

Figure 208 Convective boundary layer concept with simplification of flow modelling

For a shaft exhibiting no whirl orbit then the steady state solution for this condition can be established by equation 8.4.1 as the heat input to the oil film for any angular position around the bearing remains independent of time. However with the introduction of the orbit, the internal heat generation within the lubricant film is periodic with time which results in a non stationary periodic temperature state within the oil film. The convective heat transfer dictates the time dependant distributions as the flow velocity of the lubricant varies across the film from the journal velocity down to zero at the bearing shell boundary. From this analogy it is clear to recognise that a significant number of orbit perturbations will be required before a periodic steady state thermal condition is established.

The convective model outlined above is simulated by numerical means where the oil film is discreatised into a number of angular elements. For each of the angular elements the temperature state of the lubricant T_L will be a function of

the lubricant temperature entering that element by the dynamic boundary layer, the temperature of the 'static' boundary layer for that angular position plus the temperature perturbation at the that angular location due to the shaft orbit with assumed Couette flow :

$$T'_{dx} = \frac{T_{dx-1} + T_{dx}}{2} + \dot{T}_{dx} \quad \text{Eq. 8.6.1}$$

However it is the case that for more heavily loaded bearings that the flow consists of a nonlinear profile due to the Poiseuille flow component which is dependant on the sliding velocity and dp/dθ (i.e. pressure gradient). Such conditions will change the proportions of flow such that the level of advancing fluid and mixing from element to element will change considerably as Figure 209 highlights.

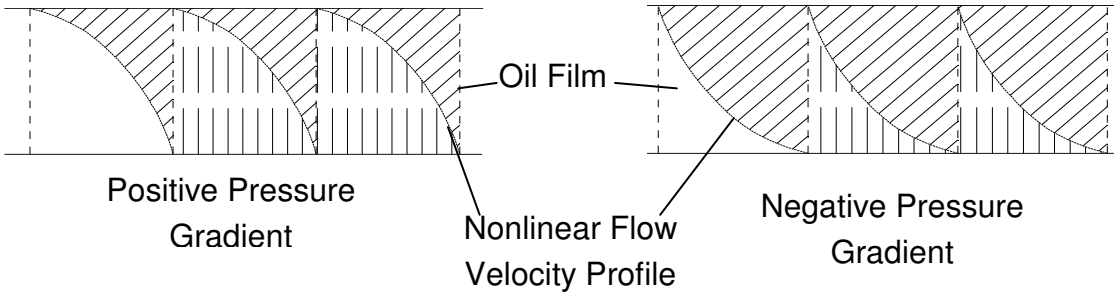

Figure 209 Couette and Poiseuille Flow Due to Pressure Gradient $\frac{\partial p}{\partial \theta}$

Providing for effects of Couette and Poiseuille flow the general form becomes:

$$T_{L(\theta,t)} = f_L.T_{L((\theta-\Delta\theta),(t-\Delta t))} + (1-f_L).T_{L(\theta,(t-\Delta t))} + T_{j(\theta,t)} \quad \text{Eq. 8.6.2}$$

Where T_o is the temperature perturbation due the shaft orbit**

and f_L is a factor to express the proportion of advancing to static boundary flow (i.e. f_L = 0.5 for Couette (linear) flow velocity profile)

** Note this can be a negative temperature due the fact it represents a distortion of periodic variation of the steady oil film temperature.

Where $$T_{j(\theta,t)} = F_{\dot{E}} \cdot \left(\frac{1}{H_{j(\theta,t)}} - \frac{1}{H_{o(\theta)}} \right) . \frac{1}{H_{j(\theta,t)}.c_L.\rho_L} \quad \text{Eq. 8.6.3}$$

And $F_{\dot{E}}$ is a factor collecting together the bearing specific terms (viscosity, speed and bearing dimensions) with $j = 1, 2$ where 1 and 2 indicate forward and backward whirl orbits respectively.

The boundary conditions applied to the perturbed film temperature model were that the temperatures of the lubricant at the oil inlet location were equal to the pad lubricant inlet temperature plus the temperature variation due the shaft orbit T_o. All convective flow was assumed to reset due the mixing occurring at the oil inlet. This condition ensures that the temperature accumulation does not continue to rise with each orbit iteration evaluated, allowing a thermal periodic steady state condition to be determined.

The numerical procedure applied to solve the perturbed heat flow conditions is by means of a time step iterative process. The oil film temperature condition within the bearing is initiated at time t=0 to the zero obit condition and then a stepwise time stepping solution is performed for the discretised angular grid. Each orbit consists of *n* increments and the time stepping procedure is continued for an integer number of obits until a converged film temperature solution is obtained.

It is now important to take the dynamic thermal conditions in the lubricant film and relate this to the temperature conditions within the journal rotor. The thermal transport from the lubricant film to the journal can be expressed as a heat flux from the lubricant to the journal. The heat flux is governed by the gradient of temperature differential at the journal lubricant boundary and the rate of heat transfer from the lubricant film into the journal. The rate of heat transfer across the lubricant film is high when compared to that of the conductive heat transfer of the journal itself, largely due to the significant difference in respective conduction time constants. However some time dependant influence results from the heat transports within the fluid film due to the small values of Δt when operating at high rotational speeds. The instantaneous heat flux from the lubricant film into the rotating journal is given by Gomiciaga et al [18] as :

$$q_{J(\theta_J,t)} = \frac{k_L}{h_{(\theta_J,t)}} . \frac{\partial T_L}{\partial \eta}(\eta = 0, \theta_J, t) \quad \text{Eq. 8.6.4}$$

$q_{(\theta_J,t)}$ = Journal heat flux W/m^2

k_L = Lubricant thermal conductivity

η = Cross film non-dimensional ordinate, where 0 = journal lubricant boundary

Equation 8.8.6.4 relates the heat transfer rate variation as a function of the associated dynamic film thickness, where increased heat transfer occurs for thinner films over a given time period *t*. The heat flux relationship described by equation 8.6.4 can be incorporated into the 1 dimensional film temperature model by substituting $\frac{\partial T_L}{\partial \eta}$ with the difference in mean cross film lubricant temperature and journal surface temperature for a given location a time *t*.

The asymmetric heating of the journal is then determined by the time averaging of the instantaneous heat fluxes, which are based on the combined steady and perturbed temperatures T_o and T_j, around the bearing for each time step Δt for each synchronous orbit. These heat fluxes are then applied as boundary conditions to the journal thermal finite difference model. This results in the temperature differential and phase angle of the hot spot. The converged heat flux conditions are representative of the temperature distribution and hot spot phase angle that results in the shaft journal. Figure 210 shows the heat flux profile for a converged solution for a forward whirl orbit, note the hot spot phase lag which now results with respect to the point of minimum dynamic film thickness.

$$T_{L(\theta,t)} = \left(T_{o(\theta)} + T_{j(\theta,t)}\right).I_{h(\theta)} \quad \text{Eq. 8.6.5}$$

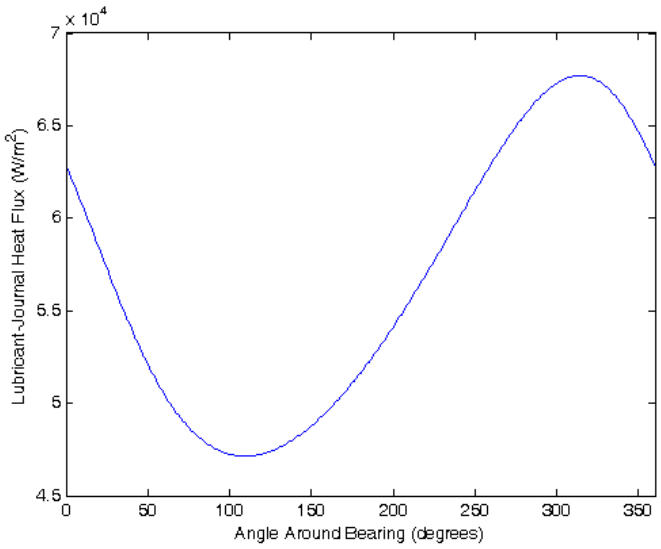

Figure 210 Plot of a converged heat lubricant-journal heat flux
$R_j = 0.0375$ m, $\Omega = 837$ rads/s, c_r=70 μm, $\varepsilon = 0.25$, $\sigma = 0.2$

Key assumptions used in convective modelling :

- Specified factor to govern flow/mixing around bearing circumference
- ISO thermal conditions at lubricant boundaries, i.e. no heat is lost within lubricant film
- No conduction takes place across or circumferentially around the oil film.
- Lubricant film considered as two boundary layers – ‘static’ layer (bearing side) and dynamic layer (journal side)
- Average cross film temperature is the volumetric mean of the dynamic and static lubricant boundary layer temperatures.
- Lubricant temperature conditions are set to be equal to the pad inlet temperature at oil inlet grooves
- Axial conditions are averaged with no axial flow effects
- Laminar flow around bearing
- ISO viscous lubricant properties

8.7 Shaft Bearing Journal Temperature Distribution Model

The analytical and numerical procedures presented in sections 8.2, 8.3 and 8.4 are now applied in a combined procedure to provide a time domain prediction of the thermal heating model of the bearing and journal. The shaft temperature differential and thermal bow are predicted for a given set of operating conditions.

The solution procedure was performed by use of a computer program developed by the author in the MatLab [49] environment as the matrix handling techniques available provide a means of efficient programming and solution times.

8.7.1 Finite Difference Grid

The finite difference grid is constructed in the polar coordinate system and the associated temperature matrices initiated from the desired initial condition temperature of the journal. The number of circumferential and radial control volumes is specified to give suitable resolution and accuracy for the condition being analysed.

The grid resolution is kept to a minimum to result in as larger Δt as possible to give the shortest possible solution times whilst keeping errors and temperature resolution within acceptable boundaries. Figure 211 shows a typical finite difference structured polar grid. The maximum time step increment required is governed by one of two factors. The first factor is that of maintaining a stable solution when stepping through time domain increments as defined by equation 8.7.1. The second consideration when specifying the time step Δt is matching the shaft rotation speed to give a suitable number of points N around the shaft during one rotation. Where the Δt is given by :

$$\Delta t = \frac{2.\pi}{\omega.N} \quad \text{Eq. 8.7.1}$$

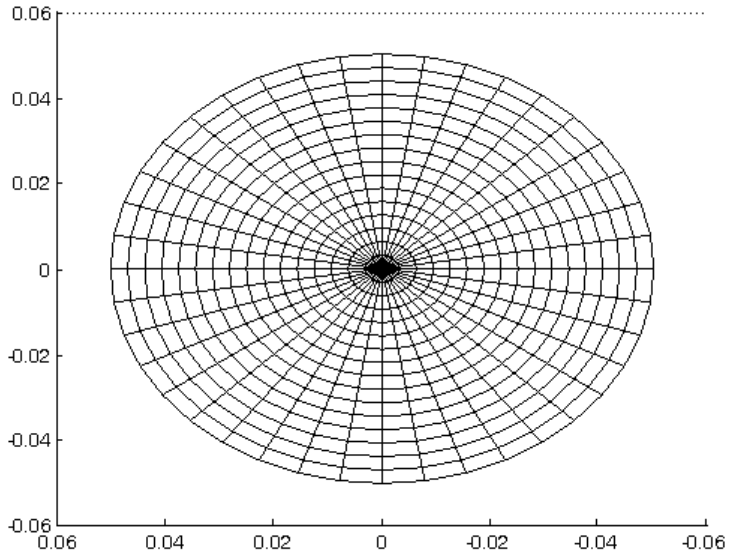

Figure 211 Structured 2D Polar Finite Difference Grid

8.7.2 Initialisation and Boundary Conditions

The temperature matrix of the finite difference grid is initialised to a constant temperature across the journal. The temperature used for the initial condition is based on mean pad oil inlet temperature resulting from the steady state temperature solution given by equation 8.4.1 for the zero orbit condition.

The boundary conditions are then applied to the grid for each time step. The boundary conditions are applied by means of a heat flux to the exterior nodes of the finite difference grid control volumes. The heat flux distribution is determined by the methods outlined in section 8.3 for each time increment and corresponding position around the shaft orbit. After each time step the boundary conditions are shifted round by $\Delta\theta$ in the direction opposite to shaft rotation to simulate the effect of the fixed finite difference grid rotating relative to the bearing.

8.7.3 Time Domain Solution

The model is then solved for a given time period of Δt increments or until convergence is obtained on the temperature within the shaft journal centre node. The temperature convergence is tracked for each orbit cycle and can be

extracted against the time *t*. The complex shaft bend angle development is also tracked against time and this observed with reference to the residual mechanical unbalance location. The development of the thermal bend angle is can then be used to provide an indication or stable and or unstable spiralling vibration for a given set of running conditions in terms of operating speeds, response characteristics and shaft orbits. No specific procedure for stability assessment is presented here, but the procedures presented by Keogh et al [9,10] and Childs et al [35] may be applied to the complex bend angle data resulting from the analysis.

A sample 2D temperature plot of a converged case from the finite difference model is shown in Figure 212. The convergence of the thermal solution is considered to have occurred when the central node temperature variation with time reduces to a predefined level. A typical plot of the central node temperature with iteration cycle (time) is presented in Figure 213. In all converged cases the cross sectional temperature distribution was seen to be of a linear profile.

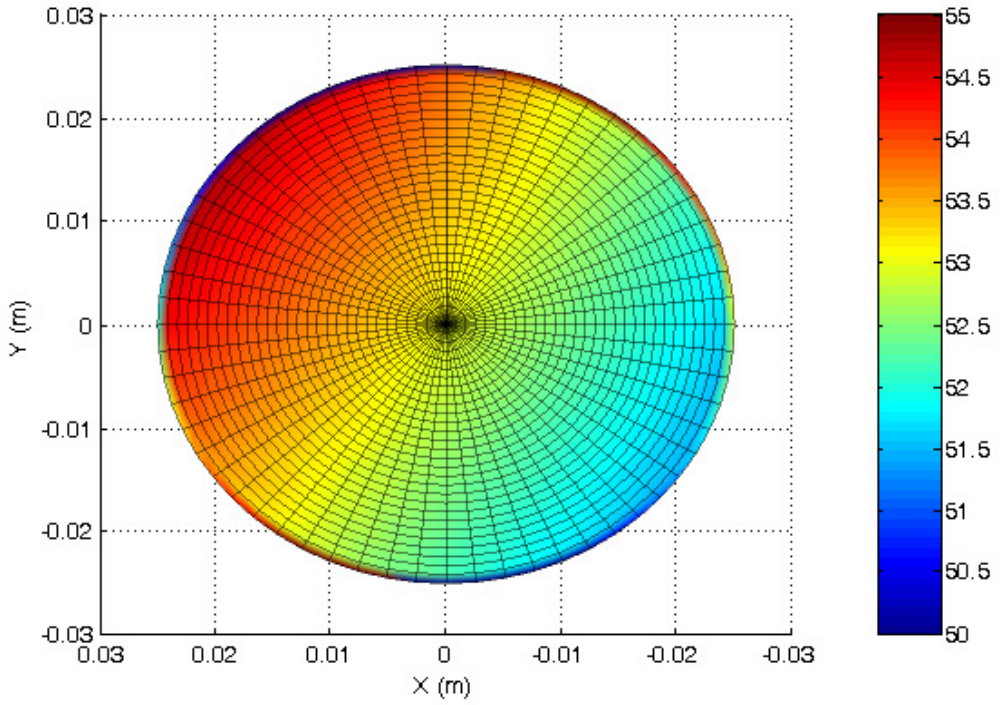

Figure 212 Finite Difference Grid Converged Journal Temperature Distribution 50mm diameter bearing, 5000 rpm, ε=0.3, σ_1=0.2, forward orbit, 2 oil inlets

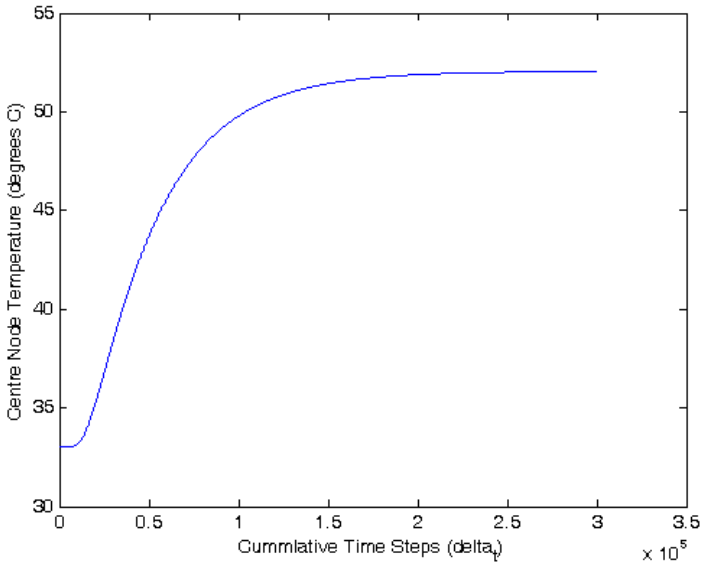

Figure 213 Typical Convergence Trend of Central Node Temperature

Chapter 9

Analysis of Results and Discussion

9. Analysis of Results and Discussion

9.1 Introduction

This chapter provides a detailed review of the experimental test results obtained within this research as presented in section 7. Experimental Results. Review of theoretically produced results, by means of the developed theoretical model, is also presented. Where possible both qualitative and quantitative comparisons are made between the various tests conditions assessed during the experimental work with respect the various key influencing parameters. Specific attention is given to the correlations between the rotordynamic behaviour of the rotor and the measured thermal conditions in the bearing and journal.

Comparison is made between the results of the theoretical models and experimental test results where possible. Attention is also given to the discussion of the methods employed in the existing theoretical work.

The analysis of the experimental and theoretical work addresses the key areas of rotordynamic performance, thermal measurements and theoretical modelling.

9.2 Rotordynamic Performance

The rotor dynamic performance of the rotors and bearings is in general agreement with the analysis performed at the design stage. The rotor critical speed points were located at the expected frequencies for both the fixed and variable geometry bearing arrangements. Figure 214 and Figure 215 present the predicted and measured rotor response for the flexible rotor in fixed geometry and variable geometry bearings respectively. The effects of the residual mechanical unbalance have been removed from the measured results to enable comparison to the calculated rotor response. The calculated and measured results data presented relate to the discrete added mass only.

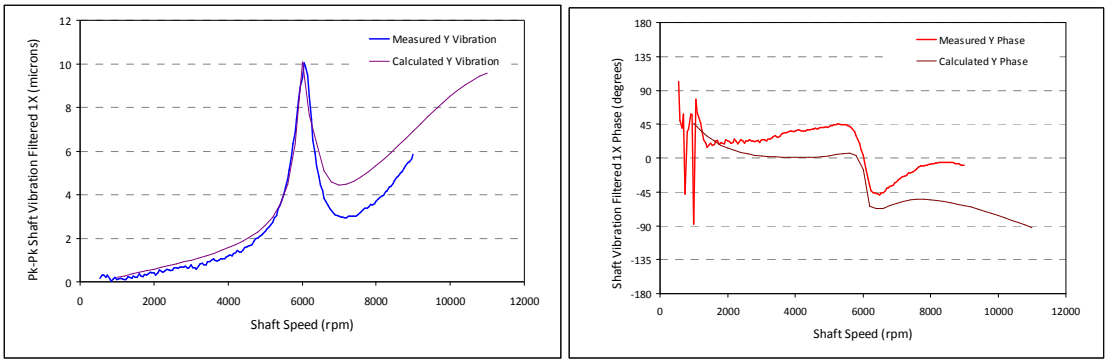

Probe X

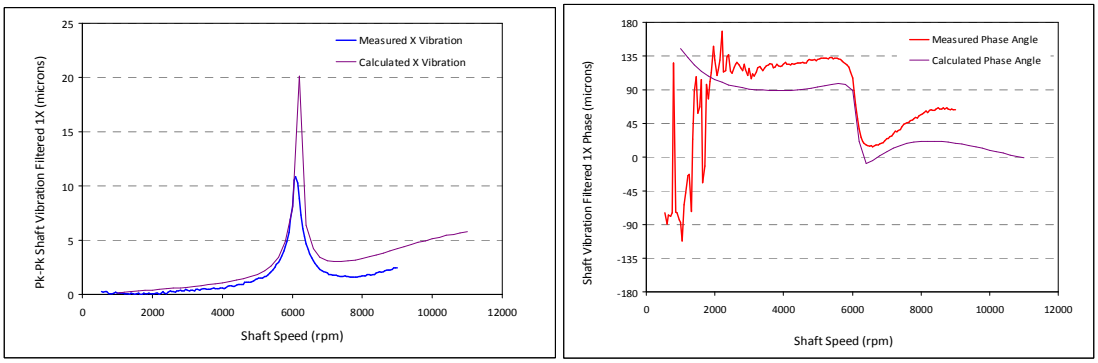

Probe Y

Figure 214 Measured and Calculated Rotordynamic Response for DR0428 (rotor residual mechanical unbalance removed)

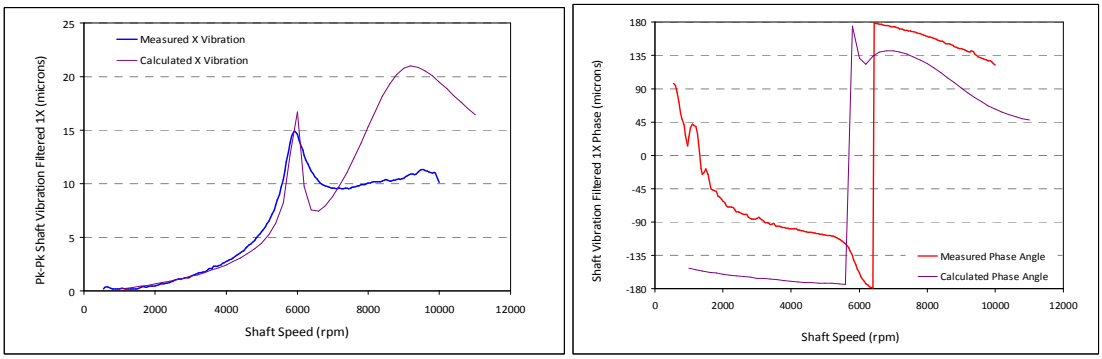

Probe X

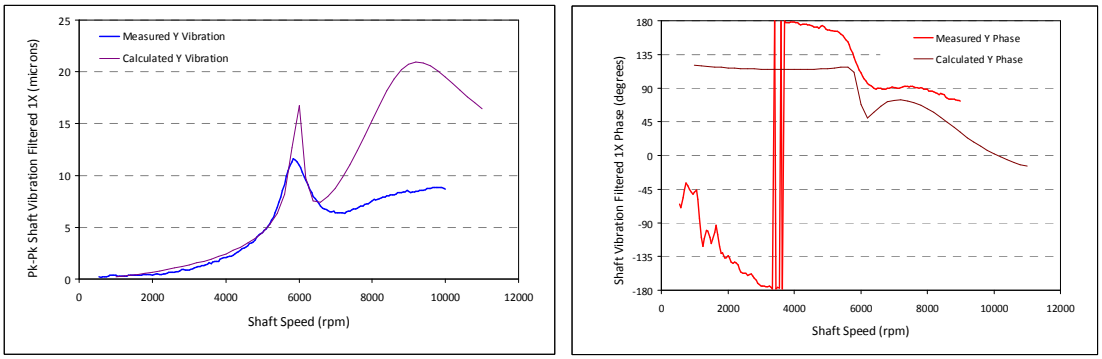

Probe Y

Figure 215 Measured and Calculated Rotordynamic Response for DR0673 (rotor residual mechanical unbalance removed)

It can be seen that for the fixed geometry bearings generally good agreement is obtained for the amplitude responses and also good correlation with the phase characteristics (it should be noted that the phase angles will have a 'bulk' shift due to the offset location of the key phasor with reference to the unbalance locations used on the test rotor and rotordynamic calculations).

For the variable geometry bearings, good agreement is obtained once again but with this case the predicted amplitudes deviate significantly from the actual levels when running at the higher speeds > ~7000 rpm. It is most likely that the cause of this is that a discrepancy exists between the predicted and actual bearing oil film parameters of stiffness and damping. In practice the rotor generally exhibits slightly higher damping characteristics than is shown in the predicted work. However, overall the rotordynamic predictions compare well to the actual measured values for both amplitude and phase.

9.3 Shaft Journal Temperature Measurements

The experimental work essentially breaks down into two distinct areas of shaft journal temperature measurement. The first area addresses the measurement of influence component journal dynamic displacement and operating speeds on the journal temperature distribution development. The aim was to isolate the rotordynamic characteristics (other than unbalance response) and any thermal bend development from the journal temperature differential development. This allows for observations and an understanding of the relationships coupling the dynamic bearing conditions and journal temperature distributions.

The second area of experimentation introduced the flexible rotor which introduces more complex rotordynamic conditions that are engineered to provide thermally sensitive conditions with respect to shaft bend stability. The same observation principles apply as outlined for the rigid rotor, for the flexible rotor tests but with the additional of the dynamic amplification effects at the bearing location with more complex rotor phase characteristics. The introduction of a second bearing geometry type, variable geometry bearings, also presents some further change in operating conditions.

Considering in detail the relationship between the journal temperature and rotor response, and more specifically the response at the bearing journal the results of the rigid rotor with the fixed geometry offset half bearings will be evaluated.

A principal point of interest when assessing the stability conditions with respect to journal thermal bend development are the relationships governing the rate of 1st harmonic temperature distribution and the response characteristics at the bearing. When considering this at the rotordynamic design stage the ability to establish steady state unbalance response is well proven but the relationships and mode of development with basic operating conditions such as speed, unbalance force, bearing response and orbit shape is less well understood at a practical level. To date no controlled experimental data has been published for journal temperature measurement for fixed geometry bearings and more specifically offset half or two lobe type configurations. In addition the theoretical modelling work presented to date in the literature considers only plain cylindrical bearing geometry which is a profile rarely applied in high speed rotating machinery, due to rotordynamic stability (half speed whirl). The test data obtained from the rigid rotor test embodies the more complex interactions the take place with non cylindrical geometry present with typical high speed plain bearings.

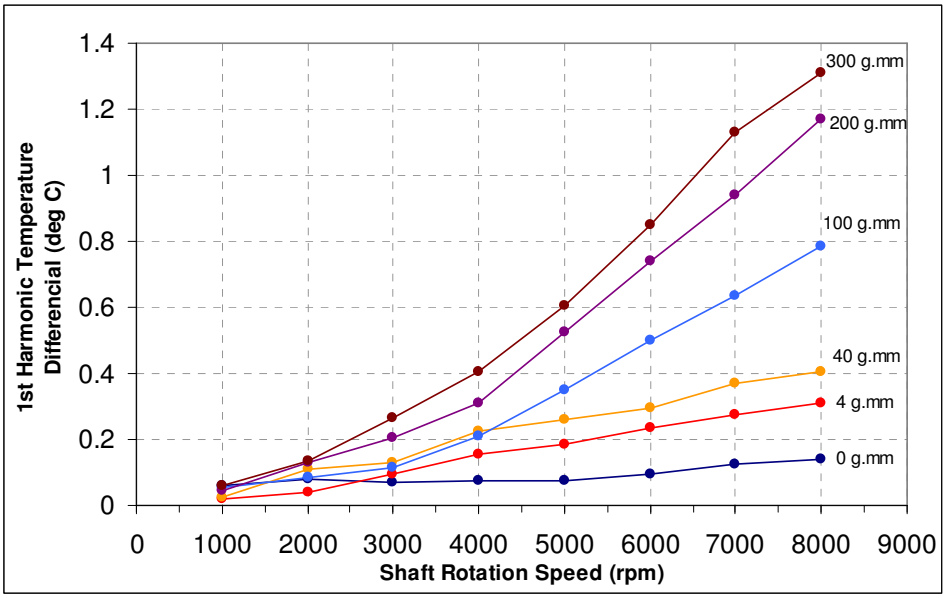

Figure 216 Measured 1st Order Shaft Journal Temperature Differential for Rigid Rotor

The experimental test data presented in section 7 and Figure 216 show the fundamental (1X) harmonic component content of the temperature distribution for the rigid test rotor NDE journal (DR03). The data is provided across a running speed range of 0-8000 rpm for a range of unbalance magnitudes of 0g to 7.5g applied at a radius of 40mm, resulting 0-300 g.mm of unbalance. Typical residual mechanical unbalance levels for an industrial rotor of this

size/weight running at 8000 rpm would be 25-100g.mm. The unbalance mass location is consistent for all conditions shown and was located at the NDE flange.

It can be clearly seen that a steady increase in temperature differential is developed as the shaft speed is increased. The temperature differential also increases in magnitude as the amount of mechanical unbalance is increased. It can be observed that the relationship of temperature differential with speed shows a near linear condition for the smaller amounts if unbalance mass. As the amount of unbalance mass is increased (100, 200 and 300 g.mm) the relationship becomes exponential.

A log-log plot (Figure 217) shows that for the higher unbalance conditions an exponential relationship fits well with the captured data. The expression $\Delta T = A_T.N^{B_T}$ describes the journal temperature differential, ΔT, where A_T is function relating the rotor vibration response to the magnitude of journal temperature differential, and B_T is the relationship of rotor journal velocity/lubricant shear stress and temperature differential characteristic. For the conditions shown here exponents of 1.75, 1.71 and 1.58 were found to correlate for 100g.mm, 200g.mm and 300g.mm unbalance conditions respectively, see Figure 217.

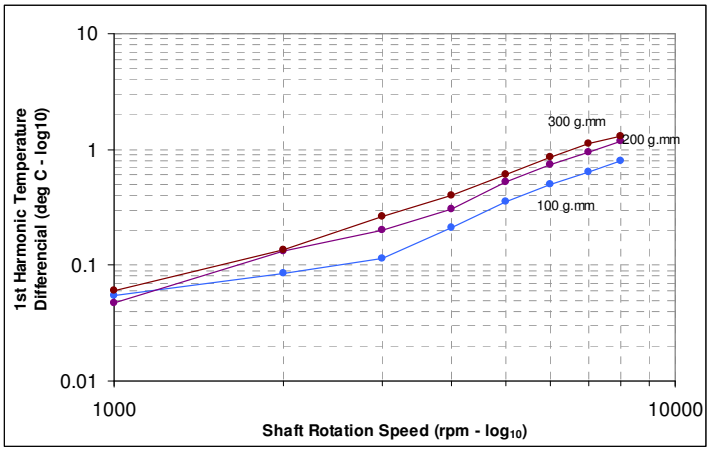

Figure 217 Log-Log Plot of DR03 Tests for 100, 200

The maximum temperature differential observed in the rotor was 1.31 ^{o}C at the maximum unbalance condition of 300 g.mm. The temperature differential in the rotor remained steady when running at constant speed under steady conditions. As seen in the rotor response vibration results, this is consistent with the steady vibration amplitude and phase measurements at both the drive and non drive end bearing.

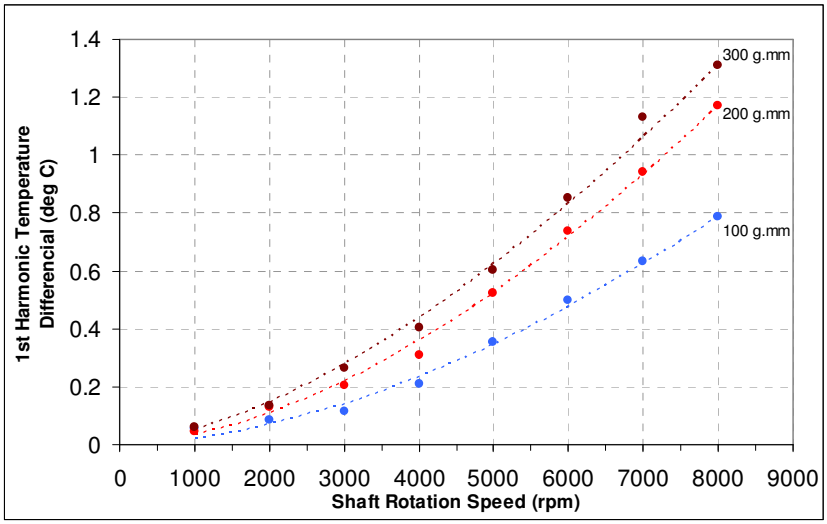

Figure 218 Analytical Curves for Rigid Rotor Unbalance Loads for 100, 200 and 300 g.mm. $\Delta T = A_T.N^{B_T}$

The relationship between journal temperature differential and the response of the rotor is shown in Figure 219 where the peak temperature differentials have been extracted for each unbalance condition when running at 8000 rpm.

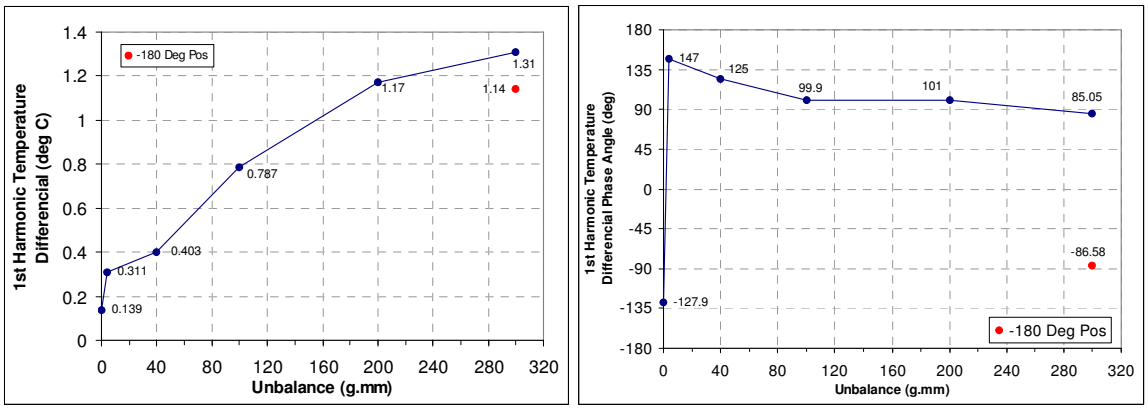

Figure 219 1st Harmonic journal temperature differential and phase angle with respect to introduced mechanical unbalance

The data in Figure 219 presents the temperature differential and phase shift with respect to the unbalance mass introduced. The phase data is taken with reference to the datum (Green) thermistor sensor and it should be noted that this not a direct measure of the phase angle with reference to the point of minimum film thickness on the journal, this is determined and presented later in this section. An additional data point is included which shows the measured temperature differential when the unbalance mass was rotated by 180 degrees. The magnitude of ΔT for the 180° location is 1.14 °C compared to 1.31 °C for the datum location, and it is also seen that the ΔT phase rotates

by some 188.3°, providing good correlation with the unbalance location and the temperature differential development. The difference in ΔT and phase for the two conditions is most likely as a result of the residual mechanical unbalance in the rotor shaft. However, the thermal conditions within the bearing are governed not by the specific forces involved but by the geometric relationships in terms of dynamic whirl orbit. As it is not easy to present the relationship of the rotor response by a single measurement, due to the interactions of the orbit shape and bearing bore profile, resulting in more complex film thickness functions, the modulus of the X and Y probes is taken as a measure of whirl orbit size. It has been stated in the literature [33,34] that a near linear relationship between whirl orbit size and journal temperature differential exists, however this does not give detail of how, if at all, the orbit shape or bearing profile affects this relationship. The peak temperature differential measured for the rigid rotor are shown in Figure 220 against the modulus of rotor dynamic response when running at 8000 rpm. The temperature differential follows a near linear increase for the low levels of response up to approximately 18% of clearance, beyond which it appears to level off above 20% C_d.

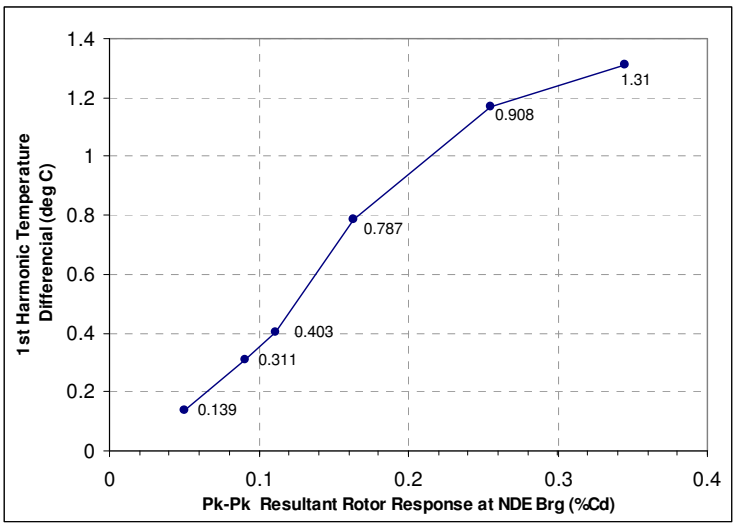

Figure 220 1st Harmonic journal temperature differential against orbit size

A key feature in the development of the thermal instability is the phase of the 'hot' spot relative to the minimum film thickness location and how this relates to the location of mechanical unbalance. In order to establish the phase lag it is necessary to understand the relationship of the shaft orbit with respect to the bearing profile. This then needs to be corrected with respect to the

rotordynamic phase lag when evaluating the thermal bow feedback and its influence on rotor stability.

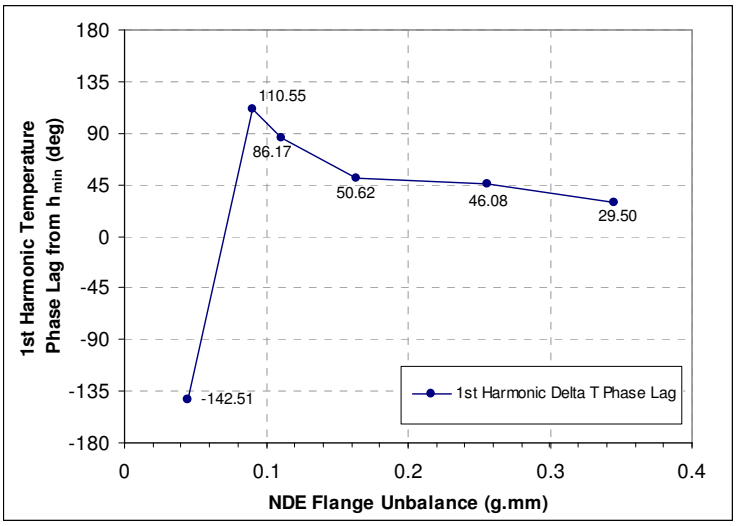

Figure 221 Rigid Rotor 1st Harmonic Temperature Phase Lag with Respect to Rotor Response at 8000 rpm

For the rigid rotor tests, once the point of minimum film thickness is determined for the given operating condition, the 'hot' spot phase lag angle is as shown in Figure 221 for six pk-pk response conditions. At the lower response conditions the phase lag is seen to exceed 90 degrees. At the higher response levels the phase lag can be seen to steadily decrease with increased rotor response. The phase lag for the conditions between 0.1-0.35 C_d ranges from 86° to 29.5°.

Considering the ΔT phase lag condition for the lower responses, the orbit shapes can be seen to differ. Figure 222 shows whirl orbits for the 0.07 and 0.34 C_d response conditions respectively. It can be seen that the whirl orbits are highly elliptical, with the high response test resulting in a greater ellipse ratio (ratio of ellipse major axis t minor axis). Significantly the ellipse angle orientation is rotated round by some 60-70 degrees in the direction of rotation for the lower response condition from that measured for the max response condition. The orbit phase angle steadily rotated in a direction opposing shaft rotation as the response orbit increased in magnitude, whilst accompanied by an increase in ellipse ratio. The dynamic h_{min} location point with reference to the bearing will have an influence on the convective heat transfer and how this relates to the location of the hot spot on the journal. As previously discussed the elliptical orbit can be considered to consist of both forward and backward circular whirl orbits. Where the forward whirl component has been associated with phase lag conditions and backward whirl with a phase lead. The

combination of these conditions with the pre-load bore geometry, gives a complex set of interactions, all of which will have an influence on the temperature differential and phase angle.

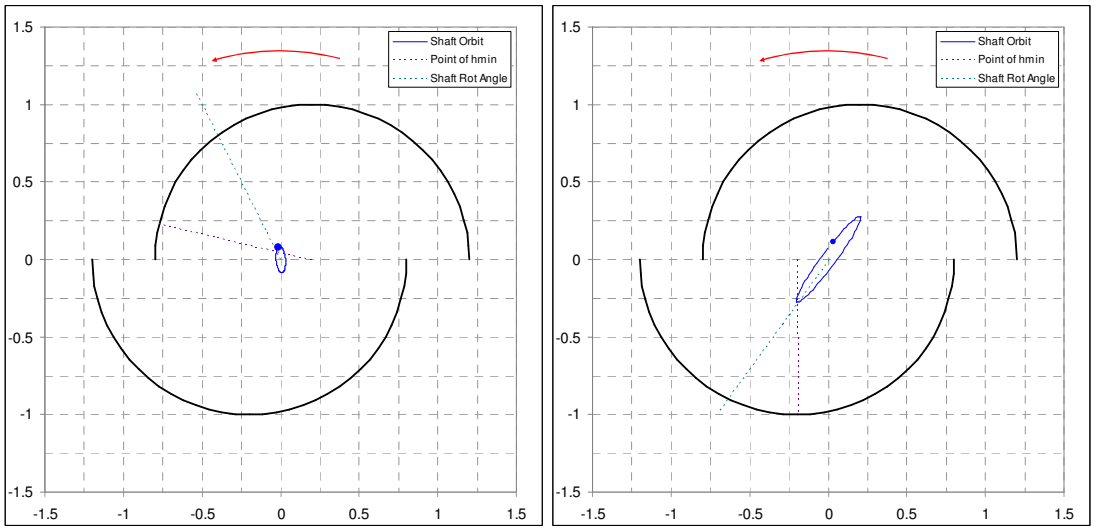

Figure 222 Rigid rotor whirl orbits for 0.07Cd and 0.35Cd conditions

Little information has been presented in the literature with respect to 'hot' spot phase angles, specifically with reference to changes in operating conditions. Gomiciaga et al [18] however, in his numerical CFD study does indicate a reduction in phase lag angle with an increase in forward whirl orbit diameter up to 0.2 C_d for a plain cylindrical bearing with two oil inlets.

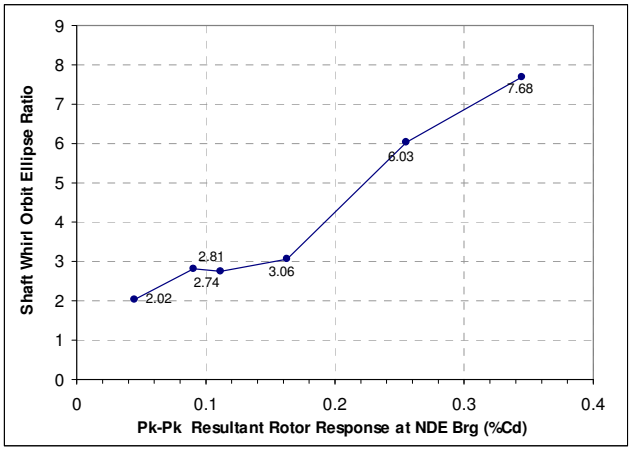

Figure 223 Peak-Peak rotor response with respect to whirl orbit ellipse ratio

Also of interest is the relationship observed for the ΔT phase lag development of the journal 'hot' spot with relation to shaft operating speed. Evaluation of several of the unbalance conditions showed that the ΔT phase lag was seen to steadily increase with an increase in shaft rotation speed. For

the conditions where notable temperature differentials (40, 100, 200 and 300 g.mmm cases) and response were observed, the increase in phase lag angle followed a linear relationship with speed. Figure 224 shows the phase lag angle with respect to shaft rotation speed for the 300 g.mm test case with imbalance positioned at the datum location. It can be seen that the phase lag increases from ~20 degrees to ~40 degrees between 3000 and 8000 rpm.

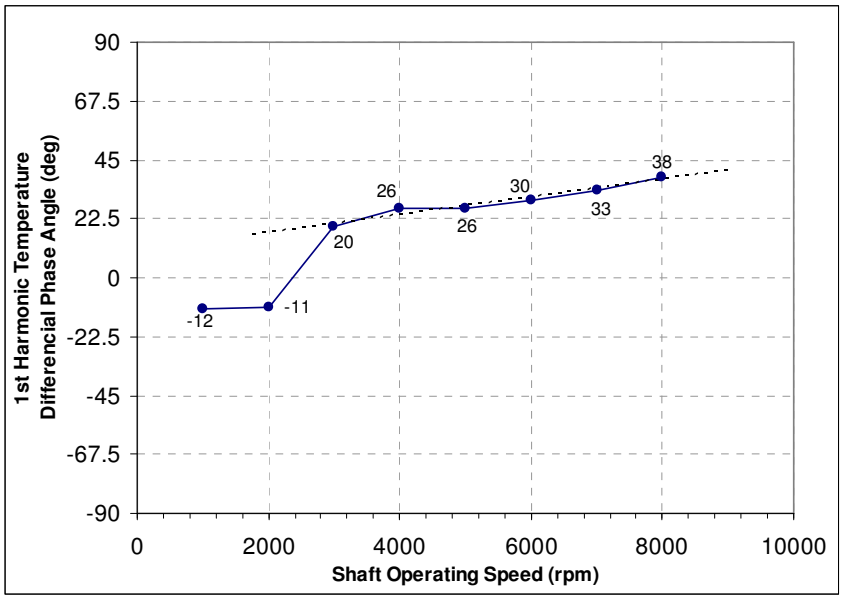

Figure 224 1st Harmonic Temperature Differential Phase Angle for 300 g.mm Unbalance of Rigid Rotor

Considering the flexible rotor arrangements, the rotors were designed to be sensitive to unbalance excitation and in particular prone to development of overhung section thermal bow. The rotor was operated in both fixed geometry and tilting pad bearings, across a speed range up to 11000 rpm. The test programme investigated a number of unbalance conditions and locations to assess the impact on rotordyanmic performance and shaft journal thermal development. Unbalance loads, up to 100 g.mm were introduced at the NDE flange of the rotor, for both bearing configurations. The rotor was operated at both shaft multi speed test runs (~10-15 minutes at each speed condition), and also for extended periods at higher operating speeds between 7000 and 11000 rpm, where zones of instability were expected. The theoretical calculations for instability of the rotor, in line with the published procedure, predicted thermal instability at operating speeds between 8000 and 10500 rpm at unbalance levels of nominally 20 g.mm, 20% of the actual maximum imbalance levels applied.

Following extensive periods of running thermal bend instability was not encounter for any condition. In areas identified as prone to instability the rotor was run for up to 60 minutes and vibration levels were always observed to maintain stable amplitude and phase parameters. Small changes in phase were observed, however these were found to be associated with small changes in oil inlet temperature. The temperature response of the rotor journal was observed to be very rapid, with stable conditions being obtained within 30-60 seconds following a speed change. Therefore it was concluded that further extended running periods were likely to result in unstable developments. The levels of rotor imbalance was limited to 100 g.mm due to reaching a predetermined limit of pk-pk vibration measured at the NDE bearing.

The rotor was initially run with no additional overhung mass applied to the NDE flange when operating in the fixed geometry bearings. As has been evaluated for the rigid rotor, the journal temperature differential development is evaluated for several whirl orbit response conditions. For the conditions assessed the maximum temperature development was at a ΔT of 1.25°C for a resultant response level of 0.17 C_d. The temperature development was observed to follow a linear relationship with respect to response magnitude, see Figure 226. This differs from the rigid rotor results where the ΔT was seen to reduce development rate at higher response levels. When a least squares fit curve is applied to the temperature differential against response it can be seen to cross the axis very close to zero, suggesting a simple linear response with orbit magnitude. It is however recognised that the response level experienced on the flexible rotor did not exceed 0.2 C_d which is the point beyond which the ΔT was seen to drop off on the rigid rotor. A similar characteristic could be displayed if response magnitudes were increased further on the flexible rotor configuration. It is also noted that the temperature differential developed at 8000 rpm on the flexible rotor of ~1°C is higher than the temperature differential measured at equivalent conditions on the rigid rotor of 0.75°C for a response of ~0.15 C_d.

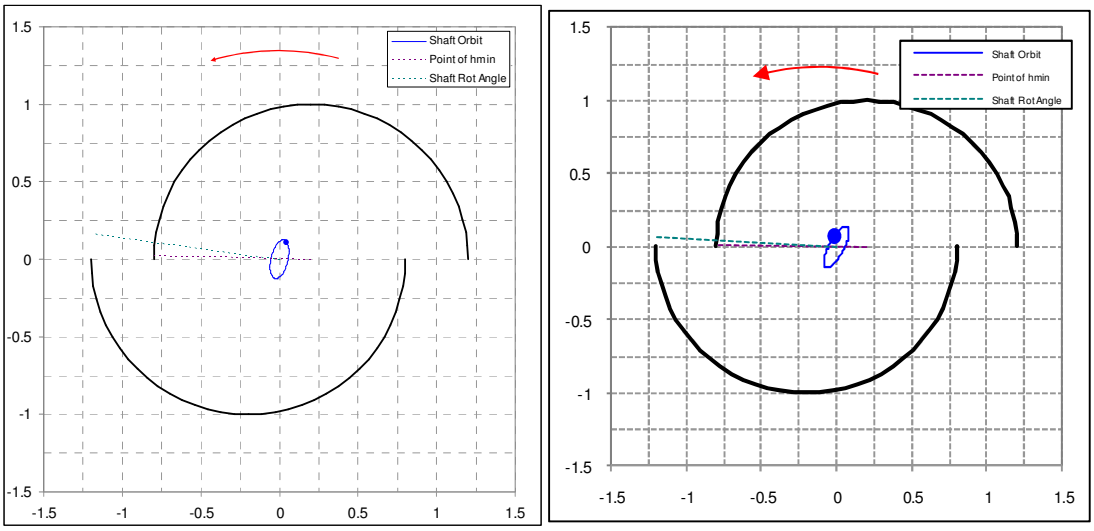

1.5 kg OHM 5.0 kg OHM

Figure 225 Shaft Whirl Orbits for the Flexible Rotor in Fixed Geometry Bearings with 1.5 kg and 5 kg OHM

A small difference can be seen between the rigid and flexible rotor conditions in that the shaft orbit is seen to be rotated (~25-30^{o}) around in the direction of rotation for the flexible rotor case. This rotation tends the orbit major axis toward the lower clearance quadrant of the bearing due the bearing bore offset profile. It cannot be concluded that this variation results in the higher temperature differential measured but it is generally considered that the orbit orientation will influence the periodic thermal development of the oil film. The influence of the more complex rotordynamics on the response conditions within the bearing should also be considered as a potential source for variations in the characteristics of the journal thermal development between the rigid and flexible rotor results.

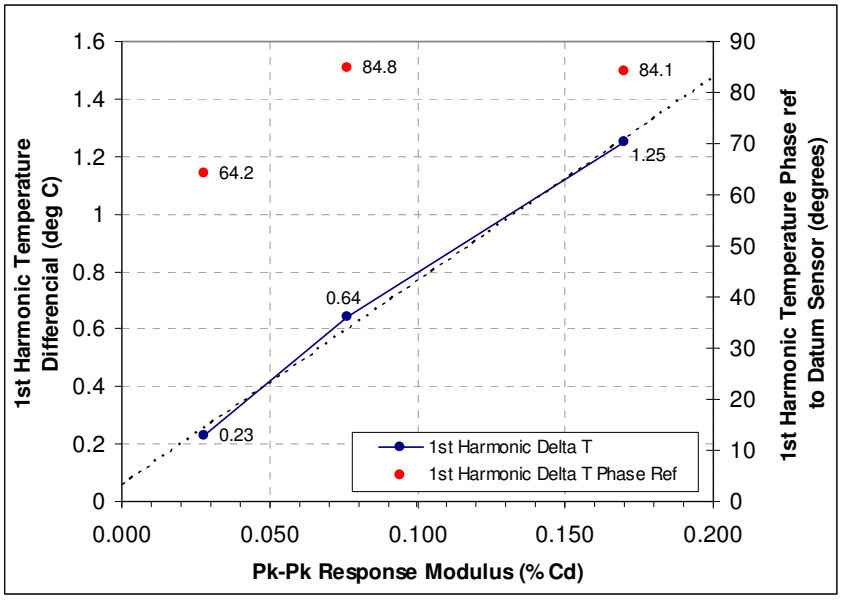

Figure 226 1st Harmonic Journal Temperature Differential for Flexible Rotor with 1.5 kg OHM with Respect to Orbit Size at 9000 rpm

As was observed with the rigid rotor results the ΔT phase lag was observed to reduce with increased unbalance response. With the phase lag varying from ~40° down to ~30° for a dynamic response range of 0.025-0.16 C_d. The phase lag observed for the flexible rotor was generally lower than that seen for the rigid rotor at the same resultant bearing response magnitudes. It should be noted that the orbit shapes and orientations are notably different for the flexible rotor conditions than those of the rigid rotor and that more complex phase changes take place across the rotor length for the flexible rotor.

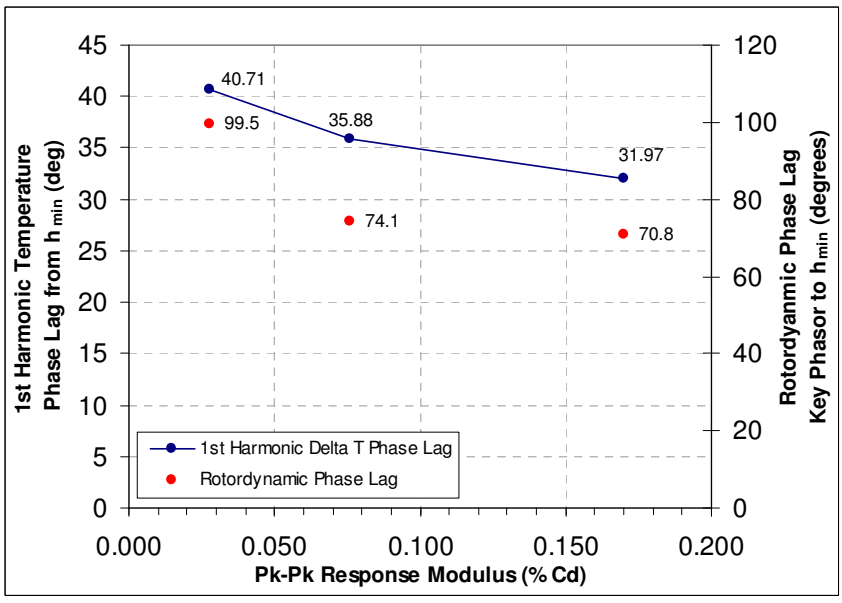

Figure 227 1st Harmonic Journal Temperature Differential Phase Lag for Flexible Rotor with 1.5 kg OHM with Respect to Orbit Size at 9000 rpm

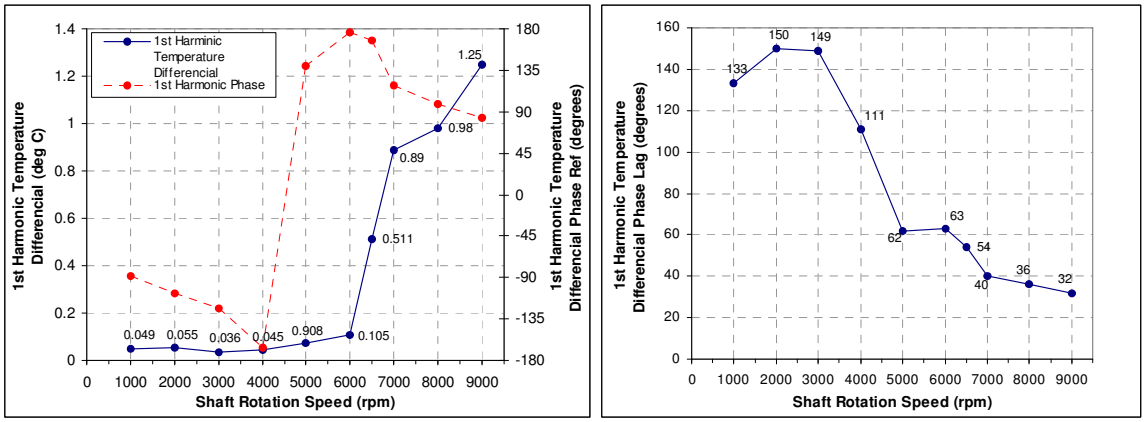

Figure 228 1st Harmonic Journal Temperature Differential and Phase Angle against Speed for a 100 g.mm Unbalance on Flexible Rotor with 1.5 kg OHM

The temperature differential developed in the journal was measured to follow a flat response up to approximately 6000 rpm with temperature differentials of less than 0.15°C being developed for an unbalance load of 100 g.mm at the NDE flange. The temperature differential then increased rapidly to a ΔT of 1.25°C at a running speed of 9000 rpm. A significant phase shift in the 'hot' spot location around the journal was observed, with a total phase movement taking place of ~175°. The temperature distribution and phase shift corresponds closely to the rotordynamic response as the shaft approaches the first and second critical speeds, with the first bending critical being located at ~6800 rpm. The rotor dynamic phase lag was seen be above 90° for the lower speed/response conditions with this dropping to between 60° and 30° as the rotor response and ΔT increased at the higher speed conditions. In this test case there was a general trend for the ΔT phase lag to reduce with increased running speed, which in some part is a contradiction to the observations of the rigid rotor tests. However, the response characteristics are now more complex and whilst speed is increasing a notable increase in dynamic amplification is also present at the bearing location which would, from earlier observations, tend to reduce the ΔT phase lag. This is also coupled with the relationship that the shaft whirl orbit form and orientation now also changes significantly for each operating condition.

Similar observations were made for the flexible rotor with the NDE additional rotor overhung mass added for both the fixed and variable geometry bearings. For the fixed geometry bearings the temperature development follows a more gradual increase with increased speed as opposed to the more 'step' type change seen for the lower overhung mass condition, see Figure 229. This correlates well with the changes observed in the rotordynamic response where a more significant amount of low speed vibration is present but a more

damped response is observed. The increase in overhung mass condition was seen to be more sensitive to unbalance where similar peak vibration levels were see for the increased mass configuration for approximately 50% of the unbalance force.

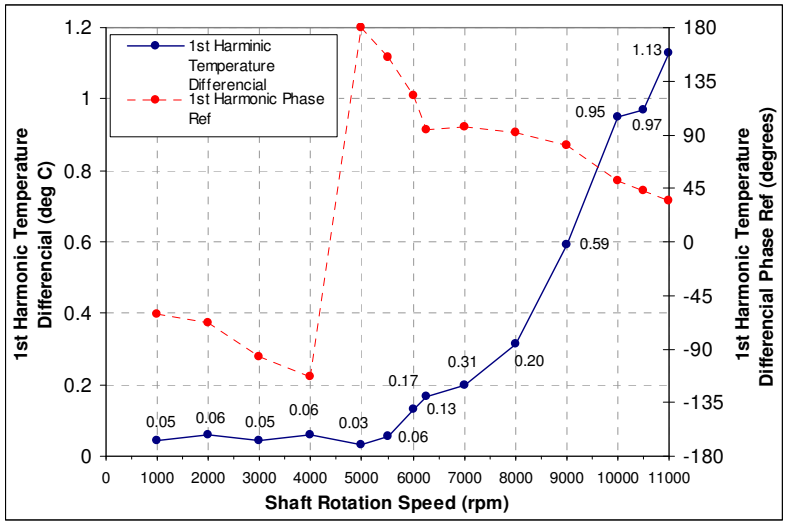

Figure 229 1st Harmonic Journal Temperature Differential against Speed for a 40 g.mm Unbalance on Flexible Rotor with 5.0 kg OHM

The ‘hot’ spot phase lag for the overhung condition is shown in Figure 229 and it can be seen that the lag angle seems more erratic than observed previously and also suggests that a phase lead angle exists for high speed conditions. Whilst it has not been conclusively stated that this case would not occur, it is in generally contradiction to the observations made here and in some of the literature.

When the rotordynamic conditions are studied in a little more detail for this more sensitive rotor configuration it becomes apparent that the relationship of the journal with respect to amplitude and phase becomes more complex, and the relationship between the measurement point and the bearing centre must be considered. Using the rotordynamic model it can be shown that a significant variation in phase condition is predicted between the bearing centre line location and the point at which the shaft displacement measurements are made. Even though this axial distance is separated by 18-20 mm the phase conditions change notably both in magnitude and characteristic. This variation is largely due to the fact that at the rotor is operating in a higher order shaft deflection mode where the NDE bearing location is close to the nodal point which results in rapid rates of change with respect to phase and amplitude. It is these conditions which identify the rotor as one that should be sensitive to

thermal heating instability. Figure 230 shows the phase angle predictions in the horizontal and vertical planes for the bearing centre location and the proximity probe measurement location. It can be seen that the shift in phase when approaching the first shaft bending critical at ~6000 rpm is significantly greater than that seen at the bearing centre.

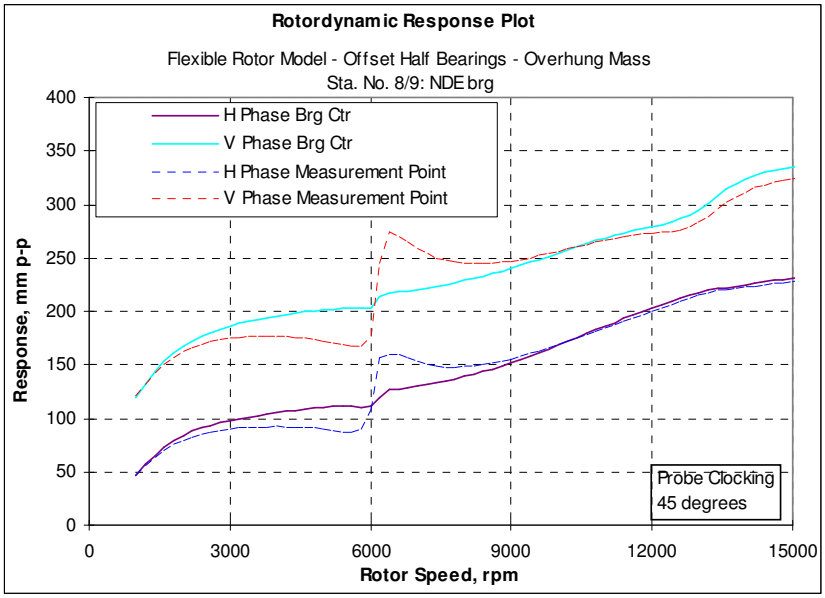

Figure 230 Calculated Phase Angles for NDE Bearing Centre and Measurement Point Locations Flexible Rotor Fixed Geometry Bearings 5kg OHM

This variance in phase angle between the two locations means that when determining the phase lag between the minimum film thickness h_{min} position on the bearing journal and the 'hot' spot, a distorted measurement will be obtained. To compensate in some way for this variation between the measurement location and the condition within the bearing, application of the rotordynamic predictions is used. Good correlation has been observed between the shaft vibration measurement and the rotordynamic response prediction, in particular the correlation of the phase angles. The phase angle prediction and measurement of the proximity probe observed location for the NDE bearing was compared to the measured rotordynamic response at this axial point. Figure 231 shows the respective phase angles for the measured and predicted cases. The predicted rotordynamic phase angles were corrected for the actual key phasor location used on the physical test rig with respect the introduced mechanical unbalance.

The correlation between the predicted and measured rotordynamic phase angles is seen to be very good at the speed conditions above ~5000 rpm with discrepancy in results being of the order of 5-10°.

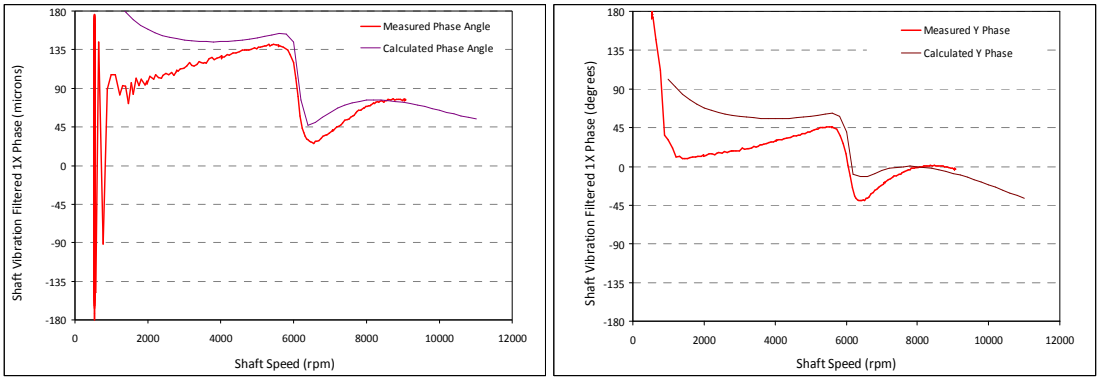

Figure 231 Measured and Calculated Phase Angles for NDE Bearing Flexible Rotor Fixed Geometry Bearings 5.0 kg OHM – DR0428

Now the ΔT phase lag angles are determined using the rotordynamic predictions for phase at the bearing centre location. Figure 232 shows the result of this change, where it can be observed that a more consistent phase lag angle is observed for the higher running speed conditions. This characteristic is more in line with expectation with regards to magnitude. However, at the lower speed conditions <5000 rpm significant errors are likely to be present due to the poorer correlation between the predicted and measured vibration phase in this operating range.

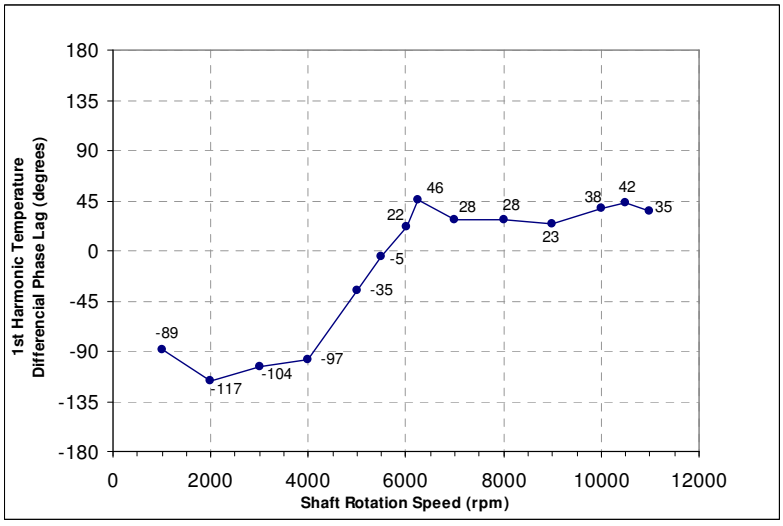

Figure 232 1st Harmonic Journal Temperature Differential Phase Angle for Flexible Rotor in Fixed Geometry Bearings – Corrected by Calculated Rotordynamic Phase Shift

The application of the predicted rotordynamic phase conditions to the determination of the ΔT phase lag can provide a more representative measure of the phase lag angle for the shaft 'hot' spot where good correlation exists between the rotordynamic model and physical measurements. The method is applied for determination of phase angles for the flexible rotor conditions where complex rotordynamic responses are observed. Whilst the procedure should provide a more accurate means of establishing the journal 'hot' spot phase lag it will embody some additional error through the numerical calculation and the precise conditions in the bearing itself remaining unknown. It is, however, considered a suitable means of establishing the characteristics and general magnitudes for the data being presented here.

The thermal differential development for the tilting pad bearing was seen to follow a more gradual increase with speed which was consistent with the response characteristics for this arrangement. The ΔT was seen to peak at a running speed of ~8500 rpm which corresponded to a point just below the second shaft bending critical. Beyond this point, the ΔT was seen to start to reduce with increasing speed. The ΔT phase angle remained constant up to the point of the rotor first bending critical, beyond which it can be seen to shift to a near linear relationship with speed by around -55°, see Figure 233. These characteristics were consistent for all tests for this bearing configuration where imbalance was introduced at the NDE flange.

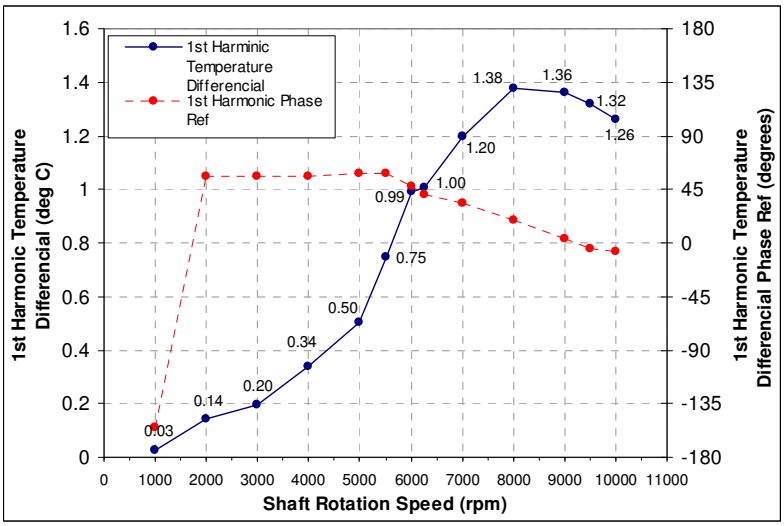

Figure 233 1st Harmonic Journal Temperature Differential for Flexible Rotor in Variable Geometry Bearings with 5.0 kg OHM

The rotordynamically corrected ΔT phase lag angle was seen to follow a fairly flat response, steadily decreasing in magnitude from 72° to 31° degrees

between 2000 to 9000 rpm. At 10000 rpm this had reduced to just 11° (Figure 234). A small oscillation in phase lag is observed as the rotor traverses the first shaft bending critical speed.

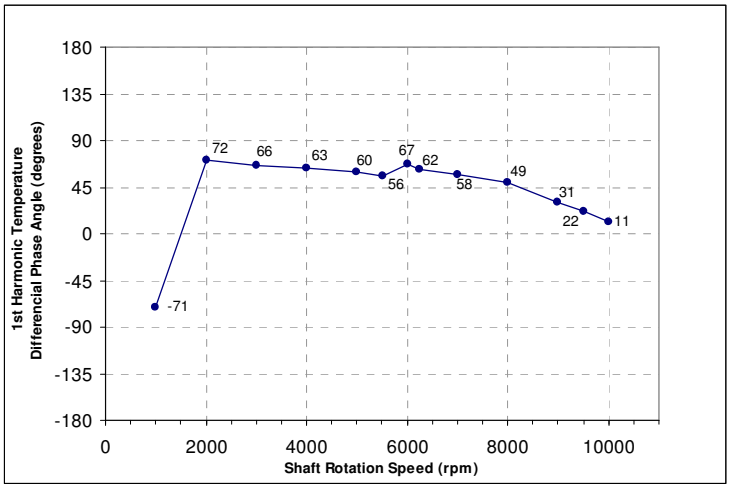

Figure 234 1st Harmonic Journal Temperature Differential Phase Angle for Flexible Rotor in Variable Geometry Bearings with 5.0 kg OHM

A comparison of the various temperature differentials for several of the test conditions for the flexible rotor is presented in Figure 236. It can be seen that for all cases that a linear trend would tend towards the 0 loci on the plot. Clearly too few data points are available to provide a numerically conclusive observation but the characteristics are consistent for all conditions of both fixed and variable geometry design. It can be seen that in general for the same nominal response magnitude, the tilting pad bearing results in higher temperature differentials. For the 5kg overhung mass condition the tilting pad bearing resulted in approximately twice the ΔT than the fixed geometry bearings for the same response level. The orbit characteristic of the tilting pad bearing remained more consistent across the running conditions of both speed and imbalance load with respect to orientation and ellipse ratio (i.e. relevant content of forward and backward whirl). The whirl orbit was much more circular than observed with the fixed geometry offset half bearing, with typical ellipse ratios of approximately 1.5. Figure 235 shows a typical shaft whirl orbit for an imbalance load applied to the NDE flange on the flexible rotor running in variable geometry bearings.

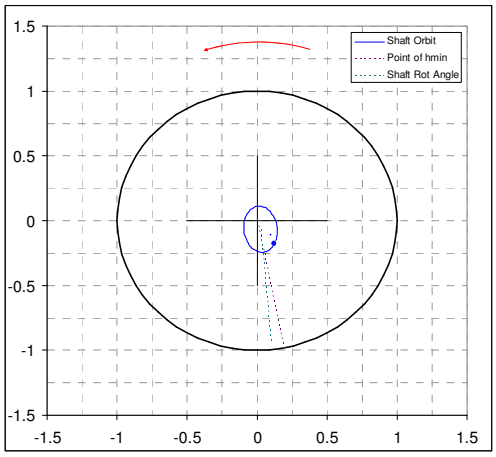

Figure 235 Shaft Whirl Orbit for the Flexible Rotor in Variable Geometry Bearings with 5 kg OHM

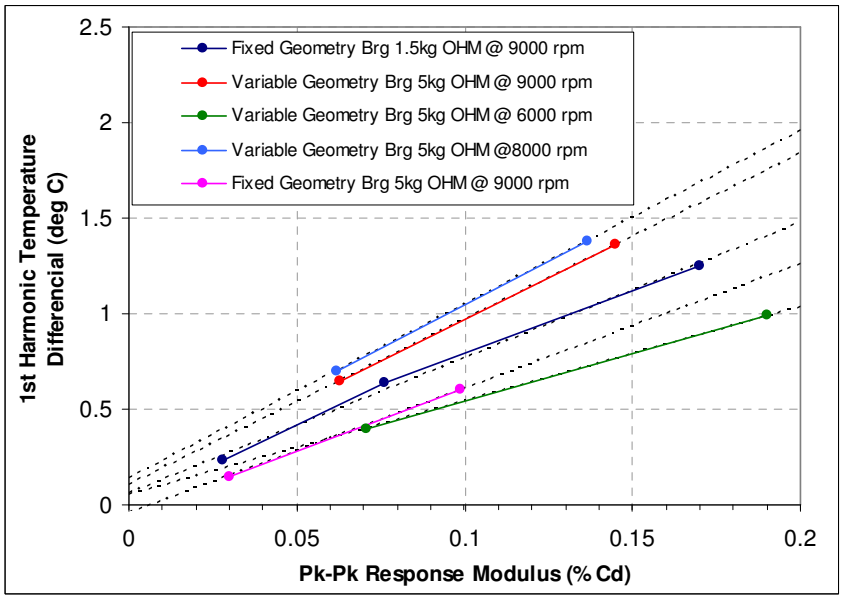

Figure 236 1st Harmonic Journal Differential Temperature with Respect to Response Modulus for Different Arrangements and Conditions

The introduction of the overhang mass on the flexible rotor when running in the fixed geometry bearings resulted in a reduction in effective ΔT for a given magnitude of response orbit. Exploring this further it is noted that whilst the whirl orbits are of a similar magnitude the orientation of the major ellipse axis was rotated by some 25-30 degrees in the direction of rotation for the lower overhung mass condition (1.5 kg). An orbit tending to this orientation would generally result in slightly lower film thickness conditions and also impact on the convective oil film heat transports. It can not be stated that this is the cause for the higher temperature differential of the lower OHM tests, but it is a systemic observation. It should also be noted that, as highlighted previously, due to rotordynamic influences on phase at the bearing centre this will also

change the conditions seen in the bearing from the orbits measured. This can influence the orbit geometry and hence temperature differential development. Figure 237 shows the orbits for the 1.5kg and 5kg overhung mass conditions for the fixed geometry bearings running at 9000 rpm with 50 g.mm of imbalance.

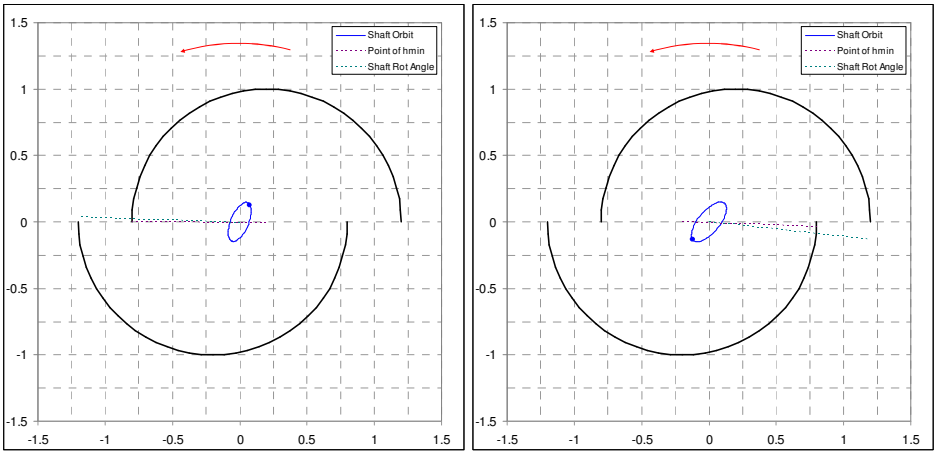

Figure 237 Flexible Rotor Shaft Whirl Orbits for 50 g.mm Unbalance at the NDE Flange Running at 9000 rpm in Fixed Geometry Bearings

Imbalance mass was also added to the shaft centre location (no imbalance was included at the NDE flange). Several imbalance magnitudes were introduced and a near linear relationship to ΔT was observed for response conditions up to 0.2 C_d. The significant difference was the notable reduction in ΔT when running above the first bending shaft critical. In Figure 238 the peak ΔT can be seen to occur at ~6500 rpm (approximately 300 rpm above the first shaft bending critical speed) with a magnitude of ~0.7°C, where it then rapidly drops down to ~0.25°C when running up to 9000 rpm. The ΔT phase lag can be seen to remain at a steady level when running in the higher ΔT region at ~40° up to a speed of ~8000 rpm where it then shifts to a phase lead of ~90°.

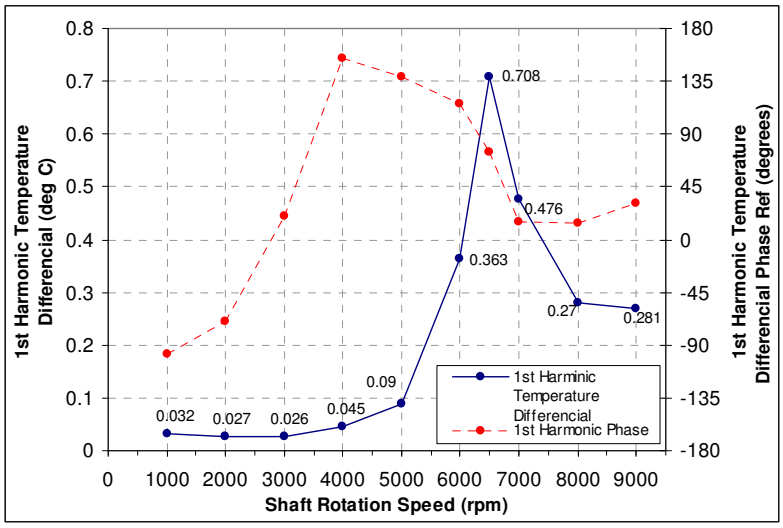

Figure 238 1st Harmonic Journal Temperature Differential Running in Fixed Geometry Bearings with 150 g.mm of Imbalance Located at the Rotor Mid-span

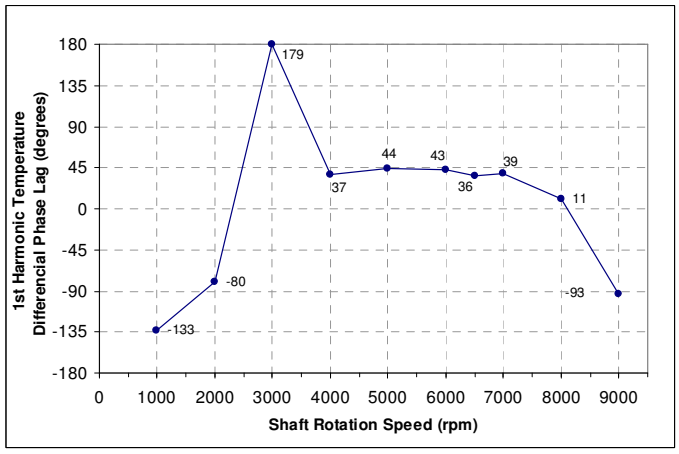

Figure 239 1st Harmonic Journal Temperature Differential Phase Running in Fixed Geometry Bearings with 150 g.mm of Imbalance Located at the Rotor Mid-span

The focus within this work has principally been on the 1st order harmonic of temperature disruption as it is this component of thermal differential that will result in a mechanical bow of the rotor. All other higher order components maintain a state of equilibrium with respect to thermally induced stress in the journal (i.e. no resultant displacements). However it was observed that for many of the tests, particularly for the conditions when running at low levels of response some form of higher order components were present in the circumferential temperature distribution. For the purposes of discussion here these shall be referred to as ‘non harmonic’ components.

Figure 240 shows the temperature distributions for the flexible rotor running at two speeds for the fixed and variable geometry bearing arrangements with an NDE flange imbalance force of 40 g.mm. Figure 240 (a) and (b) are for the fixed geometry bearing and as (c) and (d) for the variable geometry. The green line represents the residual temperature distribution once the 1st harmonic component is removed. It can be seen that the non-harmonic component contributes more to the overall measurement as the rotor response/speed is reduced. Clearly some of this non harmonic content will result from measurement error, however it can be seen that the magnitude of this component is notably in excess of the stated measurement accuracy, (which has been demonstrated by several means). Even if the error range were tripled the magnitude of the non harmonic component would remain significant.

Further insight into the presence of this non harmonic component can be derived from the measurements taken using the rigid rotor. It can be seen from Figure 241 (a) and (b) that when the unbalance mass is shifted by 180 degrees the residual component has now inverted. If this residual were as result of asymmetric measurement error then it might not be expected that the measured residual would shift phase in this manner.

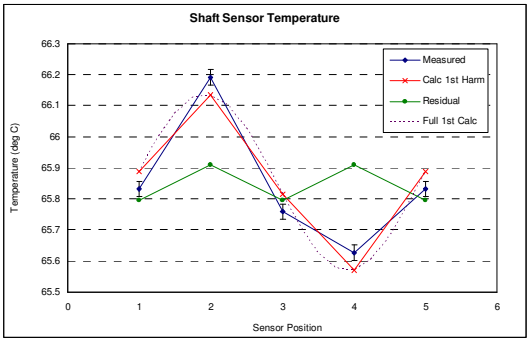

(a) DR0428 – 9000 rpm

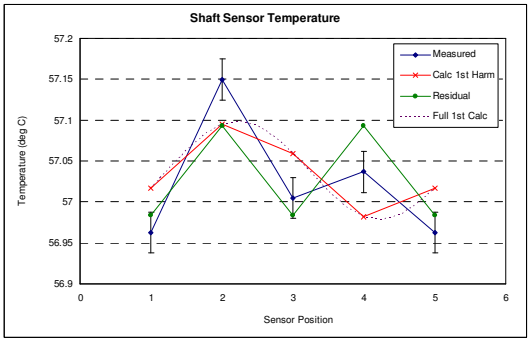

(b) DR0428 – 5000 rpm

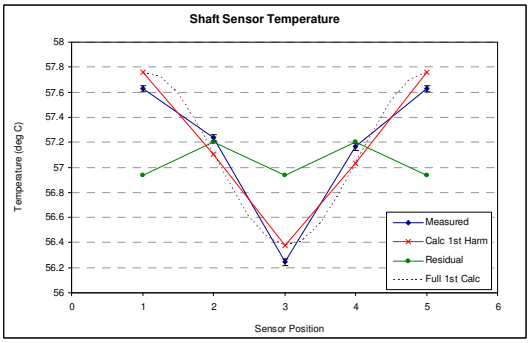

(c) DR0673 – 9000 rpm

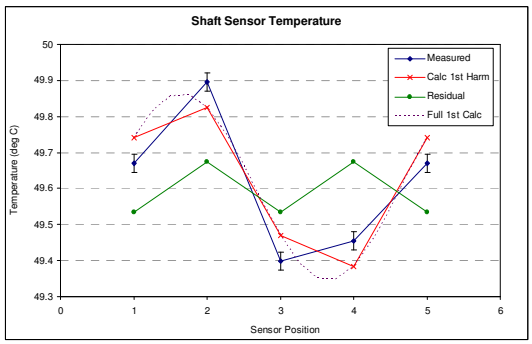

(d) DR0673 – 5000 rpm

Figure 240 Measured Journal Temperature Distributions for the Flexible Rotor

It is not possible here to attempt to determine and harmonic content of this residual as too few measurement points are used to extract anything greater than the 1st harmonic. The residual component can only be used as a guide to the amount of measured non fundamental temperature distribution present within the journal.

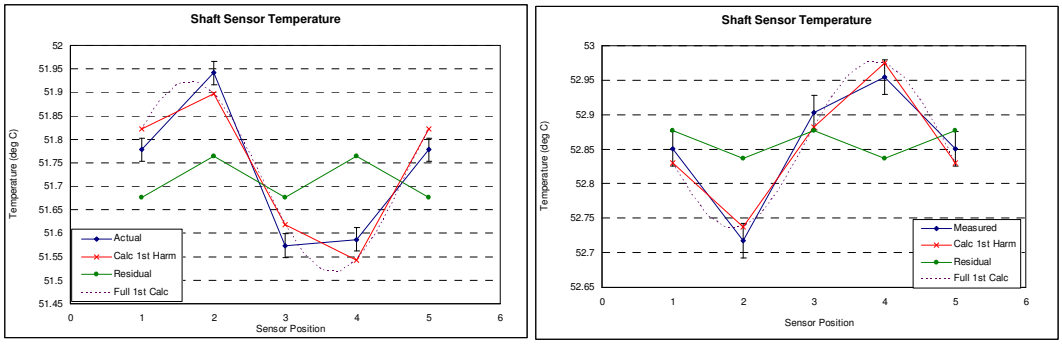

(a) DR0321 – 4000 rpm (b) DR039 – 4000 rpm

Figure 241 Measured Journal Temperature Distributions for the Rigid Rotor with 180° Phase Shift in Mechanical Unbalance

From the discussion presented here it is considered that the measurement of the presence of some non harmonic content is credible. It is not unexpected that this maybe the case as the shaft orbits have been shown to be of an elliptical nature for both the fixed and variable geometry bearings, which means some backward circular whirl is present. A backward circular whirl has been shown in the theory presented in section 8 to result in some significant non harmonic content. This coupled with the more complex bearing profile geometry results in complex periodic time dependent temperature distributions around the bearing which could quite conceivably result on non sinusoidal temperature distributions around the rotating shaft journal.

Comparison of Results to Thermal Instability Theory (Balabahdur [19])

The theoretical analysis method presented by Balbahadur [19] predicted unstable regions for the fixed geometry and variable geometry bearings of 8800-10800 rpm and 7000-9000 rpm respectively for 50 g.mm and 25 g.mm unbalance loads respectively. As previously stated the rotor remained stable across all operating conditions, and both rotors where run with unbalance loads up to 100 g.mm.

The predicted temperature differentials for the fixed and variable geometry bearings were of the order of 2.8°C and 10°C respectively for the 50 g.mm and 25 g.mm loads. As the method for establishing temperature differential is not principally driven by the unbalance force but the specified response magnitudes then it is important that these correlate to the measured conditions. As stated at the being of this chapter good correlation was obtained for both magnitude and phase conditions between the measured and predicted responses for a given level of applied unbalance. This provides some confidence in the data that was used in the analytical model of Balbahadur [19] is valid and the temperature differential predications can be safely compared to the measured levels.

The predicted and measured temperature profiles for two unbalance conditions, one with fixed geometry bearings and the other with variable geometry bearings is presented in Figure 242 and Figure 243 respectively.

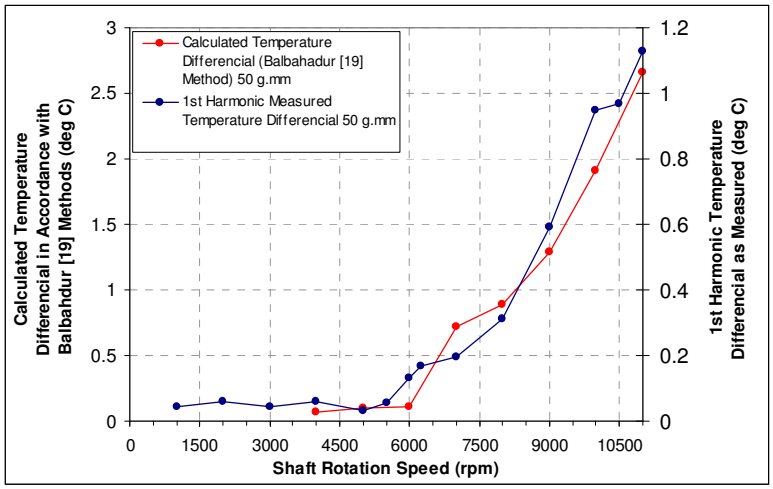

Figure 242 Measured and Calculated [19] Journal Temperature Differential Flexible Rotor in Fixed Geometry Bearings with 40 g.mm Unbalance and 5 kg OHM - DR0428

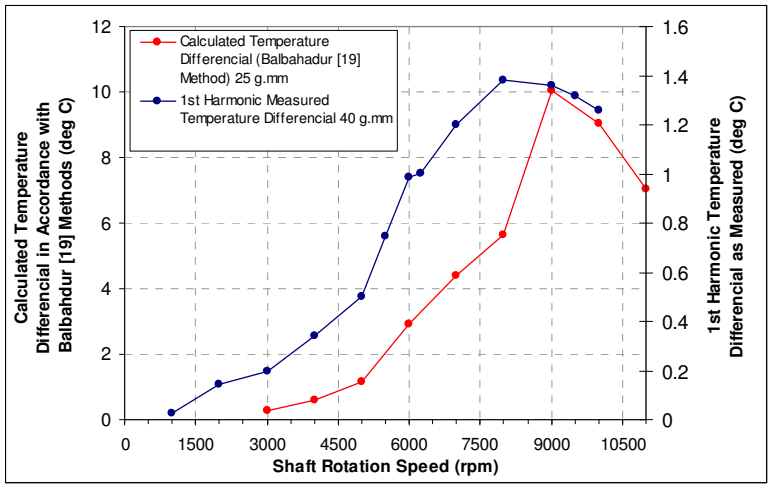

Figure 243 Measured and Calculated [19] Journal Temperature Differential Flexible Rotor in Variable Geometry Bearings with 40 g.mm Unbalance and 5 kg OHM - DR0673

It can be seen that there are significant differences in the magnitude of predicted temperature differentials. For the fixed geometry bearing the predicted temperature differential is 2.8°C which is 2.4 times that measured on the shaft journal. With the variable geometry bearing the peak predicted temperature differential is 10.1°C compared to a measured differential of 1.4°C, which is approximately a factor of 7 higher. It should also be noted that in the variable geometry case the measured temperature was for an unbalance force of 40 g.mm as opposed to a 25 g.mm unbalance in the model, which would result in a further in variation.

While the magnitudes of ΔT show significant discrepancy there is some correlation between the characteristics of the temperature development of the predicated and measured data. For the fixed geometry bearing it can be seen in Figure 242 that the trend is very well matched to that of the measured ΔT data. With the variable geometry data in Figure 243 there is some reasonable correlation between predicted and measured data, but the most notable correlation is in the drop off in ΔT at higher speeds above ~8000-9000 rpm. However it would be reasonable to assume good correlation of the temperature development trend would be attained, as the method is heavily dependent on the supplied rotordynamic amplitude and phase data, which has been shown to be of reasonable accuracy.

9.4 Comments on Existing Theoretical Models

At current with regard to the thermal modelling there are two well documented procedures. In addition to this both methods have been used to couple in some way with the shaft dynamic characteristics. In the case of Keogh [9] et al an actual rotordynamic formulation was incorporated, albeit a fairly straight forward case. Balbahadur [19] does not use analysis with respect to rotordyanmic influences but is based solely on a steady threshold for the amount of thermally induced shaft bend for the spot analysis performed. Whilst this does provide a simple method of analysis it unfortunately does not give any real account to the rotordynamic sensitivity of the rotor with respect to scale. The use of the stability threshold factor based on rotor mass to determine the unbalance force raises questions when light weight rotors are being used, and unbalance forces can quite soon reach levels which account for a significant percentage of the rotor mass. The bearing stiffness with respect to balance force also do not necessarily scale with rotor size. Which could introduce issues with the use of a constant stability threshold factor for all rotor sizes and configurations.

Whilst the method of Keogh et al [9] provides a much more thorough account of both the thermal conditions and rotordynamic interactions the procedure is analytically intensive and as such does not lend itself to easy introduction with existing rotordynamic codes/procedures. The significant advantage to the more complex method with respect to reliability, is the ability for the model to model the convective and conductive heat transports within the oil film and around the bearing. It is these elements which have been identified as being key to the prediction of the hot spot location on around the journal, which dictates the phase angle of the thermal bend. This phase angle is key to understanding how sensitive a rotor likely to be to thermally induced instability. This is a significant restriction in the current more applicable tools, where the methods do not provide any provision for determining the thermal phase angle. There is a tendency for such methods to predict higher temperature differentials and in general provide a more conservative prediction of instability. Whilst conservative design is generally a positive approach care must be taken that systematic overdesign does not result.

Some key observations from analytical procedures :

Balbahadur [19] procedure

- No account for hot spot phase angle prediction
- Uses steady state assumption for oil film temperatures at dynamic locations and as such would have a tendency to over predict the bearing temperatures and journal temperature differentials
- Method can be easily applied and built into existing rotordynamic codes/methods
- Dynamic tilting pad bearing solution provides good account for oil film functions under dynamic conditions
- No account provided for non circular geometry on fixed profile bearings
- Method suggests more centred orbits are more prone to instability which is in some contraction to other analytical studies

Keogh et al [9] procedure

- Procedure couples the thermal, hydrodynamic and rotordynamic problems giving a holistic evaluation
- Method provides for oil film conditions which allow for determination of not only temperature differentials but hot spot phase lag angle
- Procedure for coupling shaft bend angle as a feedback gain provides more definitive measure of system stability
- Method is computationally complex and does not readily apply to more complex bearing configurations without further development
- Computation time would result in difficulties to incorporate with common rotordynamic analysis methods

In summary the work presented by Keogh et al [9] provides a highly detailed account of the conditions taking place in a whirling shaft and the effects on thermal stability, although some assumptions are still introduced. However due to its highly involved nature it is generally too complex for practical implementation at an industrial level. The work and method can, however, provide a good benchmark by which to evaluate other less involved analysis procedures. The work of Balbaadur [19] introduced a method which can be built into the practical design procedures and follows the type of approach that is needed for industrial use. However, some of the assumptions and idealisations that have had to be made mean that some critical elements of the data, such as phase angle and rotordynamic interaction are omitted. To

increase the reliability of the procedure some method of account for these elements would be necessary. The works presented in the literature have clearly advanced the understanding and modelling capability of the phenomenon but further development of the analytical procedures is required along with practical test data and results with which to validate the approaches.

9.5 Shaft Journal Temperature Theoretical Model Results

The theoretical model presented in this research consist of three principal elements :

- The oil film energy model
- The orbit perturbed thermal model
- The time domain finite difference journal model

The principal focus of all of the aspects involved in this procedure is to provide as simple and as efficient solution method as possible whilst still providing results of acceptable accuracy. As it has not been part of this research to perform an extensive parametric study into the application of the presented journal hearting model, some simple case studies have been considered to provide and insight as to how well the method compares to existing data or other published work.

As the principal element in determining the temperature distributions within the shaft journal are dependant on the lubricant film thermal conditions, it is key that the energy model used to represent the heat generation within the bearing provides suitably accurate representation.

9.5.1 Oil Film Energy Model and Temperature Equation

To investigate how the presented oil fil temperature energy equation performs, a comparison to the case presented by Keogh et al [9] is made for the zero orbit condition.

Keogh et al [9] uses a complex thermohydrodynamic model incorporating CFD techniques to determine the steady and perturbed bearing lubricant film temperature around the bearing. The model used by Keogh et al [9] considers cross film temperatures in addition to circumferential temperature variation. As such, for the purposes of comparison to the current research, then the cross film mean temperature from the results presented by Keogh is used. The bearing considered is a single inlet plain cylindrical bearing, with the oil inlet positioned at 180^{o} to the point of minimum film thickness as outlined in Figure 244. The following material properties and parameters are taken for the considered load case :

$\varepsilon = 0.648$		$\Omega = 1000$	rad/s		
$R_j = 0.05$	m	$L_b = 0.035$	m	$c_r = 100$	μm
$\upsilon_{40} = 46$	cst	$\upsilon_{100} = 5.5$	cst	$T_{Lin} = 45$	°C
$\rho_L = 850$	kg/m^3	$c_L = 2000$	$J/kg/K$		

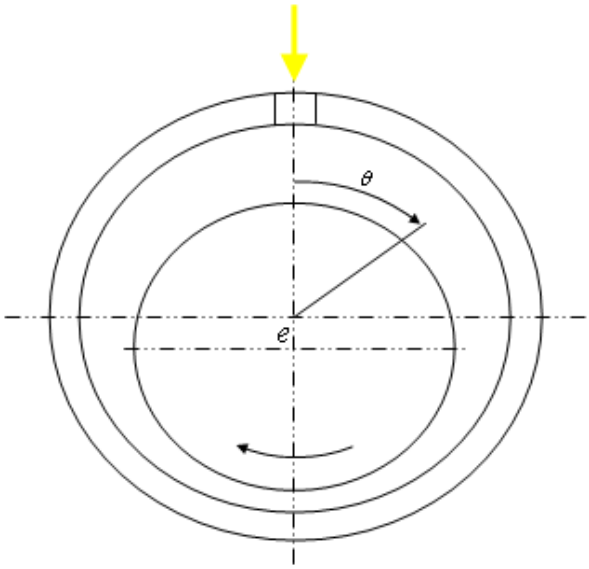

Figure 244 Keogh et al [9] Bearing Case

Using the equations set out in chapter 8, a bearing temperature rise ΔT of 45.6°C was calculated with an effective pad inlet temperature T_{o1} of 50.3°C. The mean effective viscosity used for the analysis was calculated as 12.9 Cst, where this initial condition was estimated from the mean temperature rise for a fully centred journal in the bearing. Figure 246 shows the predicted circumferential temperature distribution for both that presented by Keogh et al [9] and that of the current research.

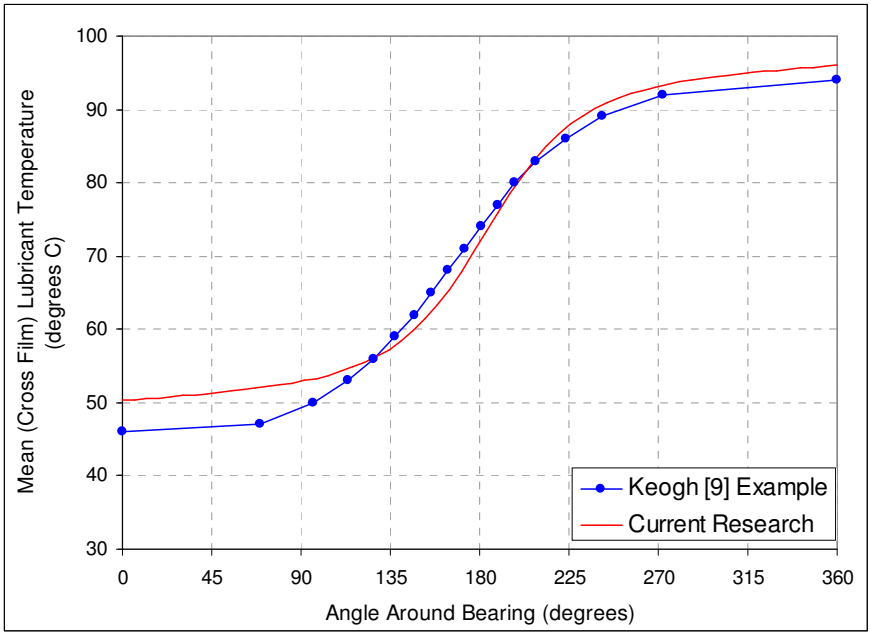

Figure 245 Circumferential Temperature Distribution for Steady Eccentricity Comparison Between Literature and Research

The results of the example case show good correlation between the mean film temperature presented by Keogh et al [9] as calculated by a comprehensive coupled fluid and thermo dynamic approach. The current research formulation appears to predict a higher pad inlet temperature by ~4.5°C than that of Keogh et al [9]. Also the overall temperature rise is slightly less than that of Keogh et al [9] with a ΔT of 48°C and 45.6°C for [9] and the current research respectively. It should be noted that the temperature distribution in Figure 245 is the actual lubricant temperature and no effect of axially averaged heat (flux due to the fractional film function in the cavitation region) is present.

For the above result, the application of the closed form energy solution of the bearing temperature distribution shows very promising results when compared to a well considered and detailed CFD type analysis. This provides a good indication that the method can provide acceptably accurate results for the prediction of the oil film temperature where the basic input parameters are defined. However, it is recognised that a much wider range of application is required to validate the model across a greater range of parameters and geometric arrangements before a definitive understanding of the scope and accuracy of the solution can be made.

9.5.2 Oil Film Temperature Perturbations

To evaluate the journal differential heating aspects in the orbit perturbed thermal model, the same case as presented by Keogh et al [9] was used. Keogh et al [9] goes on to predict the journal temperature differential for both forward and backward whirl orbits. The basic operating parameters are used as for the steady zero orbit case, but now the synchronous orbits are introduced. The following additional parameters for the dynamic perturbed case are :

$$\sigma_{1,2} = 0.1 \qquad k_L = 0.15 \quad W.m^{-1}.K^{-1} \qquad H_J = 50 \quad W.m^{-2}.K^{-1}$$

The forward orbit was solved assuming Couette flow across the oil film. The resulting temperature distribution is shown in Figure 246. As can be seen the results show an almost sinusoidal distribution with the journal surface hot spot lagging the minimum film thickness.

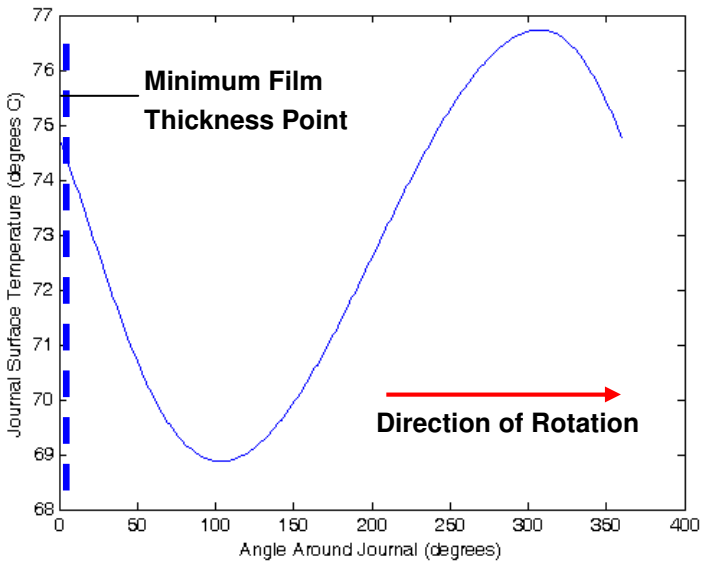

Figure 246 Calculated Journal Temperature Distribution with a Forward Whirl Orbit

A harmonic analysis of the temperature distribution is presented in Figure 247, where the 1st harmonic ΔT and associated phase angle are 7.8°C and -66.9° respectively. It can be seen that the fundamental harmonic dominates, as would be expected, but there is a small amount of 2nd harmonic component - approximately 10% of the magnitude of the 1st harmonic.

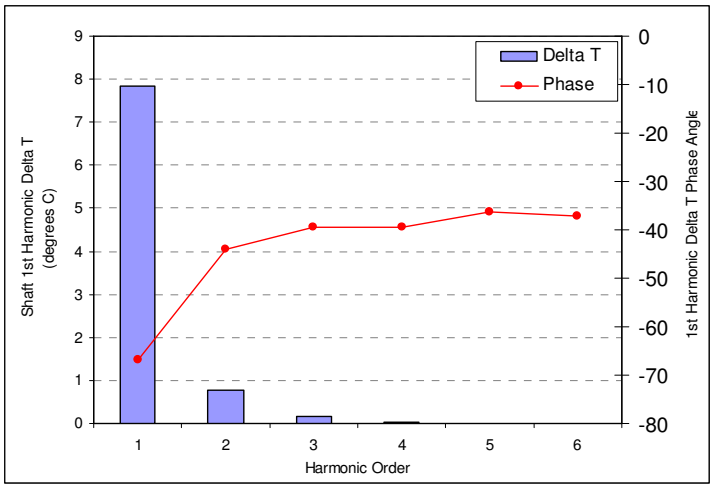

Figure 247 Journal Temperature Distribution Harmonic Analysis with a Forward Whirl Orbit

The model was also solved for the backward whirl condition. The resulting journal temperature distribution is presented in Figure 248 where the temperature distribution can again be seen to be predominantly sinusoidal. However a more significant point is that the journal hot spot now leads the point of minimum film thickness on the journal. The temperature distribution harmonic analysis is given in Figure 249. The phase angle can be seen to lead by some 55 degrees with the 1st harmonic ΔT being 3.6 °C.

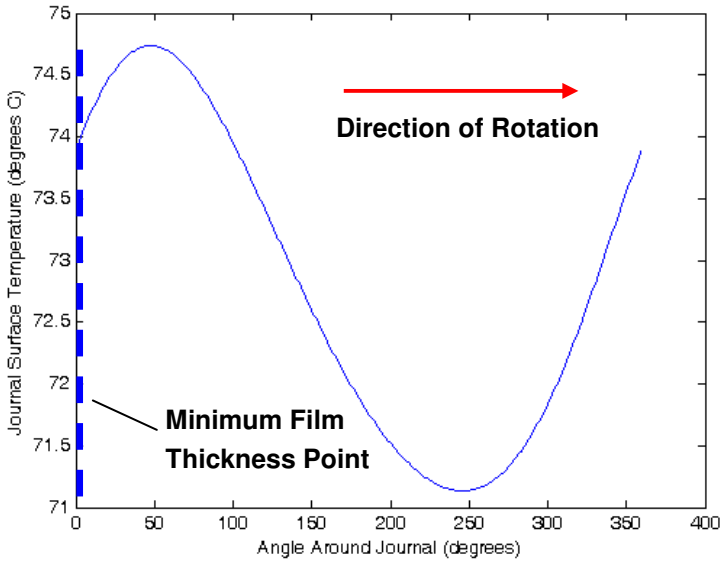

Figure 248 Calculated Journal Temperature Distribution with a Backward Whirl Orbit

The predicted ΔT and phase angles presented by Keogh et al [9] were 10 °C and 4 °C for forward and backward whirl orbits respectively. The phase lag for the forward whirl orbit was given as 55°. No specific phase angle was given

for the backward whirl orbit, but it was specified that it was leading the point of minimum film thickness on the journal.

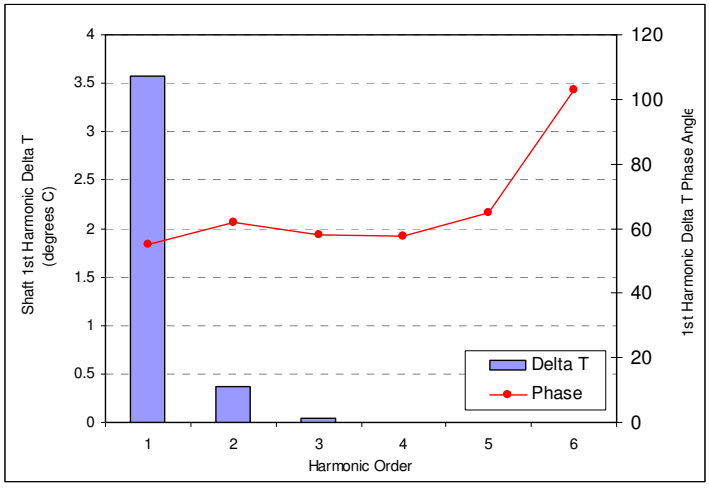

Figure 249 Journal Temperature Distribution Harmonic Analysis with a Backward Whirl Orbit

The results from the method presented within this research compare reasonably to the work presented by Keogh et al [9] for the temperature distributions. Forward whirl orbit is some 2.5 °C (25%) less than the literature and the backward whirl ~0.5 °C less (12%). The phase lag was however a little further away from that of Keogh et al [9] by some 11°.

In summary, whilst some variation does exist between the method presented within the research and the literature case, this still gives a good correlation in light of the objectives. Some discrepancy would be expected when a simplified method with greater assumptions is adopted over the more complex and costly analysis, however the results are still well within acceptable accuracy levels for such an analysis. It was noted during the evaluation of the procedure that the predicted phase angle is quite sensitive the convective flow fraction. With phase angle shifts of 10-20° observed for 10% change in f_L, highlighting the need for further investigation to this feature. However, if such levels of accuracy as have been seen in this case study can be demonstrated by this method across a wider number of cases, then use in practical rotordynamic analysis would be well justified. To account for the variations seen in phase angle and ΔT, a tolerance could be applied to the calculated phase angles and temperature differences and a sensitivity analysis performed to ensure a stable operating range is selected for a rotor. This type of sensitivity analysis is common place in rotordynamic procedures where levels of uncertainty for some specific parameters is relatively high.

Chapter 10

Conclusions

10. Conclusions

This thesis has considered the phenomenon of synchronous rotor dynamic thermal bowing initiated and propagated by thermal differential heating of the bearing journal due to unbalance induced shaft whirl, which under certain conditions has been observed to induce unstable vibration response behaviour (the 'Morton' effect). A number of industrial cases have been reported in the literature where synchronous related shaft vibrations have been observed to increases with time whilst at steady running conditions, where the phase is seen to alter with changes in vibration amplitude. This thesis has looked in detail at the theories and has analysed several of the referenced industrial cases to understand the rotordynamic and bearing performance characteristics that relate to the promotion and initiation of thermal bow induced instability. The work presents critique of existing evaluation methodology and uses a specially designed experimental rig to obtain controlled experimental data with relation to the bearing induced thermal differential heating of the shaft journal. This thesis presents an alternative procedure of theoretical modelling of the thermal development of a whirling shaft journal to determine shaft temperature differential and phase data.

It has been shown that it has been possible, using appropriate rotordynamic models, to reproduce the rotor dynamic response characteristics which correlate accurately to the measured test results for two cases published in the literature and an as yet unpublished industrial example. It has been possible to identify some of the fundamental characteristics that have been observed to be present in the rotors where thermal rotor bow and instability has been reported. The study has shown that in cases where the thermal instability exists, very specific relationships between the rotor operating deflection shapes are required in combination with the vibration phase conditions. Whilst a rotor can exhibit high rotor vibrations associated with a shaft overhung section, a more complex set of conditions relating the rotordynamic and 1^{st} harmonic temperature distribution phase at the bearing journal would be required to result in a condition of instability. The

rotordynamic study also shows that in certain rotor configurations, imbalance effects at overhung sections in shafts (where the relative distances of bearing span and overhung section are comparable) could result in unstable behaviour being observed in opposing bearing locations to those where the thermal bend development is taking place. In all cases evaluated, the rotor sensitivity to unbalance was seen in some way to correlate to the level and severity of instability observed. Where rotors were predicted as being highly sensitive to imbalance, these were shown to become fully unstable. Those where transient or cyclical unstable characteristics were displayed were predicted to be less sensitive to unbalance forces. A common characteristic in all cases was that, due to the natural vibration response of the rotors, they operated with mode shapes where dynamic shaft bending is present at or near to a bearing location. Critical speeds provided some dynamic amplification in the regions of unstable behaviour.

An experimental test rig design has been presented which has been rotordynamically engineered to replicate the dynamic conditions observed in rotors with known thermal rotor bow and unstable 'Morton' type characteristics. The test rig introduces the use of non circular fixed geometry hydrodynamic bearings, as commonly applied in high speed rotating machines. To date no controlled operational data for these bearing types has been presented in the relevant literature. The use of variable geometry bearings is also included in the test rig design analysis and specification. The rotor design is predicted to undergo unstable thermal bend conditions within the speed range for both fixed and variable geometry bearing configurations under moderate unbalance conditions when calculated in accordance with a key method presented within the literature [19]. The rig design includes a method by which journal temperature measurements can be accurately acquired from the journal for operating speeds up to 14000 rpm. This allows a range of journal temperature data to be obtained for different operating conditions for both fixed and variable geometry arrangements. This new area of experimental data is not covered in the availble literature and has been generated and presented in this thesis.

The experimental test rig and associated instrumentation has been manufactured, constructed and commissioned as per the design outlined in the above paragraph. The test rig has been operated across a speed range of 13,000 rpm in both fixed geometry offset half and variable geometry tilting pad bearings, running above the 1st bending natural frequency and within 10% of the 2nd natural bending modes of the rotor. Shaft dynamic displacement,

phase and journal temperature distribution data has been obtained for a number of operating conditions and configurations for several states of initial mechanical unbalance.

Experimental results data is presented which demonstrates good correlation with predicted rotor unbalance synchronous vibration amplitudes and phase. Specific results data is presented where the 1st harmonic rotor journal temperature distributions are extracted and the phase conditions presented with respect to the initial mechanical unbalance location and the point of journal minimum film thickness.

The work shows that it was not possible to initiate instability due to the thermal rotor bow when running in either the fixed geometry or variable geometry bearings. Magnitudes of initial unbalance mass were introduced that were consistent with those used in the theoretical model for which instability was predicted, and also higher unbalance magnitudes of up to 6-8 times greater were also applied with stable vibrations observed throughout. Running periods of over 30 minutes under steady speed and inlet conditions were performed.

Shaft journal temperature differentials were measured and a systematic increase in shaft temperature differential was observed as unbalance and shaft orbits were increased. The development of the shaft journal temperature differentials was shown to follow an almost linear relationship with shaft whirl orbit size for vibrations of <20% of the bearing diametrial clearance for the fixed profile arrangement. This is consistent with the assumptions presented in several literature sources. However, the experimental data shows that for the fixed geometry offset half bearings with orbits >20% of diametrial clearance, the rate of temperature differential development reduces to a lower rate.

Actual shaft journal temperature differentials are shown to be significantly lower than those predicted using the current theoretical model presented in the literature [19] for the same dynamic displacement conditions. Fixed geometry bearings were only 35% of predicted levels and variable geometry lower at ~15%. Maximum temperature differentials were measured of 1.5-1.7°C.

Shaft ‘hot’ spot phase angle data is measured and systematic relationships are seen to exist between unbalance conditions, shaft speeds and rotordynamic behaviour. For cases where little rotordynamic behaviour is

active at the bearing, it is shown that ‘hot’ spot phase lags reduce with increased orbit size and tend to increase with elevated speed. Whereas with flexible rotors undergoing significant rotordynamic response behaviour, it is shown that these influences create a more complex bearing-journal interaction and resulting temperature profile and ‘hot’ spot phase lag. In particular it is shown that the orbit shape and orientation relates to significant variation in temperature differential development and phase lag angles. This research shows that the tilting pad bearings produced higher temperature differentials than the fixed geometry offset halve bearing arrangement for the same orbit size ratios ($\%C_d$). The work shows that, in all cases, the circumferential temperature profile consists not only of a fundamental harmonic component, but that higher order distributions exist within the generated temperature profile.

Calculated and measured rotordynamic results show that for flexible rotors undergoing significant shaft deflections and vibration phase shifts, the phase conditions within the bearing can be significantly different from those at the measurement point of the rotor, even where the sensors are positioned at the outer edge of the bearing and the axial distances involved are small (10-15 mm). The impact of these variations result in significant errors being introduced when determining the phase angle relationships between the journal hot spot and the initial mechanical unbalance location, unless suitable compensations are made for these variations.

A novel computational modelling technique for evaluation of the thermal development within the bearing journal is presented. The technique allows for the journal temperature development to be modelled in the time domain without the requirement for complex CFD analysis techniques, enabling practical application to be made when performing more routine rotordynamic stability analysis procedures. A simplified energy model is introduced which allows the steady state bearing temperature distribution to be established by means of a closed form equation developed within this work. A numerical procedure is applied to model the dynamic temperature perturbations and convective heat transfer within the oil film. The resulting steady state and dynamic oil film temperatures and phase lag angles provide the necessary boundary conditions for solution of a transient finite difference grid model of the shaft journal. The resulting journal temperature differential and phase lag angles are then determined for specific operating conditions. This allows the necessary stability analysis to be performed. The procedure allows for correct modelling of the fixed geometry bearing bore profile - a feature which is

overlooked by means of simplifications in the non CFD techniques presented in the literature. This thesis is the first theoretical model presented which predicts the 'hot' spot phase lag angle without the need for complex and highly computationally intensive CFD procedures to be applied.

The oil film energy model in this research is compared against the theoretical results data in the literature where complex CFD techniques have been applied. The results correlate to within approximately 5 ^{o}C for the conditions considered. Similar comparisons are made for the dynamic journal temperature differential and 'hot' spot phase lag where variations of ~2.5^{o}C(~25%) ^{o}C and -11.9^{o} result.

The key contributions of this work are :

1. Presentation of a detailed characterisation of the rotordynamic and bearing performance features present within rotors where thermally induced rotor bow instabilities have occurred in industrial machines.

2. Design, development and commissioning of a dedicated high speed rotor test rig for the accurate measurement of rotating journal shaft temperatures in a whirling shaft for both rigid and flexible rotor systems. The rotordynamic conditions within the test rotor replicate those conditions identified as significant with respect to the elements necessary for the development of thermally induced rotor bow and associated instabilities.

3. The experimentally controlled generation of shaft journal temperature differential data in whirling shafts for both fixed and variable geometry bearings. The temperature differentials are presented for a range of operating parameters, with detailed information relating to the associated phase lag angles under these conditions. This data can be used to further develop and validate the theoretical models in place today and those presented within this work. To date no controlled experimental data on fixed geometry bearing journal temperature measurement has been presented in the literature. Moreover this is the first presentation of detailed phase lag angle data for a range of operating arrangements and conditions for both rigid and flexible rotor systems. Whilst it was not feasible to send the rotor unstable within this work, the rotor was seen to exhibit the desired rotordynamic characteristics identified as necessary for promotion of the Morton

Effect instability. This would enable the use of a test rotor of this design to be used for future studies where alternative bearing configurations are investigated.

4. Comparison of existing theoretical model predictions to experimental data for both fixed and variable geometry bearings. A number of significant differences have been identified between actual and calculated parameters. More fundamentally, a lack of correlation between the predicted thermal bow conditions and associated stability with that observed experimentally has been shown. This highlights the need for development of theoretical modelling tools currently available for thermal differential development and stability prediction.

5. Derivation of a closed form energy based equation to describe the cross film mean lubricant temperature for cylindrical journal bearings.

6. Following from 4 above, a new modelling procedure for the prediction of shaft journal temperature differential development is presented. The restrictions present within other procedures from the literature are addressed with respect to ‘hot’ spot phase lag angle and prediction of the journal temperature differential that result from the ‘quasi’ steady state assumption for shaft whirl orbit perturbations. The presented method uses a significantly lower complexity solution than that of the CFD approaches, which enables practically implementable evaluations to be made, whilst retaining sufficient accuracy for appropriate stability risk assessments to be performed.

Chapter 11

Further Work

11. Further Work

In addition to the work presented here, an extensive programme of work to focus on the temperature developments within the bearing should be considered. Through the use of the rigid rotor arrangement where little rotordynamic influence is present within the bearing, other than simple unbalance response, it would be possible to generate both journal temperature differential data and 'hot' spot phase lag angle data. From this a wider range of operating parameters can be considered, such as oil viscosities, oil supply temperatures, oil supply flows and more significantly bearing clearance. The work would need to cover a range of bearing types. The larger collection of acquired data would be used to provide guidance on selection of bearing configurations which would be suitable for development of instability in the flexible rotor configuration, validation and development of theoretical models and also for use as guidance in the design of industrial machine arrangements.

The introduction of several improvements or design modifications to the test arrangement and instrumentation setup should be investigated. A significant aspect which should be considered is the elimination of the mechanical slip ring configuration for the measurements of the shaft journal temperatures. Whilst it was possible to obtain acceptable temperature measurements in this research, the problems and reliability issues associated with the slip ring method of obtaining signals resulted in significant down time and extended experimental running. Investigations and development of a telemetric solution should be performed which would eliminate the mechanical elements from the data acquisition and, if appropriately designed, reduce the low level noise present within mechanical slip rings. The inclusion of additional journal temperature sensors should also be considered so that the harmonic range to which the measured temperature distribution can be described is increased beyond the fundamental.

The possibility of introducing proximity probes at the bearing centre location to enable direct, accurate measurement of the shaft vibration displacements and phase angles should be explored. It was shown in the current research that variations can exist between the measurement point and the bearing centre position in flexible rotors. These variations are sufficient to significantly affect the analysis of the phase angle measurements of the journal 'hot' spot location, even when axial distances between the bearing centre and measurement point are small (~10-15 mm). The introduction of this feature can be applied without too much difficulty for the variable geometry arrangements but some special consideration and testing will be required where this is to be applied to typical fixed geometry arrangements. The inclusion of direct measurement of pad angle for the variable geometry arrangement would also provide a validation of the conditions present within the oil film function which has a direct influence on the predicted temperature differential generation. Some current models in the literature assume this aspect to follow a 'quasi' steady state position for the orbit perturbations, where in practice inertial effects in the pads will influence the dynamic tilt angles presented within the bearing.

Using the experimental results presented within this research, the results of any further testing in the rigid rotor design and the developed theoretical models should focus on investigating different bearing configurations, clearances and overhung sections. The aim of this should be to define an arrangement where the conditions required for instability of the test rotor can be replicated. This information should be used to provide data enabling validation of the relationships between actual instability thresholds and those predicted in theoretical models.

Further benchmarking and development is required of the newly presented theoretical model to address a more widely spread number of validation cases. A more extensive study using some CFD case studies could be used for comparison when looking to further develop the convective element in the analytical procedure, specifically with respect to different bearing profile geometries and where high levels of backward whirl are present. Also more extensive comparison of the model is needed to experimentally determine data and greater understand the accuracy and scope of the new procedure presented here.

Further development of the specific procedures and computer codes necessary to integrate the techniques for the evaluation of tilting pad bearings

is required and also the inclusion of an integrated Reynolds solution into the calculation procedures would improve the functionality of the routine. This could also be extended to incorporate a more comprehensive stability assessment and method for closer integration to rotordynamic modelling tools, which would provide a further significant step forward in the practical analysis of rotors for Morton stability assessment.

References and Bibliography

References

1. Newkirk, B.L., 'Shaft Rubbing', Mechanical Engineering, Vol. 48, 1926, p.830.

2. Kroon, R.P. and W.A. Williams, 'Spiral Vibration of Rotating Machinary' Proceedings of 5th International Congress of Applied Mechanics, Wiley, New York, 1939, p. 712 – 718.

3. Dimarogonas, A.D., 'An Analytical Study into the Packing Rub Effect in Rotating Machinery', Dissertation, Rensselaer Polytechnic Institute, Troy, N.Y., 1970.

4. Dimarogonas, A.D., 'Newkirk Effect : Thermally Induced Dynamic Instability of High Speed Rotors', ASME, 1973.

5. Dimarogonas, A.D., 'Heat Distribution and Flash Temperatures in Radial Seals', Wear, Vol. 23, No. 1, 1972.

6. Kellenberger W., 'Spiral Vibrations Due to Seal Rings in Turbogenerators Thermally Induced Interaction Between Rotor and Stator', Journal of Mechanical Design, Vol. 102, p.177-184, January 1980.

7. Ericsson U., 'Temperature Distribution in the oil Film of a Vibrating Tilting Pad Bearing', Thesis Report, Chalmers University of Technology Goteborg, Sweden, 1980.

8. Schimied, J., 'Spiral Vibration of Rotors', Rotating Machinery Dynamics, ASME, Vol. 2, p.449-456, September 1987.

9. Keogh P.S. and Morton P.G., 'Journal Bearing Differential Heating Evaluation with Influence on Rotor Dynamic Behaviour', Proc. R. Soc. Lond. A 441, p. 527-548, 1993.

10. Keogh P.S. and Morton P.G., 'The Dynamic Nature of Rotor Thermal Bending due to Unsteady Lubricant Shearing within a Bearing', Proc. R. Soc. Lond. A 445, p. 273-290, 1994.

11. de Jongh F.M. and Morton P.G., 'The Synchronous Instability of a Compressor Rotor Due to Bearing Journal Differential Heating', ASME Int. Gas Turbine and Aeroengine Cong. and Exp.', The Hague, Netherlands, Paper 94 GT-35, 1994.

12. Faulkner H.B., Strong W.F. and Kirk R.G., 'Thermally Introduced Synchronous Instability of a Radial Inflow Overhung Turbine, Part I', Proceedings of DETC'97, 1997.

13. Faulkner H.B., Strong W.F. and Kirk R.G., 'Thermally Introduced Synchronous Instability of a Radial Inflow Overhung Turbine, Part I', Proceedings of DETC'97, 1997.

14. de Jongh F.M. and van de Hoeven P., 'Application of a Heat Barrier Sleeve to Prevent Synchronous Rotor Instability', Proc. of the 27th Turbomachinary Symposium, 1998.

15. Larsson B., 'Journal Asymmetric Heating – Part I : Nonstationary Bow', Journal of Tribology,Vol. 121, p. 157-163, January 1998.

16. Larsson B., 'Journal Asymmetric Heating – Part II : Alteration of Rotor Dynamic Properties', Journal of Tribology,Vol. 121, p. 164-168, January 1998.

17. Tucker P.G. and Keogh P.S., 'On the Dynamic Thermal Sate in a Hydrodynamic Bearing With a Whirling Journal Using CFD Techniques', ASME Tribology Conf., 1995.

18. Gomiciaga R. and Keogh P.S., 'Orbit Induced Journal Temperature Variation in Hydrodynamic Bearings', Journal of Tribology, Vol. 121, p. 77-84, 1999.

19. Balbahadur A.C. , 'A Thermoelastohydrodynamic Model of the Morton Effect Operating in Overhung Rotors Supported by Plain or Tilting Pad Journal Bearings', PhD Thesis, Virginia Polytechnic Institute and University, 2001.

20. Balbahadur A.C. and Kirk R.G. , 'Part I : Theoretical Model for a Synchronous Thermal Instability Operating in Overhung Rotors', 2002.

21. Balbahadur A.C. and Kirk R.G., 'Part II : Case Studies for a Synchronous Thermal Instability Operating in Overhung Rotors', 2002.

22. Taylor H.D., 'Rubbing Shafts Above and Below Resonant Speed', G.E. Technical Information Series, 16709, 1924.

23. Balbahadur A.C., Z Guo and Kirk R.G., 'Synchronous Thermal Instability Prediction for Overhung Rotors', Proc. of the 32nd Turbomachinary Symposium, 2003

24. Kirk R.G., Balbahadur A.C., 'Thermal distorition syncrounous rotor instability', 7th International Conference on Vibrations in Rotating Machinary, 2000

25. Jeffcott H.H., 'The lateral vibration of loaded shafts in the neighbourhood of a whirling speed – The effect of want of balance', Philosophical Magazine Ser. 6-37 p. 304-314, 1919

26. Reynolds O., 'On the theory of lubrication and its application to Mr Beauchamp Tower's experiments including and experimental determination of the viscosity of olive oil, Phil. Trans. 177 (i) p. 157-234, 1886.

27. J. W. Lund and B. Sternlicht, 'Rotor-Bearing Dynamics with Emphasis on Attenuation,' Journal of Basic Engineering, Trans. ASME, Vol. 84, Series D, 1962, pp. 491–502.

28. J. W. Lund, 'Stability and Damped Critical Speeds of a Flexible Rotor in Fluid-Film Bearings,' Journal of Engineering for Industry, Trans. ASME, Vol. 96, Series B, No. 2, May 1974, pp. 509517

29. Thoma D., Zeitschrift des Vereines deutscher Ingenieure, p. 985, July 25 1925.

30. Kirk G.R., 'Morton Effect Analysis – Theory, Program and Case Study', ISCORMA-3, Cleveland, Ohio, 19-23 September 2005.

31. Marscher W., Illis B., 'Journal Bearing "Morton Effect" Cause of Cyclic Vibration in Compressors', Tribology Transactions, 50 : p. 104-113, 2007.

32. Schmied J., Pozivil J., Walch J., 'Hot spots in turboexpander bearings: case history, stability analysis, measurements and operational experience', ASME Turbo Expo, Berlion Germany, 2008

33. de Jongh F., 'The synchronous rotor instability phenomenon – Morton Effect' Proceedings of the 37th Turbomachinery Symposium 2008

34. Morton P.G., 'Recent advances in the study of oil lubricated journal bearings', Proceedings of fourth international conference on rotordynamics, IFFToMM, Chicago, Illinois, p. 299-305.

35. Childs W.C., Saha R., 'A new, iterative, synchronous-response algoritham for analyzing the Morton Effect', Proceedings of ASME Turbo Expo, Vancouver, British Columbia, Canada, June 2011

36. Murphy B.T., Lorenz J.A., 'Simplified Morton Effect analysis for synchronous spiral instability', ASME Power Division Special Section, December 2009

37. Murphy B.T., Lorenz J.A., 'Case study effect shaft differential heating in a variable-speed rotating electric machine', Proceedings of ASME Turbo Expo, Vancouver, British Columbia, Canada, June 2011.

38. Lorenz, J.A., 'Implementation of fluid-film bearing shaft differential heating calculations using commercial CFD software', MSc Thesis, B.M.E., University of Minnesota, 2009

39. Dowson D., Hudson J.D., Hunter B., March C.N., 'An experimental investigation of the thermal equilibrium of steadily loaded journal bearings', Proceedings of the Institute of Mechanical Engineers, Vol 181, p. 70-80, 1966.

40. Sommerfeld A., 'Zur hydrodynamishen theorie der Schiermittelreibung', Z.Math. u. Physik, Vol. 50, p. 97, 1904

41. Ocvirk F.W., Dubois G.B., 'Analytical derivation and experimental evaluation of short bearing approximation for full journal bearings', NACA Report 1157, 1953

42. Garner D.R., 'The use of design procedures for plain bearings', Industrial Unit of Tribology, University of Leeds, September 1908

43. Cameron A., 'The Principles of Lubrication' Longmans, 1996

44. Stachowiak G.W., Batchelor A.W., 'Engineering Tribology' Third Edition , Elsevier Butterworth-Heinemann, 2005

45. Cole J.A., Hughes C.J., 'Oil Flow and Film Extent in Complete Journal Bearings', Proceedings of the Institute of Mechanical Engineers, Vol 170, p. 499-510, 1956.

46. Wright K., 'Chebyshev collocation methods for ordinary differential equations', Computer Journal, Vol. 6, Issue 4, p. 358-365, 1964

47. San Andres L., 'An Overview of Tilting Pad Journal Bearings', Dept. of Mechanical Engineering, Texas A&M University, Febuary 2000

48. Vance J.M., 'Rotordynamics of Turbomachinery', John Wiley & Sons, 1988

49. MATLAB, 'Programming Environment Software', The MathWorks Inc

50. Ettles C.M., 'The analysis of pivoted pad journal bearing assemblies considering thermoelastic deformation and heat transfer effects', Tribology Transactions, Vol. 35, No. 1, p. 156-162

51. XLRotor, 'Rotordynamic Software Package', Rotating Machinery Inc (RMA).

52. JPU, 'Vickers – JPU Tilting Pad Journal Bearing Performance Program' V3.21'' – Custom AGSL code

53. API Standard 617, 'Axial and centrifugal compressors and expander-compressors for petroleum chemical and gas industry services', 7th Edition, American Petroleum Institute, Washington D.C.

54. HYBJRN, 'Rotordynamic and Hydrodynamic Bearing Calculation Program', Franklin Institute AGSL custom code

55. ISO 1940-1:2003 'Mechanical vibration -- Balance quality requirements for rotors in a constant (rigid) state - Part 1: Specification and verification of balance tolerances', International Organisation for Standardisation

56. Steinhart I.S., Hart S.R. 'Calibration curves for thermistors', Deep Sea Research Vol.15(3), p. 497-503, 1968

57. 'Industrial Temperature Sensors Datasheet', Industrial Sensors Ltd, www.itsirl.com

58. Biggs D.H., 'Electrical Runout and Eddy Current Displacement Proximity Transducers (Bently Nevada Literature No. L0360)', ASME Paper, September 1975

59. Shannon C.E., 'Communication in the Presence of Noise', Proceedings of the IEEE, Vol. 86, No. 2, February 1998 (reprinted from earlier paper)

60. www.cdeep.iitb.ac.in

61. Muneer T., Kubie J., Grassie T., 'Heat Transfer : A problem solving approach, Volume 1', Taylor & Francis, 2003

62. Li Z., 'Finite Difference Methods Basics', Centre for Research in Scientific Computation & Department of Mathematics North Carolina State University Raleigh, NC 2769

63. Martin F.A., 'Developments in Engine Bearing Design', Tribology International, Vol. 16. no. 3, p. 147-164, 1983

64. Martin F.A., Lee C.S., 'Feed-Pressure Flow in Plain Journal Bearings' Tribology International, Vol. 26, No. 3, p. 381-392, 1983

65. Marscher D., McGinley J.J., 'Vibration Troubleshooting of an Air Compressor', Sound and Vibration Journal, May 2006

66. Sundqvist H., Veronis G., 'A simple finite-difference grid with non-constant intervals', Tellus XXII (1970), 1

67. Blake R. E., 'Basic Vibration Theory', Shock and Vibration Handbook, Fourth Edition, Chapter 2 – p. 2.18, 1995

Bibliography

1. Stroud Engineering Mathematics, K.A. Stroud, Fourth Edition, 1995

2. Stroud Further Engineering Mathematics, K.A. Stroud, Third Edition, 1996

3. Mechanics of Materials Volume 1: An Introduction to the Mechanics of Elastic and Plastic Deformation of Solids and Structural Materials: v. 1 by E.J. Hearn (9 Jul 1997)
4. Rotordynamics of Turbomachinery by John M. Vance (1988)

5. Machine Dynamics MSc Course Notes Part 1&2, Cranfield University

6. Signal Processing MSc Course Notes, Cranfield University

7. Shock and Vibration Handbook by Cyril M. Harris (Hardcover - Dec 1995)

8. Applied Thermodynamics for Engineering Technologists by T.D. Eastop and A. Mcconkey (1993)

9. Handbook of Numerical Heat Transfer by W. J. Minkowycz, E. M. Sparrow, G. E. Schneider and R. H. Pletcher (1988)

10. Basic Lubrication Theory (Ellis Horwood series in engineering science) by A CAMERON (1977)

Appendix A

Numerical Procedure for Measurement of Bearing Pre-load

This appendix details the numerical procedure used to measure the bearing bore geometry of the fixed pad offset half bearing. The procedure is based around using traditional clock or CMM readings in the bearing radial plane to then use a curve fitting approach to determine the shaft preload and clearance conditions.

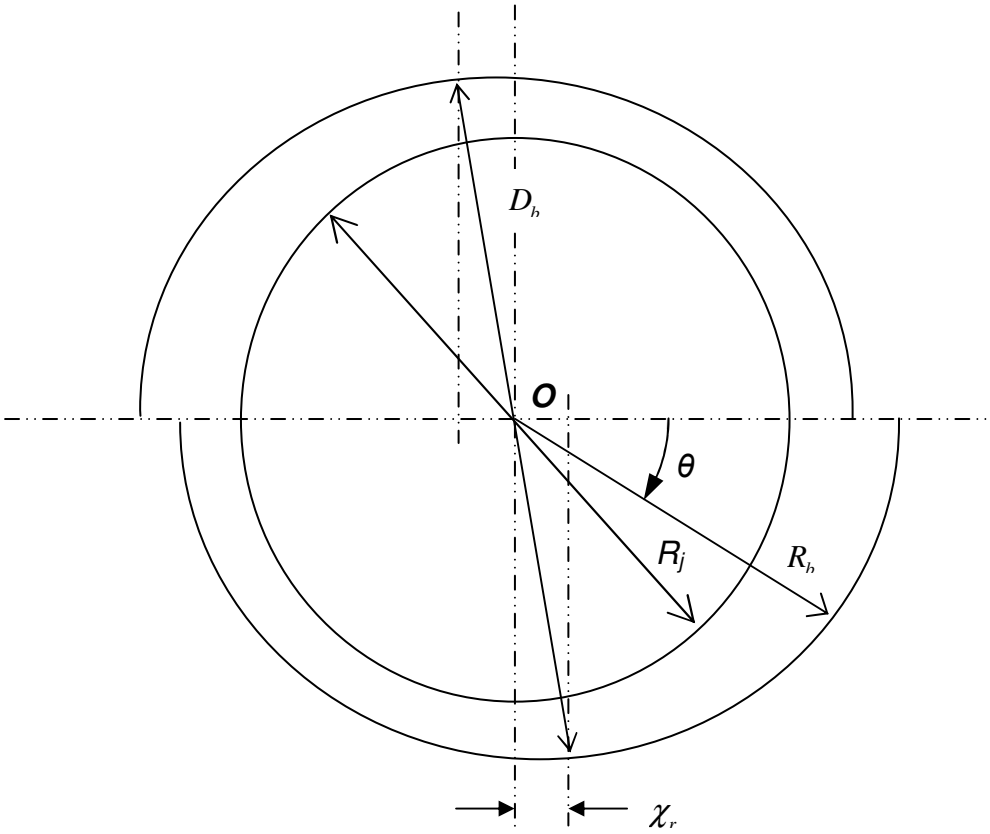

Figure A1. Offset Half Bearing Bore Profile System of Coordinates

Where

$$C_\theta = R_b - R_j$$

$$C_r = D_b - 2.R_j$$

Assuming that the radial clearance around the bearing has the following form :

$$C_\theta = C_r + \chi_r.\cos(\theta - \phi_m) \quad \text{Eq. A1}$$

Where

C_θ = theoretical radial clearance from bearing centre

C_r = machined radial clearance

χ_r = bore offset value

θ = angle around bearing

ϕ_m = bore offset cant angle

Applying trig identities :

$$\begin{aligned} C_\theta &= C_r + \chi_r.(\cos(\theta).\cos(\phi_m) - \sin(\theta).\sin(\phi_m)) \\ &= C_r + \chi_r.\cos(\theta).\cos(\phi_m) - \chi_r.\sin(\theta).\sin(\phi_m) \end{aligned} \quad \text{Eq. A2}$$

The error between the theoretical clearance and the measured clearance distribution is assumed to be given by :

$$\in_m = C_H = -C_r - \chi_r.\cos(\theta).\cos(\phi_m) - \chi_r.\sin(\theta).\sin(\phi_m) \quad \text{Eq A3}$$

Where

C_H = the measured radial clearance at angle θ

Applying the method of least squares fit :

$$\in_r = \sum (C_H = -C_r - \chi_r.\cos(\theta).\cos(\phi_m) - \chi_r.\sin(\theta).\sin(\phi_m))^2 \quad \text{Eq A4}$$

Where $\frac{\partial \in_r}{\partial C_r} = \frac{\partial \in_r}{\partial(\chi_r.\cos(\phi_m))} = \frac{\partial \in_r}{\partial(\chi_r.\sin(\phi_m))} = 0$ to give the least error

Therefore integrating with respect to $C_r, \chi_r.\cos(\phi_m), \chi_r.\sin(\phi_m)$ gives :

$$\frac{\partial \in_r}{\partial C_r} = \sum 2.(C_H = -C_r - \chi_r.\cos(\theta).\cos(\phi_m) - \chi_r.\sin(\theta).\sin(\phi_m)).(-1) = 0 \quad \text{Eq. A5}$$

$$\frac{\partial \in_r}{\partial\left(\chi_r.\cos\left(\phi_m\right)\right)} = \sum 2.\left(C_H = -C_r - \chi_r.\cos\left(\theta\right).\cos\left(\phi_m\right) - \chi_r.\sin\left(\theta\right).\sin\left(\phi_m\right)\right).\left(-\cos\left(\theta\right)\right) = 0$$

Eq. A6

$$\frac{\partial \in_r}{\partial\left(\chi_r.\sin\left(\phi_m\right)\right)} = \sum 2.\left(C_H = -C_r - \chi_r.\cos\left(\theta\right).\cos\left(\phi_m\right) - \chi_r.\sin\left(\theta\right).\sin\left(\phi_m\right)\right).\left(-\sin\left(\theta\right)\right) = 0$$

Eq. A7

Rearranging from 1

$$\begin{aligned}&\sum\left(-C_H\right) + \sum C_r + \sum \chi_r.\cos\left(\phi_m\right).\cos\left(\theta\right) + \sum \chi_r.\sin\left(\phi_m\right).\sin\left(\theta\right) = 0\\ &\sum\left(-C_H\right) + n.C_r + \chi_r.\cos\left(\phi_m\right).\sum\cos\left(\theta\right) + \chi_r.\sin\left(\phi_m\right).\sum\sin\left(\theta\right) = 0\end{aligned}$$ Eq. A8

Rearranging from 2

$$\begin{aligned}&-\sum C_H.\cos\left(\theta\right) + \sum C_r.\cos\left(\theta\right) + \sum \chi_r.\cos\left(\phi_m\right).\cos^{\,2}\left(\theta\right) + \sum \chi_r.\sin\left(\phi_m\right).\sin\left(\theta\right).\cos\left(\theta\right) = 0\\ &-\sum C_H.\cos\left(\theta\right) + C_r.\sum\cos\left(\theta\right) + \chi_r.\cos\left(\phi_m\right).\sum\cos^{\,2}\left(\theta\right) + \chi_r.\sin\left(\phi_m\right).\sum\sin\left(\theta\right).\cos\left(\theta\right) = 0\end{aligned}$$

Eq A9

Rearranging from 3

$$\begin{aligned}&-\sum C_H.\cos\left(\theta\right) + \sum C_r.\sin\left(\theta\right) + \sum \chi_r.\cos\left(\phi_m\right).\sin\left(\theta\right).\cos\left(\theta\right) + \sum \chi_r.\sin\left(\phi_m\right).\sin^2\left(\theta\right) = 0\\ &-\sum C_H.\sin\left(\theta\right) + C_r.\sum\sin\left(\theta\right) + \chi_r.\cos\left(\phi_m\right).\sum\sin\left(\theta\right).\cos\left(\theta\right) + \chi_r.\sin\left(\phi_m\right).\sum\sin^2\left(\theta\right) = 0\end{aligned}$$

Eq. A10

Putting the above equations into matrix from

$$\begin{bmatrix} n & \sum\cos\left(\theta\right) & \sum\sin\left(\theta\right) \\ \sum\cos\left(\theta\right) & \sum\cos^2\left(\theta\right) & \sum\sin\left(\theta\right).\cos\left(\theta\right) \\ \sum\sin\left(\theta\right) & \sum\sin\left(\theta\right)\cos\left(\theta\right) & \sum\sin^2\left(\theta\right) \end{bmatrix}.\begin{bmatrix} C_r \\ \chi_r.\cos\left(\theta\right) \\ \chi_r.\sin\left(\theta\right) \end{bmatrix} = \begin{bmatrix} \sum C_H \\ \sum C_H.\cos\left(\theta\right) \\ \sum C_H.\sin\left(\theta\right) \end{bmatrix}$$ Eq. A11

Where n = number of data points

From xx the equations can now be solved for $C_r, \chi_r.\cos(\phi_m), \chi_r.\sin(\phi_m)$ and $\chi_r.\sin(\phi_m)$ from which χ_r and ϕ_m can be given by A12 andA13.

$$\chi_r = \left(\left(\chi_r.\cos(\phi_m) \right)^2 + \left(\chi_r.\sin(\phi_m) \right)^2 \right)^{\frac{1}{2}} \quad \text{Eq. A12}$$

$$\phi_m = \tan^{-1}\left(\frac{\chi_r.\sin(\phi_m)}{\chi_r.\cos(\phi_m)} \right) \quad \text{Eq. A13}$$

Where pad pre-load = $m = \frac{\chi_r}{C_r}$

Appendix B
Test Rig Production Drawings

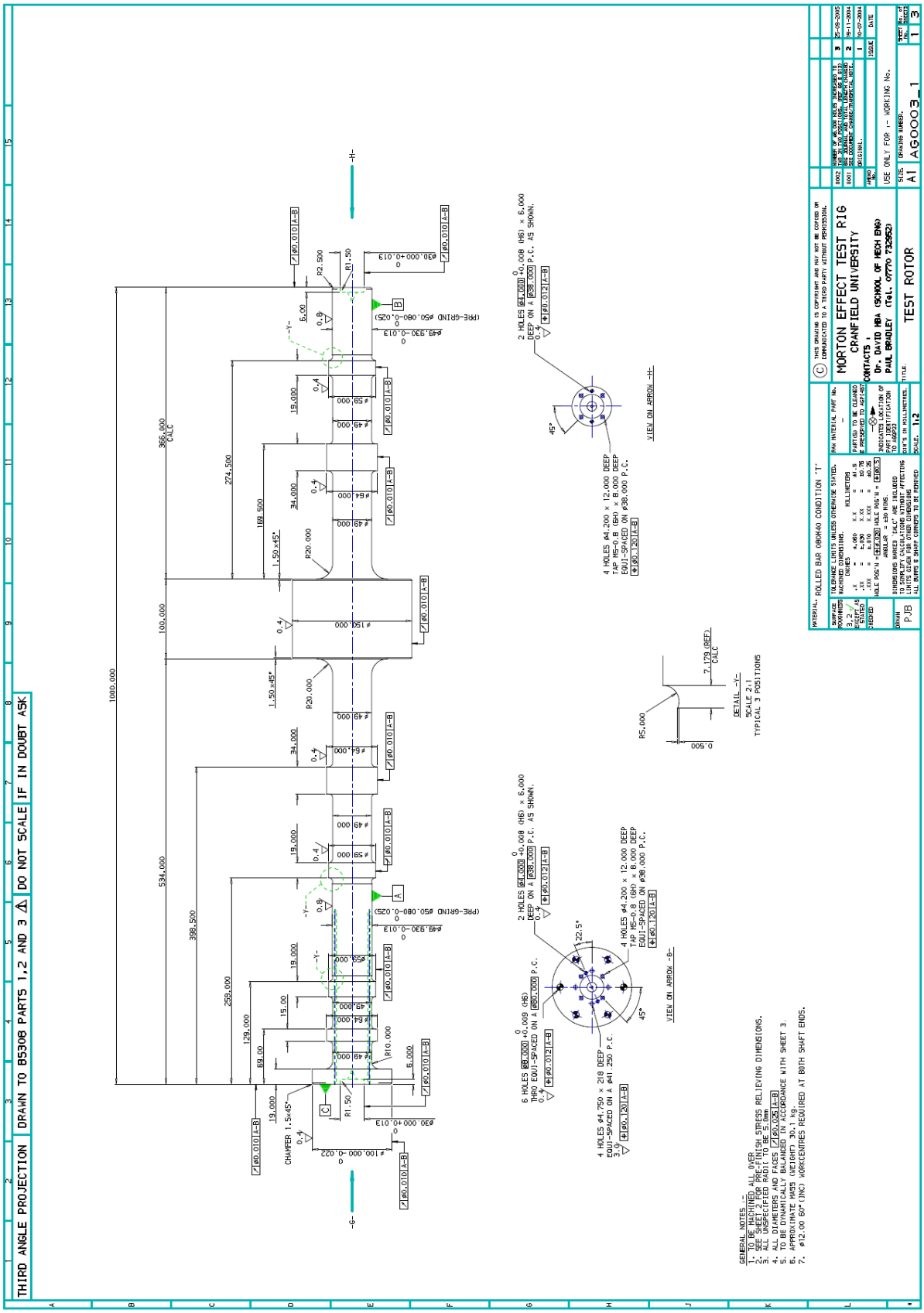

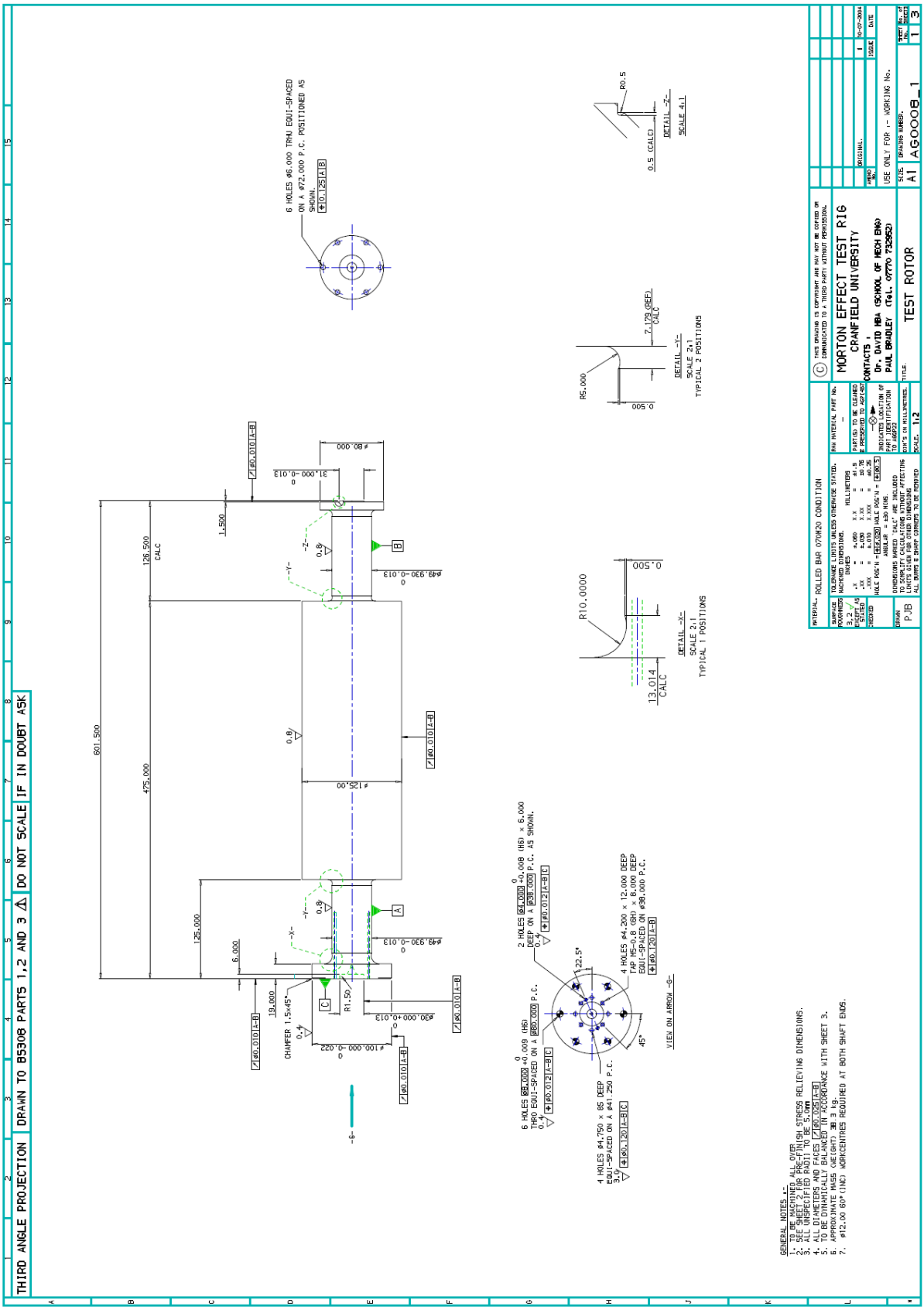
THIRD ANGLE PROJECTION
DRAWN TO BS308 PARTS 1,2 AND 3
DO NOT SCALE
IF IN DOUBT ASK
MORTON EFFECT TEST R16
CRANFIELD UNIVERSITY
CONTACTS :
Dr. DAVID MBA (SCHOOL OF MECH ENG)
PAUL BRADLEY (Tel. 07770 732852)
TEST ROTOR
A1 AG0008_1
USE ONLY FOR :- WORKING No.
PJB
SCALE 1:2
MATERIAL ROLLED BAR 070M20 CONDITION
GENERAL NOTES :-
1. TO BE MACHINED ALL OVER
2. SEE SHEET 2 FOR PRE-FINISH STRESS RELIEVING DIMENSIONS.
3. ALL UNSPECIFIED RADII TO BE 5.0mm
4. ALL DIMENSIONS ARE FOR FINISHED PART
5. TO BE DYNAMICALLY BALANCED IN ACCORDANCE WITH SHEET 3.
6. APPROXIMATE MASS (WEIGHT) 38.3 kg.
7. ø12.00 60° (INC) WORKCENTRES REQUIRED AT BOTH SHAFT ENDS.

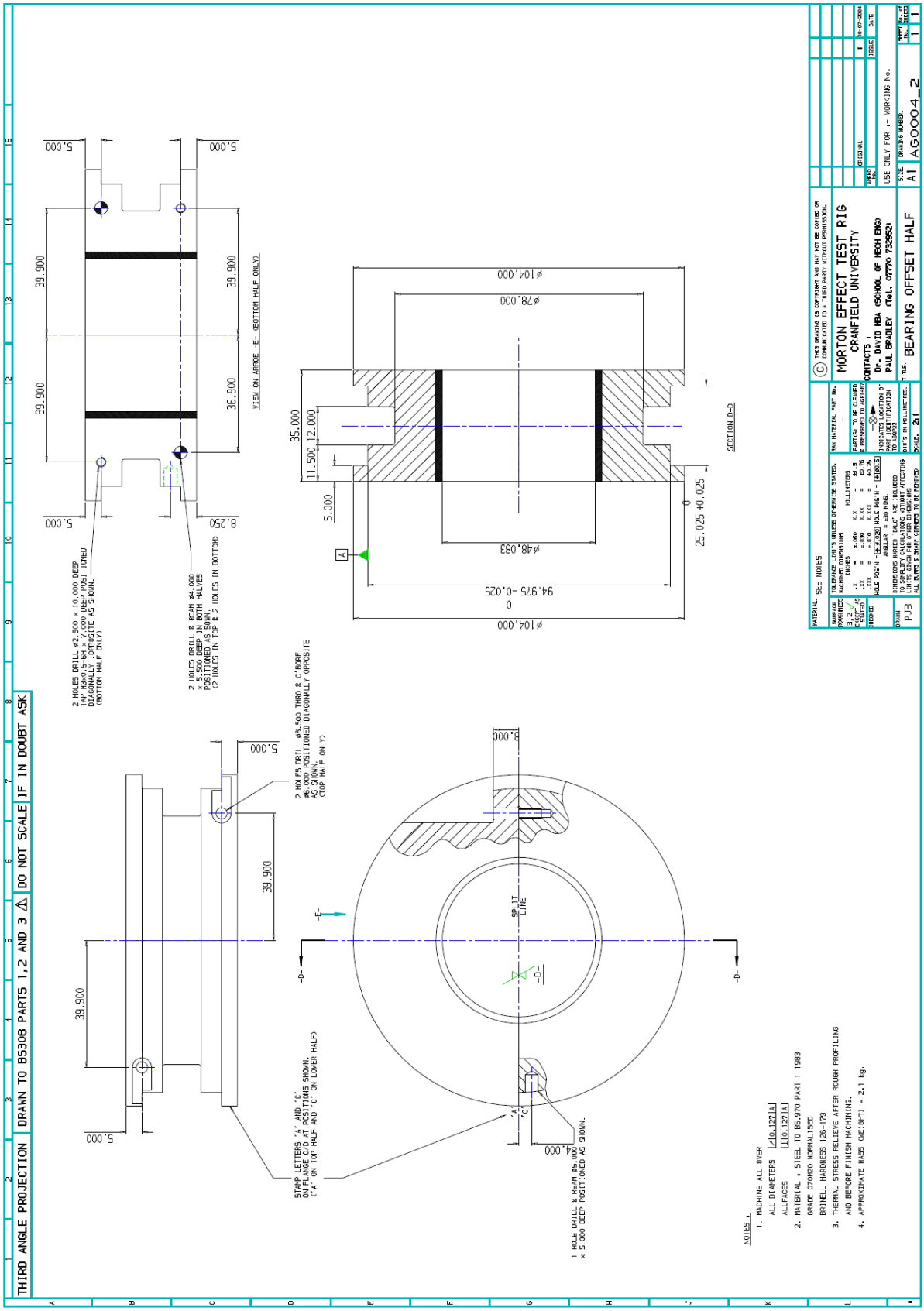
THIRD ANGLE PROJECTION
DRAWN TO BS308 PARTS 1,2 AND 3
DO NOT SCALE
IF IN DOUBT ASK
MORTON EFFECT TEST R16
CRANFIELD UNIVERSITY
CONTACTS :
Dr. DAVID MBA (SCHOOL OF MECH ENG)
PAUL BRADLEY (Tel. 07770 732552)
BEARING OFFSET HALF
A1 A60004_2
SEE NOTES
PJB
SPLIT LINE
SECTION D-D
VIEW ON ARROW -E- (BOTTOM HALF ONLY)
NOTES :-
1. MACHINE ALL OVER
ALL DIAMETERS
ALL FACES
2. MATERIAL : STEEL TO BS.970 PART 1 1983
GRADE 070M20 NORMALISED
BRINELL HARDNESS 126-179
3. THERMAL STRESS RELIEVE AFTER ROUGH PROFILING
AND BEFORE FINISH MACHINING.
4. APPROXIMATE MASS (WEIGHT) = 2.1 kg.

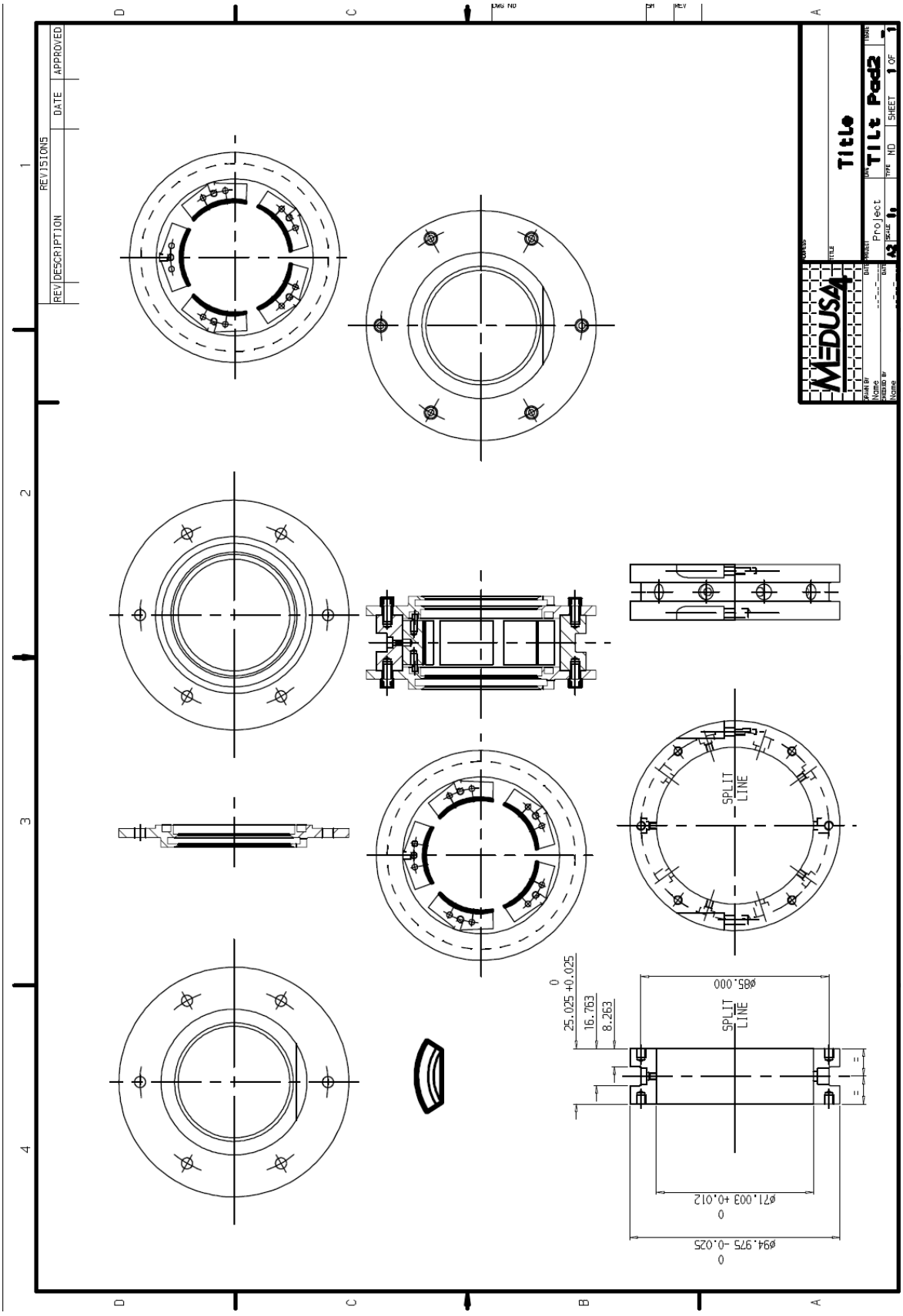
REVISIONS
REV
DESCRIPTION
DATE
APPROVED
MEDUSA
Title
Tilt Pad2
Project
SHEET
1 OF
SPLIT LINE
SPLIT LINE
Ø85.000
25.025 +0.025 0
16.763
8.263
Ø71.003 +0.012 0
Ø94.975 -0.025 0

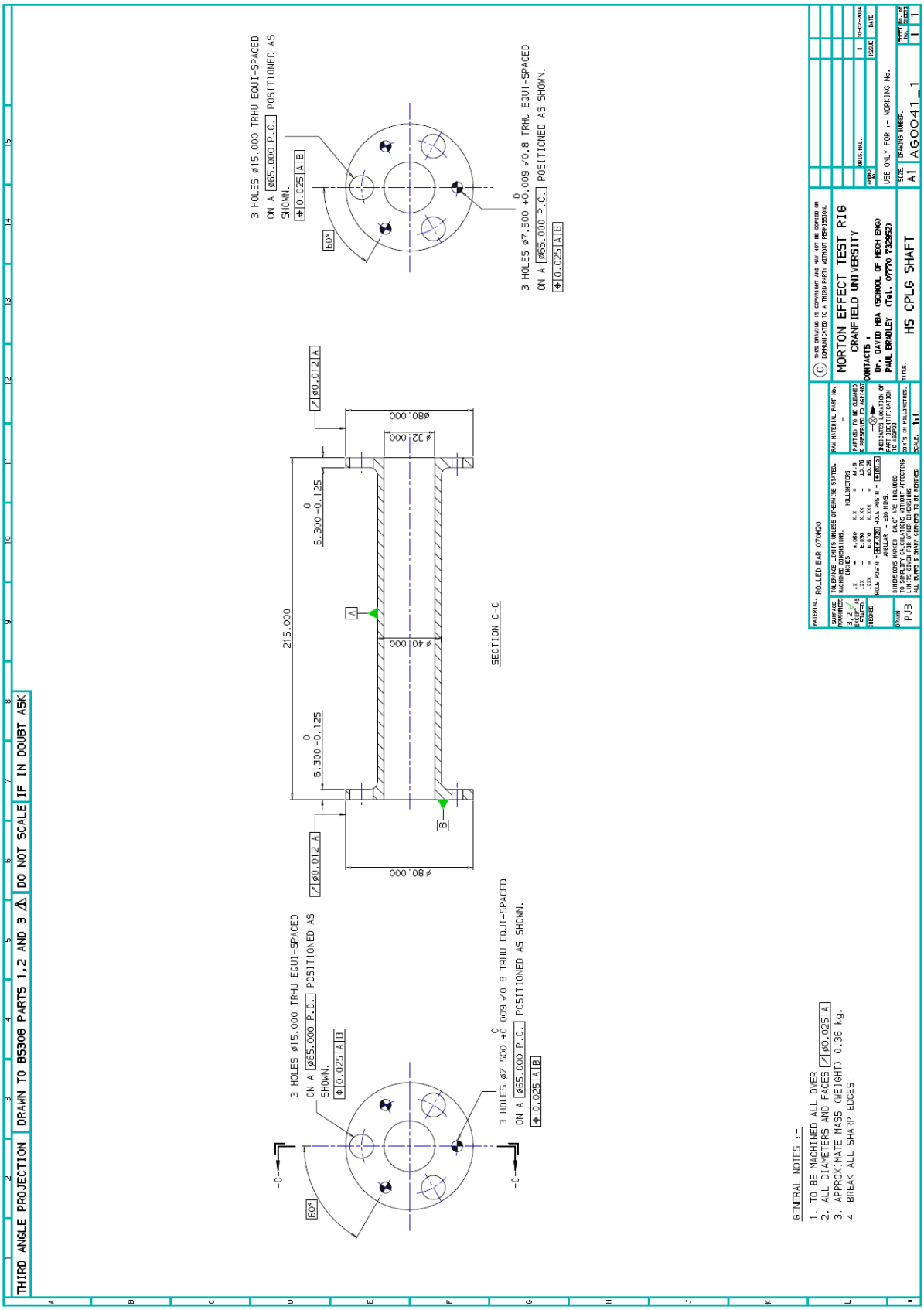
THIRD ANGLE PROJECTION
DRAWN TO BS308 PARTS 1,2 AND 3
DO NOT SCALE
IF IN DOUBT ASK
3 HOLES ø15.000 THRU EQUI-SPACED ON A ø65.000 P.C. POSITIONED AS SHOWN. ⌖ 0.025 A B
3 HOLES ø7.500 +0.009 0 ø0.8 THRU EQUI-SPACED ON A ø65.000 P.C. POSITIONED AS SHOWN. ⌖ 0.025 A B
60°
215.000
6.300 -0.125 0
ø80.000
ø32.000
ø40.000
⌭ ø0.012 A
SECTION C-C
GENERAL NOTES :-
1. TO BE MACHINED ALL OVER
2. ALL DIAMETERS AND FACES ⌭ ø0.025 A
3. APPROXIMATE MASS (WEIGHT) 0.36 kg.
4 BREAK ALL SHARP EDGES.
MATERIAL ROLLED BAR 070M20
TOLERANCE LIMITS UNLESS OTHERWISE STATED.
MACHINED DIMENSIONS. MILLIMETERS
.X = ±.060 X.X = ±0.15
.XX = ±.030 X.XX = ±0.76
.XXX = ±.010 X.XXX = ±0.25
HOLE POS'N = ⌖ ø0.05 M
ANGULAR = ±30 MINS.
DIMENSIONS MARKED 'CALC' ARE INCLUDED TO ASSIST CALCULATIONS. TOLERANCE APPLICATION LIMITS GIVEN FOR OTHER DIMENSIONS
ALL BURRS & SHARP CORNERS TO BE REMOVED
Rm MATERIAL PART No. -
PARTS TO BE CLEANED & PRESERVED TO AGP1467
INDICATES LOCATION OF PART IDENTIFICATION TO AGP23
DIM'S IN MILLIMETRES.
SCALE. 1:1
TITLE: H5 CPL6 SHAFT
SIZE A1
DRAWING NUMBER: AG0041_1
ISSUE 1
DATE 14-07-2004
SHEET No. 1 OF 1
ORIGINAL
USE ONLY FOR :- WORKING No.
MORTON EFFECT TEST R16
CRANFIELD UNIVERSITY
CONTACTS :
Dr. DAVID MBA (SCHOOL OF MECH ENG)
PAUL BRADLEY (Tel. 07770 732952)
THIS DRAWING IS COPYRIGHT AND MAY NOT BE COPIED OR COMMUNICATED TO A THIRD PARTY WITHOUT PERMISSION.

Appendix C

Derivation of $\int \frac{1}{\left(1+\varepsilon.\cos(\phi)\right)^2}.d\phi$

The information in this appendix follows through the integration of the film function term from the oil film energy equation derived in chapter 8 of this thesis.

The problem to be solved is the integration of the term given by C1. The arrangement does not allow for the application of a standard integral so a more involved integration process is required. The approach taken here is to manipulate the fundamental term by means of trigonomic substitutions using partial fractions to provide a series of steps which allow the terms to be solved using standard integrals.

$$\int \frac{1}{\left(1+\varepsilon.\cos(\phi)\right)^2}.d\phi \quad \text{Eq C1}$$

Let us first consider the trigonomic substitution :

$$s = \tan\left(\frac{\phi}{2}\right) \quad \text{Eq C2}$$

$$ds = \frac{\sec^2\left(\phi/2\right)}{2}.d\phi \quad \text{Eq C3}$$

Then we have :

$$d\phi = \frac{2}{s^2+1}.ds \quad \text{Eq C4}$$

$$\cos(\phi) = \frac{1-s^2}{s^2+1} \quad \text{Eq C5}$$

$$\sin(\phi) = \frac{2s}{s^2+1} \quad \text{Eq C6}$$

Substituting into C1 :

$$\int \frac{1}{\left(1+\varepsilon.\cos(\phi)\right)^2}.d\phi = 2.\int \frac{1}{\left(s^2+1\right).\left(1+\frac{\varepsilon.\left(1-s^2\right)}{s^2+1}\right)^2}.ds$$

$$= 2.\int \frac{s^2+1}{\left(-s^2-1+\varepsilon.s^2-\varepsilon\right)}.ds \quad \text{Eq. C7}$$

Breaking out C7 into partial fractions :

$$= 2.\int \left(\frac{1}{(1-\varepsilon).\left(s^2+1-\varepsilon.s^2+\varepsilon\right)} - \frac{2.\varepsilon}{(1-\varepsilon).\left(s^2+1-\varepsilon.s^2+\varepsilon\right)^2} \right).ds$$

Taking constants outside integral and integrating term by term :

$$= \frac{4.\varepsilon}{\varepsilon-1}.\int \frac{1}{\left(s^2-\varepsilon.s^2+\varepsilon+1\right)^2}.ds - \frac{2}{\varepsilon-1}.\int \frac{1}{s^2-\varepsilon.s^2+\varepsilon+1}.ds$$

Grouping squared terms of s :

$$= \frac{4.\varepsilon}{\varepsilon-1}.\int \frac{1}{\left((1-\varepsilon).s^2+\varepsilon+1\right)^2}.ds - \frac{2}{\varepsilon-1}.\int \frac{1}{(1-\varepsilon).s^2+\varepsilon+1}.ds$$

First considering the LHS integral term $\frac{1}{\left((1-\varepsilon).s^2+\varepsilon+1\right)^2}$:

Substituting with t :

Where

$$t = \frac{\sqrt{1-\varepsilon}.s}{\sqrt{1+\varepsilon}}.ds \quad \text{Eq. C8}$$

And

$$dt = \frac{\sqrt{1-\varepsilon}}{\sqrt{1+\varepsilon}}.ds \quad \text{Eq. C9}$$

Substituting, with some work, gives :

$$= \frac{4.\varepsilon.\sqrt{1+\varepsilon}}{\sqrt{1-\varepsilon}.(\varepsilon-1).|1+\varepsilon|^2}.\int \frac{1}{\left(t^2+1\right)^2}.dt - \frac{2}{\varepsilon-1}.\int \frac{1}{(1-\varepsilon).s^2+\varepsilon+1}.ds \quad \text{Eq. C10}$$

Now considering the integral term $\frac{1}{\left(t^2+1\right)^2}$:

Substituting with w :

$$w = \tan^{-1}(t) \quad \text{Eq. C11}$$

and

$$dw = \frac{1}{t^2+1}.dt \quad \text{Eq. C12}$$

Where

$$\cos^2\left(\tan^{-1}(t)\right)=\frac{1}{t^2+1}$$

and

$$\frac{1}{\left(t^2+1\right)^2}=\cos^2(w).dw$$

Substituting into C10 :

$$=\frac{4.\varepsilon.\sqrt{1+\varepsilon}}{\sqrt{1-\varepsilon}.(\varepsilon-1).|1+\varepsilon|^2}.\int\cos^2(w).dw-\frac{2}{\varepsilon-1}.\int\frac{1}{(1-\varepsilon).s^2+\varepsilon+1}.ds \quad \text{Eq. C13}$$

Recognising standard integral of $\cos^2(w)=\frac{w}{2}+\frac{\sin(2.w)}{4}$ yields :

$$=\frac{2.\varepsilon.\sqrt{1+\varepsilon}.w}{\sqrt{1-\varepsilon}.(\varepsilon-1).|1+\varepsilon|^2}+\frac{\varepsilon.\sqrt{1+\varepsilon}.\sin(2.w)}{\sqrt{1-\varepsilon}.(\varepsilon-1).|1+\varepsilon|^2}-\frac{2}{\varepsilon-1}.\int\frac{1}{(1-\varepsilon).s^2+\varepsilon+1}.ds \quad \text{Eq. C14}$$

Now considering the RHS integral term $\frac{1}{(1-\varepsilon).s^2+\varepsilon+1}$:

Using trigonomic substitution

$$t=\frac{\sqrt{1-e}.s}{\sqrt{1+e}} \quad \text{Eq. C15}$$

and

$$dt=\frac{\sqrt{1-e}}{\sqrt{1+e}}.ds \quad \text{Eq. C16}$$

Substituting into C14

$$=\frac{2.\varepsilon.\sqrt{1+\varepsilon}.w}{\sqrt{1-\varepsilon}.(\varepsilon-1).|1+\varepsilon|^2}+\frac{\varepsilon.\sqrt{1+\varepsilon}.\sin(2.w)}{\sqrt{1-\varepsilon}.(\varepsilon-1).|1+\varepsilon|^2}-\frac{2.\sqrt{1+\varepsilon}}{(\varepsilon-1).\sqrt{1-\varepsilon}.|1+\varepsilon|}.\int\frac{1}{t^2+1}.dt \quad \text{Eq. C16}$$

Where using the standard integral of $\int\frac{1}{t^2+1}.dt=\tan^{-1}(t)+C$

We complete the integration to give :

$$= \frac{2.\varepsilon.\sqrt{1+\varepsilon}.w}{\sqrt{1-\varepsilon}.(\varepsilon-1).|1+\varepsilon|^2} + \frac{\varepsilon.\sqrt{1+\varepsilon}.\sin(2.w)}{\sqrt{1-\varepsilon}.(\varepsilon-1).|1+\varepsilon|^2} - \frac{2.\sqrt{1+\varepsilon}.\tan^{-1}(t)}{(\varepsilon-1).\sqrt{1-\varepsilon}.|1+\varepsilon|} + C \quad \text{Eq. C17}$$

Now substituting back for $w = \tan^{-1}(t)$:

$$= \frac{2.\varepsilon.\sqrt{1+\varepsilon}.\tan^{-1}(t)}{\sqrt{1-\varepsilon}.(\varepsilon-1).|1+\varepsilon|^2} + \frac{\varepsilon.\sqrt{1+\varepsilon}.2.t}{\sqrt{1-\varepsilon}.(\varepsilon-1).|1+\varepsilon|^2.(t^2+1)} - \frac{2.\sqrt{1+\varepsilon}.\tan^{-1}(t)}{(\varepsilon-1).\sqrt{1-\varepsilon}.|1+\varepsilon|} + C$$

Where $\sin\left(2.\tan^{-1}(t)\right) = \frac{2.t}{t^2+1}$

Substitute back for $t = \frac{\sqrt{1-\varepsilon}.s}{\sqrt{1+\varepsilon}}$:

$$= \frac{2.\varepsilon.\sqrt{1+\varepsilon}.\tan^{-1}\left(\frac{\sqrt{1-\varepsilon}.s}{\sqrt{1+\varepsilon}}\right)}{\sqrt{1-\varepsilon}.(\varepsilon-1).|1+\varepsilon|^2} + \frac{\varepsilon.2.s}{(\varepsilon-1).|1+\varepsilon|^2.\left(\frac{(1-\varepsilon).s^2}{(1+\varepsilon)}+1\right)} - \frac{2.\sqrt{1+\varepsilon}.\tan^{-1}\left(\frac{\sqrt{1-\varepsilon}.s}{\sqrt{1+\varepsilon}}\right)}{(\varepsilon-1).\sqrt{1-\varepsilon}.|1+\varepsilon|} + C$$

And finally substituting back in for $s = \tan\left(\frac{\phi}{2}\right)$

$$= \frac{2.\varepsilon.\sqrt{1+\varepsilon}.\tan^{-1}\left(\frac{\sqrt{1-\varepsilon}.\tan\left(\frac{\phi}{2}\right)}{\sqrt{1+\varepsilon}}\right)}{\sqrt{1-\varepsilon}.(\varepsilon-1).|1+\varepsilon|^2} + \frac{\varepsilon.2.\tan\left(\frac{\phi}{2}\right)}{(\varepsilon-1).|1+\varepsilon|^2.\left(\frac{(1-\varepsilon).\tan^2\left(\frac{\phi}{2}\right)}{(1+\varepsilon)}+1\right)} - \frac{2.\sqrt{1+\varepsilon}.\tan^{-1}\left(\frac{\sqrt{1-\varepsilon}.\tan\left(\frac{\phi}{2}\right)}{\sqrt{1+\varepsilon}}\right)}{(\varepsilon-1).\sqrt{1-\varepsilon}.|1+\varepsilon|} + C$$

Eq. C18

Grouping terms and simplifying, following some work, the general solution can be given as :

$$\int \frac{d\phi}{\left(1+\varepsilon.\cos(\phi)\right)^2} = -\frac{2.\sqrt{\eta}}{\left(\varepsilon^2-1\right)}.\tan^{-1}\left(\frac{\tan\left(\frac{\phi}{2}\right)}{\sqrt{\eta}}\right).\left[\frac{\varepsilon}{1+\varepsilon}-1\right]+\frac{2.\varepsilon.\tan\left(\frac{\phi}{2}\right)}{\left(\varepsilon^2-1\right).(1+\varepsilon).\left(\frac{1}{\eta}.\tan^2\left(\frac{\phi}{2}\right)+1\right)}+C$$

Eq. C19

Where $\eta = \frac{1+\varepsilon}{1-\varepsilon}$

The above equation C19 can now be substituted back into the energy equation to complete the lubricant film temperature expression.